Title
Three-Dimensional Modeling of Ground-Pile Systems and Bridge Foundations

Author
Wang, Ning

Publication Date
2015

Peer reviewed|Thesis/dissertation

UNIVERSITY OF CALIFORNIA, SAN DIEGO

Three-Dimensional Modeling of Ground-Pile Systems and Bridge Foundations

A dissertation submitted in partial satisfaction of the requirements for the degree of

Doctor of Philosophy

in

Structural Engineering

by

Ning Wang

Committee in charge:

Professor Ahmed Elgamal, Chair
Professor J. Enrique Luco
Professor Hidenori Murakami
Professor Peter Shearer
Professor P. Benson Shing

2015

The Dissertation of Ning Wang is approved, and it is acceptable in quality and form for publication on microfilm and electronically:

____

Chair

University of California, San Diego

2015

DEDICATOIN

To all my family members:
my grandfather,
my parents,
my husband Chu Wang and my daughter Xinnuo Wang,
for their love and support.

TABLE OF CONTENTS

SIGNATURE PAGE ..... **iii**

DEDICATOIN ..... **iv**

TABLE OF CONTENTS ..... **v**

LIST OF FIGURES ..... **xi**

LIST OF TABLES ..... **xxiii**

ACKNOWLEDGEMENTS ..... **xxv**

VITA ..... **xxviii**

ABSTRACT OF THE DISSERTATION ..... **xxix**

Chapter 1 Introduction and Literature Review **1**

1.1 Brief Overview of Soil-Structure-Interaction 2

1.2 Past Research on Pile Foundation under Lateral Load 3

1.2.1 Experimental Research 3

1.2.2 Analytical Methods 4

1.2.3 Numerical Methods 5

1.3 Strong Motion Data and SSI Analysis 7

1.3.1 Recorded Data from Geotechnical Downhole Arrays 8

1.3.2 Recorded Data from Bridge Instrumentation 9

1.4 Current Approaches for Simulation of Ground-Foundation Systems 10

1.5 Objectives and Scope 12

1.6 Organization 13

Chapter 2 Three-Dimensional Finite Element Modeling of Pile and Pile Group System Response **19**

2.1 Introduction 20

2.2 Computational Framework 21

2.3 Lateral Pile Response Calibration 22

2.3.1 Configuration of the Pile-Soil System 22

2.3.2 Finite Element Model 23

2.3.3 Nonlinear Soil Modeling 24

2.4 Modeling of Pile Group Effects 24
2.4.1 Benchmark Lateral Response of Single Pile 24
2.4.2 3×3 Pile Group Configuration 25
2.4.3 3×3 Pile Group Response 26
2.5 Conclusion 29
2.6 Acknowledgements 30
Chapter 3 Lateral Load on a Large Pile Group 38
3.1 Introduction 39
3.2 General Information of Dumbarton Bridge Pier 23 40
3.2.1 Bridge Structure 40
3.2.1 Pile Group Configuration at Dumbarton Bridge Pier 23 41
3.3 Finite Element Model 42
3.4 Loading Scenario I: Lateral Loading 42
3.4.1 Pile Group Load Efficiency 43
3.4.2 Deformed Mesh 43
3.4.3 Pile Displacements at the Mudline 44
3.4.4 Load Distribution 44
3.5 Loading Scenario II: Combination of Lateral Load and Bending Moment 45
3.5.1 Load Combination 45
3.5.2 Summary of Main Numerical Results 46
3.6 Conclusions 48
3.7 Acknowledgements 49
Chapter 4 Effects of Permeability and Loading Rate on Lateral Pile Response 58
4.1 Introduction 59
4.2 Constitutive Soil Model with Cyclic Mobility Mechanism 61
4.2.1 Pressure-Dependent Model 61
4.2.2 Soil-Water Interaction 62
4.3 Variation of Pore Water Pressure 62
4.4 Finite Element Model 63
4.4.1 Configuration of the Pile-Soil System 63

4.4.2 Pile Properties 64
4.4.3 Soil Profile 65
4.5 Parametric Study for Effect of Soil Permeability and Loading Rate 66
4.5.1 Effect of Permeability 67
4.5.2 Effect of Loading Rate 69
4.6 Lateral Resistance for Piles with Wings 71
4.6.1 Configuration of Finite Element Model for Piles with Wings 72
4.6.2 Numerical Results for Pile with Wings 73
4.7 Conclusion 74
4.8 Acknowledgements 75
Chapter 5 Eureka Geotechnical Downhole Array Data Analysis 106
5.1 Introduction 108
5.2 Site Description and General Information 109
5.2.1 Geotechnical Downhole Array at Eureka Station 89734 109
5.2.2 Available Earthquake Records 110
5.2.3 Site Description 110
5.3 Evaluation of Strong Motion Data 111
5.3.1 Recorded Time Histories 111
5.3.2 Cross Correlation Analysis 112
5.3.3 Site Resonant Characteristics 115
5.4 1-D site amplification numerical response 116
5.5 Discussion 117
5.6 Summary and Conclusions 117
5.7 Acknowledgements 118
Chapter 6 Recorded Seismic Response of the Samoa Channel Bridge System. 152
6.1 Introduction 153
6.2 Strong-Motion Instrumentations at the Samoa Channel Bridge and Adjacent Downhole Array 155
6.2.1 General Bridge Information 155
6.2.2 Instrumentations of the Samoa Channel Bridge 156

6.2.3 The Adjacent Eureka Geotechnical Array 157
6.2.4 Recorded Earthquake Motions 157
6.3 Evaluation of the Earthquake Records 158
6.3.1 Ground Motions at the Bridge and Adjacent Downhole Sites 159
6.3.2 Seismic Response along the Bridge Deck 160
6.3.3 Seismic Response of Pier S-8 162
6.3.4 Abutment and Bridge Response along Mud-line 164
6.4 System Identification for the Ground-Foundation-Bridge System.................... 165
6.4.1 Site Response and Nonlinearity.. 165
6.4.2 Bridge Sub-system Resonances.. 165
6.5 Discussion and Conclusions 168
6.6 Acknowledgements 169
Chapter 7 Numerical Analysis of the Samoa Channel Bridge System.............. 206
7.1 Introduction 207
7.2 General Bridge Information.. 208
7.2.1 The Bridge Layout.. 208
7.2.2 Geology and Site Description.. 209
7.2.3 Original Construction and Seismic Retrofit 210
7.3 Insights from the FE Analysis of Pier S-8... 211
7.3.1 Finite Element Modeling... 211
7.3.2 Calibration of the Pier Column Model at Pier S-8 213
7.3.3 Calibration of the Pile Foundation Model at Pier S-8 214
7.4 Numerical Simulation of the Bridge and Optimization with SNOPT 214
7.4.1 Optimization of Pier S-8 FE Model... 216
7.4.2 Spatial Variation of Bridge Foundation Stiffness.................................. 217
7.4.3 Comparison with Other Similar Foundation Stiffness Estimates 218
7.5 Conclusions 219
7.6 Acknowledgements 219
Chapter 8 Recorded Seismic Response and Numerical Analysis of the Eureka Channel Bridge.. 240

8.1 Introduction 241
8.2 General Bridge Information.. 242
8.2.1 The Bridge Description 242
8.2.2 Geology and Site Description.. 244
8.2.3 Seismic Retrofit Effort.. 244
8.3 Strong-Motion Instrumentations at the Eureka Channel Bridge 245
8.3.1 Instrumentations of the Eureka Channel Bridge.................................. 245
8.3.2 Recorded Earthquake Motions 246
8.4 Evaluation of Earthquake Records 247
8.4.1 Ground Motions at the Bridge and Adjacent Downhole Sites 247
8.4.2 Seismic Response along the Bridge Deck 249
8.4.3 Seismic Response of Pier E-7... 250
8.4.4 Abutment and Bridge Response along Mud-line 251
8.5 System Identification for the Ground-Foundation-Bridge System................... 251
8.5.1 Site Response and Nonlinearity.. 251
8.5.2 Bridge Sub-system Resonances.. 251
8.6 Finite Element Analysis... 252
8.6.1 Finite Element Modeling.. 252
8.6.2 Structural Modeling of the Column at Pier E-7.................................. 253
8.6.3 Structural Modeling of the Pile Foundation below Pier E-7 254
8.7 Numerical Simulation for the Eureka Channel Bridge.................................. 255
8.8 3D FE Modeling of Pile Groups at Pier E-7... 258
8.9 Conclusions 259
8.10 Acknowledgements 260
Chapter 9 Conclusions and Future Work.. 299
9.1 Conclusions 299
9.1.1 3D Finite Element Modeling of Pile Groups....................................... 300
9.1.2 Strong Motion Data Analysis 302
9.1.3 Numerical Modeling for Ground-Foundation-Structure system 303
9.2 Future work.. 304

BIBLIOGRAPHY **305**
Appendix A. **Additional Parametric Study for Effects of Loading Rate** **322**
Appendix B. **Estimation of Soil Shear Modulus and Raleigh Damping** **329**
Appendix C. **Moment Curvature (M−φ) Analysis for Pier Column S-8** **334**
Appendix D. **3D Modeling of Pile Groups below Pier S-8** **344**

LIST OF FIGURES

Figure 1.1: Substructure approach to analyze the SSI problem (from Stewart et al. 1998) 16

Figure 1.2: Analysis procedure using an equivalent single pile and p-y curves (from Caltrans 2012a) 16

Figure 1.3: Translational and rotational pile group stiffness matrix logic (from Novak 1991) 17

Figure 1.4: Seismic soil-pile-foundation-structure interaction: (a) the whole system, (b) Pile group dynamic impedances and (c) superstructure inertia response (from Gazetas et al. 1993) 18

Figure 2.1: OpenSeesPL user interface (Lu et al. 2006, http://cyclic.ucsd.edu/openseespl/) 31

Figure 2.2: Employed half mesh configuration (due to symmetry) for the single pile simulation (a) 3D isometric view (b) illustration of pile model with rigid links 31

Figure 2.3: Comparison of pile deflection profiles for the linear-response calibration scenario (Elgamal and Lu 2009) 32

Figure 2.4: Multi-surface plasticity J_2 model: (a) Von Mises multi-surfaces, (b) Hysteretic shear response (Elgamal et al. 2008), and (c) illustration of tension cut-off logic ... 32

Figure 2.5: Computed pile head load-deflection curves for the single pile simulation 32

Figure 2.6: Pile deflection, bending moment and shear force profiles for the linear, nonlinear, and nonlinear with tension cut-off soil cases at the maximum applied lateral load of 420.36 kN 33

Figure 2.7: Finite element mesh (half-mesh configuration) employed for 3×3 pile group (3Dia spacing case) with pile numbering scheme and close-up of the pile group.... 33

Figure 2.8: Tension cut-off case: stress ratio for 3×3 pile group at the maximum lateral load (displacements as shown are magnified by a factor of 8): (a) 3Dia pile spacing, (b) 5Dia pile spacing, and (c) 7Dia pile spacing 34

Figure 2.9: Pile head displacement efficiency of the 3×3 pile group for different spacing under the maximum applied lateral load of 420.36 kN per pile (the single pile head deflection is 0.003 m, 0.012 m, and 0.027 m for the linear, nonlinear and nonlinear with cut-off cases respectively) 34

Figure 2.10: Linear, nonlinear, and nonlinear with tension cut-off cases: (a) Load-deflection curves, (b) corresponding displacement efficiency, and (c) load or force-based efficiency 35

Figure 2.11: Distribution of pile head lateral force at the maximum applied load for (a) 3Dia pile spacing and (b) 7Dia pile spacing (Pile numbers are shown in Figure 2.7) 36

Figure 2.12: Bending moment profiles at maximum load in the 3×3 pile group of Figure 2.7 for (a) 3Dia pile spacing and (b) 7Dia pile spacing 37

Figure 3.1: Dumbarton Bridge (http://www.mtc.ca.gov) 51

Figure 3.2: Large 8x4 pile group: (a) soil profile used for the FE simulation with 8 piles in the direction of applied lateral load, (b) the FE mesh employed for the simulation, and (c) plan view of pile group layout 51

Figure 3.3: Average longitudinal shear load at pile head versus displacement curve 52

Figure 3.4: Final deformed mesh (factor of 30) for shear stress ratio contour (red color shows yielded soil elements): (a) nonlinear soil and (b) nonlinear with tension cutoff 52

Figure 3.5: Displacement at the mudline at 0.3 m pile cap deflection............................. 53

Figure 3.6: Shear force and bending moment at the 0.3 m pile cap deflection 53

Figure 3.7: Pile axial forces: (a) at the initial vertical dead load and (b) after application of the 0.30 m lateral pile cap deflection.. 54

Figure 3.8: Shear forces and moments in each pile: (a) peak shear force, (b) peak bending moment, (c) residual shear force (after removal of lateral load), and (d) residual bending moment (after removal of lateral load) 55

Figure 3.9: Axial force distribution: (a) under gravity load, (b) under the applied peak lateral load, and (c) after removal of the applied lateral 56

Figure 3.10: Lateral pile displacements (m) at the mudline: (a) at the maximum lateral load and (b) upon removal of lateral load.. 56

Figure 3.11: Vertical displacement (m) contour (magnified by a factor of 50): (a) at the maximum lateral load and (b) upon load removal 57

Figure 4.1: Multi-yield surface and constitutive model: (a) conical yield surface in principal stress space and (b) schematic of undrained constitutive model response (Yang 2000; Yang and Elgamal 2002; Yang et al. 2003)... 78

Figure 4.2: Finite element mesh (half-mesh configuration) and a close-up view employed in this study 78

Figure 4.3: Shear loading on single element (a) employed 9-node quadrilateral plane-strain element and boundary conditions, (b) shear stress-strain (drained versus undrained), and (c) shear stress-strain response, pore water pressure (pwp) and effective confinement relationship under undrained situation................................. 79

Figure 4.4: Cavitation allowed: (a) Pile head displacement-time relationship and (b) load-displacement curve.. 80

Figure 4.5: Pile deflection profiles and shear force profiles at: (a) t = 1 sec, (b) t = 2.5 sec, and (c) t = 5 sec... 81

Figure 4.6: Pile bending moment profiles at: (a) t = 1 sec, (b) t = 2.5 sec, and (c) t = 5 sec 82

Figure 4.7: Without cavitation: (a) Pile head displacement-time relationship and (b) load-displacement curve.. 83

Figure 4.8: Time histories of excess pore pressure adjacent to soil-pile interfacing layer for permeability coefficients: (a) k = 50 m/s and (b) k = 1 m/s at 4 different elevations 84

Figure 4.9: Time histories of excess pore pressure adjacent to soil-pile interfacing layer for permeability coefficients: (a) k = 1e-2 m/s and (b) k = 1e-3 m/s at 4 different elevations 85

Figure 4.10: Time histories of excess pore pressure adjacent to soil-pile interfacing layer for permeability coefficients k = 6.6e-5 m/s at 4 different elevations...................... 86

Figure 4.11: Time histories of excess pore pressure adjacent to soil-pile interfacing layer for permeability coefficients k = 1e-7 m/s at 4 different elevations......................... 86

Figure 4.12: Pore water distribution for permeability coefficient of 6.6e-5 m/s w/o and with cavitation cutoff (close up side view 24.96 m×7.35 m)................................... 87

Figure 4.13: Excess water distribution for permeability coefficient of 6.6e-5 m/s w/o and with cavitation cutoff (close up side view 39.64 m×27.38 m)................................. 88

Figure 4.14: Loading scenarios for pushover analysis... 89

Figure 4.15: Secant Stiffness versus load for 3 different constant loading rate scenarios 89

Figure 4.16: EPP versus lateral load behind (dashed line) and in front of (solid line) the pile for three loading rate cases: (a) k = 1e-2 m/s and (b) k = 6.6e-5 m/s 90

Figure 4.17: Pile response for medium dense sand with water table at ground surface and at 10 meters above 91

Figure 4.18: PWP and EPP versus lateral load behind and in front of the pile 92

Figure 4.19: Pore water pressure contour for permeability coefficient of 6.6e-5 m/s for loading scenarios 1, 2 and 3 on deformed mesh (factor = 200) up to 6.2 m depth... 93

Figure 4.20: Excess pore water pressure contour for permeability coefficient of 6.6e-5 m/s for loading scenarios 1, 2 and 3 on deformed mesh (factor = 100)) up to 10 m depth.. 94

Figure 4.21: (a) Full mesh, (b) close-up plan view around the pile, and (c) side view for the pile with wings. 95

Figure 4.22: Effect of pile wings on load-displacement curves for permeability (a) k = 1e-3 m/s and (b) k = 6.6e-5 m/s with loading rate 30kN/0.005 s. 96

Figure 4.23: Change of pile head displacement vs time for with and without pile wings cases for permeability (a) k = 1e-3 m/s and (b) k = 6.6e-5 m/s with loading rate 30kN/0.005 s. 97

Figure 4.24: Pile deflection profile at t = 0.25 s for permeability (a) k = 1e-3 m/s and (b) k = 6.6e-5 m/s with loading rate 30kN/0.005 s... 98

Figure 4.25: Shear Force Profile at t = 0.25 s for permeability (a) k = 1e-3 m/s and (b) k = 6.6e-5 m/s with loading rate 30kN/0.005 s. ... 99

Figure 4.26: Bending Moment Profile at t = 0.25 s for permeability (a) k = 1e-3 m/s and (b) k = 6.6e-5 m/s with loading rate 30kN/0.005 s ... 100

Figure 4.27: Deformed mesh for (a) no wing case and (b) with wing of b_w = 0.685 m and h_w = 3 m, and (c) with wing of b_w = 1.370 m and h_w = 3 m (factor = 200) for permeability k = 1e-3 m/s ... 101

Figure 4.28: Deformed mesh for (a) no wing case and (b) with wing of b_w = 0.685 m and h_w = 3 m, and (c) with wing of b_w = 1.370 m and h_w = 3 m (factor = 200) for permeability k = 6.6e-5 m/s ... 102

Figure 4.29: PWP on deformed mesh for (a) no wing case and (b) with wing of b_w = 0.685 m and h_w = 3 m, and (c) with wing of b_w = 1.370 m and h_w =3 m for permeability k = 1e-3 m/s (factor = 200) ... 103

Figure 4.30: EPP on deformed mesh for (a) no wing case and (b) with wing of b_w = 0.685 m and h_w = 3 m, and (c) with wing of b_w = 1.370 m and h_w = 3 m for for permeability k = 1e-3 m/s (factor = 200) ... 103

Figure 4.31: PWP on deformed mesh for (a) no wing case and (b) with wing of b_w = 0.685 m and h_w = 3 m, and (c) with wing of b_w = 1.370 m and h_w = 3 m for permeability k = 6.6e-5 m/s (factor = 200) ... 104

Figure 4.32: EPP on deformed mesh for (a) no wing case and (b) with wing of b_w = 0.685 m and h_w = 3 m, and (c) with wing of b_w = 1.370 m and h_w = 3 m for permeability k = 6.6e-5 m/s (factor = 200) ... 105

Figure 5.1: Location of the Eureka Geotechnical Downhole Array (Map data @ 2015 Google) and station photograph (http://www.strongmotioncenter.org) ... 122

Figure 5.2: The Eureka Geotechnical Downhole Array (http://www.strongmotioncenter.org) ... 123

Figure 5.3: Velocity profile along the depth at the Eureka Geotechnical Array (elevation is referenced to MSL) (http://www.strongmotioncenter.org) ... 124

Figure 5.4: Google Earth image of the M_w 6.5 2010 Ferndale Earthquake (Google Imagery @2015 NASA, TerraMetrics) ... 125

Figure 5.5: Soil profile at the Eureka geotechnical Array site (Caltrans 2002a) ... 125

Figure 5.6: Recorded (a) acceleration and (b) displacement time histories during the moderate event in NS direction ... 126

Figure 5.7: Recorded (a) acceleration and (b) displacement time histories during the moderate event in EW direction ... 127

Figure 5.8: Recorded (a) acceleration and (b) displacement time histories during the 2000 Eureka Offshore Earthquake in NS direction ... 128

Figure 5.9: Recorded (a) acceleration and (b) displacement time histories during the 2000 Eureka Offshore Earthquake in EW direction 129

Figure 5.10: Overall average cross-correlation based on the 2000 Cape Mendocino Earthquake, the 2005 Crescent City Earthquake, the 2010 Ferndale Earthquake [b], the 2007 Ferndale Earthquake, and the Ferndale Offshore Earthquake 2000 130

Figure 5.11: Cross-correlation of accelearations (with respect to the ground surface records) during the moderate event (t = 0 s – 90 s) in (a) NS and (b) EW directions 131

Figure 5.12: Cross-correlation of accelearations (with respect to the ground surface records) during the moderate event with the 23 s - 60 s time window in (a) NS and (b) EW directions 132

Figure 5.13: Cross-correlation of accelearations (with respect to the ground surface records) during the moderate event with the 20 s - 30 s time window in (a) NS and (b) EW directions 133

Figure 5.14: Stress-strain histories for soil layer 1, 2 and 3 during the moderate event in (a) NS and (b) EW directions 134

Figure 5.15: Stress-strain histories for (a) soil layer 1 and (b) soil layer 2 during the moderate event 135

Figure 5.16: Typical range for modulus reduction curves after EPRI (1993) for sand .. 136

Figure 5.17: Variation of estimated incident shear wave velocities with time (time window = 5 seconds) for the moderate event in (a) NS and (b) EW directions 137

Figure 5.18: Cross-correlation of accelearations (between adjacent sensor records) during the 2000 Eureka Offshore Earthquake in (a) NS and (b) EW directions 138

Figure 5.19: Cross-correlation of accelearations (with respect to the ground surface records) during the 2000 Eureka Offshore Earthquake in (a) NS and (b) EW directions 139

Figure 5.20: Estimates of shear wave velocity in comparison with the geophysical measurements 140

Figure 5.21: Transfer function of acceleration (Layer 1) in NS direction 141

Figure 5.22: Transfer function of acceleration (Layer 1) in EW direction 142

Figure 5.23: Nonlinear soil response of the topmost stratum during the moderate event in NS direction 143

Figure 5.24: Nonlinear soil response of the topmost stratum during the moderate event in EW direction 144

Figure 5.25: Short time Fourier transform analysis during the moderate event in (a) NS and (b) EW directions 145

Figure 5.26: Linear soil response of the topmost stratum during the Ferndale Earthquake on Feb, 2010 in NS direction 146

Figure 5.27: Linear soil response of the topmost stratum during the Ferndale Earthquake on Feb, 2010 in EW direction 147

Figure 5.28: Nonlinear analysis for the moderate event (damping ratio of 5% at the frequencies of 2.5 Hz and 7.5 Hz) in (a) NS and (b) EW directions 148

Figure 5.29: Linear analysis for the moderate event (damping ratio of 20% at the frequencies of 2.5 Hz and 7.5 Hz) in (a) NS and (b) EW directions 149

Figure 5.30: Linear analysis for the 2000 Eureka Offshore Earthquake (damping ratio of 8% at the frequencies of 2.5 Hz and 7.5 Hz) in (a) NS and (b) EW directions 150

Figure 5.31: Linear analysis for the 2000 Cape Mendocino Earthquake (damping ratio of 8% at the frequencies of 2.5 Hz and 7.5 Hz) in (a) NS and (b) EW directions 151

Figure 6.1: Bridge Configuration: (a) Samoa Channel Bridge, Eureka Geotechnical Array, Middle Channel Bridge and Eureka Channel Bridge (Map Data @ 2015 Google) and (b) photo of the Samoa Channel Bridge (http://www.strongmotioncenter.org) 176

Figure 6.2: Layout of instrumentation at the Samoa Channel Bridge (http://www.strongmotioncenter.org) 177

Figure 6.3: Layout of instrumentation at the Samoa Channel Bridge Pier S-8 (Caltrans 2002a) 178

Figure 6.4: Soil Profile along the bridge (Caltrans 2002a) and shear wave velocity profile at Eureka Downhole array (http://www.strongmotioncenter.org) 179

Figure 6.5: Soil Profile (Caltrans 2002a) and shear wave velocity profile at Eureka Downhole array (http://www.strongmotioncenter.org) 180

Figure 6.6: Transversal time histories: (a) acceleration and (b) displacement at the BGS, BPF and GDA stations during the moderate event 181

Figure 6.7: Longitudinal time histories: (a) acceleration and (b) displacement at the BGS, BPF and GDA stations during the moderate event 182

Figure 6.8: Response Spectra of acceleration of BGS, BPF and GDA at different depths in the transverse and longitudinal directions for: (a) the moderate event and (b) the 2007 Trinidad Earthquake 183

Figure 6.9: Response Spectra of acceleration of BGS, BPF and GDA at different depths in the transverse and longitudinal directions for (a) the 2007 Ferndale Earthquake and (b) the 2005 Crescent City Earthquake 184

Figure 6.10: Response Spectra of acceleration of BGS, BPF and along bridge deck during the moderate event: (a) Transverse and (b) Longitudinal 185

Figure 6.11: Power spectral density (PSD) of BGS, BPF and GDA at different depths in the transverse direction during (a) the moderate event and (b) the 2007 Trinidad Earthquake 186

Figure 6.12: Variation of relative displacement time histories at the bridge deck level for the 2007 Ferndale Earthquake: (a) Transverse and (b) Longitudinal 187

Figure 6.13: Variation of relative displacement time histories at the bridge deck level for the moderate event: (a) Transverse and (b) Longitudinal 188

Figure 6.14: Recorded acceleration and relative longitudinal/transversal displacement of deck across the separation joint near Pier 8 for the moderate event (a) before and (b) after filtering 189

Figure 6.15: Peak displacement along bridge deck referenced to BPF: (a) Transverse and (b) Longitudinal 190

Figure 6.16: Displacement time histories along Pier S-8 during the moderate earthquake in the transverse direction 191

Figure 6.17: Displacement time histories along Pier S-8 during the 2007 Ferndale Earthquake in the transverse direction 192

Figure 6.18: Displacement time histories along Pier S-8 during the moderate Earthquake in the longitudinal direction 193

Figure 6.19: Displacement time histories along Pier S-8 during the 2007 Ferndale Earthquake in the longitudinal direction 194

Figure 6.20: Displaced configuration of Pier S-8 for selected time instants during the moderate event in (a) Transverse and (b) Longitudinal 195

Figure 6.21: Displaced configuration of Pier S-8 for selected time instants during the 2007 Ferndale Earthquake: (a) Transverse and (b) Longitudinal 195

Figure 6.22: Transverse direction: (a) time histories and (b) displaced configuration of Pier S-8 for selected time instants during the moderate event................................ 196

Figure 6.23: Transverse direction: (a) time histories and (b) displaced configuration of Pier S-8 for selected time instants during the 2007 Ferndale Earthquake 196

Figure 6.24: Longitudinal direction: (a) time histories and (b) displaced configuration of Pier S-8 for selected time instants during the moderate event................................ 197

Figure 6.25: Longitudinal direction: (a) time histories and (b) displaced configuration of Pier S-8 for selected time instants during the 2007 Ferndale Earthquake 197

Figure 6.26: Variation of (a) acceleration and (b) displacement time histories along ground surface in the transverse direction for the moderate event 198

Figure 6.27: Variation of (a) acceleration and (b) displacement time histories along ground surface in the longitudinal direction for the moderate event 199

Figure 6.28: Response Spectra of acceleration of along bridge base line during the moderate event: (a) Transverse and (b) Longitudinal 200

Figure 6.29: Response Spectra of acceleration of along bridge base line during the 2007 Trinidad Earthquake: (a) Transverse and (b) Longitudinal 201

Figure 6.30: Transfer function in the transverse direction for deck response over pile cap response ... 202
Figure 6.31: Short time transfer function during the moderate event (deck to pile cap) in the transverse direction ... 203
Figure 6.32: Short time transfer function during the 2007 Ferndale Earthquake (deck to pile cap) in the transverse direction ... 203
Figure 6.33: Transfer function in the transverse direction for deck response (a) over free field response and (b) over pile response at -16.46 m ... 204
Figure 6.34: Short time transfer function during the moderate event (deck to pile -16.45 m) in the transverse direction ... 205
Figure 6.35: Short time transfer function during the 2007 Ferndale Earthquake (deck to pile -16.45) in the transverse direction ... 205
Figure 7.1: Faults near Eureka Area and Geological map of Eureka area (McLaughlin et al. 2000) ... 226
Figure 7.2: Samoa Channel Bridge Pier S-8 and adjacent soil profile ... 227
Figure 7.3: Samoa Channel Bridge retrofit information for Piers S-2, 3 and 14 through 20 (Caltrans 1968; 2002b) ... 228
Figure 7.4: Samoa Channel Bridge retrofit information Piers S-4 through 13 (Caltrans 1968; 2002b) ... 229
Figure 7.5: Pier S-8 single column type pier model ... 230
Figure 7.6: Transverse mode shapes of pile-column system (at Pier S-8) with fixed base at the elevation of -16.46 m with (a) f_1=0.74 Hz and (b) f_2=2.37 Hz... 230
Figure 7.7: Time histories comparisons for at Pier S-8 (at the deck level) during earthquakes: (a) the moderate event (b) the 2007 Trinidad Earthquake, and (c) the 2008 Willow Creek Earthquake ... 231
Figure 7.8: Time histories comparisons along Pier S-8 from deck level to elevation of -16.46 m during: (a) the moderate event, (b) the 2007 Trinidad Earthquake, and (c) the 2008 Willow Creek Earthquake ... 232
Figure 7.9: Beam-column model of the Samoa Channel Bridge ... 233
Figure 7.10: Bridge Deck Section ... 233
Figure 7.11: Estimation of the spring value at the base of Pier S-8 using SNOPT ... 233
Figure 7.12: The recorded and optimized time histories at Pier S-8 ... 234
Figure 7.13: Variation of Spring Stiffness during during the moderate event ... 235
Figure 7.14: Locations of recorded pile cap and bridge deck responses for objective function ... 235
Figure 7.15: Base spring values along deck for earthquake Ferndale 2010 ... 236

Figure 7.16: Base spring values along deck during the Trinidad 2007 and Trinidad 2008 earthquakes in sequence ... 236

Figure 7.17: Comparison of computed and measured displacement time histories at (a) Pier S-8, (b) S-14 during the moderate event ... 237

Figure 7.18: Comparisons of computed and measured displacement time histories at Pier S-4, S-9 and S-17 (deck level) during the moderate event ... 238

Figure 7.19: Side view of (a) the Middle Channel Bridge and (b) the Samoa Channel Bridge (http://www.strongmotioncenter.org) ... 239

Figure 8.1: Bridge Configuration: (a) Samoa Channel Bridge, Eureka Geotechnical Array, Middle Channel Bridge and Eureka Channel Bridge (Map Data @ 2015 Google) and (b) photo of the Eureka Channel Bridge (http://www.strongmotioncenter.org) ... 266

Figure 8.2: Layout of instrumentation at the Eureka Channel Bridge: (a) deck level plan and (b) elevation (http://www.strongmotioncenter.org) ... 267

Figure 8.3: Soil Profile along the bridge (Caltrans 2002b) ... 268

Figure 8.4: Layout of instrumentation and retrofit efforts at the Eureka Channel Bridge Pier E-7 (Caltrans 2002b) ... 268

Figure 8.5: Displacements at the ground surface of the Samoa Channel Bridge (SCB), the Geotechnical downhole array (GDA), the Middle Channel Bridge (MCB) and the Eureka Channel Bridge (ECB) in the (a) NS and (b) EW directions during the moderate event ... 269

Figure 8.6: Accelerations at the ground surface of SCB, GDA, MCB and ECB in the (a) NS and (b) EW directions during the moderate event ... 270

Figure 8.7: Fourier transformation of ground surface response of SCB, GDA, MCB and ECB in the (a) NS and (b) EW directions during the moderate event ... 270

Figure 8.8: Displacement time histories in the (a) east-west (EW) and (b) north- south (NS) directions during the moderate event ... 271

Figure 8.9: Displacement time histories in the (a) east-west (EW) direction and (b) north-south (NS) directions during the 2007 Ferndale Earthquake ... 271

Figure 8.10: Eureka Channel bridge response spectra of free-field in the transverse and the longitudinal directions of Pier E-7 during the moderate event ... 272

Figure 8.11: Variation of time histories at bridge deck level during the moderate event for (a) acceleration and (b) relative displacement time histories (Transverse shown) . 273

Figure 8.12: Variation of time histories at bridge deck level during the moderate event for (a) acceleration and (b) relative displacement time histories (Longitudinal shown) ... 274

Figure 8.13: Variation of time histories at bridge deck level during the 2007 Ferndale Earthquake for (a) acceleration and (b) relative displacement time histories (Transverse shown) 275

Figure 8.14: Variation of time histories at bridge deck level during the 2007 Ferndale Earthquake for (a) acceleration and (b) relative displacement time histories (Longitudinal shown) 276

Figure 8.15: Displacement time histories along Pier E-7: (a) in the transverse direction, (b) in the longitudinal direction during the moderate event 277

Figure 8.16: Relative displacement time histories (referenced to the motions at EBPF station) along Pier E-7: (a) in the transverse direction, (b) in the longitudinal direction during the moderate event 277

Figure 8.17: Displacement time histories along Pier E-7: (a) in the transverse direction, (b) in the longitudinal direction during the 2007 Ferndale Earthquake 278

Figure 8.18: Relative displacement time histories (referenced to the motions at EBPF station) along Pier E-7 during the 2007 Ferndale Earthquake: (a) Transverse and (b) Longitudinal 278

Figure 8.19: Displaced configuration of Pier E-7 for selected time instants during (a) the 2007 Ferndale Earthquake and (b) the 2007 Trinidad Earthquake (Transverse) 279

Figure 8.20: Displaced configuration of Pier E-7 for selected time instants during (a) the moderate event and (b) the 2007 Ferndale Earthquake (Longitudinal) 280

Figure 8.21: Variation of (a) acceleration and (b) displacement time histories along ground surface for the moderate event (in Tran direction of Pier E-7 shown) 281

Figure 8.22: Variation of (a) acceleration and (b) displacement time histories along ground surface for the moderate event (in Long direction of Pier E-7 shown) 282

Figure 8.23: Short time transfer function plots in the transverse direction for deck response over pile cap response during (a) the 2007 Ferndale Earthquake and (b) the 2007 Trinidad Earthquake 283

Figure 8.24: Short time transfer function plots in the transverse direction for (a) deck response over free field response and (b) deck response over pile response at -16.46 m during the 2007 Ferndale Earthquake 284

Figure 8.25: Short time transfer function plots in the transverse direction for (a) deck response over free field response and (b) deck response over pile response at -16.46 m during the 2007 Trinidad Earthquake 285

Figure 8.26: Transfer function in the transverse direction for deck response over pile cap response 286

Figure 8.27: Transfer function in the transverse direction for (a) deck response over pile response at -16.46 m and (b) deck response over free field response 286

Figure 8.28: Pier E-7 single column type pier model 287

Figure 8.29: Pier E-7 foundation-pier model 287

Figure 8.30: Transverse mode shapes of pile-column system (at Pier E-7) with fixed base at the elevation of -16.46 m with (a) f_1=1.51 Hz and (b) f_2=3.50 Hz........ 288

Figure 8.31: Comparison of computed and measured response at Pier E-7 during the 2007 Trinidad Earthquake........ 289

Figure 8.32: Time histories comparisons along Pier E-7 from deck level to elevation of -16.46 m during the 2007 Trinidad Earthquake 290

Figure 8.33: Time histories comparisons along Pier E-7 from deck level to elevation of -16.46 m during the 2007 Ferndale Earthquake 291

Figure 8.34: Beam-Column Model of the Eureka Channel Bridge 292

Figure 8.35: Estimation of the spring value at the base of Pier E-7 using SNOPT 292

Figure 8.36: The recorded and optimized time histories at Pier E-7 during the 2007 Trinidad Earthquake........ 293

Figure 8.37: The recorded and optimized time histories at Pier E-7 during the 2007 Ferndale Earthquake 294

Figure 8.38: Identified lateral base spring values along the bridge 295

Figure 8.39: Comparison of computed and measured displacement time histories at Pier E-7 in (a) Transverse and (b) Longitudinal during the moderate event........ 296

Figure 8.40: Comparison of computed and measured displacement time histories at Pier E-7 in (a) Transverse and (b) Longitudinal during the moderate event........ 296

Figure 8.41: Comparison of computed and measured displacement time histories at E-10 and E-13 in (a) Transverse and (b) Longitudinal during the moderate event........ 296

Figure 8.42: Soil Profile at Pier E-7 of Eureka Channel Bridge........ 297

Figure 8.43: Plan view of pile group layout after retrofit 297

Figure 8.44: Finite element mesh and close-up view of pile group........ 298

Figure A.1: Load-displacement for 1500 kN in 0.25 s with EI=2×10^7 kN-m^2, EI=2×10^6 kN-m^2 (more realistic) and EI=2×10^6 kN-m^2 (with interfacing layer) 323

Figure A.2: Load-displacement curve for k=6.6e-5 m/s and k=1e-2 m/s (with interfacing layer) 324

Figure A.3: Pile head displacement-time relationship for k=1e-2 m/s (with interfacing layer) 324

Figure A.4: EPP versus lateral load behind (dash line) and in front of (solid line) the pile for three loading rate cases for (a) k=1e-2 m/s and (b) k=6.6e-5 m/s (with interfacing layer) 325

Figure A.5: Secant Stiffness versus load for 3 different constant loading rate scenarios (with interfacing layer) 326

Figure A.6: Pore Water Pressure contour for permeability coefficient of 6.6e-5 m/s (with interfacing layer) ... 327

Figure A.7: EPP contour for permeability coefficient of 6.6e-5 m/s (with interfacing layer) ... 327

Figure A.8: Soil response at 0.685 m from pile center in transverse direction at 0.7887 m depth (with interfacing layer) ... 328

Figure B.1: OpenSees2DPS main window ... 331

Figure B.2: The moderate event - Linear analysis (Damping ratio of 20% at f_1 = 2.13 Hz, f_2 = 6.3 Hz) ... 332

Figure B.3: The 2000 Eureka Offshore Earthquake - Linear analysis (Damping ratio of 5% at f_1 = 2.63 Hz, f_2 = 6.75 Hz) ... 333

Figure C.1: Moment Curvature Curve (Caltrans) ... 340

Figure C.2: Concrete Stress-Strain Model (Caltrans) ... 340

Figure C.3: Pier Columns before retrofit ... 341

Figure C.4: Pier Columns after retrofit ... 342

Figure C.5: Comparison of EI of pier S-8 and S-9 from FE and Moment curvature analysis ... 343

Figure C.6: Moment curvature analysis for pier columns cross section ... 343

Figure D.1: Soil Profile at Pier S-8 of Samoa Channel Bridge ... 348

Figure D.2: Plan view of pile group layout (a) before and (b) after retrofit ... 348

Figure D.3: Finite element mesh and close-up view of pile group ... 348

LIST OF TABLES

Table 3.1: Soil Model Properties 50

Table 4.1: Suggested permeability coefficient values in OpenSeesPL and Cyclic1D 76

Table 4.2: Soil material properties employed in the 3D analysis 76

Table 4.3: Pile wing geometry 77

Table 4.4: Percentage reduction of lateral pile head displacement 77

Table 4.5: Percentage reduction of maximum bending moment 77

Table 5.1: Earthquakes recorded by station 89734 Eureka Geotechnical Array 119

Table 5.2: Measured shear and pressure wave velocities and Poisson's ratio 119

Table 5.3: Estimated resonant frequency and average shear wave velocity (*Vs*) for the topmost stratum (Layer 1) in NS direction 120

Table 5.4: Estimated resonant frequency and average shear wave velocity (*Vs*) for the topmost stratum (Layer 1) in EW direction 120

Table 5.5: Soil layer properties for the 1D FE model 121

Table 6.1: Recorded peak acceleration for recent earthquakes at the Bridge Site (arranged by order of peak acceleration) 170

Table 6.2: Recorded peak displacement for recent earthquakes at the Bridge Site 171

Table 6.3: Rotation of sensors at the elevation of -16.46 m on retrofitted pile in degree 172

Table 6.4: Rotation of sensors at the elevation of -16.46 m on retrofitted pile in degree 172

Table 6.5: Deflection of substructure components at pier S-8 in the transverse direction 173

Table 6.6: Identified resonant frequency of bridge pier in the transverse direction 174

Table 6.7: Identified resonant frequency of bridge system in the transverse direction .. 174

Table 6.8: Identified resonant frequency of bridge pier in the longitudinal direction 175

Table 7.1: Diameter and height of pier and pile foundation 220

Table 7.2: Concrete material parameters for the FE model (Caltrans 2002a) 221

Table 7.3: Steel material parameters for the FE model (Caltrans 2002a) 221

Table 7.4: Uncracked section properties for bridge pier columns (Caltrans 2002a) 221

Table 7.5: Identified stiffness factor for pier and pile foundation at Pier S-8 222

Table 7.6: Employed Bridge Deck Properties for the FE Model (Caltrans 2002a) 222

Table 7.7: Optimized frequency and stiffness factor at Pier S-8 based on EI of uncracked section (FEM1) 223

Table 7.8: Optimized frequency and spring value representing pile foundation below Pier S-8 (Figure 7.11) 223

Table 7.9: Employed weighting factors of the objective function for each sensor 223

Table 7.10: Optimized foundation stiffness and values based on Caltrans report for the Middle Channel Bridge (Caltrans 2000b) for the 4×4 pile group configuration with 4 CISS retrofitted piles (Table 7.1 and Figure 7.3) 224

Table 7.11: Optimized foundation stiffness and values based on Caltrans report for the Middle Channel Bridge (Caltrans 2000b) for the concrete pile groups with 4 CISS retrofitted piles (Table 7.1 and Figure 7.4) 225

Table 8.1: Recorded peak acceleration for recent earthquakes at the Bridge Site (arranged by order of peak acceleration) 261

Table 8.2: Identified resonant frequency of bridge pier in the transverse direction 261

Table 8.3: Identified resonant frequency of bridge system in the transverse direction 262

Table 8.4: Optimized frequency and stiffness factor for pier at Pier E-7 based on uncracked section 262

Table 8.5: Optimized spring value representing pile foundation below Pier E-7 263

Table 8.6: Employed Bridge Deck Properties for the FE Model 264

Table 8.7: Bridge Pier Column Properties 264

Table 8.8: Optimized spring value representing pile foundation below Pier E-7 265

Table 8.9: Soil Material Properties 265

Table 8.10: Effects of nonlinearity of pile and soil 265

Table B.1: Soil Layer Properties (Linear Soil Case, Optimized value) for the moderate event 330

Table C.1: Constitutive model parameters for concrete materials and steel material before Retrofit 338

Table C.2: Constitutive model parameters for concrete materials and steel material after Retrofit 339

Table D.1: Soil Material Properties 347

Table D.2: Effects of nonlinearity of pile and soil 347

ACKNOWLEDGEMENTS

It is truly my pleasure to have had the opportunity to join the University of California, San Diego and to pursue my PhD degree in the department of Structural Engineering. My deepest gratitude goes to my advisor, Professor Ahmed Elgamal for all his guidance, encouragement, and generous support through all these years. It is hard to count how many times I went into his office full of confusion, but came back with confidence and exciting ideas. His invaluable knowledge and professional attitude made the long journey possible. Working with Professor Elgamal has been a great and cherished experience in my life.

I would like to thank all my committee members, Professor Enrique Luco, Professor Hidenori Murakami, Professor Peter Shearer, and Professor Benson Shing for their helpful suggestions and technical guidance on this project. I am grateful for the advice and assistance provided by Mr. Tom Shantz of Caltrans, and by Mr. Tony Shakal and Dr. Moh Huang of the USGS. Special thanks to my fellow colleagues in the Elgamal Group, Dr. Zhaohui Yang, Dr. Jinchi Lu, Dr. Ian Prowell, Dr. James Gingery and Dr. Kyungtae Kim for both technical discussions and friendships. Last but most importantly, I would like to express my gratitude to my family: my parents, my husband Chu Wang and my daughter Ellie for their endless love, support and confidence in me.

Chapter 2 of this dissertation contains material from the published proceedings of the Geo-Congress 2014 titled “Three-Dimensional Finite Element Modeling of Pile and Pile Group System Response” with authors Ning Wang, Ahmed Elgamal and Jinchi Lu (2014). The dissertation author is the first author of this paper.

Chapter 3 of this dissertation is based on material published in two proceedings: (1) the Geo-Congress 2014 titled “Three-Dimensional Finite Element Modeling of Pile and Pile Group System Response” with authors Ning Wang, Ahmed Elgamal and Jinchi Lu and (2) 2nd International Conference on Geotechnical and Earthquake Engineering titled “Lateral Load on a Large Pile Group: A 3D Finite Element Model” authored by Ning Wang, Jinchi Lu and Ahmed Elgamal. The dissertation author is the first author of these papers.

Chapter 4 of this dissertation is based on material from a manuscript under preparation for publication, tentatively titled “Numerical study on effects of permeability and loading rate on lateral pile response”, with a preliminary author list of Ning Wang, Ahmed Elgamal and Jinchi Lu. The dissertation author is the first author of this paper.

Chapter 6 of this dissertation is an extended version of the material published in the proceedings of the 10th International Conference on Urban Earthquake Engineering, titled “Bridge and Adjacent Downhole Array Response During Earthquakes at Eureka, California” with co-author Ahmed Elgamal (2013), and a manuscript under preparation for publication as a journal article, tentatively titled “Finite Element Based Seismic Assessment of the Samoa Channel Bridge-Foundation System”, with preliminary author list of Ning Wang and Ahmed Elgamal. The dissertation author is the first author of this paper.

Chapter 7 of this dissertation is based on material from a manuscript under preparation for publication, tentatively titled “Finite Element Based Seismic Assessment of Samoa Channel Bridge-Foundation System”, with co-author Ahmed Elgamal. The dissertation author is the first author and primary investigator of this paper.

Chapter 8 of this dissertation is based on material from a manuscript under preparation for publication, tentatively titled “Recorded Seismic Response of Eureka Channel Bridge-Foundation System and Adjacent Downhole Array”, with co-author Ahmed Elgamal. The dissertation author is the first author and primary investigator of this paper.

The research presented in this dissertation was funded partially by the Pacific Earthquake Engineering Research (PEER) Center, the U.S. Geological Survey (USGS award G13AP00050), the California Department of Transportation (Caltrans), and the U.S. National Science Foundation (NSF award CMMI-1201195). This support is gratefully acknowledged.

VITA

2001 Bachelor of Science, Tongji University, Shanghai, China

2006 Master of Science, Darmstadt University of Technology, Germany

2015 Doctor of Philosophy, University of California, San Diego

PUBLICATIONS

Wang, N., Elgamal, A., and Lu, J. (2014) "Three-Dimensional Finite Element Modeling of Pile and Pile Group System Response." *Soil Behavior Fundamentals to Innovations in Geotechnical Engineering*, ASCE, 570-584.

Wang, N., Lu, J., and Elgamal, A. (2013) "Lateral Load on a Large Pile Group: A 3D Finite Element Model." *Proceedings of IACGE 2013 Challenges and Recent Advances in Geotechnical and Seismic Research and Practices*, ASCE GSP 232, 677-684.

Wang, N. and Elgamal, A. (2013) "Bridge and Adjacent Downhole Array Response During Earthquakes at Eureka, California." *10th International Conference on Urban Earthquake Engineering*, *Tokyo Institute of Technology*, Tokyo, Japan

ABSTRACT OF THE DISSERTATION

Three-Dimensional Modeling of Ground-Pile Systems and Bridge Foundations

by

Ning Wang

Doctor of Philosophy in Structural Engineering

University of California, San Diego, 2015

Professor Ahmed Elgamal, Chair

Continued advancements in high-speed computing and increased availability of earthquake strong motion data have been allowing for further progress in the area of soil-structure-interaction (SSI). Efforts in this dissertation are mainly concerned with three-dimensional (3D) computational analyses of pile foundations and bridge-foundation-ground systems. This includes Finite Element (FE) modeling of ground-pile foundation systems, documentation and assessment of recorded bridge strong motion data, and identification of dynamic bridge-foundation system characteristics.

Currently, simplified approaches, such as p-y curves or the foundation stiffness matrix representation, are employed mainly when considering Soil-Structure-Interaction. However, there is much interest in more representative modeling techniques in order to improve our assessments of seismic pile foundation response.

In an effort to address this challenge, 3D FE numerical investigations are conducted related to the response of piles and pile groups under lateral load. Distribution of loads and moments among the piles within the group is investigated. Effects of permeability and loading rate on lateral pile response are addressed for saturated relatively impervious cohesionless soil condition. Insights concerning the soil-pile interaction mechanisms are obtained based on the conducted analyses of the soil-pile foundation subsystems.

Furthermore, numerical studies are conducted of long-span highway bridge-foundation systems under seismic loading conditions. Three-dimensional FE models of two existing bridges at Eureka California (the Samoa Channel Bridge and the Eureka Channel Bridge) are developed. Methodologies combining numerical modeling with insights gained from strong motion sensor records are investigated to capture the essential structure-foundation-ground system-response mechanisms. Focus is placed on the evaluation of dynamic properties and validation of the bridge FE models based on the recorded earthquake response. An optimization tool (SNOPT) is employed to evaluate the bridge foundation lateral stiffness. The studies show that computational modeling, along with analysis of the recorded ground-pile foundation data, provide an effective mechanism for understanding the entire structure-foundation-ground system response.

The OpenSees platform and the user-interfaces OpenSeesPL, MSBridge, as well as SNOPT are employed in various sections of the study. In the domain of highly expensive and time consuming foundation design and/or retrofit, major beneficial outcomes can result from adoption of analysis tools which have been calibrated/verified by actual recorded seismic performance data sets.

Chapter 1

Introduction and Literature Review

While the research field of Geotechnical Earthquake Engineering has been developing significantly in the past 40 years, impact of soil-structure-interaction (SSI) on the seismic response of structures is still not fully understood. In practice, it is challenging to predict the dynamic response of bridge-foundation-ground systems due to the difficulties encountered in modeling SSI, such as representation of the soil profile large spatial configuration, complexity of the soil-foundation interface mechanisms, and scarcity of advanced nonlinear soil behavior tools.

In this chapter, a brief overview of SSI research is provided. Existing literature on numerical simulation for ground-pile foundation systems is discussed. Motivation and scope of this research are outlined. Finally, the outline of this dissertation is presented.

1.1 Brief Overview of Soil-Structure-Interaction

Soil-structure interaction (SSI) and wave propagation during an earthquake have been shown to affect the seismic response of structures (e.g., Stewart et al. 1998; Datta 2010). For instance, many bridges either collapsed or incurred severe damage resulting from failure or movement of the foundation during past earthquakes (Caltrans 2001). Over the years, many analytical techniques have been developed to evaluate SSI effects for linear soil-structure systems (Luco and Contesse 1973; Luco 1975; Gazetas 1983; Wong and Luco 1985; 1986; Luco et al. 1987; Luco and Wong 1992). These efforts have provided valuable insights to complement the traditional structural analysis approaches using the fixed-base boundary condition. In addition, numerous full-scale or small-scale tests have been conducted to assess SSI effects. However, the analytical methods and experimental studies have limitations (e.g., difficulties in capturing the nonlinearities of SSI during strong earthquake motions). As such, advances in high-speed computing, 3D nonlinear constitutive soil models and strong motion sensing techniques in the last two decades, are increasingly facilitating and allowing for further understanding of soil-structure-interaction for large-scale structures.

In general, effects of SSI on bridge-foundation-ground systems can be numerically evaluated using either a *comprehensive model approach* or an *equivalent substructure approach* (Stewart et al. 1998; Zhang and Makris 2002). In the *comprehensive model approach*, the soil, pile foundation and superstructure are included within the same model and analyzed as a system. For this approach, material and geometric nonlinearities of both the structure and the surrounding soil can be captured with coupling effects considered. Therefore, this type of analysis conceptually stands to be more accurate in estimation of the system response (Elgamal et al. 2008; Bao et al. 2012). However, this modeling procedure is computationally quite expensive. In the *equivalent substructure approach*, analysis for the SSI effect is broken down into three individual steps (Mylonakis et al. 1997): (1) evaluation of the foundation kinematic response, (2) determination of the spring/dashpot properties based on the inertia mechanism, and (3) dynamic analysis of the structure supported on a compliant base (Figure 1.1). The major advantage of the substructure approach is the independency of each step so that the analyst can focus on the most significant aspects of the problem (Stewart et al. 1998).

1.2 Past Research on Pile Foundation under Lateral Load

For years, numerous experimental, theoretical and numerical investigations have been conducted to predict the behavior of laterally loaded piles. In this section, a literature review of representative investigations of laterally loaded pile foundations is presented.

1.2.1 Experimental Research

Experimental approaches (such as full-scale field test, centrifuge test, as well as shaking table test) provide valuable data for understanding the complex mechanisms of laterally loaded pile response, calibrating the analytical/numerical analysis tools and improving the design procedures. In particular, experimental studies are noteworthy for investigating special problems of laterally loaded piles, such as soil-pile separation

/slipping and pile group effects, which are difficult to study using analytical solutions. Due to the high cost of conducting tests on laterally loaded pile groups, most experimental research has been focused on response of single piles (Ting 1987; Chai and Hutchinson 2002; Bouafia 2007). Relatively few studies (Brown et al. 1987; Rollins et al. 1998; Rollins et al. 2006; Travis and Kyle 2008) were conducted to explore the performance of pile groups subjected to lateral loading.

1.2.2 Analytical Methods

During the last six decades, a number of analytical methods have been proposed in the area of lateral response of piles. For example, the *limit state method* (Hansen 1961; Broms 1964) calculates the ultimate lateral resistance of piles in cohesive and cohesionless soils based on the assumed distribution of ultimate soil pressure along the pile (SSI at lower loads is not addressed however). The *Elastic method* (Poulos 1971; Banerjee and Davies 1978; Pise 1984; Budhu and Davies 1988) assumes that the soil is elastic and continuous. The soil Young's modulus varies with the level of stress at the pile-soil interface. Poulos (1971) proposed an elastic method for the horizontal displacement and rotation of a laterally loaded pile group. The distribution of horizontal forces within the group is discussed with the assumption that all piles in the group are of same diameter and length.

The analytical approaches mentioned above are either semi-empirical or employ considerable simplifications, and have limitations with respect to taking account the soil continuum and nonlinearity at the same time (Mokwa 1999). As a result, the response of the pile foundation is often overestimated or underestimated based on the assumptions adopted (Mokwa 1999).

1.2.3 Numerical Methods

Numerical methods enable researchers to approach problems in a detailed way, combining many factors and parameters together to simulate the lateral pile foundation behavior. Generally, there are two main approaches: the Winkler spring (or p-y spring methods) and the Finite Element Method (FEM).

a) The Winkler Spring Model

One of the earliest attempts to model soil-pile interaction was to idealize the soil as a series of springs. In this model, there is no coupling of soil resistance from point to point along the pile (i.e. the soil resistance at any point on the pile is simply proportional to the displacement of that point) as employed in Reese and Matlock 1956, Broms 1964, Petrasovits and Awad 1972, Reese et al. 1984, Basu and Salgado 2007, Allotey and El Naggar 2008, and Zhang 2009.

While oversimplified, the Winkler model has been viewed to capture some of the basic physics of the system. Budek et al. (2000) compared the analytical results based on a Winkler beam with the solutions from an inelastic finite element analysis. It was reported that the linear soil models are adequate for most pile/column design applications. The influence of the coupling for the p-y and t-z (spring model in the vertical direction) responses on the cyclic/dynamic response of piles was investigated by Allotey and Foschi (2005).

The p-y method is currently among the most popular approaches in practice (Matlock 1970; Reese and Welch 1975; Reese and Wang 1986), using a beam to represent the pile and independent nonlinear springs along the pile to take account for the soil resistance. This approach requires the input of a series of p-y curves, which relate the soil reaction to pile displacement along the length of the pile. Over the years, researchers have proposed p-y curves for different types of soil from a number of well-instrumented field tests (Matlock 1970; Reese and Welch 1975; Reese 1997). In addition, the existing p-y relationships for sand were evaluated through experiments and numerical analysis (Briaud et al. 1984; Georgiadis et al. 1992; Gerolymos et al. 2009).

This method is widely used due to its simplicity and the possibility to incorporate factors such as nonlinearity, variation of subgrade reaction with depth, and representation of layered systems (Kumar et al. 2006). It could easily be implemented on computers to assess the performance of piles subjected to lateral loading (Reese and Wang 2006). However, this method ignores the continuous nature of the soil medium and dependency of the spring modulus on the foundation size and deflections (e.g., Elfass et al. 2004). Thus, the accuracy of this method is not guaranteed for complex problems.

b) The Finite Element Method

Computer-aided finite element analysis provides a versatile tool, allowing for use of advanced nonlinear constitutive soil models (Randolph 1981; Bezgin et al. 2004), simulation of soil-structure interface behavior and studies of lateral pile group behavior. In the past decades, computational simulations have helped to bring insight into the complex mechanisms of soil-pile response. For example, Muqtadir and Desai (1986) studied the behavior of a pile-group using a 3D FE program with a nonlinear soil model.

Interaction effects and relative slip are discussed. The response of closely spaced piles subjected to lateral loading in either one or two rows has been analyzed (Brown and Shie 1990) with two types of plasticity soil models: un-drained loading of saturated clay and drained loading of sands. Effects of spacing and development of plastic deformation areas around the piles were evaluated.

Zhang et al. (1999a) predicted the response of both the single pile and 3 × 3 to 7 × 3 pile groups using the finite element code FLPIER (Hoit et al. 1997). Validation of the 3D FEM by comparisons with experimental data from a prototype test of laterally loaded pile groups was also performed (Wakai et al. 1999; Chae et al. 2004). In this thesis, the OpenSees Finite Element computational analysis framework (Mazzoni et al. 2006), with capabilities of implementing 3D constitutive linear and nonlinear models for the soil and pile (http://opensees.berkeley.edu,) is used to simulate pile-soil-system response throughout.

1.3 Strong Motion Data and SSI Analysis

In the United States, bridges constructed before 1970 were designed with little or no consideration of seismic resistance (Itani 2003). In the 1971 San Fernando Earthquake (M_w = 6.6), more than 60 bridges were damaged in California (http://www.fhwa.dot.gov). In the 1989 Loma Prieta Earthquake, 10 bridges near Santa Cruz were closed due to major structural damage (http://earthquake.usgs.gov). To better understand the bridge seismic response mechanisms, the California Geological Survey Strong Motion Instrumentation Program (SMIP) was established in 1971 (http://www.consrv.ca.gov). Instrumentations installed on highway bridges, free-field sites near major bridges and subsurface geotechnical arrays all together provide valuable insights into the performance of the Ground-Foundation-Bridge Systems during earthquake events (http://www.consrv.ca.gov).

1.3.1 Recorded Data from Geotechnical Downhole Arrays

Throughout the years, researchers have been studying the effects of local soil conditions, aiming to improve the prediction of seismic site response. Traditionally, in-situ tests (Nazarian and Desai 1993) or laboratory tests (NRC 1985) are conducted to obtain soil characteristics with limitations and restraints. With the development of computational analysis technologies and improvement of sensor technologies, downhole array recording site seismic response becomes a promising source to fully understand the associated mechanisms in the in-situ state (e.g., Elgamal et al. 1995). Numerous research efforts have been focused on identification of soil seismic behavior with more and more geotechnical downhole arrays available at seismically active locations (Elgamal et al. 2001).

For example, downhole array below the foundation or in the vicinity of a structure was used to calibrate convolution and deconvolution processes by studying the spatial variation of motions (Power et al. 1986; Çelebi et al. 1992). Inverse analysis schemes was developed (Seed et al. 1988; Zeghal and Elgamal 1994; Elgamal et al. 1995; Elgamal et al. 1995; Zeghal et al. 1995; Chang et al. 1996; Glaser and Baise 2000; Harichane et al. 2005) to identify dynamic soil behavior, such as shear wave velocity and resonant frequencies. Using downhole array data in the Los Angeles basin, Assimaki et al. (2008) and Li and Assimaki (2010) developed stochastic models of elastic and nonlinear dynamic soil properties. In addition, various novel techniques, such as SUMDES (Li et al. 1998) and SelfSim (Tsai and Hashash 2009), were applied to perform ground response analysis at the Lotung downhole array site (Chang et al. 1989; Chang et al. 1990).

1.3.2 Recorded Data from Bridge Instrumentation

For over two decades, strong motion sensors have been deployed on Caltrans bridges and nearby free-field/downhole sites (Hipley and Huang 1997), through the joint efforts of the California Department of Transportation (Caltrans) and the California Geological Survey (CGS). The recorded data sets along with system identification techniques are permitting the evaluation of the bridge and surrounding ground seismic responses (Wilson 1986; Wilson and Tan 1990; Werner et al. 1994).

Numerous works on identification of structural systems utilizing recorded motion have been conducted to estimate the vibration properties of bridges and to elucidate the effects of the soil-structure interaction. For example, the seismic characteristics of the heavily instrumented Meloland Road Overpass have been evaluated with various identification methodologies (Werner et al. 1987; Werner et al. 1994; Kwon and Elnashai 2008; Mosquera et al. 2012). Fenves and DesRoches (1994 and 1995) evaluated the response of the Northwest Connector during the Landers and Big Bear earthquakes in 1992 based on an extensive strong motion instrumentation network. With these invaluable recorded data sets, relative bridge deflection, modal frequencies, and mode shapes can be identified (Şafak 1991; Arici and Mosalam 2000; Arici and Mosalam 2003; Kim and Stewart 2003), and our understanding of soil-structure interaction (SSI) effects has been further advanced (Crouse and Hushmand 1989; Spyrakos 1990; Goel and

Chopra 1997; Hipley et al. 1998; Chaudhary et al. 2001; Van Den Einde et al. 2004; Pandey et al. 2012; Shamsabadi and Taciroglu 2013; Shamsabadi et al. 2014).

1.4 Current Approaches for Simulation of Ground-Foundation Systems

It has been shown that the dynamic behavior of the surrounding soil and supporting foundations has a significant influence on the seismic response of the bridge superstructure (Zhang 2006; Zhang et al. 2008). As such, many modern design standards and recommendations have included provisions to consider the contribution of SSI effects (ASCE 2010). In general, the configurations of pile groups may vary along a long-span bridge. This makes it impossible to perform full-scale experiments for all employed pile groups. Therefore, numerical simulation can become a main useful tool to predict the dynamic foundation response for large bridge.

As discussed in section 1.1, it is not feasible to employ a FE model including every individual pile and surrounding soil. To simplify the computational simulation procedure, a wide variety of approaches using an equivalent substructure (representing the Ground-Foundation system) have been proposed. Broadly, these methods can be classified into two categories: 1) soil springs (p-y curves) approach or 2) foundation matrix approach.

The design procedure for bridge foundations in industry mainly relies on the soil springs approach (e.g., Caltrans 2012a). In this procedure, the pile is modeled as linear elastic beam elements and the interaction between soil and foundation is modeled with nonlinear soil springs (details in section 1.2.3, Figure 1.2).

To further simplify the numerical model, the foundation matrix approach is proposed using a 6×6 stiffness matrix to replace the pile foundation and to reduce the degrees of freedom for the entire system. In 1986, Lam and Martin proposed this approach for single pile analysis, where the pile is modeled with linear elastic beam elements, and the interaction between the pile and the surrounding soil is modeled by nonlinear force-deflection relationships (p-y, t-z and q-z curves). Based on a force (moment) vs. deflection (rotation) curve, a tangent or secant modulus for pile head is computed which is assumed to be equal to the pile head stiffness. Later, Lam et al. (1991) developed a simpler method using charts as a function of soil reaction and flexural rigidity (EI) to obtain lateral and rotational pile-head stiffness. However, the vertical pile-head stiffness, which is critical for estimating rotational stiffness of the pile group, was not computed. Novak (1991) estimated the 6×6 pile-head stiffness matrix using the computer program PILAY for single piles and program DYNA for pile groups. The stiffness k_{ij} term is defined as the amplitude of the force (or moment) that has to be applied to the pile head in order to generate a unit displacement in the specified direction (Novak 1991). The concept of translational and rotational stiffness is illustrated in Figure 1.3. Norris et al. (1991) investigated the lateral and vertical-rotational stiffness of pile foundations. Nonlinear uncoupled lateral and vertical-rotational pile group stiffness, which are displacement or rotation dependent, were evaluated via p-y and t-z analyses. To perform a linear dynamic analysis for a bridge, a series of iterations were undertaken to choose the boundary element spring stiffness that is compatible with the resulting relative displacements or rotations. The lateral stiffness of a pile group is derived from that of the average pile in the group multiplied by the number of piles. In addition, a number of issues (pile cap contribution, group effect, and head fixity) are considered when evaluating the laterally loaded pile stiffness. Capabilities and shortcomings are discussed based on the failure analysis of the Cypress Street Viaduct (Norris et al. 1993).

Figure 1.4 (Gazetas et al. 1993) provides an overview of the earthquake design idea for pile foundations using the substructuring technique. In the MCEER report (Lam and Law 2000), a procedure for the foundation matrix approach was described in detail. Two steps are involved in this technique to simplify the foundation in the global bridge model: (1) linearization of the p-y curves by performing pushover analysis of the single pile to a representative displacement level expected during the earthquake, and (2) construction of the condensed stiffness matrix (Lam and Law 2000; Lam et al. 2007).

The stiffness matrix obtained using the method above has the disadvantage that the group effect, the stiffness of the pile cap and gapping issues are not easily implemented. Therefore, a more rigorous but efficient methodology is needed with consideration of the coupling effect between the super-structure and pile foundation.

1.5 Objectives and Scope

Recognizing that soil-structure interaction affects the structure's seismic response, numerous investigations have been conducted to advance the related simulation techniques. While remarkable success has been achieved, there are still challenges and notable unsolved issues (such as soil-pile separation, pile group effects, etc.). The objective of the research presented in this dissertation is to further advance the procedures for numerical simulation of soil-foundation-structure systems by conducted the following studies:

- Large-scale 3D nonlinear finite element analyses of pile groups are performed to provide insights concerning laterally loaded pile response. Pile group effects, load distribution among the piles and permeability effects (for saturated cohesionless soils) on the overall ground-foundation system are discussed;
- Strong motion data of two instrumented bridges in Eureka, CA and one adjacent downhole array collected through the joint efforts of the California Strong Motion Instrumentation Program and Caltrans are documented and analyzed;
- Seismic response of the downhole site and the two instrumented bridges during the observed earthquake events is evaluated using system identification techiniques;
- FE models for the two bridges (Samoa Channel Bridge and Eureka Channel Bridge) are developed and calibrated;
- Optimization of equivalent base springs is carried out to document the corresponding exerted lateral pile-group resistance, and explore the salient characteristics of the ground-foundation system.

1.6 Organization

The dissertation has been organized into 9 chapters in the following manner:

This chapter presented general information regarding the effects of SSI on Ground-Foundation-Bridge systems. Past research efforts on pile-soil interaction are briefly reviewed. Current practice for strong motion data analysis and ground-foundation system simulation is discussed. Finally, the objectives, research scope and organization of the dissertation are included.

Chapter 2 presents the behavior of a laterally loaded 3×3 pile group at different pile-spacing scenarios with comparisons to the corresponding single pile response. Load distribution among the piles and group efficiency under linear and nonlinear soil behavior representations are investigated.

In Chapter 3, a 3D FE model representing salient characteristics of the pile-foundation at the Dumbarton Bridge (California) Pier 23 is developed. The behavior of this large (8×4) pile group foundation supporting a high-clearance bridge deck is addressed. For seismic response evaluation, push-over combined axial/lateral loads along with a substantial moment are imposed. Primarily, pile group behavior in nonlinear soil with and without a soil model tension-cutoff logic is discussed. Distribution of load within the pile and the group interaction effects are examined.

Chapter 4 attempts to show that the relation between soil permeability and loading rate can be among the critical factors controlling stiffness of the soil-pile system. The response of a laterally loaded single pile embedded in a range of saturated soils from gravel-like to clay-like permeability is investigated based on a nonlinear 3D FE model.

In Chapter 5, the Eureka Geotechnical Downhole Array installed by the California Strong Motion Instrumentation Program (CSMIP) in cooperation with Caltrans is employed to identify the site dynamic characteristics with the help of system identification techniques (e.g., cross-correlation and response spectral analysis). FE based site seismic response analysis is performed using the identified soil parameters.

Chapters 6 - 8 discuss two instrumented bridges in California, the Samoa Channel Bridge and Eureka Channel Bridge, which have strong motion records available at a selected pile-group (each), in close proximity to the nearby Eureka Geotechnical Array.

With the aid of system identification and optimization approaches, seismic response of the pile foundation and the Samoa/Eureka Channel bridges is evaluated.

Chapter 9 summarizes the conclusions from the preceding chapters. The current limitations of numerical simulation for soil-structure interaction are discussed. Finally, recommendations for related future research studies are proposed.

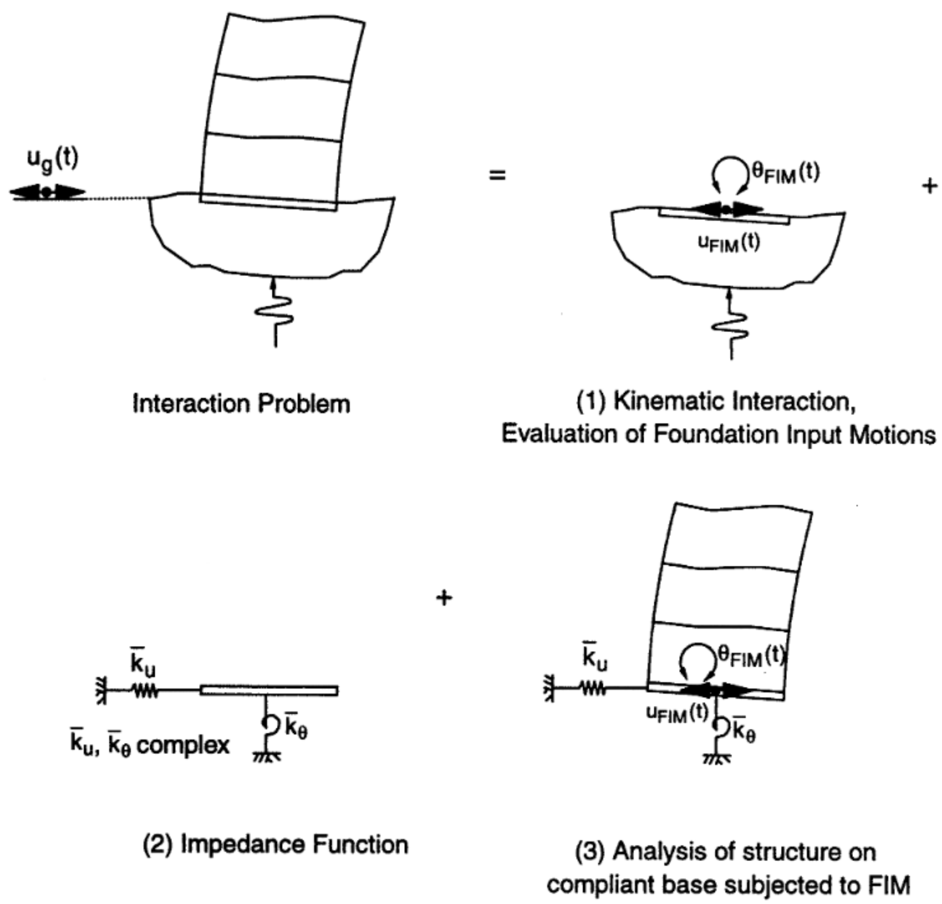

Figure 1.1: Substructure approach to analyze the SSI problem (from Stewart et al. 1998)

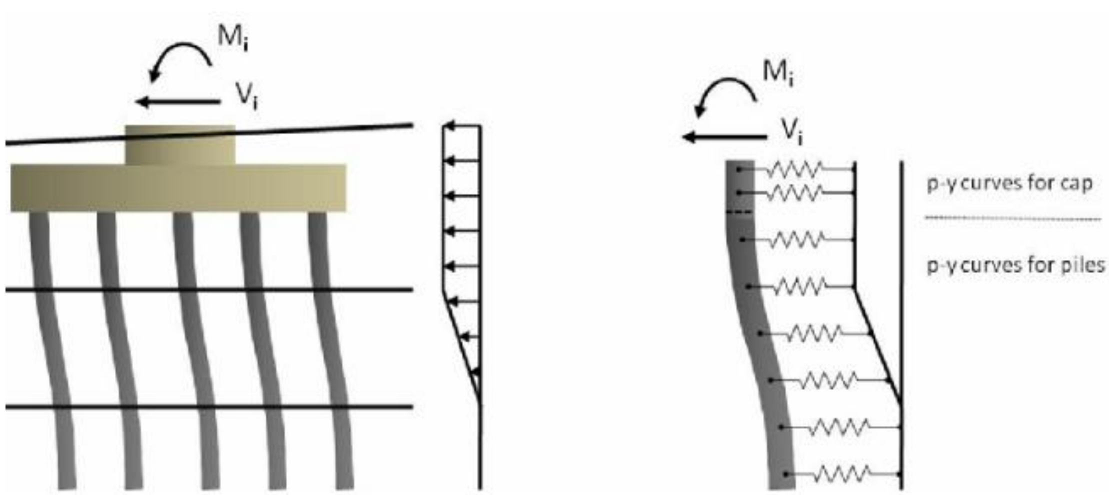

Figure 1.2: Analysis procedure using an equivalent single pile and p-y curves (from Caltrans 2012a)

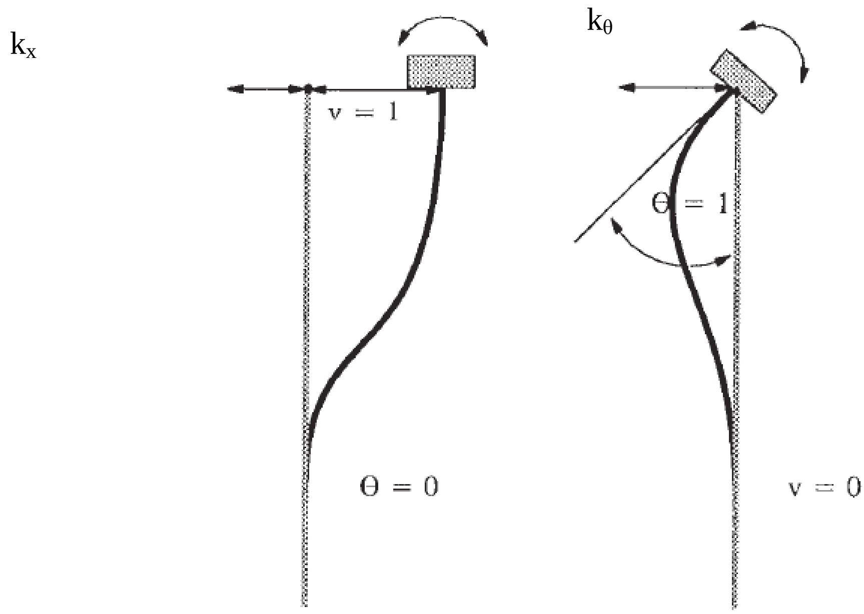

Figure 1.3: Translational and rotational pile group stiffness matrix logic (from Novak 1991)

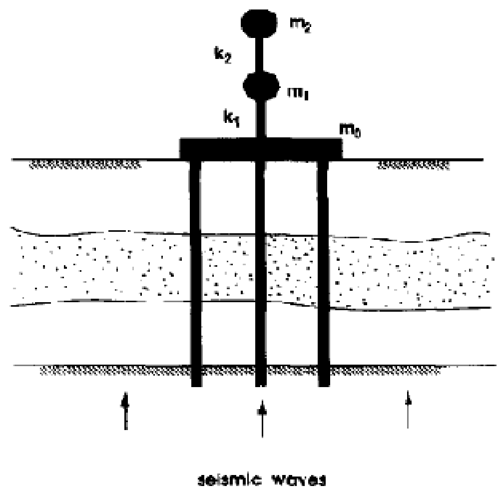

(a)

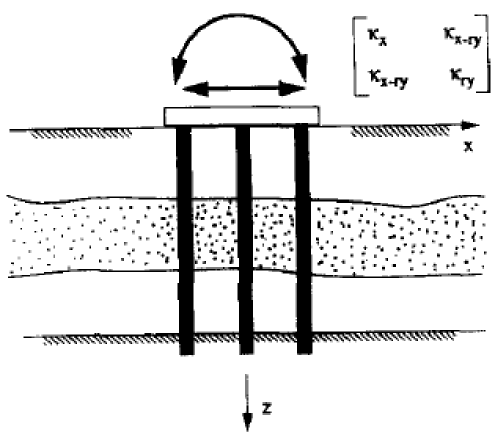

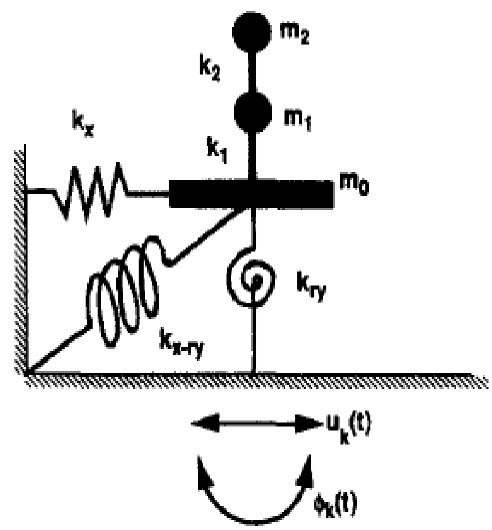

(b) (c)

Figure 1.4: Seismic soil-pile-foundation-structure interaction: (a) the whole system, (b) Pile group dynamic impedances and (c) superstructure inertia response (from Gazetas et al. 1993)

Chapter 2

Three-Dimensional Finite Element Modeling of Pile and Pile Group System Response

Advancements in high-speed computing and developments in material modeling techniques are increasingly allowing for large-scale three-dimensional (3D) linear and nonlinear geotechnical finite-element (FE) simulations. The open-source computational platform OpenSees provides such 3D simulation capabilities for static/seismic ground-foundation analyses. With the aid of the graphical user interface OpenSeesPL (http://cyclic.ucsd.edu/openseespl), 3D computations for pile and pile group studies are greatly facilitated. Using this FE framework, an effort is made to capture key features associated with lateral loading on piles and pile groups. For that purpose, the behavior of a laterally loaded 3×3 pile group at different pile-spacing scenarios is presented first, and contrasted with that of the corresponding single pile scenario. Response under linear and nonlinear soil behavior representations is discussed. Lateral pile-group performance and efficiency considerations are investigated. All studies are presented within a scope that highlights current modeling capabilities and directions for further research.

2.1 Introduction

Soil-structure interaction (SSI) plays a major role in the response of structures subjected to earthquakes (e.g., Wolf 1985; Mylonakis and Gazetas 2000). The analysis of a pile under lateral loading is complicated since the soil reaction at any point along a pile is a function of pile deflection. The pile deflection in turn depends on the soil resistance. The conditions of equilibrium and compatibility have to be satisfied for the ground-pile system (Amiri 2008). Therefore, numerical FE investigations have been conducted for piles and pile groups to further understand the involved SSI mechanisms within an environment that attempts to represent the actual involved geometric configuration (Muqtadir and Desai 1986; Brown and Shie 1990; Wakai et al. 1999; Yang and Jeremic 2003; Chae et al. 2004; Maheshwari et al. 2004; Maheshwari et al. 2004; Peng et al. 2004; Dodds 2005; Yang and Jeremic 2005; Maki et al. 2006; Uzuoka et al. 2007; Elgamal et al. 2008; Elgamal and Lu 2009; Elgamal et al. 2009; Lu et al. 2010).

For seismic pile-ground analyses, advanced 3D nonlinear constitutive material models that are applicable to arbitrary cyclic loading scenarios are needed (e.g., Yang 2000; Yang and Elgamal 2003). In this regard, the open-source platform OpenSees (Open

System for Earthquake Engineering Simulation) of the Pacific Earthquake Engineering Research (PEER) Center (Mazzoni et al. 2006) allows for such capabilities and is employed herein. Developed for 3D pile-ground analyses, the user friendly interface OpenSeesPL is utilized to facilitate the pre- and post-processing efforts (Lu et al. 2010, http://cyclic.ucsd.edu/openseespl/).

Using this numerical analysis framework, this chapter aims to present a number of pilot investigations related to the response of piles and pile groups. Soil is represented by three alternative idealizations, in the form of linear as well as nonlinear (undrained clay-type) models, with and without a tension cut-off logic.

Additional details of the employed analysis framework are presented briefly below. Influence of pile group spacing on basic system behavior mechanisms is then illustrated using a relatively simple 3×3 configuration. Distribution of load between the piles is analyzed and the group interaction effects are discussed. As such, it is important to note that FE mesh refinement is among the important considerations behind overall accuracy. In this regard, effort has been made throughout to develop and employ adequately refined FE meshes for the purpose of the above-mentioned pilot investigations. Along with the insights gained from this study, the reported results highlight the current analysis framework capabilities and range of potential applications.

2.2 Computational Framework

The Open System for Earthquake Engineering Simulation (OpenSees), an open-source platform developed for simulation of structural and geotechnical systems subjected to seismic load (http://opensees.berkeley.edu, Mazzoni et al. 2006) is employed throughout. The reported pre- and post-processing scenarios were generated by the user friendly interface OpenSeesPL (Figure 2.1) which allows for: i) convenient generation of the mesh (for surface load/footing, single pile, or pile group) and associated boundary conditions, ii) simplified selection of soil/pile linear/nonlinear (e.g., Yang et al. 2003; Elgamal et al. 2008) material modeling parameters (i.e., the FE input file), iii) execution of the computations using the OpenSees platform, iv) single pile and pile group simulations under seismic excitation as well as push-over studies in prescribed displacement or prescribed force modes, v) study of various ground modification scenarios by appropriate specification of the material within the pile zone (Elgamal et al. 2009b, Rayamajhi et al. 2012), and vi) graphical display of the results for the footing/pile and the ground system (Elgamal et al. 2009a).

2.3 Lateral Pile Response Calibration

Elgamal and Lu (2009) employed the analytical elastic solution of Abedzadeh and Pak (2004) to develop a satisfactory 3D FE model for the purpose of lateral pile response studies. Details of this calibration effort are described briefly in this section.

2.3.1 Configuration of the Pile-Soil System

A circular steel-pipe free-head pile with steel Young's Modulus E_p = 199.95 GPa, outer radius (a) of 203.20 mm and wall thickness (h) of 20.32 mm was studied (cross-sectional moment of inertia $I = \pi a^3 h = 5.36\times10^{-4}$ m^4). The pile length (l) was selected to be 10.15 m in order to numerically model the analytical elastic solution (case of l/a=50). The pile was fully embedded in a homogeneous isotropic linearly elastic soil domain with submerged unit weight $\gamma' = 9.87$ kN/m^3, shear modulus of soil $G_s = 5.50\times10^4$ kPa, and Poisson's ratio $\nu_s = 0.25$ (i.e., Bulk modulus $B_s = 9.17\times10^4$ kPa). In this linear-response calibration scenario, a horizontal load H of 140.12 kN (31.5 kips according to Elgamal and Lu 2009) was applied to the free pile head (at ground surface).

2.3.2 Finite Element Model

In view of symmetry, a half-mesh was employed as shown in Figure 2.2 (lateral load was applied along the longitudinal direction of this mesh). Both 8-node and 20-node brick elements were used to model the soil domain. The pile was modeled by beam-column elements, in order to easily view axial loads, moments, and shear forces. Within this configuration, essentially rigid beam-column elements (links) were used to represent the pile cross-sectional spatial domain (diameter) and the interface with the surrounding 3D soil elements. As such, these links were defined to be 10^4 times stiffer (both axially and flexurally) than the pile elements. Away from the pile centerline beam-column elements, the edge nodes of these rigid links are tied to the coincident nodes of the adjacent 3D soil brick element in the three translational degrees of freedom (Law and Lam 2001; Elgamal et al. 2008; Rollins and Brown 2011). In total there were 2900 brick elements, 20 beam-column elements, and 189 rigid links in this FE model (Figure 2.2).

The boundary conditions of the model were defined as: i) Base of the ground domain was fixed in the longitudinal (x), transverse (y), and vertical (z) directions, ii) Left, right and back sides of the mesh were fixed in the x and y directions, and iii) Plane of symmetry was fixed in the transverse (y) direction. A satisfactory numerical solution was obtained for a mesh of 158.19 m in lateral extent and 20.12 m in depth (i.e., the bottom of the soil domain was 9.97 m below the pile tip). The numerical pile deflection profile obtained using OpenSeesPL is shown in Figure 2.3 along with the analytical elastic solution (Abedzadeh and Pak 2004).

2.3.3 Nonlinear Soil Modeling

In addition to the elastic soil simulations, a multi-surface pressure-independent J_2 plasticity model (Von-Mises) was employed (undrained clay-type soil material) to demonstrate the influence of nonlinear ground response (Figure 2.4). Response using this nonlinear model was also explored in the presence of a tension cut-off mechanism where shear strength vanishes upon occurrence of tensile effective confinement (Figure 2.4c). Along with the elastic properties of the calibrated model, cohesion c= 40.68 kPa in the range of a Medium Clay, was specified. Using a hyperbolic backbone curve model, the maximum shear strength was specified to occur at an octahedral shear strain (γ_{max}) of 3%.

2.4 Modeling of Pile Group Effects

2.4.1 Benchmark Lateral Response of Single Pile

Numerical single pile simulations for linear, nonlinear, and nonlinear with tension cut-off soil cases were conducted first to provide a reference for the pile group behavior comparison. A lateral load (H) was applied to the pile head (free head condition), located essentially at the ground surface, in 40 increments up to a final load of 420.36 kN (94.5 kips according to Elgamal and Lu 2009) to clearly demonstrate the effects of nonlinear soil response.

Figure 2.5 illustrates the influence of nonlinear soil response on the pile head computed deflections. As the load increases, the difference in pile head deflection becomes more pronounced. At maximum applied load, the nonlinear soil tension cut-off scenario appears to be nearing ultimate capacity. In this case, the back-soil zones (adjacent soil that the pile is moving away from at any depth) provide minimal support, leading to a marked reduction in overall lateral resistance.

The corresponding pile deflection, bending moment, and shear force profiles are shown in Figure 2.6. Compared to the linear case, the nonlinear scenarios displayed: i) a significant increase in lateral pile head displacement and maximum moment, and ii) a clear increase in depth to the location where maximum moment occurs. The soil nonlinear yielding response and the tension cut-off logic (when activated) decrease lateral soil resistance, and thus account for these mechanisms.

2.4.2 3×3 Pile Group Configuration

Lateral resistance may be significantly reduced for a closely spaced pile group (Rollins et al. 2006). ASCE (2010) suggested that pile group effects on pile nominal strength shall be included for closed spaced pile group (8Dia or less center-to-center spacing in the direction of lateral force for lateral nominal strength; 3Dia or less for vertical nominal strength), where Dia is the pile diameter. In order to model this mechanism and explore the resulting pile group efficiency, the behavior of a 3×3 pile group (Figure 2.7) at different pile-spacing configurations was studied (based on above single pile scenario). The 3×3 pile group (free head condition rigidly connected by a pile cap) was subjected to a horizontal load (H) of 3,783.21 kN, nine times that of the single pile case.

The pile group functionality implemented in the user-interface OpenSeesPL allows for convenient study of pile spacing effects. Up to about 6 hours of computational time was needed using a 3GHz CPU PC Desktop for the more challenging nonlinear soil cases with the tension cut-off logic activated (in terms of the needed number of iterations for convergence).

2.4.3 3×3 Pile Group Response

For representative pile spacing configurations (the tension cut-off case at maximum applied load), Figure 2.8 depicts the attained stress ratio (J_2 computed shear stress divided by failure stress counterpart). As such, the pile-group interaction mechanism is illustrated in terms of influence on the surrounding soil. At close pile spacing (3Dia), it is evident that the entire soil between the piles is highly stressed with more noticeable overall lateral translation (Lu et al. 2011). As the spacing increases, each pile is surrounded by an adequate soil domain (independent from the influence of surrounding piles).

Based on this logic, the peak-load displacement efficiency (deflection of single pile/deflection of pile group) as a function of pile spacing (Figure 2.9) displays higher values with the increase in pile spacing. When the spacing reaches 10 Dia, the pile group efficiency approaches its maximum (1.0) for the tension cut-off soil condition. At close pile spacing, it is of interest to note that linear case shows the highest displacement efficiency (Figure 2.9).

As the pile spacing increases, this efficiency increases for all cases. However, the rate of this increase appears to be highest for the nonlinear case with tension cut-off logic activated. On this basis, it may be inferred that (at the presented maximum load situation of Figure 2.9): a) closely spaced piles intensify nonlinear soil response in the immediate surrounding soil, further reducing the group efficiency compared to their single pile counterpart, and b) as spacing increases, nonlinear soil behavior tends to localize the influence of each pile on the surrounding soil domain, gradually leading to increased pile-group efficiency compared to the linear soil case (i.e., liner behavior tends to engage a larger domain of the ground around each pile).

Figure 2.10 displays salient response characteristics as a function of the level of applied load and resulting pile head displacement. Load-deflection curves (Figure 2.10a) clearly show that the pile group (PG) undergoes considerably more displacement than the single pile (SP) under the same average load/pile (Brown et al. 1987; McVay et al. 1995). This is particularly evident (Figure 2.10a) in the highly nonlinear tension cut-off case. As spacing increases, the pile group response tends toward the single pile situation (Figure 2.10a).

In Figure 2.10b, pile group displacement efficiency is seen to change with the level of applied lateral load (the nonlinear soil situations). At close pile spacing, efficiency decreases as the load increases, as the influence zone of each pile overlaps with the other thus causing higher levels soil shear stress and yielding (Figure 2.8). As the pile spacing increases, the opposite occurs, and group efficiency is seen to increase with the level of applied load. Apparently, for the larger pile spacing scenarios, further localization of the pile influence on the surrounding soil occurs with the increase in nonlinear soil response, resulting in a corresponding increase in efficiency. As such, it may be concluded that group efficiency is dependent on the level of applied load, soil nonlinearity, and pile group spacing (McVay et al. 1998). It may increase or decrease as the level of applied load increases depending on spacing.

Efficiency may be assessed alternatively based on sustained force by the single pile and the pile group at equal levels of lateral displacement. For the case under discussion, this force-based efficiency (Average load per pile in group / Single pile load) as shown in Figure 2.10c reveals that initially, the group efficiency increases markedly as deflection increases (the nonlinear soil scenarios). At such relatively low levels of deflection, compared to the pile group with overall large lateral dimensions, the single pile appears to cause higher levels of stress concentration and soil yielding in the immediate surrounding ground. For large spacing (the shown 7Dia scenario), this effect remains evident as deflection continues to increase with the efficiency sustained at high values above about 0.9. For close spacing (the shown 3Dia scenario), efficiency shows a more noticeable gradual decrease with the increase in deflection due to the increased soil nonlinearity and yielding around the entire pile group.

Lateral loads carried by each pile are shown in Figure 2.11 for the 3Dia and 7Dia spacing scenarios, and bending moment profiles are presented in Figure 2.12. For the linear and nonlinear soil cases, the front (3 and 6) and back (1 and 4) piles show similar load patterns. Being on the outer edges, away from the influence of other piles, the corner piles (4 and 6) are seen to shoulder a higher portion of the load (Figure 2.11). Upon activation of the tension cut-off mechanism, the front corner pile (6) shoulders a higher portion of the overall load compared to the back corner pile (4). This is especially obvious in the closely-spaced 3Dia pile group scenario. As the pile spacing increases, a more uniform loading sharing pattern takes place.

2.5 Conclusion

From the results of this 3x3 pile-group simulation, the following response patterns were observed:

1. Displacement efficiency of the pile group dropped to as little as about 27% (Figure 2.10b) for close pile-spacing scenarios (3Dia spacing tension cut-off case). Such decrease in efficiency would be expected as the immediate soil regions providing resistance around each pile heavily overlap.

2. For such close spacing, displacement efficiency of the nonlinear and tension cut-off soil cases was lower than that of the linear counterpart. For these nonlinear cases, the overlapping influence of each closely-spaced pile results in increased loads and yielding of the immediate surrounding soil.

3. As spacing increased, group displacement efficiency becomes higher and more rapidly so in the nonlinear soil cases. This observation implies that the loaded zone of influence around each pile decreases with the level of nonlinearity in soil response.

4. The center pile (pile 2 in Figure 2.11 and Figure 2.12) shoulders a lower share of the overall load. Soil within this zone translates laterally due to the action of all surrounding piles, a mechanism that reduces available resistance to the center pile translation (Scott 1981).

5. The mechanism of tension cut-off plays a major role in dictating the analysis outcome. Along with reduced overall lateral stiffness, the front piles shoulder a higher

portion of the overall load, and experience higher bending moments and shear forces (Figure 2.11 and Figure 2.12).

2.6 Acknowledgements

Chapter 2 of this dissertation contains material from the published proceedings of the Geo-Congress 2014 titled “Three-Dimensional Finite Element Modeling of Pile and Pile Group System Response” with authors Ning Wang, Ahmed Elgamal and Jinchi Lu (2014). The dissertation author is the first author of this paper.

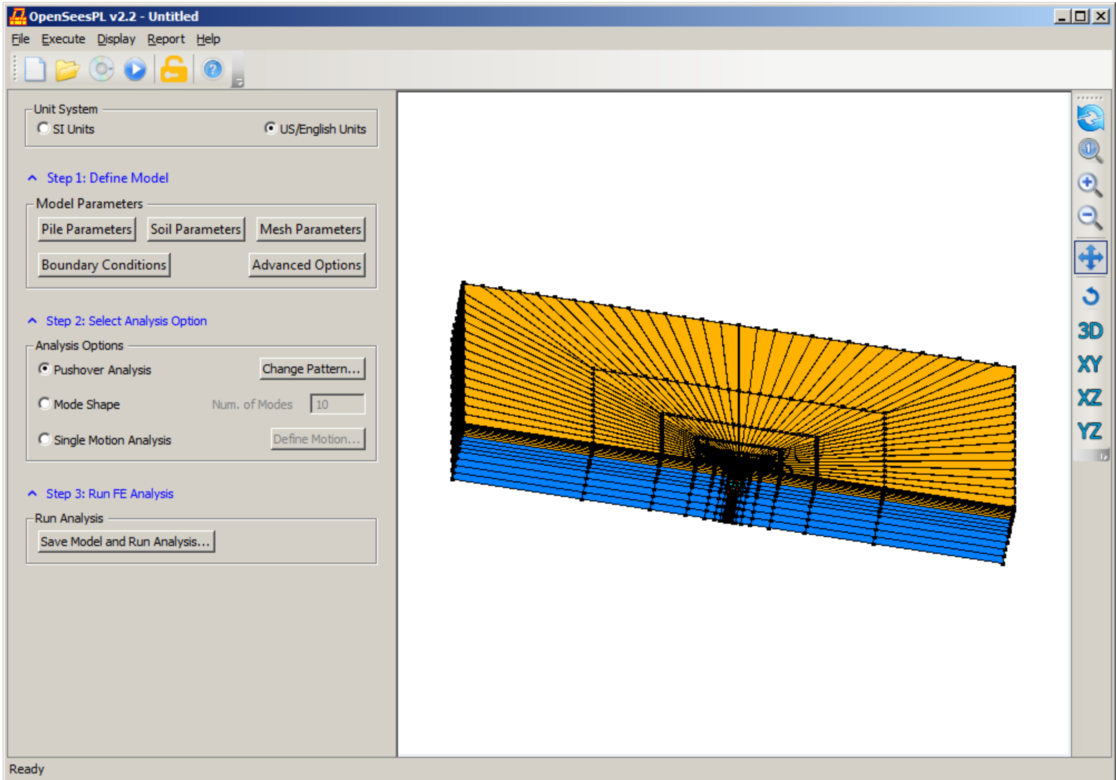

Figure 2.1: OpenSeesPL user interface (Lu et al. 2006, http://cyclic.ucsd.edu/openseespl/)

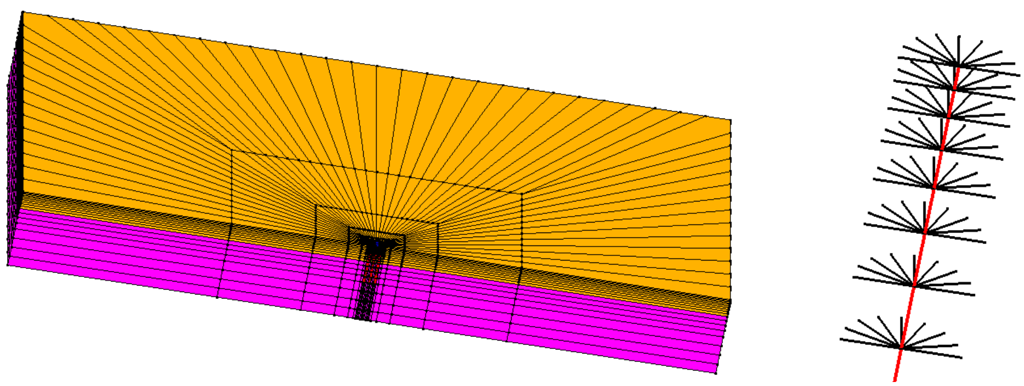

(a) (b)

Figure 2.2: Employed half mesh configuration (due to symmetry) for the single pile simulation (a) 3D isometric view (b) illustration of pile model with rigid links

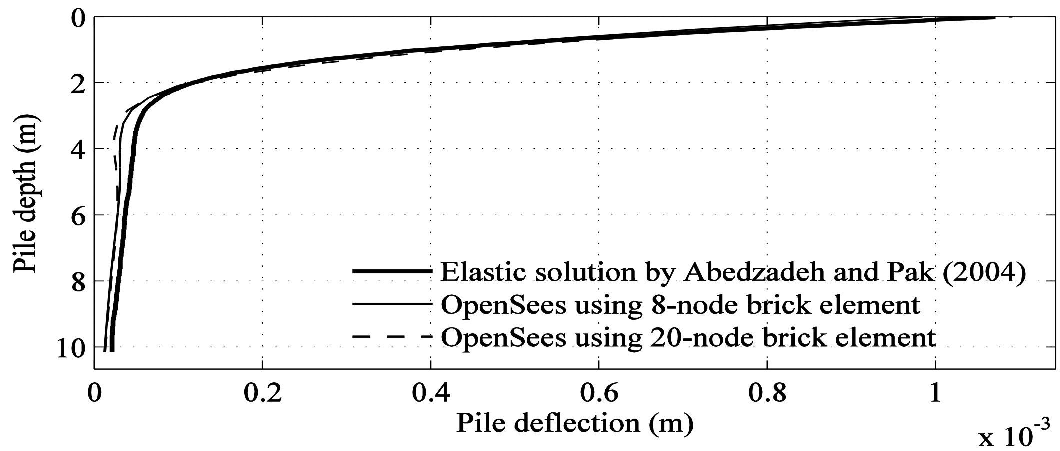

Figure 2.3: Comparison of pile deflection profiles for the linear-response calibration scenario (Elgamal and Lu 2009)

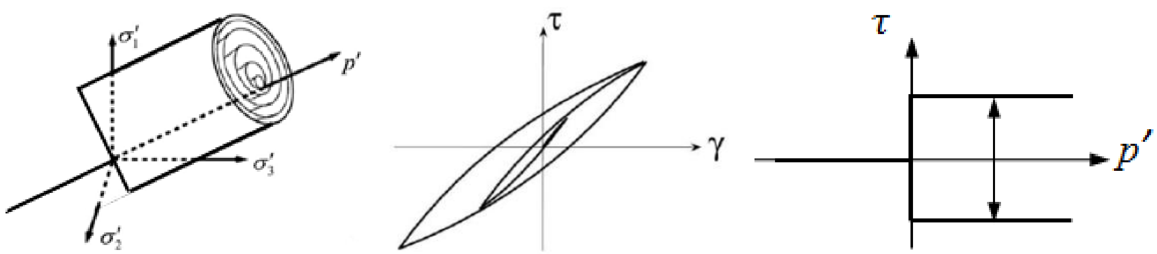

(a) (b) (c)

Figure 2.4: Multi-surface plasticity J_2 model: (a) Von Mises multi-surfaces, (b) Hysteretic shear response (Elgamal et al. 2008), and (c) illustration of tension cut-off logic

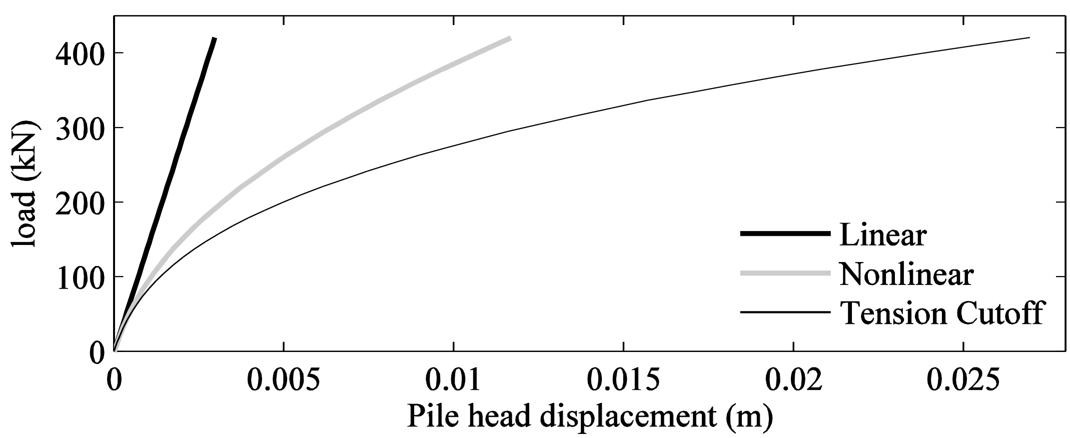

Figure 2.5: Computed pile head load-deflection curves for the single pile simulation

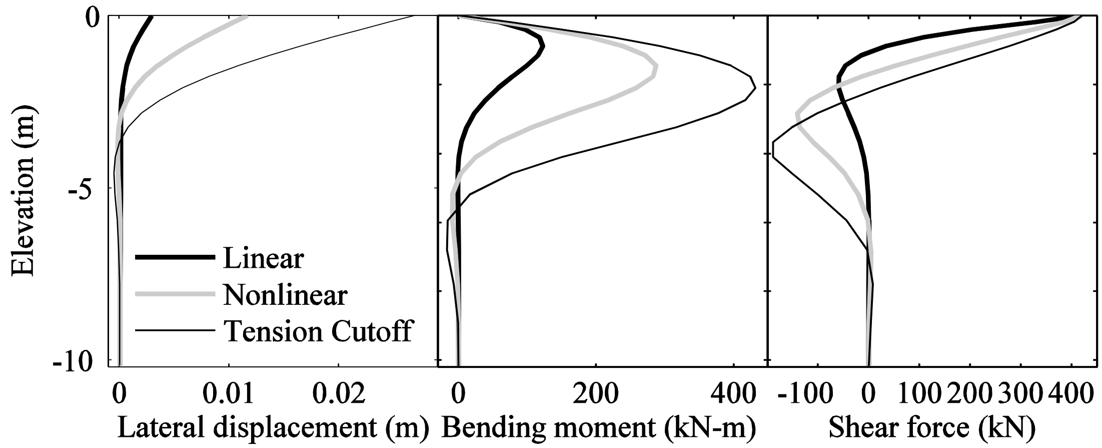

Figure 2.6: Pile deflection, bending moment and shear force profiles for the linear, nonlinear, and nonlinear with tension cut-off soil cases at the maximum applied lateral load of 420.36 kN

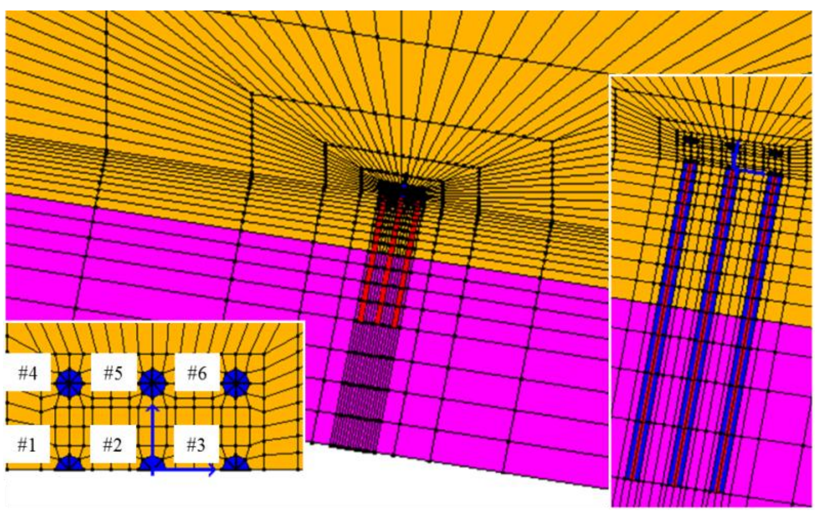

Figure 2.7: Finite element mesh (half-mesh configuration) employed for 3×3 pile group (3Dia spacing case) with pile numbering scheme and close-up of the pile group

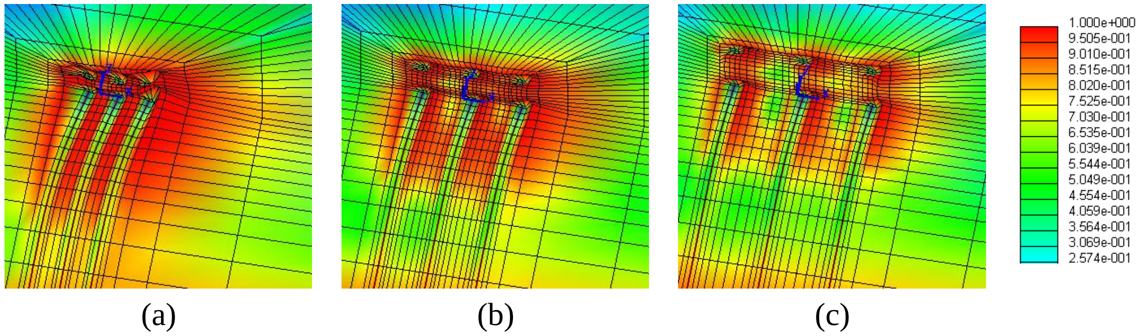

Figure 2.8: Tension cut-off case: stress ratio for 3×3 pile group at the maximum lateral load (displacements as shown are magnified by a factor of 8): (a) 3Dia pile spacing, (b) 5Dia pile spacing, and (c) 7Dia pile spacing

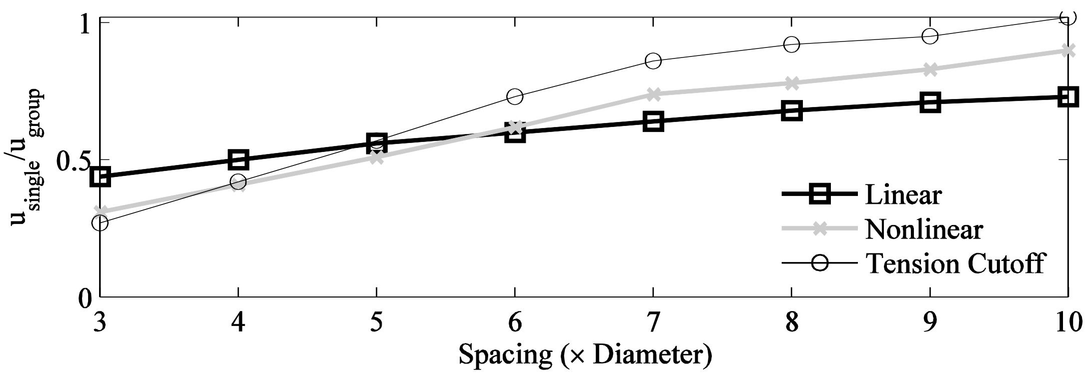

Figure 2.9: Pile head displacement efficiency of the 3×3 pile group for different spacing under the maximum applied lateral load of 420.36 kN per pile (the single pile head deflection is 0.003 m, 0.012 m, and 0.027 m for the linear, nonlinear and nonlinear with cut-off cases respectively)

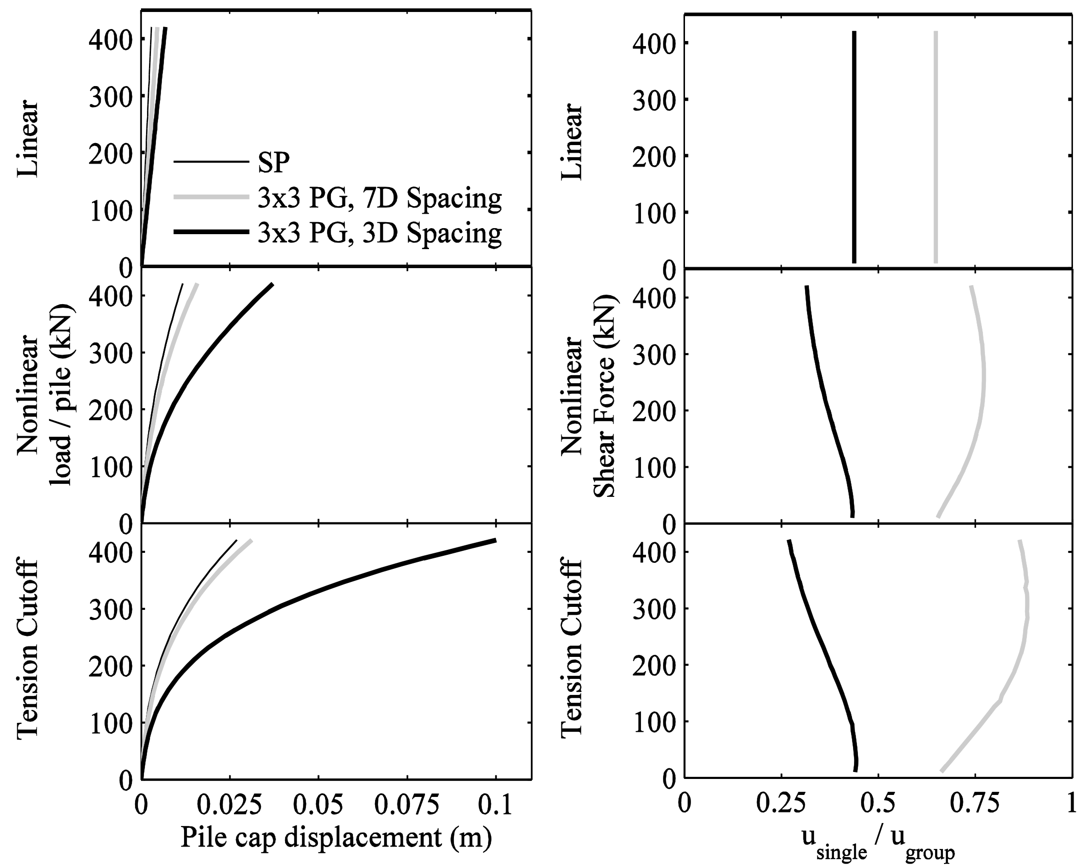

(a)

(b)

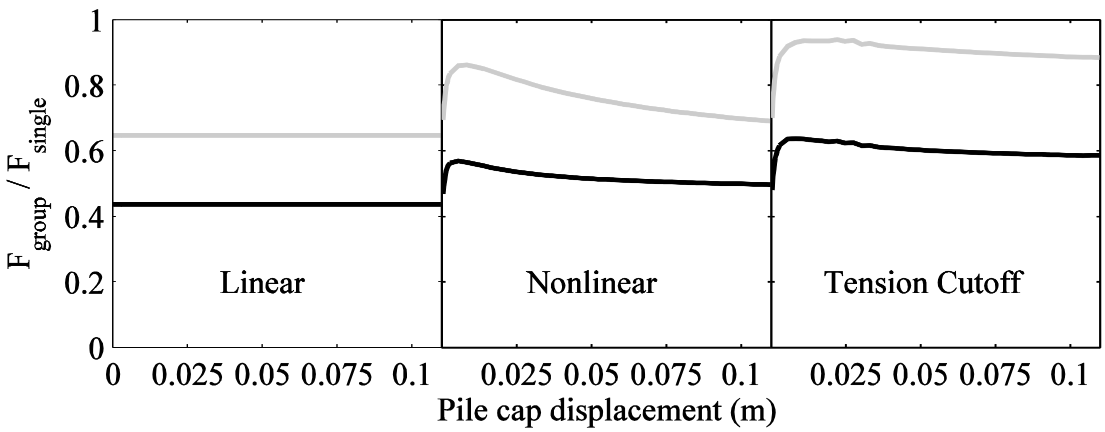

(c)

Figure 2.10: Linear, nonlinear, and nonlinear with tension cut-off cases: (a) Load-deflection curves, (b) corresponding displacement efficiency, and (c) load or force-based efficiency

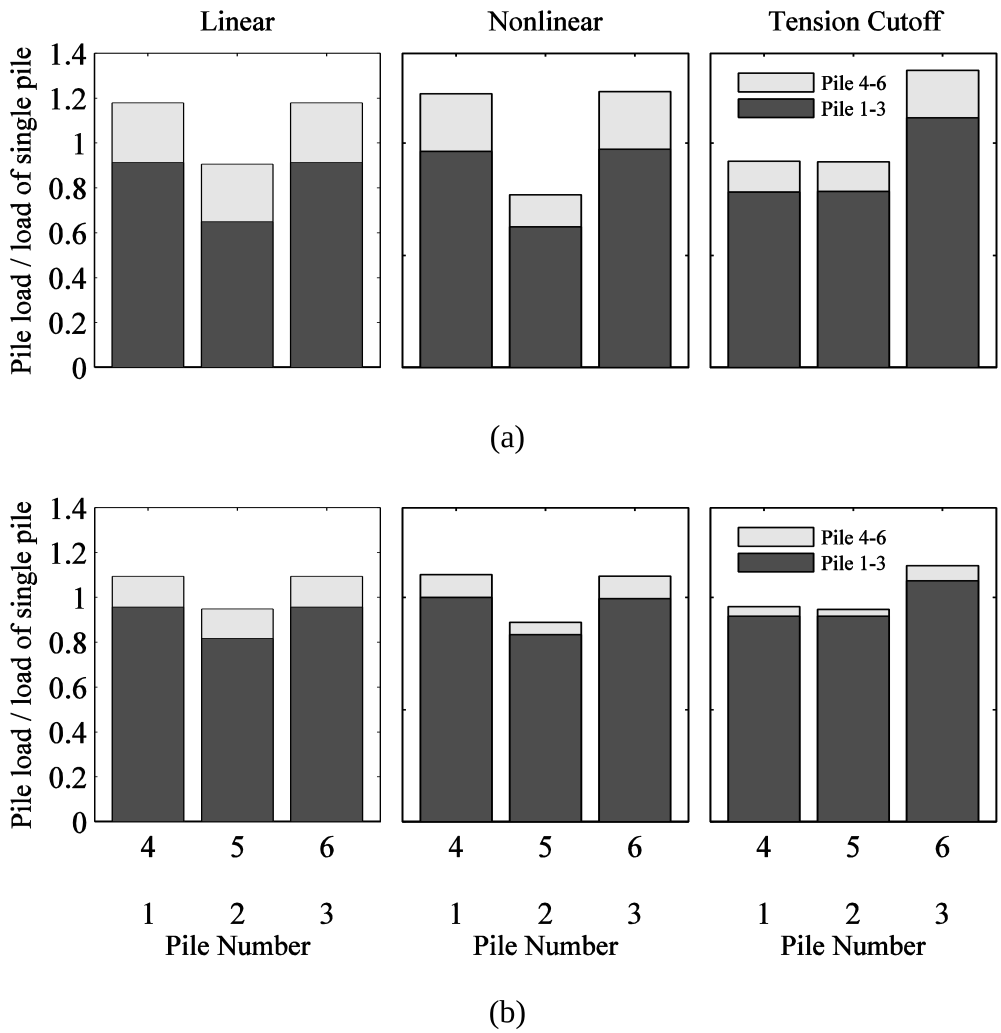

Figure 2.11: Distribution of pile head lateral force at the maximum applied load for (a) 3Dia pile spacing and (b) 7Dia pile spacing (Pile numbers are shown in Figure 2.7)

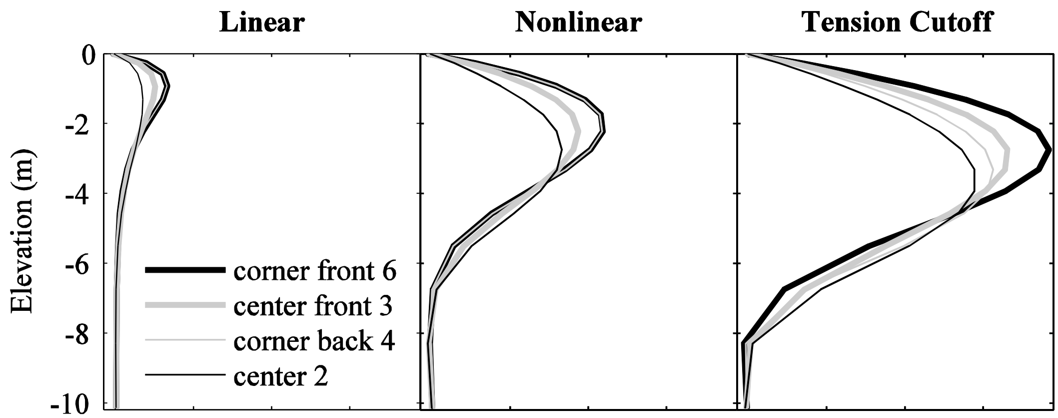

(a)

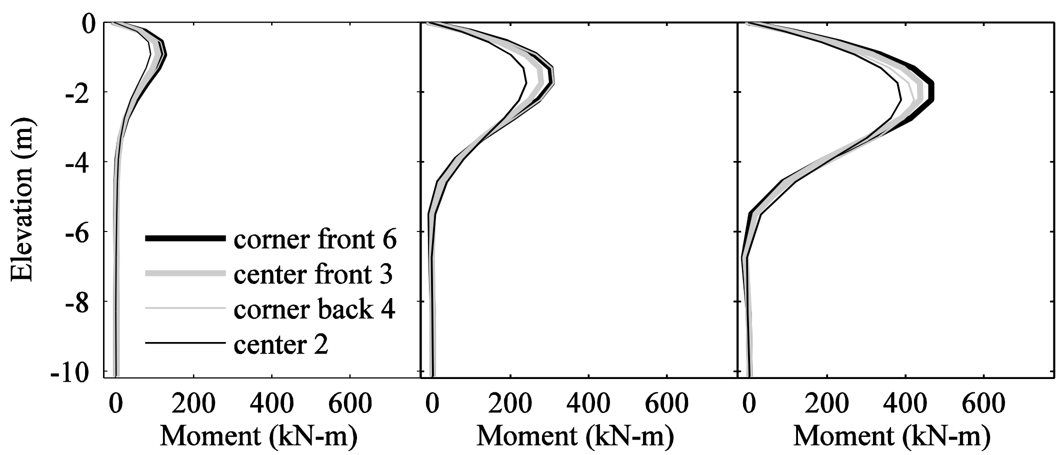

(b)

Figure 2.12: Bending moment profiles at maximum load in the 3×3 pile group of Figure 2.7 for (a) 3Dia pile spacing and (b) 7Dia pile spacing

Chapter 3

Lateral Load on a Large Pile Group

Practice shows that the analysis of laterally loaded pile foundations is critically important. For years, numerous experimental, theoretical and numerical investigations have been conducted to predict the behavior of such systems. In this chapter, a model that represents salient characteristics of the Dumbarton Bridge (California) Pier 23 pile-foundation geometric configuration is developed. The behavior of this large (8×4) pile group foundation supporting a high-clearance (for marine navigation) bridge deck is addressed. Primarily, pile group behavior in nonlinear soil with and without a tension-cutoff logic is discussed. Distribution of load within the pile group is analyzed and the group interaction effects are examined.

3.1 Introduction

In order to satisfactorily reproduce SSI effects computationally, it is often necessary to model a large domain of the soil surrounding the structure of interest. With the developments in material modeling techniques, linear and nonlinear three-dimensional (3D) finite-element (FE) methods are becoming a promising technique for understanding the involved SSI mechanisms. In particular, special attention is given to the soil-pile response mechanisms and the pile group interaction effects. Pressley and Poulos (1986) employed an axially symmetric model to study group effects. Brown and Shie (1990) conducted a series of 3D FE studies on the behavior of single piles and closely spaced pile groups. Wakai et al. (1999) studied the behavior of free- and fixed-head 3×3 pile groups based on model tests. Yang and Jeremic (2003) simulated the response of 3×3 and 4×3 pile groups in loose and medium dense sands and investigated the interaction effects for large pile groups.

This chapter presents a systematic 3D FE study of a large pile group under lateral loading, embedded into a nonlinear soil domain (with an implemented tension cut-off logic). The piles are modeled by beam-column elements, and rigid beam-column elements are used to model the pile size (diameter). For comparison, a representative single-pile reference simulation is also studied. For seismic response evaluation, push-over combined axial/lateral loads along with a substantial moment are imposed. The open-source computational platform OpenSees (Mazzoni et al. 2006) is employed to conduct the 3D FE analysis. In order to facilitate the pre- and post-processing phases, an user interface OpenSeesPL is employed (Lu et al. 2006; Elgamal et al. 2009).

3.2 General Information of Dumbarton Bridge Pier 23

3.2.1 Bridge Structure

The current Dumbarton Bridge (Figure 3.1) across the San Francisco Bay was opened to traffic in 1982 connecting city of Newark in Alameda County and East Palo Alto in San Mateo County. This 1.6-mile long multi-span bridge has six lanes (three in each direction) and an eight-foot bicycle/pedestrian pathway (http://www.asce.org). Dumbarton Bridge is a combination of three bridge types: 1) reinforced concrete slab approaches supported on multiple pile extension columns, 2) precast-prestressed concrete delta girders, and 3) steel box girders supported on reinforced concrete piers. Seismic evaluations of this bridge were conducted recently by Ke et al. (2007 and 2010) in which conventional p-y springs were used to represent the involved kinematic soil-pile interaction mechanisms at selected piers. The current retrofit strategy (completed in 2013) includes (Caltrans 2012b):

- Structural steel is being added to the bridge to strengthen it during the next large earthquake and allow for the installation of new seismic isolation bearings;
- The main bridge structure between piers 16-31 is raised approximately 5 inches for isolation bearings to be installed;
- The bridge piers are being widened with reinforced concrete to accommodate the new bearings;
- The bent caps are being extended and tied to retrofitted 48-inch diameter steel piles;
- 6 friction pendulum bearings installed at each pier to isolate the superstructure from the substructure during seismic events.

- Replacement of two existing deck joints with seismic joints at Pier 16 and Pier 31 to accommodate the increased freedom of lateral movement;
- The height of the footings of Pier 17 through 30 was increasing by adding a foot of concrete on top. Two feet of concrete and steel were added to each side of the pier caps between Pier 16 and 31.

3.2.1 Pile Group Configuration at Dumbarton Bridge Pier 23

The Pier 23 pile-group foundation is configured in an 8 × 4 arrangement with a longitudinal (the 8 piles direction) spacing of 2 pile diameters and transversal (the 4 piles direction) spacing of 2.15 pile diameters on center, respectively (Figure 3.2). Each pile is 1.37 m in diameter and 30.8 m long. The group is essentially rigidly connected at the pile cap, 14.3 m above the mudline. A FE model that is representative of salient characteristics of the Pier 23 pile-group foundation geometry was developed. A vertical load of 28,900 kN was estimated to represent the tributary own weight of the bridge deck.

Each concrete pile is encased by a prestressed concrete shell (wall thickness h = 0.1778 m) and filled with cast-in-place concrete up to 19.8 m below the ground surface (Ke et al. 2010). To simplify the FE model, in this study the pile response is assumed to remain linear with an effective bending stiffness of $EI = 2 \times 10^6$ kN-m^2 for each pile (average value of actual stiffness along the pile height).

As modeled in this study (Table 3.1), the upper 2 layers were 6.7 m each in thickness and the bottom layer had a thickness of 30.5 m. The pressure-independent (J_2) multi-yield surface plasticity model in OpenSees was employed in which a hyperbolic relationship describes the soil shear stress-strain backbone response. A Poisson’s ratio of

0.4 was specified for all soil strata. In this soil model, the influence of an imposed no-tension strength cutoff (details in section 2.3.3) can be activated (where shear strength vanishes upon occurrence of tensile effective confinement).

3.3 Finite Element Model

In Figure 3.2, length of the mesh in the longitudinal 8-pile direction is 393 m, with 191 m transversally (in this half-mesh configuration, resulting in a 393 m x 382 m soil domain in plan view). Total thickness of the soil layers was 43.9 m (i.e., the base of the soil domain is 27.4 m below the pile tip). The soil domain was modeled by eight-node brick elements (23,040 in total) and the piles were modeled by beam-column elements (512 in total). Rigid beam-column elements (1,664 in total) were used around each pile to model the actual circumferential pile size (diameter). Boundary conditions for this mesh (Figure 3.2b) were defined as described earlier in this document. For comparison, a fixed head single pile was studied with the same geometrical and material properties and a vertical dead load of -903.5 kN (= -28900 kN / 32 piles).

3.4 Loading Scenario I: Lateral Loading

In the employed ½ mesh of Figure 3.2 (due to symmetry), the vertical dead load was imposed initially (after applying the soil domain own weight). A lateral pile cap longitudinal displacement was then applied (at the center of the pile cap) up to a maximum of 0.30 m in 30 steps, in order to clearly demonstrate the effects of nonlinear soil response. In the section below, results from the following three different computational simulations are contrasted: linear soil, nonlinear soil, and nonlinear soil with tension-cutoff.

3.4.1 Pile Group Load Efficiency

Figure 3.3 shows lateral load versus displacement for the entire pile group at the pile cap elevation. In this figure, average load is shown for the pile group (total pile-group load/32 piles). This average load corresponds to a total pile group load of 19,518 kN (i.e., approximately 70% of the bridge own weight is applied laterally) at the pile cap longitudinal displacement of 0.30 m (tension-cutoff scenario). At this level of displacement, pile-group lateral force in the tension cutoff case is about 92% of the nonlinear and 50% of the linear analysis case. Compared to the single pile scenario, it may be concluded (tension-cutoff scenario) that the pile group load efficiency ηe (lateral resistance of the pile group versus that of the single pile at equal levels of final deflection) for this case is 19518 / (909.9 x 32) = 0.67 which agrees well with efficiencies obtained from experimental studies under the maximum applied load (e.g. η_e in the range of 0.5 - 0.68 based on full-scale experiments of Brown et al. (1987) and Rollins et al. (1998)). In the nonlinear simulations (Figure 3.3), it might be noted that the tension-cutoff logic has a large impact on the single pile response, compared with that of the pile group.

3.4.2 Deformed Mesh

The final deformed mesh is shown along with the stress-ratio contour fill (red color shows yielded soil elements) for the nonlinear soil (Figure 3.4a) and the tension-cutoff (Figure 3.4b) cases. As expected, more soil behind the pile group is clearly engaged in the case without the tension cutoff logic. Along with translation, the pile group is seen to also undergo some overall rotation for both cases.

3.4.3 Pile Displacements at the Mudline

As for the pile displacements at the mudline at the 0.30 m pile cap longitudinal displacement, inner piles (2-5) experience the most lateral movement whereas the corner front pile 16 translates the least due to the resistance provided by the surrounding soil (Figure 3.5). The tension-cutoff scenario allows the back piles to move a bit easier with the movement of piles 2-5 and 10-13.

3.4.4 Load Distribution

At the 0.30 m pile cap longitudinal displacement, the corresponding shear force and bending moment distributions between piles in the pile group are shown in Figure 3.6. The outer (corner) front pile (pile 16) carries the highest portion of shear force and bending moment. The edge front pile 8, and back piles 1 and 9 also sustain relatively higher levels of load. Conversely, the inner piles (3-6) carry the least burden (about 80% of the share of pile 16 approximately).

Axial force distribution between piles in the pile group is shown in Figure 3.7. Even in the initial axial load static state, the share of each pile varies in a wide range. Piles along the circumference carry most of the load and the corner piles shoulder the biggest burden. At the prescribed 0.30m pile cap displacement, the compressive axial forces increase dramatically in the front piles (6-8 and 14-16). Conversely, the back piles experience tensile forces in the range of 0.5-1.2 of the initial static compressive force.

3.5 Loading Scenario II: Combination of Lateral Load and Bending Moment

Thereafter, pushover computational analysis of this large pile group system was performed under combined: a) bridge tributary self weight vertical load, and b) lateral load along with overturning moment in the 8-pile longitudinal direction of the FE mesh. In the sections below, distribution of load within the pile group is analyzed and the group interaction effects are examined.

3.5.1 Load Combination

Imposed initially, a vertical dead load of 28,900 kN was estimated to represent the tributary self weight of the bridge deck at Pier 23 (after applying the soil domain self weight). In order to clearly demonstrate the effects of nonlinear soil response and the associated permanent displacement effects of the foundation, a lateral load of 11,677.6 kN (approximately 40% of the tributary bridge-deck self weight) was applied at the bridge deck level (27.6 m above the pile cap) in the 8-pile direction (Figure 3.2). As such, lateral loading along with a substantial bending moment of 321,800 kN-m was imposed on the pile group at the pile cap elevation. In this lateral direction, load was applied gradually in 40 equal increments, and thereafter removed in the same fashion (i.e., loading followed by un-loading was explored).

3.5.2 Summary of Main Numerical Results

3.5.2.1 Shear Force and Bending Moment Distribution

Under the maximum applied lateral load, the corresponding shear force and bending moment distribution between piles in the pile group is shown in Figure 3.8a and Figure 3.8b. The front corner pile 16 carries the highest portion of shear force (-416.23kN) and bending moment (4028.04 kN-m at the pile cap). The edge front pile 8, and back piles 1, 9 also sustain relatively high levels of load. Due to the soil tension cut-off mechanism, the back piles 1, 9 were found to sustain a slightly lower portion of shear force and bending moment compared to their front pile 8, 16 counterparts. The inner piles 3-6 carry the least burden (each, about 80% of the share of pile 16).

Upon removal of the applied lateral load, distribution of residual shear forces and bending moments are shown in Figure 3.8c and Figure 3.8d. While relatively small (about 4% of the maximum), residual shear forces are seen to vary in sign between the front and back sectors of the pile group Figure 3.8c). In the back sector, the piles return towards their original position a bit more than the surrounding soil, resulting in this positive/negative distribution (Figure 3.8c). Residual moments in the range of 5-10% of the maximum also remained (Figure 3.8d).

3.5.2.2 Axial Force Distribution

Axial force distribution between piles in the pile group is shown in Figure 3.9. In the initial axial load static state (bridge-deck self weight), piles along the circumference carry most of the load and the corner piles shoulder the biggest burden (Scott 1981). At the prescribed 11,677.6 kN peak lateral load, the compressive axial forces increase dramatically in the front piles 6-8 and 13-16. Conversely, the back piles experience tensile forces in the range of 0.2-2.4 of the initial static compressive force. Such lower compressive or even tensile axial forces in the back piles may greatly weaken the confinement-dependent structural reinforced concrete properties (Priestley et al. 1994). Upon removal of the applied lateral load, a noticeable redistribution of axial forces is observed with the center piles carrying more load compared to corner and edge piles (Figure 3.9a and Figure 3.9c).

3.5.2.3 Lateral Displacement

As for peak lateral displacements at the mudline, inner piles 2-6 experienced the most lateral movement, whereas the corner front pile 16 translated the least due to the resistance provided by the surrounding soil (Figure 3.10). Compared to their front pile counterparts, the back piles 1, 9 moved a bit easier with the movement of the preceding piles 2-6 and 10-14. Overall the inner piles moved as much as 25 % more than the front corner pile. Upon removal of the applied lateral load, about 40 % of the peak displacement remains (Figure 3.10b).

Peak and residual vertical displacements are shown in Figure 3.11 (at the maximum lateral load and upon removal). Variation of the pile and surrounding soil displacements highlight the mechanism of load transfer from the pile group to the surrounding soil.

3.6 Conclusions

A pilot computational study of a large pile group system (Dumbarton Bridge Pier 23) under combined axial/lateral loads with/without associated moment was presented. An idealized linear-behavior pile group model was assumed, embedded within a 3-layer stratified soil stratum represented by linear as well as nonlinear J_2 elasto-plastic behavior. A tension cut-off shear strength logic was also exercised. A single pile scenario was studied for comparison. Overall, the computed results indicate:

1. At an equal level of applied longitudinal displacement, a large soil domain surrounding the pile group was engaged with substantial potential yielding (compared to the single pile scenario).

2. With the tension-cutoff logic activated, a reduction in shear force and moment was noted in the back piles.

3. In the conducted study with close pile spacing (2 pile diameters), piles along the circumference of the 8 x 4 pile group carried much of the axial load (Scott 1981).

4. Due to application of lateral load, back piles may experience a significant reduction in compressive axial load, resulting eventually in possible tensile axial forces. This may in turn adversely affect the reinforced concrete pile bending stiffness and strength.

Generally, the conducted investigations bring insight into the behavior of a large pile group under lateral load, where theoretical solutions and/or experimental/field data may be scarce or nonexistent today. Lateral and axial load distribution among piles in the pile group was examined. With linear and nonlinear three-dimensional (3D) finite-element (FE) methods becoming a promising technique for understanding the involved SSI mechanisms, further studies, to be conducted efficiently with the aid of OpenSeesPL, may be directed towards effects of soil/pile stiffness properties, mesh refinement, pile geometric parameters (diameter, length, pile spacing and pile cap contribution), as well as soil-pile boundary conditions. Validation and refinement of this numerical analysis framework can result in higher fidelity and more robust foundation analysis/design principles.

3.7 Acknowledgements

Chapter 3 of this dissertation is based on material published in two proceedings: (1) the Geo-Congress 2014 titled "Three-Dimensional Finite Element Modeling of Pile and Pile Group System Response" with authors Ning Wang, Ahmed Elgamal and Jinchi Lu and (2) Second International Conference on Geotechnical and Earthquake Engineering titled "Lateral Load on a Large Pile Group: A 3D Finite Element Model" authored by Ning Wang, Jinchi Lu and Ahmed Elgamal. The dissertation author is the first author of these papers.

Table 3.1: Soil Model Properties

Material Property	Top layer	Middle layer	Bottom layer
Thickness (m)	6.7	6.7	30.5
Mass density (kg/m^3)	1300	1500	1800
Shear wave velocity (m/s)	120	250	300
Shear strength (kPa) at a specified octahedral shear strain γ_{max} = 3%	25	60	75

Figure 3.1: Dumbarton Bridge (http://www.mtc.ca.gov)

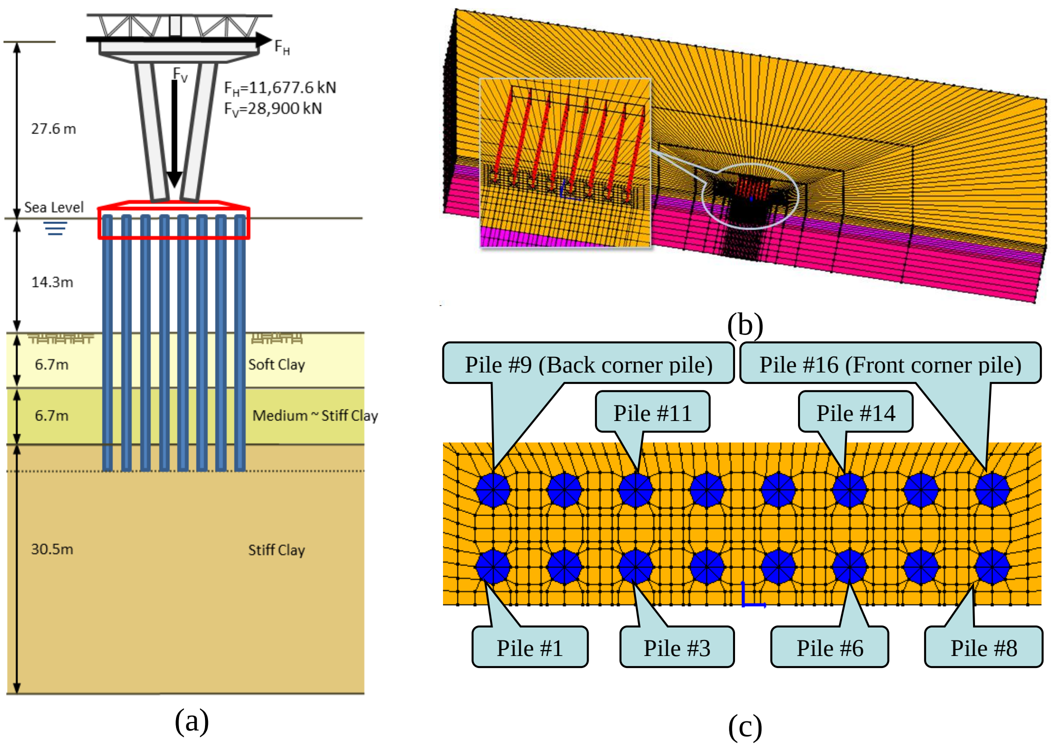

Figure 3.2: Large 8x4 pile group: (a) soil profile used for the FE simulation with 8 piles in the direction of applied lateral load, (b) the FE mesh employed for the simulation, and (c) plan view of pile group layout

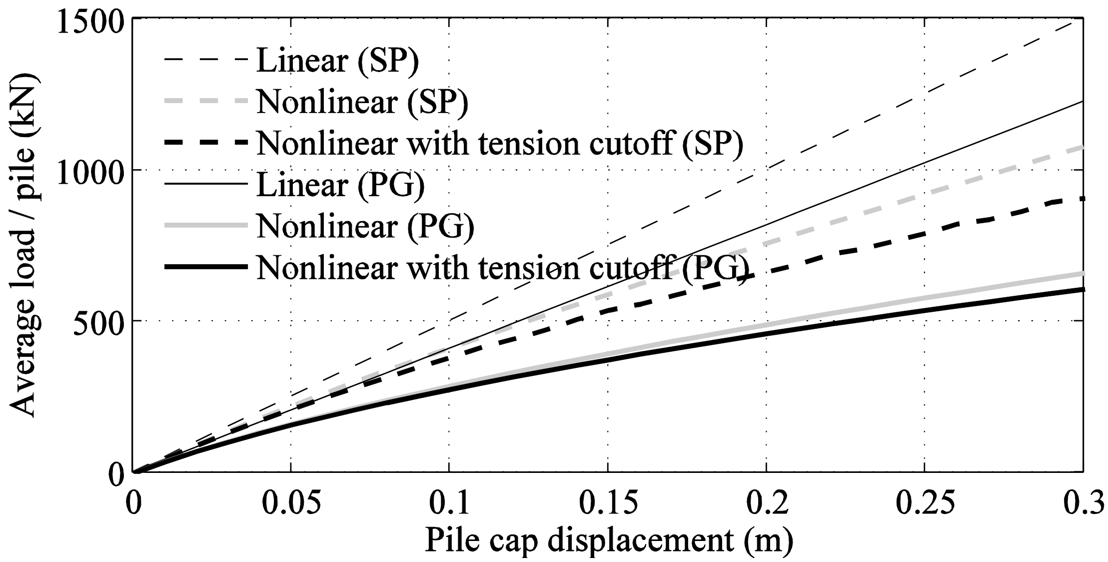

Figure 3.3: Average longitudinal shear load at pile head versus displacement curve

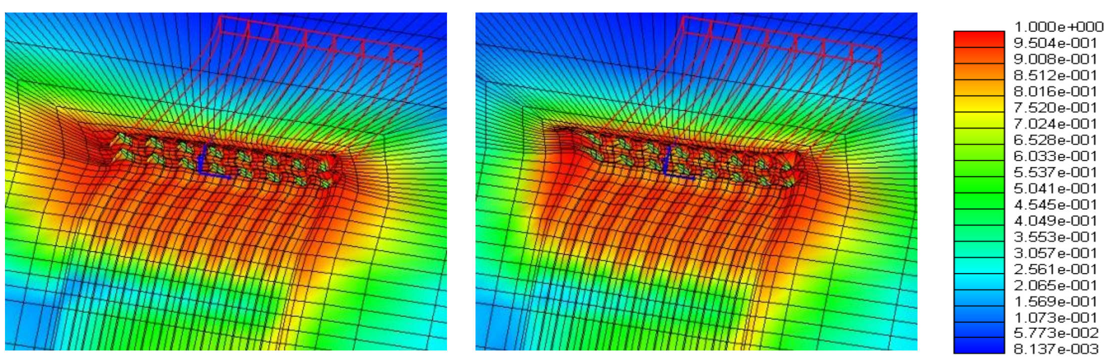

(a) (b) (c)

Figure 3.4: Final deformed mesh (factor of 30) for shear stress ratio contour (red color shows yielded soil elements): (a) nonlinear soil and (b) nonlinear with tension cutoff

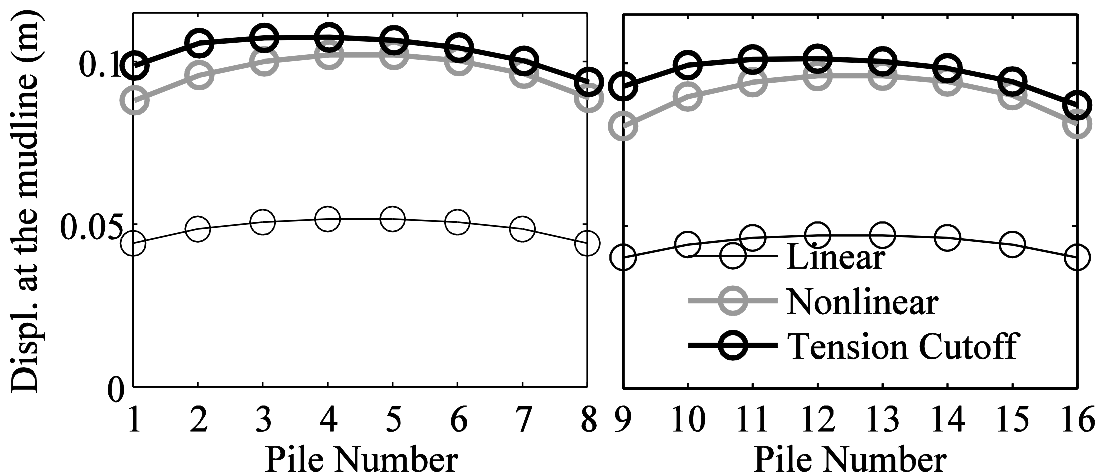

Figure 3.5: Displacement at the mudline at 0.3 m pile cap deflection

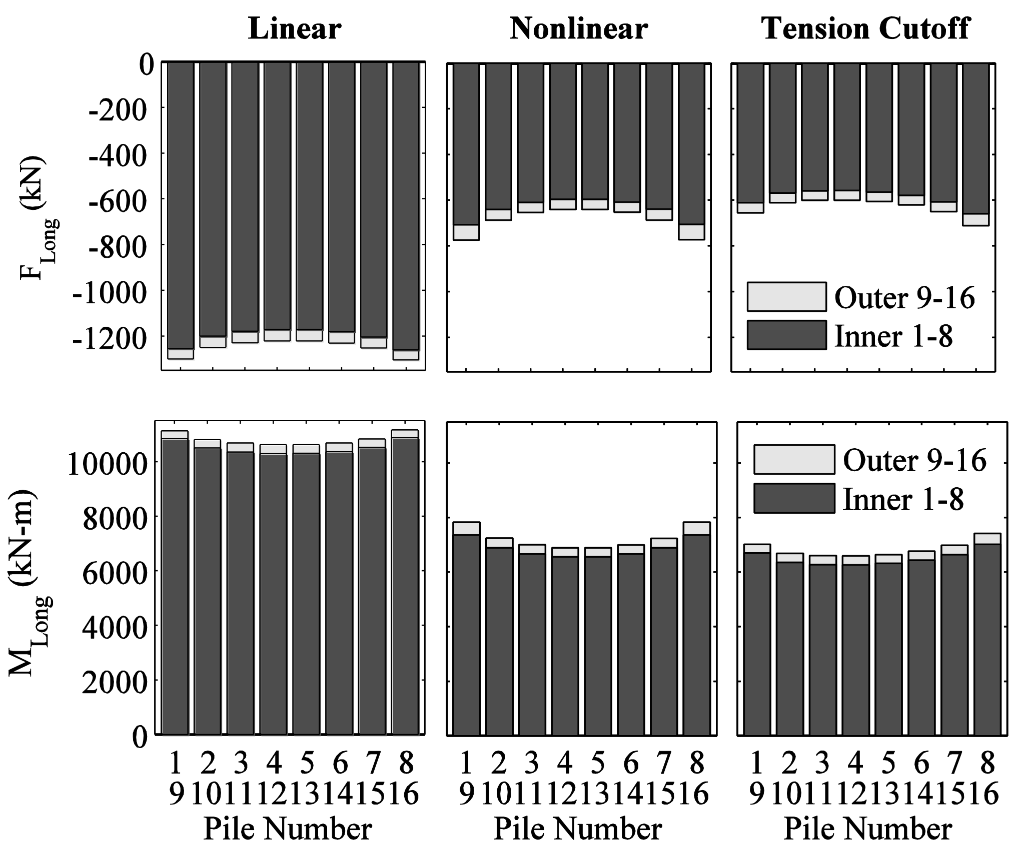

Figure 3.6: Shear force and bending moment at the 0.3 m pile cap deflection

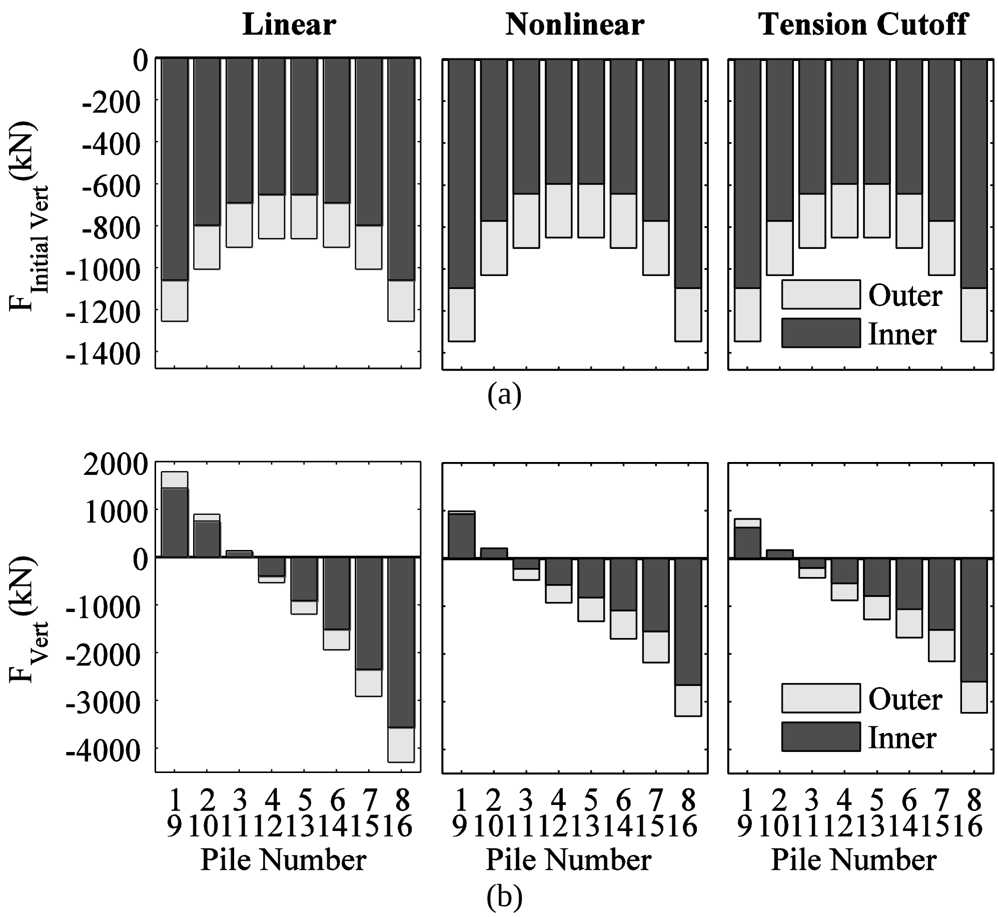

Figure 3.7: Pile axial forces: (a) at the initial vertical dead load and (b) after application of the 0.30 m lateral pile cap deflection

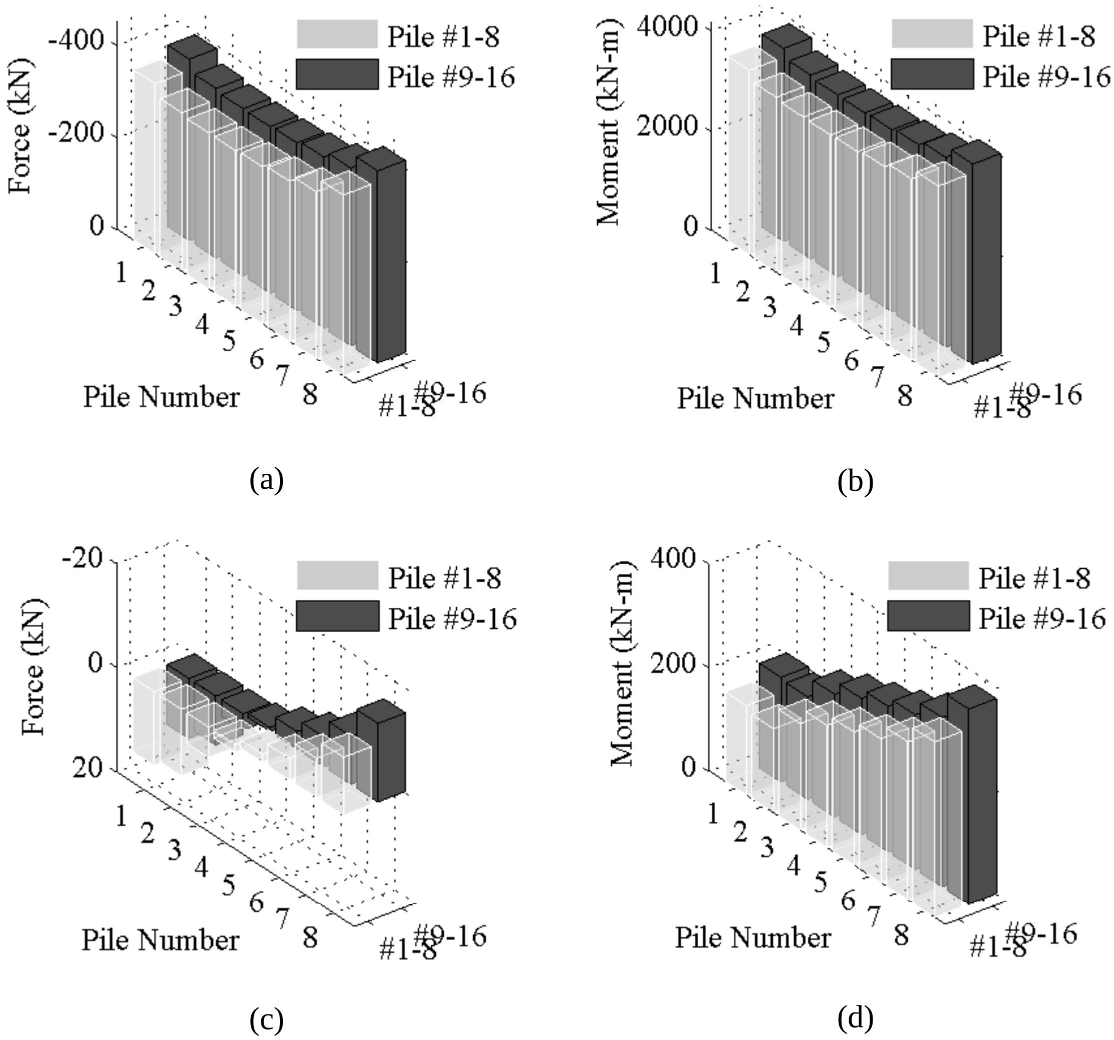

Figure 3.8: Shear forces and moments in each pile: (a) peak shear force, (b) peak bending moment, (c) residual shear force (after removal of lateral load), and (d) residual bending moment (after removal of lateral load)

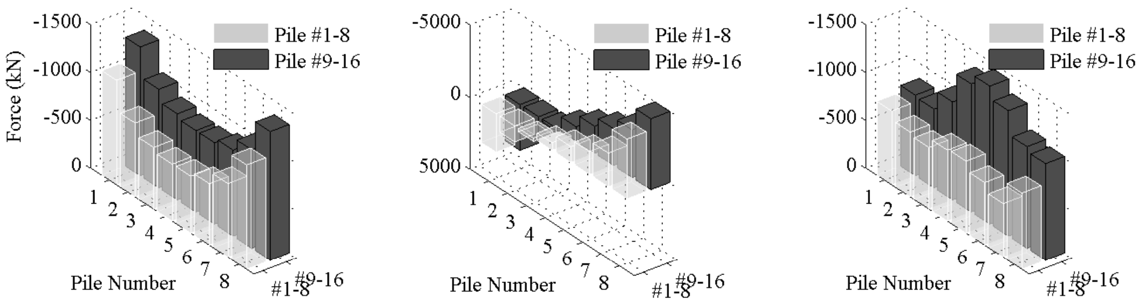

(a) (b) (c)

Figure 3.9: Axial force distribution: (a) under gravity load, (b) under the applied peak lateral load, and (c) after removal of the applied lateral

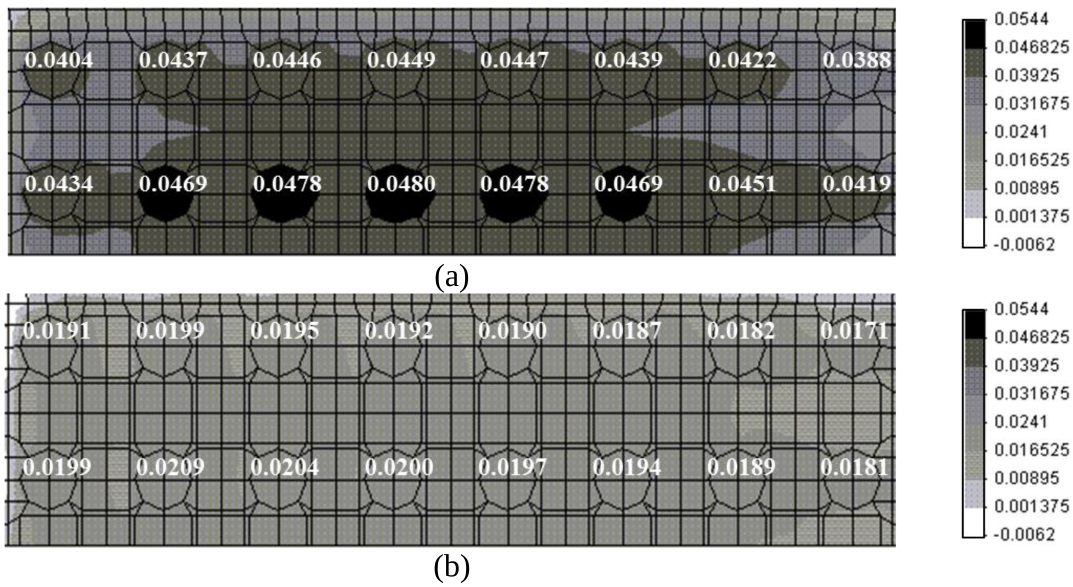

Figure 3.10: Lateral pile displacements (m) at the mudline: (a) at the maximum lateral load and (b) upon removal of lateral load

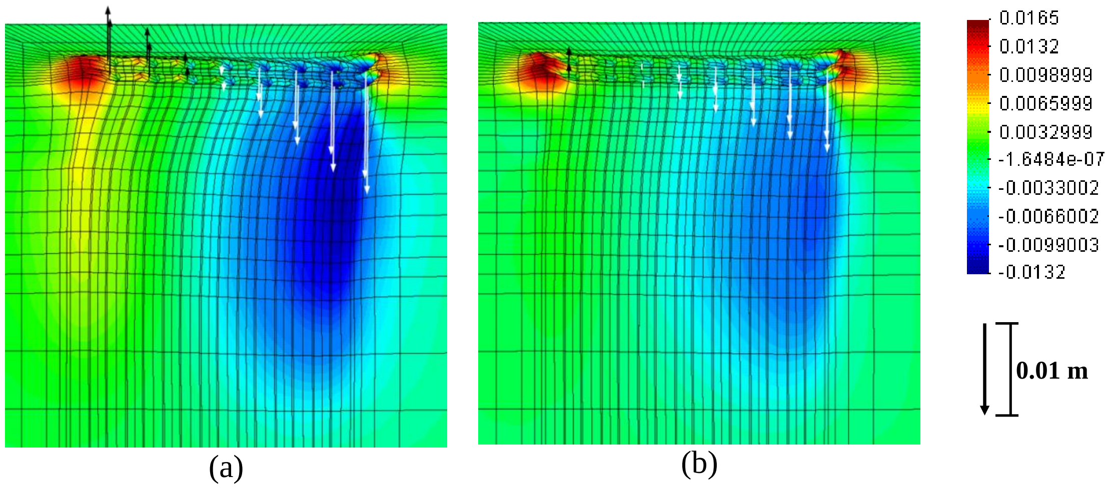

Figure 3.11: Vertical displacement (m) contour (magnified by a factor of 50): (a) at the maximum lateral load and (b) upon load removal

Chapter 4

Effects of Permeability and Loading Rate on Lateral Pile Response

A great number of pile-supported waterfront structures, such as piers, wharves, and wind turbines are embedded in saturated sandy soils. Earthquakes, waves and wind may impose cyclic lateral load demands on such structures. As such, the lateral resistance exerted by the saturated soil plays an important role in determining the overall system response. Shear loading in saturated soil is associated with a tendency for volume change, thus engaging the mechanisms that depend on permeability. In particular, the relation between soil permeability and loading rate may become one of critical factors that control excess pore water pressure, the resulting effective confinement, and the corresponding shear stiffness of the pile-soil system.

In this chapter, effects of important influencing factors such as soil permeability and loading rate on the pile foundation-soil-water system are studied based on nonlinear 3 dimensional (3D) finite element (FE) analysis. The behavior of a laterally loaded single pile embedded in a variety of saturated soils from gravels to silts (in terms of permeability) was investigated. Instantaneous larger pile resistance is observed when the surrounding soil is less pervious and/or the loading rate is high. Lateral response of statically and dynamically loaded piles embedded in dry soil was addressed as a reference. As a scenario that amplifies this permeability-induced lateral stiffness effect, a pile with a vertical steel plate (wing) attached near the pile head is also studied. The FE model is developed using the open-source platform OpenSees (Mazzoni et al. 2006). The user interface OpenSeesPL (Elgamal and Lu 2009) is employed to facilitate the pre- and post-processing phases.

4.1 Introduction

Much work has been performed to study the role of soil permeability on soil behavior (Liu et al. 2005; Menéndez et al. 2010). However, relatively few efforts have been done to investigate the interaction between saturated soil and deep foundations under lateral loading. Common geotechnical numerical approaches (such as the p-y spring method) generally consider the soil condition as liquefied or non-liquefied. The effects of permeability and loading rate on the performance of pile foundations buried in saturated soils has yet to be fully investigated from the seismic response point of view.

Actually, the progressive buildup and redistribution of pore water pressure (PWP) in the soil during seismic loading can be marked with significant time dependence (based on soil permeability and loading rate), which in turn will affect the short-term lateral stiffness of the pile-soil system. Evidence on the crucial role played by the interplay between the soil permeability and the rate of loading was observed in reported experimental investigations (Elgamal et al. 2005; Dungca et al. 2006). Results of shaking table test performed by Dungca et al. (2006) showed that as the loading rate becomes higher, the soil response near the pile tends to be undrained and a larger lateral soil resistance is mobilized. Gonzalez et al. (2005 and 2009) pointed out that permeability of soil is an extremely important but poorly understood factor. They investigated the effect of soil permeability on the response of end-bearing single piles and pile groups based on six model centrifuge experiments (liquefaction-induced lateral spreading pile loading scenario). Significant negative excess pore pressure near the foundation at a shallow depth was found in the low permeability soil. The stiffening of soil due to the reduction in pore pressure in turn allows for a larger force against the foundation. To this end, 3-6 times larger pile head displacements and bending moments were observed for low permeability soil at the end of shaking (due to lateral spreading of the liquefied soil).

Motivated by the discussions in the papers mentioned above, the role of soil permeability and loading rate on pile response is addressed computationally in this chapter. The studies show that the magnitude of excess water pressure (EPP) due to pile lateral movement (pushover or shaking) changes significantly depending on the permeability of the soil. Variation of pore water pressure in the different soil modeling cases (simulating undrained, partially drained and drained conditions) is evaluated. The pile-soil interaction during the generation of pore water pressure is discussed. Thereafter, the benefits from pile wings are presented on the basis of 3D FE pushover analysis. It should be noted that liquefaction and its effect on pore water pressure is not discussed throughout this chapter (as the study is focused on relatively dense soils only).

4.2 Constitutive Soil Model with Cyclic Mobility Mechanism

Contemporary geotechnical modeling software might include advanced nonlinear soil constitutive with yield functions, shear stress-strain backbone curves, hardening laws and flow rules (Stewart et al. 2008). As such, tracking the change of pore water pressure is possible when conducting effective stress analyses (Pyke 1980; Prevost 1985). Among these nonlinear soil model codes, PressureDependMultiYield material model (Parra 1996; Yang 2000; Yang 2002; Yang and Elgamal 2002; Elgamal et al. 2003; Yang et al. 2003) implemented in Opensees, is an elastic-plastic material to simulate the essential response characteristics of pressure sensitive soil materials. Fully undrained and partially drained condition can be simulated upon combination of this pressure dependent material in a solid-fluid fully coupled element (brick u-p Element) using appropriate permeability values (Yang 2002; Elgamal et al. 2003).

4.2.1 Pressure-Dependent Model

Plasticity of this pressure-dependent soil model is formulated based on the multi-surface concept (Drucker-Prager type). A number of similar conical yield surfaces with different tangent shear moduli are employed to represent shear stress-strain nonlinearity and the confinement dependence of shear stiffness and shear strength (Figure 4.1). For the hysteretic response of the soil under cyclic shear loading, a purely deviatoric kinematic hardening rule is employed. This model (Yang 2002; Elgamal et al. 2003) is capable of representing the shear-induced volumetric deformation (contraction or dilation) with a non-associated flow rule. This pressure-dependent material model has been extensively calibrated for medium Nevada Sand based on monotonic/cyclic laboratory tests and centrifuge experiments (Parra 1996; Yang 2000).

4.2.2 Soil-Water Interaction

Dynamic response of solid-fluid fully coupled materials in the *u*-*p* element (Chan 1988) is simulated based on Biot's theory of porous media, where displacement of the soil skeleton *u* and pore pressure *p* are the primary unknowns (Yang and Elgamal 2002). For this solid-fluid fully coupled element, there are four degrees-of-freedom (DOF) at each node where DOFs 1 to 3 defines the solid displacement (*u*) and DOF 4 captures the fluid pore pressure (*p*).

Numerical simulations in this chapter are performed using this PressureDependMultiYield material along with the BrickUP element (an 8-node hexahedral solid-fluid element) in OpenSees to illustrate the permeability/loading rate dependent soil-pile response.

4.3 Variation of Pore Water Pressure

Due to the relative incompressibility of the fluid, the tendency to dilate or to contract of the soil will induce pore water pressure variations. In general, with the increase in pore water pressure, the ability of the soil-water system to support foundation loads temporally increases (if there is a tendency for volume increase) and then decreases with the dissipation of the water. This soil dilation tendency can build up negative excess pore water pressure (reported pore water pressure in this chapter will be zero-referenced against ambient air pressure, i.e. gauge pressure) which helps to keep soil particles together and has the effect of increasing the soil effective confinement and strength.

It should be noted that water is conventionally thought be have little tensile strength and will cavitate at a negative pressure of about -101 kPa (atmospheric air pressure). If soil response is essentially undrained, the tendency for dilation can eventually drop pore pressure to the minimum value of -101 kPa (i.e., cavitation). This cavitation will prevent the effective confining pressure from further increase. As will be shown below, comparisons of pile response and EPP contours within the soil with and without this cavitation threshold illustrate its potential significant effect on the overall pile-ground system response.

4.4 Finite Element Model

4.4.1 Configuration of the Pile-Soil System

In view of symmetry, a half mesh configuration is used (Figure 4.2). Length of the mesh in the longitudinal direction is 194.466 m, with 97.233 m transversally (in this half-mesh configuration, resulting in a 194.466 m x 194.466 m soil domain in plan view). Total soil layer thickness is 43 m (the base of the soil domain is 25 m below the pile tip). The soil is modeled by eight-node brick elements and the piles are modeled by beam-column elements. Essentially rigid beam-column elements are used around each pile to model the pile size (diameter). This FE model has 2891 nodes which define 2184 brickUP elements and 190 elastic beam column elements.

In this employed ½ mesh (due to symmetry) configuration of Figure 4.2 , the following boundary conditions were enforced:

a) The bottom of the domain is fixed in the longitudinal (X), transverse (Y), and vertical (Z) directions,

b) Left, right and back planes of the mesh are fixed in X and Y directions (the lateral directions) and free in the Z direction,

c) In this half mesh configuration, the plane of symmetry is fixed in Y and free in Z and X directions (to model the full-mesh 3D scenario),

d) The pore pressure DOF of the nodes on the ground surface is fixed (zero prescribed fluid pore pressure) to model the traction free situation, and

e) The bottom and lateral boundaries are impervious (simulating no drainage)

The numerical modeling procedure is divided into 2 individual steps: (1) application of gravity load (and static loads if any) where material behavior is defined as linear elastic, with the resulting stress-state applied to the elasto-plastic soil model representation; (2) subsequent dynamic loading phase in which the stress-strain response is elasto-plastic.

4.4.2 Pile Properties

A linear elastic circular pile with a diameter of 1.37 m and a total length of 18.01 m (0.01m of the pile is above ground surface) is employed in the OpenSees simulation. There is neither a pile head mass nor an axial load applied at pile head. Linear beam-column elements are used with the bending stiffness of EI = 2×10^7 kN-m^2 (10 times larger than the EI employed in the Dumbarton Pier 23 simulation). This high lateral pile stiffness further engages the soil response at depth and thus accentuates the role of the permeability-induced mechanisms. Pile head connection is considered to be free in all cases.

The employed properties of the pile are summarized below:

Pile Geometry:

Pile diameter (D)	= 1.37 m
Total pile length	= 18.01 m
Pile height above surface	= 0.01 m
Pile head mass	= 0 ton
Axial load applied at pile head	= 0 kN

Linear Beam Element Properties:

Bending Stiffness EI	$= 2 \times 10^7$ kN-m^2
Mass density	= 0 ton/m^3 (for simplicity in this push-over study)

4.4.3 Soil Profile

The pile is assumed to be embedded in a homogeneous, isotropic half-space. The coefficient of soil permeability depends on soil type (grain size distribution of the soil). According to the reference values for permeability coefficients in Table 4.1, six permeability coefficients are employed to perform this parametric study, which are 50m/s (drained condition), 1m/s, 1×10^{-2} m/s (Gravel), 1×10^{-3} m/s (sand permeability), 6.6×10^{-5} m/s (silty sand permeability) and 1×10^{-7} m/s (silt permeability), respectively. All other soil parameters (representing medium dense sand) used in this study were maintained constant throughout as listed in Table 4.2.

A preliminary single element simulation (9-4 node effective stress fully coupled quad element) representing saturated dense sand (e.g., Elgamal et al. 2005) is employed to demonstrate the influence of dilation on shear stress-strain response. For this type of element, all 9 nodes describe the translational degrees of freedom whereas the 4 nodes at the corner describe the fluid pressure. Strain-controlled monotonic lateral shear simulations are conducted. A high permeability of 10 m/s is adopted to represent the drained scenario. In comparison, a relatively low permeability coefficient of 1e-8 m/s was employed representing the undrained scenario. Four different initial confinements (20 kN, 40 kN, 60 kN and 80 kN) are applied to the element top to emulate overburden soil pressures. The boundary conditions are defined as: (1) the base is fixed and impervious, (2) the top edge is free draining when applying the vertical confining pressure. The shear stress-strain response under drained/undrained conditions is displayed in Figure 4.3. During the shearing process, the soil element with low permeability (undrained condition) exhibits a much larger shear resistance due to the dilation tendency (volume increase). Overall, the soil permeability along with the tendency for dilation results in remarkable difference in shearing resistance.

4.5 Parametric Study for Effect of Soil Permeability and Loading Rate

Effects of soil permeability and loading rate on the lateral pile response are numerically presented below. As discussed below, comparisons of lateral pile response (pile head displacement, shear force and bending moment) and soil response (displacement, PWP and EPP) reveal that the soil permeability/loading rate has a significant impact on the behavior of the entire pile-soil-water system.

4.5.1 Effect of Permeability

4.5.1.1 Applied Loading Rate

To illustrate the desired effects, a loading rate of 10,000 kN/s is employed for the following study. The applied lateral load reaches 25000kN in 2.5 second and is kept constant thereafter.

4.5.1.2 Pile and Soil Response

Time histories of pile head displacement are shown in Figure 4.4. It is found that the pile head displacement for the high permeability scenarios (e.g., k = 50 m/s and k= 1m/s) remain approximately constant after 2.5 second where the applied load reaches ultimate value of 25000 kN and stops increasing. In contrast, the pile head displacement for the k = 1e-2 m/s scenario is 26.8% smaller than the dry soil case at 2.5 seconds and pile head displacement continues thereafter. For this permeability case, the pile head displacement essentially reaches that of the dry soil at a time of about 25 seconds.

The corresponding load-displacement curves are shown in Figure 4.4b. Pile deformation profiles, shear force profiles and bending moment profiles at 3 selected instants during the pushover analysis are shown in Figure 4.5 and Figure 4.6. For the undrained situation, the decrease in maximum shear force and bending moment along with the decrease in depth to the location where the maximum moment occurs (low permeability case) suggests an enhanced lateral resistance of the overall system.

For the highly pervious soil, minimal excess pore pressure appears throughout the loading process. Due to the complete dissipation of pore pressure during the loading phase, there is no significant change of pile head displacement after the applied load stops increasing. When the permeability becomes smaller (k<1 m/s), excess pore pressures are sustained during the loading phase. Appreciable additional displacement is observed due to the gradual excess pore pressure dissipation even after the load stops increasing and is kept constant. Once the pore pressure is eventually dissipated (could take several minutes), the pile head displacement remains constant thereafter. These observations agree well with the conclusion of Dungca et al. (2006).

It should be noted that effect of soil permeability is less obvious for the low permeability soil scenario when cavitation is considered (Figure 4.4b vs Figure 4.7b). As can be seen, cavitation prevents the effective confining pressure from further increase.

In conclusion, high permeability precludes significant variation in excess pore pressures and results in higher pile head displacement. In contrast, low permeability results in a lower level of pile deformation (during the loading process). To this point, it can be concluded that the pile response is dependent on the soil permeability, the higher the permeability the larger short-term pile head displacement.

4.5.1.3 Pore Water Pressure Variation

Figure 4.8-Figure 4.11 show how the excess pore pressure changes with time for the different permeability scenarios. As mentioned before, excess pore pressure decays quickly with time resulting in insignificant EPP for the permeable soil. When permeability is low (e.g., when k = 6.6x10-5 m/s or less), it will take a longer time to eliminate the pore water pressure and larger pile resistance is temporarily mobilized. The negative pore water pressure limit (-101 kPa at the water table elevation) is observed

adjacent to the pile area for the low permeability soil. Once the upper soil layer reaches cavitation, PWP tends to change within the lower soil layers (compared to the scenario where the cavitation logic is inactive). In addition, for the low permeability scenarios (e.g., k = 6.6e-5 m/s and 1e-7 m/s representing the undrained situation) the pore pressure on the side of the movement direction in the upper soil layer increased slightly due to the sand contraction. Thereafter, it showed rapid decrease of PWP as a result of the sand dilation and the suction force on the backside of the pile. The pressure on the back side of the pile monotonically decreased till cavitation happens. Overall, the pore pressure decreased on both sides though the pressure on the side of the movement was larger than that on the other side.

Pore water pressure and excess pore water pressure contours at selected instants are shown in Figure 4.12 and Figure 4.13. It is observed that negative excess pore pressure developed near the ground surface (mainly the upper 1/3 of the pile) on both sides of the pile for this essentially undrained case. Strong dilative response was observed with sharp pore pressure drop in the soil section behind the foundation.

In summary, pile resistance changes dramatically with the change in pore water pressure. Increase in permeability results in weaker dilation tendency effects. Thus, less instantaneous support is provided by the soil leading to a larger pile displacement.

4.5.2 Effect of Loading Rate

In order to investigate the influence of loading rate on the distribution of excess pore water pressure, variations of pile head displacement and excess pore water pressure were examined over different loading frequencies as well as different soil permeability conditions. To maintain simplicity, only ¼ of a presumed triangular wave loading up to a max load of 1500 kN was employed. In the following numerical studies, cavitation was allowed with a negative pore water pressure limit of -101 kPa (at the water table elevation). Excess Pore water pressure is not allowed to decrease further below this threshold limit (at the water table elevation).

Three different constant loading rates are employed which are 3000 kN/s, 6000 kN/s and 12000 kN/s (Figure 4.14). Changes of secant stiffness along with lateral load are shown Figure 4.15. It is observed that the larger the loading rate, the higher the lateral pile stiffness (especially clear up to a load of about 200 kN or more).

Comparing the pore pressure responses along with the pile head displacement shows:

(1) The effect of loading rate is more obvious for the k = 1e-2 m/s scenario. Under the maximum applied load (1500 kN), pile head displacement is 7% for the fastest loading rate (Figure 4.16).

(2) Effect of loading rate is weakened for the permeability coefficient of 1e-7 m/s scenario in vicinity of pile due to the cavitation phenomenon. If the water table is 10 m above the ground surface, to preclude the occurrence of cavitation, higher pile-soil stiffness is observed (Figure 4.17 and Figure 4.18).

(3) Contours of excess pore water pressure around the pile area with k = 6.6e-5 m/s are illustrated in Figure 4.19 and Figure 4.20 at selected loading instants. During the applied pushover loading, cavitation occurs with both negative as well as positive excess pore pressures observed depending on location along the pile/ soil depth (Hansen and

Gislason 2007). The time taken to reach cavitation is dependent on the permeability and loading rate.

(4) As a matter of fact, the overall resistance of the system relies on both the soil permeability and the loading rate (Takahashi et al. 2002).

(5) In the Appendix A, the influence of an interfacing layer, with a tension cut-off logic between the pile and the soil, is discussed.

4.6 Lateral Resistance for Piles with Wings

Many experimental and numerical studies have shown that tapered piles improve the lateral loading behavior of pile foundations (El Naggar and Wei 1999; Sakr et al. 2005; Ismael 2010). The pile geometry, in particular, the pile shape near ground surface affects the lateral resistance of piles. Inspired by the idea that enlargement or strengthening of the upper section of piles leads to higher lateral load capacity and less lateral deflections, an innovative system, pile with wings (Irvine et al. 2003), is drawing some attention recently. Practically, pile wings can be realized by welding wings to the steel pile or integrating steel plates into the reinforcement of concrete piles. Significant improvement of the lateral bearing capacity can be achieved through attaching vertical steel plates near the pile head.

Irvine et al. (2003) first presented the concept of pile of wings. Small-scale tests and computation simulations were carried out. The results show that the lateral load capacity and stiffness of the pile was enhanced by attaching the wings to a pile just below the soil surface. Dührkop and Grabe (2008) conducted several small scale tests showing that the laterally loaded piles with wings help to increase the ultimate bearing capacity and minimizes pile deformations or the required embedded length.

Lateral capacity of pile with wings are estimated using numerical and experimental methods (Peng 2006; Peng et al. 2010). Peng et al. (2011) evaluated the performance of pile wings under cyclic lateral load. Small-scale tests on monopole and wing piles with different wing size were carried out. It was found that the wings reduced the lateral displacement by at least 50% after 10000 cycles.

In this section, Finite Element Analysis was performed to investigate the effect of pile wings (Figure 4.21) for the saturated soil scenarios discussed above. Variables for the parametric study include width of pile wings, location of pile wings and soil permeability. Efficiency of the pile wings was evaluated using lateral pile head displacement as reference.

4.6.1 Configuration of Finite Element Model for Piles with Wings

Same soil properties (medium dense sand) and pile properties were employed. Layout of the pile with four-wings is shown in Figure 4.21 where the four wings are arranged at 90º intervals around the pile circumference. Lateral load was applied in the longitudinal direction at the pile head (0.01 m above the ground surface) up to 1500 kN in 0.25 s. Due to the symmetry, two wings perpendicular to the loading directions were considered in the simulation. The pile wings were assumed to be rigid steel plates which lead to same translations along the plate at the same depth. Increased bending stiffness owing to the existence of pile wings was considered through using relatively rigid pile elements along the pile wing. Different pile wing geometries (Table 4.3) were employed to evaluate the benefits from additional pile wings. Two different wing widths ($b_w = \frac{D}{2}$ and $b_w = D$, where D is the diameter of the pile) were considered with wings located just below the soil surface or 1 m below the surface. Effects of soil permeability (with cases scenarios k = 1e-3 m/s and k = 6.6e-5 m/s) are investigated.

4.6.2 Numerical Results for Pile with Wings

Comparisons were made between a conventional circular pile and a pile with wings. Pile-soil response was evaluated based on the load-deflection relationship, bending moment and shear force profile along the pile.

It is found that the lateral resistance of the pile is significantly improved when the pile wings are introduced. A stiffer load-deformation behavior is observed for piles with wings (Figure 4.22). For a given load (1500 kN), the lateral pile head displacement decreases with increasing size of the wing. The pile head displacements at 0.25 s (1500 kN) decrease 23% (with 0.685 m × 3 m rectangular plate – PW0685a) and 40% (with 1.37 m × 3 m rectangular plate – PW1370a) as the piles with wings embedded in saturated soil (k = 1e-3 m/s) are employed (Figure 4.22a). The pile bending moments decrease 10% and 19% for PW0685a and PW1370a. For the pile embedded in dry sand, the pile head displacements decrease 25% for PW0685a and 44% for PW1370a respectively. Change of pile head displacement with time, deformed profiles, shear force profiles and bending moment profiles with and without wings are shown in Figure 4.23-Figure 4.26. In all cases, the effective enlarged cross-section increases the lateral stiffness and therefore decreases the pile deformation up to 46%. Moreover, deeper embedment of the pile wings helps to further reduce the lateral displacement. However, maximum bending moment of the pile stays more or less the same or even becomes larger with pile wings 1 m below the ground surface.

Lateral displacement contours representing pile-wing-soil response especially the soil reaction around the wings are presented in Figure 4.27. For two different soil permeability scenarios, a larger area of influence is observed due to the presence of the pile wing, though with smaller magnitude of movement. PWP and EPP contours are shown in Figure 4.28 - Figure 4.32. Generally, the conducted numerical simulations demonstrate the potential of this innovative foundation for seismic loading applications, when the soil/site conditions are appropriate (Table 4.4 and Table 4.5).

4.7 Conclusion

Permeability and loading rate is shown to be of potential significance for piles in relatively dense saturated cohesionless soil, subjected to lateral inertial structural load. In this chapter, numerical simulations are conducted to explore the lateral response of such single piles embedded in a uniform medium dense cohesionless soil. Response under different loading rate and soil permeability condition are investigated. The effect of the existence of pile wings and their dimensions on the lateral behavior of piles is explored. The main findings of this numerical study can be summarized as follows:

- In saturated low permeability cohesionless soils, pile lateral stiffness and strength can be much enhanced under short duration inertial structural loading scenarios.
- No (or very little) change occurs in pile head displacement (once the load becomes constant) for the cases where loading is relatively slow or permeability is high (because of the minimal sustained excess pore pressure).

- For low permeability soil, it will take a longer time for dissipation of excess pore pressure and the pile head continues to move even after the load stops increasing (i.e., the low permeability beneficial effect is only helpful for instantaneous loading conditions).
- A fluid cavitation logic is necessary in order to prevent erroneous unrealistic decreases in excess pore pressure and resulting unrealistic cohesionless soil effective confinement and strength.
- The concept of pile with wings and its advantages is introduced for scenarios of saturated cohesionless soils (and rapid dynamic load applications).
- The observations in this study can serve as a reference for practical engineers when defining simplified approaches such as p-y curves or a representative foundation stiffness matrix.

4.8 Acknowledgements

Chapter 4 of this dissertation is based on material from a manuscript under preparation for publication, tentatively titled “Numerical study on effects of permeability and loading rate on lateral pile response”, with a preliminary author list of Ning Wang, Ahmed Elgamal and Jinchi Lu. The dissertation author is the first author of this paper.

Table 4.1: Suggested permeability coefficient values in OpenSeesPL and Cyclic1D

Cohesionless Soil	**Permeability* (m/s)**
Loose, Medium, Medium-dense and Dense Gravel permeability	1.0×10^{-2}
Loose, Medium, Medium-dense and Dense Sand permeability	6.6×10^{-5}
Loose, Medium, Medium-dense and Dense Silt permeability	1.0×10^{-7}
Cohesive Soil	**Permeability (m/s)**
Soft, Medium, Stiff and U-Clay/Rock	1.0×10^{-9}

***** Permeability values are based on Fig. 7.6 (Holtz and Kovacs 1981)

Table 4.2: Soil material properties employed in the 3D analysis

Material Property	Soil Type: USand1
Saturated Mass density (ton/m^3)	2.0
Poisson’s Ratio	0.33
Reference Shear Modulus (kPa)	100000
Reference Bulk Modulus (kPa)	300000
Fluid-Solid Combined Bulk Modulus (kPa)	2200000
Friction Angle (degrees)	37
Permeability (m/s)	50, 1, 1e-2, 1e-3, 6.6e-5, and 1e-7
Number of Yield Surfaces	20
Contraction Parameter	0.05
Dilation 1	0.6
Dilation 2	3
Liquefaction1	0.000725
Liquefaction2	0.003
Liquefaction3	1

Table 4.3: Pile wing geometry

Pile Wing Type	Wing length (m)	Wing width (m)	Wing top below ground surface (m)
PW0685a	3	0.685	0
PW1370a	3	1.370	0
PW0685b	3	0.685	1
PW1370b	3	1.370	1

Table 4.4: Percentage reduction of lateral pile head displacement

Pile Wing Type	Dry Soil	k = 1e-3 m/s	k = 6.6e-5 m/s
PW0685a	25%	23%	17%
PW1370a	44%	40%	33%
PW0685b	28%	26%	20%
PW1370b	46%	42%	36%

Table 4.5: Percentage reduction of maximum bending moment

Pile Wing Type	Dry Soil	k = 1e-3 m/s	k = 6.6e-5 m/s
PW0685a	13%	10%	4%
PW1370a	25%	19%	9%
PW0685b	2%	-1%	-9%
PW1370b	10%	5%	-5%

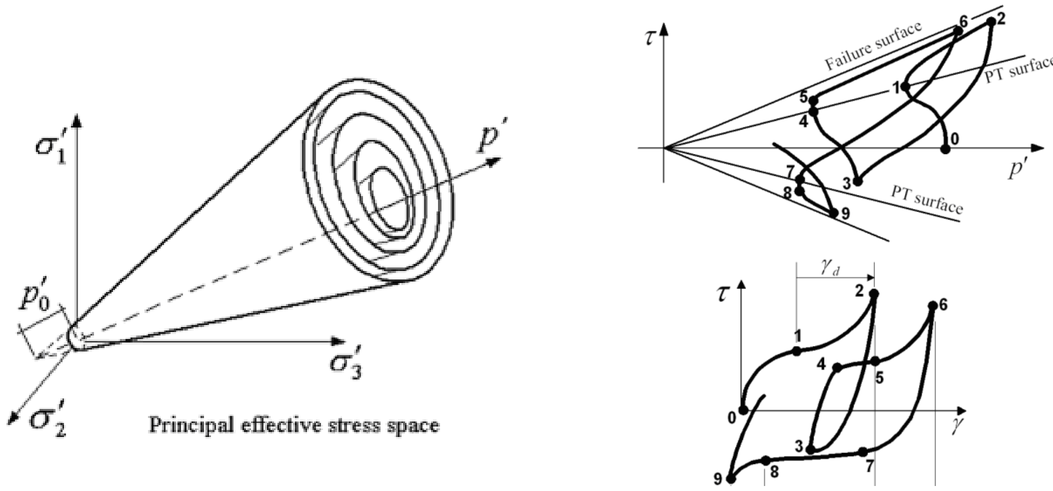

(a) (b)

Figure 4.1: Multi-yield surface and constitutive model: (a) conical yield surface in principal stress space and (b) schematic of undrained constitutive model response (Yang 2000; Yang and Elgamal 2002; Yang et al. 2003)

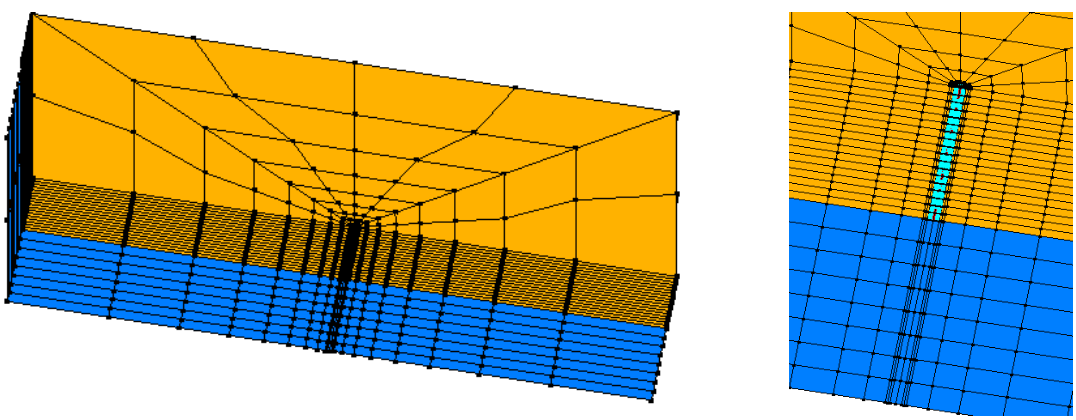

Figure 4.2: Finite element mesh (half-mesh configuration) and a close-up view employed in this study

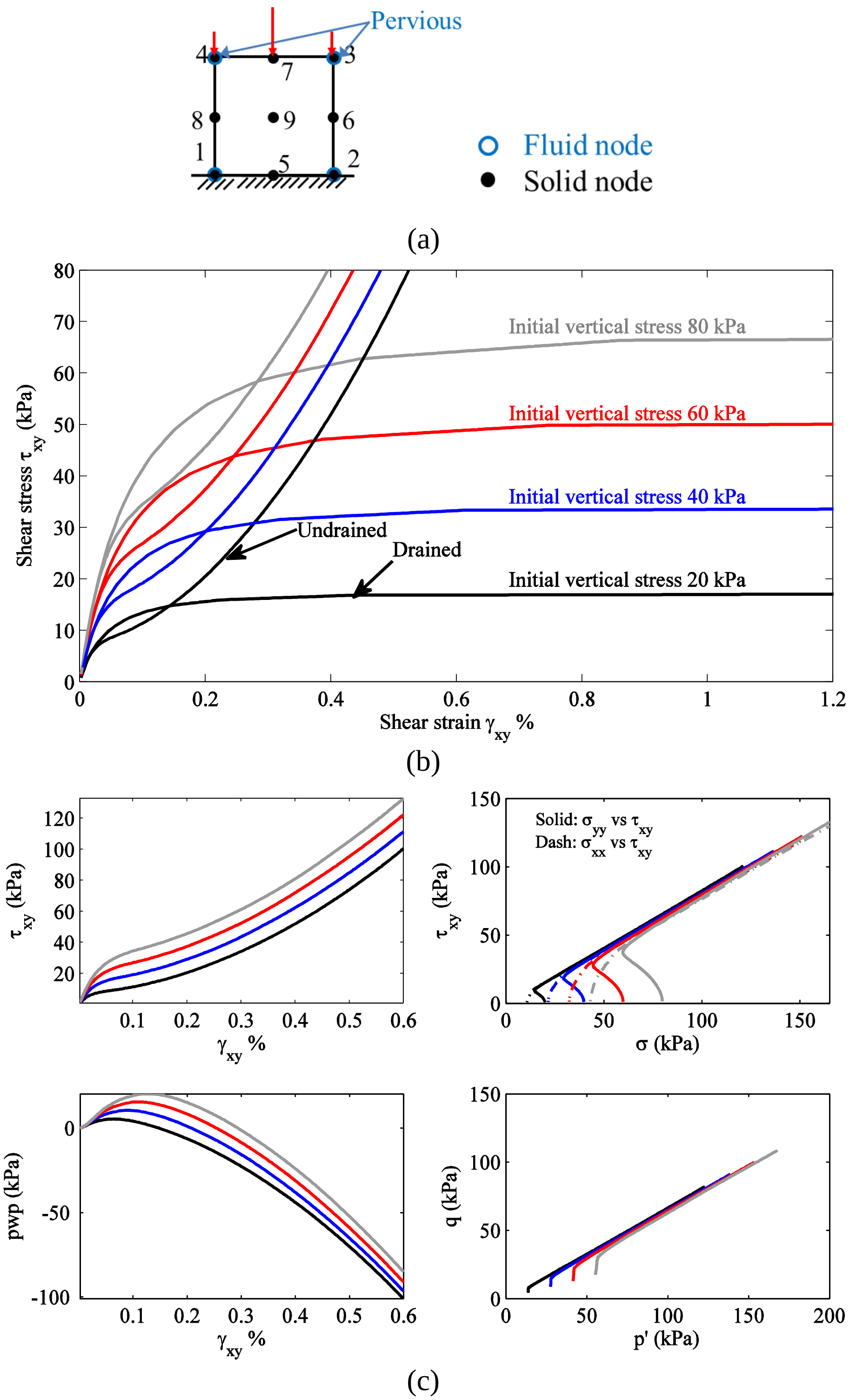

Figure 4.3: Shear loading on single element (a) employed 9-node quadrilateral plane-strain element and boundary conditions, (b) shear stress-strain (drained versus undrained), and (c) shear stress-strain response, pore water pressure (pwp) and effective confinement relationship under undrained situation

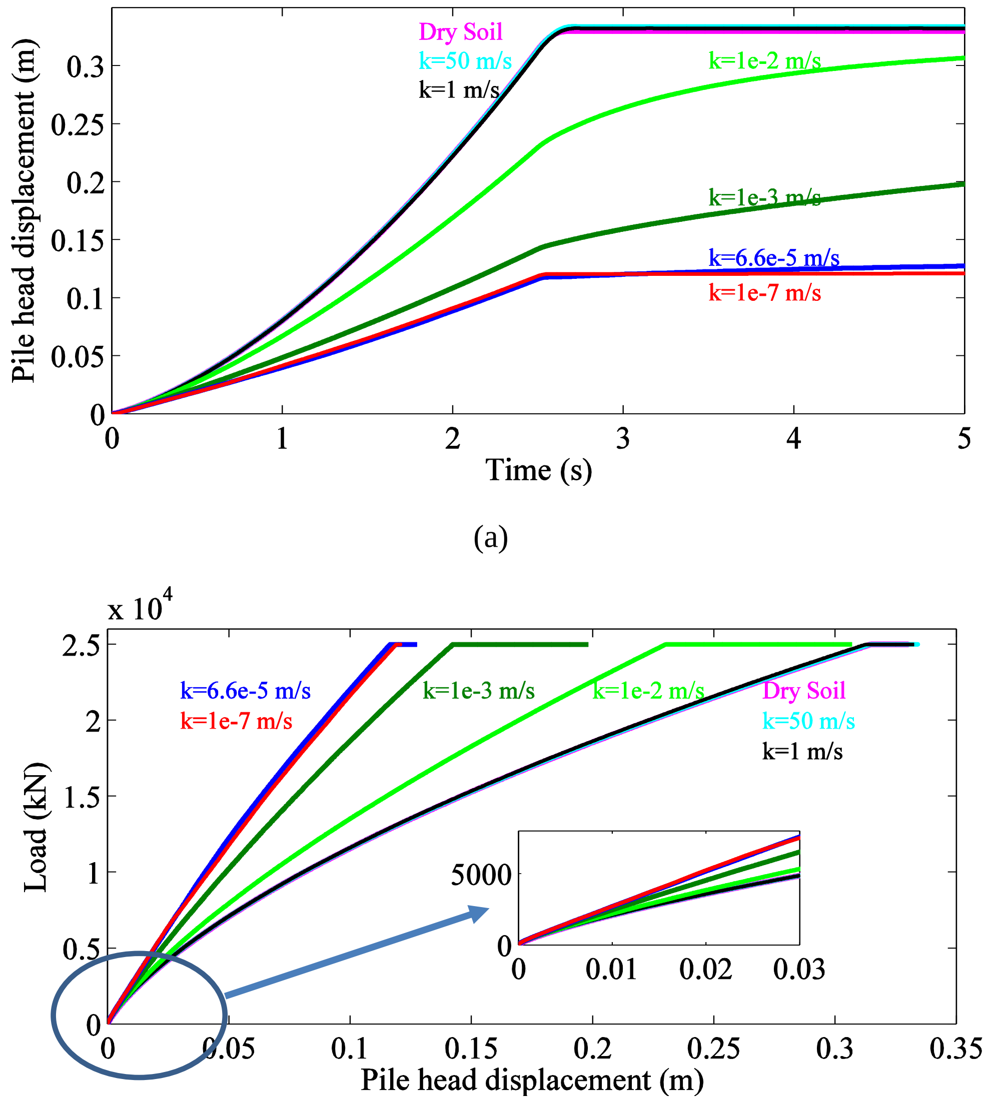

(b)

Figure 4.4: Cavitation allowed: (a) Pile head displacement-time relationship and (b) load-displacement curve

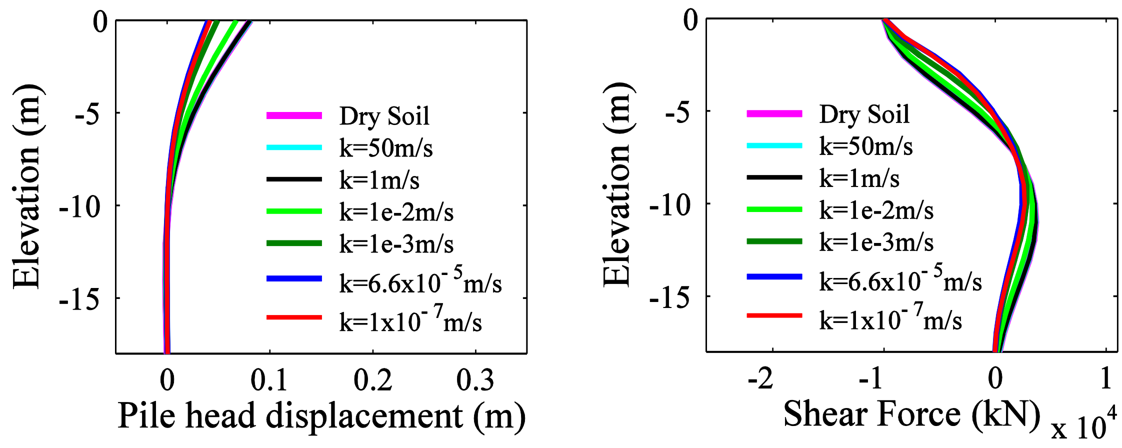

(a)

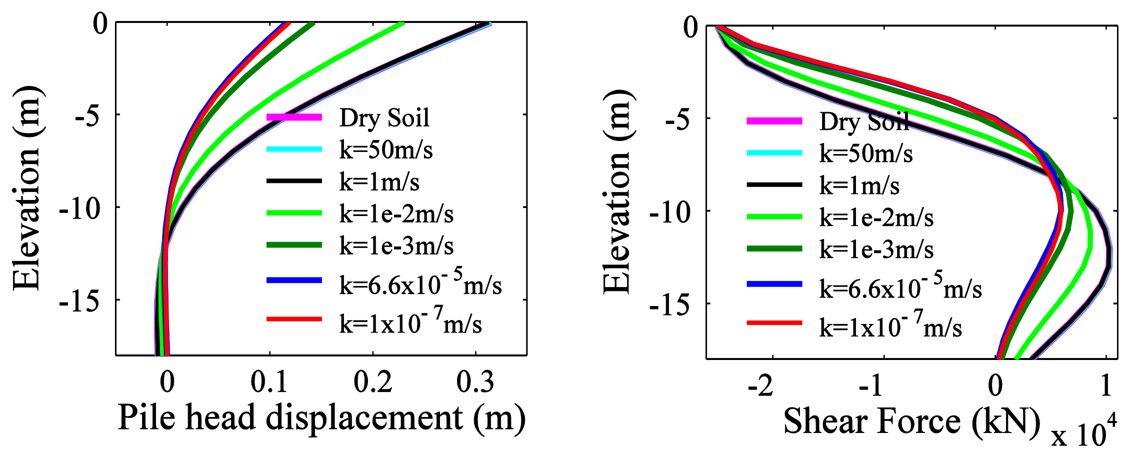

(b)

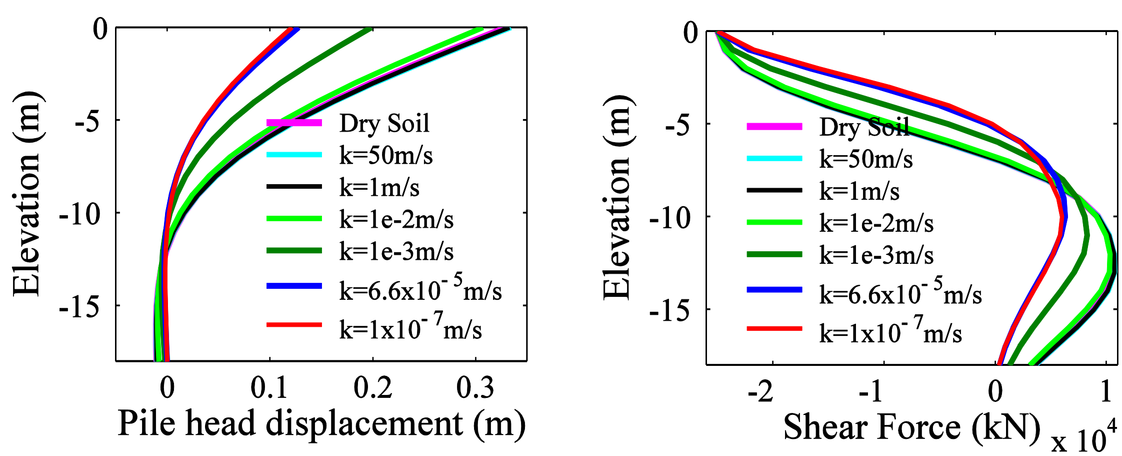

(c)

Figure 4.5: Pile deflection profiles and shear force profiles at: (a) t = 1 sec, (b) t = 2.5 sec, and (c) t = 5 sec

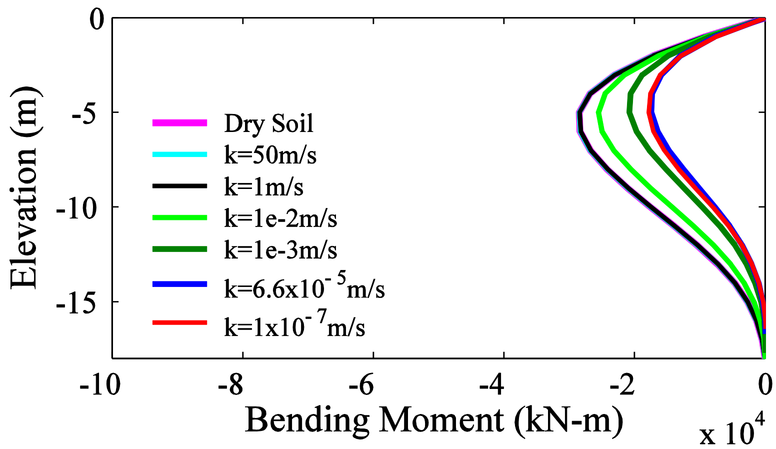

(a)

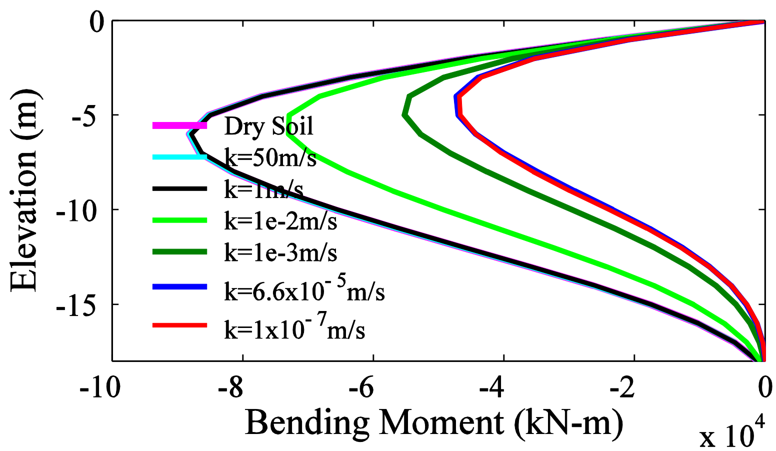

(b)

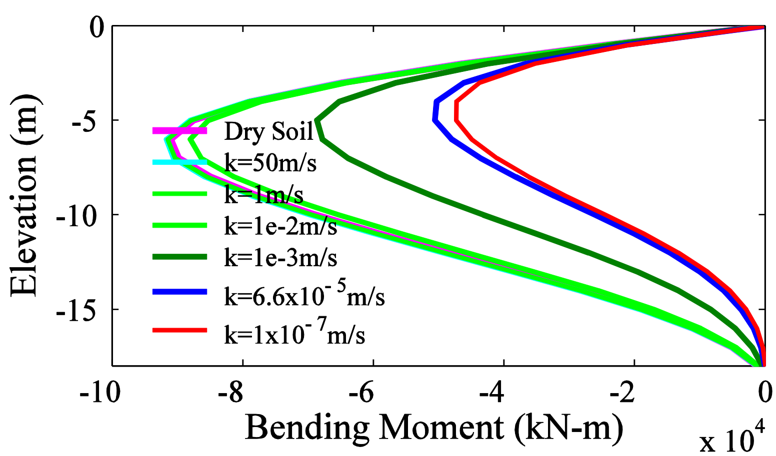

(c)

Figure 4.6: Pile bending moment profiles at: (a) t = 1 sec, (b) t = 2.5 sec, and (c) t = 5 sec

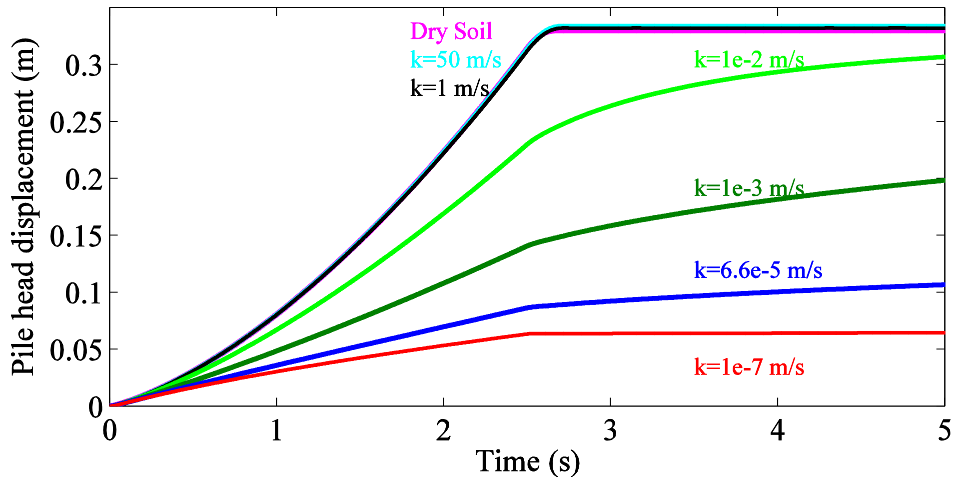

(a)

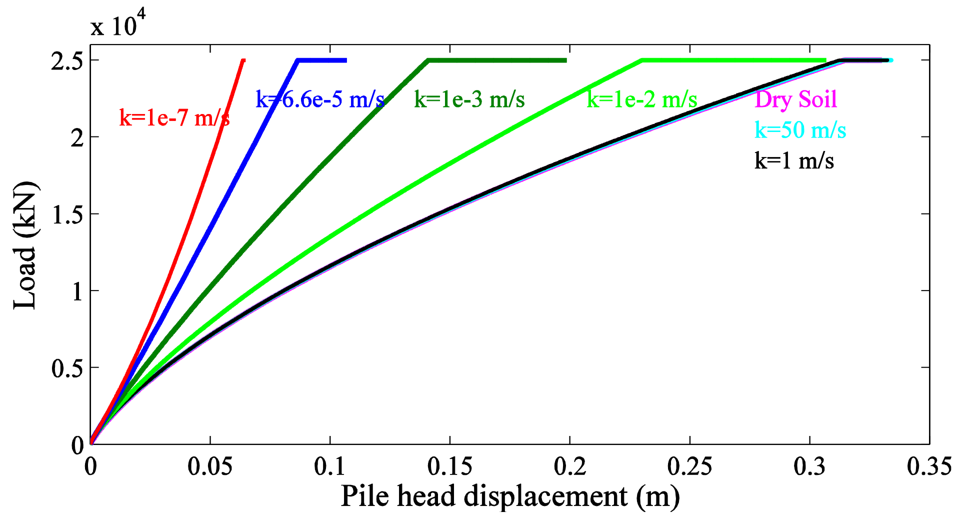

(b)

Figure 4.7: Without cavitation: (a) Pile head displacement-time relationship and (b) load-displacement curve

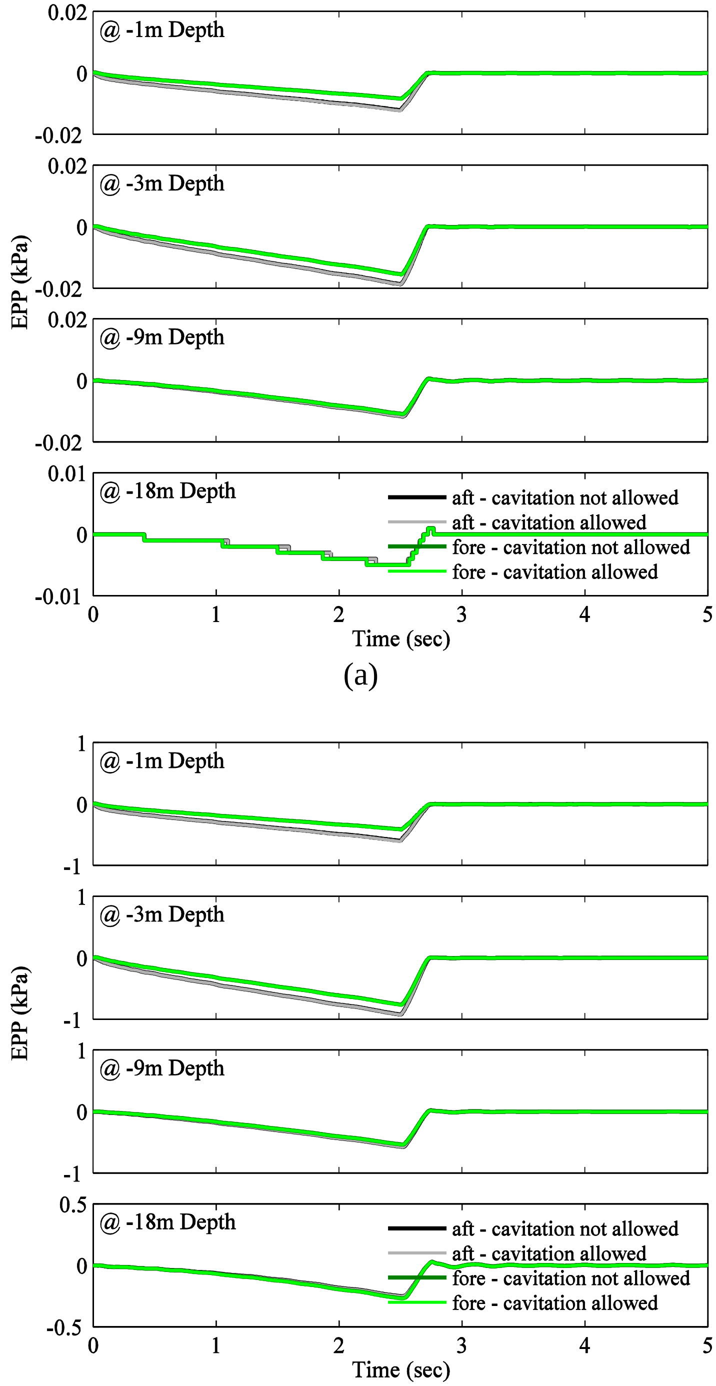

(a)

(b)

Figure 4.8: Time histories of excess pore pressure adjacent to soil-pile interfacing layer for permeability coefficients: (a) k = 50 m/s and (b) k = 1 m/s at 4 different elevations

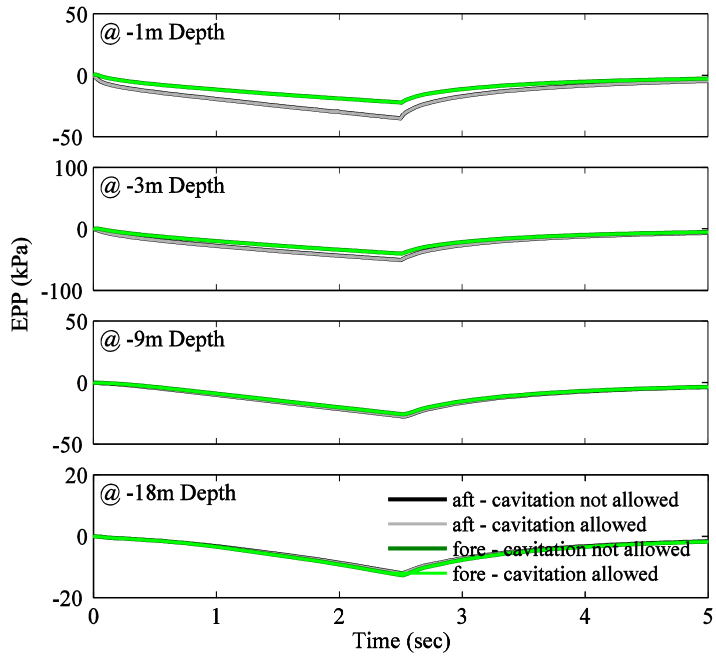

(a)

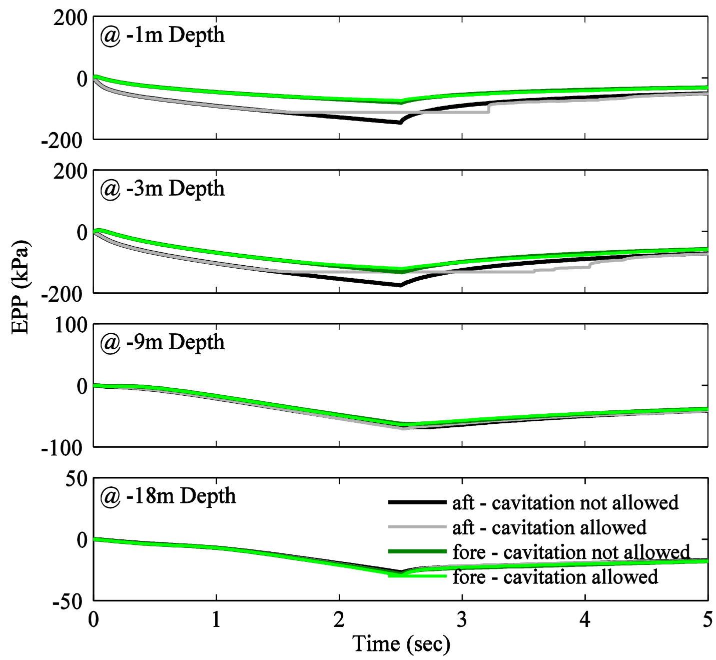

(b)

Figure 4.9: Time histories of excess pore pressure adjacent to soil-pile interfacing layer for permeability coefficients: (a) k = 1e-2 m/s and (b) k = 1e-3 m/s at 4 different elevations

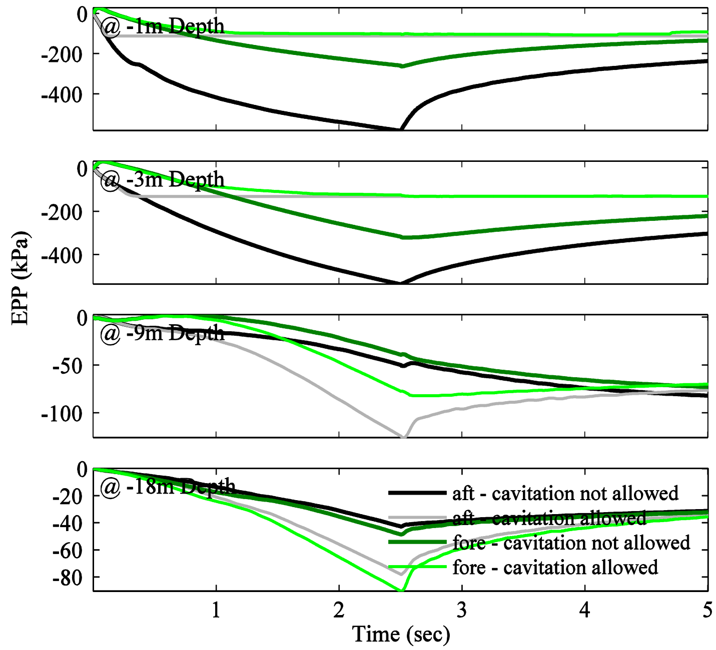

Figure 4.10: Time histories of excess pore pressure adjacent to soil-pile interfacing layer for permeability coefficients k = 6.6e-5 m/s at 4 different elevations

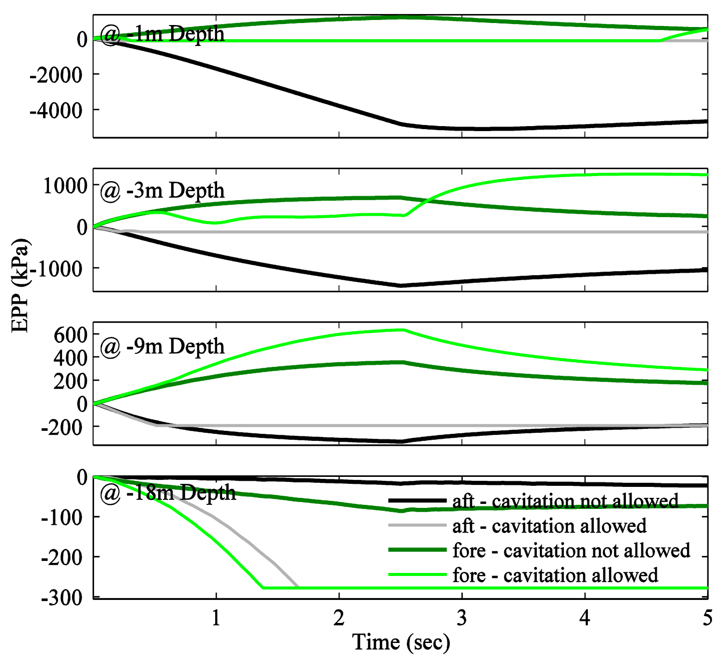

Figure 4.11: Time histories of excess pore pressure adjacent to soil-pile interfacing layer for permeability coefficients k = 1e-7 m/s at 4 different elevations

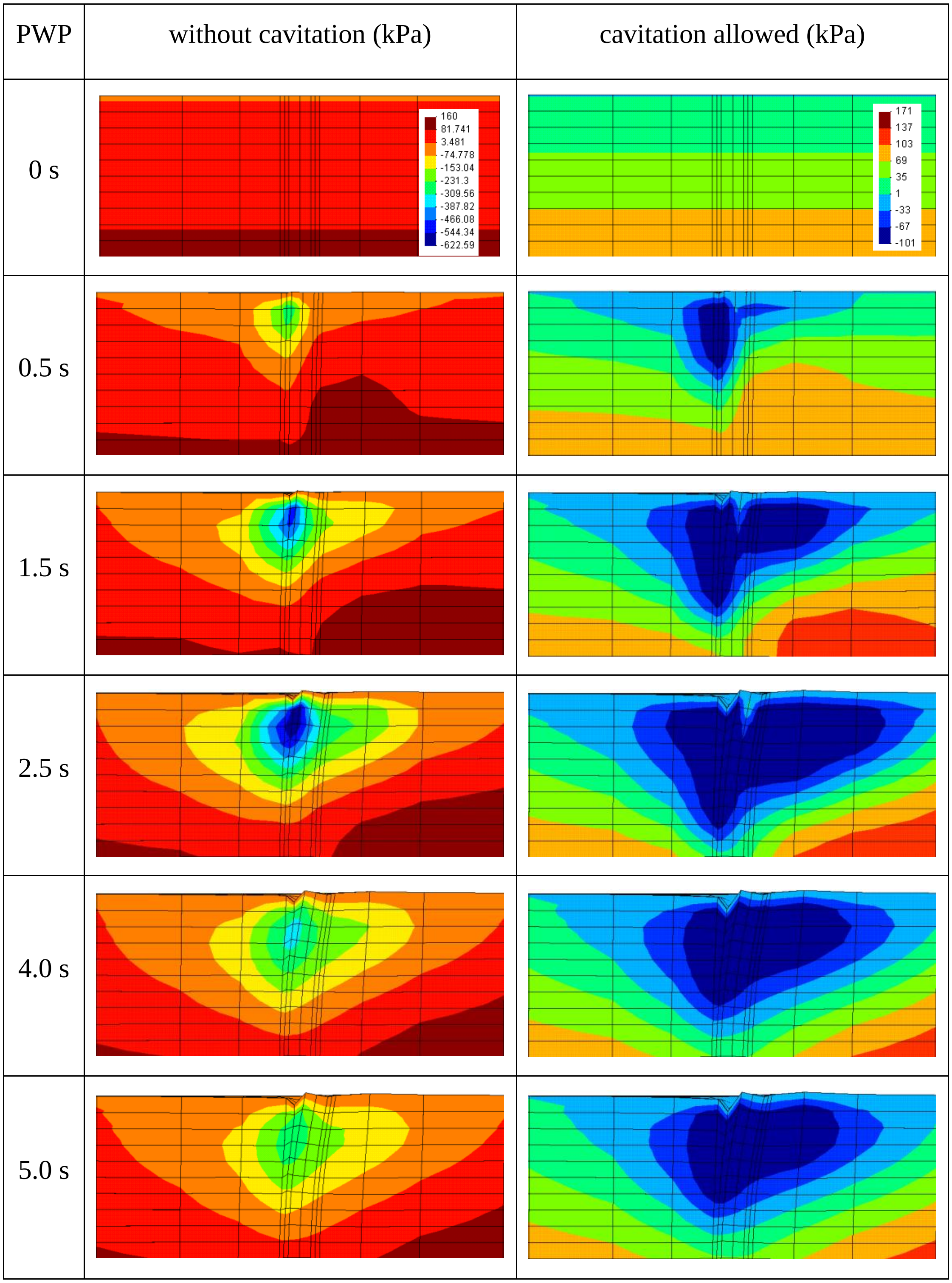

Figure 4.12: Pore water distribution for permeability coefficient of 6.6e-5 m/s w/o and with cavitation cutoff (close up side view 24.96 m×7.35 m)

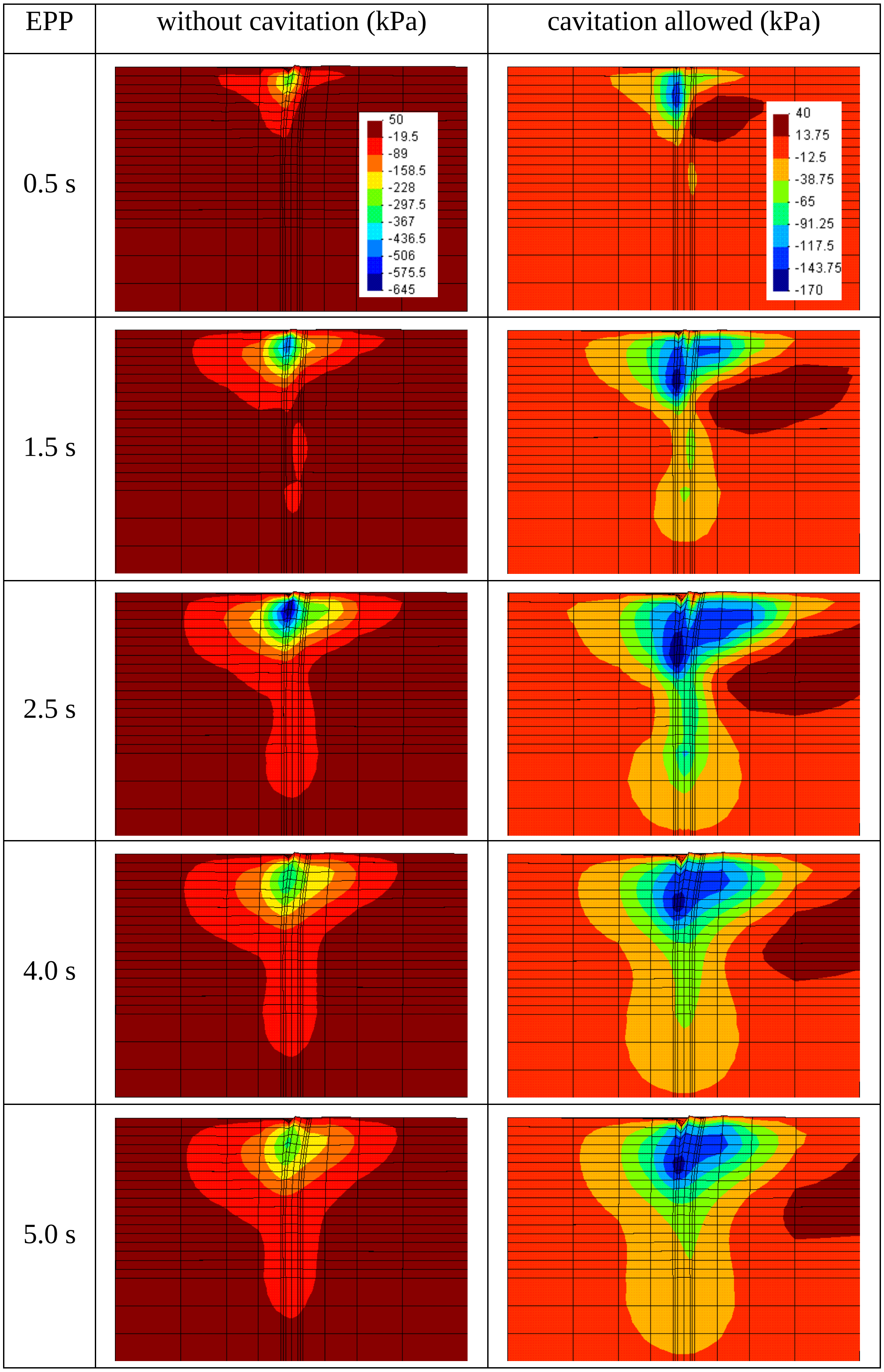

Figure 4.13: Excess water distribution for permeability coefficient of 6.6e-5 m/s w/o and with cavitation cutoff (close up side view 39.64 m×27.38 m)

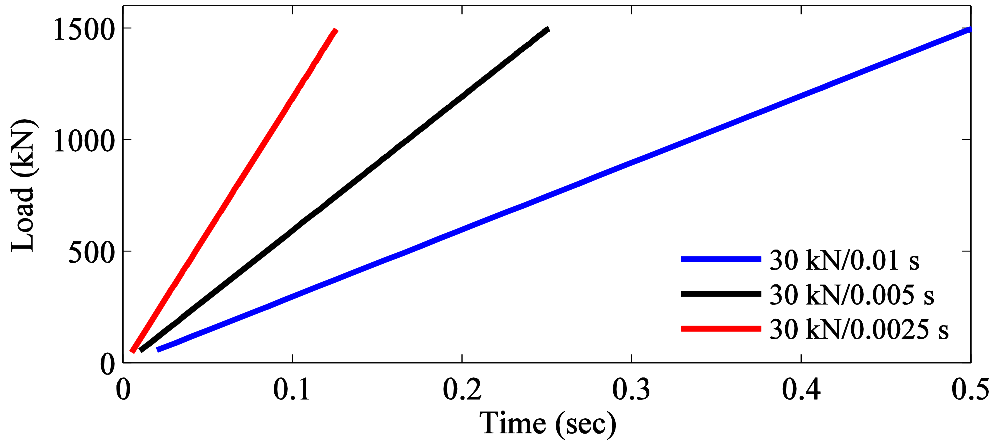

Figure 4.14: Loading scenarios for pushover analysis

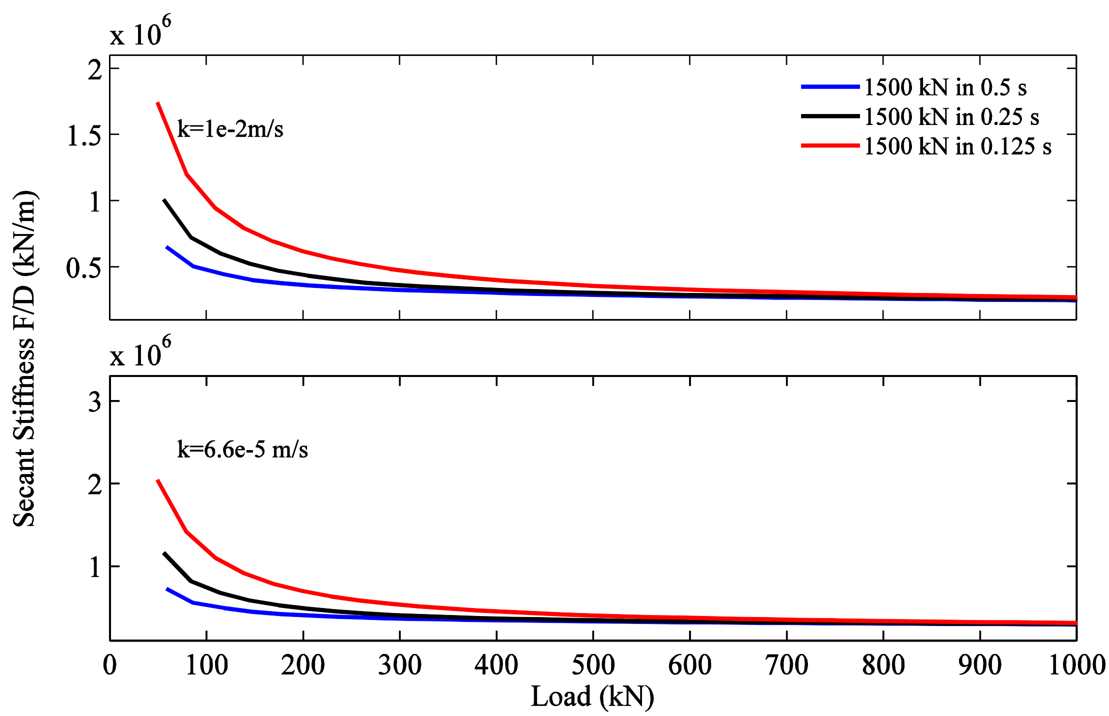

Figure 4.15: Secant Stiffness versus load for 3 different constant loading rate scenarios

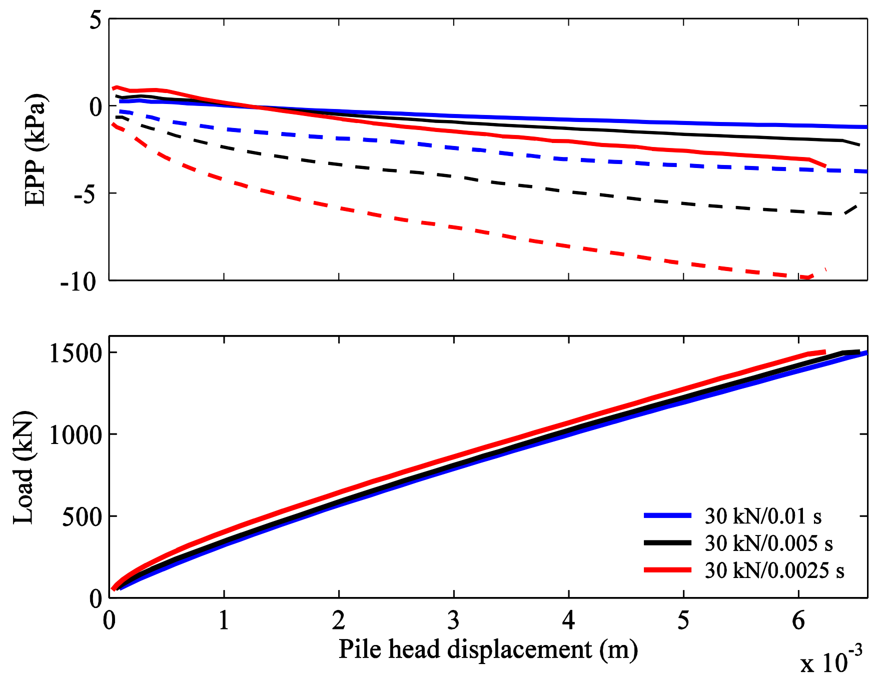

(a)

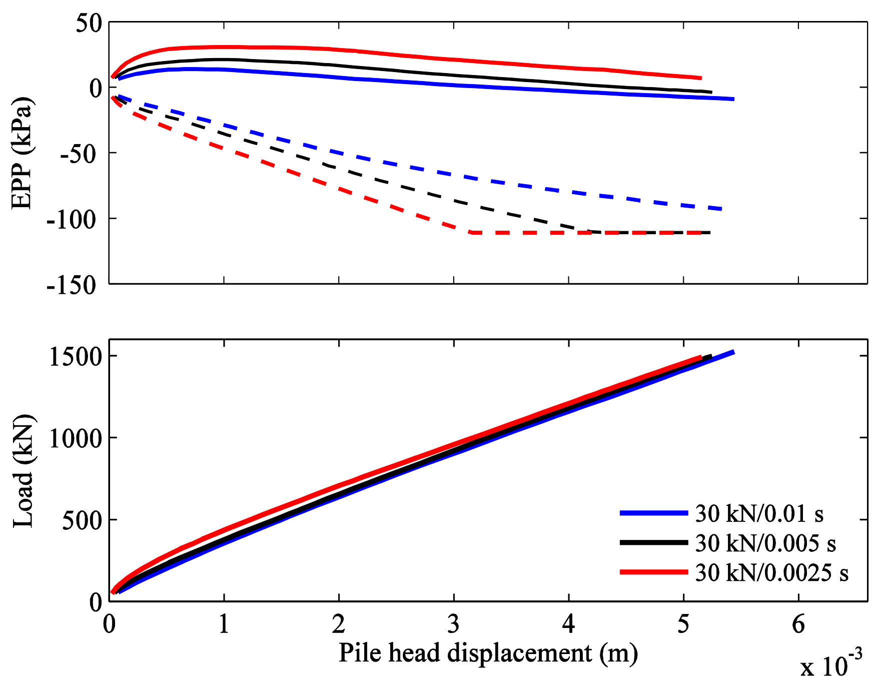

(b)

Figure 4.16: EPP versus lateral load behind (dashed line) and in front of (solid line) the pile for three loading rate cases: (a) k = 1e-2 m/s and (b) k = 6.6e-5 m/s

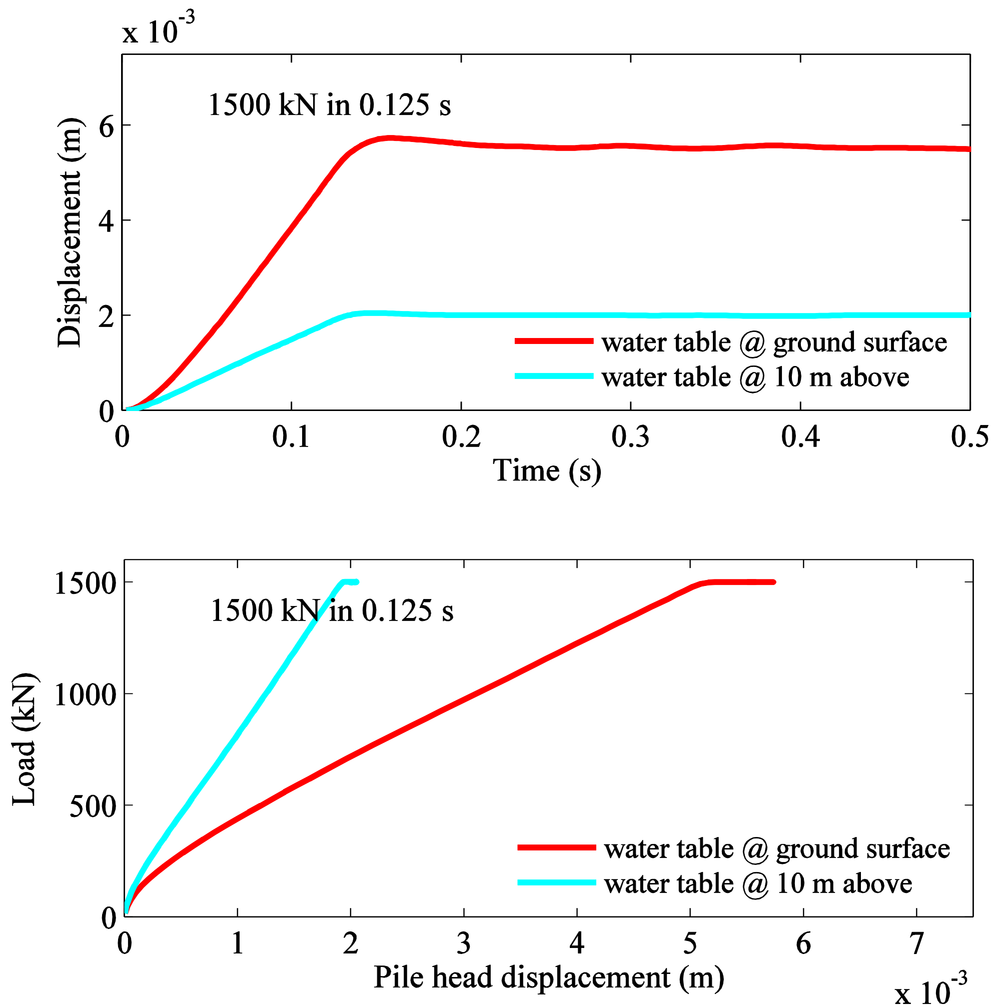

Figure 4.17: Pile response for medium dense sand with water table at ground surface and at 10 meters above

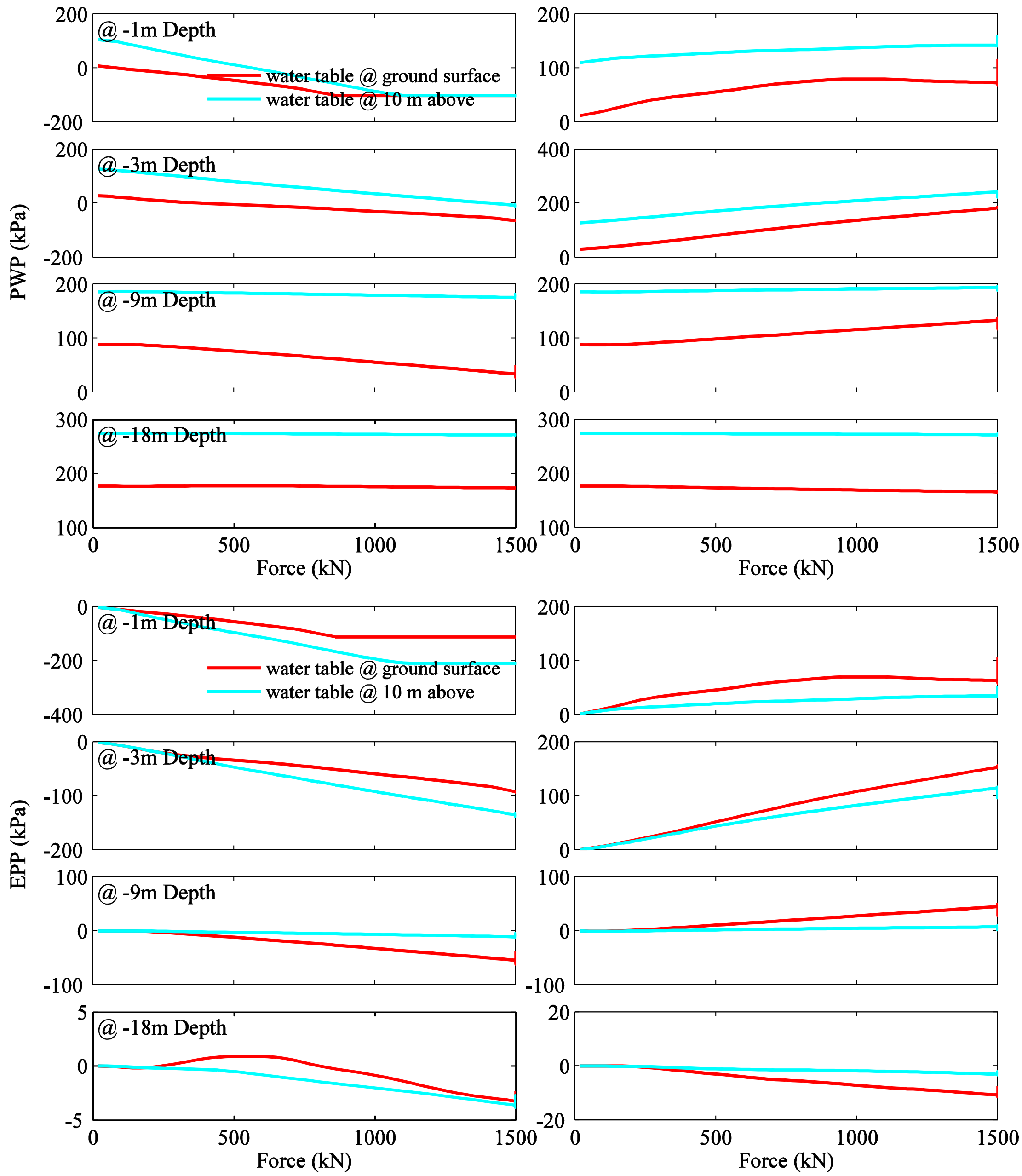

Figure 4.18: PWP and EPP versus lateral load behind and in front of the pile

PWP (kPa) / F (kN)	Case 1 1500 kN in 0.5 s	Case 2 1500 kN in 0.25 s	Case 3 1500 kN in 0.125 s
300	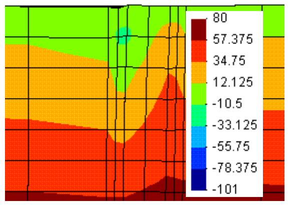	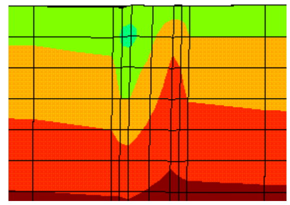	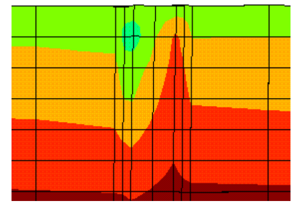
600	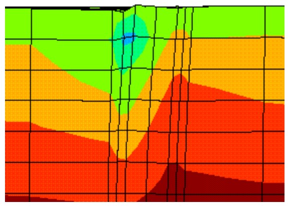	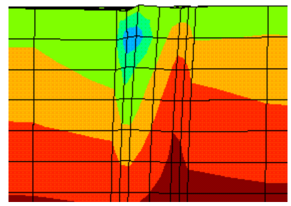	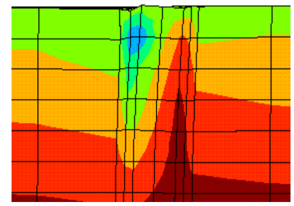
900	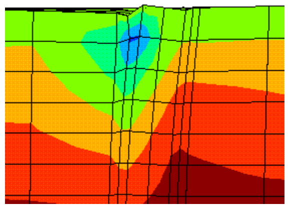	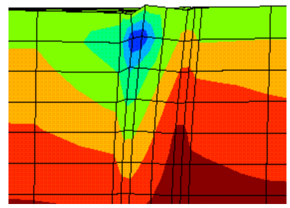	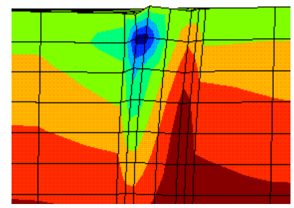
1200	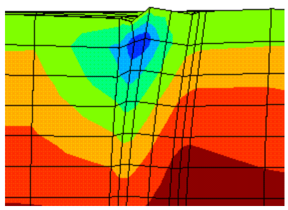	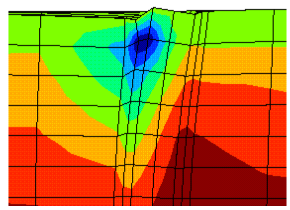	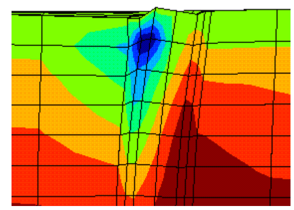
1500	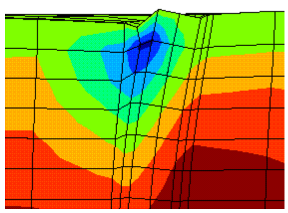	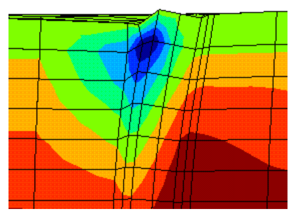	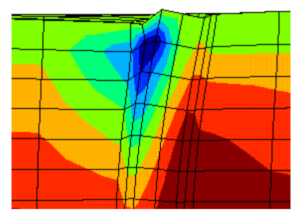

Figure 4.19: Pore water pressure contour for permeability coefficient of 6.6e-5 m/s for loading scenarios 1, 2 and 3 on deformed mesh (factor = 200) up to 6.2 m depth

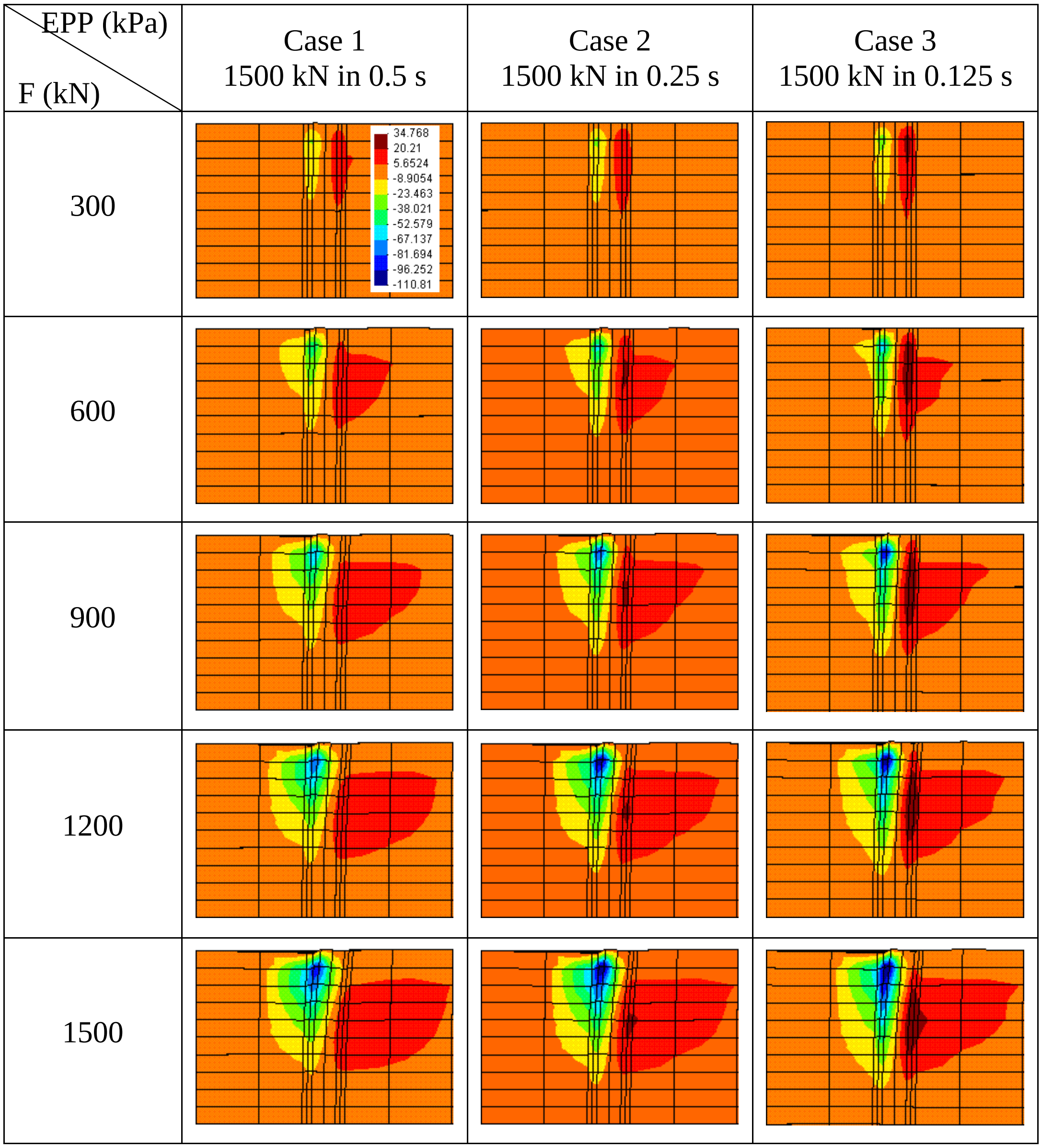

Figure 4.20: Excess pore water pressure contour for permeability coefficient of 6.6e-5 m/s for loading scenarios 1, 2 and 3 on deformed mesh (factor = 100)) up to 10 m depth

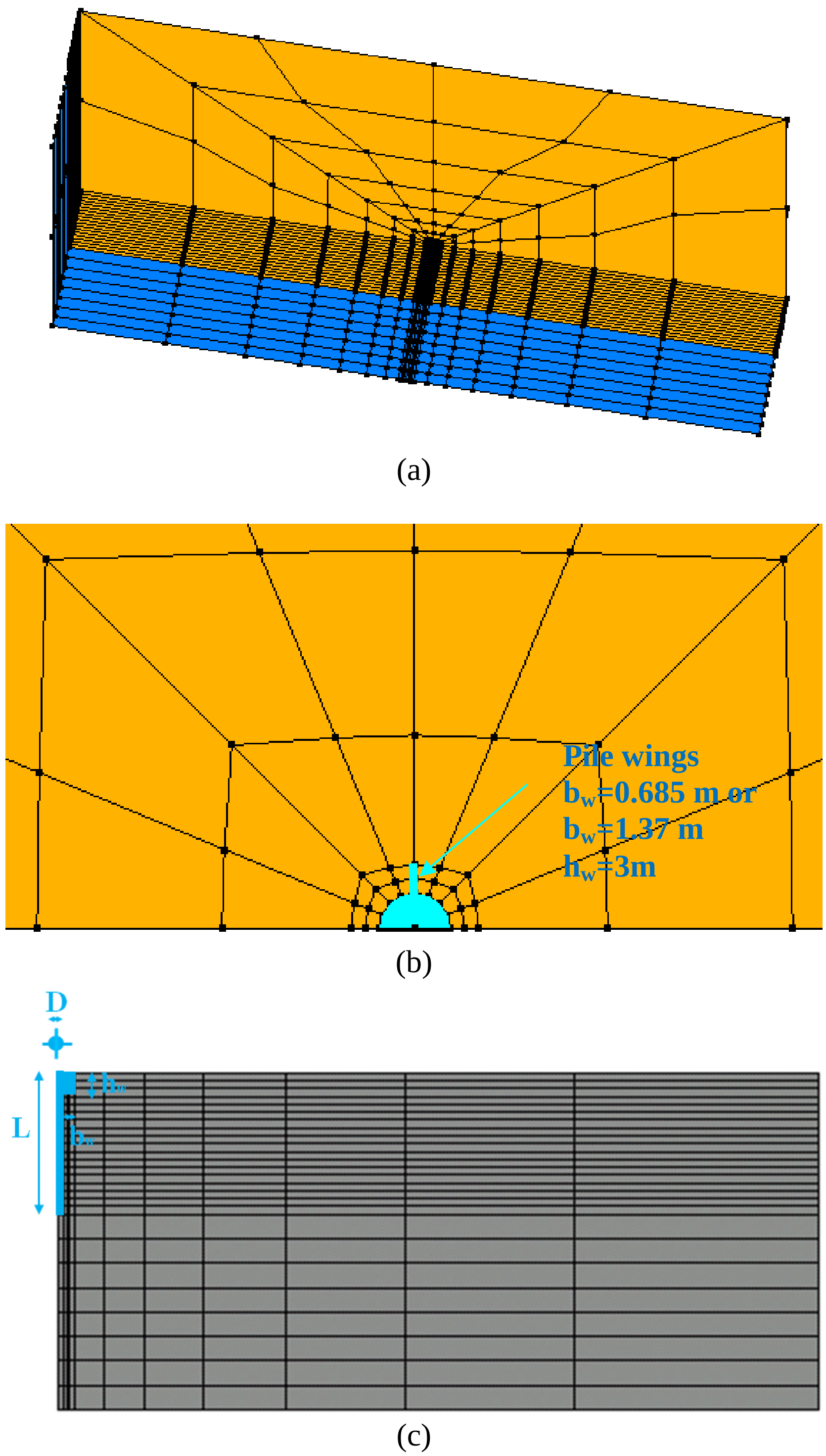

Figure 4.21: (a) Full mesh, (b) close-up plan view around the pile, and (c) side view for the pile with wings

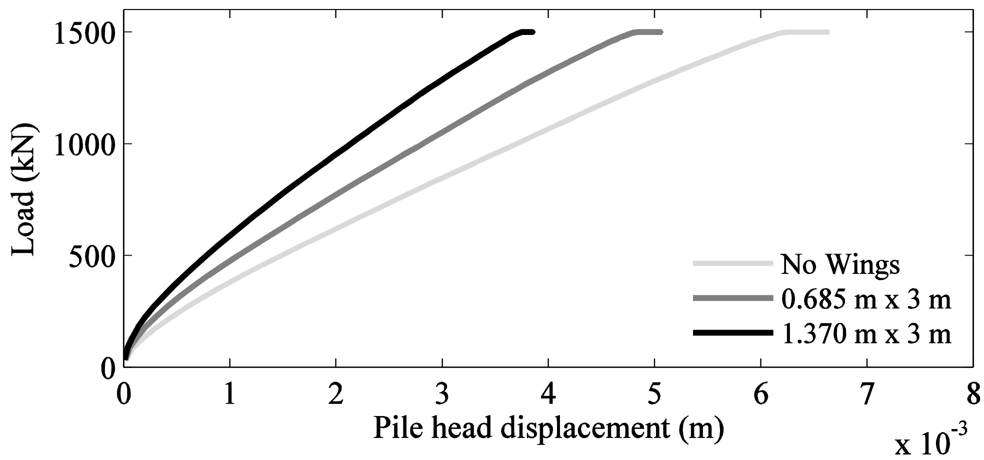

(a)

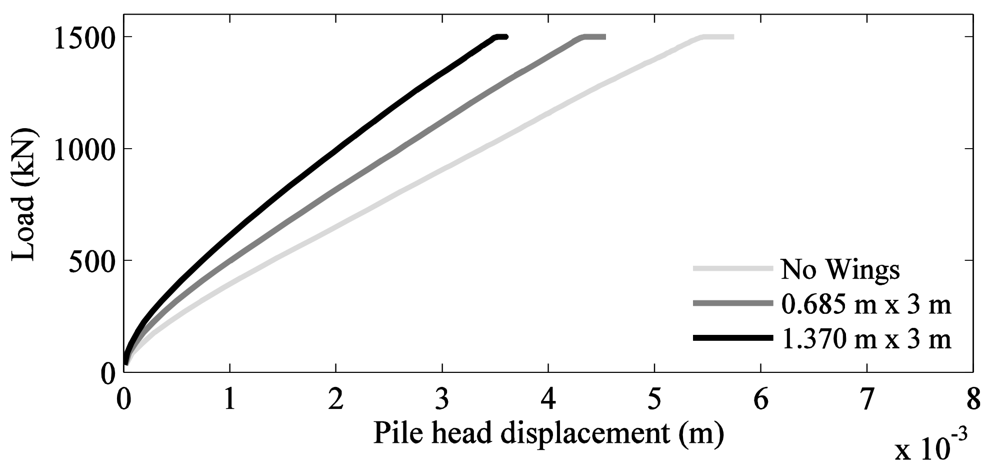

(b)

Figure 4.22: Effect of pile wings on load-displacement curves for permeability (a) k = 1e-3 m/s and (b) k = 6.6e-5 m/s with loading rate 30kN/0.005 s

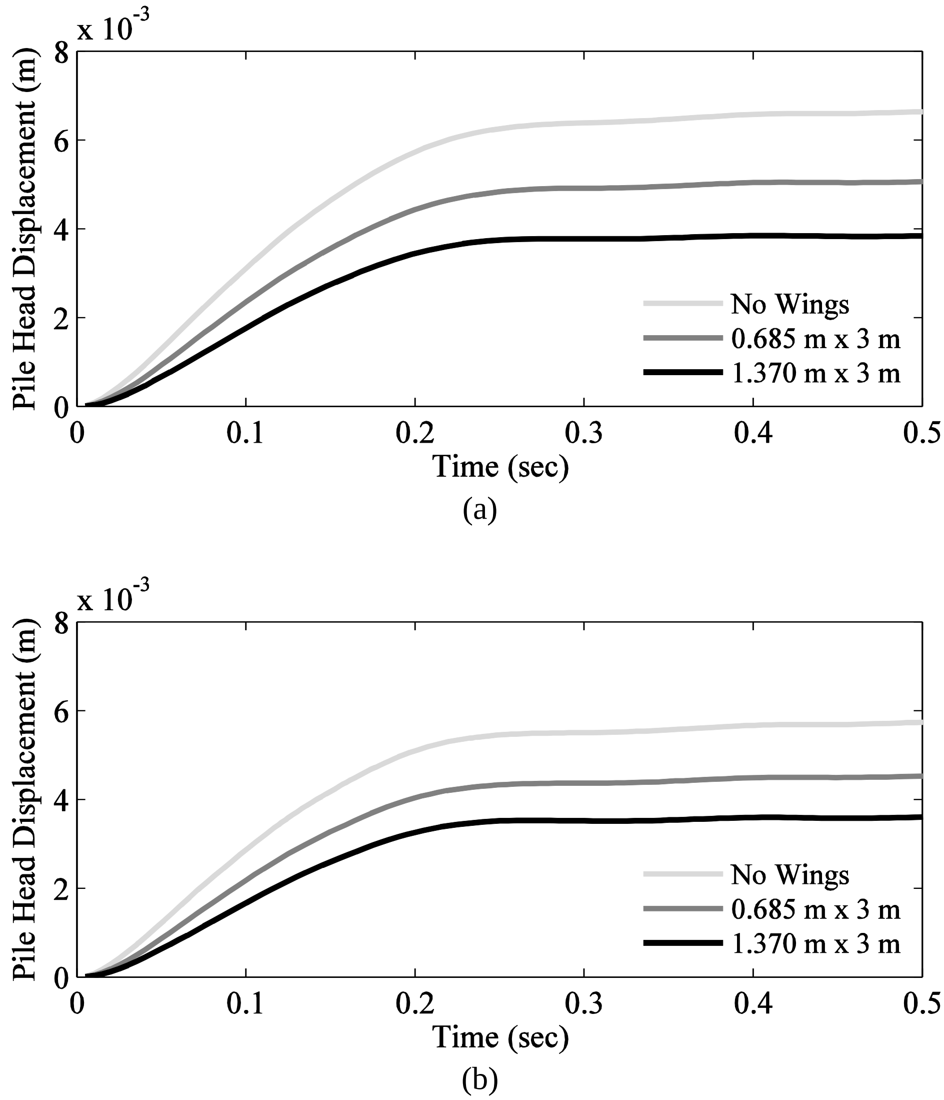

Figure 4.23: Change of pile head displacement vs time for with and without pile wings cases for permeability (a) k = 1e-3 m/s and (b) k = 6.6e-5 m/s with loading rate 30kN/0.005 s

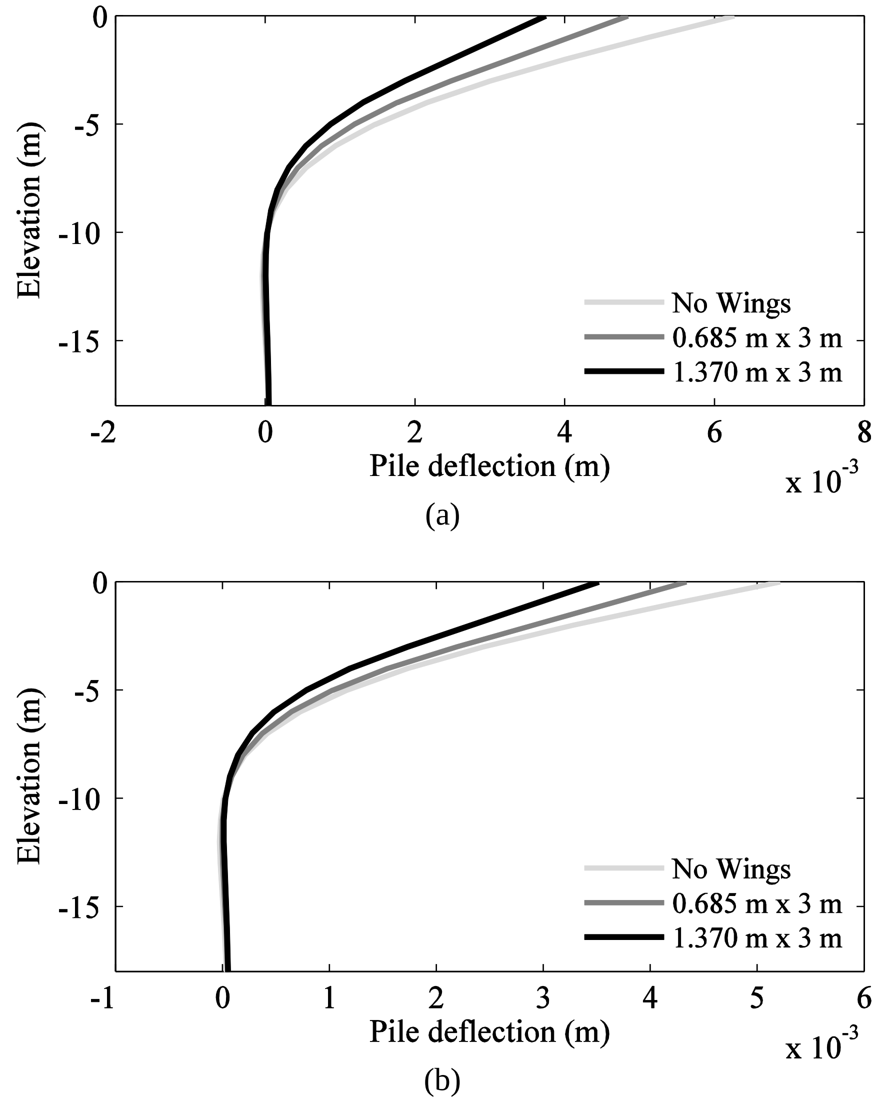

Figure 4.24: Pile deflection profile at t = 0.25 s for permeability (a) k = 1e-3 m/s and (b) k = 6.6e-5 m/s with loading rate 30kN/0.005 s

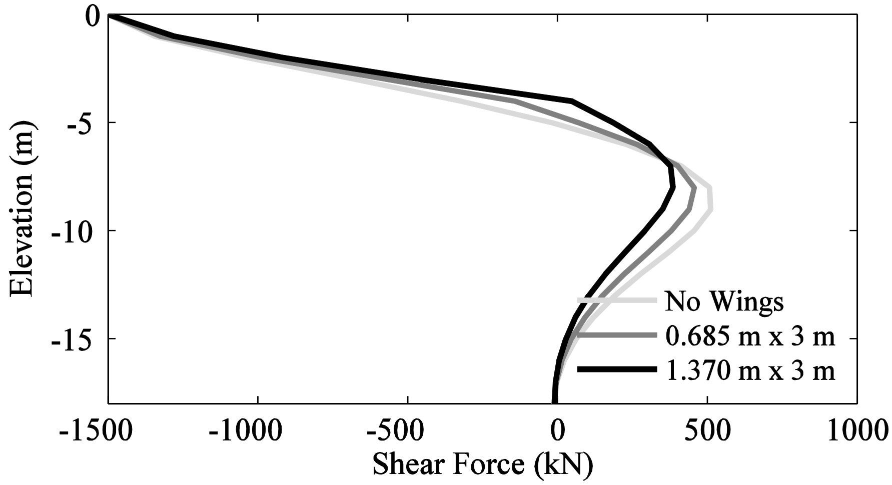

(a)

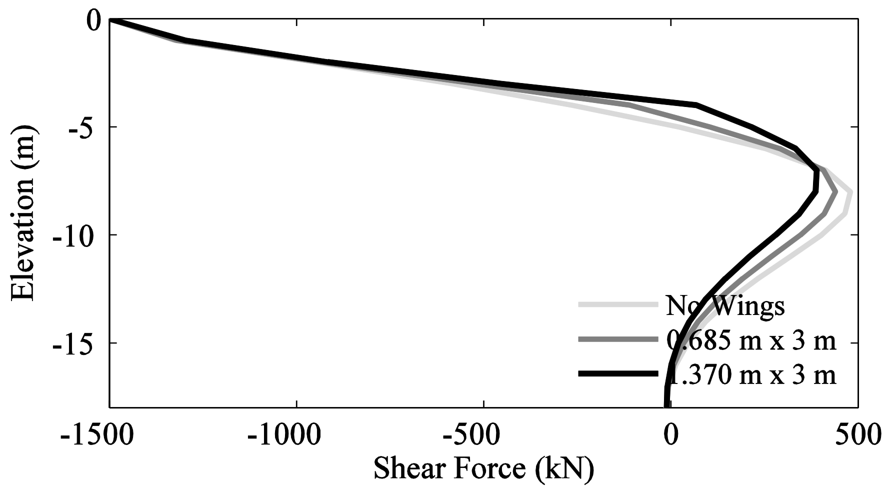

(b)

Figure 4.25: Shear Force Profile at t = 0.25 s for permeability (a) k = 1e-3 m/s and (b) k = 6.6e-5 m/s with loading rate 30kN/0.005 s

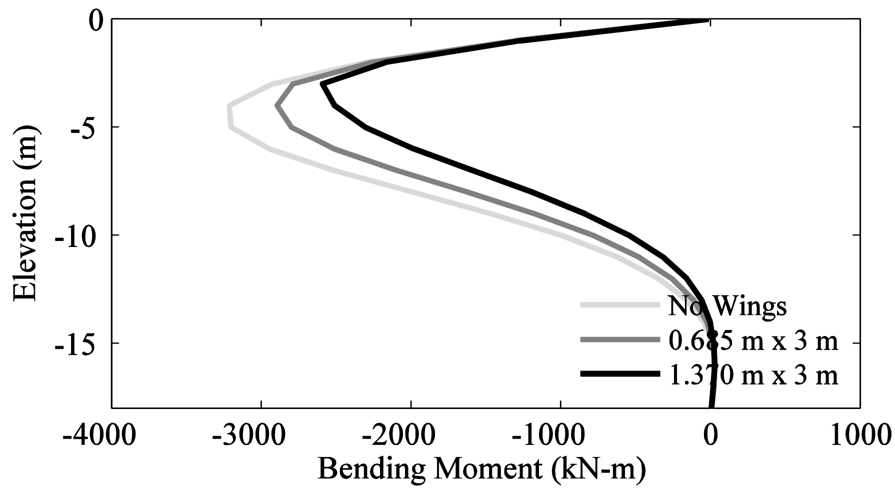

(a)

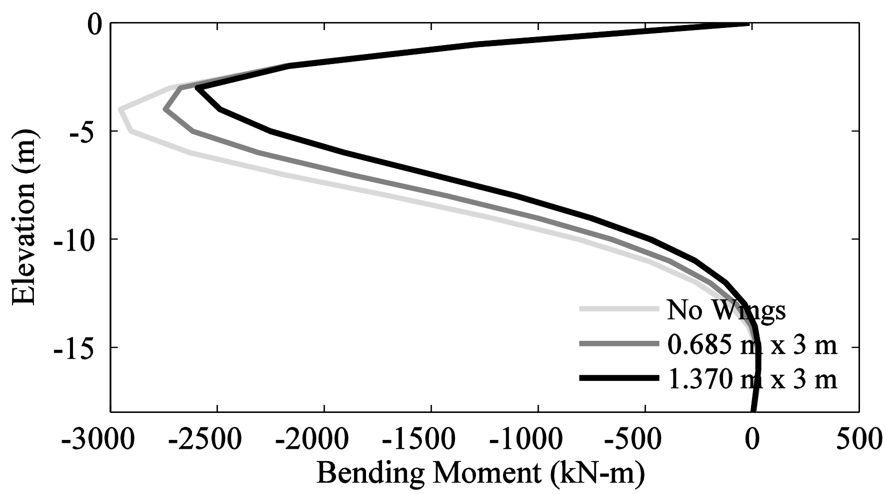

(b)

Figure 4.26: Bending Moment Profile at t = 0.25 s for permeability (a) k = 1e-3 m/s and (b) k = 6.6e-5 m/s with loading rate 30kN/0.005 s

F (kN)	Displacement (m)		
500	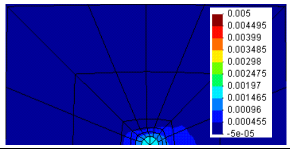	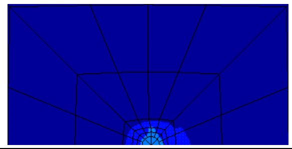	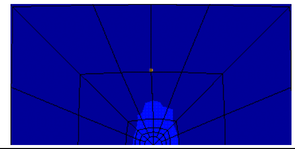
1000	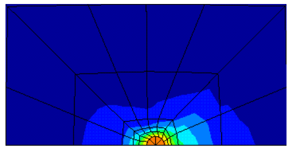	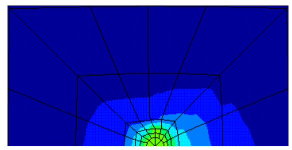	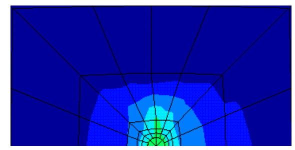
1500 @ 0.25 s	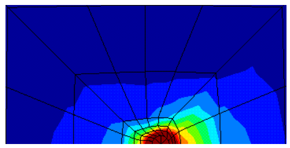	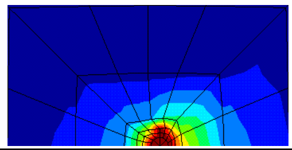	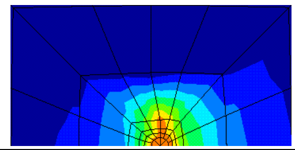
1500 @ 0.5 s	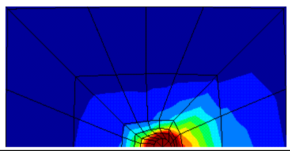	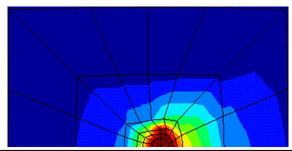	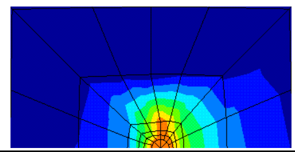
	(a)	(b)	(c)

Figure 4.27: Deformed mesh for (a) no wing case and (b) with wing of $b_w = 0.685$ m and $h_w = 3$ m, and (c) with wing of $b_w = 1.370$ m and $h_w = 3$ m (factor = 200) for permeability k = 1e-3 m/s

F (kN)	Displacement (m)		
500	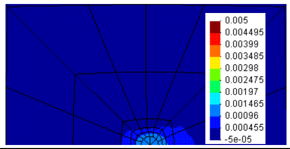	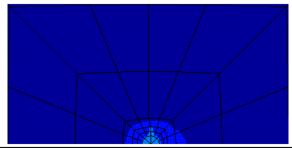	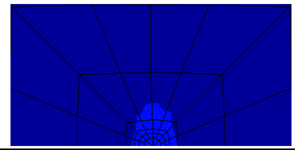
1000	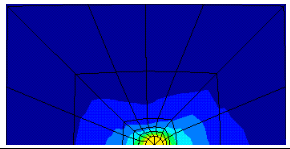	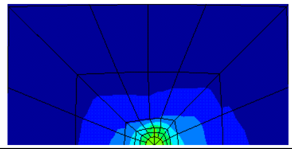	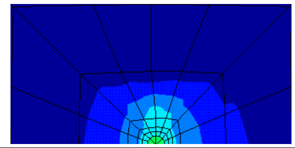
1500 @ 0.25 s	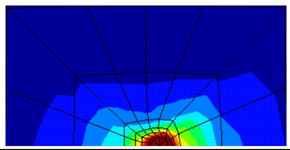	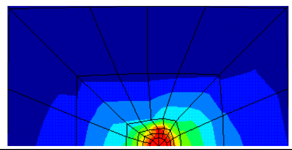	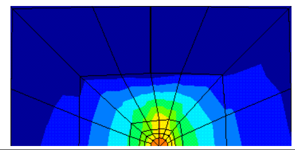
1500 @ 0.5 s	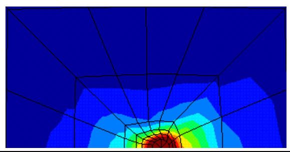	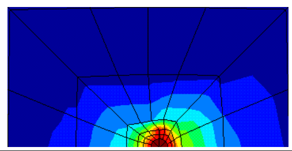	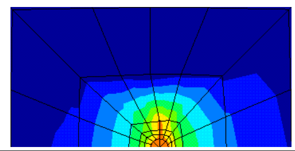
	(a)	(b)	(c)

Figure 4.28: Deformed mesh for (a) no wing case and (b) with wing of $b_w = 0.685$ m and $h_w = 3$ m, and (c) with wing of $b_w = 1.370$ m and $h_w = 3$ m (factor = 200) for permeability k = 6.6e-5 m/s

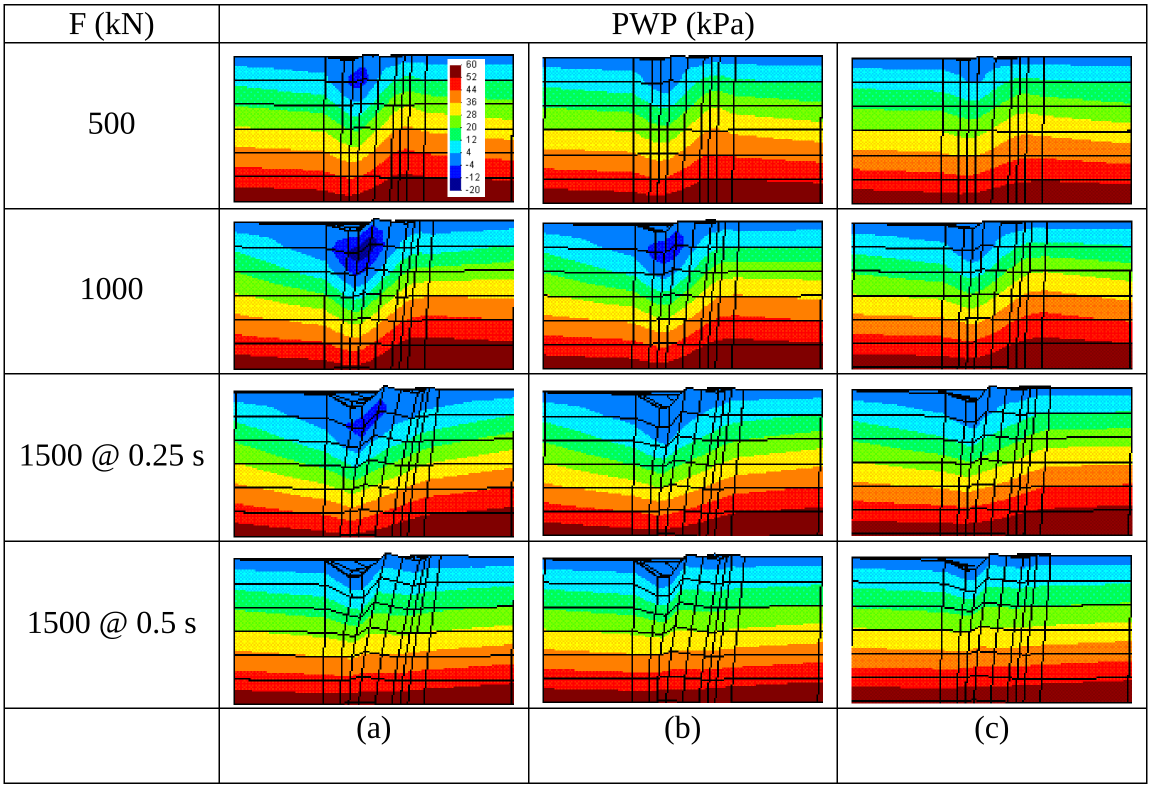

Figure 4.29: PWP on deformed mesh for (a) no wing case and (b) with wing of b_w = 0.685 m and h_w = 3 m, and (c) with wing of b_w = 1.370 m and h_w =3 m for permeability k = 1e-3 m/s (factor = 200)

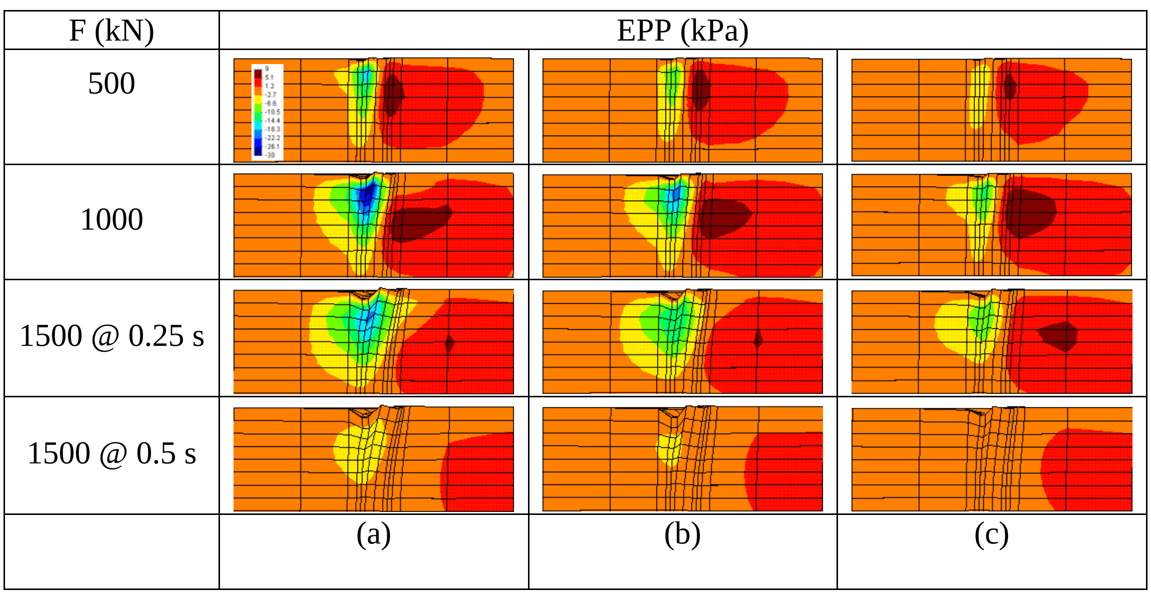

Figure 4.30: EPP on deformed mesh for (a) no wing case and (b) with wing of b_w = 0.685 m and h_w = 3 m, and (c) with wing of b_w = 1.370 m and h_w = 3 m for for permeability k = 1e-3 m/s (factor = 200)

F (kN)	PWP (kPa)		
500	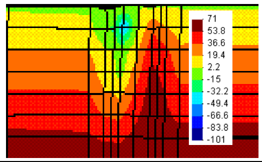	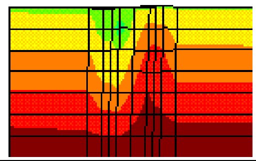	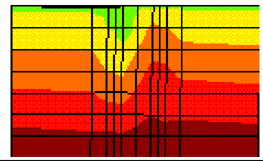
1000	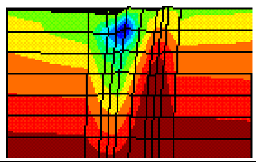	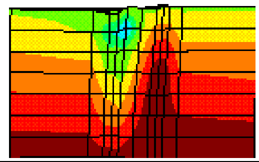	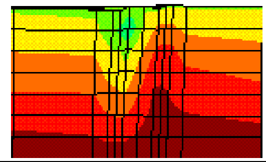
1500 @ 0.25 s	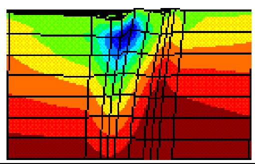	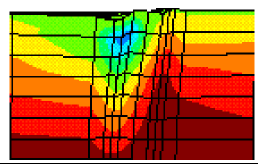	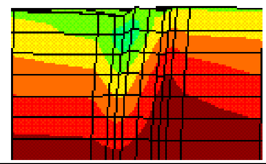
1500 @ 0.5 s	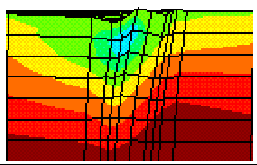	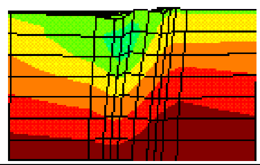	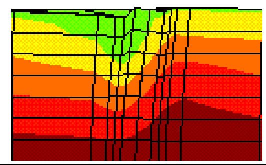
	(a)	(b)	(c)

Figure 4.31: PWP on deformed mesh for (a) no wing case and (b) with wing of b_w = 0.685 m and h_w = 3 m, and (c) with wing of b_w = 1.370 m and h_w = 3 m for permeability k = 6.6e-5 m/s (factor = 200)

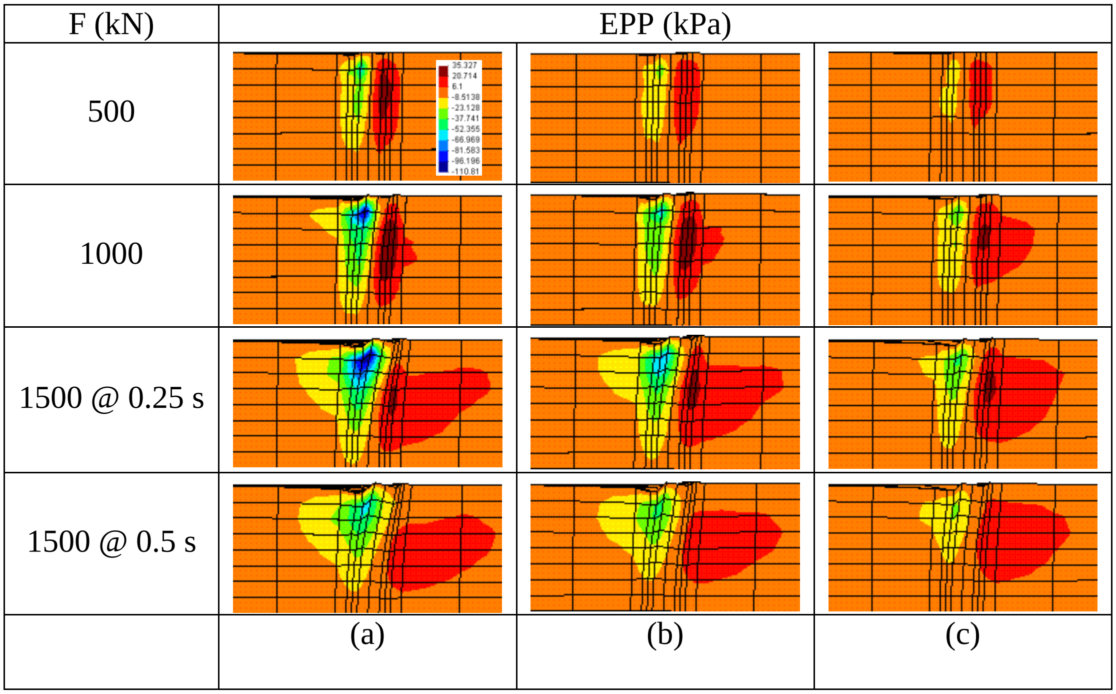

Figure 4.32: EPP on deformed mesh for (a) no wing case and (b) with wing of $b_w = 0.685$ m and $h_w = 3$ m, and (c) with wing of $b_w = 1.370$ m and $h_w = 3$ m for permeability k = 6.6e-5 m/s (factor = 200)

Chapter 5

Eureka Geotechnical Downhole Array Data Analysis

The geotechnical downhole-array monitoring seismic response in near-surface strata provides valuable information on local soil dynamic characteristics. In particular, insights into the relationships between site geologic conditions and actual ground seismic behavior can be obtained with the help of system identification techniques. In this chapter, downhole array records at the Eureka, California site are employed to examine the linear/nonlinear ground response. This Eureka geotechnical array was installed by California Strong Motion Instrumentation Program (CSMIP) in cooperation with California Department of Transportation (Caltrans) in 1995. Ten earthquakes were recorded during the period 2000 - 2012. Cross-correlation analyses and spectral system identification are performed to evaluate the average shear wave velocities and site resonant frequencies. Nonlinear site response during the moderate shaking event of Ferndale Earthquake (M_w 6.5) on Jan 9, 2010 was observed. In addition, a 1-D numerical model of the site is developed using the finite element (FE) program - Cyclic1D. This FE model is calibrated using the identified site characteristics and shows a good agreement between the computed and recorded ground response.

5.1 Introduction

Local soil conditions can greatly affect the site seismic response, resulting in significant impact on the behavior of adjacent foundation-structure systems during earthquakes. Soil properties obtained from in-situ or laboratory testing procedures are always associated with limitations, such as disturbance of soil sampling or difficulty of reproducing seismic loading history (Elgamal et al. 1995). On the other hand, recorded site response provides unique insights into local soil behavior subjected to a wide range of earthquake loading scenarios. As such, data collected by geotechnical downhole arrays along with system identification techniques could further advance our understanding of the site dynamic mechanisms.

In this chapter, records of a geotechnical downhole array located in Eureka were employed to perform cross-correlation analyses and site resonant analysis. This downhole array was installed by California Strong Motion Instrumentation Program (CSMIP) in cooperation with California Department of Transportation in 1995 (Graizer et al. 2000). Objectives of this study include: (1) evaluation of shear wave velocities; (2) assessment of soil/site dynamic properties, such as resonant frequencies and seismic shear stress-strain histories; (3) examination of the nonlinear soil response during the moderate shaking event; and (4) development of a FE model to simulate the site seismic response.

General information of downhole instrumentation as well as variations of ground motion records along the depth is provided in the first part of the chapter. Thereafter, cross-correlation analysis is performed to estimate the average shear wave velocities. Seismic shear stress-strain histories are evaluated using a simple identification procedure developed earlier in the Lotung downhole array studies (Zeghal et al. 1995; Elgamal et al. 1996). Transfer function is used to assess resonant frequencies of soil layers. A 1-D FE model is developed based on the identified soil properties. Computational simulation results are presented, discussed, and compared to the recorded seismic site response.

5.2 Site Description and General Information

5.2.1 Geotechnical Downhole Array at Eureka Station 89734

The Eureka Geotechnical Downhole Array (GDA, CSMIP Station 89734) located between the Samoa Channel Bridge and the Middle Channel Bridge (Figure 5.1) was instrumented through the joint efforts of CSMIP and the California Department of Transportation (Caltrans) in 1995. Horizontal and vertical motion sensor layouts as well as shear/pressure wave velocity profiles of the underlying soil from geophysical test are shown in Figure 5.2 and Figure 5.3. This downhole array consists of 15 accelerometers at five different depths (ground surface, 19 m, 33 m, 56 m, and 136 m) oriented in the north-south (NS), east-west (EW) and vertical directions. Elevation of the ground surface sensors is +1 m with respect to the MSL (Mean Sea Level, personal communication with USGS). Due to the grade in the immediate area, elevation of the ground at the location of the downhole sensors near the road is estimated to be +3 m with respect to MSL (Figure 5.2). Therefore, elevations for the downhole sensors are +1 m, -16 m, -30 m, -53 m and -133 m all referenced to MSL.

5.2.2 Available Earthquake Records

A total of ten earthquakes have been recorded in the period of March 2000 through October 2012 with magnitudes from 4.1M_w to 7.2 M_w (M_w: regional moment magnitude). Varying in peak acceleration (from 0.004 g to 0.197 g), epicentral distances (from 22.2 km to 153.8 km), shaking duration, and frequency content bandwidth, these earthquakes provide valuable information on the site seismic behavior over a broad range of excitations (Elgamal et al. 1995). Table 5.1 presents time, magnitude, epicentral distance and peak horizontal acceleration at ground surface of the recorded earthquakes. Notable is the 2010 Ferndale Earthquake (hereafter, referred to as “the moderate event”) causing a peak ground motion of around 20% g at this site. This M_w 6.5 Ferndale earthquake occurred off the coast of the Humboldt Bay Area, California (Figure 5.4) where the epicenter of this strike-slip earthquake is located northwest of the Mendocino Fracture Zone at a depth of about 29 km (Pitarka et al. 2012). It is the largest earthquake in Humboldt County since the Crescent City Offshore Earthquake in 2005 with an epicenter that is farther away (153.8 m) from the downhole site.

5.2.3 Site Description

A deep soft alluvium geological profile with high water table exists at this location. Subsurface data from a boring test conducted by of the Caltrans show 10 m of very soft clayey silt underlain by slightly compact gray materials. The very dense soil layer is approximately 22 m below the ground surface (Figure 5.5).

Shear velocity (V_s) and pressure wave velocity (V_p) profiles down to a depth of 225 meters are provided by USGS (Figure 5.3). The shear wave velocities are about 158 m/s -230 m/s in the upper 20 meters, and lie in the range of 210 m/s to 460 m/s at the depths of 20 to 60 meters. Bedrock appears to be at a depth of 220 m where the shear wave velocity reaches 870 m/s. The calculated Poisson's ratio (Eq. 5-1) at the elevation of each downhole sensor is listed in Table 5.2, generally indicating saturated soil conditions.

$$\upsilon = \frac{0.5 \times (\frac{v_p}{v_s})^2 - 1}{(\frac{v_p}{v_s})^2 - 1} \qquad (5\text{-}1)$$

5.3 Evaluation of Strong Motion Data

5.3.1 Recorded Time Histories

Sensors of the geotechnical downhole array installed at different depths provide acceleration time histories during earthquake events which can be used to study the local soil profile. Corrected time series (http://www.strongmotioncenter.org), where the raw data have preliminarily been processed with baseline correction and bandpass filters (3 dB pts, 0.17/0.3 Hz ~ 40/46 Hz), are employed. Figure 5.6 - Figure 5.9 depict the recorded time histories along the depths (at the free field surface, 19m, 33m, 56m and 136m) during the moderate 2010 Ferndale Earthquake and a representative weaker shaking event on September 22, 2000, in the two horizontal directions. As shown, the ground movement was amplified from 3.71 cm at the depth of 136 m (Elev. = -133 m) to 9.98 cm at the surface (Elev. = +1 m) during the moderate 2010 Ferndale Earthquake (an increase of 1.7 fold).

Site response between downhole stations along the depth was evaluated using time and frequency domain analyses. Overall, analyses of 8 earthquake records were performed to investigate site low strain properties and the nonlinear soil behavior during the moderate 2010 Ferndale event.

5.3.2 Cross Correlation Analysis

There are various methods to estimate shear wave velocities using the recorded acceleration time histories, such as Fourier spectral ratio, travel time of local peaks, time lag for the maximum cross correlation, phase angle of cross covariance, stress-strain hysteretic loops, etc. (Chang et al. 1996). In this study, seismic shear waves are assumed to propagate vertically. Cross correlation analysis is performed to estimate time needed for shear waves to propagate upwards (incident waves) or downwards (reflected waves) between downhole stations.

The cross-correlation coefficient $C_{a_i a_j}$ between two acceleration time histories *a(i)* and *a(j)* collected from sensor channel *i* and j can be expressed as (Bendat and Piersol 1980; Elgamal et al. 1995):

$$C_{a_i a_j}(\tau = m\Delta t) = \frac{\frac{1}{N-m}\sum_{n=1}^{N-m} a_i(n\Delta t)a_j((n+m)\Delta t)}{\frac{1}{N}\sqrt{\sum_{n=1}^{N} a_i^{\,2}(n\Delta t)}\sqrt{\sum_{n=1}^{N} a_j^{\,2}(n\Delta t)}} \quad , \text{m=0, 1, 2, ..., N-1} \qquad (5\text{-}2)$$

where N is number of time history samples, Δt is the time step of acceleration records, $m\Delta t$ is the time delay at which cross-correlation is calculated. Assuming that a major peak of the cross-correlation appears at a time delay of τ_d, the average incident shear wave velocity between *i* and *j* with a distance of *d* apart can be calculated as:

$$V_s = \frac{d}{\tau_d} \tag{5-3}$$

Low frequency components of the recorded accelerations were filtered before evaluating the cross-correlation functions to separate the incident and reflected wave peaks. Based on recorded downhole acceleration, shear wave velocities are estimated in the north-south and east-west directions. It is observed that the time lag at peak correlation increases with depth. The correlation peaks of incident waves (positive time lags) are higher than those of reflected waves (negative time lags). Identical estimated shear wave velocities using different time windows indicate stability of the velocity estimates. The average cross-correlation function for four of the low-acceleration earthquakes is shown in Figure 5.10 in the two horizontal directions (for the 2007 Ferndale, the 2005 Crescent City, the 2000 Ferndale Offshore, and the 2000 Cape Mendocino earthquakes).

Nonlinearity of the site seismic response was particularly evident during the moderate event (Table 5.3, Table 5.4, and Figure 5.11). Lower average shear wave velocities are obtained when the strong motion phase of the moderate 2010 Ferndale Earthquake is included (Figure 5.12 vs Figure 5.13). The estimated average shear wave velocity decreased during the 30 s - 35 s time window (V_S = 121.4 m/s), leading to a reduction of shear modulus of about 60% (ground surface (+1 m) to -16 m elevation). Average shear strain (Elgamal et al. 1995; Zeghal et al. 1995) during this strong motion time window reached a maximum of about 0.09% (Figure 5.14 and Figure 5.15). The estimated shear modulus (40 percent of the initial shear modulus at shear strain of 0.09%) agrees with the shear modulus degradation curves for sand after Seed and Idriss (1970) as well as after EPRI (1993), which is in a range of 27% -38% for depths ranging from 0 m to 15.24 m (Figure 5.16).

A moving time window of 5 seconds width allows for monitoring the nonlinear soil response during this moderate shaking event (Figure 5.17). The horizontal gray lines indicate the estimated shear wave velocity range obtained on the basis of all available earthquake records and the black points represent variation of shear wave velocity using a 5-second time window.

Figure 5.18 shows cross-correlation between adjacent sensors for the 2000 Eureka Offshore Earthquake. The peaks at 0.05 s and 0.26 s correlate incident waves at depth of 33 m to 19 m incident and reflected waves. Thus, V_s = (33-19)/0.05 = 280 m/s is estimated between the depth of 33 m and 19 m. Time lag between the two peaks (0.26-0.05 = 0.21 s), is the time for a shear wave to travel from elevation of -16 m to the ground surface (Elev. = +1 m) and back. As such, an average velocity of V_s = 34/0.21 = 161.9 m/s for the topmost stratum is obtained and agrees well with the estimated shear wave velocity (170 m/s) on the basis of correlation between ground surface (Elev. = +1 m) and -16 m elevation (Figure 5.19).

Overall, estimated incident shear wave velocities between sensors (Figure 5.3) are found to be in the range (low values below correspond to the moderate event):

Soil layer 1: V_{s1} = 121.4 m/s – 188.9 m/s;

Soil layer 2: V_{s2} = 233.3 m/s – 311.1 m/s;

Soil layer 3: V_{s3} = 328.6 m/s – 460.0 m/s;

Soil layer 4: V_{s4} = 363.6 m/s – 500.0 m/s.

The geophysical measurements of shear wave velocity are within this estimated range as shown in Figure 5.20. Since only slightly difference is observed for shear wave velocities in the NS and in EW directions, no appreciable azimuthal anisotropy of the soil at this location is evident. The mean shear wave velocities from geophysical measurements for the first 3 soil layers are 190.5 m/s, 290 m/s and 373 m/s.

5.3.3 Site Resonant Characteristics

Resonant frequency analyses utilizing a fast Fourier transform algorithm for the topmost stratum (ground surface to 19 m depth) are conducted (Figure 5.21 and Figure 5.22) in two directions. Fourier Spectral ratio analyses based on selected earthquakes are shown in Table 5.3 and Table 5.4 where the predicted first resonance is in a range of 2.30-3.11 Hz for the low amplitude shaking events. The identified first resonant frequency is in the neighborhood of that estimated by the simple constant shear modulus resonant shear beam formula of $f_1 = V_s/(4H)$ = 2.27-2.78 Hz (where f_1 is first resonant frequency, and H is vertical distance between sensors). The predominant frequency of the moderate event shifted to a lower frequency of f_1 = 1.90 Hz ($f_1 = V_s/(4H)$ =1.79 Hz). Such shift reflects a decrease in modulus and indicates the nonlinearity of soil during this moderate shaking event (Elgamal et al. 1995; Elgamal et al. 1996).

Fourier spectral ratios between the top two stations (elevation of +1 m to -16 m) were computed with a 5-second time window for the moderate event (Figure 5.23 and Figure 5.24). During the early and late parts of the recorded motion, natural frequency reached as much as 2.60 Hz, similar to the estimates from the other small shaking events. During the strong motion phase (30 s - 35 s), a lower natural frequency (decrease of soil stiffness) is noted (~1.8 Hz). Short-time Fourier transform analysis (Figure 5.25) indicates the nonlinearity of the site seismic response. For the low amplitude earthquake, resonant frequency between the top two sensors is quite stable (Figure 5.26 and Figure 5.27). The reduction of resonant frequency due to the softening of the soil domain during the moderate shaking event (Figure 5.23 and Figure 5.24) may contribute to changes in the adjacent bridge foundation stiffness.

5.4 1-D site amplification numerical response

In order to verify the estimated shear wave velocity, FE program Cyclic1D is employed to model the ground motion. A shear-beam model with calibrated soil properties is developed to represent the site dynamic response. NS and EW seismic motions measured by downhole array at the depth of 56 m are considered as the input excitation. The soil profile used for the simulations is summarized in Table 5.5. Newmark time integration is employed with $\gamma = 0.55$ and $\beta = 0.276$. Rayleigh damping is employed with specified damping ratio at the frequencies of 2.5 Hz and 7.5 Hz.

Site response during the moderate 2010 Ferndale Earthquake, the 2000 Ferndale Offshore Earthquake and the 2000 Cape Mendocino Earthquake are simulated (Figure 5.28-Figure 5.31). It is seen that there is a good degree of agreement between the time domain recorded and computed response.

Additional estimates of the soil shear modulus and Raleigh damping ratio are included in Appendix B using the SNOPT optimization tool (further details included in Chapter 7).

5.5 Discussion

The collected strong motion data from the geotechnical downhole array along with system identification techniques allow for better evaluation of the soil response under ground shaking. In this chapter, cross-correlation and site resonance analyses using recorded accelerations are performed to identify average soil dynamic characteristics between sensors. It is found that:

1. Identified soil characteristics depend highly on the availability and spacing of the sensors. Thus, due to the large distance between sensors (17 m, 14 m, 23 m and 80 m), spatial changes of soil properties may not be captured. Even so, estimated shear wave velocities show good agreement with the downhole profile provided by the US Geological Survey and Caltrans

2. Recorded motion at the depth of 56 m consists of two main phases: incident wave and reflected wave from the ground surface. Thus using it as an incident motion may not be very accurate (i.e., for site analysis, it must be used as total base motion).

5.6 Summary and Conclusions

Post-earthquake ground response analysis using system identification techniques is shown to be an efficient and effective method to examine the soil nonlinear behavior and to investigate in-situ dynamic properties. Based on recorded ground motions of a five-level downhole array located in the Eureka area, soil shear wave velocities were back-calculated and site resonant frequencies are estimated. The identified site seismic characteristics are found to be in reasonable agreement with earlier in-situ measured data.

Both shear-wave analysis and resonant frequency analysis illustrate nonlinear dynamic soil behavior during the moderate 2010 Ferndale earthquake event. A shear-beam model was developed using Cyclic1D to simulate site seismic response. Computed site response is comparable to the actual recorded counterpart.

5.7 Acknowledgements

Chapter 5 of this dissertation is an extended version of the material published in the following proceedings conference and a manuscript under preparation for publication as a journal article: (1) 10th International Conference on Urban Earthquake Engineering, titled “Bridge and Adjacent Downhole Array Response During Earthquakes at Eureka, California” with co-author Ahmed Elgamal (2013), and (2) tentatively titled “Finite Element Based Seismic Assessment of the Samoa Channel Bridge-Foundation System”, with preliminary author list of Ning Wang and Ahmed Elgamal. The dissertation author is the first author of this paper.

Table 5.1: Earthquakes recorded by station 89734 Eureka Geotechnical Array

Earthquake	Date	Record length (s)	Magnitude	Epic. Dist. (km)	Horiz PGA** (g)	
					NS	EW
Ferndale [a]	01/09/2010	90.0	6.5 (M_w)	54.0	0.195	0.143
Trinidad	06/24/2007	60.0	5.1 (M_L)	64.3	0.055	-----*
Weitchpec	02/13/2012	60.0	5.6 (M_w)	47.9	0.029	0.038
Ferndale [b]	02/04/2010	66.0	5.9 (M_w)	77.6	0.025	0.021
Bluelake	10/21/2012	56.0	3.5 (M_L)	22.2	0.013	0.008
Eureka Offshore	09/22/2000	40.0	4.4 (M_L)	24.4	0.011	0.010
Ferndale [c]	02/26/2007	59.0	5.4 (M_L)	62.6	0.007	0.010
CrescentCity	06/14/2005	104.0	7.2 (M_L)	153.8	0.006	0.008
Ferndale Offshore	12/27/2000	37.0	4.1 (M_w)	46.4	0.007	0.005
Cape Mendocino	03/16/2000	75.0	5.6 (M_w)	102.6	0.004	0.004

* malfunction of accelerometer at the ground surface
** PGA = Peak Ground Acceleration
Ferndale [a]: Ferndale Earthquake on Jan 09, 2010
Ferndale [b]: Ferndale Earthquake on Feb 04, 2010
Ferndale [c]: Ferndale Earthquake on Feb 26, 2007

Table 5.2: Measured shear and pressure wave velocities and Poisson's ratio

Depth (m)	V_s (m/s)	V_p (m/s)	$\upsilon = \dfrac{0.5 \times (\frac{V_p}{V_s})^2 - 1}{(\frac{V_p}{V_s})^2 - 1}$
19	205	1540	0.49
33	353	1820	0.48
56	420	1700	0.47
136	640	1861	0.43

Table 5.3: Estimated resonant frequency and average shear wave velocity (Vs) for the topmost stratum (Layer 1) in NS direction

Earthquake	Time step (s)	V_s (m/s)	1st resonant frequency (Hz)		Shear Modulus G** (MPa)
			$\frac{V_s}{4H}$	Identified	
Ferndale [a]	0.01	154.5 141.7*	2.27 2.08*	2.13	35.3 29.7*
Weitchpec	0.005	161.9	2.38	2.30	38.8
Bluelake	0.005	161.9	2.38	3.11	38.8
EurekaOffshore	0.01	170.0	2.50	2.62	42.8
Ferndale [c]	0.01	188.9	2.78	2.47	52.8
FerndaleOffshore	0.01	188.9	2.78	2.75	52.8

* during the strong shaking phase 30 s – 35 s.
** using a soil mass density of 1480 kg/m^3

Table 5.4: Estimated resonant frequency and average shear wave velocity (Vs) for the topmost stratum (Layer 1) in EW direction

Earthquake	Time step (s)	V_s (m/s)	1st resonant frequency (Hz)		Shear Modulus G (MPa)
			$\frac{V_s}{4H}$	Identified	
Ferndale [a]	0.01	121.4 121.4*	1.79 1.79*	1.90	21.8 21.8*
Weitchpec	0.005	178.9	2.63	2.83	47.4
Bluelake	0.005	154.5	2.27	2.86	35.3
Eureka Offshore	0.01	170.0	2.50	2.65	42.8
Ferndale [c]	0.01	188.9	2.78	3.03	52.8
Ferndale Offshore	0.01	170.0	2.50	2.89	42.8

* during the strong shaking phase 30 s – 35 s.

Table 5.5: Soil layer properties for the 1D FE model

Soil layer	Mass density* (kg/m^3)	V_s (m/s)	Poisson's ratio	Shear strength s_u * (kPa)	Octahedral shear strain* at s_u (%)
Layer 1	1480	190.00	0.4	35.1	3
Layer 2	1740	280.00	0.4	67.4	3
Layer 3	2100	383.33	0.4	80.0	3

* selected values to generally provide a close match to the observed nonlinear response, and the hyperbolic relation is used to define the backbone curve

Figure 5.1: Location of the Eureka Geotechnical Downhole Array (Map data @ 2015 Google) and station photograph (http://www.strongmotioncenter.org)

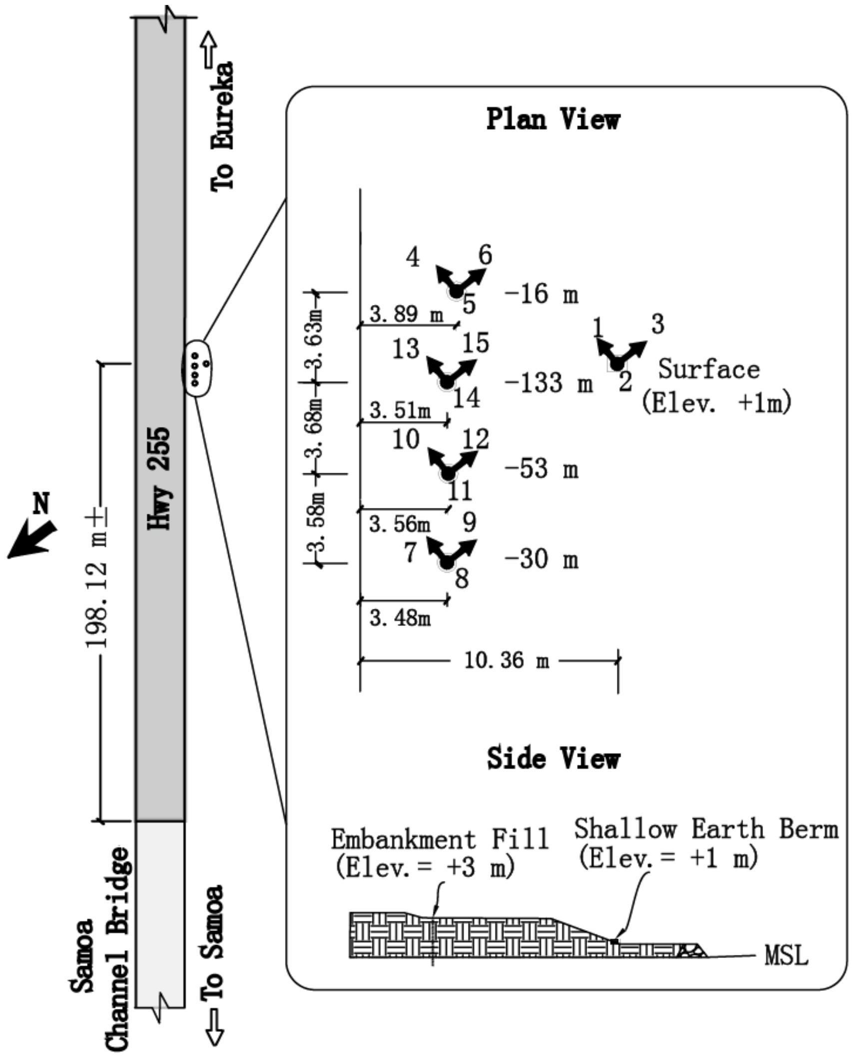

Figure 5.2: The Eureka Geotechnical Downhole Array
(http://www.strongmotioncenter.org)

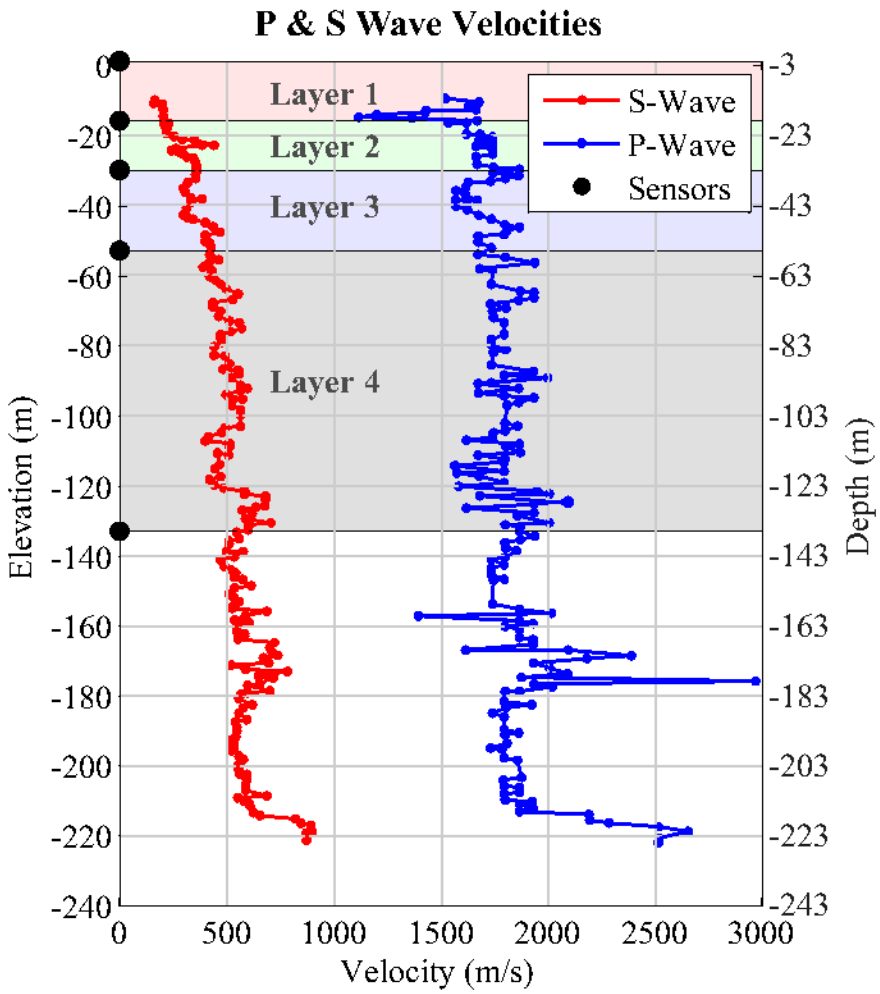

Figure 5.3: Velocity profile along the depth at the Eureka Geotechnical Array (elevation is referenced to MSL) (http://www.strongmotioncenter.org)

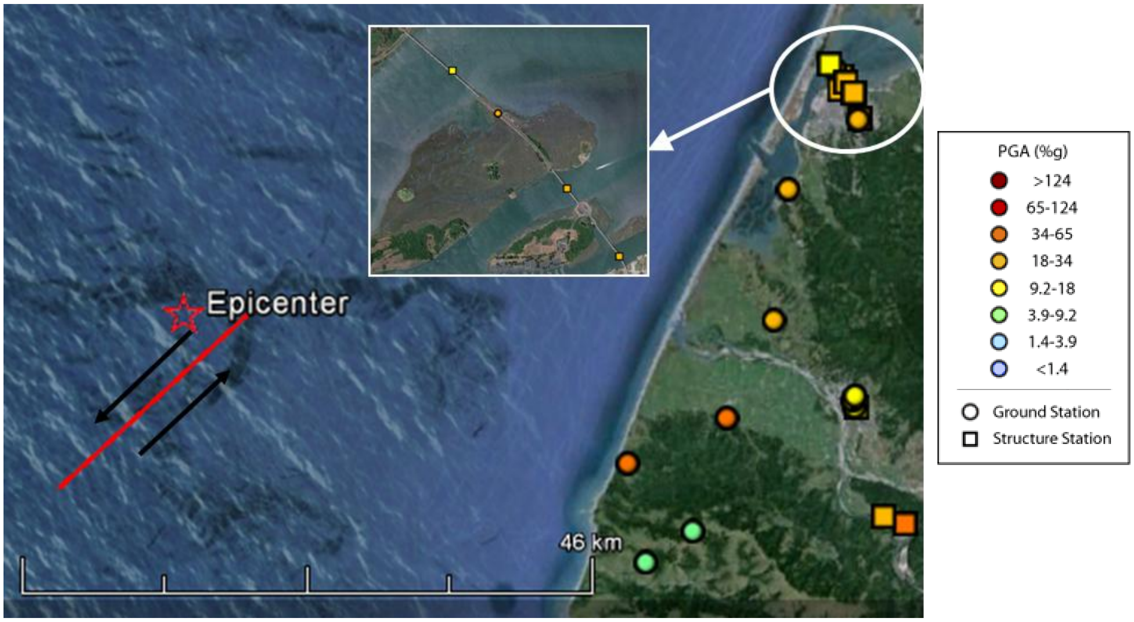

Figure 5.4: Google Earth image of the M_w 6.5 2010 Ferndale Earthquake (Google Imagery @2015 NASA, TerraMetrics)

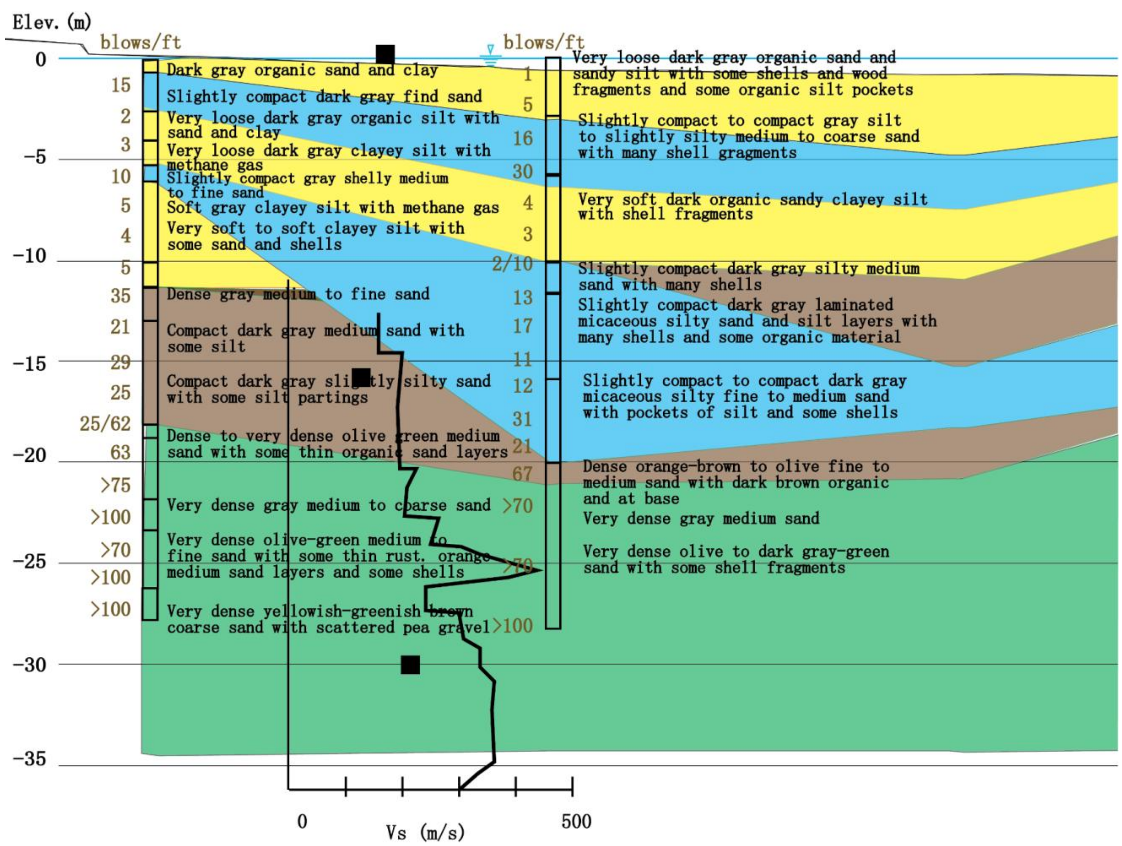

Figure 5.5: Soil profile at the Eureka geotechnical Array site (Caltrans 2002a)

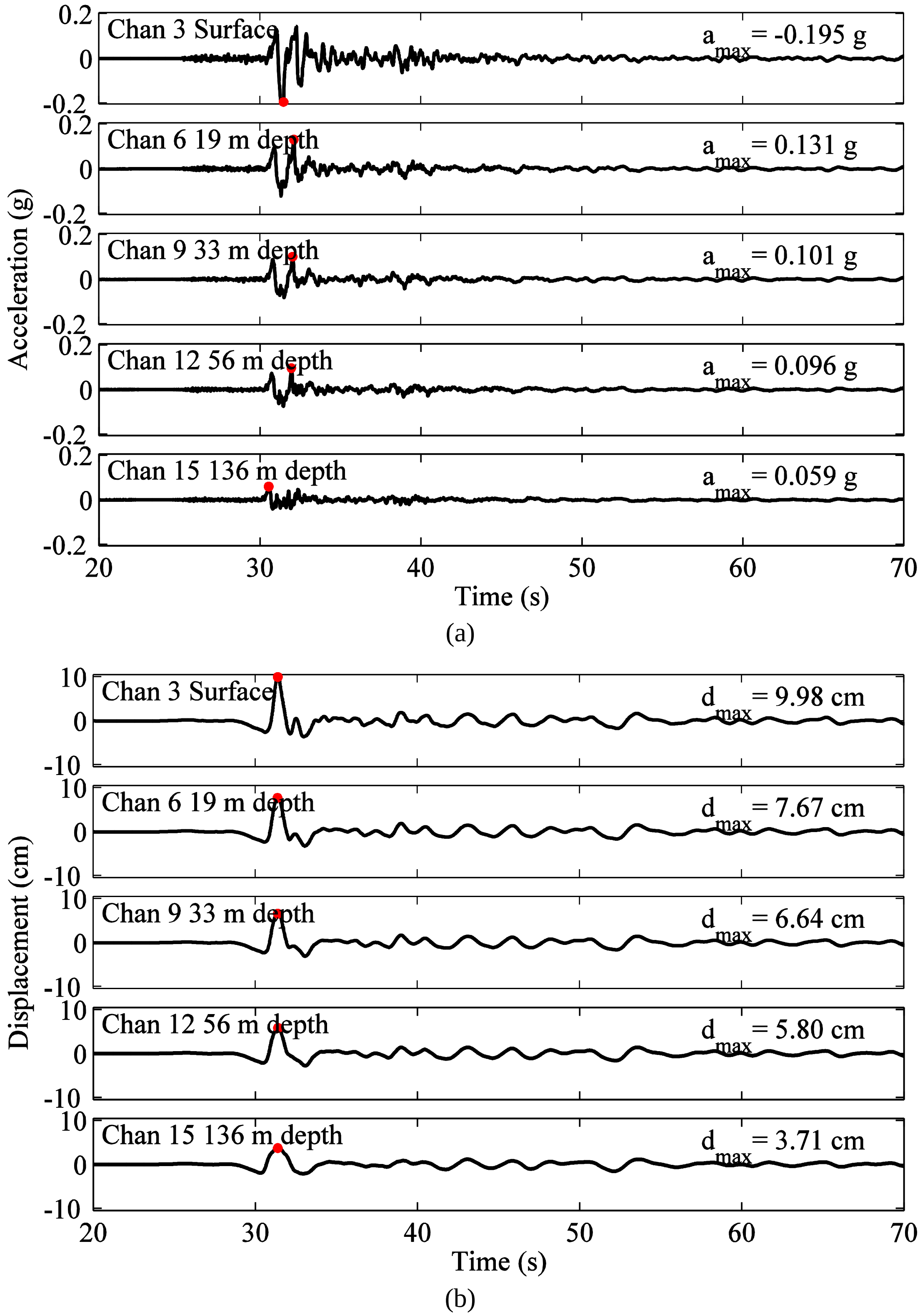

Figure 5.6: Recorded (a) acceleration and (b) displacement time histories during the moderate event in NS direction

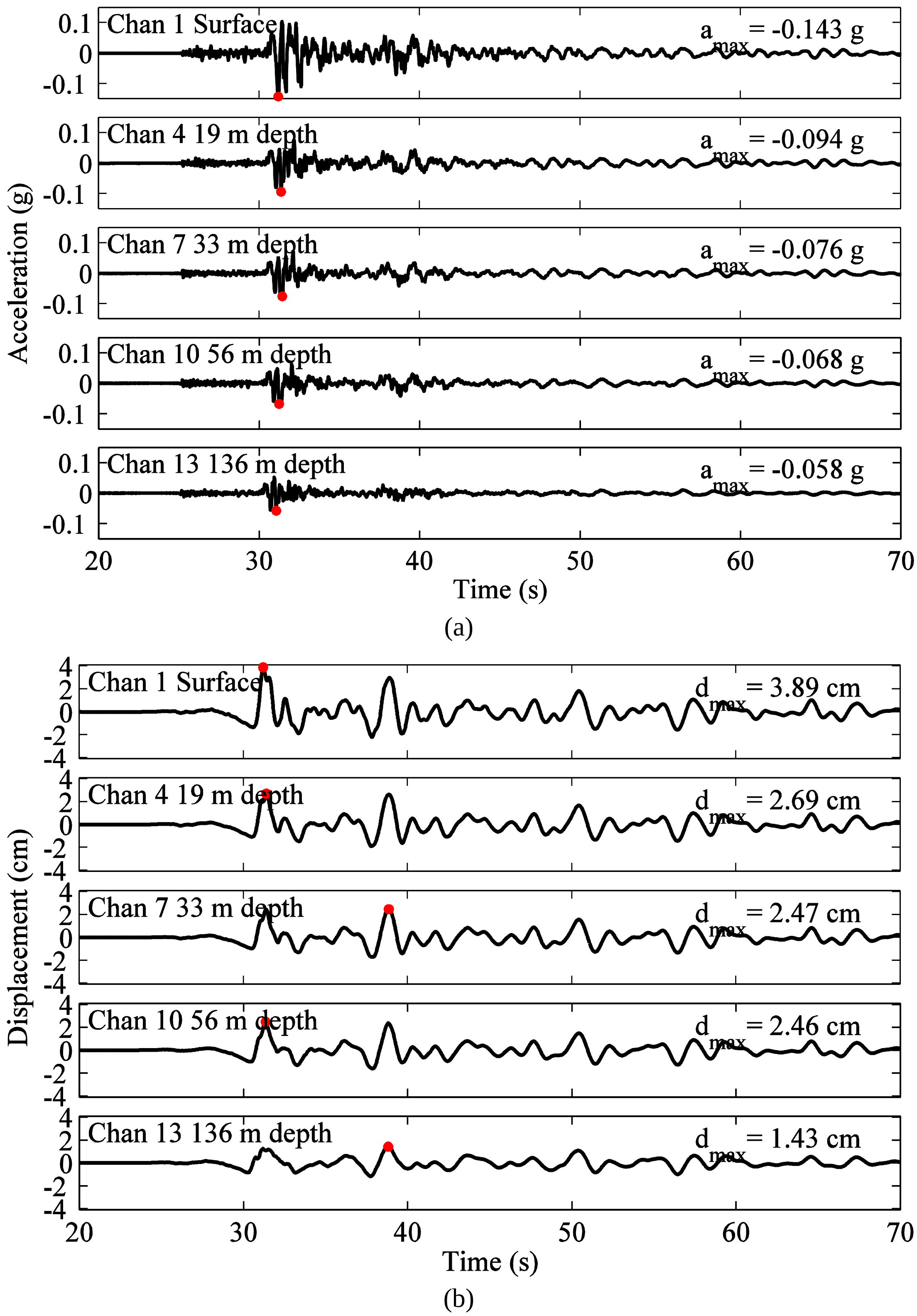

Figure 5.7: Recorded (a) acceleration and (b) displacement time histories during the moderate event in EW direction

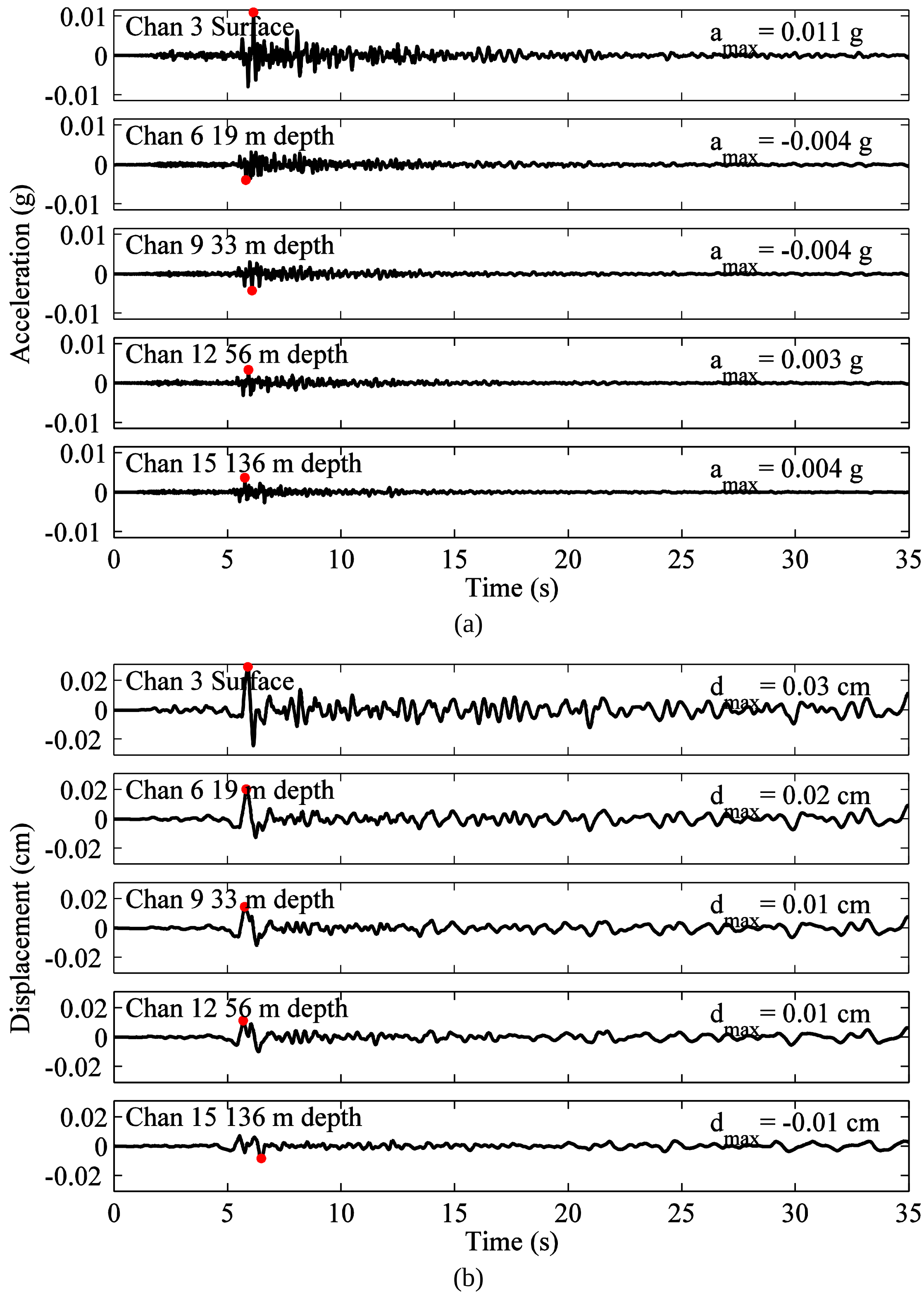

Figure 5.8: Recorded (a) acceleration and (b) displacement time histories during the 2000 Eureka Offshore Earthquake in NS direction

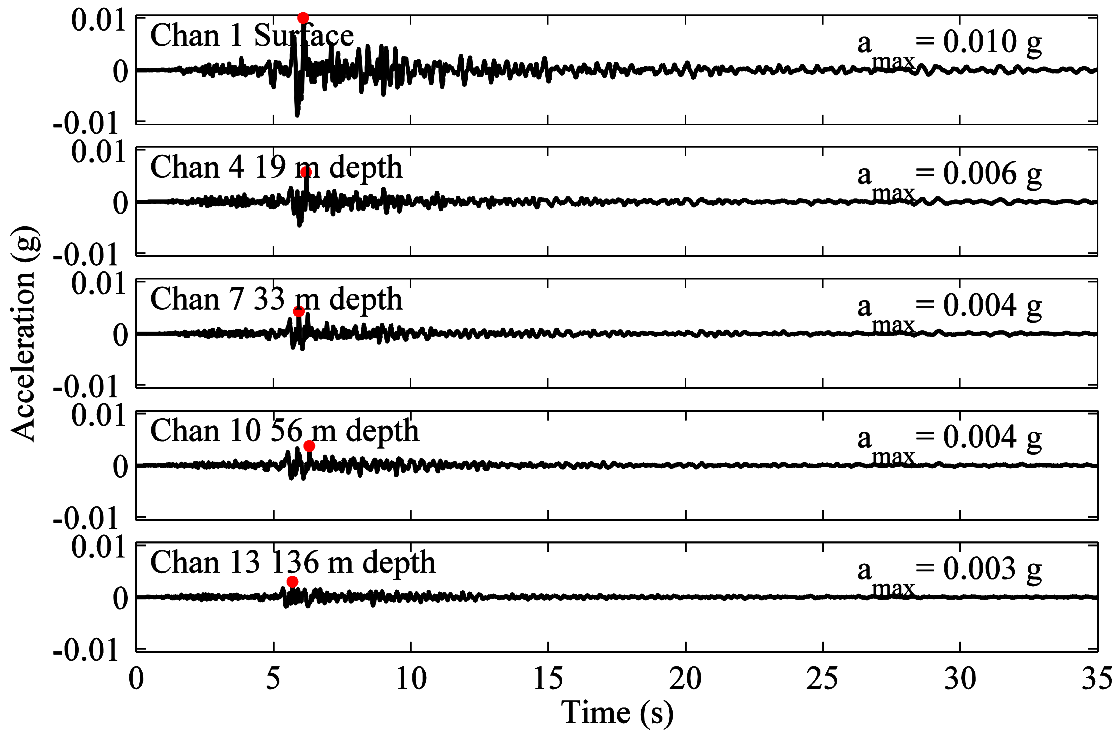

(a)

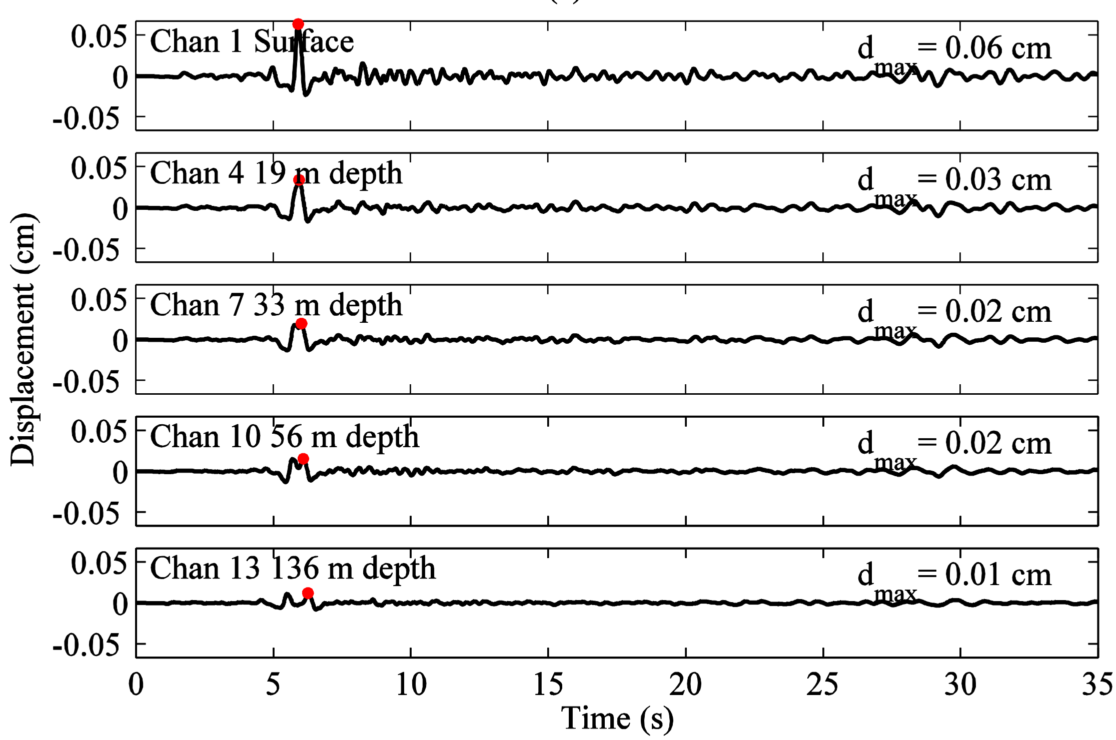

(b)

Figure 5.9: Recorded (a) acceleration and (b) displacement time histories during the 2000 Eureka Offshore Earthquake in EW direction

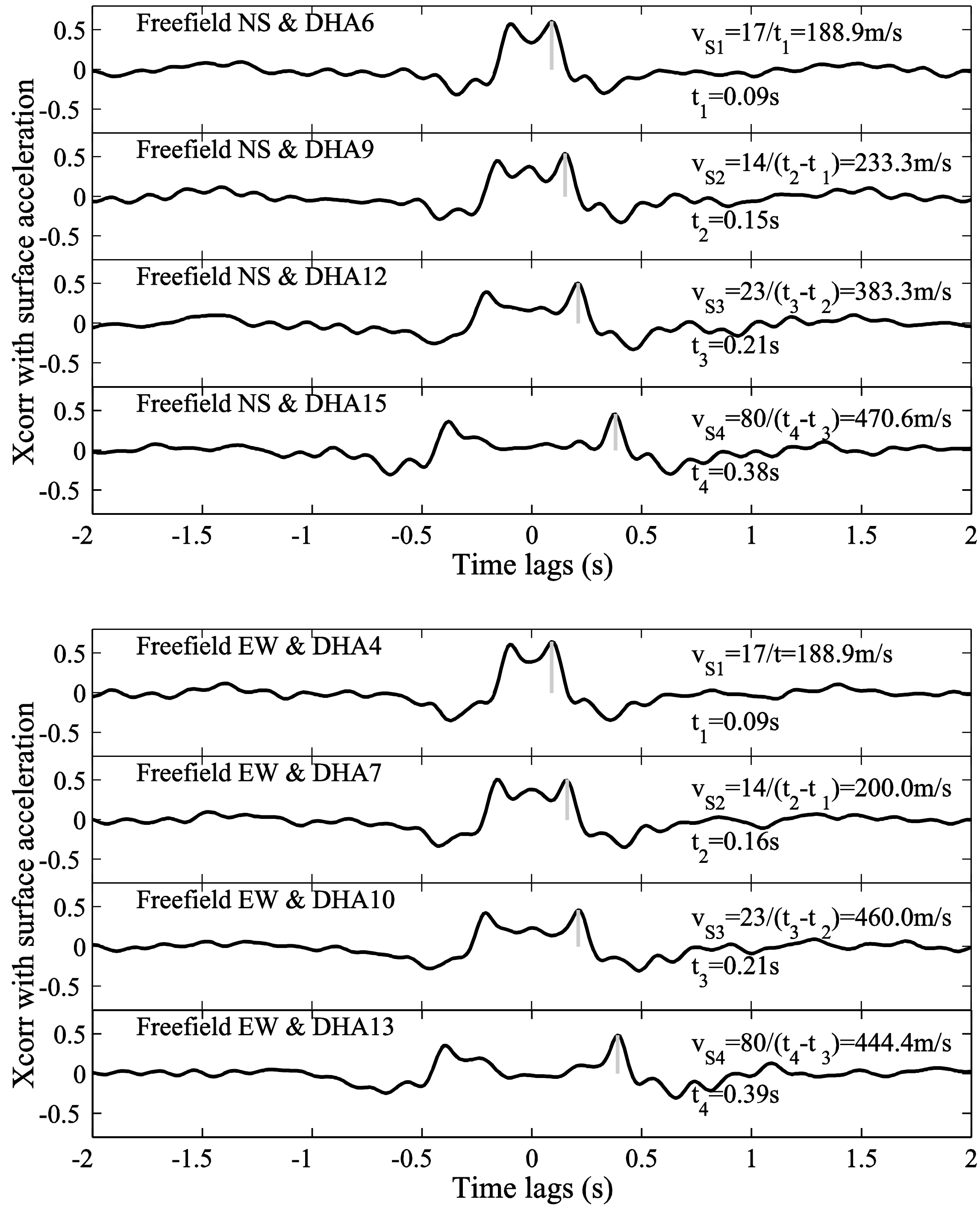

Figure 5.10: Overall average cross-correlation based on the 2000 Cape Mendocino Earthquake, the 2005 Crescent City Earthquake, the 2010 Ferndale Earthquake [b], the 2007 Ferndale Earthquake, and the Ferndale Offshore Earthquake 2000

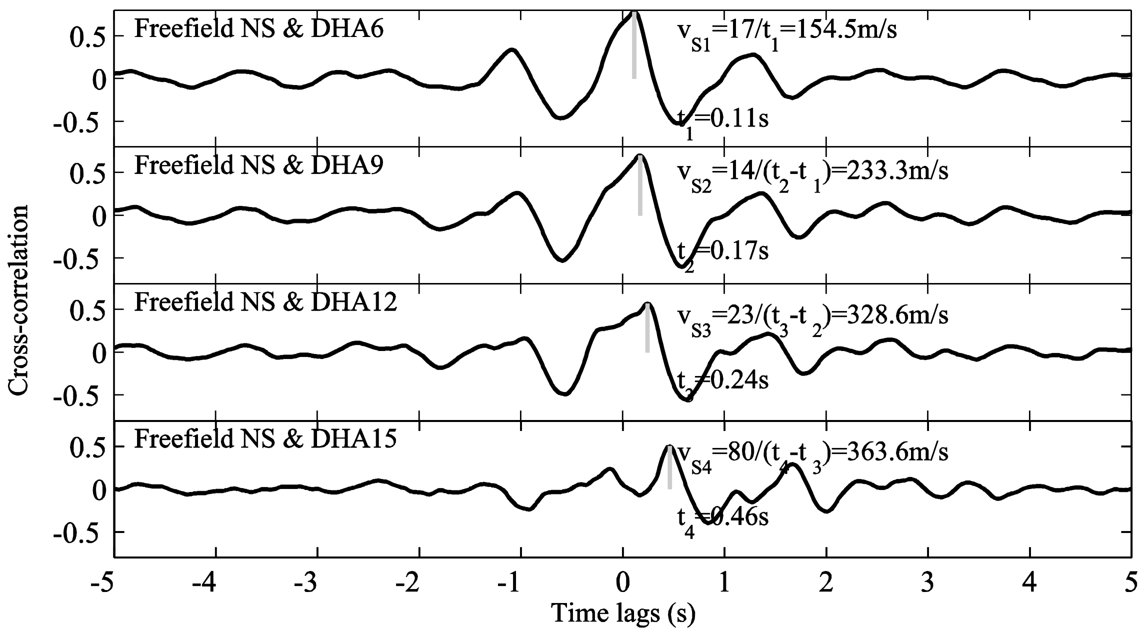

(a)

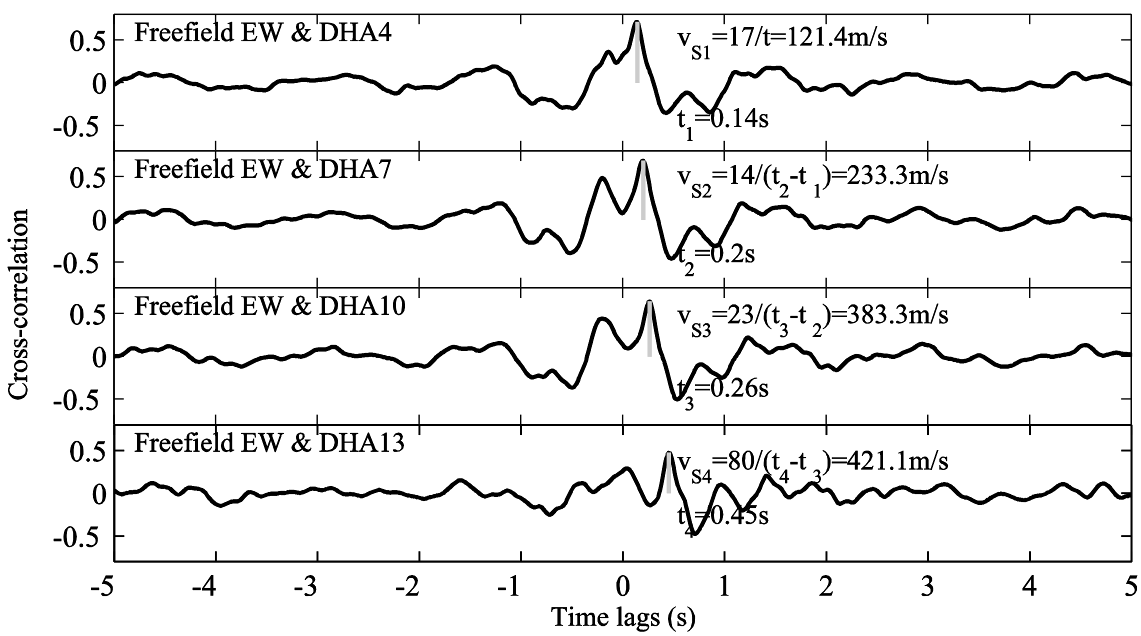

(b)

Figure 5.11: Cross-correlation of accelearations (with respect to the ground surface records) during the moderate event (t = 0 s – 90 s) in (a) NS and (b) EW directions

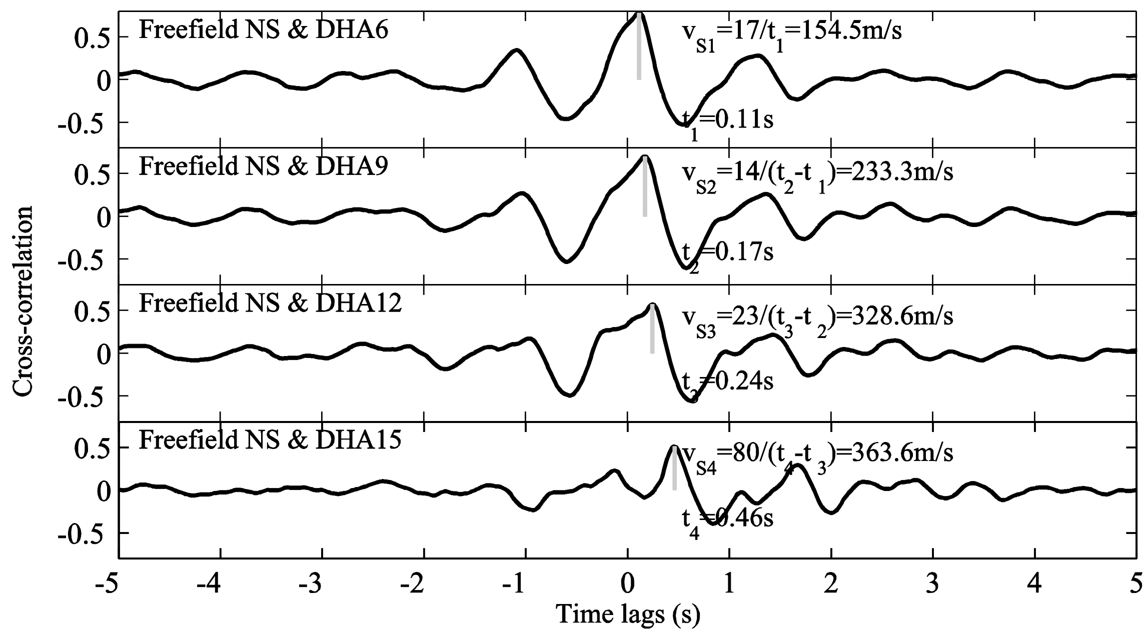

(a)

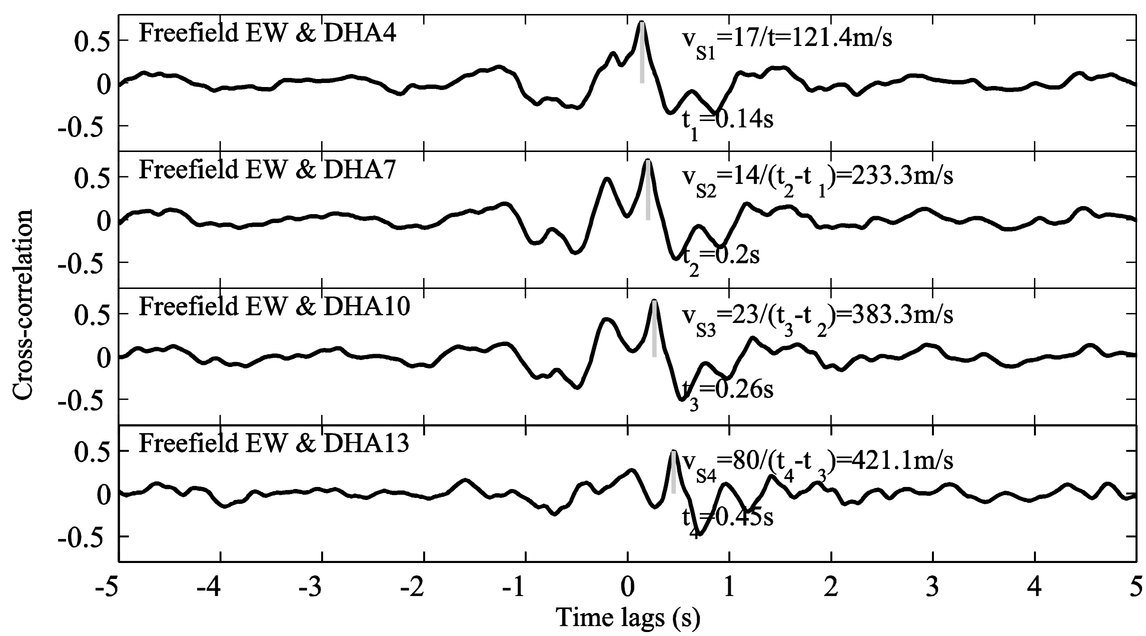

(b)

Figure 5.12: Cross-correlation of accelearations (with respect to the ground surface records) during the moderate event with the 23 s - 60 s time window in (a) NS and (b) EW directions

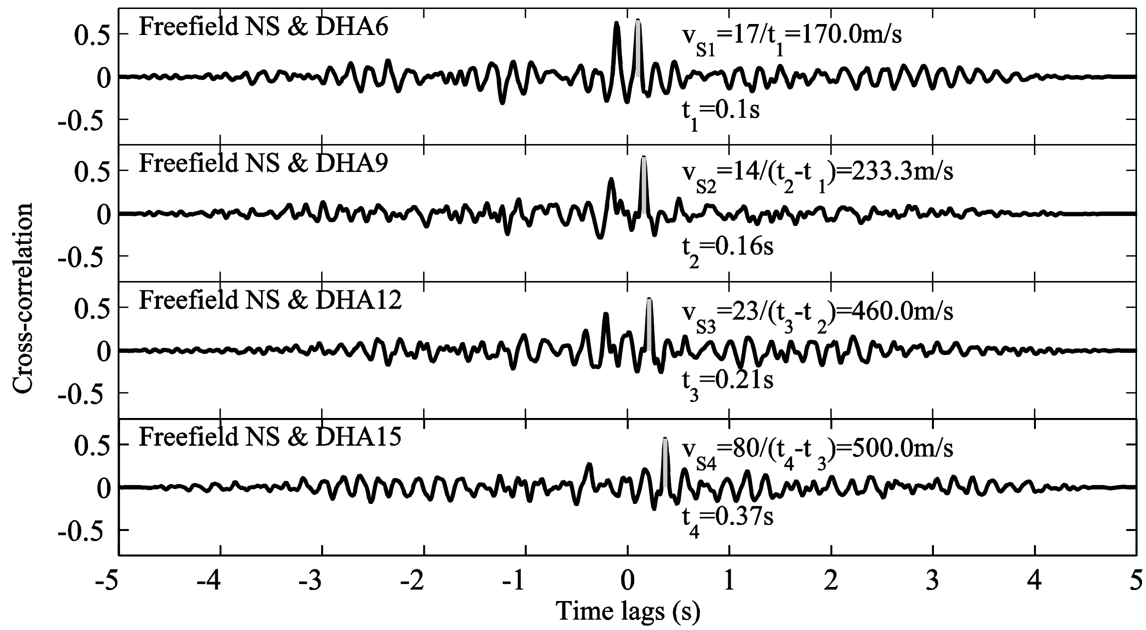

(a)

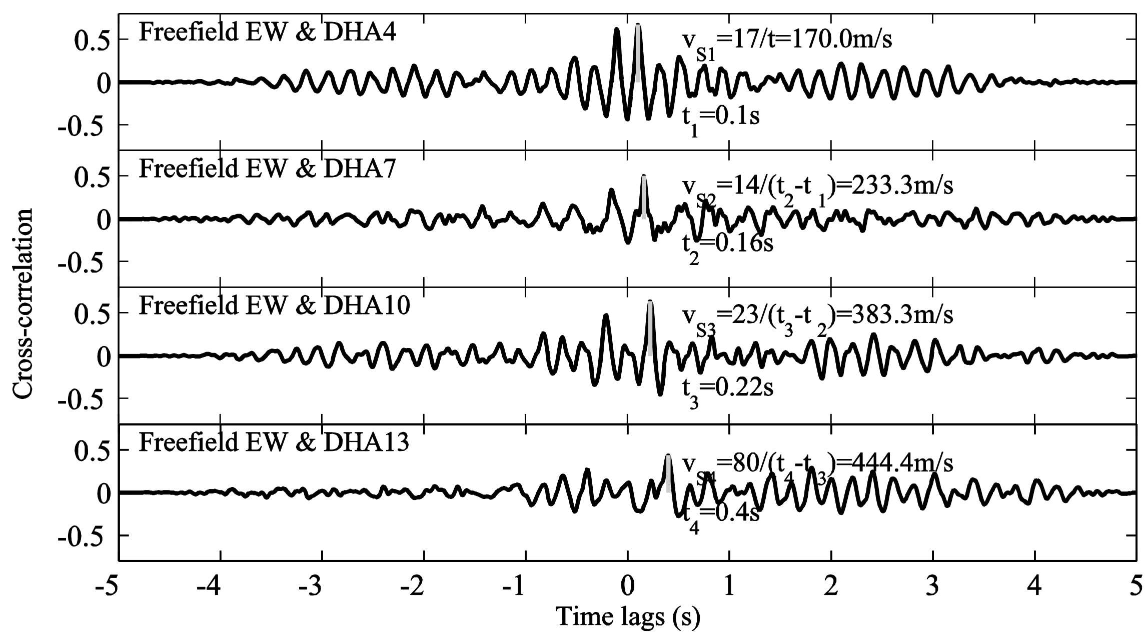

(b)

Figure 5.13: Cross-correlation of accelearations (with respect to the ground surface records) during the moderate event with the 20 s - 30 s time window in (a) NS and (b) EW directions

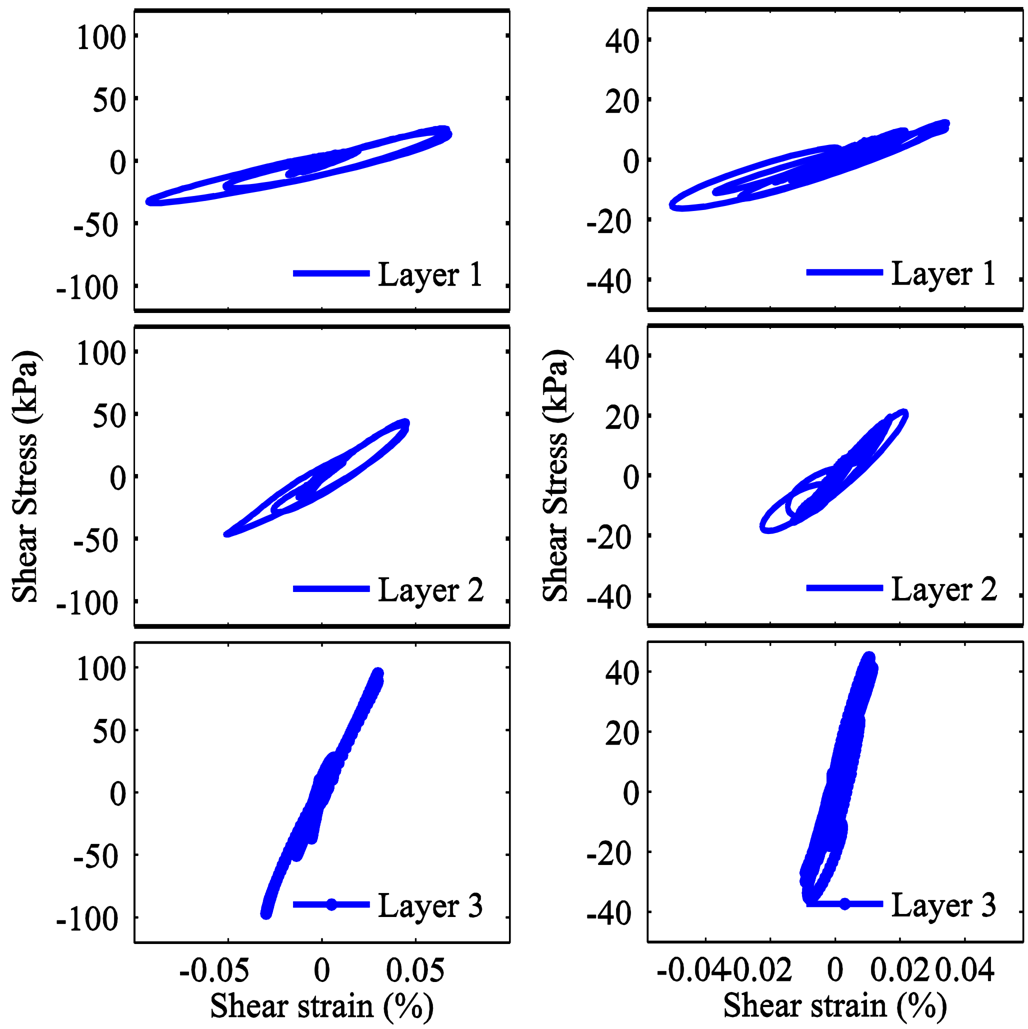

(a) (b)

Figure 5.14: Stress-strain histories for soil layer 1, 2 and 3 during the moderate event in (a) NS and (b) EW directions

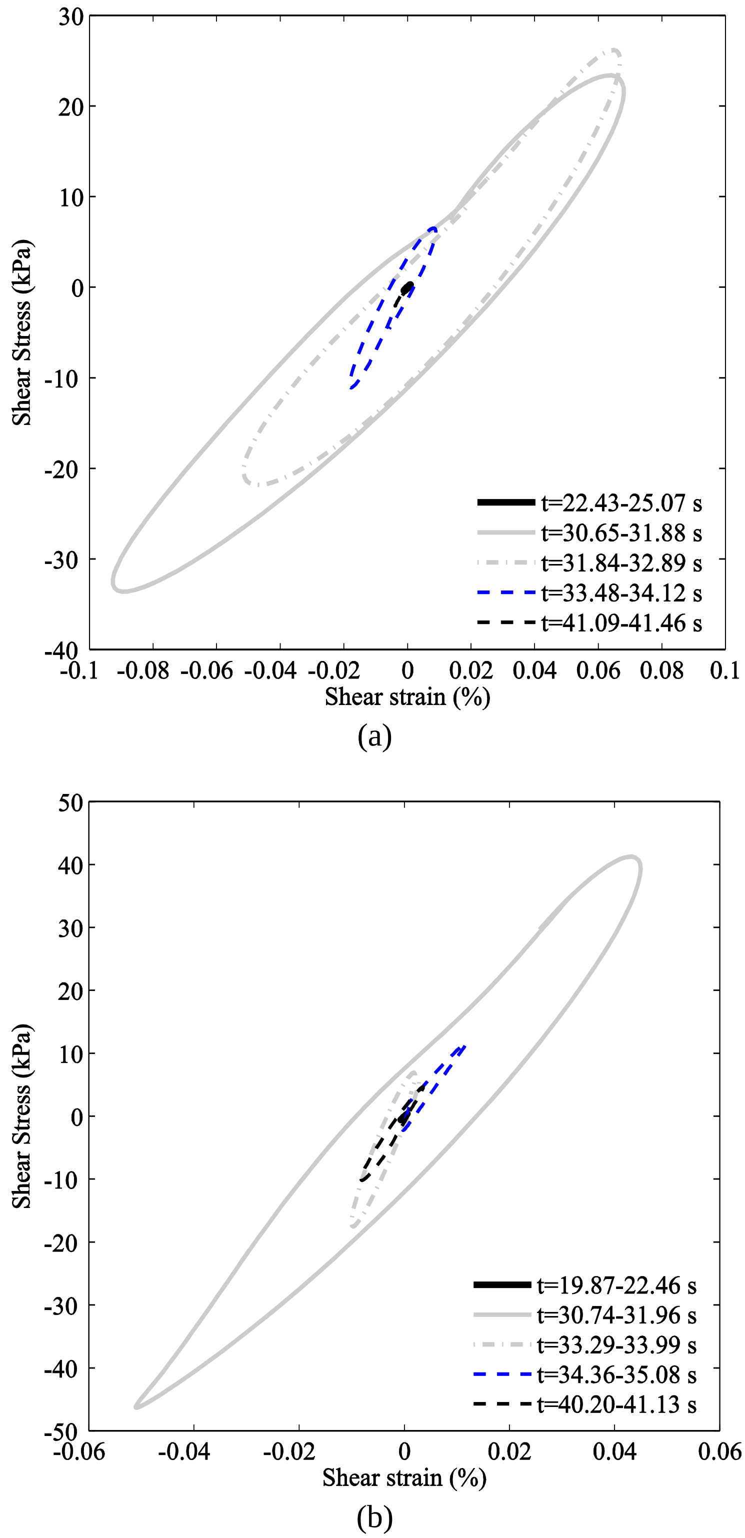

Figure 5.15: Stress-strain histories for (a) soil layer 1 and (b) soil layer 2 during the moderate event

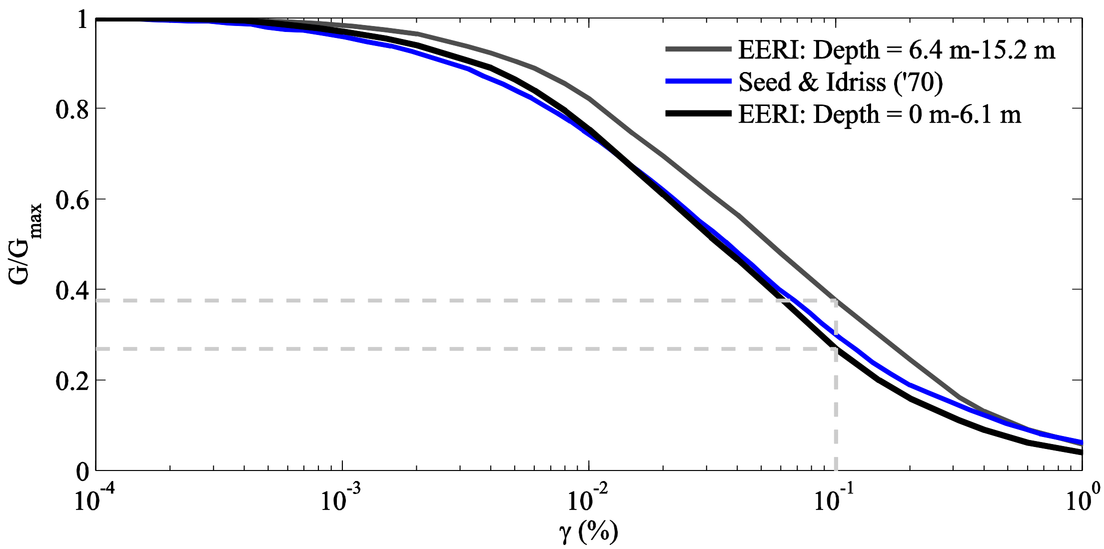

Figure 5.16: Typical range for modulus reduction curves after EPRI (1993) for sand

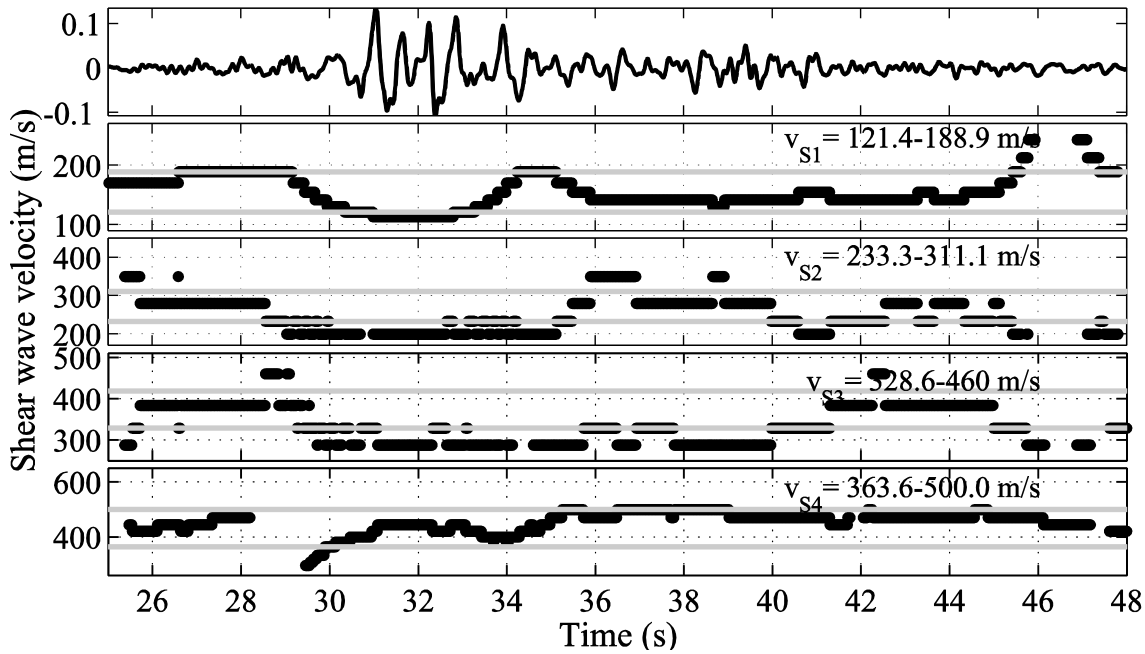

(a)

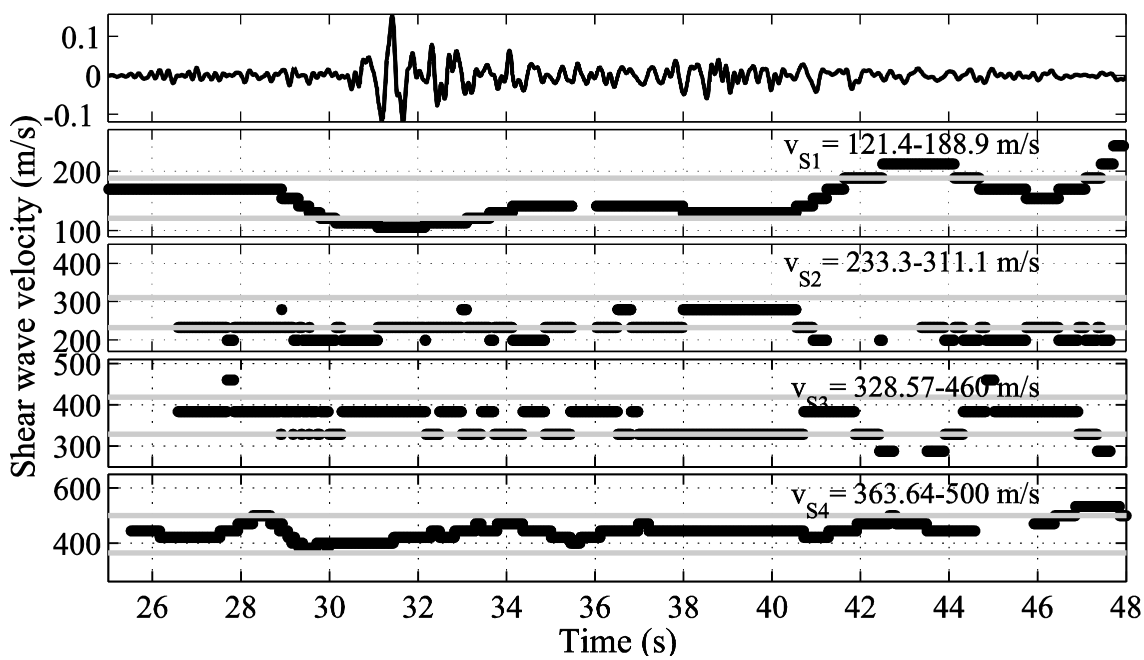

(b)

Figure 5.17: Variation of estimated incident shear wave velocities with time (time window = 5 seconds) for the moderate event in (a) NS and (b) EW directions

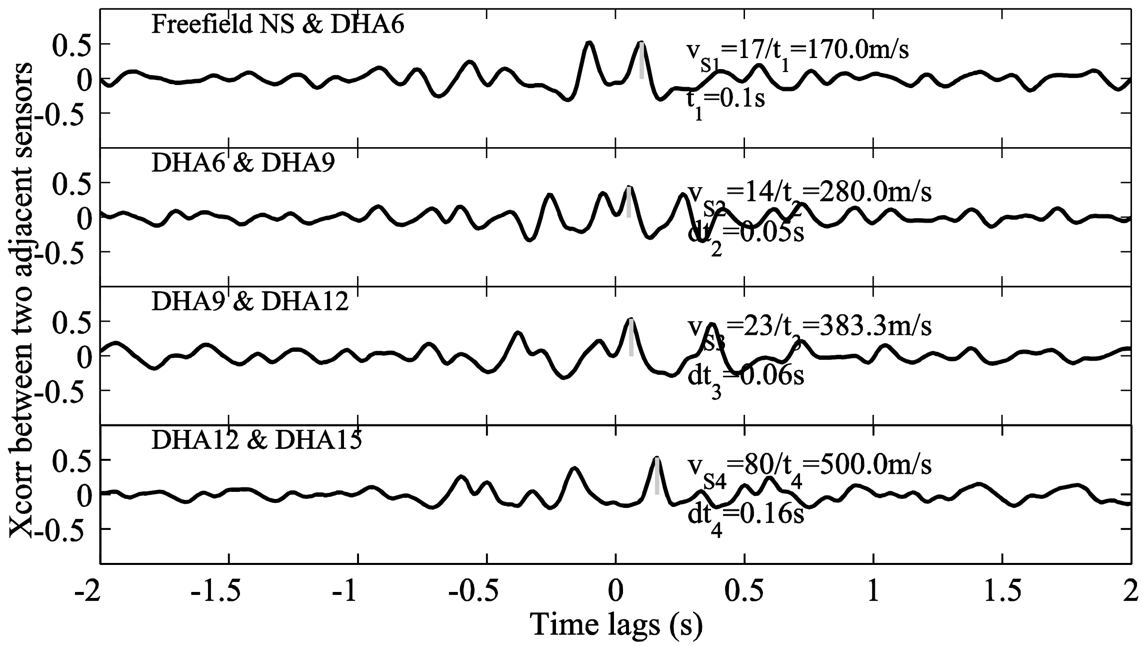

(a)

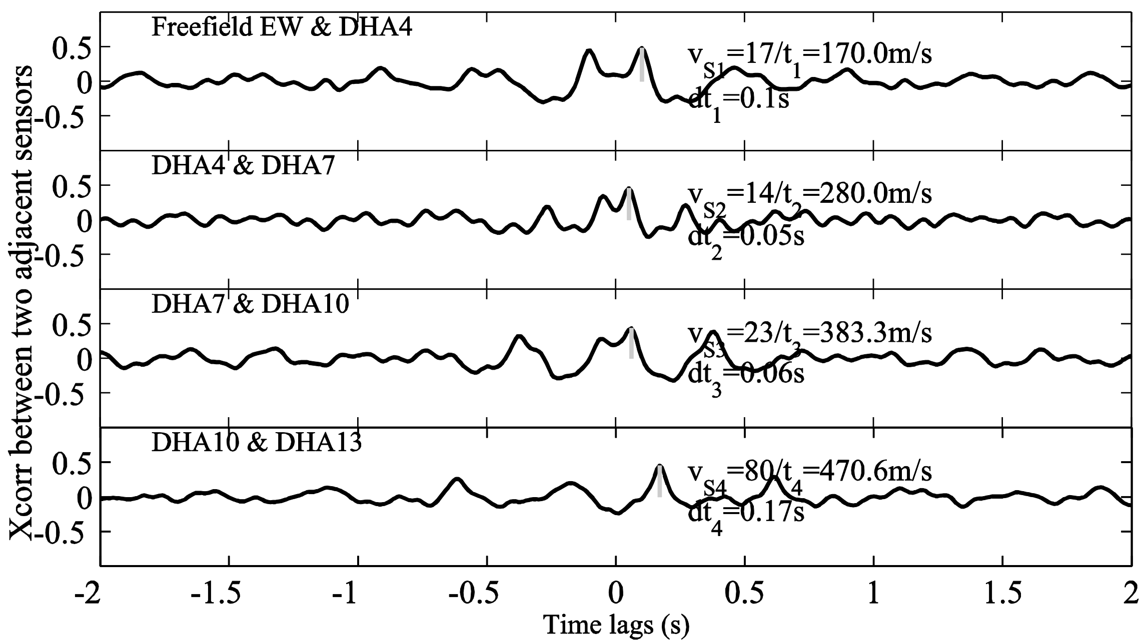

(b)

Figure 5.18: Cross-correlation of accelearations (between adjacent sensor records) during the 2000 Eureka Offshore Earthquake in (a) NS and (b) EW directions

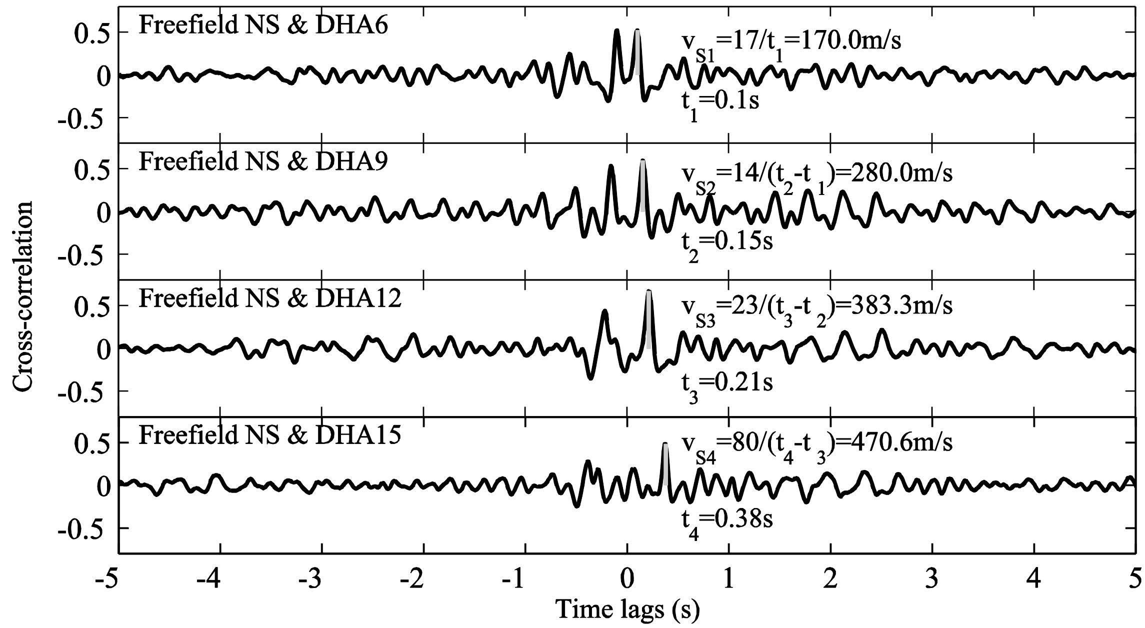

(a)

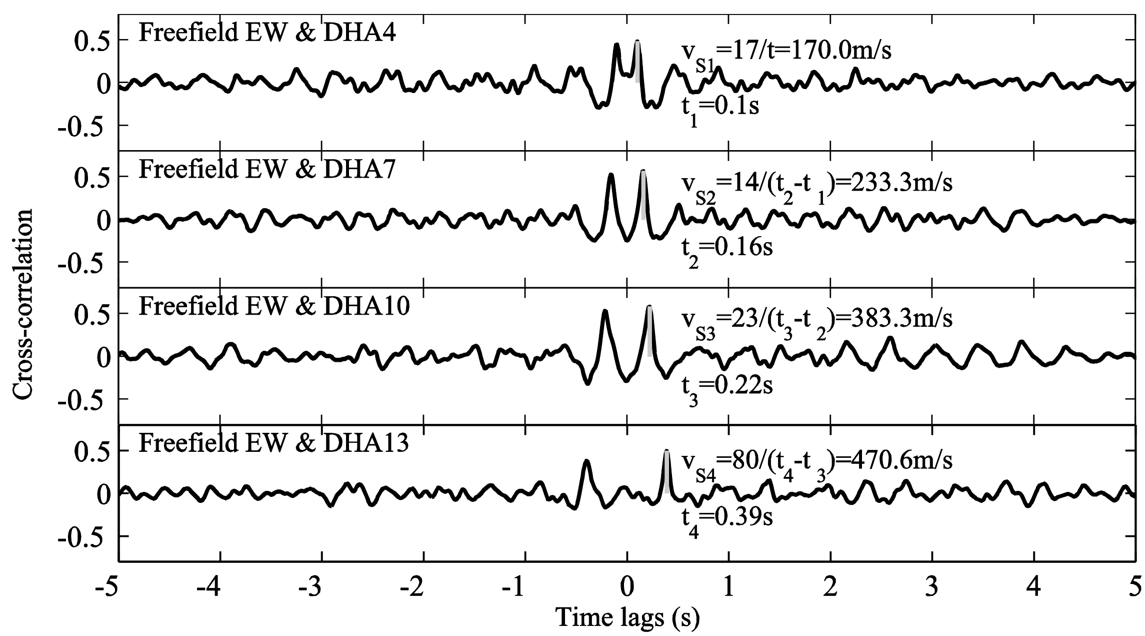

(b)

Figure 5.19: Cross-correlation of accelearations (with respect to the ground surface records) during the 2000 Eureka Offshore Earthquake in (a) NS and (b) EW directions

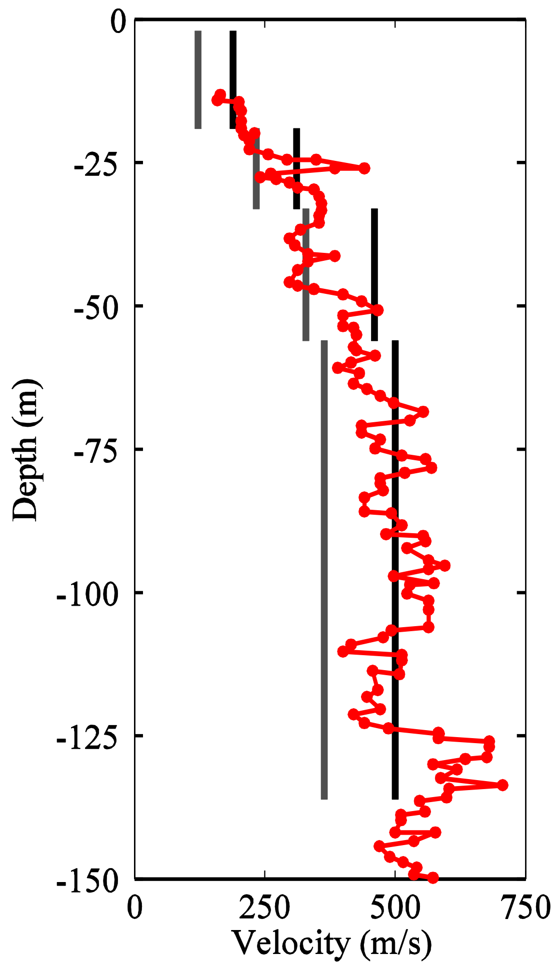

Figure 5.20: Estimates of shear wave velocity in comparison with the geophysical measurements

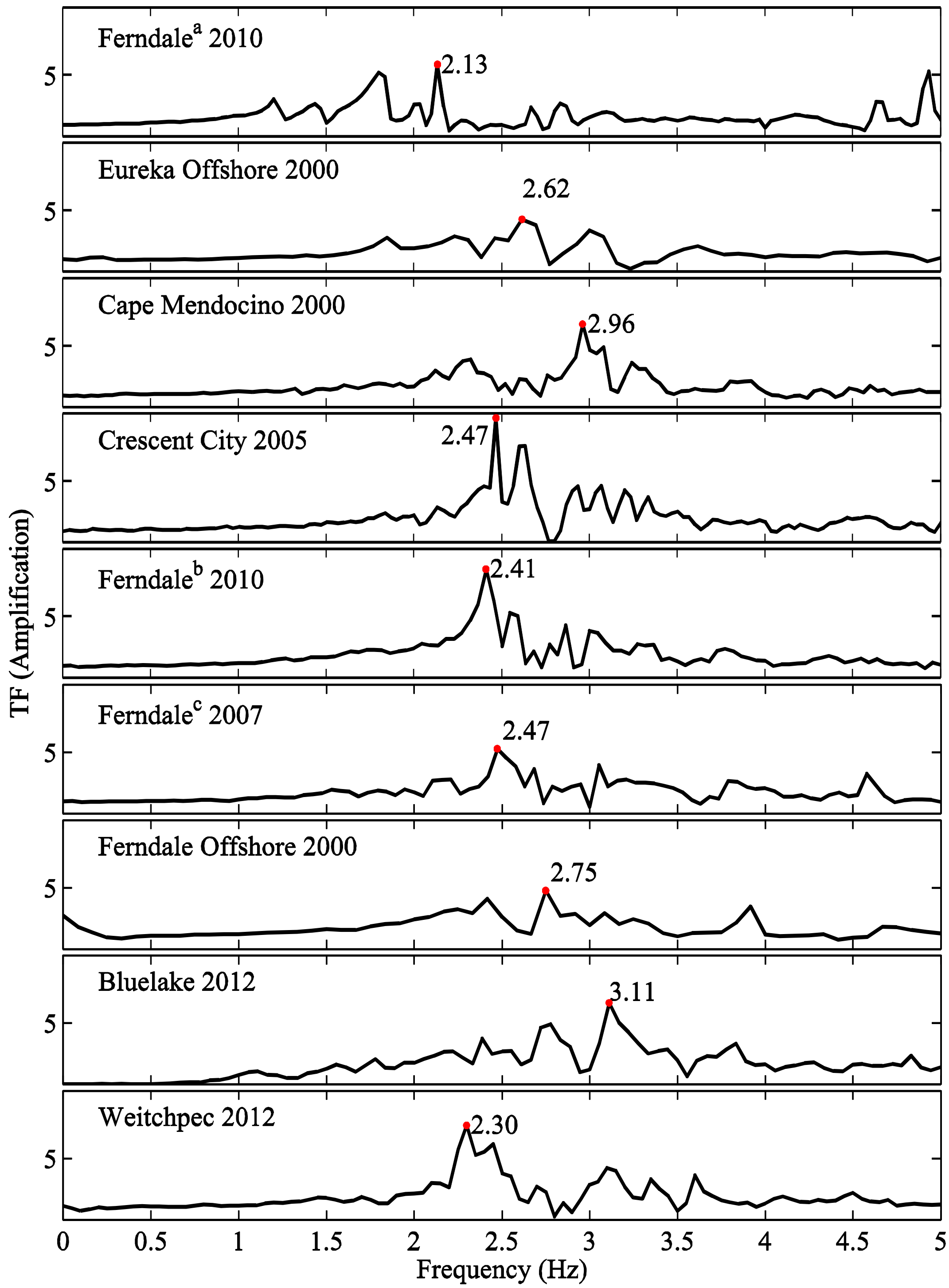

Figure 5.21: Transfer function of acceleration (Layer 1) in NS direction

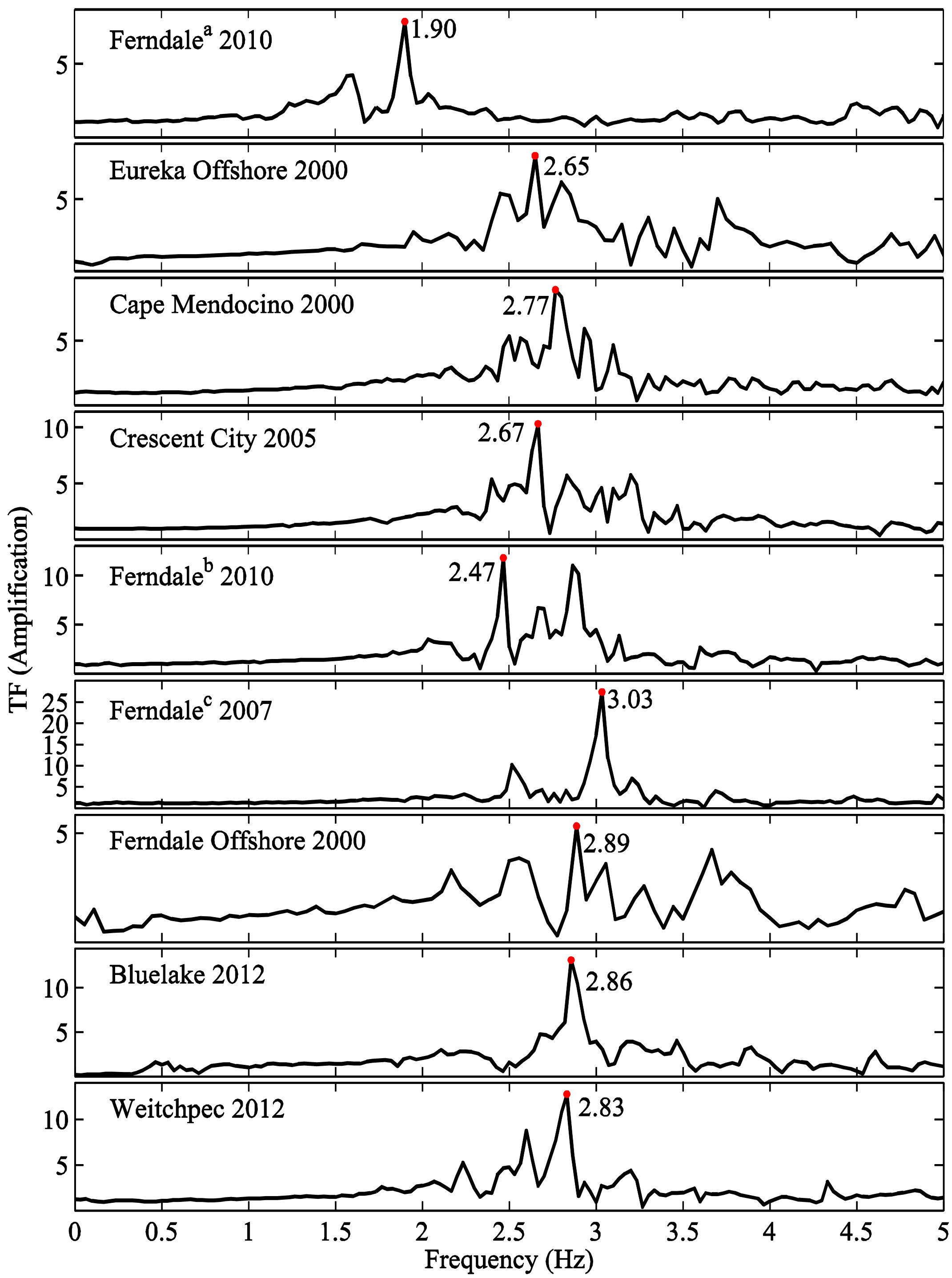

Figure 5.22: Transfer function of acceleration (Layer 1) in EW direction

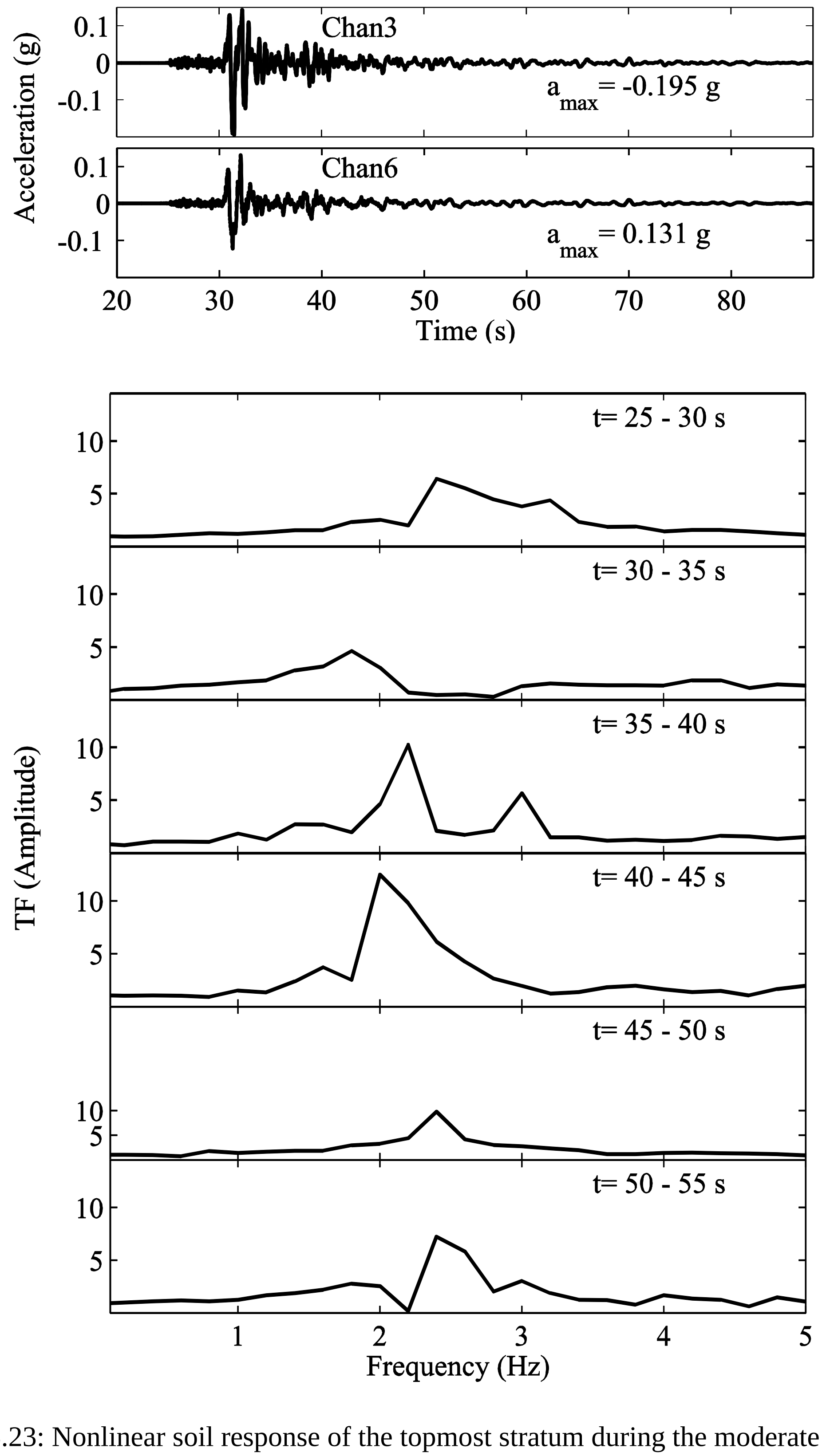

Figure 5.23: Nonlinear soil response of the topmost stratum during the moderate event in NS direction

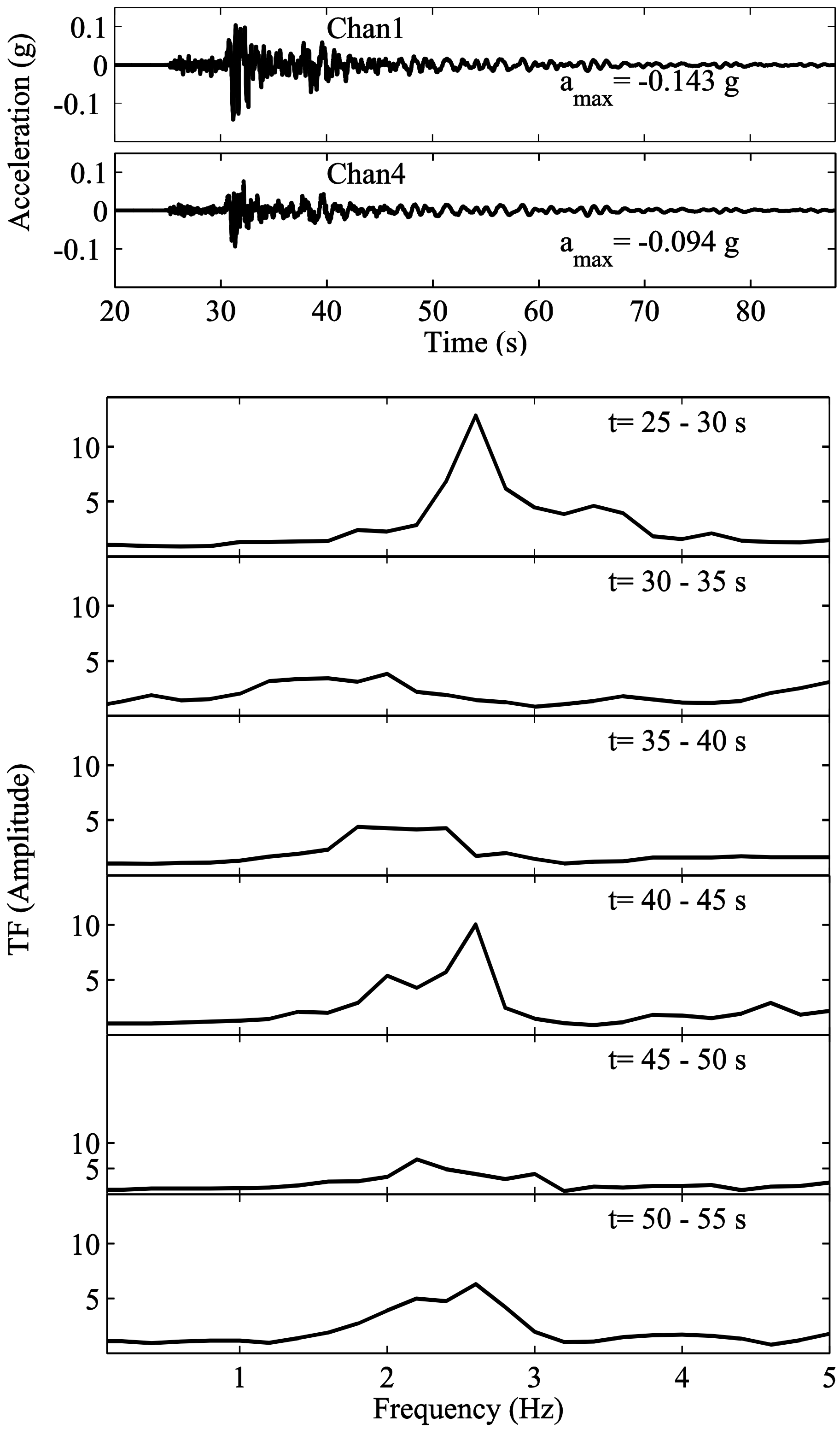

Figure 5.24: Nonlinear soil response of the topmost stratum during the moderate event in EW direction

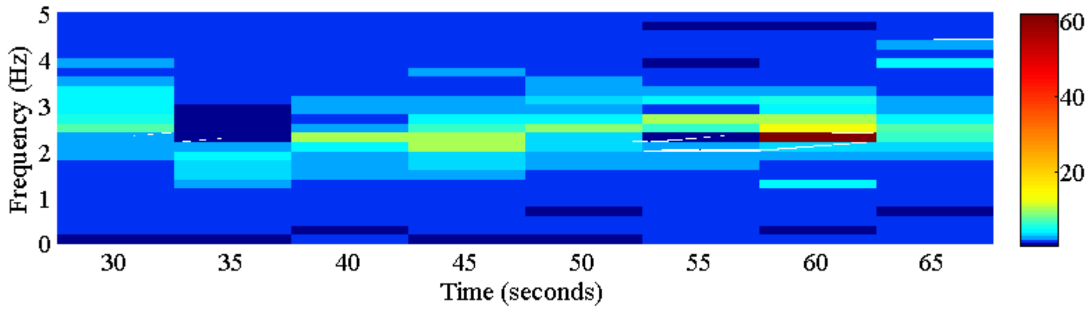

(a)

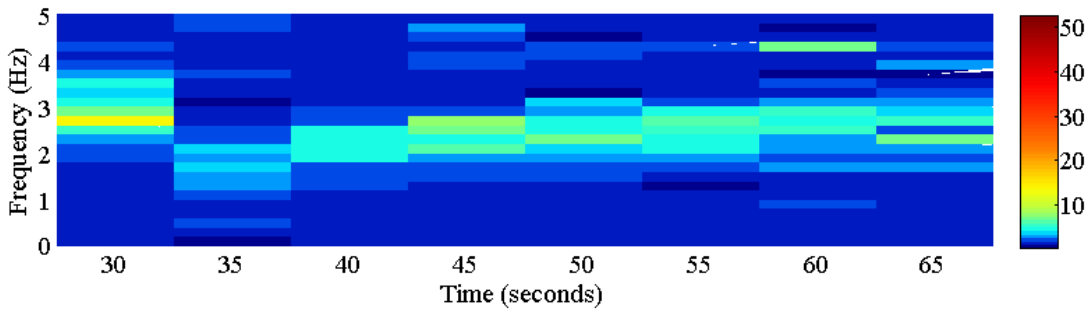

(b)

Figure 5.25: Short time Fourier transform analysis during the moderate event in (a) NS and (b) EW directions

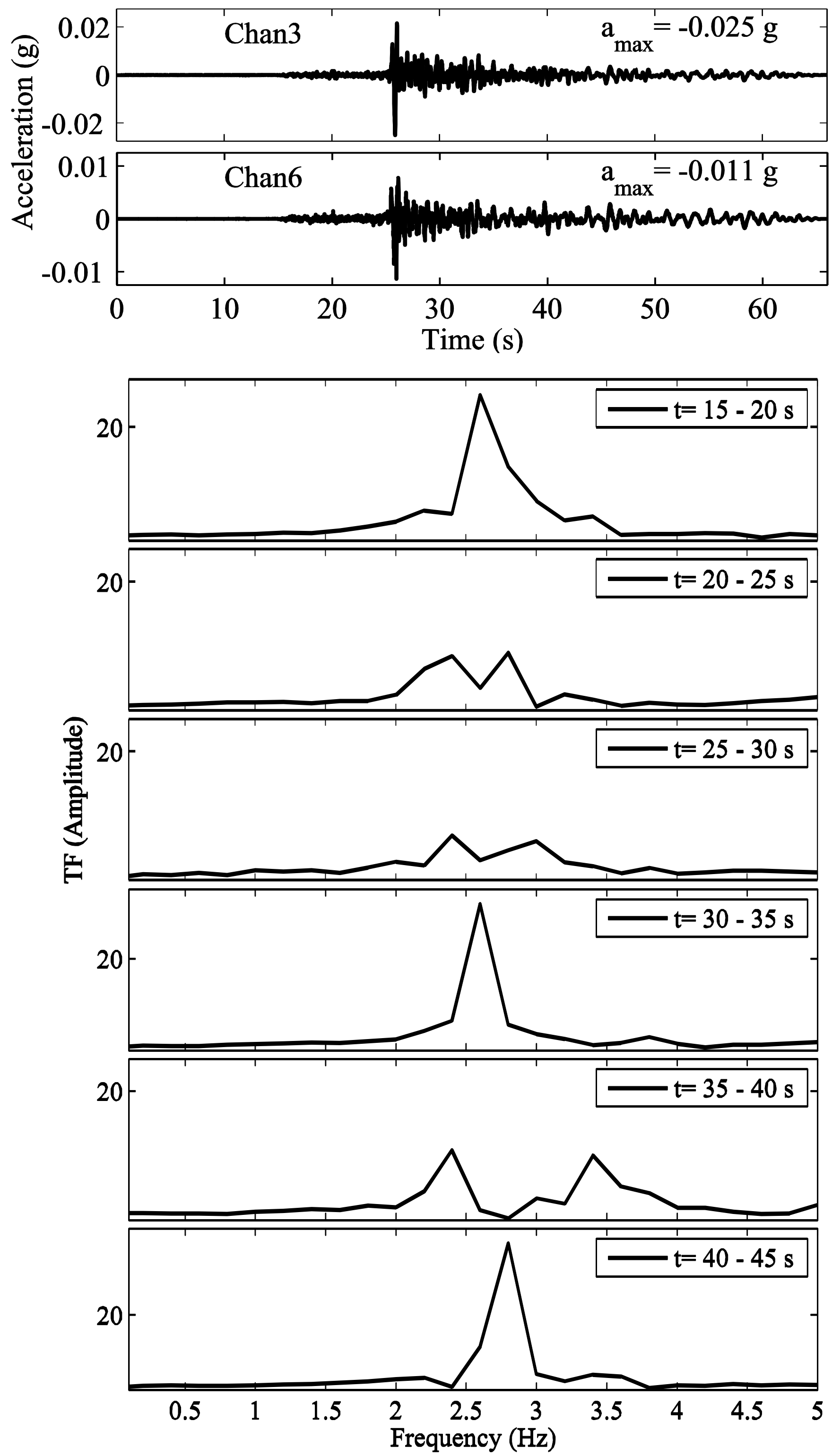

Figure 5.26: Linear soil response of the topmost stratum during the Ferndale Earthquake on Feb, 2010 in NS direction

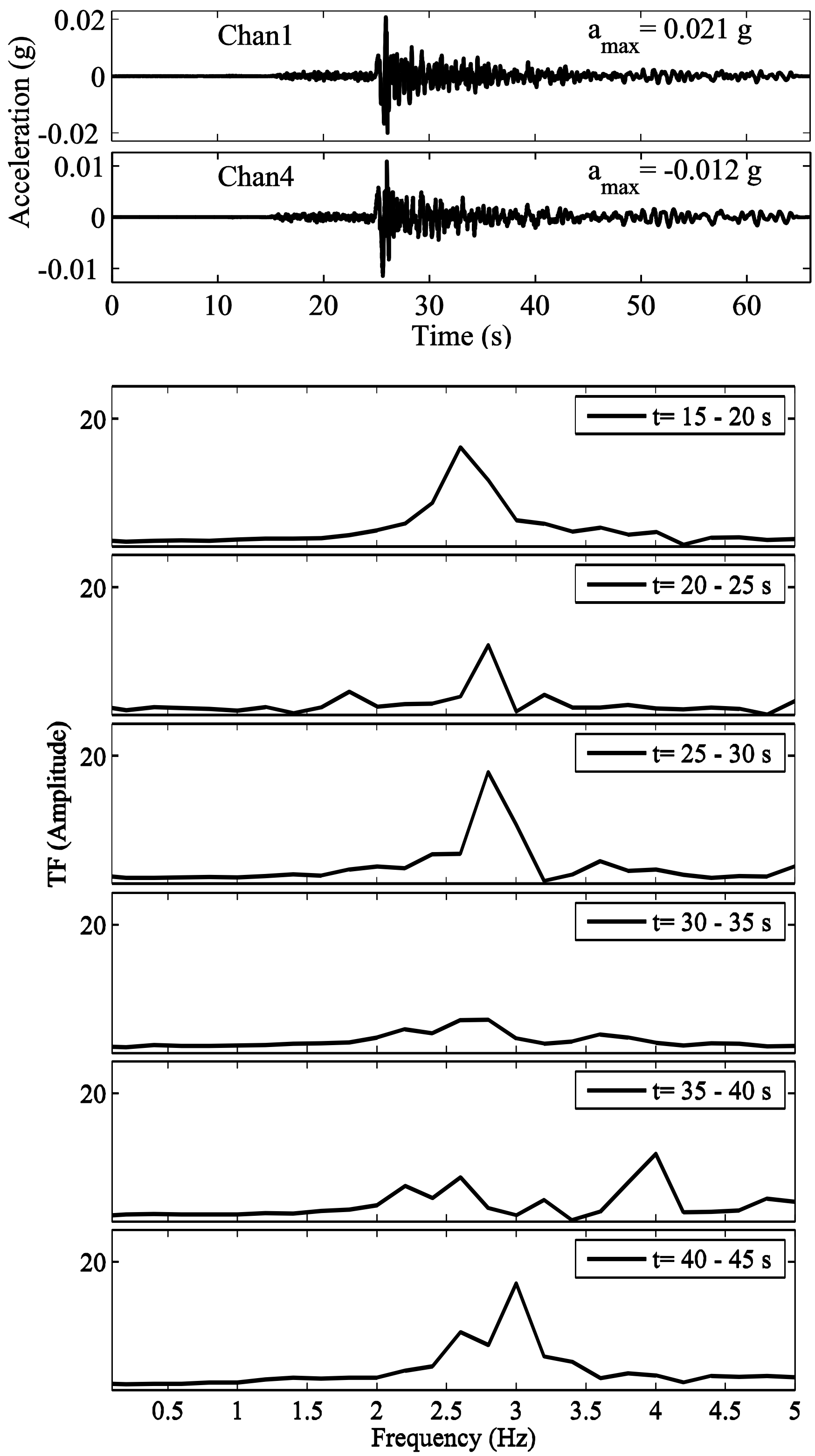

Figure 5.27: Linear soil response of the topmost stratum during the Ferndale Earthquake on Feb, 2010 in EW direction

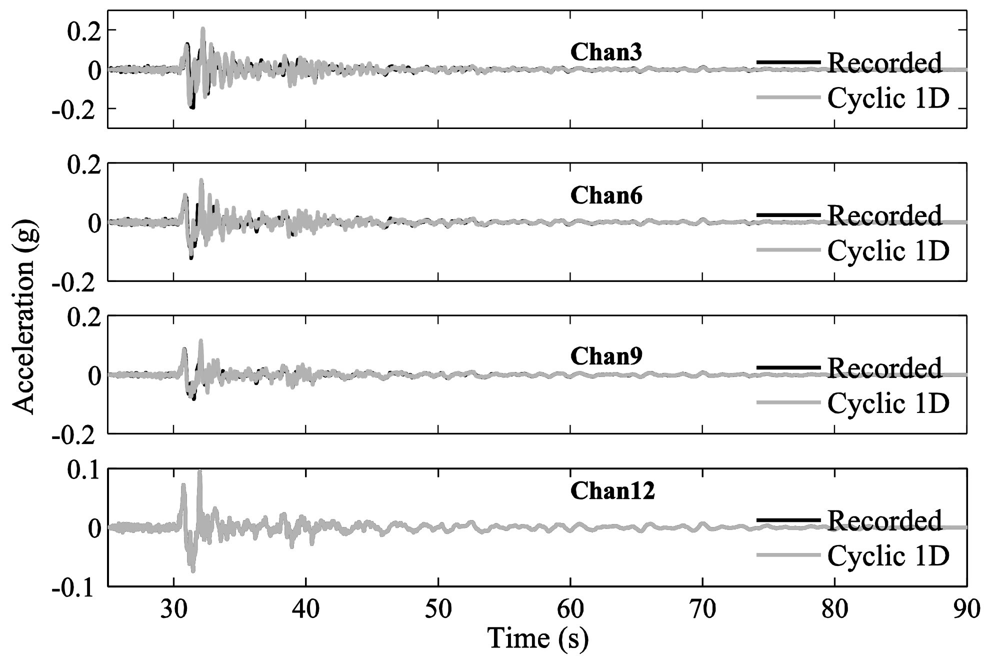

(a)

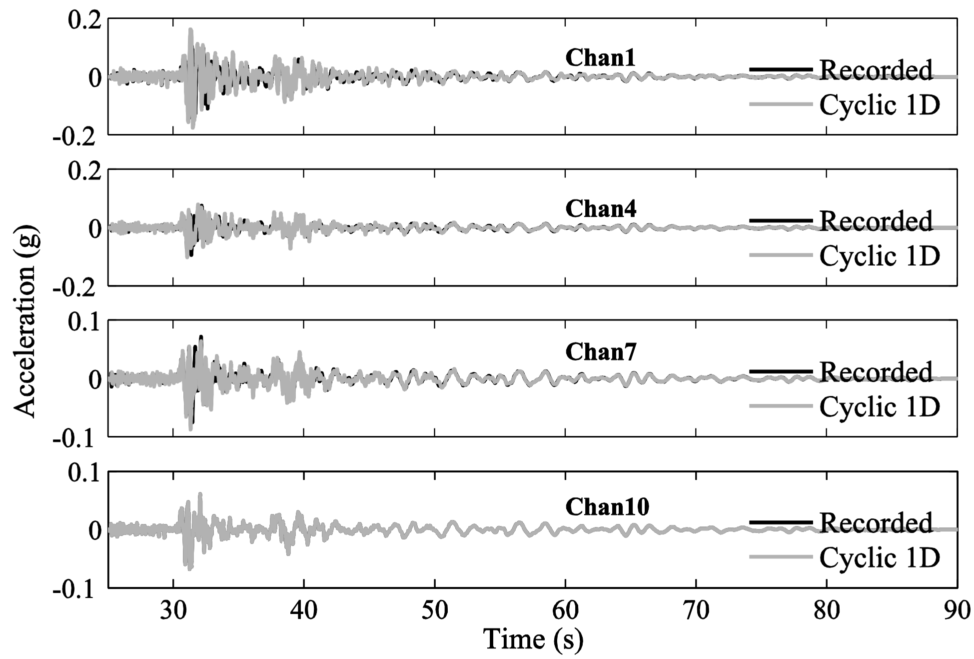

(b)

Figure 5.28: Nonlinear analysis for the moderate event (damping ratio of 5% at the frequencies of 2.5 Hz and 7.5 Hz) in (a) NS and (b) EW directions

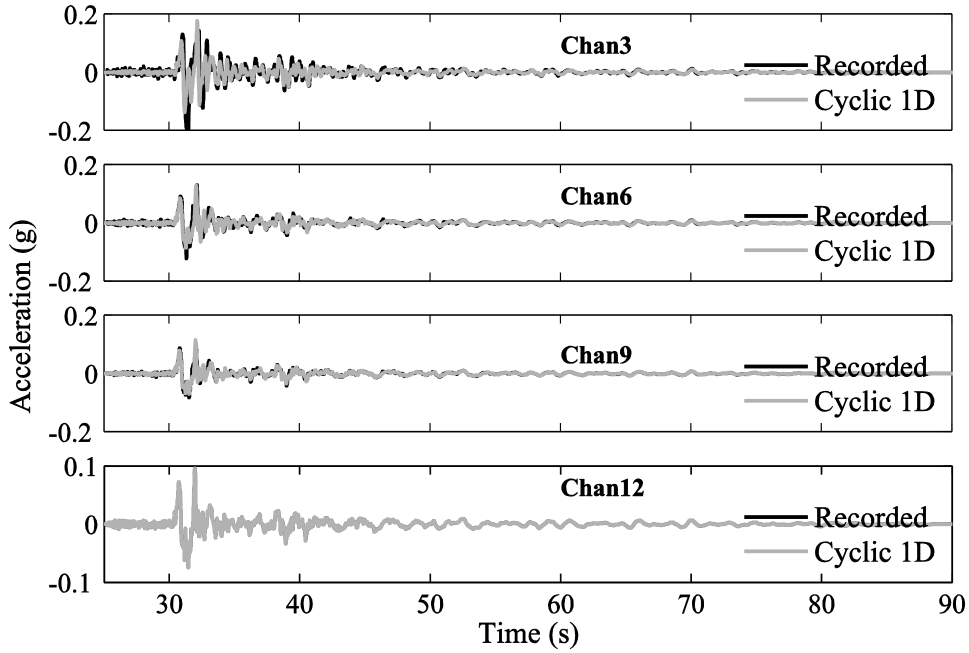

(a)

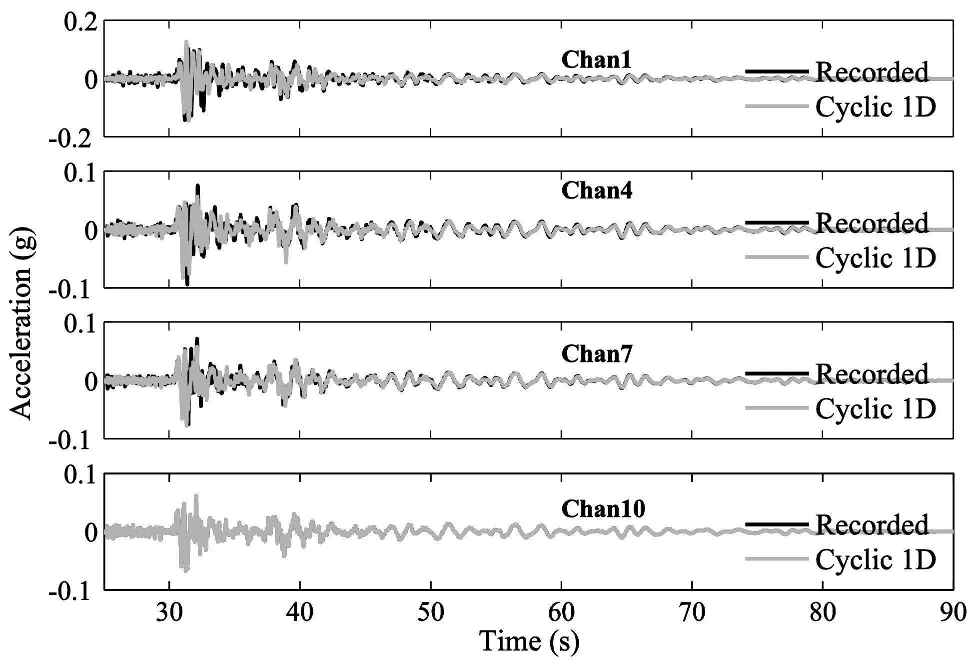

(b)

Figure 5.29: Linear analysis for the moderate event (damping ratio of 20% at the frequencies of 2.5 Hz and 7.5 Hz) in (a) NS and (b) EW directions

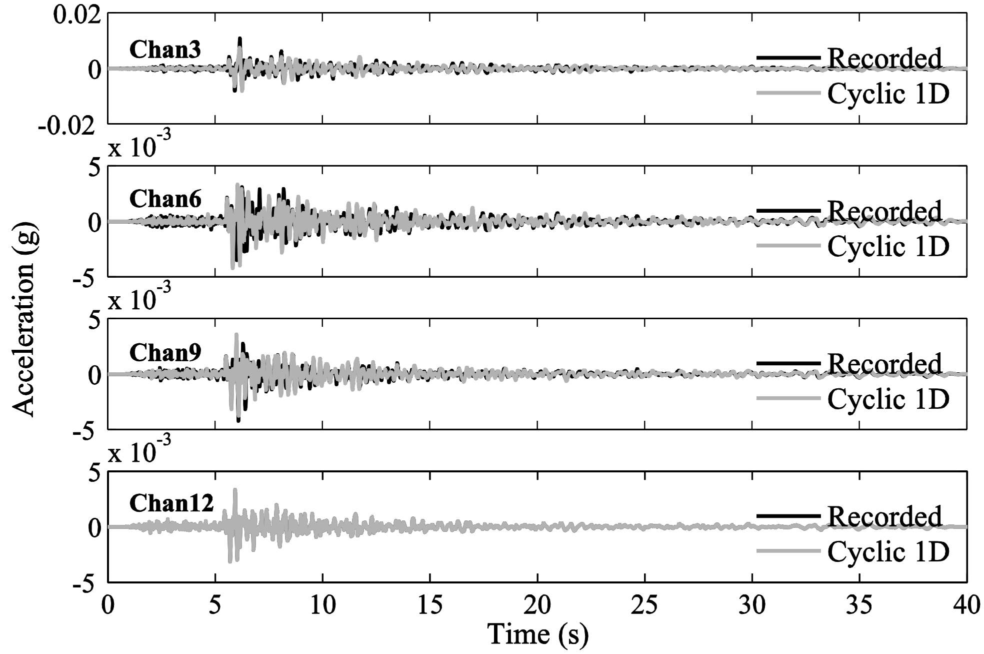

(a)

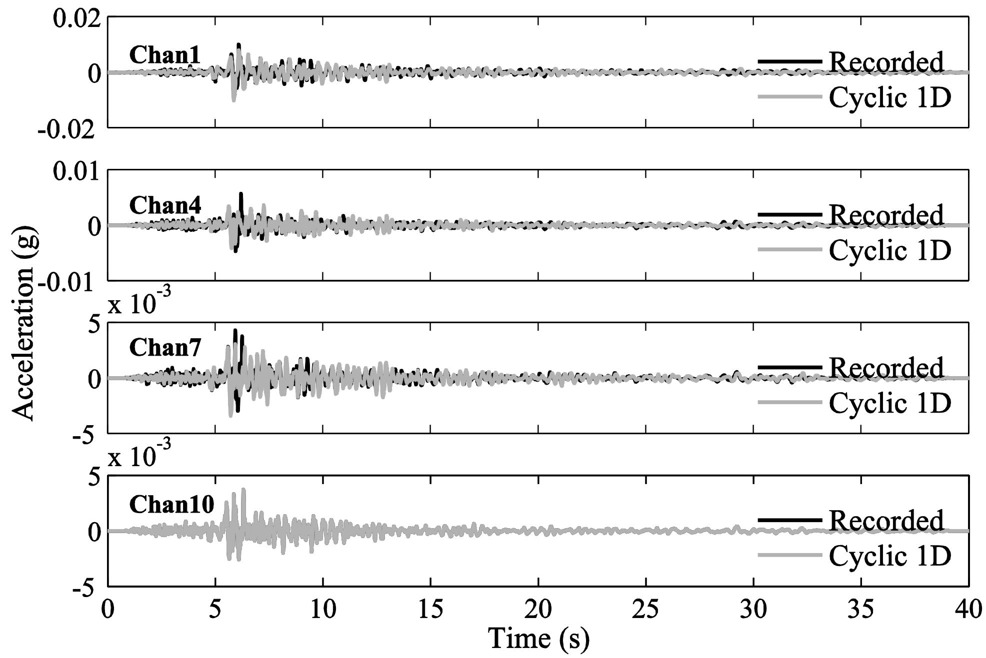

(b)

Figure 5.30: Linear analysis for the 2000 Eureka Offshore Earthquake (damping ratio of 8% at the frequencies of 2.5 Hz and 7.5 Hz) in (a) NS and (b) EW directions

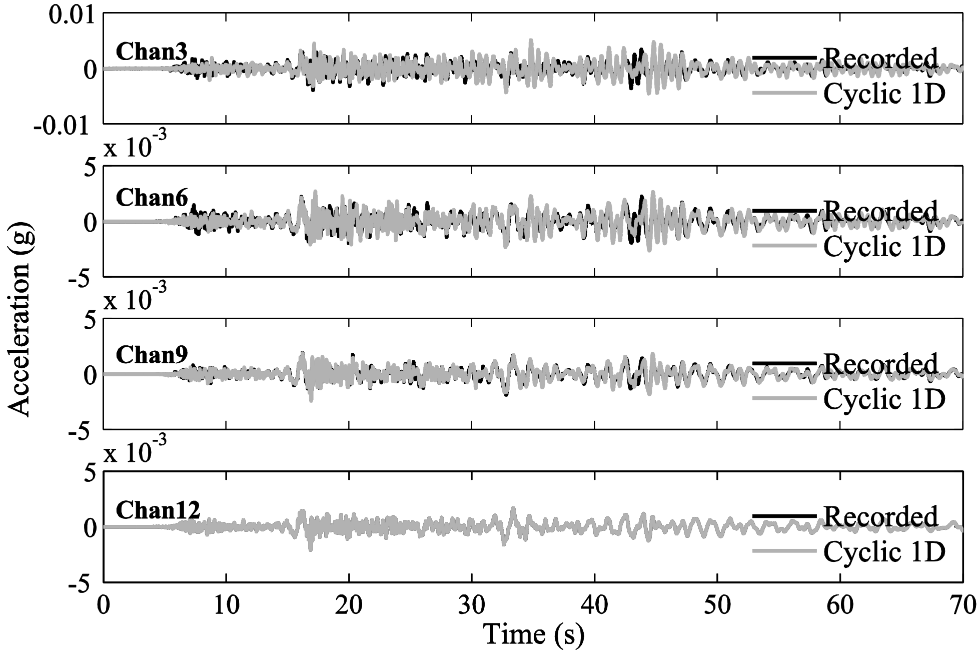

(a)

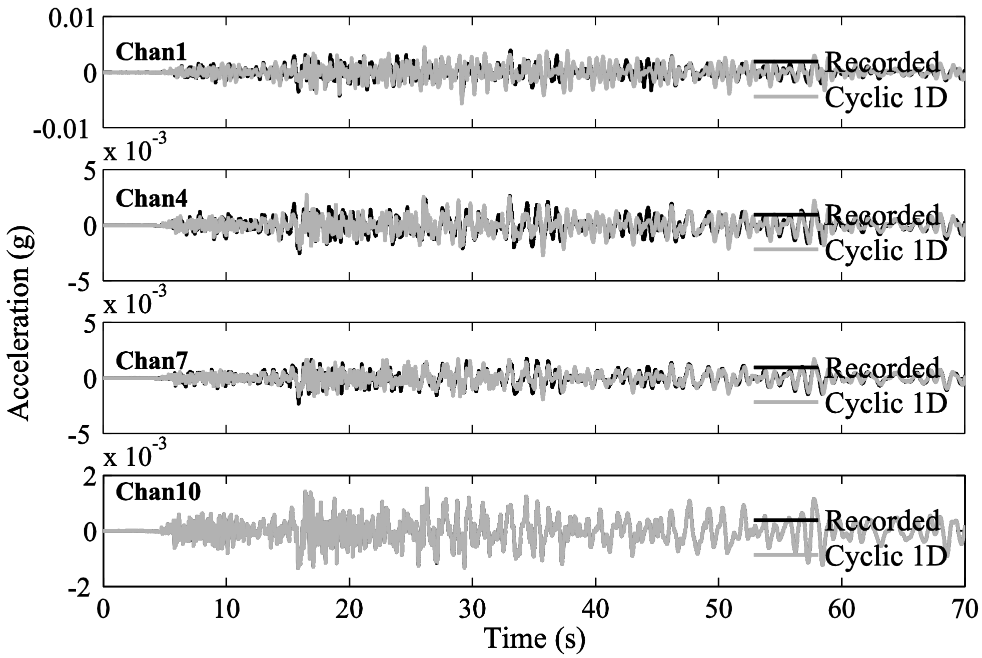

(b)

Figure 5.31: Linear analysis for the 2000 Cape Mendocino Earthquake (damping ratio of 8% at the frequencies of 2.5 Hz and 7.5 Hz) in (a) NS and (b) EW directions

Chapter 6

Recorded Seismic Response of the Samoa Channel Bridge System

Recorded earthquake motions from the highly instrumented Samoa Channel bridge-ground system are providing valuable insights concerning the response characteristics during seismic excitation. During eight seismic events, more than 30 data channels have been documenting the seismic response of the bridge deck, abutments, and adjacent free-field. Of special interest is the response of one of the intermediate piers with records at the deck level, two pile group caps, and within an underlying pile foundation. Response of this pile foundation within the ground is compared to that of the nearby Eureka geotechnical downhole array. Records of the moderate level 2010 Ferndale earthquake (PGA of about 0.15g), along with all other available low-amplitude shaking events (2007-2014) are employed to evaluate the ground, pile foundation, and overall bridge seismic responses. Spatial variation of the recorded motions is examined. Linear and nonlinear response of the ground and the bridge are assessed using system identification techniques. Increased flexibility of the pile foundation is identified clearly during the Ferndale Earthquake in 2010.

6.1 Introduction

For over two decades, strong motion sensors have been deployed on Caltrans bridges and nearby free-field/downhole sites (Hipley and Huang 1997), through the joint efforts of the California Department of Transportation (Caltrans) and the California Geological Survey (CGS). As of 2013, 65 highway bridges, 13 toll bridge structures and 28 downhole geotechnical arrays have been instrumented in California (Caltrans 2008; 2012c; Shakal and Huang 2013). The bridge instrumentation sensors are attached to various locations to record bridge dynamic response during the seismic events (Olson 2005). The recorded data sets along with system identification techniques are permitting the evolution of insights into the bridge seismic response mechanisms (Wilson 1986; Wilson and Tan 1990; Werner et al. 1994).

More recently, instrumentation within bridge pile foundations is being deployed. As of 2014, eight bridge structures were instrumented as such, along with a nearby geotechnical downhole array (the Benicia-Martinez East Bridge, the Benicia-Martinez West Bridge, the Carquinez Bridge West Span, the Oakland - SF Bay Bridge/East, the San Francisco - Bay Bridge/West, the San Rafael Bridge, the Samoa Channel Bridge and the Eureka Channel Bridge). Among these, only the Samoa Channel Bridge and the Eureka Channel Bridge have multiple earthquake records available, varying in peak ground acceleration, epicentral distance, shaking duration, and frequency content bandwidth.

The recorded seismic motions of bridge deep foundations along with adjacent downhole-arrays provide a unique opportunity for documenting and analyzing salient ground-foundation-structure response mechanisms. Structural and geotechnical seismic performance issues which are not readily extrapolated from testing or analytical solutions, can be further elucidated based on the recorded earthquake response (Van Den Einde et al. 2004).

In this chapter, seismic response of the instrumented Samoa Channel Bridge and a nearby geotechnical array (Eureka Geotechnical Array) is investigated. Time history response along the bridge deck and underlying ground is presented. Performance of the bridge structure and the effects of local site geology during this earthquake are discussed. Response of an instrumented Pier (S-8) is closely studied. Focus is placed on the bridge seismic response during the Ferndale Earthquake of January 9, 2010 which resulted in a moderate but substantial level of earthquake excitation. Depending on the measured input-output motions of the system, resonance parameters were identified to describe the behavior of the downhole site, the structure alone and the soil-foundation-structure system. Records of other available low amplitude seismic motions are addressed as references for comparison.

6.2 Strong-Motion Instrumentations at the Samoa Channel Bridge and Adjacent Downhole Array

6.2.1 General Bridge Information

The Samoa Channel Bridge (SCB) connecting the Samoa Peninsula and Indian Island (Figure 6.1) is one of three bridges crossing Humboldt Bay in Eureka, California. It was designed in 1968, constructed in 1971 and underwent a seismic retrofit in 2002 (Caltrans 1968; 2002b).

This 20-span bridge is a 764 m long and 10.4 m wide structure (Figure 6.2). The superstructure consists of cast-in place reinforced concrete deck and four precast, prestressed concrete I-girders. As shown in Figure 6.2b, there are eight separation joints along the bridge superstructure. The bridge I-girders are supported on 19 concrete single column type piers and seat-type abutments. The piers and abutments are numbered S-1 through S-21 from the Indian Island side to the Samoa Peninsula side (Figure 6.2).

The abutments and piers were founded originally on pile-group foundations consisting of driven pre-cast prestressed concrete piles. Referenced to the mean sea level (MSL), elevation of the mud line varies from -15.8 m below Pier S-8 to +0.9 m at Pier S-20 (Figure 6.2a). Eleven pile groups (from S-3 to S-13) have a pile cap located above the mudline with a maximum value of +16.72 m (elevation of cap base) at Pier S-8 (Figure 6.2b and Figure 6.3).

The seismic retrofit work completed in 2002 included (Figure 6.3): (1) strengthening of the foundations by installing additional cast-in-steel shell (CISS) piles (e.g. 6 additional 1.52 m diameter, 19 mm shell thickness piles at Pier S-8), (2) adding or enlarging pile caps to cover the new piles, and (3) encasing the bridge columns in reinforced concrete column jackets. Detailed design drawings, retrofit information along with soil borings are reported by Caltrans (Caltrans 1968; 2002b).

6.2.2 Instrumentations of the Samoa Channel Bridge

To obtain insights for both the properties of earthquake and seismic response of the structure, the Samoa Channel Bridge is heavily instrumented with a total of 33 accelerometers (deployed mostly in 1996). Side view and deck level plan view of the sensor network layout for the bridge are shown in Figure 6.2. Locations of sensors are marked with numbered arrows indicating the direction of measured motion.

There are 24 sensors placed on the Samoa Channel Bridge to measure the translational motions of the structure, including 16 on the deck, 3 at the abutments and 5 at the pile caps of Pier S-8 and Pier S-14. Sensors on the structure are oriented in the longitudinal and transverse direction of the bridge. At a nearby ground surface station (denoted here as BGS, 48.77 m west of the Abutment S-21), three sensors were installed at elevation of +2.5 m approximately, oriented in the north-south (NS), east-west (EW) and vertical directions. In addition, 6 accelerometers were embedded inside one of the retrofitted CISS piles at Pier S-8 (Figure 6.3). As such, foundation seismic response at two different elevations (-10.36 m and -16.46 m) was recorded after the structural retrofit.

Of particular interest in this instrumentation is the dynamic response of the foundation relative to bridge structure at the mid-span of Samoa Channel Bridge (Pier S-8). For this purpose records from sensors 10, 8, 30 and 33 (transverse direction) are studied in details in this chapter to obtain salient resonant frequencies for both the superstructure and the entire ground-foundation-bridge system.

6.2.3 The Adjacent Eureka Geotechnical Array

As discussed in detail in Chapter 5, the Eureka Geotechnical Downhole Array (denoted here as GDA, CSMIP Station 89734) is located approximately 198 m south-east of the Samoa Bridge Abutment S-1 (Figure 6.4). A relatively deep soft alluvium geological profile with high water table is noted at this location. The very dense soil layer appears approximately 22 m below the ground surface (Figure 6.5). Nonlinearity of the site seismic response was evident through analysis of this nearby downhole array data. The recorded data at this site allows for a better understanding of the ground seismic response (details provided in Chapter 5) in which the Samoa Channel Bridge foundations are embedded.

6.2.4 Recorded Earthquake Motions

The bridge is located in a seismically active area of Northern California. Records from a total of eight earthquakes in the period of March 2000 through March 2014 are currently available with Magnitudes from 4.6 M_w to 7.2 M_w (M_w: regional moment magnitude). Corrected acceleration, velocity, displacement and acceleration response spectra are available. Varying in peak ground acceleration (from 0.006 g to 0.150 g), epicentral distance (from 40.2 km to 153.4 km), shaking duration, and frequency content bandwidth, these earthquakes provide valuable information on the soil-foundation-structure seismic behavior over a broad range of excitations. Table 6.1 and Table 6.2

depict time, magnitude, epicentral distance, peak horizontal acceleration/displacement of the recorded earthquakes.

Notable is the 2010 Ferndale ($M_w = 6.5$) Earthquake (hereafter, referred to as “the moderate event”) which occurred approximately 35 km away from Ferndale, CA in a deformation zone of the southernmost Gorda plate (http://earthquake.usgs.gov, Storesund et al. 2010). The bridge site at a distance of 53.8 km from the epicenter of this earthquake recorded peak acceleration of 0.15 g at the ground surface and 0.37 g on the bridge deck. During this earthquake, the largest relative movement on the bridge structure was 9.6 cm longitudinally and 7.2 cm transversely referenced to the motion of at -16.46 m within the instrumented pile. This moderate event is the first significant earthquake to occur since the retrofit in 2002 resulting in the largest motion recorded on the bridge. However, no significant damage was reported during this earthquake (Storesund et al. 2010).

6.3 Evaluation of the Earthquake Records

All available records, except the 2000 Cape Mendocino earthquake (which happened before the 2002 seismic retrofit and no instrumentation on pile foundation yet), are employed to evaluate the seismic response of the bridge. In the section below, displacement and acceleration time histories during the Ferndale Earthquake in 2010 (the moderate event) and the Ferndale Earthquake in 2007 (low amplitude shaking event) are selected to demonstrate the significant findings.

6.3.1 Ground Motions at the Bridge and Adjacent Downhole Sites

Some insights may be derived from comparison of the recorded ground motions at the bridge and the downhole array sites (Figure 6.4). Synchronization between the bridge and GDA records was done based on the actual digital time stamp for each site (resulting in a time shift of about 2 seconds during the moderate event). In order to compare with the recorded motions along pier S-8, the ground surface records at the bridge site (BGS) and the GDA records were re-oriented in the bridge transverse (Tran) and longitudinal (Long) directions.

On this basis, Figure 6.6 and Figure 6.7 present the moderate event records of: 1) the bridge ground surface station (BGS, Figure 6.2), 2) the bridge pile foundation (BPF) near the mudline at the elevation of -16.46 m (after azimuthal orientation error corrections as discussed below in section 6.3.3), and 3) the adjacent geotechnical downhole array (GDA). In general, arrival time of the ground surface seismic waves at the GDA and bridge sites differed by around 0.1 second (as judged by cross-correlation analysis).

For the GDA records, there is a clear increase in displacement/acceleration amplitudes as the seismic waves approach the ground surface. Keeping the topography and site stratification in mind (Figure 6.4 and Figure 6.5), response at the pile foundation is seen to more closely align with that of the downhole stations (more so than at ground surface). As such, this location along the pile depth appears to be practically moving along with the ground, indicating a level of relatively firm embedment (fixity) at this depth. Similar conclusions can be deduced based on comparison of records from the other available low amplitude earthquake events (Table 6.1 and Table 6.2).

The pseudo-acceleration response spectra (4 different earthquake events), with 5% damping, for the recorded free field motions of the bridge as well as those of the adjacent downhole arrays are shown in Figure 6.8 and Figure 6.9. There is a noticeable amplification effect for the motion at the downhole ground surface compared to those at depths. In particular, spectral acceleration of the BPF generally falls between those of the downhole at the ground surface and elevation of -30 m in the short period range. It is noteworthy that the pseudo-acceleration of the bridge at the ground surface station is significantly high for periods less than 0.33 second for all four earthquakes. This observed high energy response at low period might be partially due to the soil characteristics at the site (Figure 6.4 and Figure 6.5) and partially from the impact of being close to the bridge (Figure 6.10).

Welch's Power spectral density (PSD) at these three locations was evaluated (Figure 6.11) for two representative events. It can be seen that there is a clear peak at around the frequency of 3.8 Hz for the BGS station which actually occurs during all shaking events.

6.3.2 Seismic Response along the Bridge Deck

As shown in Figure 6.12 and Figure 6.13, relative displacement time histories (referenced to the motions at the -16.46 BPF station) display in-phase behavior in both directions for the two representative earthquake events. Overall, the bridge is noticeably flexible in the mid-span (Channels 10 and 12). For the moderate event, maximum relative displacement at Pier S-8 is 60% larger in amplitude compared to that at the abutment (Chan 3).

In addition, transverse displacement time histories demonstrate clearly the period of vibration due to the pronounced response of the structure in this direction. The observed resonance (Chan 12) is particularly obvious during the small shaking events with a period of 1.10 second for the entire vibration phase (Figure 6.12a). During the moderate event, the bridge structure displays a period of 1.57 second during the strong shaking phase of this event (about 28 s – 33 s), which is then reduced to about 1.29 thereafter (Figure 6.13a).

In the longitudinal direction, the displacement (Figure 6.12b and Figure 6.13b) displays a period of 0.75 second for the small shaking events and 1.27 – 1.50 second for the moderate event. In general, the bridge structure is stiffer in this direction with a lower response period. However, the bridge displays some flexibility during the moderate event, potentially due to partial opening/closing of the separation joints.

Sharp spikes were observed from the deck acceleration time histories in the translational directions (both Long and Tran) for the moderate event (Figure 6.14). As shown in Figure 6.2b, motions across the separation joints are measured by Chan 11 and 13 in the longitudinal direction and by Chan 10 and 12 in the transverse direction. It was observed that the spikes occur simultaneously in sets in the both directions. Among these, the highest spike is 2.23g at Chan13 in the longitudinal direction and -0.67g at Chan10 in the transversal direction, whereas the peak ground acceleration at the bridge site is only about 0.17g (Table 6.1). Such spikes were likely caused by head-on impact between adjacent bridge deck segments (Huang and Shakal 1995; Malhotra et al. 1995). The opening and closing of in-span separation joints (near Pier S-8) in terms of relative displacement between adjacent bridge segments is also shown in Figure 6.14. No spikes were observed during the low-amplitude shaking event.

Figure 6.15 marked the location of sensors along the bridge deck and the peaks of 6 earthquakes from the processed records referenced to BPF motions. High amplification factor is observed at pier S-8 indicating the most vulnerable location of the bridge.

6.3.3 Seismic Response of Pier S-8

Given the discontinuity of the bridge structure due to existence of separation joints near Pier S-8, transverse motion of the corresponding central intermediate bent may be analyzed individually in order to glean some initial insights (independent of the rest of the bridge). Additionally, the high transverse motion observed at Pier S-8 (Figure 6.12 and Figure 6.13), indicates the deck support flexibility at this location. As such, of particular interest in this study was the dynamic response of the bridge structure relative to the pile foundation in the transverse direction at mid-span Pier S-8. The observed behavior of this full-scale pile-deck foundation system during actual earthquake events is extremely valuable and will contribute considerably to our current understanding of this important SSI mechanism.

Displacements of the bridge along Pier S-8 (including deck level, pile cap level and the pile below ground) are shown in Figure 6.16 - Figure 6.19. It is observed that the data from the retrofitted pile at elevations of -10.36 m and -16.46 m were out of phase (Figure 6.20 and Figure 6.21). Due to the uncertainty of sensor orientations on the retrofitted pile, cross-correlation analyses were performed first, as detailed below:

- o Rotation of data at Elev.= -16.46 m: since the displacement time histories at -16.46 m is closer to those of the free field, any necessary re-orientation of these time histories was based on cross-correlation between the BGS motions and the BPF response (in the lateral directions). Table 6.3 shows that peaks of cross-correlations appear when the records of the pile were re-oriented by 90-110 degrees based on the 6 investigated earthquakes. Therefore, it was assumed that sensors at the BPF station need to be rotated 103 degrees (counterclockwise).
- o Rotation of data at Elev.= -10.36 m: due to the flexibility of the pile foundation, the response at -10.36 m is correlated to the motions at the pile cap level. Table 6.4 indicates that about 144 degrees of rotation (counterclockwise) would be needed at the elevation of -10.36 m to achieve peak cross-correlation.

After rotation, motions along Pier S-8 display in-phase behavior in the transverse and longitudinal directions (Figure 6.16 - Figure 6.19). Shamsabadi et al. (2014) obtained similar orientation angles using the Fourier Spectra method.

Transverse displacement records along Pier S-8 at four different elevation are shown in Figure 6.22a and Figure 6.23a with a clear in-phase dominant fundamental response period. With the motion of BPF as “input”, the pile cap as well as the bridge deck displacements display significant amplification.

As shown in Figure 6.22b and Figure 6.23b, much of the bridge displacements at Pier S-8 are due to deformation occurring at the pile cap level, with the bridge deck motions only slightly different from those of the pile cap. Under the maximum deflection of the substructure (displacement of deck, pile-cap and BPF station, marked as time instant 1 in Figure 6.22b), the bridge pier (between the deck and the pile cap) only contributes about 1.4% of the total deformation (Table 6.5). This may be taken as an indication that the pier above the pile cap is quite stiff in comparison to the lateral stiffness afforded by the underlying pile group. In the longitudinal direction, the displacements are more evenly accounted for by the pile group and the column, potentially due to the reduced column stiffness in this direction (Figure 6.24 and Figure 6.25). In general, foundation flexibility can have a significant influence on the seismic response of Pier S-8 and should be considered in the seismic analysis.

6.3.4 Abutment and Bridge Response along Mud-line

Figure 6.26 and Figure 6.27 compare the acceleration/ displacement time histories of bridge base along the ground surface (including motions at the BGS, the BPF, on the pile cap near ground surface and at the bridge abutments). It was observed that displacement time histories are in the same pattern with larger peak values near abutment S-1. In addition, high frequency components were observed from acceleration time histories as well as the pseudo-acceleration response spectra (Figure 6.28 and Figure 6.29) at BGS and at abutment. In the longitudinal direction, spikes were observed at abutment and on the pile cap of Pier S-14 during the moderate event. All these observations indicate that the motions recorded at nearby ground surface as well as motions on S-14 pier footing: i) are affected by the bridge response, and ii) are influenced by the varying topography and irregular soil profile stratification under the extended bridge domain. As such, typical modeling procedures using a nearby ground surface response spectrum may not fully reflect the actual input excitation complexities.

6.4 System Identification for the Ground-Foundation-Bridge System

6.4.1 Site Response and Nonlinearity

Nonlinearity of the site seismic response was evident through analysis of the nearby Eureka downhole array data (details in section 5.3). Lower resonant site (o m – 19 m) frequency (decrease of soil stiffness) is observed (~1.8 Hz) during the strong motion phase (28 s – 33 s) compared to other time windows (reaching as much as 2.6 Hz). The recorded data at this downhole site allows for a better understanding of the ground seismic response in which the Samoa Channel Bridge foundations are embedded.

6.4.2 Bridge Sub-system Resonances

For applications to bridge structures, system identification techniques can be used to estimate modal frequencies, damping ratios, and mode shapes (Şafak 1991). Depending on the measured input-output motions, modal vibration parameters were identified to describe the behavior of the structure alone or the whole ground-foundation-structure system.

In general, system identification can be classified in two general categories based on a given input-output motion pair (Fenves and DesRoches 1994; Arici and Mosalam 2000). The non-parametric system identification procedure estimates the ratio of output/input motions in the frequency domain without fitting an underlying model (Tileylioglu 2008). This frequency-domain method does not explicitly consider the nonlinearity of the investigated structural system. The parametric identification method achieves the best estimates of vibration properties by fitting with the measured response in the discrete time domain (Ljung 1999).

6.4.2.1 Non-parametric Identification

Transfer Function (TF) defined as the ratio of the cross power spectral density ($P_{yx}(f)$ with seismic input signal x and output response y) and the power spectral density ($P_{xx}(f)$) is employed to assess the system and sub-system resonant frequencies.

In the transverse direction, the fundamental frequency for the Deck-Pier sub-system (deck response referenced to pile cap response) at the Pier S-8 is 1.60 Hz during the moderate event and in range of 1.96 - 2.00 Hz (refer as the first mode frequency of the fixed-base superstructure) for all of the other low amplitude earthquakes. A summary of the TF results for 6 earthquake events employing a Hanning window and 25% -50% overlap (time histories is divided into 3 sections but not exceed 30 s) to reduce the effects of spectral leakage is presented in Table 6.6 and Figure 6.30. The lower predominant frequency during the moderate event reflects nonlinear behavior in the structure (the Pier Deck sub-system). Short time Fourier transfer function contour in Figure 6.31 and Figure 6.32 reveals the variation of frequency with time.

The first transverse natural frequency of the foundation-bridge system at Pier S-8 is obtained by relating the response of bridge deck at Pier S-8 to that of the pile at elevation -16.46 m (taken here to be a fixed base as discussed above). Since the nearby bridge ground surface (BGS) is potentially somewhat affected by the bridge structure (Figure 6.8 and Figure 6.9), transfer function between the bridge deck and the BGS is also evaluated.

The fundamental transverse frequency for the bridge was found to be around 0.97 Hz during all of the low amplitude earthquakes and 0.73 Hz during the moderate event (Figure 6.33 and Table 6.7). The lower predominant frequency during the moderate event (Figure 6.33) reflects nonlinear behavior in the structure as well as in the pile-group response. Short time Fourier transfer function contour in Figure 6.34 and Figure 6.35 reveals the variation of frequency with time, where a lower dominant frequency is noted during the strong motion shaking phase. The identified structure resonant frequency generally agrees with the recently reported ambient vibration testing result (Turek et al. 2014).

Longitudinal resonance was also assessed using the Transfer function technique. Table 6.8 displays the identified primary resonance.

6.4.2.2 Parametric Identification

To determine vibration frequencies of the bridge structure using this technique, a single input, single output model is used (Stewart and Fenves 1998) in this report. The model parameters can be estimated with least-squares procedures in the discrete time domain. One of the properties determined from the best-fit parameters of the auto-regressive model (ARX) is the vibration frequency (ω) of mode j (Fenves and DesRoches 1994; Ljung 1999). In this study, MATLAB's system identification toolbox is employed. Fundamental frequencies based on the records of Pier S-8 in the transverse direction were listed in Table 6.6.

6.5 Discussion and Conclusions

Post-earthquake ground/structure response analysis with the aid of system identification methods provides useful information to investigate site and structure dynamic behavior. In this chapter, unique insights into the salient seismic response characteristics of the Samoa Ground-Foundation-Bridge system were obtained on the basis of strong motion records from the bridge and the adjacent geotechnical downhole array (Caltrans 2013).

Comparisons of the measured time-history indicate that: (1) despite the moderately high levels of shaking, the relative displacement between the top and bottom of the bridge column at Pier S-8 remain relatively small; (2) at Pier S-8, much of the bridge lateral deflections are due to movement of the pile cap. Therefore, foundation flexibility should be considered in the seismic assessment for this bridge structure; and (3) displacement time histories at the BGS station and the BPF station follow similar patterns to those at the downhole array, although BGS motions reveal some additional energy around the high frequency of3.8 Hz . As such, the BPF motion could be a candidate input motion for a computer model of this simplified foundation-structure system.

System identification techniques are applied to the recorded bridge motions to estimate the structure resonant frequencies. The primary findings on the basis of spectral analysis include: (1) Nonlinearity of surrounding soil during the moderate shaking event; (2) Variation of stiffness for bridge column/foundation for different earthquakes and (3) Effects of pile foundation flexibility on the seismic response of the Samoa Channel Bridge.

The results of this research are of significance to the current state of practice in seismic ground-foundation-structure analysis. The performance of bridges during the earthquake events can be explicitly interpreted based on studied full-scale ground/structural response records. In this domain of highly expensive and time consuming foundation design and retrofit methodology, valuable insights into the ground-foundation-structure seismic response can be obtained with increased availability of strong motion data sets in the future.

6.6 Acknowledgements

Chapter 6 of this dissertation is an extended version of the material published in the proceedings of the 10th International Conference on Urban Earthquake Engineering, titled "Bridge and Adjacent Downhole Array Response During Earthquakes at Eureka, California" with co-author Ahmed Elgamal (2013), and a manuscript under preparation for publication as a journal article, tentatively titled "Finite Element Based Seismic Assessment of the Samoa Channel Bridge-Foundation System", with preliminary author list of Ning Wang and Ahmed Elgamal. The dissertation author is the first author of this paper.

Table 6.1: Recorded peak acceleration for recent earthquakes at the Bridge Site (arranged by order of peak acceleration)

Earthquake	Epicentral Distance (km)	Tran. Peak Acc. (g)		Long. Peak Acc. (g)		Vert. Peak Acc. (g)	
		Ground	Structure	Ground	Structure	Ground	Structure
Ferndale* Jan 09, 2010	53.8	0.158	0.665** 0.216***	0.167	2.225** 0.660***	--	1.003
Trinidad June 24, 2007	63.8	0.025	0.063	0.015	0.021	0.008	0.072
Ferndale Mar 09, 2014	81.3	0.019	0.069	0.015	0.033	--	0.064
Trinidad August 16, 2008	40.2	0.016	0.026	0.018	0.043	--	0.056
Willow Creek April 29, 2008	56.6	0.014	0.032	0.010	0.019	--	0.025
Ferndale Feb 26, 2007	62.4	0.011	0.022	0.009	0.016	0.004	0.013
Crescent City June 14, 2005	153.4	0.009	0.031	0.007	0.018	0.004	0.026
Cape Mendocino March 16, 2000	102.4	0.008	0.018	0.004	0.020	0.004	0.009

* the January 2010 Ferndale Earthquake will be referred to as “the moderate event” in this study
** large peak acceleration due to spikes from separation joints
*** estimated after removing spikes using a band pass filter

Table 6.2: Recorded peak displacement for recent earthquakes at the Bridge Site

Earthquake	Epicentral Distance (km)	Tran. Peak Disp. (cm)		Long. Peak Disp. (cm)		Vert. Peak Disp. (cm)	
		Ground	Structure	Ground	Structure	Ground	Structure
Ferndale Jan 09, 2010	53.8	4.519	9.068	6.808	15.927	---	1.847
Trinidad June 24, 2007	63.8	0.152	0.445	0.051	0.124	0.015	0.275
Ferndale Mar 09, 2014	81.3	2.148	3.974	1.370	1.788	---	0.608
Trinidad August 16, 2008	40.2	0.052	0.302	0.084	0.203	---	0.217
Willow Creek April 29, 2008	56.6	0.102	0.652	0.092	0.317	---	0.141
Ferndale Feb 26, 2007	62.4	0.087	0.364	0.156	0.438	0.029	0.060
Crescent City June 14, 2005	153.4	0.128	0.518	0.081	0.275	0.079	0.121
Cape Mendocino March 16, 2000	102.4	0.095	0.604	0.050	0.343	0.035	0.072

Table 6.3: Rotation of sensors at the elevation of -16.46 m on retrofitted pile in degree

Earthquake Events	Rotation in Degree			
	Trans. (Channel 33)		Long. (Channel 31)	
	Accel.	Displ.	Accel.	Displ.
Jan 09, 2010 Ferndale	73	90	102	117
June 24, 2007 Trinidad	114.5	108	108	99.5
March 09, 2014 Ferndale	111	101	98.5	102
August 16, 2008 Trinidad	106.5	114	99	104
April 29, 2008 Willow Creek	91.5	111	96.5	101
Feb 26, 2007 Ferndale	99.5	98.5	97.5	107

Table 6.4: Rotation of sensors at the elevation of -16.46 m on retrofitted pile in degree

Earthquake Events	Rotation in Degree			
	Trans. (Channel 30)		Long. (Channel 28)	
	Accel.	Displ.	Accel.	Displ.
Jan 09, 2010 Ferndale	138.5	135.5	147	154
June 24, 2007 Trinidad	153	146	144	144.5
March 09, 2014 Ferndale	145	140.5	145	142.5
August 16, 2008 Trinidad	157	145.5	134.5	145.5
April 29, 2008 Willow Creek	138.5	146	146.5	145
Feb 26, 2007 Ferndale	140	138	145	146

Table 6.5: Deflection of substructure components at pier S-8 in the transverse direction

Earthquake	Deformation (cm)			
	Substructure deck vs pile -16.46 m	Pier deck vs pile cap	Pile pile cap vs pile -16.46 m	Pier contribution
Ferndale Jan 09, 10	7.15	0.10	7.05	1.4%
Trinidad June 24, 07	0.32	0.13	0.19	39.3%
Ferndale Mar 09, 14	-1.76	0.35	-2.11	-19.8%
Trinidad Aug 16, 08	0.27	0.09	0.18	34.0%
Willow Creek April 29, 08	0.57	0.06	0.51	10.8%
Ferndale Feb 26, 07	0.33	0.03	0.30	9.7%

Table 6.6: Identified resonant frequency of bridge pier in the transverse direction

Earthquake	Pier S-8 Fundamental Frequency (Hz) $\frac{\text{Deck}}{\text{Pile Cap}}$		
	50% overlapping*	25% overlapping*	parametric identification
Ferndale Jan 09, 10	1.60	1.67	---
Trinidad June 24, 07	2.00	1.96	2.10
Ferndale Mar 09, 14	1.97	1.97	1.88
Trinidad Aug 16, 08	1.96	2.00	2.16
Willow Creek April 29, 08	1.93	2.00	2.01
Ferndale Feb 26, 07	1.93	1.96	2.14

* time window is divided into 3 sections but not exceed 30 s

Table 6.7: Identified resonant frequency of bridge system in the transverse direction

Earthquake	Pier S-8 Fundamental Frequency (Hz) $\frac{\text{Deck}}{\text{Pile Cap}}$	
	$\frac{\text{Deck}}{\text{Pile @} - 16.46\text{ m}}$	$\frac{\text{Deck}}{\text{Free Field}}$
Ferndale Jan 09, 10	0.73	0.73
Trinidad June 24, 07	0.93	0.93
Ferndale Mar 09, 14	0.90	0.87
Trinidad Aug 16, 08	1.00	0.96
Willow Creek April 29, 08	0.97	0.93
Ferndale Feb 26, 07	0.93	0.93

Table 6.8: Identified resonant frequency of bridge pier in the longitudinal direction

Earthquake	Pier S-8 Fundamental Frequency (Hz) $\frac{\text{Deck}}{\text{Pile Cap}}$	
	50% overlapping	25% overlapping
Ferndale Jan 09, 10	2.80	2.87
Trinidad June 24, 07	2.61	2.61
Ferndale Mar 09, 14	2.97	2.97
Trinidad Aug 16, 08	2.86	3.11
Willow Creek April 29, 08	2.90	2.93
Ferndale Feb 26, 07	2.56	2.44

* time window is divided into 3 sections but not exceed 30 s

(a)

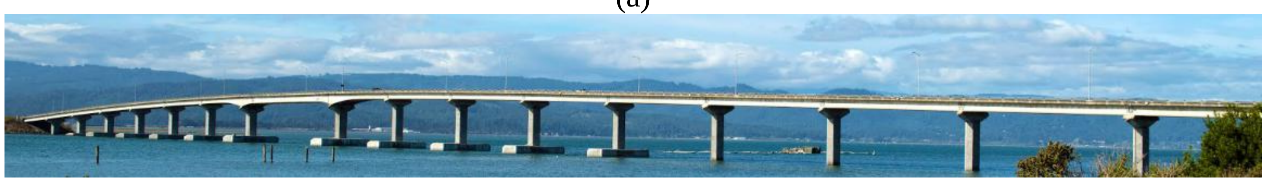

(b)

Figure 6.1: Bridge Configuration: (a) Samoa Channel Bridge, Eureka Geotechnical Array, Middle Channel Bridge and Eureka Channel Bridge (Map Data @ 2015 Google) and (b) photo of the Samoa Channel Bridge (http://www.strongmotioncenter.org)

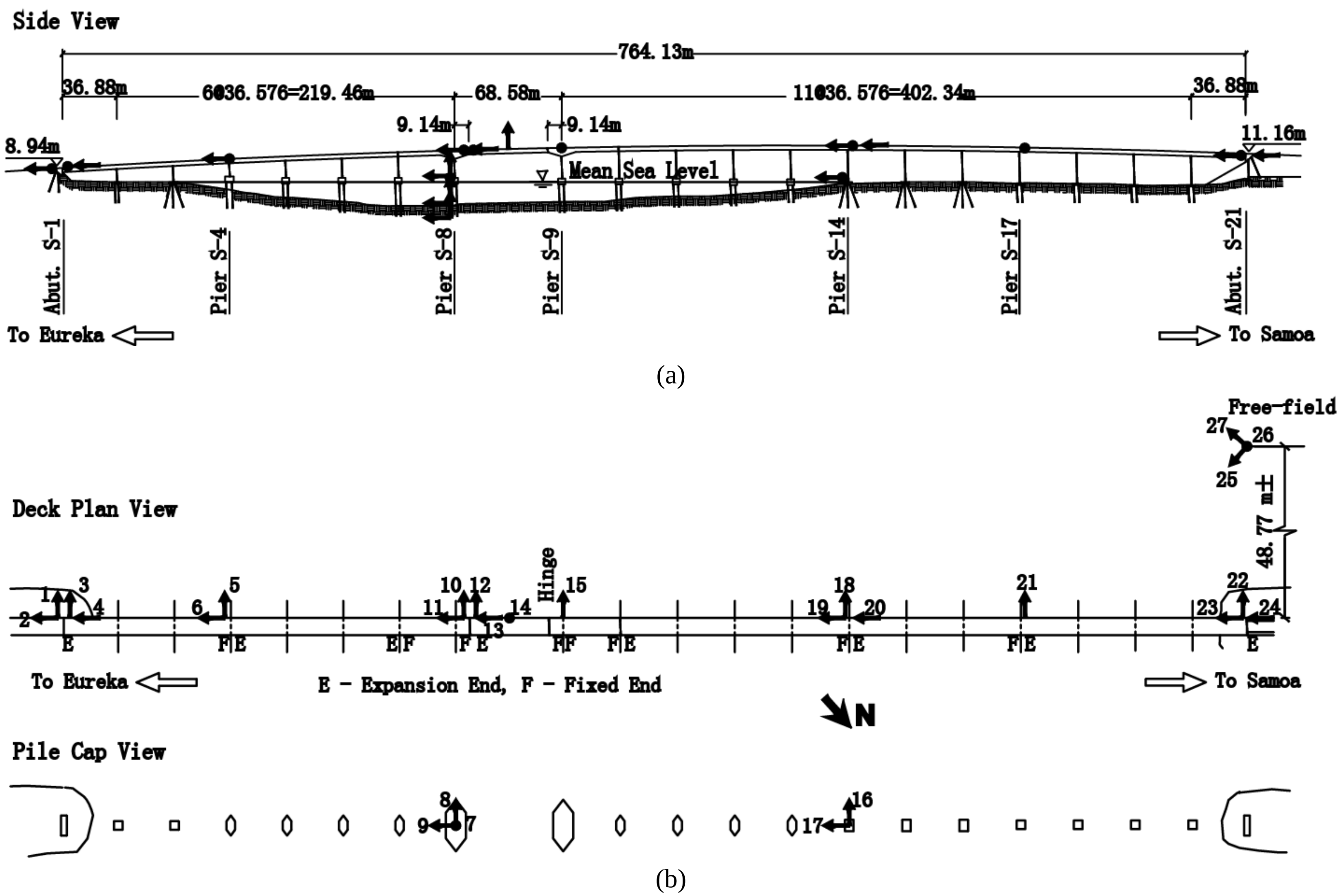

Figure 6.2: Layout of instrumentation at the Samoa Channel Bridge (http://www.strongmotioncenter.org)

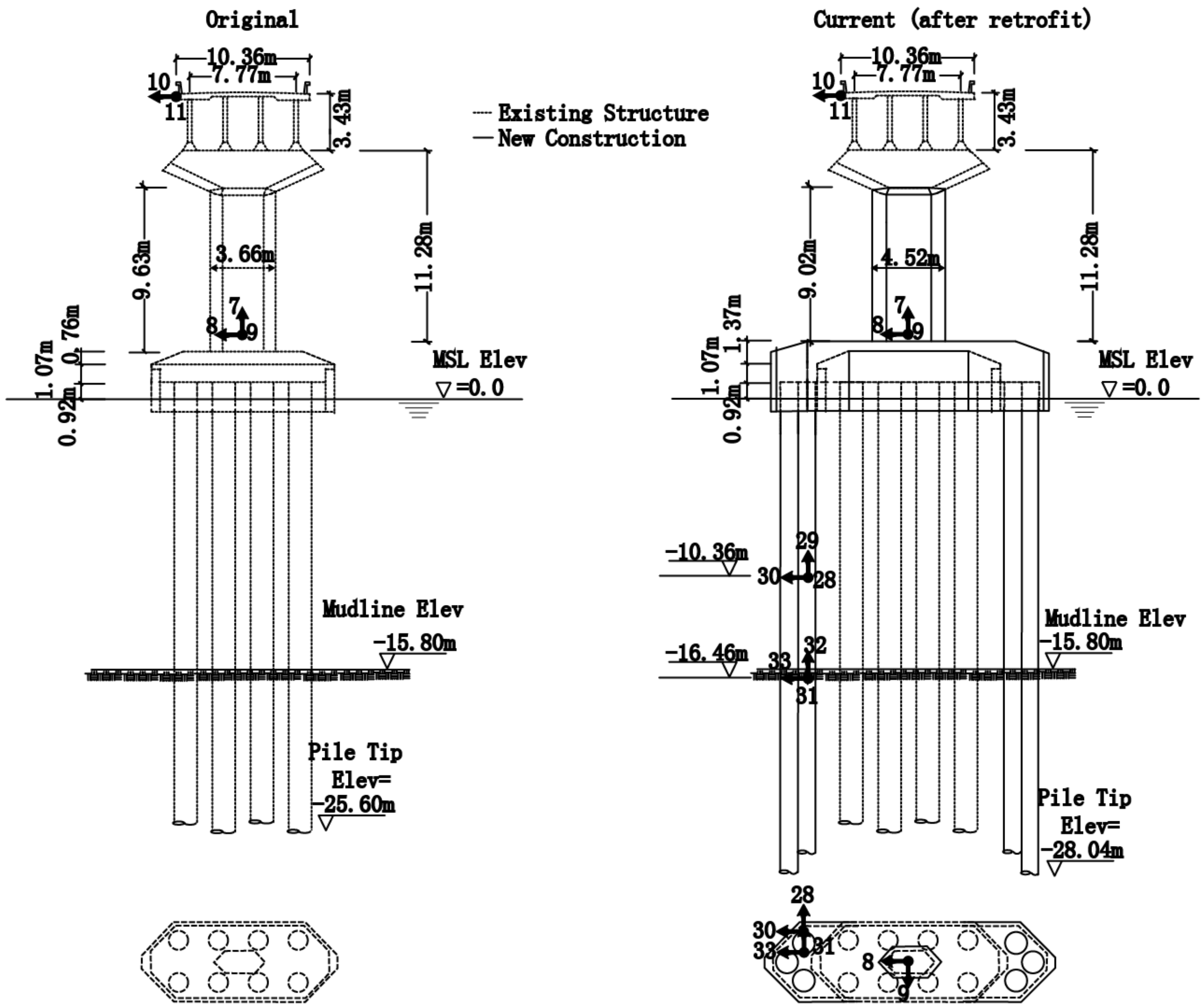

Figure 6.3: Layout of instrumentation at the Samoa Channel Bridge Pier S-8 (Caltrans 2002a)

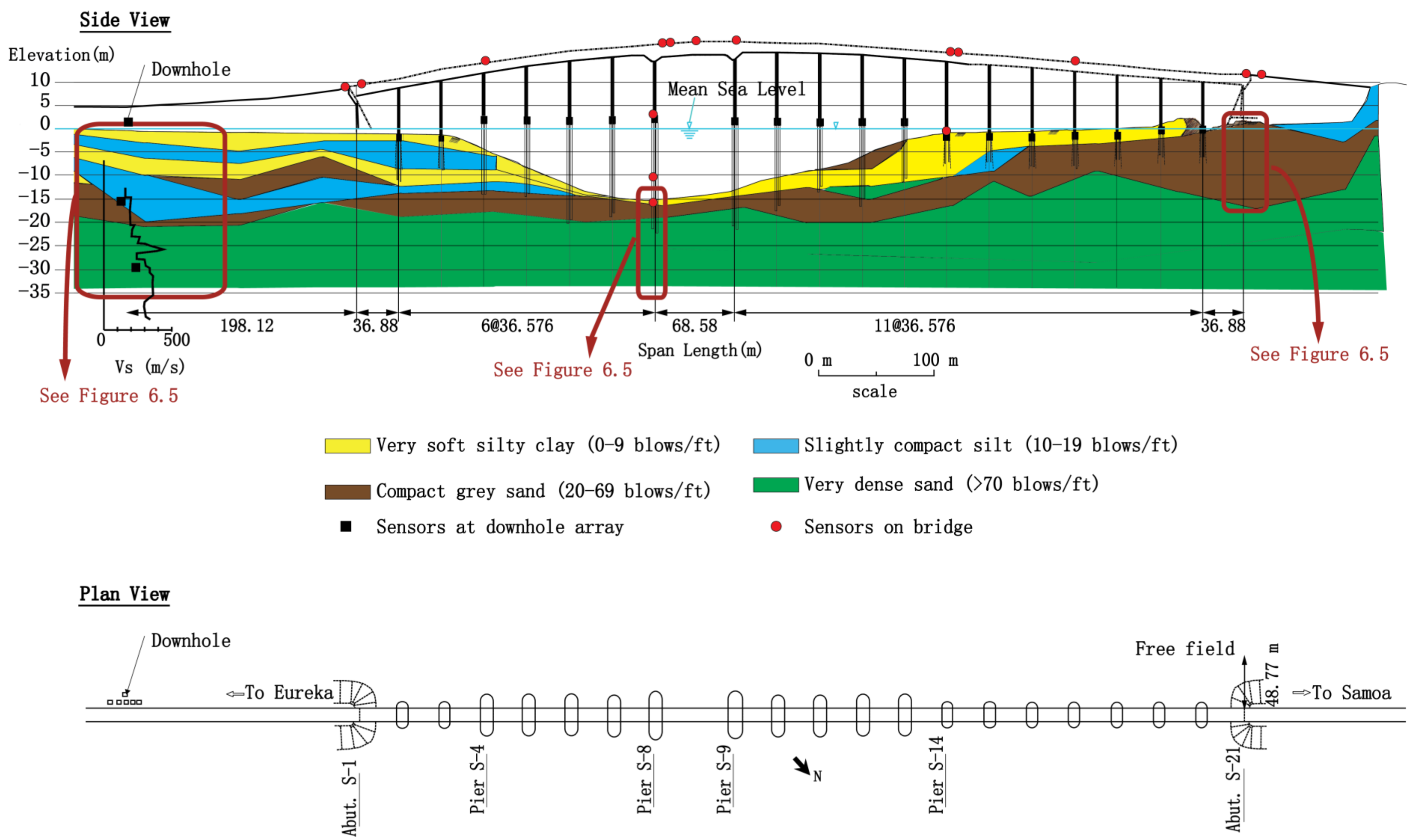

Figure 6.4: Soil Profile along the bridge (Caltrans 2002a) and shear wave velocity profile at Eureka Downhole array (http://www.strongmotioncenter.org)

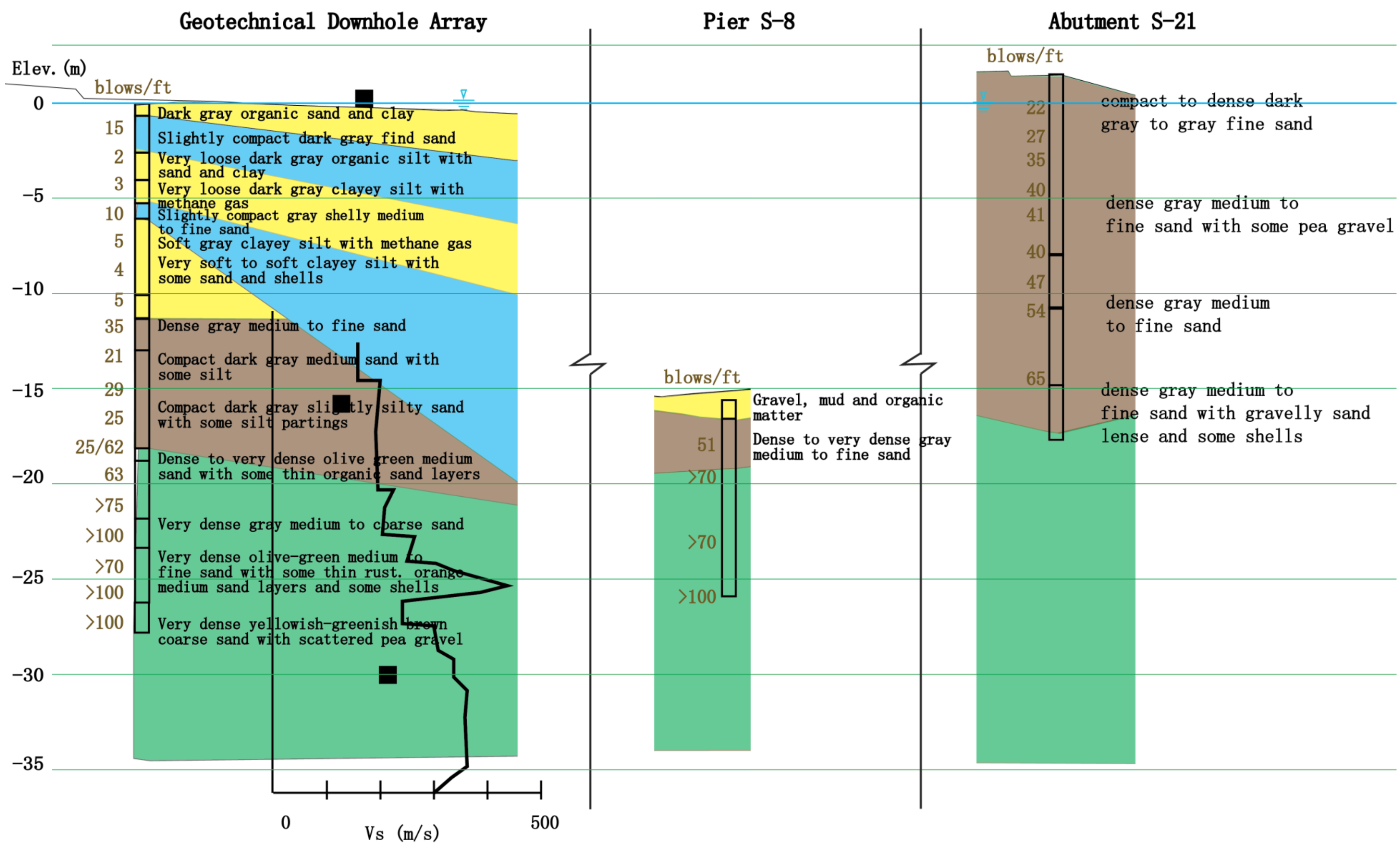

Figure 6.5: Soil Profile (Caltrans 2002a) and shear wave velocity profile at Eureka Downhole array (http://www.strongmotioncenter.org)

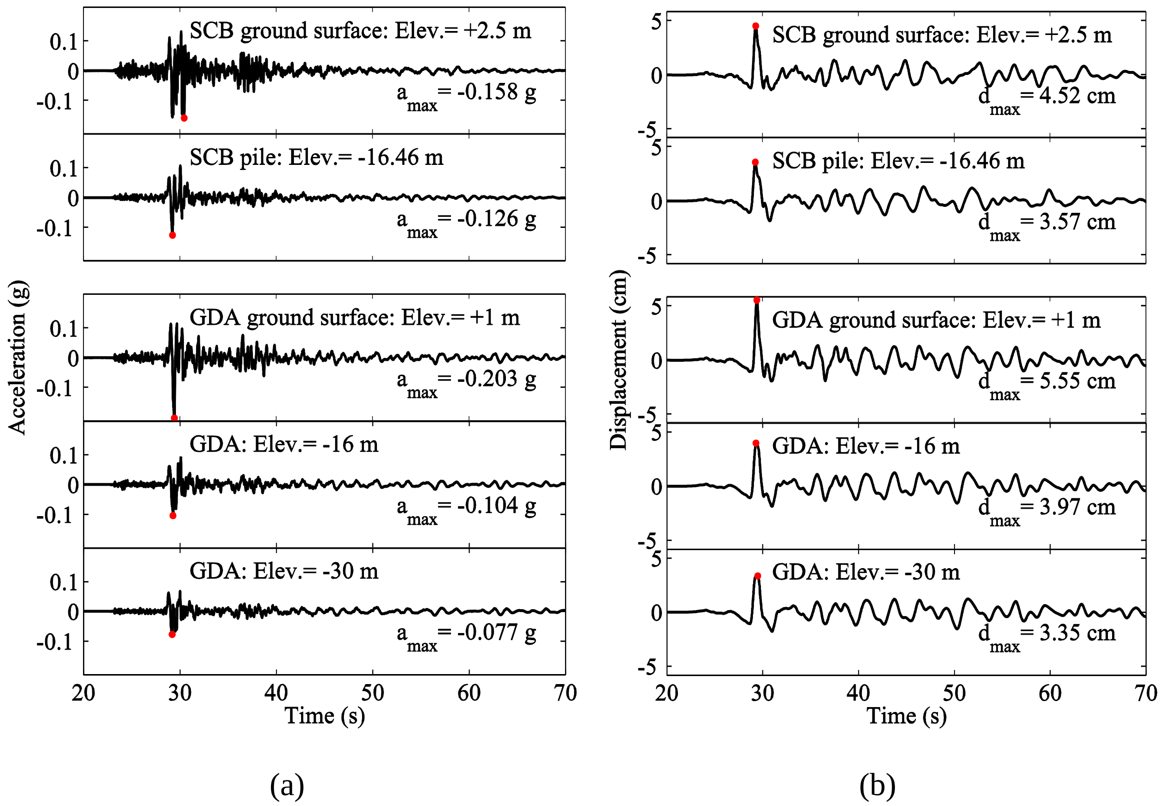

Figure 6.6: Transversal time histories: (a) acceleration and (b) displacement at the BGS, BPF and GDA stations during the moderate event

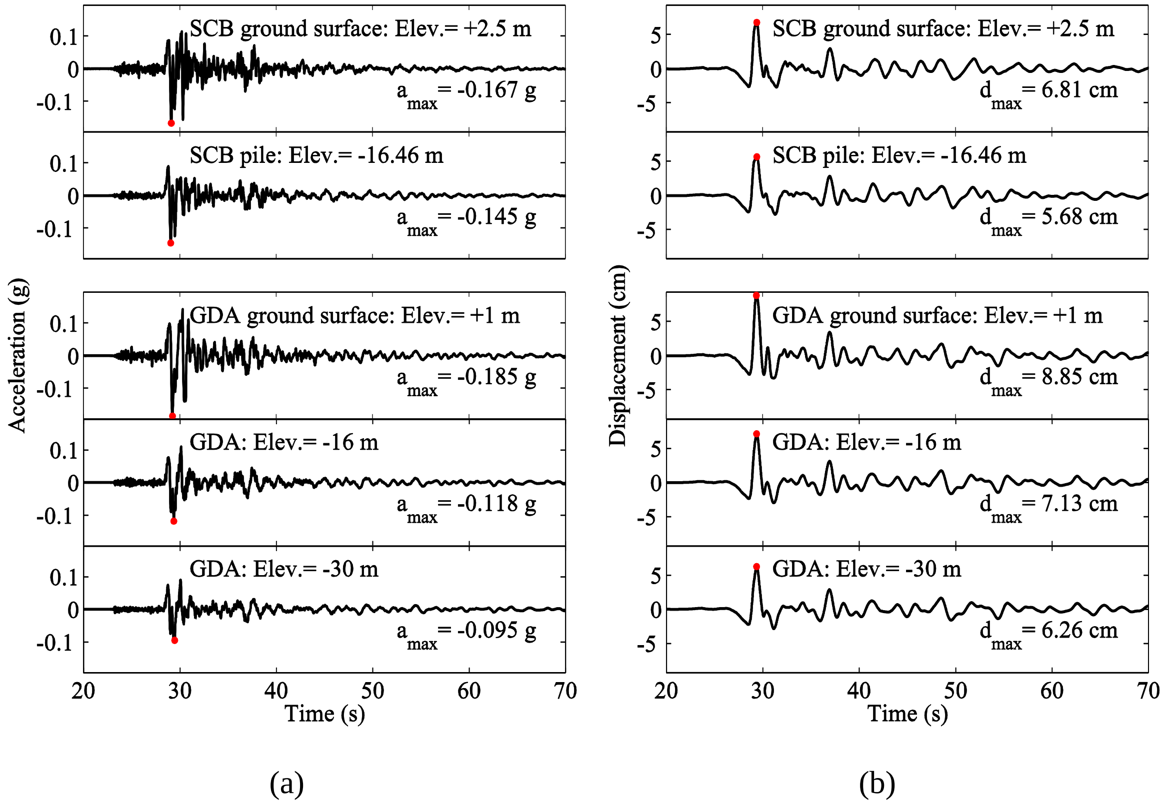

Figure 6.7: Longitudinal time histories: (a) acceleration and (b) displacement at the BGS, BPF and GDA stations during the moderate event

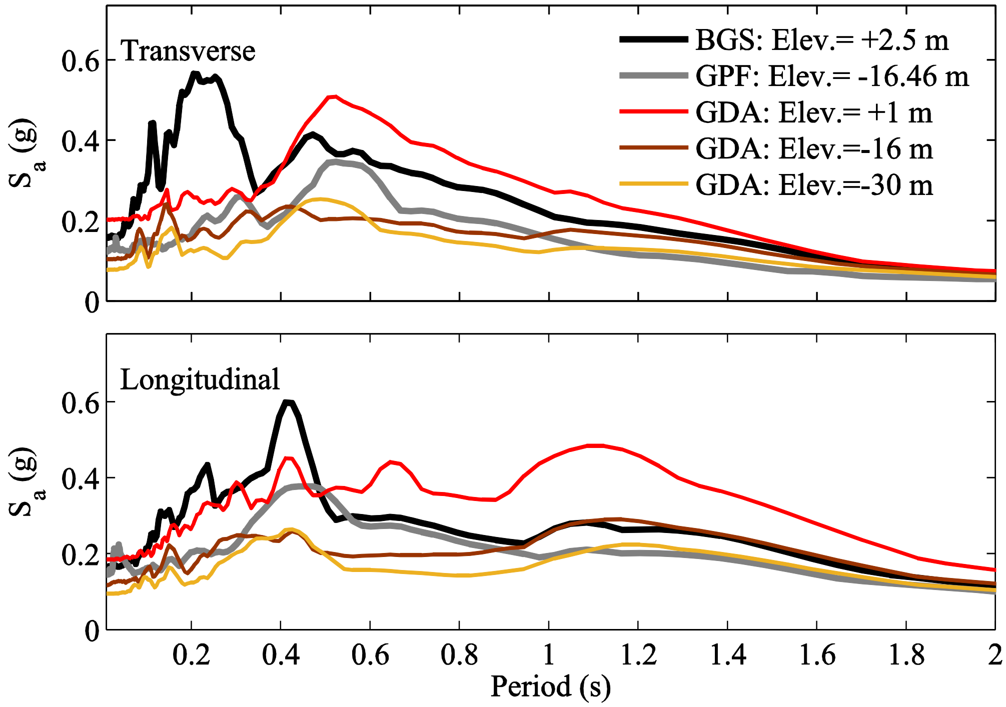

(a)

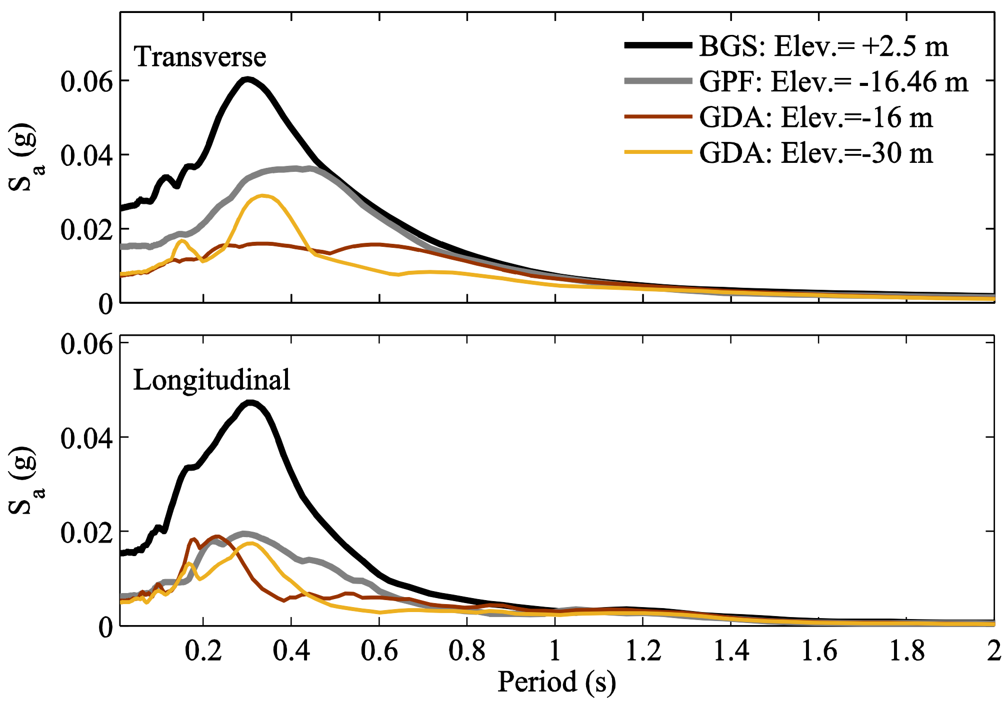

(b)

Figure 6.8: Response Spectra of acceleration of BGS, BPF and GDA at different depths in the transverse and longitudinal directions for: (a) the moderate event and (b) the 2007 Trinidad Earthquake

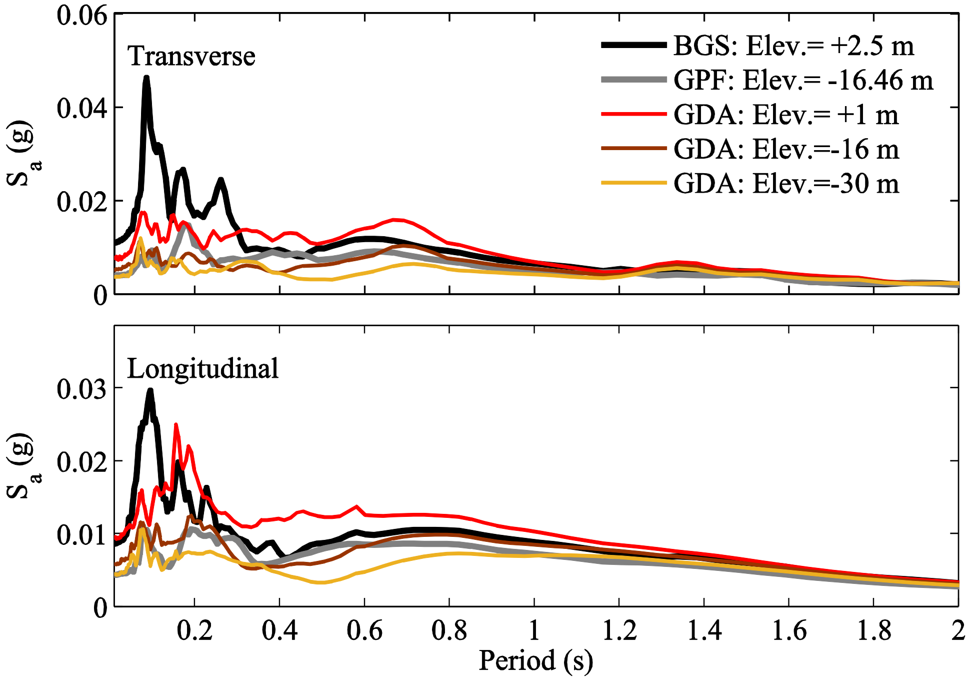

(a)

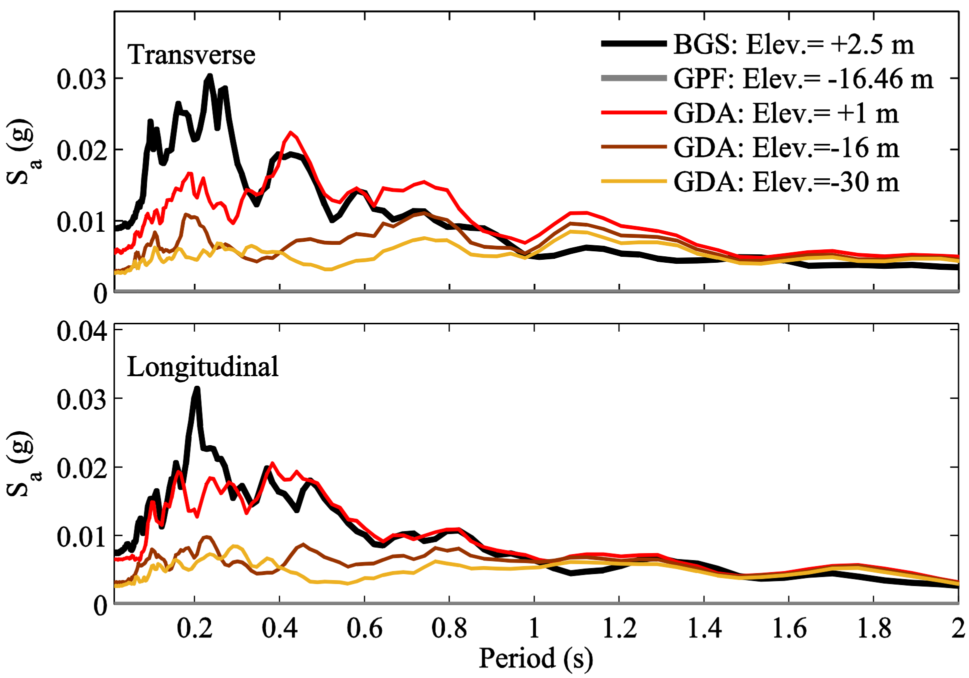

(b)

Figure 6.9: Response Spectra of acceleration of BGS, BPF and GDA at different depths in the transverse and longitudinal directions for (a) the 2007 Ferndale Earthquake and (b) the 2005 Crescent City Earthquake

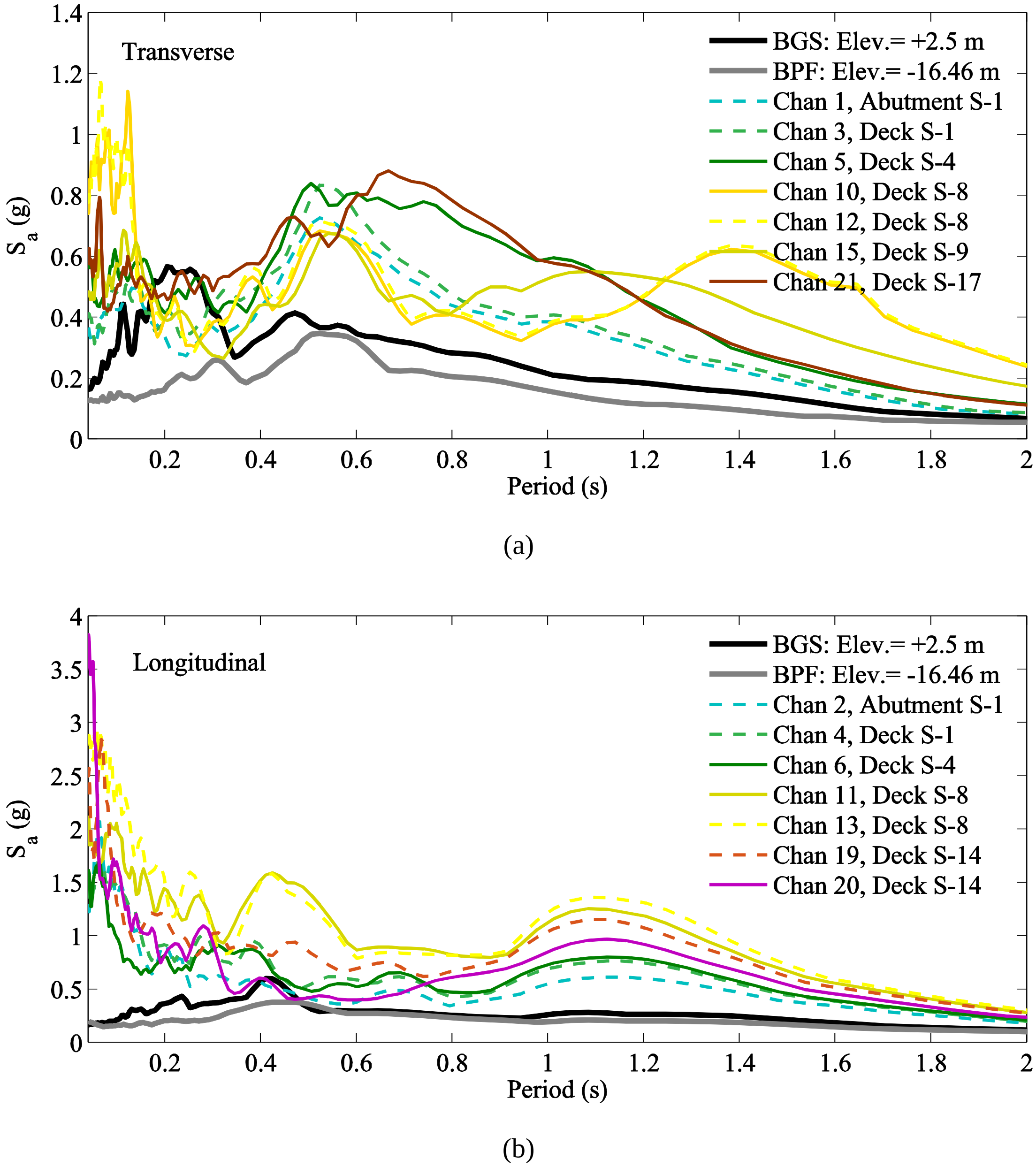

Figure 6.10: Response Spectra of acceleration of BGS, BPF and along bridge deck during the moderate event: (a) Transverse and (b) Longitudinal

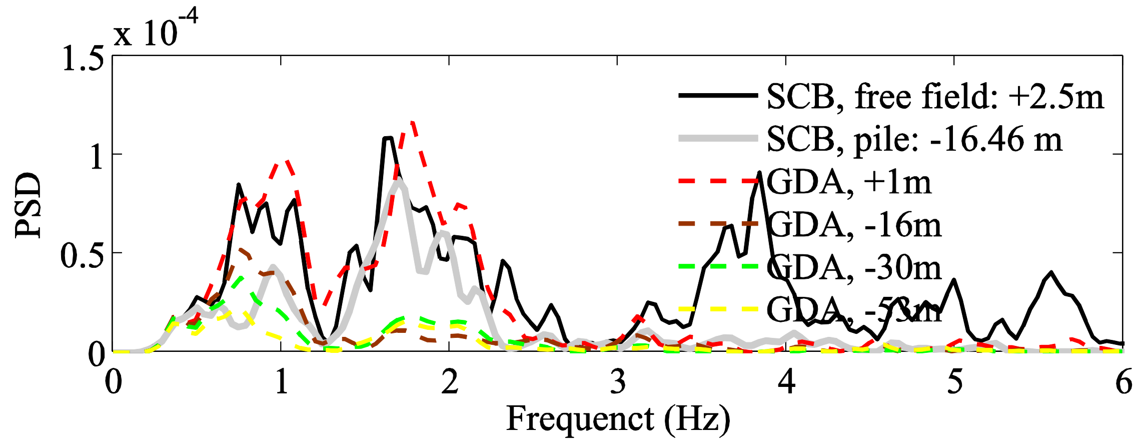

(a)

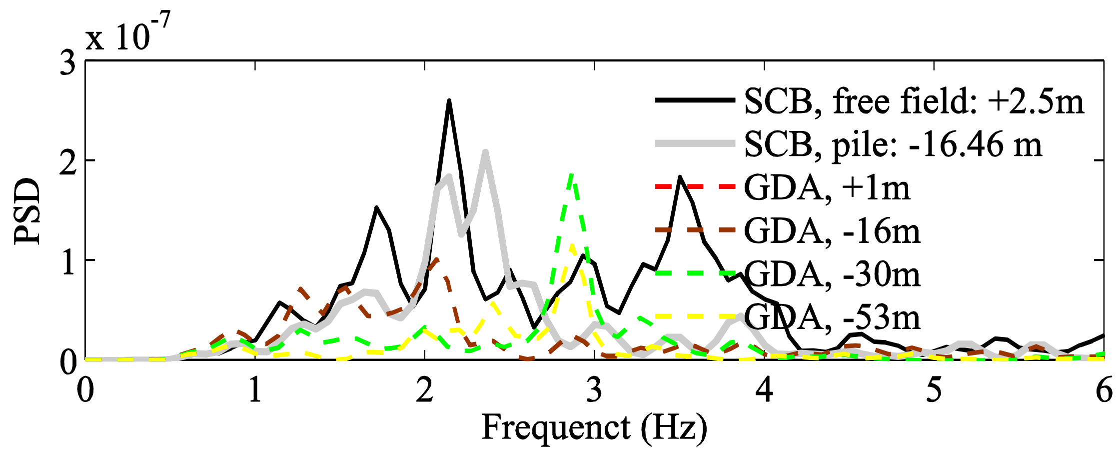

(b)

Figure 6.11: Power spectral density (PSD) of BGS, BPF and GDA at different depths in the transverse direction during (a) the moderate event and (b) the 2007 Trinidad Earthquake

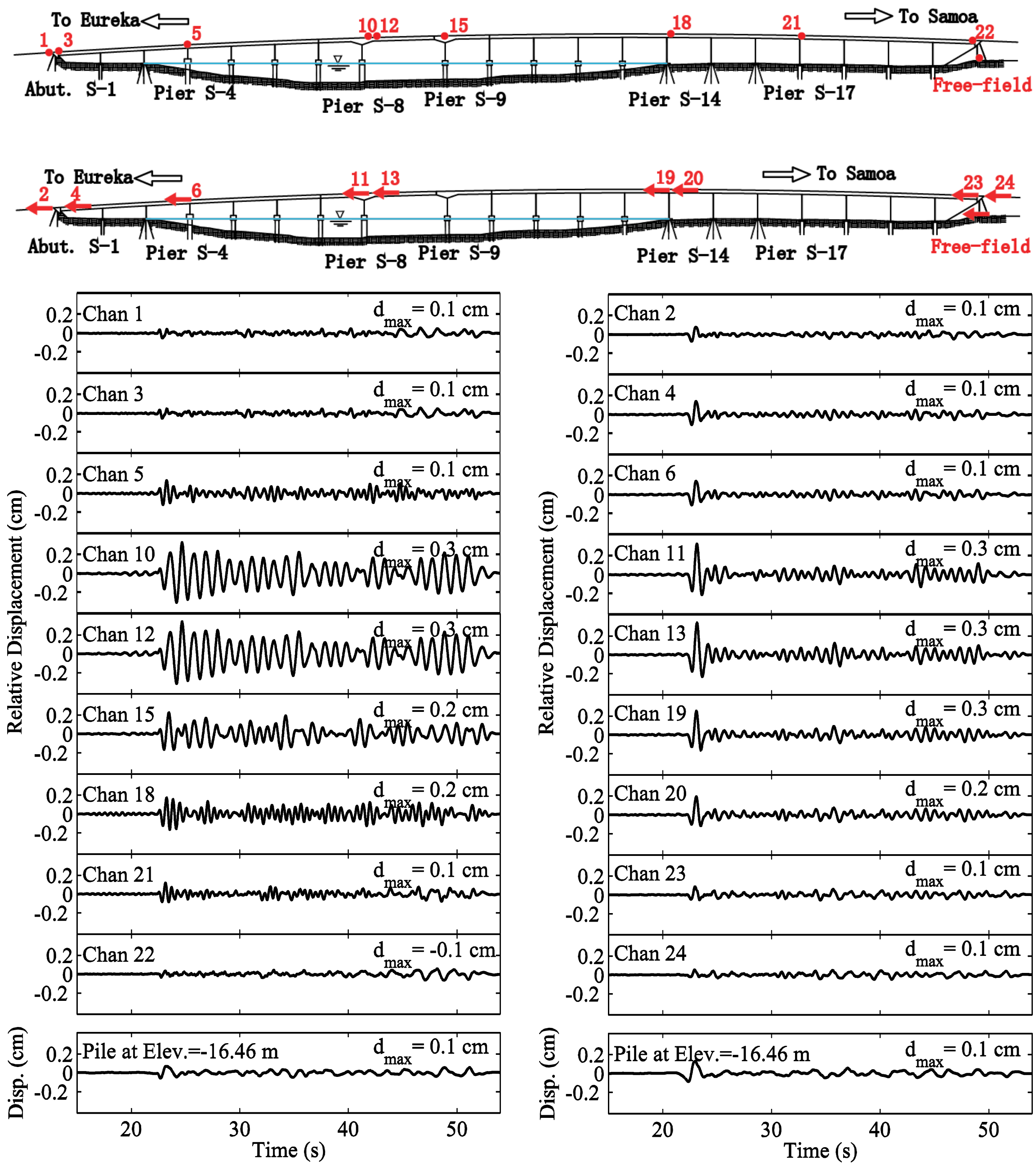

(a) (b)

Figure 6.12: Variation of relative displacement time histories at the bridge deck level for the 2007 Ferndale Earthquake: (a) Transverse and (b) Longitudinal

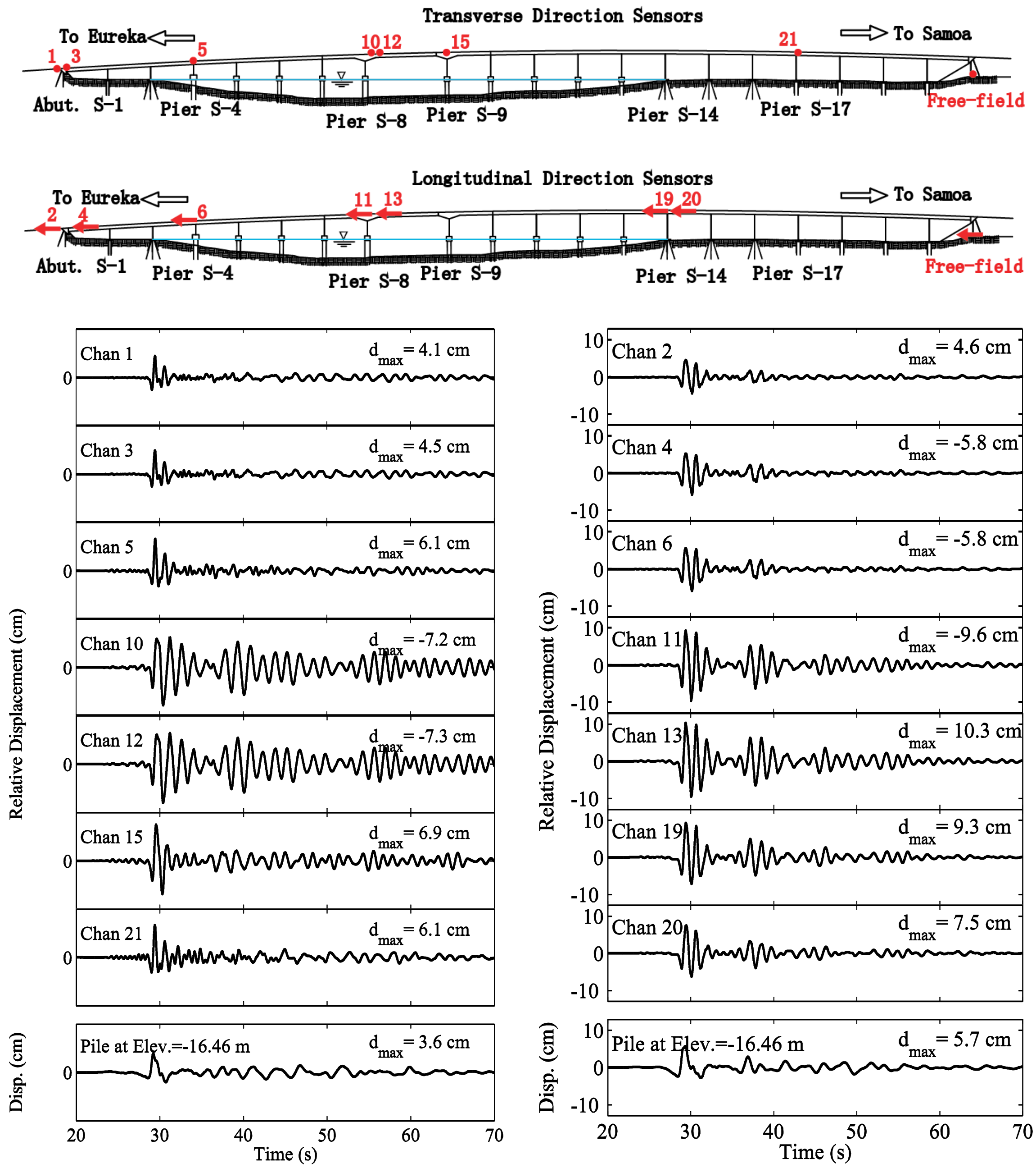

(a) (b)

Figure 6.13: Variation of relative displacement time histories at the bridge deck level for the moderate event: (a) Transverse and (b) Longitudinal

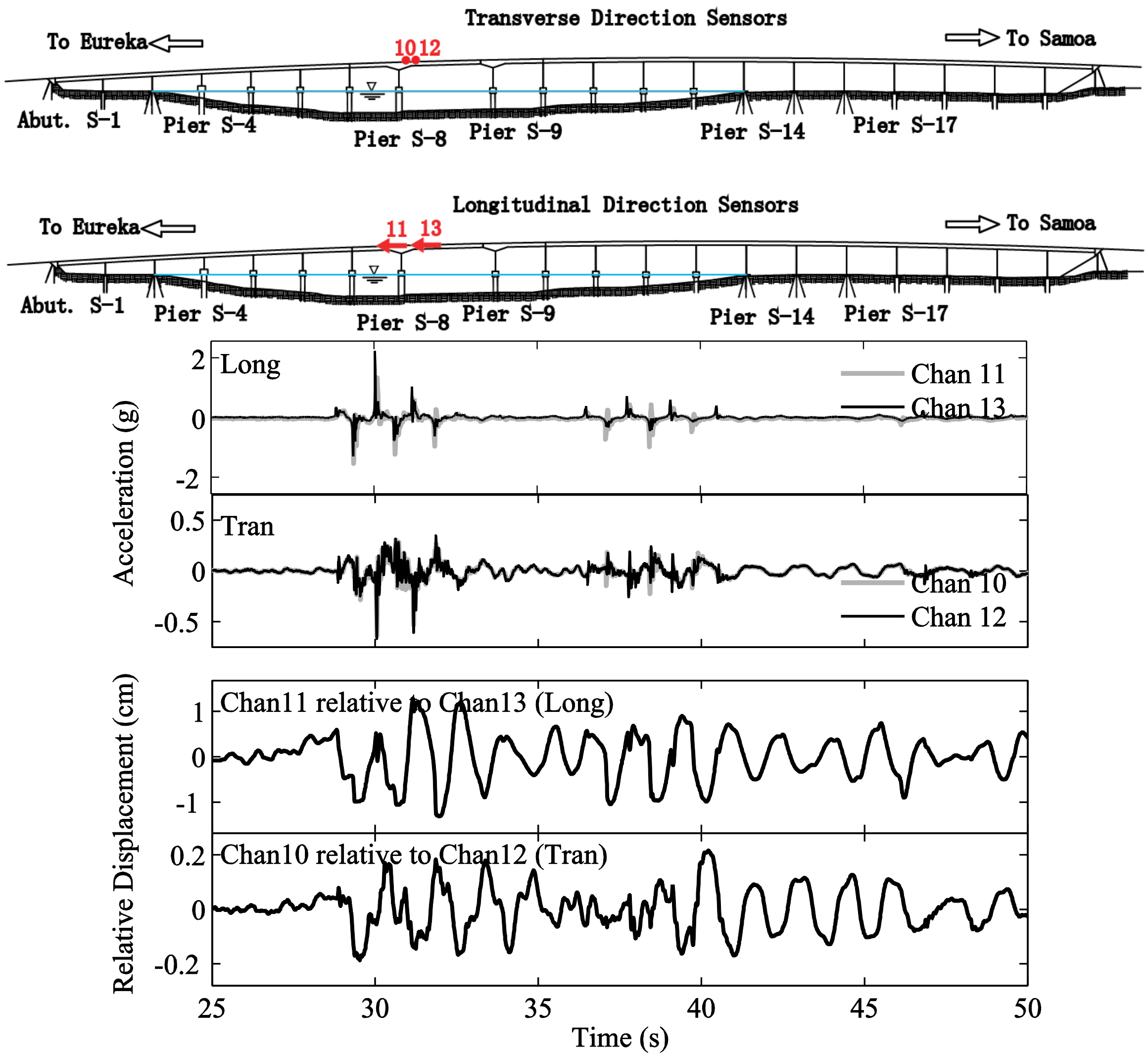

(a)

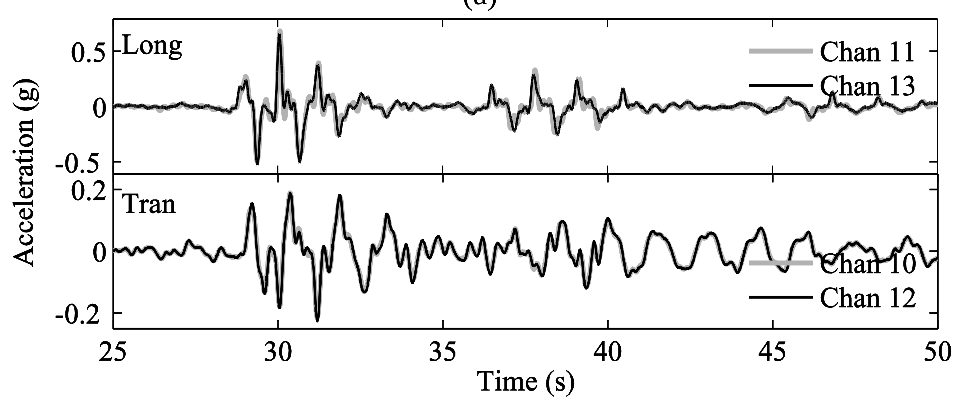

(b)

Figure 6.14: Recorded acceleration and relative longitudinal/transversal displacement of deck across the separation joint near Pier 8 for the moderate event (a) before and (b) after filtering

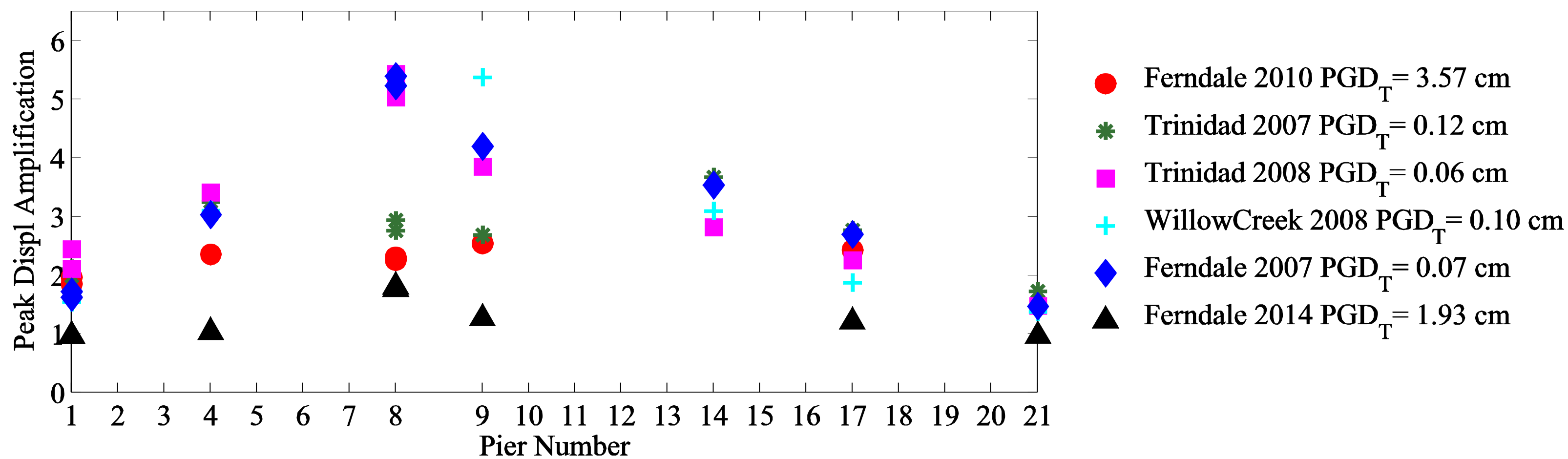

(a)

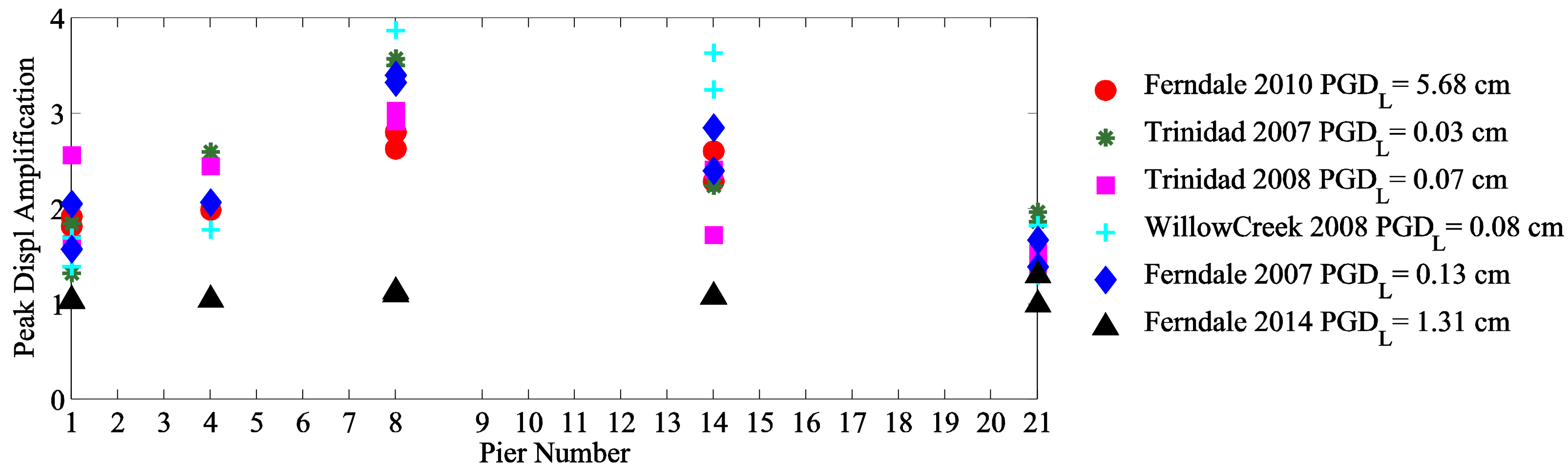

(b)

Figure 6.15: Peak displacement along bridge deck referenced to BPF: (a) Transverse and (b) Longitudinal

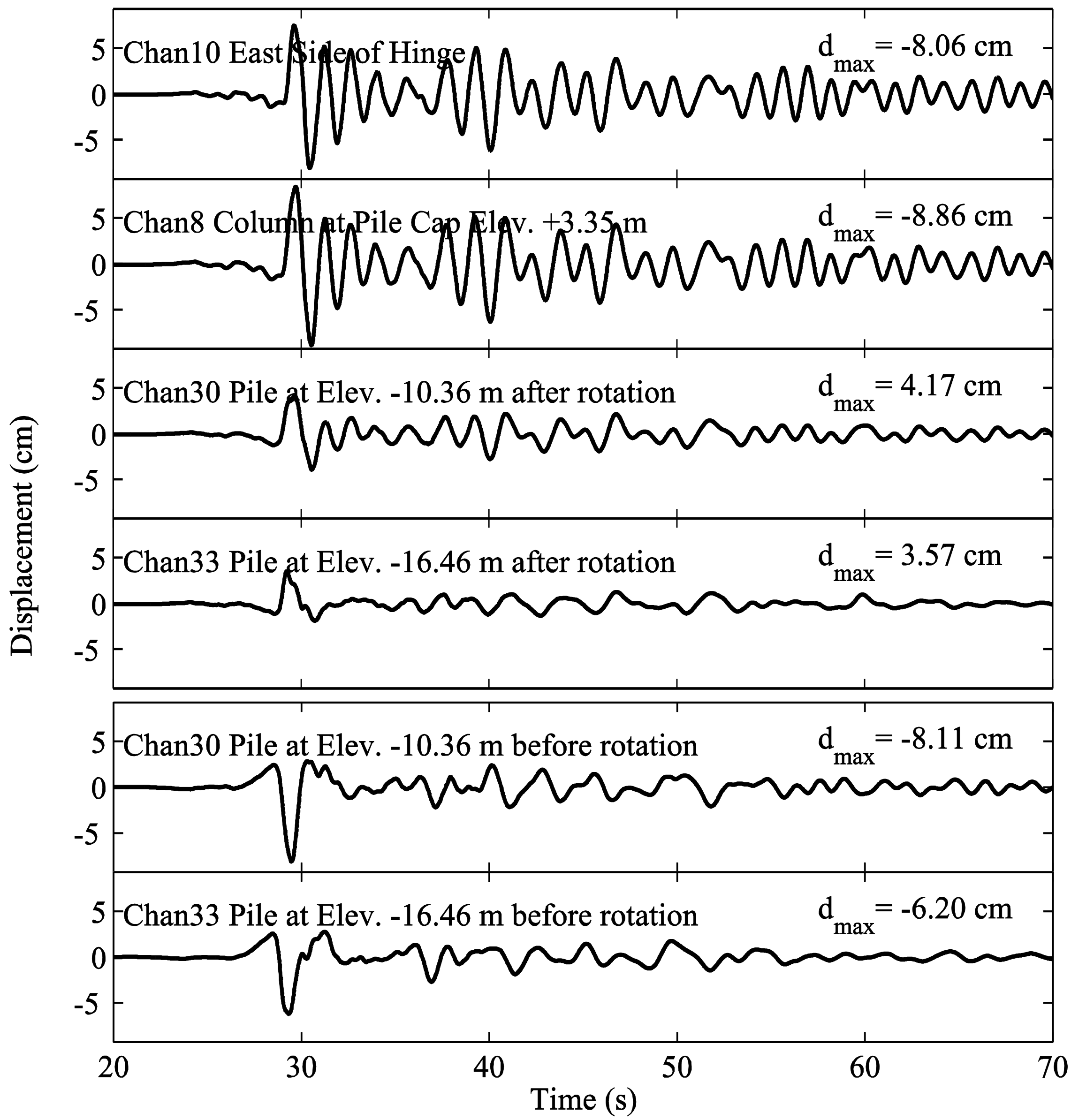

Figure 6.16: Displacement time histories along Pier S-8 during the moderate earthquake in the transverse direction

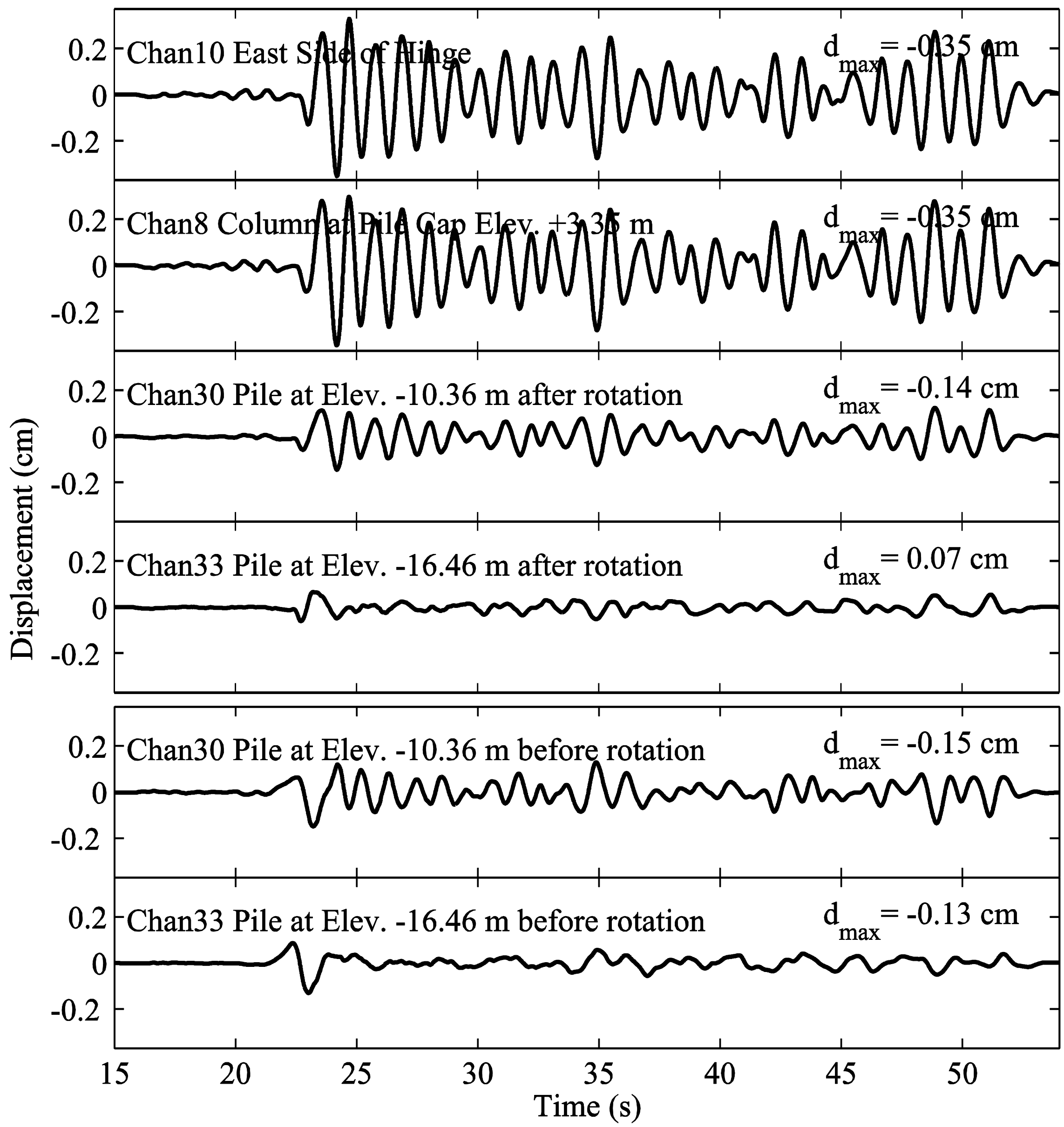

Figure 6.17: Displacement time histories along Pier S-8 during the 2007 Ferndale Earthquake in the transverse direction

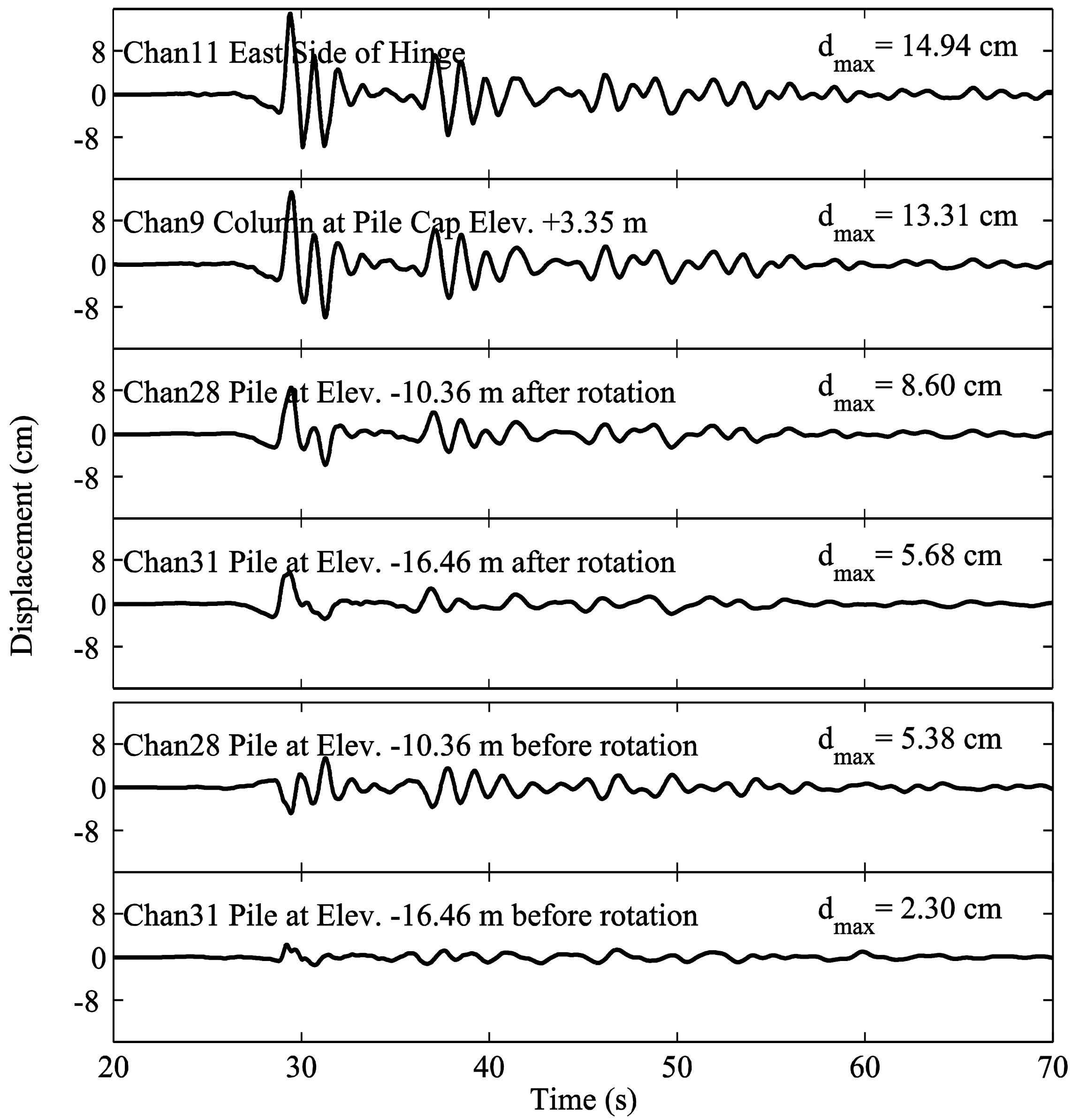

Figure 6.18: Displacement time histories along Pier S-8 during the moderate Earthquake in the longitudinal direction

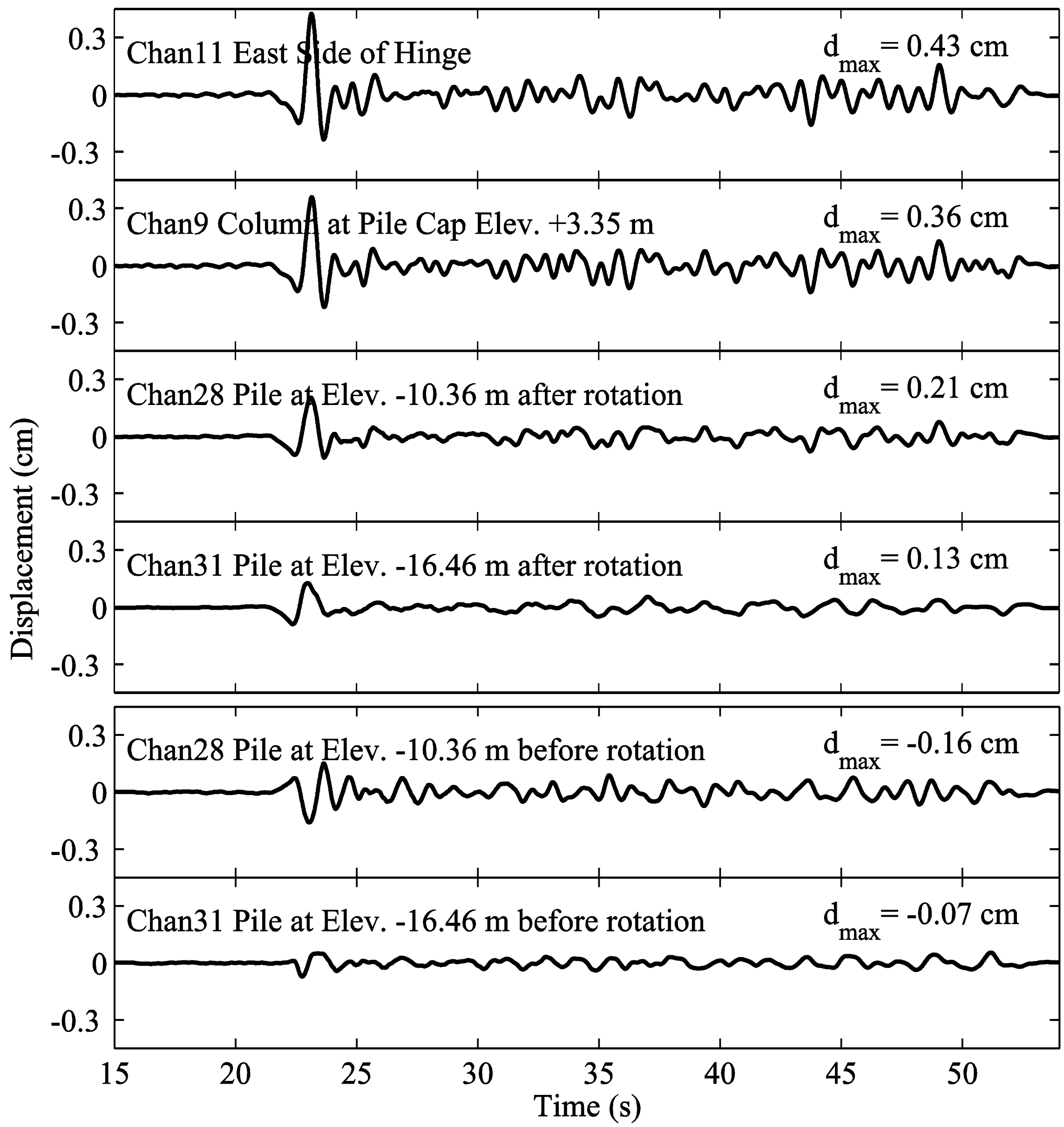

Figure 6.19: Displacement time histories along Pier S-8 during the 2007 Ferndale Earthquake in the longitudinal direction

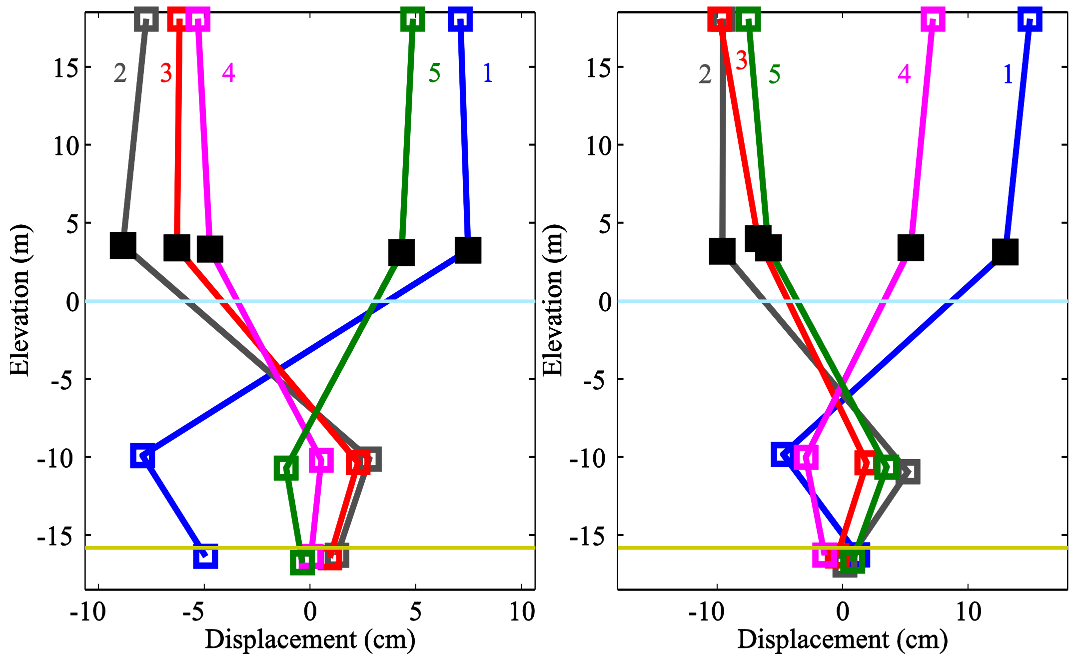

(a) (b)

Figure 6.20: Displaced configuration of Pier S-8 for selected time instants during the moderate event in (a) Transverse and (b) Longitudinal

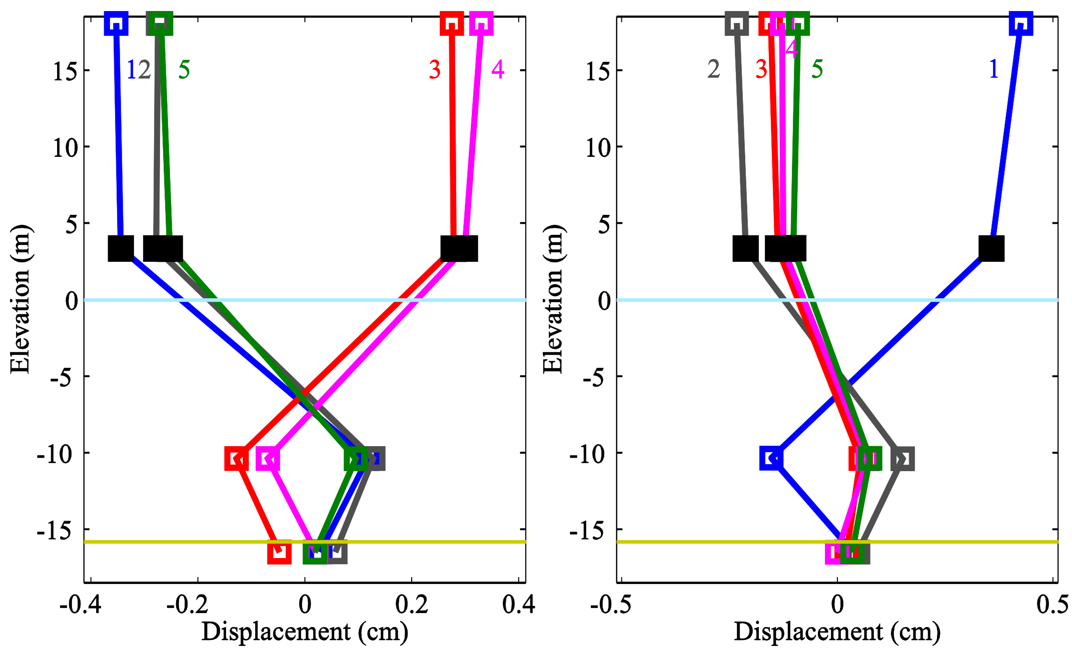

(a) (b)

Figure 6.21: Displaced configuration of Pier S-8 for selected time instants during the 2007 Ferndale Earthquake: (a) Transverse and (b) Longitudinal

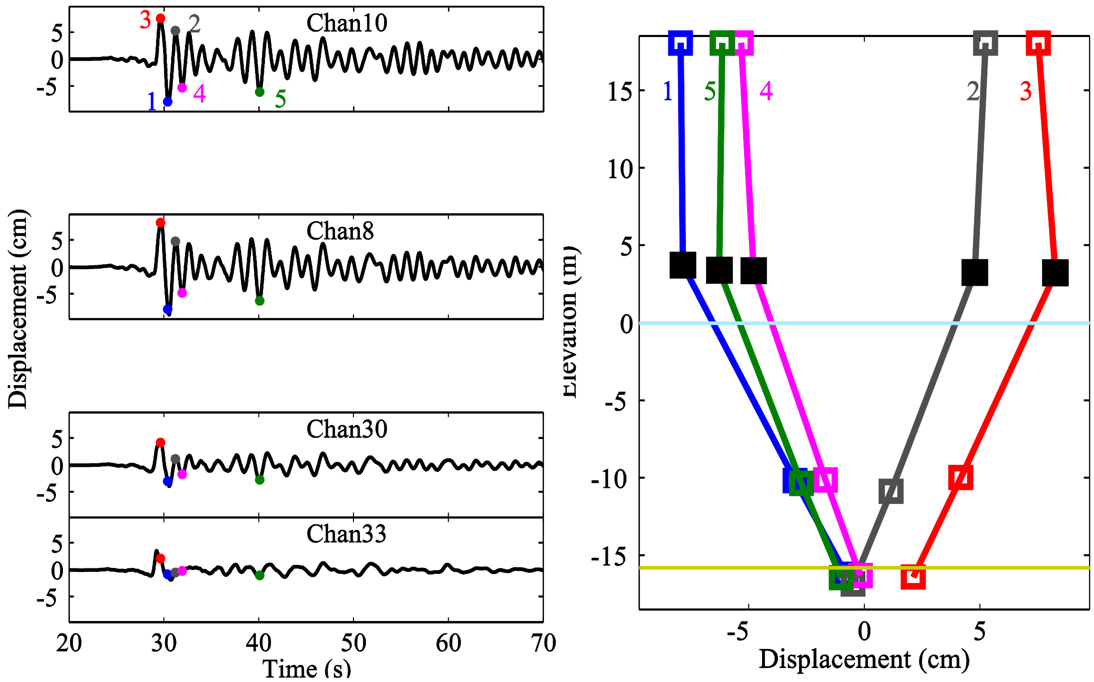

(a) (b)

Figure 6.22: Transverse direction: (a) time histories and (b) displaced configuration of Pier S-8 for selected time instants during the moderate event

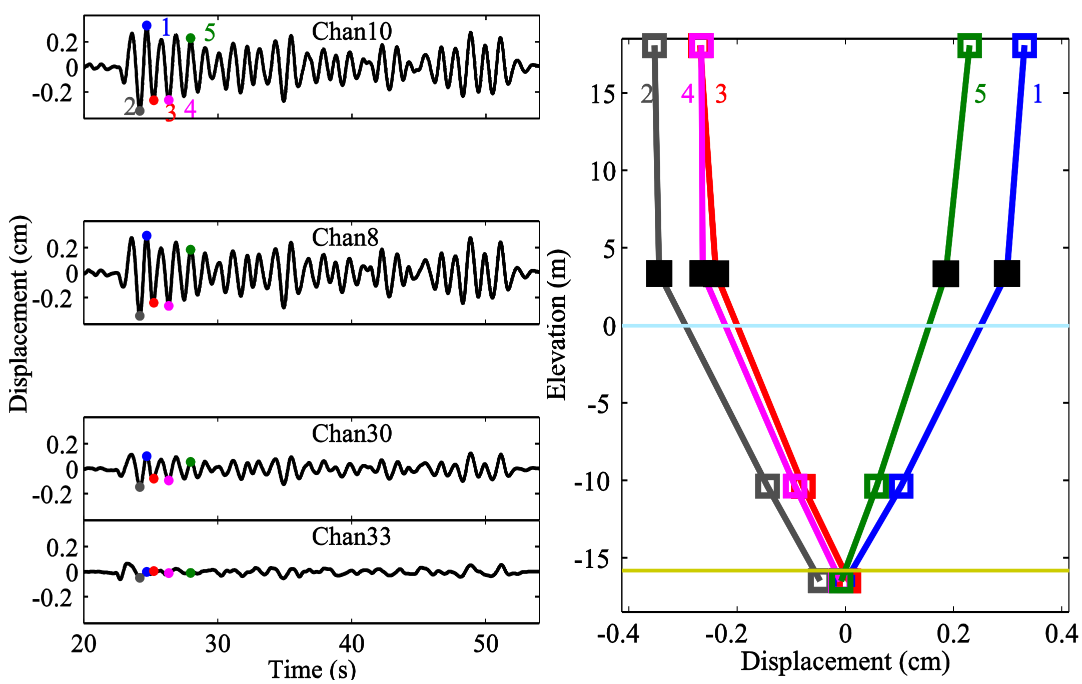

(a) (b)

Figure 6.23: Transverse direction: (a) time histories and (b) displaced configuration of Pier S-8 for selected time instants during the 2007 Ferndale Earthquake

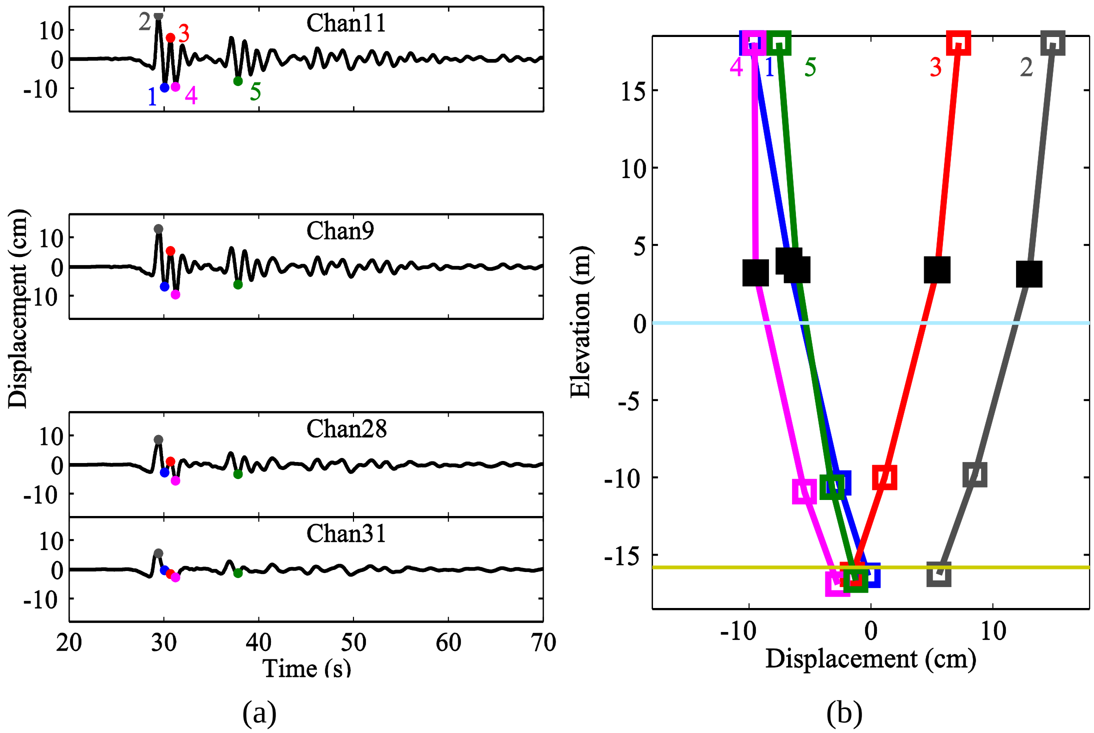

Figure 6.24: Longitudinal direction: (a) time histories and (b) displaced configuration of Pier S-8 for selected time instants during the moderate event

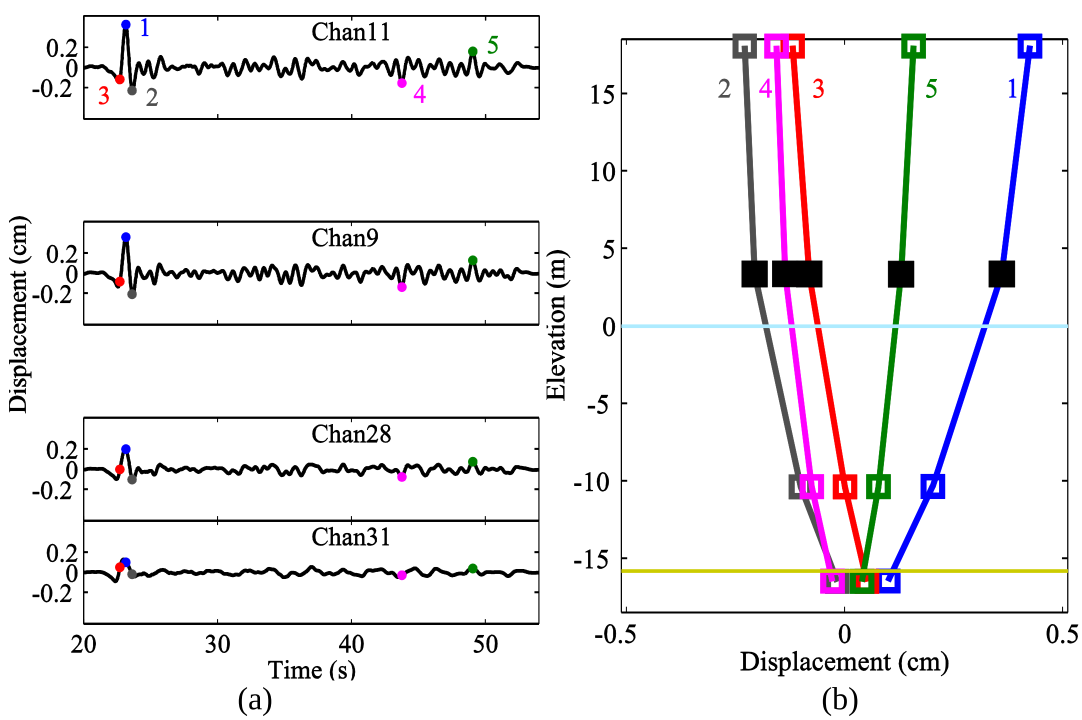

Figure 6.25: Longitudinal direction: (a) time histories and (b) displaced configuration of Pier S-8 for selected time instants during the 2007 Ferndale Earthquake

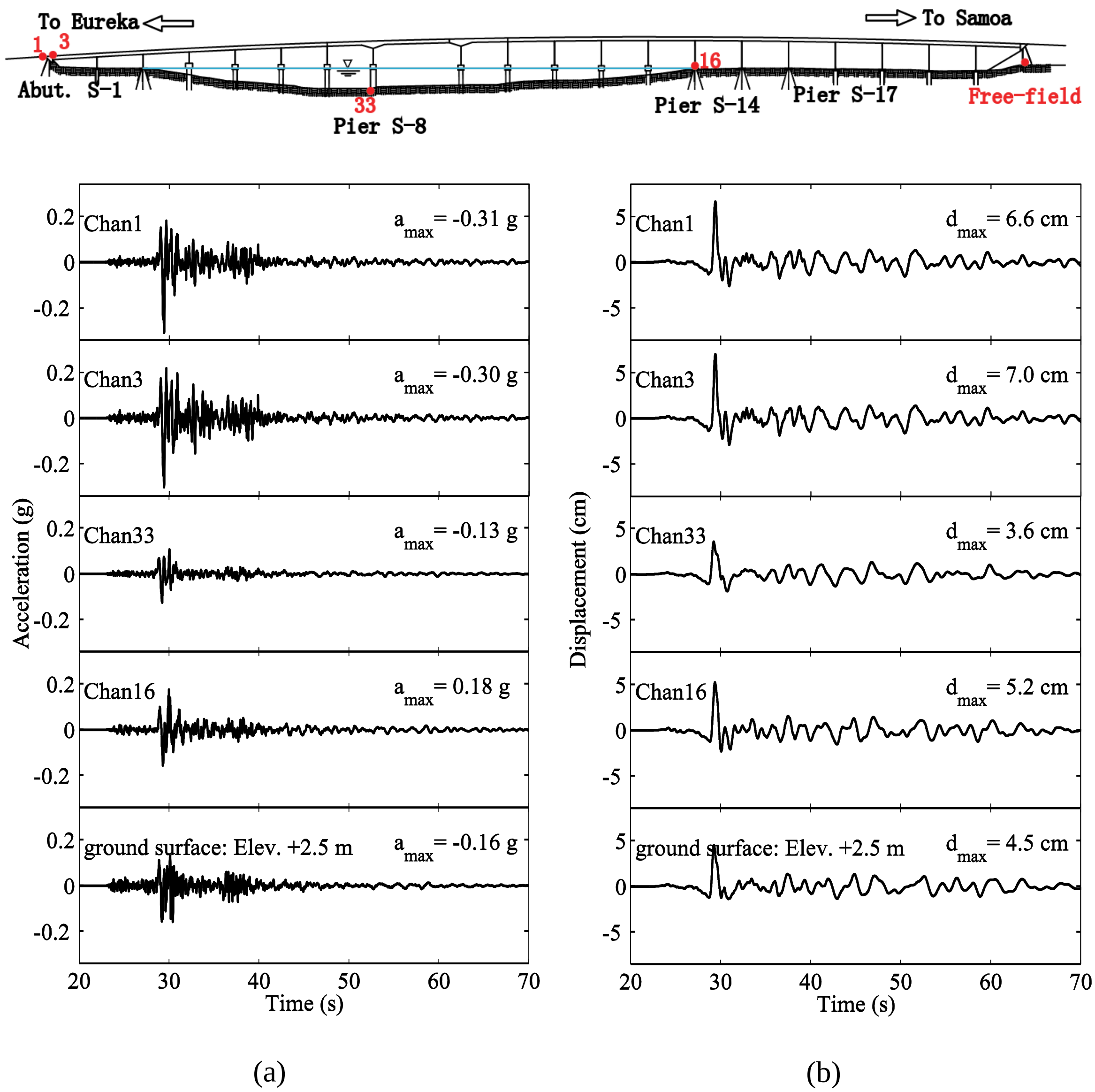

Figure 6.26: Variation of (a) acceleration and (b) displacement time histories along ground surface in the transverse direction for the moderate event

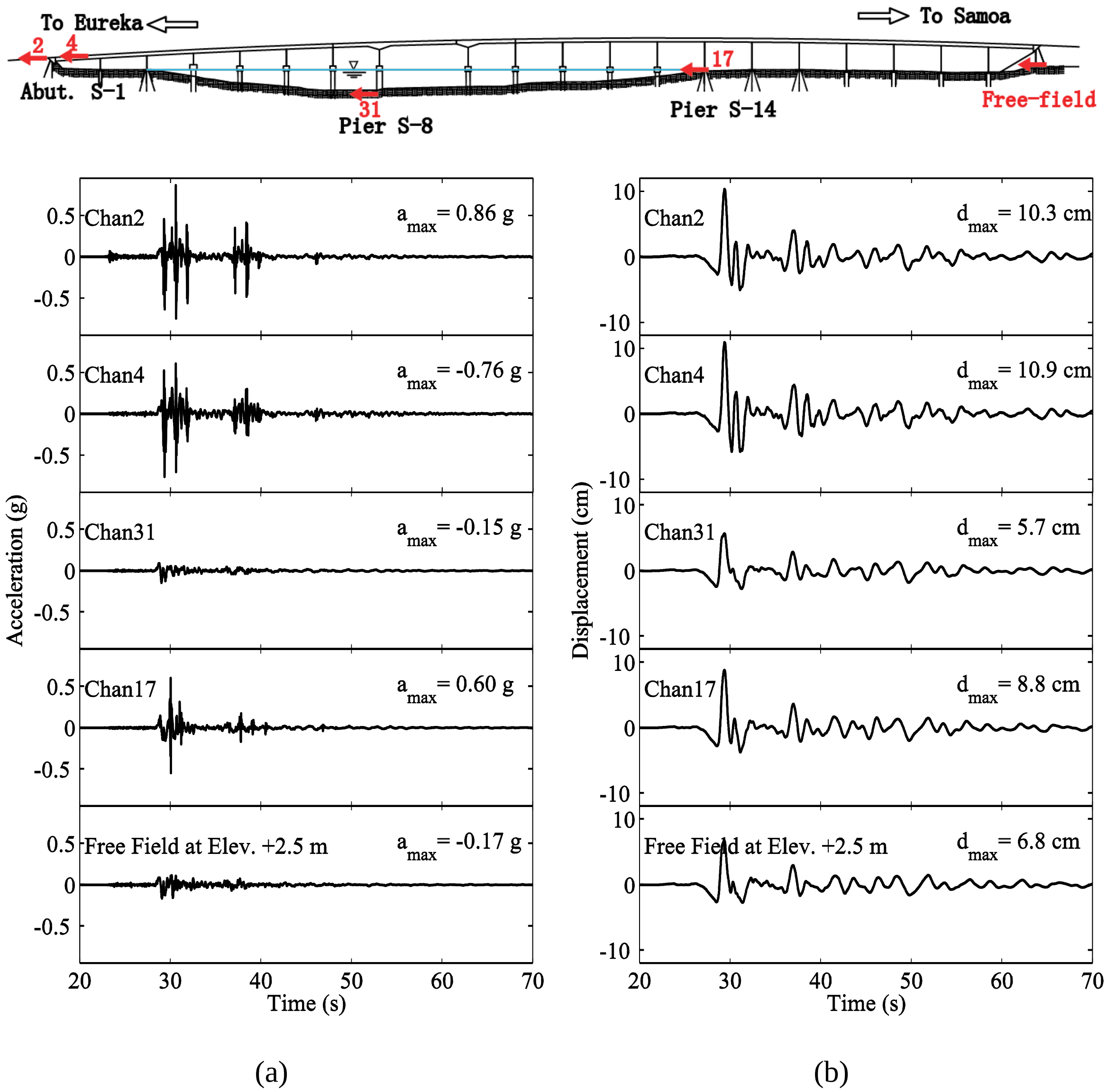

Figure 6.27: Variation of (a) acceleration and (b) displacement time histories along ground surface in the longitudinal direction for the moderate event

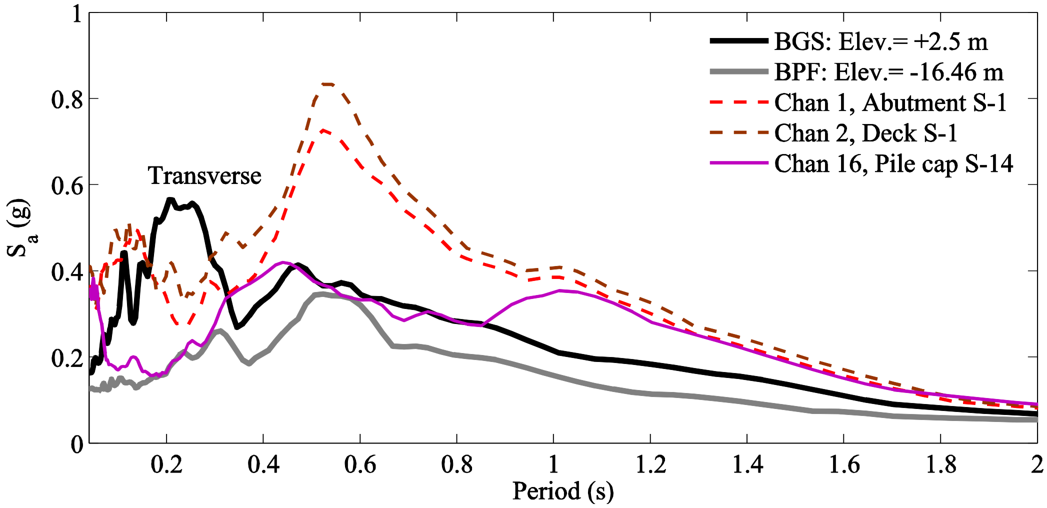

(a)

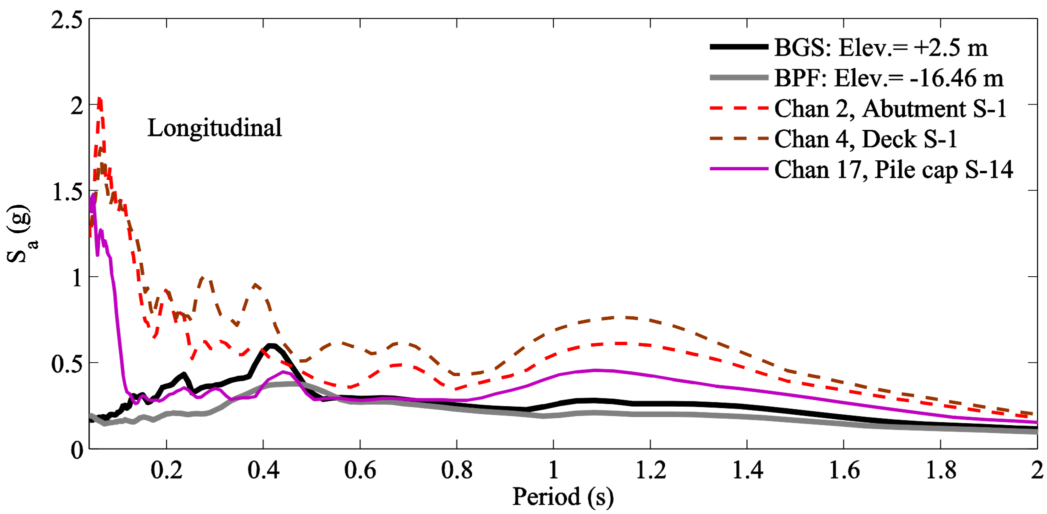

(b)

Figure 6.28: Response Spectra of acceleration of along bridge base line during the moderate event: (a) Transverse and (b) Longitudinal

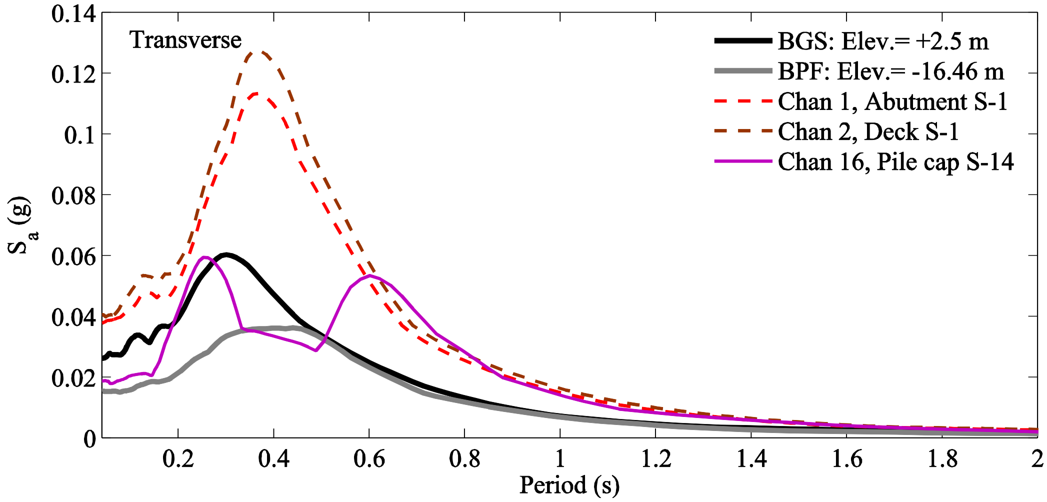

(a)

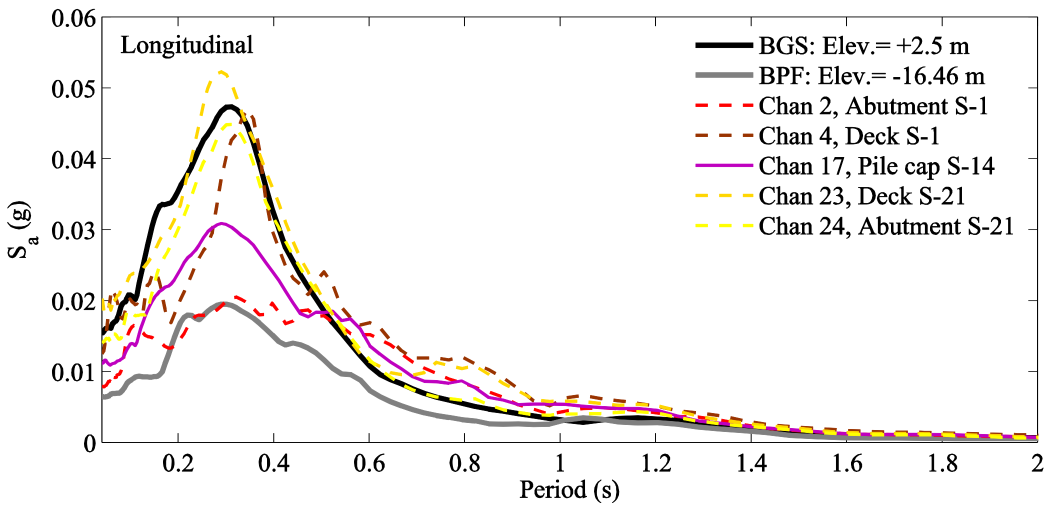

(b)

Figure 6.29: Response Spectra of acceleration of along bridge base line during the 2007 Trinidad Earthquake: (a) Transverse and (b) Longitudinal

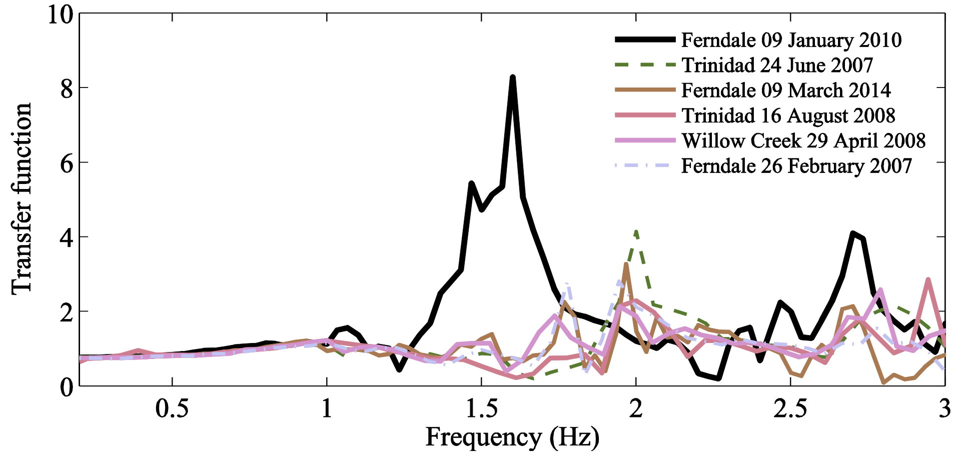

Figure 6.30: Transfer function in the transverse direction for deck response over pile cap response

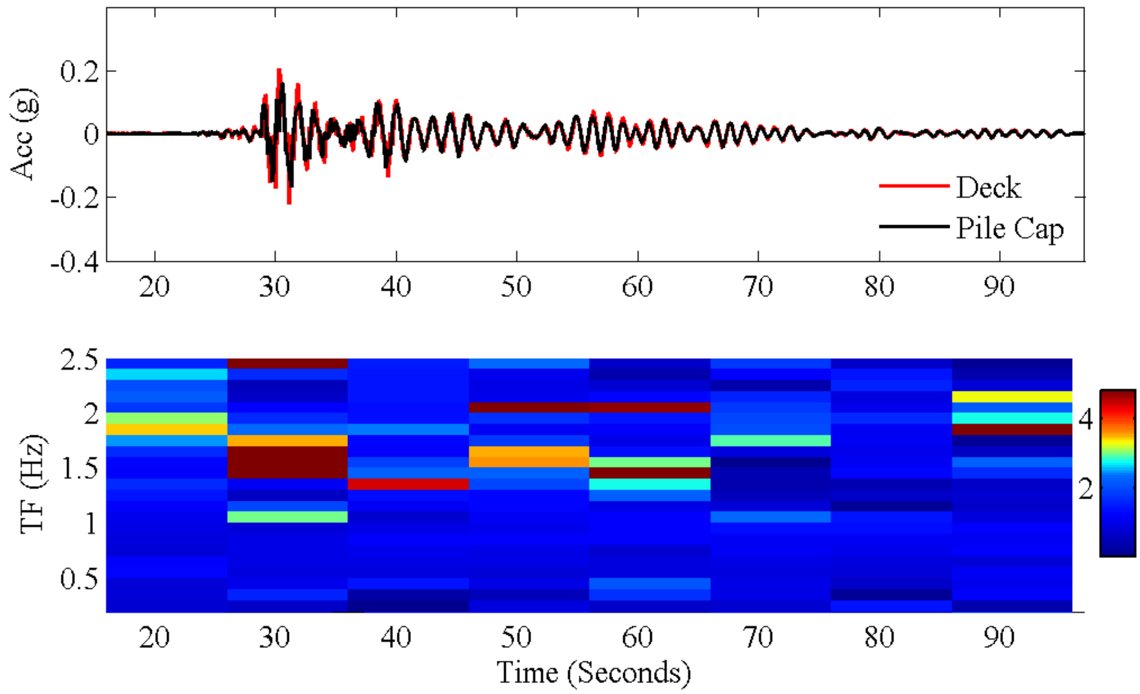

Figure 6.31: Short time transfer function during the moderate event (deck to pile cap) in the transverse direction

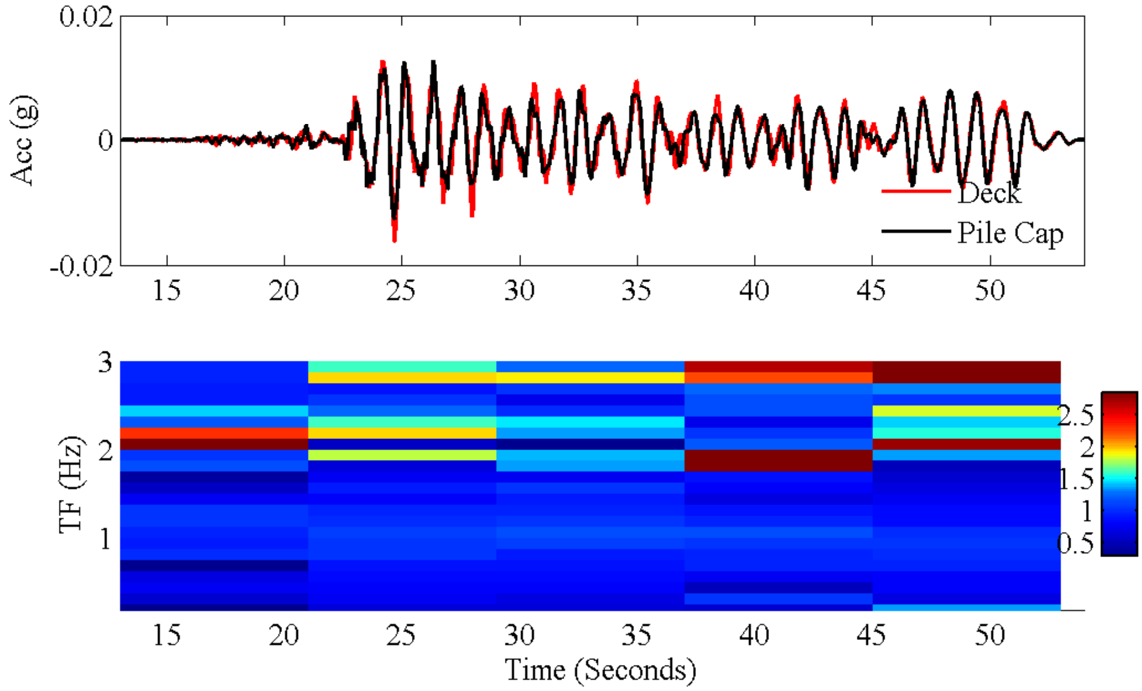

Figure 6.32: Short time transfer function during the 2007 Ferndale Earthquake (deck to pile cap) in the transverse direction

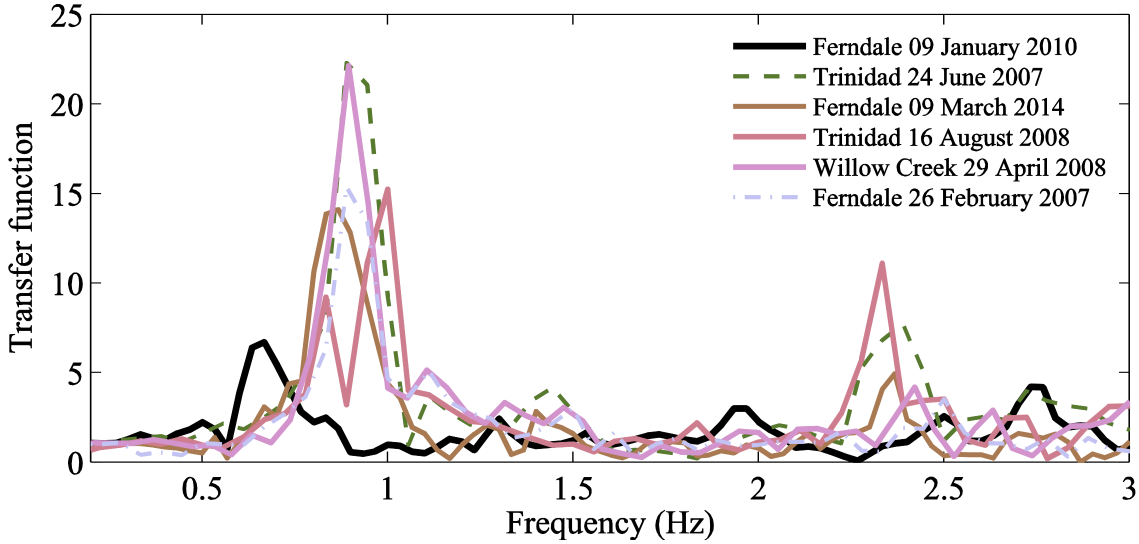

(a)

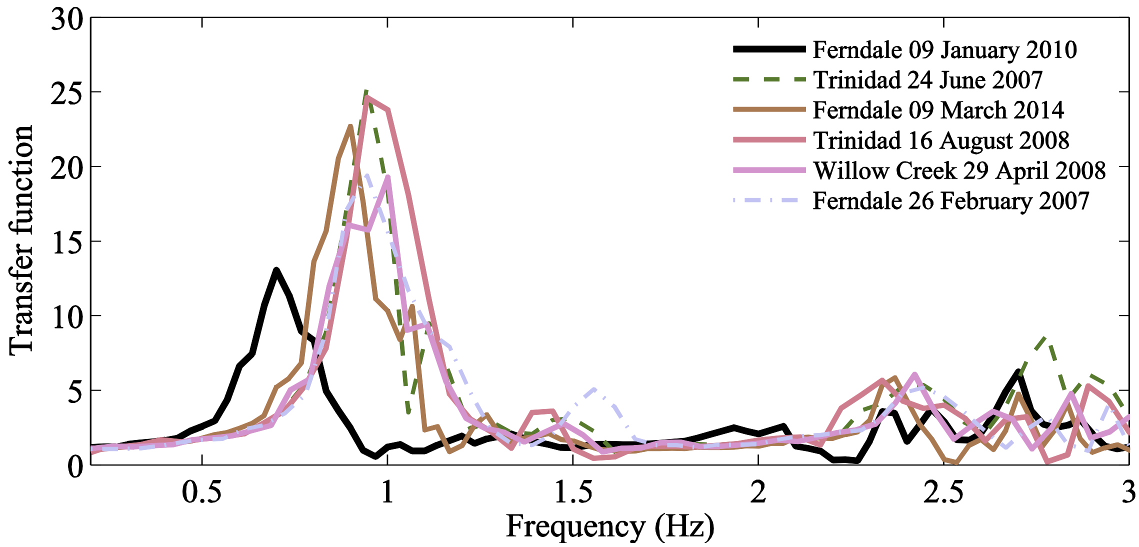

(b)

Figure 6.33: Transfer function in the transverse direction for deck response (a) over free field response and (b) over pile response at -16.46 m

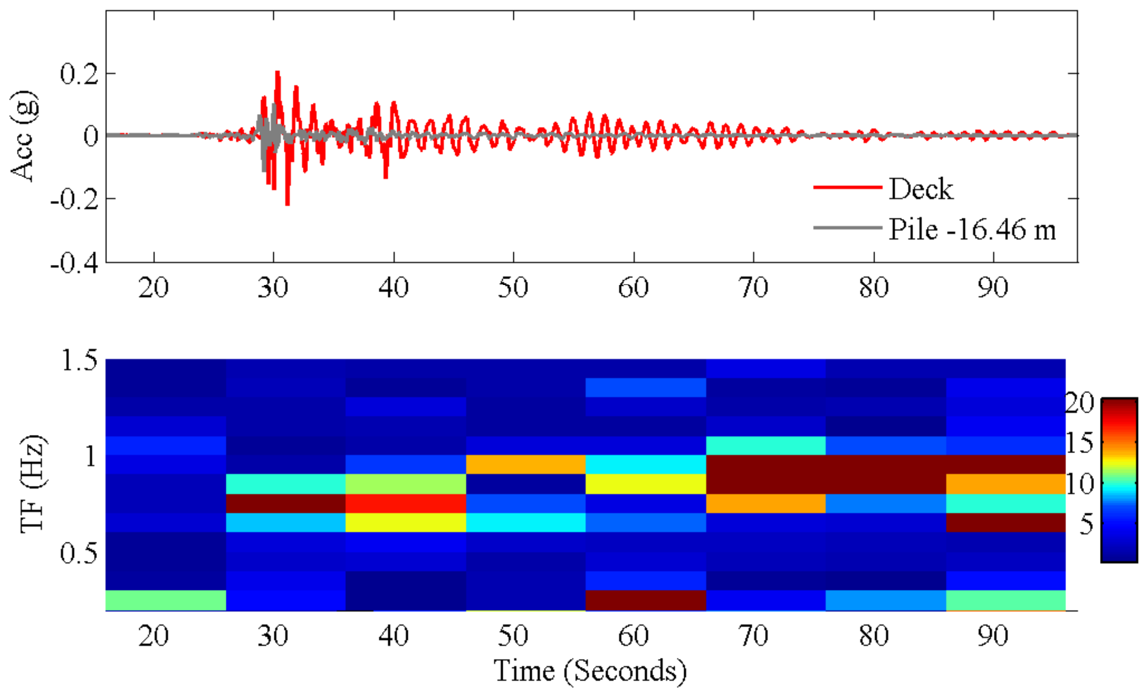

Figure 6.34: Short time transfer function during the moderate event (deck to pile -16.45 m) in the transverse direction

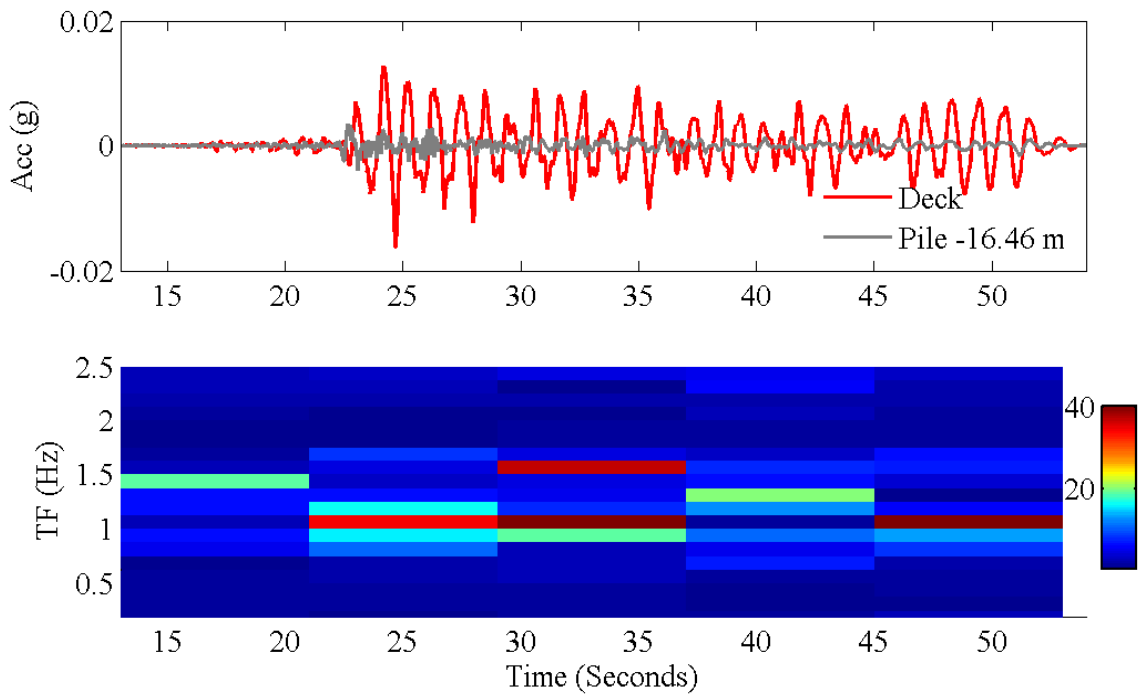

Figure 6.35: Short time transfer function during the 2007 Ferndale Earthquake (deck to pile -16.45) in the transverse direction

Chapter 7

Numerical Analysis of the Samoa Channel Bridge System

In this chapter, the spatial geometry and structural characteristics of the Samoa Channel Bridge in California Eureka area are presented in detail. Linear Finite Element (FE) models of the foundation-bridge system are developed and calibrated based on the recorded motions and identified bridge/foundation characteristics. Flexibilities of the bridge column and pile foundation are evaluated based on the recorded seismic response of this bridge using system identification and optimization techniques. The change of identified bridge column and pile foundation stiffness due to the nonlinearity of structure/foundation response during the moderate shaking event is addressed. The ground-pile-system behavior is explored in terms of equivalent foundation spring values based on the recorded data. The calibrated FE model of the bridge is shown to replicate the measurements during the 2010 Ferndale Earthquake with reasonable agreement.

7.1 Introduction

Effects of soil, abutments and pile foundations are studied on a relatively crude basis due to the lack of seismic records available at/within the foundation (Wilson and Tan 1990; Werner et al. 1994; Elgamal et al. 2008; Gomez et al. 2013). In practice, the foundation stiffness is assessed numerically with the aid of soil response codes, such as LPILE, or DFSAP (Lam and Martion 1986; Lam et al. 1998; Zafir 2002; WSDOT 2014). The estimated foundation stiffness depends on the level/combination of applied loads and depends on the pile head boundary condition.

In Chapter 6, extensive seismic records of the Samoa Channel Bridge and the adjacent Eureka Downhole-array are investigated. Resonant frequencies of the foundation-bridge system were identified (Wang and Elgamal 2013). On that basis, a linear FE model of Pier S-8 was developed and calibrated. Focus is placed on the transverse response of this bent and the estimation of representative stiffness for the bent column and the underlying pile-group foundation. The analyses indicate that during the 2010 Ferndale Earthquake (hereafter, referred to as “the moderate event”), the estimated lateral stiffness of the pile foundation at Pier S-8 is around 56 percent of that during the other low-amplitude shaking events.

In this chapter, a FE model of the entire bridge with springs at the column base is developed. Optimization techniques are employed to estimate the base spring values based on the available recorded seismic response. As such, the identified spring values represent the effects of the soil-foundation system. Computed seismic response of the bridge shows good agreements with the recorded earthquake data from the CGS (California Geological Survey) station 89686. Generally, the results of this research are of significance for validation and refinement of deep-foundation soil-structure interaction analyses (FEMA 2005; 2009; ASCE 2010; FHWA 2011).

7.2 General Bridge Information

7.2.1 The Bridge Layout

The 20-span Samoa Channel Bridge is a 764 m long and 10.4 m wide structure connecting Samoa Peninsula and Indian Island (details in Figure 6.2b of Chapter 6). The superstructure consists of a cast-in place reinforced concrete deck (16.5 cm of thickness) resting on four precast, prestressed concrete I-girders. The bridge I-girders are supported on 19 hammerhead cap single column type piers and concrete seat-type abutments. The length of span ranges from 36.576 m to 68.58 m. Between Pier S-8 and Pier S-9, there is a 50.292 m long prestressed precast concrete drop-in span. Separation joints allowing movement during seismic events are located at the top of Piers S-4, S-7, S-8, S-10, S-14, S-17 and two abutments supports as shown in Figure 6.2b of Chapter 6.

Height of the single hexagonal concrete pier columns ranges from 6.19 m at Pier S-3 to 12.9 m at Pier S-14 (Table 7.1). Originally, the abutments and pier columns were supported on pile-group foundations consisting of driven pre-cast prestressed concrete piles. Referenced to the mean sea level (MSL), elevation of the mud-line varies from -15.8 m below Pier S-8 to +0.9 m at Pier S-20 (Figure 6.2a). Eleven pile groups (from S-3 to S-13) have a pile cap located above the mudline with a maximum value of +16.72 m (elevation of pile cap base) at Pier S-8.

When designed in 1968 (Caltrans 2002a), pile groups under the main span (below Pier S-8 and Pier S-9) consisted of 8 (2x4) prestressed concrete cylinder piles (with diameter D=1.37 m) piles, concrete filled along the entire length, with a 2D center to center spacing. At the reinforced concrete seat type abutments S-1 and S-21, there are 12 square-shaped concrete piles (D=35.6 cm), with 7 battered piles (at a 1:3 ratio) in the front row and 5 vertical piles in the back.

To help in monitoring seismic response, the bridge is heavily instrumented (33 sensors, CSMIP Station 89686). By 2014, data from eight different earthquakes (magnitudes in a range of 4.6 to 7.2) was recorded. Salient seismic response characteristics of the bridge and a nearby geotechnical array (Eureka Geotechnical Array) were studied in detail in Chapter 6 (Wang and Elgamal 2013).

7.2.2 Geology and Site Description

The Samoa Channel Bridge is located in an area of complex interaction among three tectonic plates (North American, Pacific and Gorda) with high seismic activities. The ‘Little Salmon’ fault is the nearest seismic source (approximately 5 km away) from the site (Caltrans 2000a). Severe ground shaking may be generated by the Little Salmon or the Mad River Faults.

Numerous studies on tectonics and geology near the Eureka Bridges site in the vicinity of the Humboldt Bay Repowering Project were performed in the past 50 years (PG&E 2006). The geology map of Eureka area (Figure 7.1b) shows that alluvial deposits

(Qal) are identified (Clay, silt, sand, gravel, and boulders, deposited in stream beds, alluvial fans, terraces, flood plains and ponds) on Indian Island. Gravel and sand (Qm) were deposited along the shoreline Samoa Peninsula. Holocene bay deposits of Humboldt Bay were found in the channel (PG&E 2006).

Nineteen borings were drilled to a maximum depth of about 34 m below mean sea level (MSL) along HWY 255 in 1968 (Caltrans 1968). Profile Grade of the Samoa Channel Bridge based on the log of test borings (LTB) is shown in Figure 6.4 and Figure 6.5 (Caltrans, Personal communications). It reveals that the bridge site (Figure 7.2) is mantled by organic fill underlain by dense gray medium to compact gray sand (Caltrans 1968). Very dense coarse gravelly sand was encountered in the bottom layer. Soil layers vary in thickness and are not continuous horizontally. In particular, the surficial foundation soil below Pier S-8 is mainly composed of very soft to soft organic silt with clay (0.9 m). Soil layers consisting of dense to very dense gray medium and sand underlie the surficial soil layer and continue to the maximum explored depth (Figure 7.2).

7.2.3 Original Construction and Seismic Retrofit

The Eureka Channel Bridge was designed in 1968 and the construction was completed in 1971. Minor damage was reported after earthquakes in 1992 and 1994. Some repairs and subsequently an initial seismic retrofit were completed by Caltrans prior to 1997. For instance, the bent caps were reinforced and transversely stressed; pipe extenders and cable assemblies were added to selected bents (Caltrans 2002a).

In order to further strengthen the Eureka bridges, an extensive seismic retrofit program was carried out by Caltrans (Caltrans 2002a). The seismic retrofit work completed in 2002 included (Figure 7.3 and Figure 7.4): (1) strengthening of the foundations by installing additional cast-in-steel shell (CISS) piles (e.g. 6 additional 1.52 m diameter and 19 mm shell thickness piles at Pier S-8, as shown in Table 7.1), (2) adding or enlarging pile caps to cover the new piles, and (3) encasing the bridge columns in reinforced concrete column jackets to improve ductility. Accelerometers were installed inside one of the retrofitted CISS piles at Pier S-8 at two different elevations (-10.36 m and -16.46 m) during the structural retrofit. Detailed design drawings, retrofit information along with soil borings are reported by Caltrans (Caltrans 1968; 2002b).

7.3 Insights from the FE Analysis of Pier S-8

7.3.1 Finite Element Modeling

In an effort to gain preliminary insights, transverse motion of the intermediate Pier S-8 was studied, independently of the rest of the bridge, based on recorded seismic data (Wang and Elgamal 2013). This idealization is partially substantiated by the extended length of the bridge (764.1 m) and presence of separation joints at adjacent bents, as well as the observed relatively high transverse response flexibility at this near-mid-span location.

As mentioned earlier, the pile cap at this location was observed to undergo significant lateral displacement during the moderate event. As such, one of the key aspects to investigate is the lateral stiffness of the pile foundation. Utilizing the earthquake records in conjunction with model-based system identification techniques, the dynamic transverse response is investigated in view of stiffness for the column and the foundation at this location.

Based on the "as-built" geometry of the bridge, two linear elastic FE models of Pier S-8 (Figure 7.5) are developed using the FE framework OpenSees. These models consist of lumped masses at (1) the center of gravity for the deck I-girders, (2) the pier top, and (3) the pile cap level, connected by bending beams. The masses define center-to-center mass of the superstructure above S-8 (including bridge deck, longitudinal and transversal girders, and hammerhead beam of pier), mass of pier column, pile cap, and pile foundation. Calculations of mass are based on the density and volume of structural components.

The 1st FE model (FEM1 in Figure 7.5) represents the pier column at S-8. The boundary condition at the base of the pier column is considered to be fixed in all DOFs with prescribed input motion (recorded pile cap motion at Chan 8). Possible rotation at the pile cap level was assumed to be negligible due to the underlying spatially large pile group configuration.

The 2nd FE model (FEM2 in Figure 7.5) includes the pier column and the pile group below. Since it has been shown that seismic motion of the retrofitted pile at the elevation of -16.46 m has the same pattern as the motions of the nearby geotechnical downhole array, it was taken as the input excitation for this model. Therefore, boundary condition for the 2nd FE model (FEM2) is considered to be fixed in all DOFs with prescribed transverse motion defined by the record of Chan 33 at the -16.46 m location. In addition, pile cap mass location is assumed to be fixed against rotation (translation allowed only in view of the underlying spatially large pile group configuration).

Relatively high bending stiffness (EI) of the pile cap beam-column element is defined to achieve rigidity (this additional element represents the pile cap height).

Material parameters for the simplified FE models were defined based on the as-built drawings as (Caltrans 2002a) : reinforced concrete mass density ρ= 2560 kg/m^3, Young's modulus E=2.79x10^7 kPa (compressive strength $f_c' = 34\text{MPa}$) for existing reinforced concrete and Young's modulus E=2.53x107 kPa (compressive strength $f_c' = 28\text{MPa}$) for reinforced concrete of retrofit (Table 7.2), Poisson's ratio ν=0.2 for concrete and Steel Young's modulus E_s=2.0x10^8 kPa (Table 7.3).

7.3.2 Calibration of the Pier Column Model at Pier S-8

Eigenvalue analyses were performed (FEM1) to calibrate the stiffness of pier column (Table 7.4) by matching the fundamental frequency of the FE model with the identified values in section 6.4. The pier column stiffness defined in this fashion includes contributions from interaction (resistance) due to the overall bridge connectivity. The identified flexural stiffness (EI) of the pier column (Table 7.5) is contrasted with estimates based on the uncracked section estimates (Table 7.4). The employed quantities amounted to a factor varying from 0.46 (the moderate event) to 0.65 (low amplitude earthquake events). The reduced pier column stiffness agrees with the estimation from moment-curvature analysis of the fiber-section with nonlinear materials under the gravity load (details provided in Appendix C). In addition, these factors are in a range of cracked properties of common Caltrans practice where effective section properties are employed for concrete pier columns (Caltrans 2012; 2013).

7.3.3 Calibration of the Pile Foundation Model at Pier S-8

For the FEM2, the pile foundation is taken as a single equivalent super-pile with the union of the cross section of all the piles (Shantz 2013), assuming linear elastic pile behavior. Large EI is set for the pile cap bending stiffness to achieve rigidity. As such, the defined pile foundation flexibility implicitly accounts for SSI.

With identified column stiffness from FEM1, one might calibrate the pile group foundation lateral stiffness to match with the identified bridge resonant frequencies (Figure 7.6). It turns out that the pile group foundation stiffness (Table 7.5) appears to be noticeably lower than calculations might imply (only 25% of the estimated EI is engaged) for the moderate event. For the small shaking events, where the corresponding identified pier stiffness is 0.65 of the uncracked section, the identified pile foundation stiffness reached a higher factor of 0.41 (Table 7.5).

Figure 7.7 and Figure 7.8 show good agreements between the computational results and the actual measurement for both FE models. Lower stiffness factors during the moderate event highlight the nonlinear response of the structure.

7.4 Numerical Simulation of the Bridge and Optimization with SNOPT

As shown in Figure 7.9, an elastic beam-column model representing the Samoa Channel Bridge was developed. Focus is placed on the transverse response of the bridge in this study. Linear lateral springs were attached to the base of bridge structure (bottom of the pier column) to account for stiffness of the underlying pile foundations and the soil-foundation-structure interaction. Recorded motion at the elevation of -16.46 m on the retrofitted pile (Chan 33) is employed as base dynamic excitation at the end of each spring along the bridge. The recorded motions at the bridge abutment (Chan 3 and Chan 22) were specified as an input boundary condition at the bridge ends. Properties of uncracked section for pier columns and bridge deck (Figure 7.10) are listed in Table 7.4 and Table 7.6 based on of blue prints provided by Caltrans. The separation joint at Pier S-8 is modeled as a "Perfect hinge" (equalDOF constraints for the three translations). At the pile cap level, a lumped mass is added, taken to represent masses of the pile caps.

A challenging task is to calibrate the spring values at individual locations along the bridge base to satisfactorily match the recorded data sets simultaneously. Determination of linear foundation stiffness was achieved through the extended OpenSees-SNOPT (Sparse Nonlinear Optimization) framework (Gill et al. 2002). SNOPT is a general-purpose system for solving optimization problems. Adopting a Sequential Quadratic Programming technique, it searches for an optimal point at each step by minimizing a quadratic model of the objective function (Gu 2008). The major advantage of SNOPT is that it requires relatively fewer evaluations of the objective function which helps to speed up our time-consuming dynamic FE simulation (Gu 2008). In our study, the objective function in SNOPT is defined to be the sum of squared errors by comparing the computed and recorded seismic response at the location of sensors for the selected observation period:

$$\mathrm{F} = \sum_{i}^{Sensors} w_i \sum_{n=1}^{time\ step} (u_i(t_n) - u_i^{Rec}(t_n))^2$$

in which u is the computed response (displacement or acceleration) from OpenSees, u^{Rec} is the recorded response from the instrumentation, and w_i is a weighting factor.

7.4.1 Optimization of Pier S-8 FE Model

Using the OpenSees-SNOPT optimization tool (Gill et al. 2002; Gu 2008), the stiffness of pier S-8 is investigated in the time domain with 5% damping ratio at the frequencies of 1.7 Hz (f_1) and 6.0 Hz, with model FEM1. The Objective function is defined to minimize the difference between the computed and measured displacement/acceleration time histories at the bridge deck (Chan 10). The pier column stiffness factor ranges from 0.39 to 0.67 (Table 7.7) with a fixed base boundary condition. It agrees well with the factor determined from system identification analysis in the frequency domain.

On this basis, the lateral spring value for the isolated Pier S-8 is evaluated (Figure 7.11) due to the extensive measurements along the depth (at deck level, pile cap level and in retrofitted pile). The objective function is defined as the total error squared (deck response and pile cap response) for the entire length of record. The optimized spring value (below Pier S-8) is listed in Table 7.8 for six earthquakes. Comparisons between the recorded and the optimized time histories are shown in Figure 7.12 for the moderate event. It is noted here that these SNOPT optimized spring values were found to closely match the lateral stiffness provided by the pile group with the properties defined in Table 7.5, via simple pushover analysis comparisons (with the pile group assumed fixed at the elevation of -16.46 m as discussed earlier).

Variation of spring stiffness is investigated by matching time histories for every 3 seconds window using SNOPT (Figure 7.13). It was found that during the moderate event, spring value below S-8 is as high as 7.53e+4kN/m before the strong shaking starts (close to the overall value obtained from the low amplitude earthquake event in Table 7.8) and as low as 3.08e+4 kN/m during the strong shaking time window. Decrease and then increase of stiffness with time is observed. For all other 4 small earthquake events, stiffness of the spring is relatively stable with time (around 7.50e+4 kN/m).

7.4.2 Spatial Variation of Bridge Foundation Stiffness

With pre-defined pier column stiffness and pile foundation stiffness at pier S-8 (determined from the analysis above), the stiffness of lateral springs along the bridge (12 unknowns) is optimized so that the computational response of the bridge is compatible with the recorded motions. In this regard, the objective function in SNOPT is defined to be the sum of squared errors at the location of the sensors marked by a red dot on Figure 7.14) for the entire length of record.

A relatively high weighting factor (Table 7.9) was applied to the error squared components at Pier S-8 since measurements at Pier S-8 are available at the deck level, the pile cap level and along the pile. The optimization procedure systematically searches for a set of spring values that minimize the objective function and optimize the agreement between the computed and measured bridge deck and pile cap response at the locations specified.

The evaluated base spring values obtained from the twelve-variable optimization problem described above are summarized in Figure 7.15. Due to the nonlinear behavior of the ground-foundation system for the investigated earthquake, this set of spring values are applicable to the moderate shaking event. For the low amplitude seismic records, two earthquakes in sequence (case 1: Trinidad 2007 and Trinidad 2008, case 2: Ferndale 2007 and Trinidad 2008) were employed to optimize the spring values. Between the 2 earthquake motions, 15 seconds free vibration with a high Rayleigh Damping is applied to damp the free vibration as soon as possible.

Overall, it was found that spring values are larger for the low amplitude earthquakes (Figure 7.16). The calibrated global bridge model based on recorded data in 2007 and 2008 provides insights into the characteristics of SSI during these shaking events. Computed time histories depicted in Figure 7.17 and Figure 7.18 are promising with a reasonable agreement with the recorded counterparts during the moderate event.

7.4.3 Comparison with Other Similar Foundation Stiffness Estimates

The assessed equivalent foundation stiffness at different levels of shaking is compared with available calculated estimates (Caltrans 2000b) of pile stiffness for the nearby Middle Channel Bridge (Figure 7.19a) with relatively similar pile group configuration and surrounding soil profile (Table 7.10 and Table 7.11). The Middle channel foundation stiffness is evaluated based on laterally loaded pile group analysis utilizing the computer program GROPU 4.0 (Caltrans 2000b). Some useful insights might be gleaned from this comparison.

For the pile group of Pier S-8, a 3D FE linear model of the ground-foundation system was developed to evaluate the numerically predicted lateral response (details are provided in Appendix D). In this highly idealized representation, a 0.3 cracked concrete factor for the pile bending stiffness produced comparable results.

7.5 Conclusions

In this chapter, salient effects of the ground-foundation system on bridge response are assessed with the help of recorded strong motion data and optimization techniques. In particular, bridge pier and foundation lateral stiffness coefficients are estimated.

The results of this research are of significance to the current state of practice in seismic pile-ground-structure analysis. While the identified stiffness estimates might remain subject to further improvements, reference to values derived analytically or by other techniques might prove to be quite beneficial.

7.6 Acknowledgements

Chapter 7 of this dissertation is based on material from a manuscript under preparation for publication, tentatively titled “Finite Element Based Seismic Assessment of the Samoa Channel Bridge-Foundation System”, with co- author Ahmed Elgamal. The dissertation author is the first author and primary investigator of this paper.

Table 7.1: Diameter and height of pier and pile foundation

Pier Number	Pier Height (m)	Existing Piles		Retrofitted Cast-In-Steel Shell Pile*		
		Configuration	D (m)	D (m)	Pile Length (m)	Pile Above Mudline (m)
S-2	7.37	4×4	0.36	0.914[b]	14.63	-2.45
S-3	6.19	4×4[d]	0.36	0.914[b]	16.31	7.32
S-4	7.13	5	1.37[a]	1.524[c]	22.86	7.62
S-5	8.46	5	1.37[a]	1.524[c]	26.22	10.52
S-6	9.58	5	1.37[a]	1.524[c]	28.65	14.32
S-7	10.29	2×3	1.37[a]	1.524[c]	28.04	16.52
S-8	9.02	2×4	1.37[a]	1.524[c]	28.96	16.72
S-9	9.55	2×4	1.37[a]	1.524[c]	26.22	15.22
S-10	11.43	2×3	1.37[a]	1.524[c]	25.30	12.42
S-11	11.10	2×3	1.37[a]	1.524[c]	23.78	9.82
S-12	10.52	2×3	1.37[a]	1.524[c]	22.56	8.02
S-13	10.01	5	1.37[a]	1.524[c]	18.60	4.22
S-14	12.93	4×5 [d]	0.36	0.914[b]	13.72	-2.14
S-15	12.09	4×5 [d]	0.36	0.914[b]	13.72	-2.14
S-16	11.15	4×4 [d]	0.36	0.914[b]	12.19	-2.44
S-17	10.52	4×4	0.36	0.914[b]	11.74	-2.29
S-18	9.81	4×4	0.36	0.914[b]	12.35	-2.29
S-19	8.33	4×4	0.36	0.914[b]	12.19	-1.83
S-20	7.67	4×4	0.36	0.914[b]	12.19	-2.43

* See Figure 7.3 and Figure 7.4 for geometric pile group configurations
[a] Prestressed concrete cylinder pile with wall thickness h=0.127 m
[b] Four new Cast-In-Steel Shell Pile with wall thickness h=0.013 m
[c] Cast-In-Steel Shell Pile with wall thickness h=0.019 m
[d] 1:3 Batter

Table 7.2: Concrete material parameters for the FE model (Caltrans 2002a)

Condition	Compressive Strength (f_c') (MPa)	Elastic modulus (MPa)
existing	34	2.79×10^4
retrofit	28	2.53×10^4

Table 7.3: Steel material parameters for the FE model (Caltrans 2002a)

Condition	Yield Strength (f_y) (MPa)	Elastic modulus (MPa)
existing	303	2.0×10^5
retrofit	414	2.0×10^5

Table 7.4: Uncracked section properties for bridge pier columns (Caltrans 2002a)

Cross Section	S-8 and S-9	S-1 ~ S-7 S-10 ~ S-20
Area of Cross Section (m^2)	7.01	5.66
Transverse Moment of Inertia (m^4)	7.06	5.11
Longitudinal Moment of Inertia (m^4)	1.88	1.11
Torsion Constant (m^4)	5.77	3.53

Table 7.5: Identified stiffness factor for pier and pile foundation at Pier S-8

Earthquake Event	Stiffness factor based on EI of uncracked section	
	Pier ($EI=1.79\times10^8$ kN-m^2)	Pile Foundation ($EI=8.95\times10^7$ kN-m^2)
Ferndale 01/09/2010	0.46	0.25
Trinidad 06/24 /2007	0.65	0.42
Ferndale 03/09/2014	0.65	0.41
Trinidad 08/16/2008	0.65	0.44
Ferndale 02/26/2007	0.63	0.44
Willow Creek 04/29/2008	0.65	0.41

Table 7.6: Employed Bridge Deck Properties for the FE Model (Caltrans 2002a)

Cross Section	between S-8 and S-9	all other locations
Area of Cross Section (m^2)	5.05 m^2	3.76 m^2
Moment of Inertia @ Longitudinal Axis (m^4)	6.78 m^4	1.68 m^4
Moment of Inertia @ Vertical Axis (m^4)	41.89 m^4	31.72 m^4
Torsion Constant (m^4)	0.98 m^4	0.34 m^4

Table 7.7: Optimized frequency and stiffness factor at Pier S-8 based on EI of uncracked section (FEM1)

Earthquake Event	Frequency (Hz)	Column Stiffness Factor
Ferndale 01/09/2010	1.54	0.39
Trinidad 06/24 /2007	1.93	0.61
Trinidad 08/16/2008	1.88	0.59
Willow Creek 04/29/2008	1.91	0.60
Ferndale 02/26/2007	2.01	0.67
Ferndale 03/09/2014	1.87	0.58

Table 7.8: Optimized frequency and spring value representing pile foundation below Pier S-8 (Figure 7.11)

Earthquake	Computed Frequency (Hz)	Optimized spring value K (kN/m)
Ferndale 01/09/2010	0.70	3.96×10^4
Trinidad 06/24 /2007	0.95	7.50×10^4
Ferndale 03/09/2014	0.86	5.95×10^4
Ferndale 02/26/2007	0.94	7.32×10^4
Trinidad 08/16/2008	0.94	7.37×10^4
Willow Creek 04/29/2008	0.93	7.10×10^4

Table 7.9: Employed weighting factors of the objective function for each sensor

Sensor	Chan8	Chan16	Chan10	Chan5	Chan15	Chan21
w	37.5%	25%	18.75%	6.25%	6.25%	6.25%

Table 7.10: Optimized foundation stiffness and values based on Caltrans report for the Middle Channel Bridge (Caltrans 2000b) for the 4×4 pile group configuration with 4 CISS retrofitted piles (Table 7.1 and Figure 7.3)

Middle Channel Bridge (Figure 7.19a)				Samoa Channel Bridge (Figure 7.19b)			
Pier #	Pile above mudline (m)	Soil profile for top 6 meters	Caltrans k ($\times 10^4$kN/m)	Pier #	Pile above mudline (m)	Soil profile for top 6 meters	SNOPT k ($\times 10^4$kN/m)
M-2	-0.44	• organic silt • slightly compact find sand	6.97* 40.21	S-2	-2.445	• very soft organic silt • compact sand	10.94** 40.63
M-8	-0.355	• very loose organic silt	65.97	S-16 to S-20	-2.4	• very soft organic silt • compact sand	12.34** 184.40
M-9	-1.23	• very loose organic silt	47.28				
				S-3	7.315	• very soft organic silt • compact sand	1.37** 48.48

* considering liquefaction
** optimized spring value for the moderate event

Table 7.11: Optimized foundation stiffness and values based on Caltrans report for the Middle Channel Bridge (Caltrans 2000b) for the concrete pile groups with 4 CISS retrofitted piles (Table 7.1 and Figure 7.4)

Middle Channel Bridge (Figure 7.19a)				Samoa Channel Bridge (Figure 7.19b)			
Pier #	Pile above mudline (m)	Soil profile for top 6 meters	Caltrans k ($\times10^4$kN/m)	Pier #	Pile above mudline (m)	Soil profile for top 6 meters	SNOPT k ($\times10^4$kN/m)
M-3	5.115	• loose silty fine sand • fine sand	11.12				
M-4	7.615	• organic clay • dense fine sand	12.07	S-4	7.615	• loose sand • slightly compact sand	11.73* 24.62
M-5	8.815	• slightly compact sand • compact sand	7.76	S-5	10.515	• loose sand • slightly compact sand	5.08* 7.38
M-6	7.915	• slightly compact fine sand • dense sand	7.93	S-6	14.315	• organic matter • dense sand	2.66* 6.25
M-7	6.415	• loose fine sand • compact sand	9.09	S-13	4.215	• very loose silty sand • slightly compact sand	3.88* 15.00

* optimized spring value for the moderate event

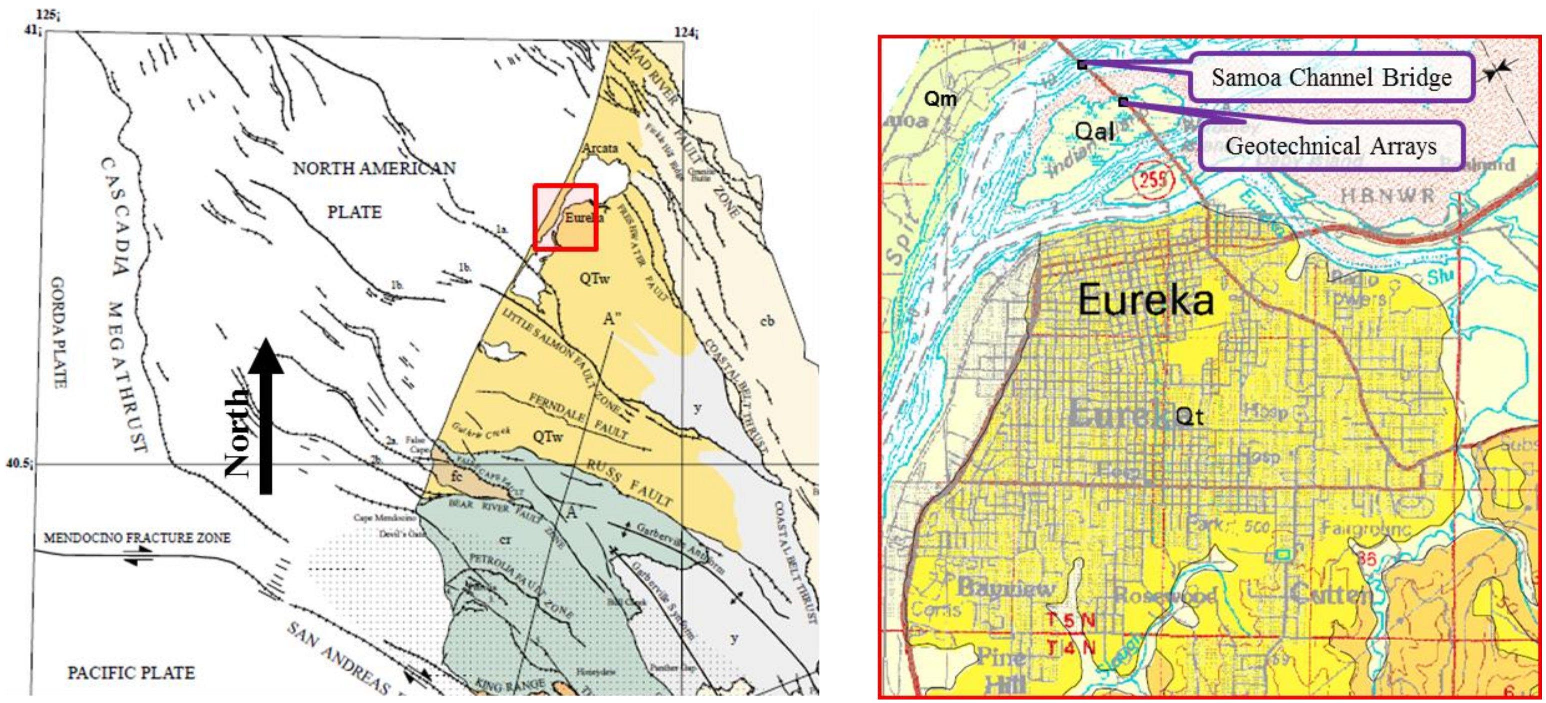

(a) **(b)**

Figure 7.1: Faults near Eureka Area and Geological map of Eureka area (McLaughlin et al. 2000)

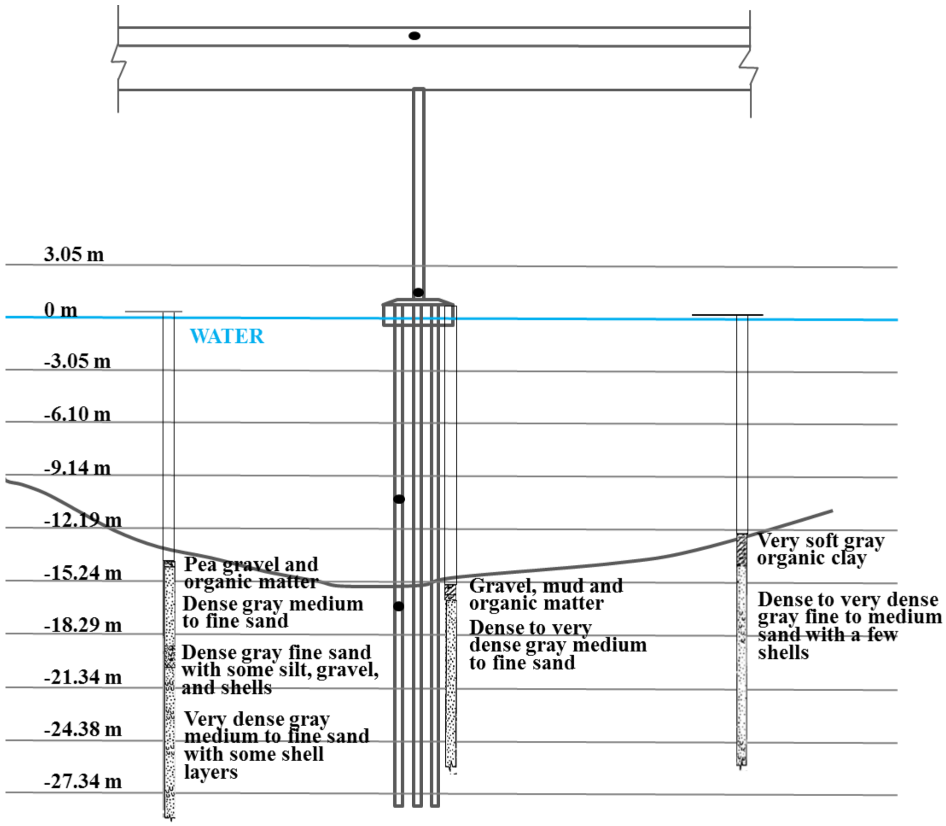

Figure 7.2: Samoa Channel Bridge Pier S-8 and adjacent soil profile

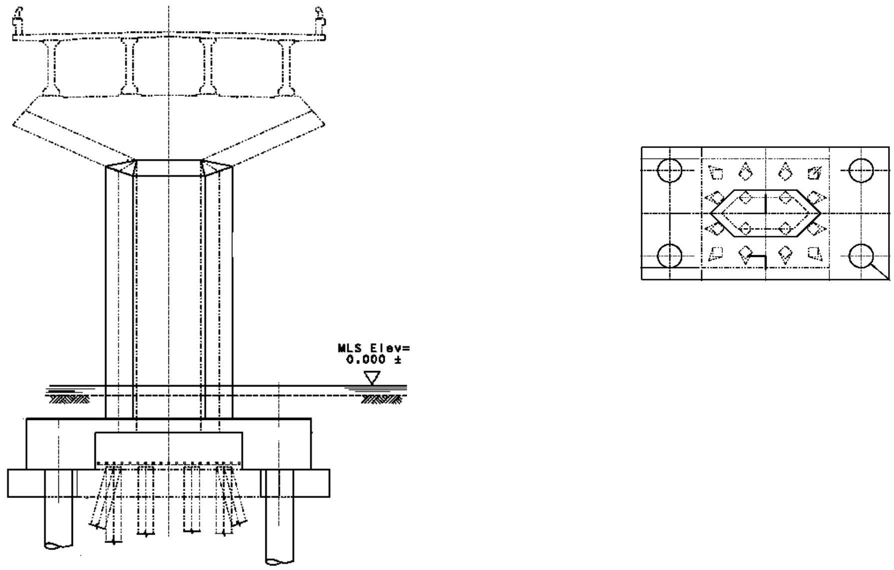

(a) Pier S-2 & 16 - 20

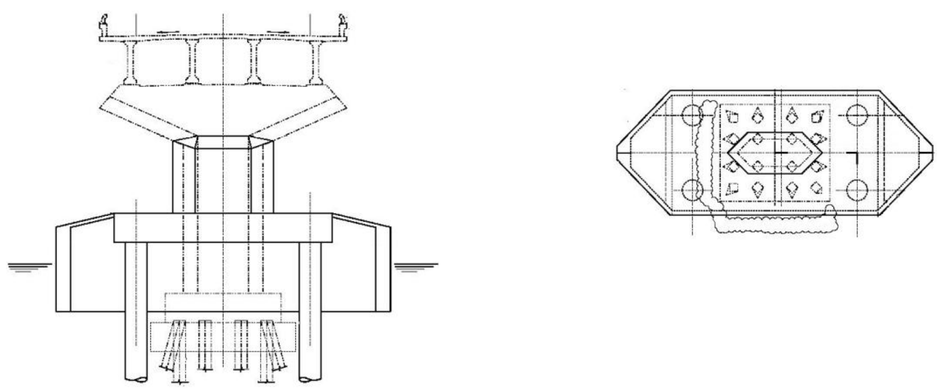

(b) Pier S-3

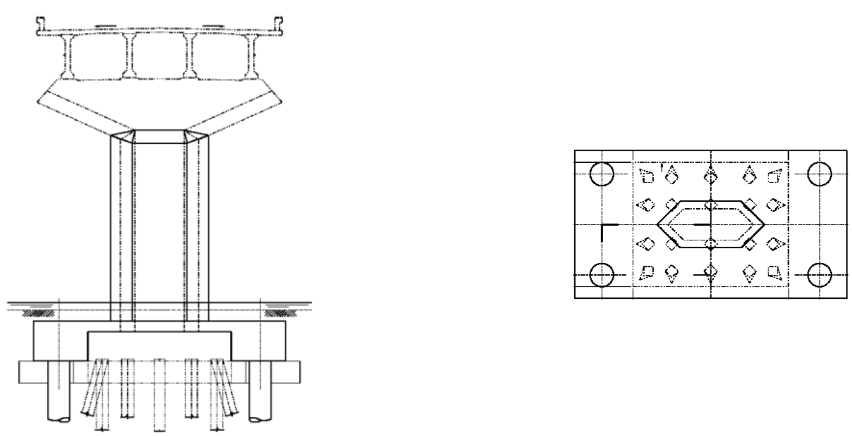

(c) Pier S-14 & S-15

Figure 7.3: Samoa Channel Bridge retrofit information for Piers S-2, 3 and 14 through 20 (Caltrans 1968; 2002b)

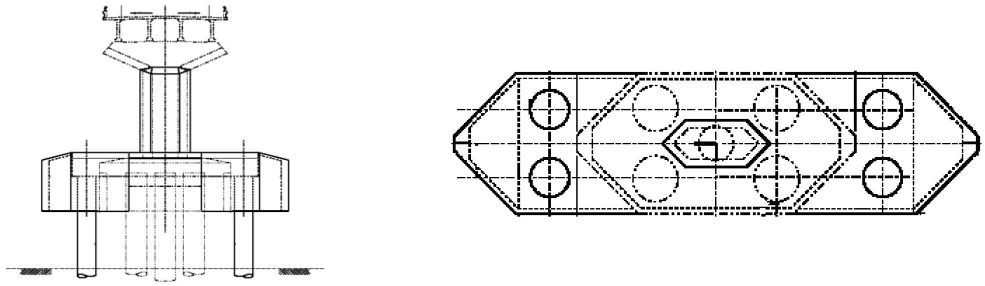

(a) Pier S-4, 5, 6 & S-13

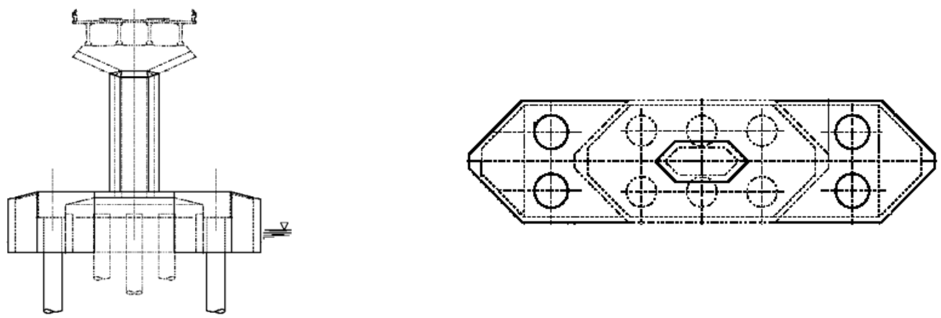

(b) Pier S-7 & 10 - 12

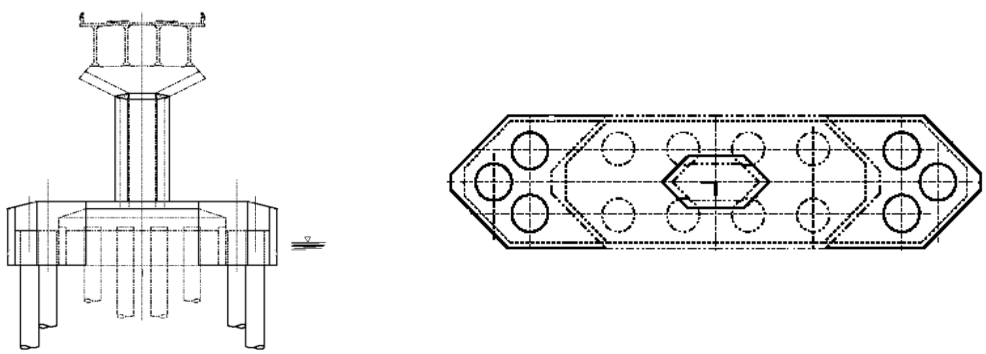

(c) Pier S-8 & 9

Figure 7.4: Samoa Channel Bridge retrofit information Piers S-4 through 13 (Caltrans 1968; 2002b)

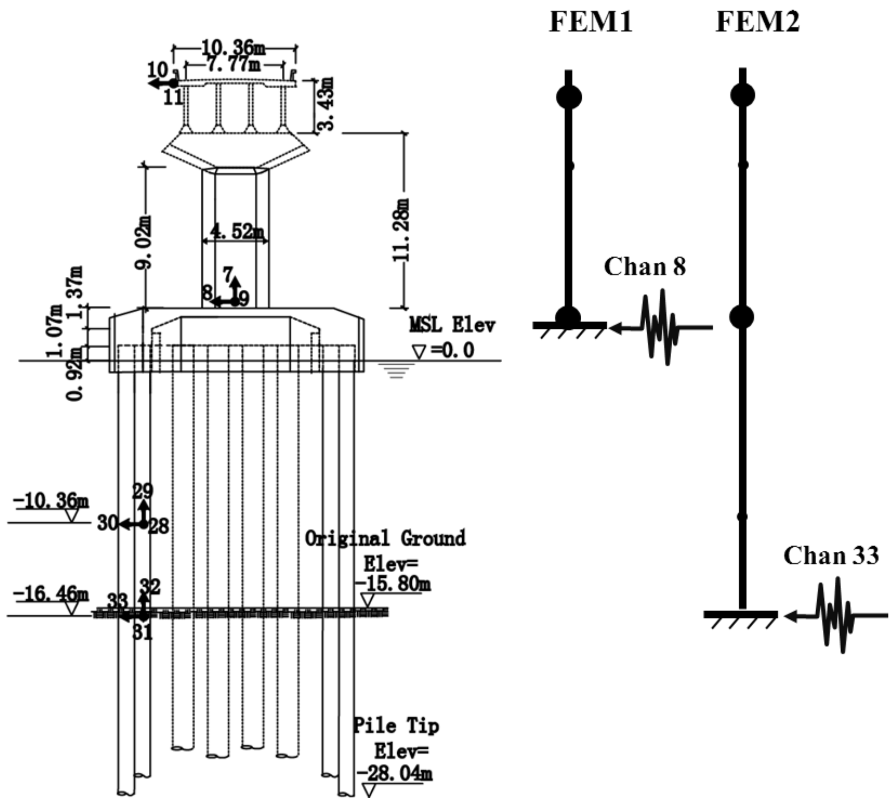

Figure 7.5: Pier S-8 single column type pier model

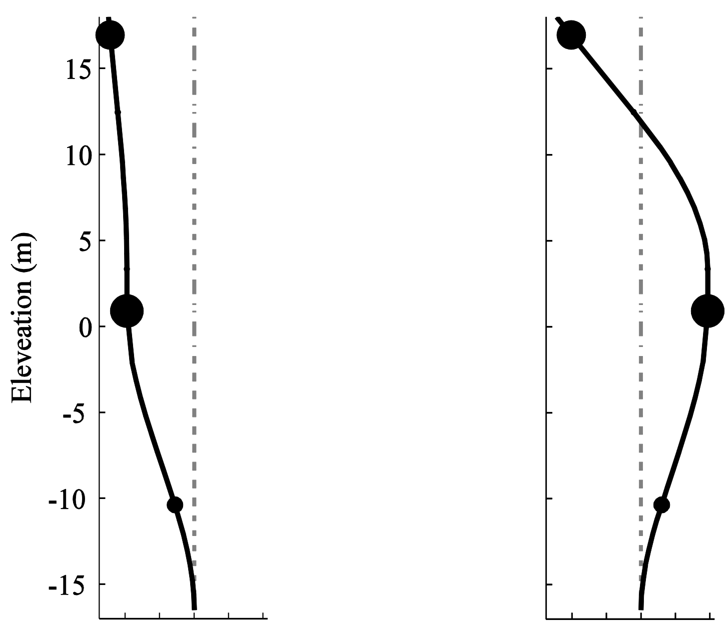

Figure 7.6: Transverse mode shapes of pile-column system (at Pier S-8) with fixed base at the elevation of -16.46 m with (a) f_1=0.74 Hz and (b) f_2=2.37 Hz

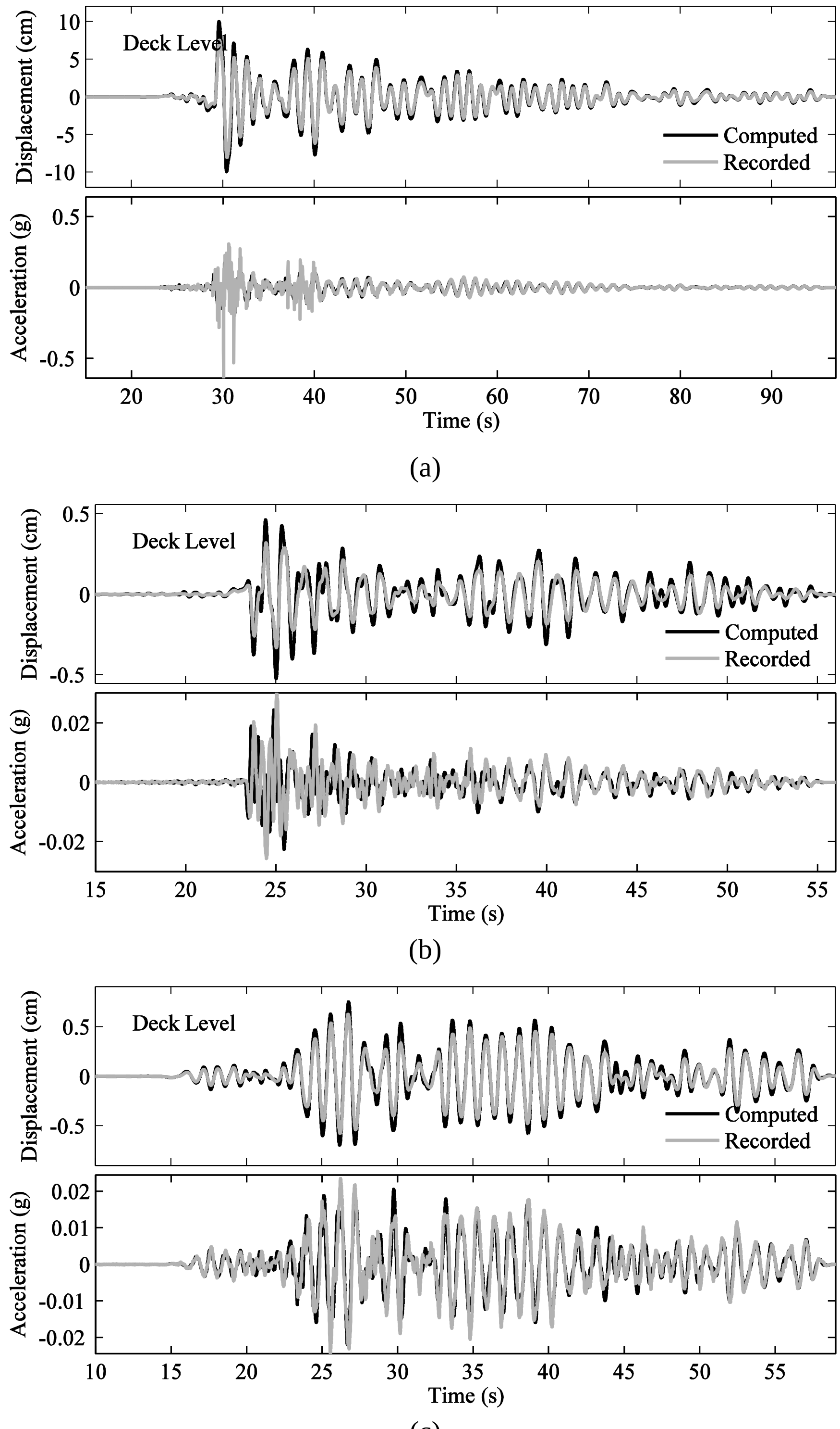

Figure 7.7: Time histories comparisons for at Pier S-8 (at the deck level) during earthquakes: (a) the moderate event (b) the 2007 Trinidad Earthquake, and (c) the 2008 Willow Creek Earthquake

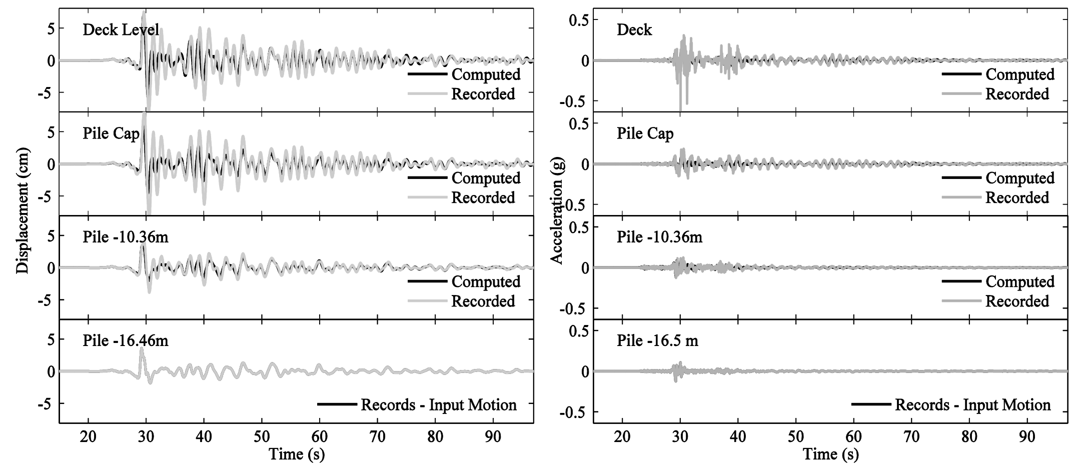

(a) Ferndale 09 Jan 2010

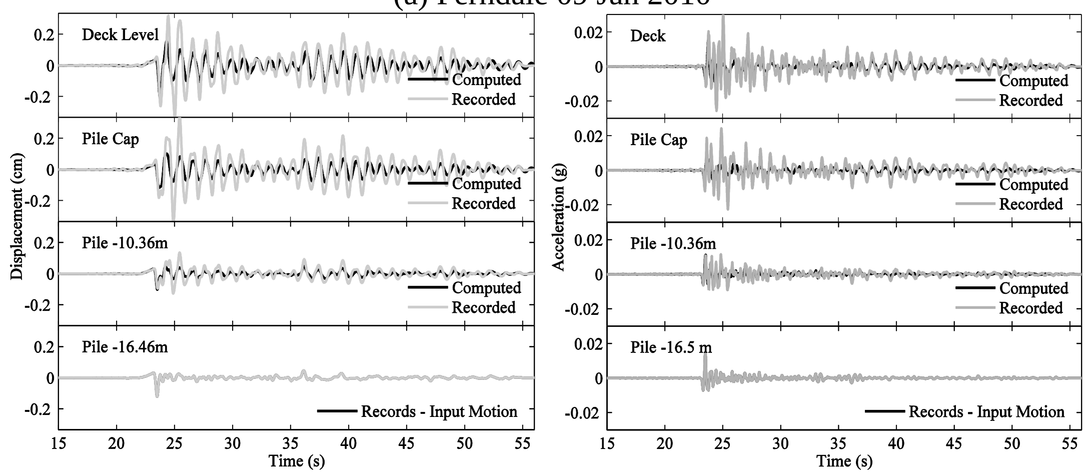

(b) Trinidad 24 Jun 2007

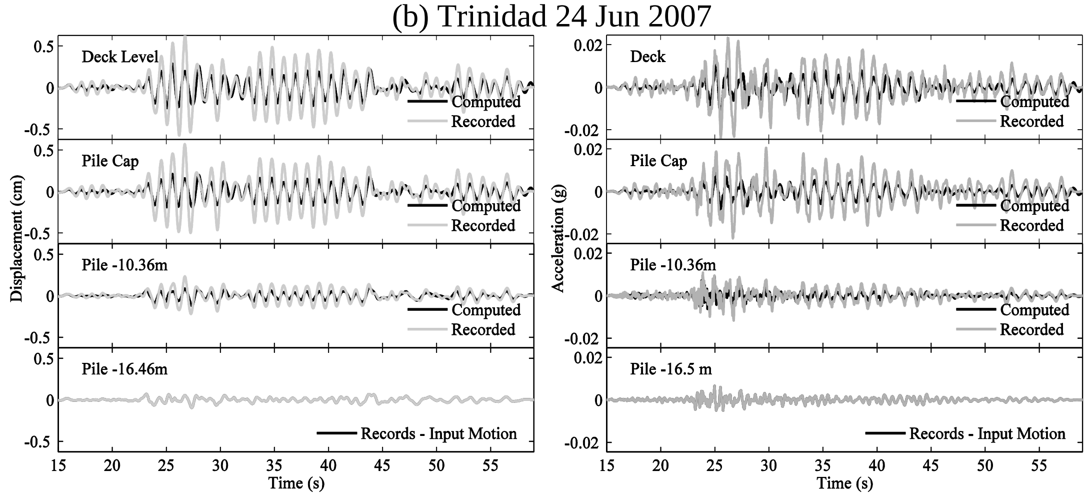

(c) WillowCreek 29 Apr 2008

Figure 7.8: Time histories comparisons along Pier S-8 from deck level to elevation of -16.46 m during: (a) the moderate event, (b) the 2007 Trinidad Earthquake, and (c) the 2008 Willow Creek Earthquake

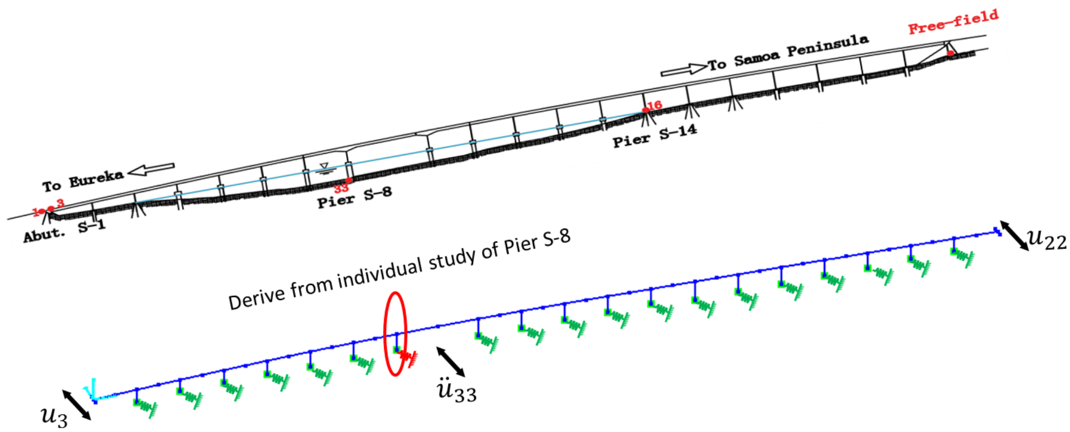

Figure 7.9: Beam-column model of the Samoa Channel Bridge

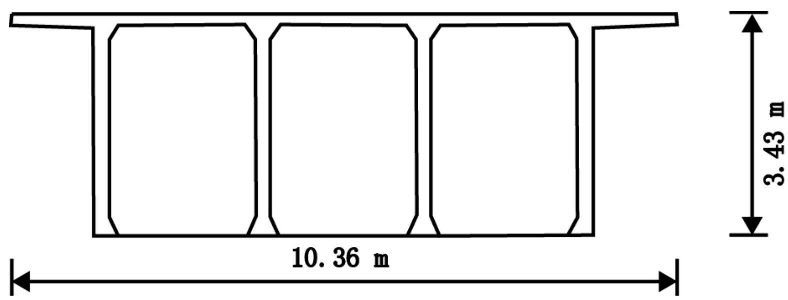

Figure 7.10: Bridge Deck Section

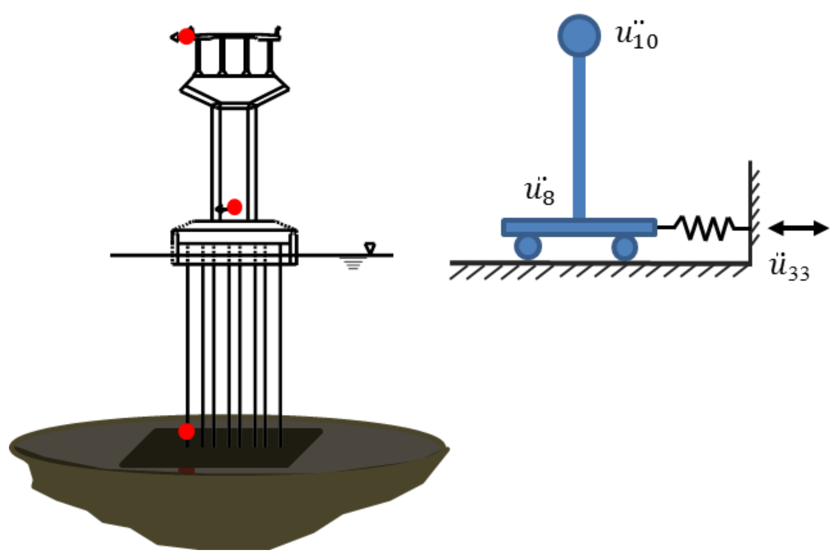

Figure 7.11: Estimation of the spring value at the base of Pier S-8 using SNOPT

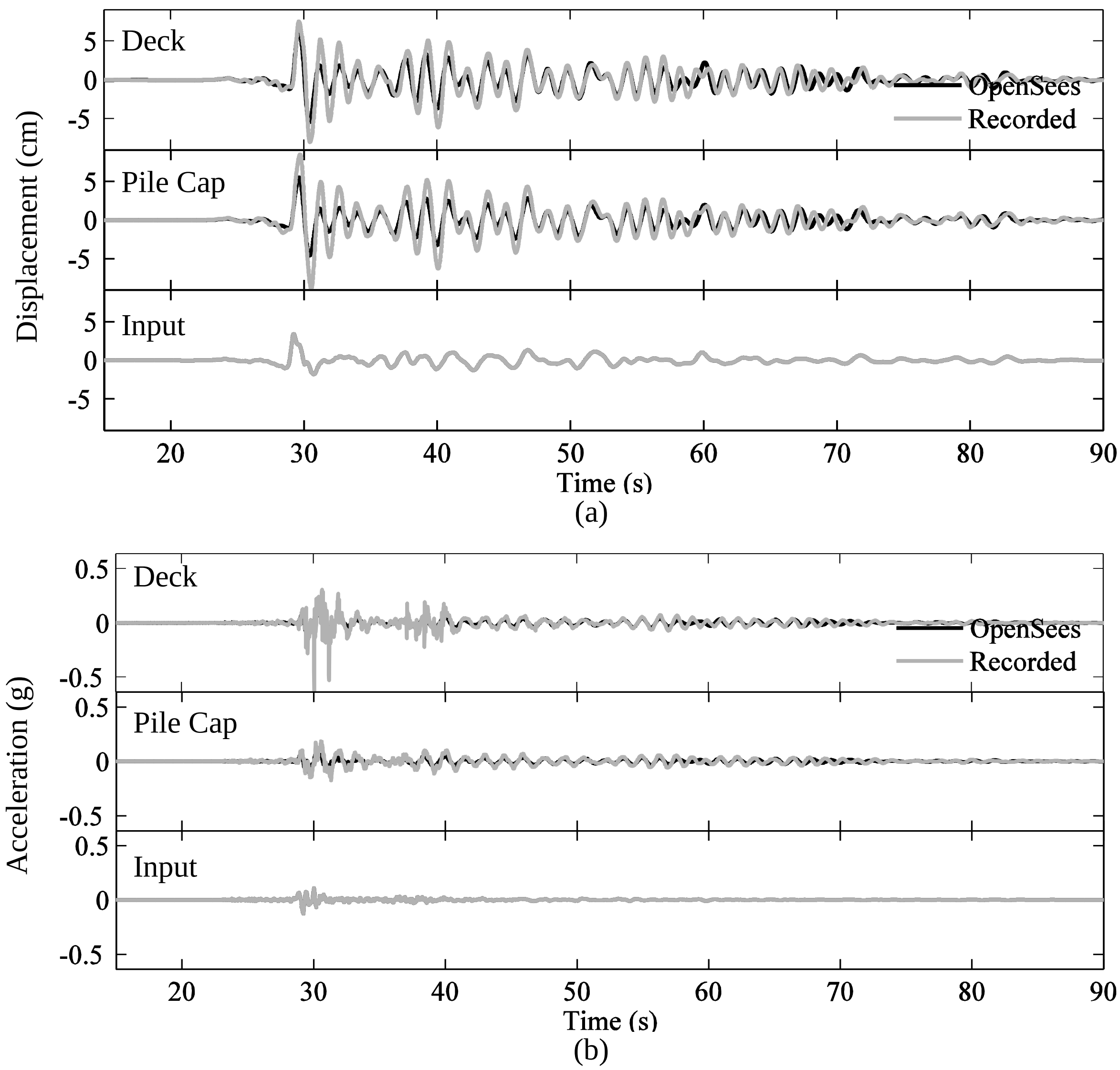

Figure 7.12: The recorded and optimized time histories at Pier S-8

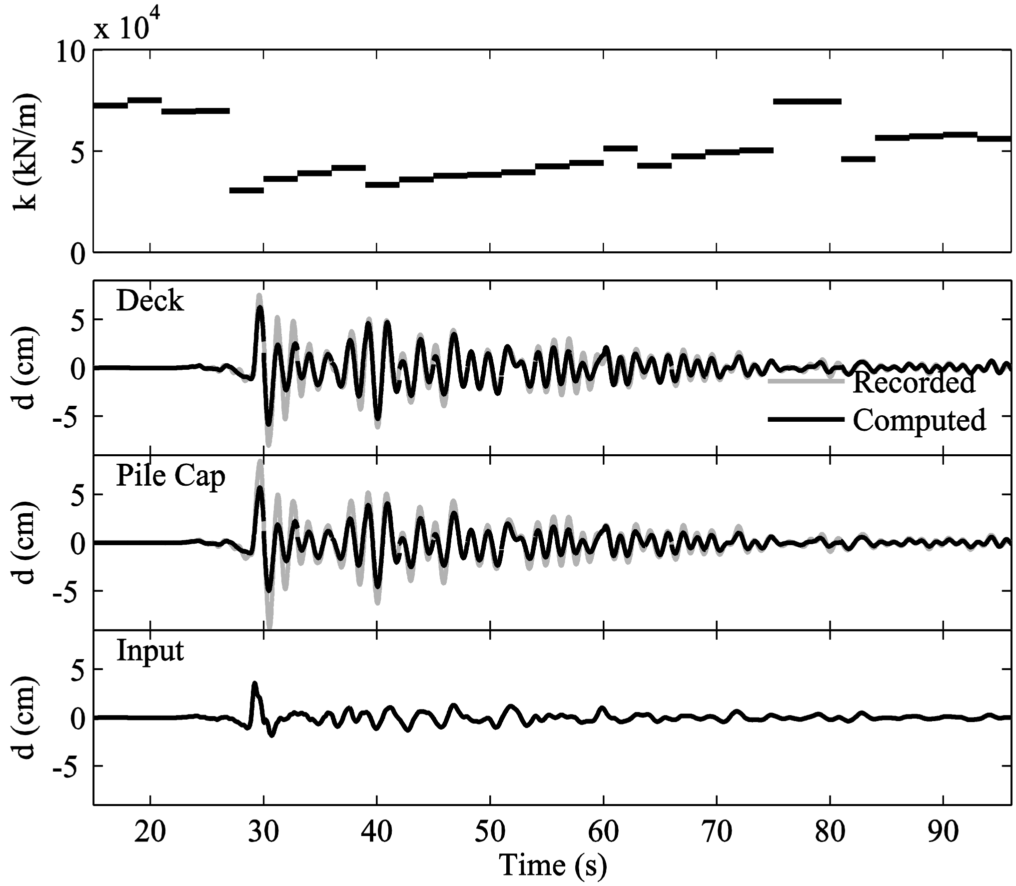

Figure 7.13: Variation of Spring Stiffness during the moderate event

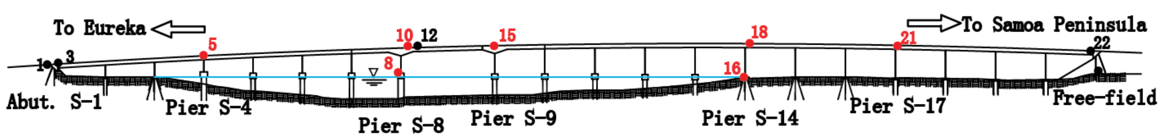

Figure 7.14: Locations of recorded pile cap and bridge deck responses for objective function

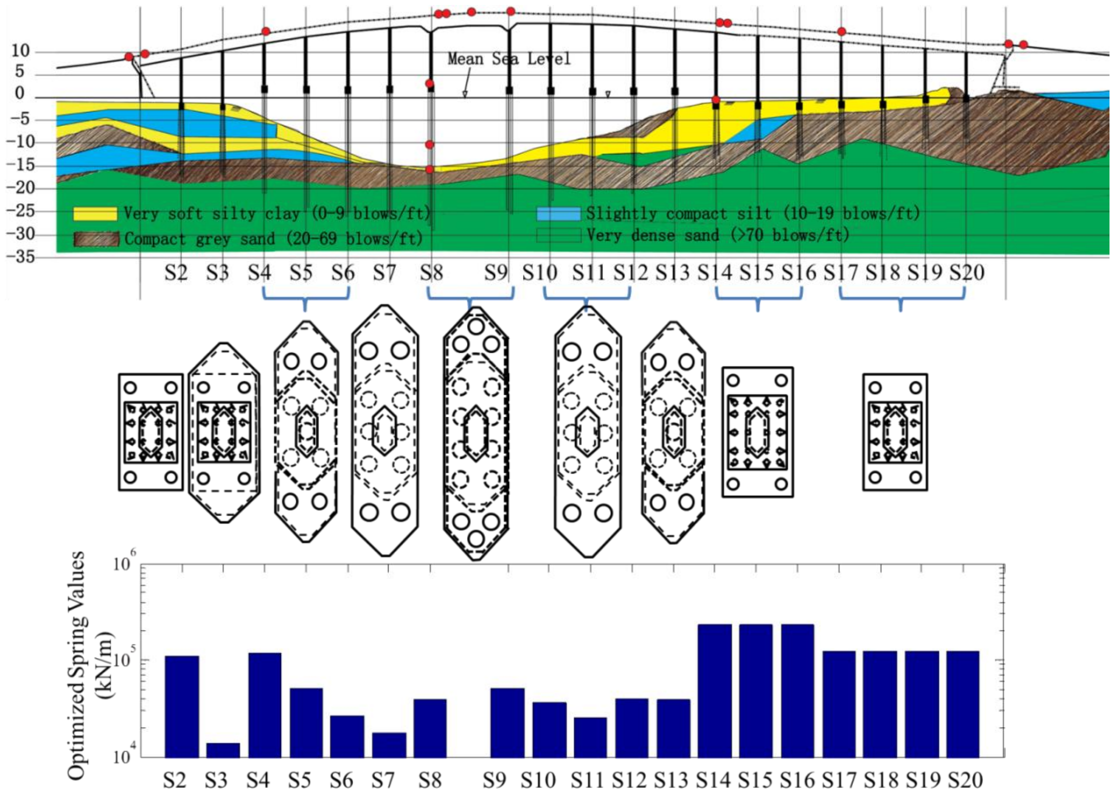

Figure 7.15: Base spring values along deck for earthquake Ferndale 2010

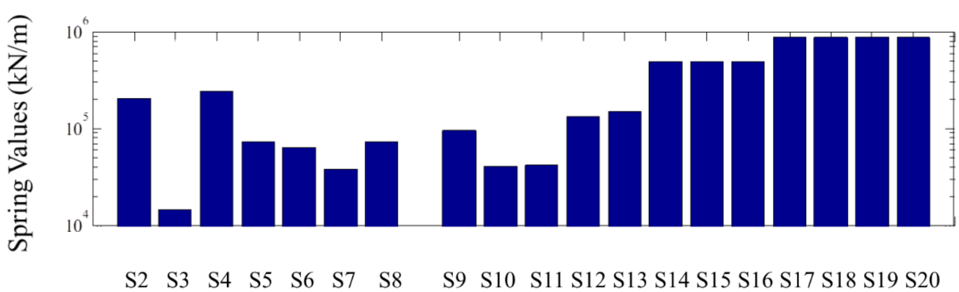

Figure 7.16: Base spring values along deck during the Trinidad 2007 and Trinidad 2008 earthquakes in sequence

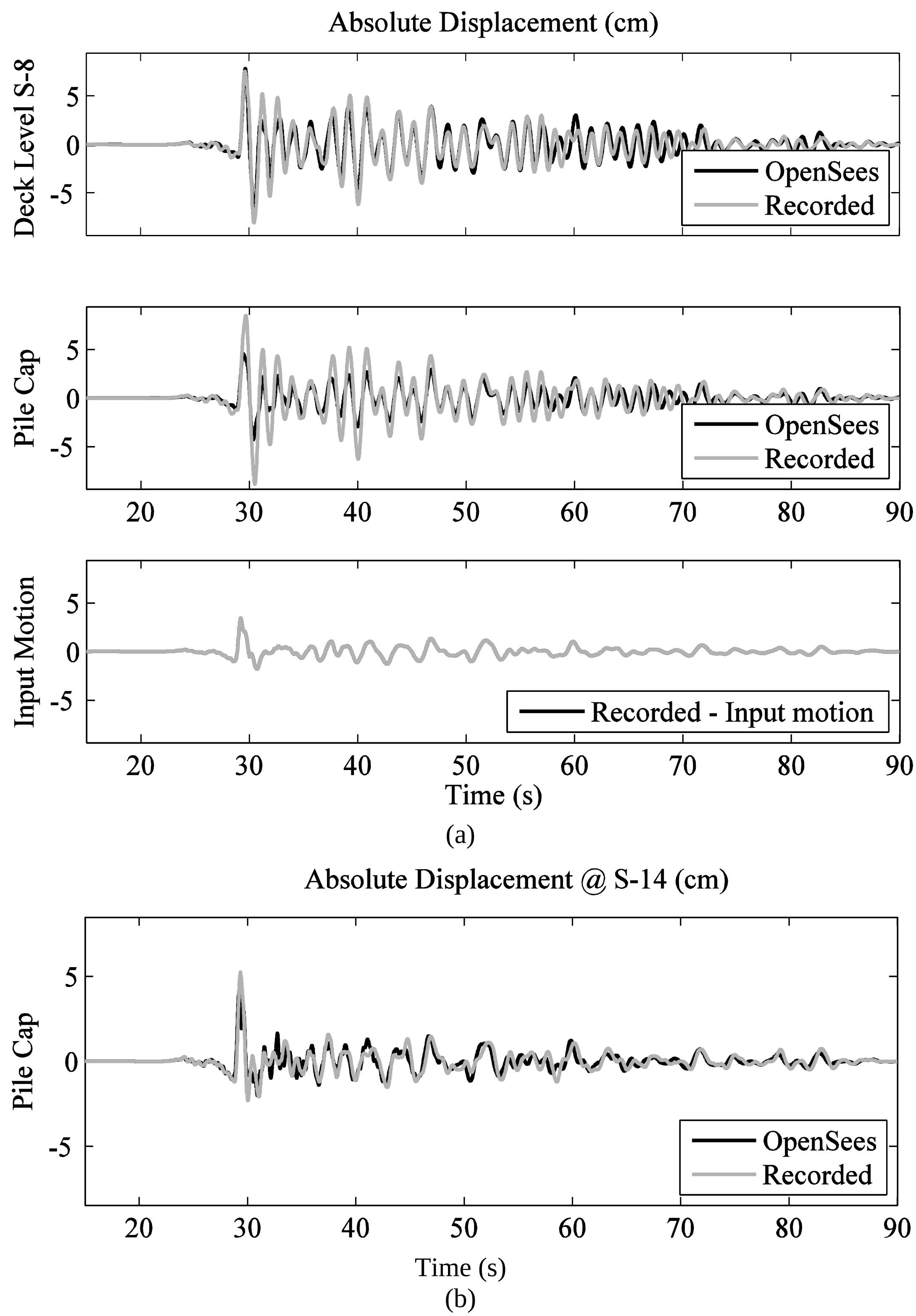

Figure 7.17: Comparison of computed and measured displacement time histories at (a) Pier S-8, (b) S-14 during the moderate event

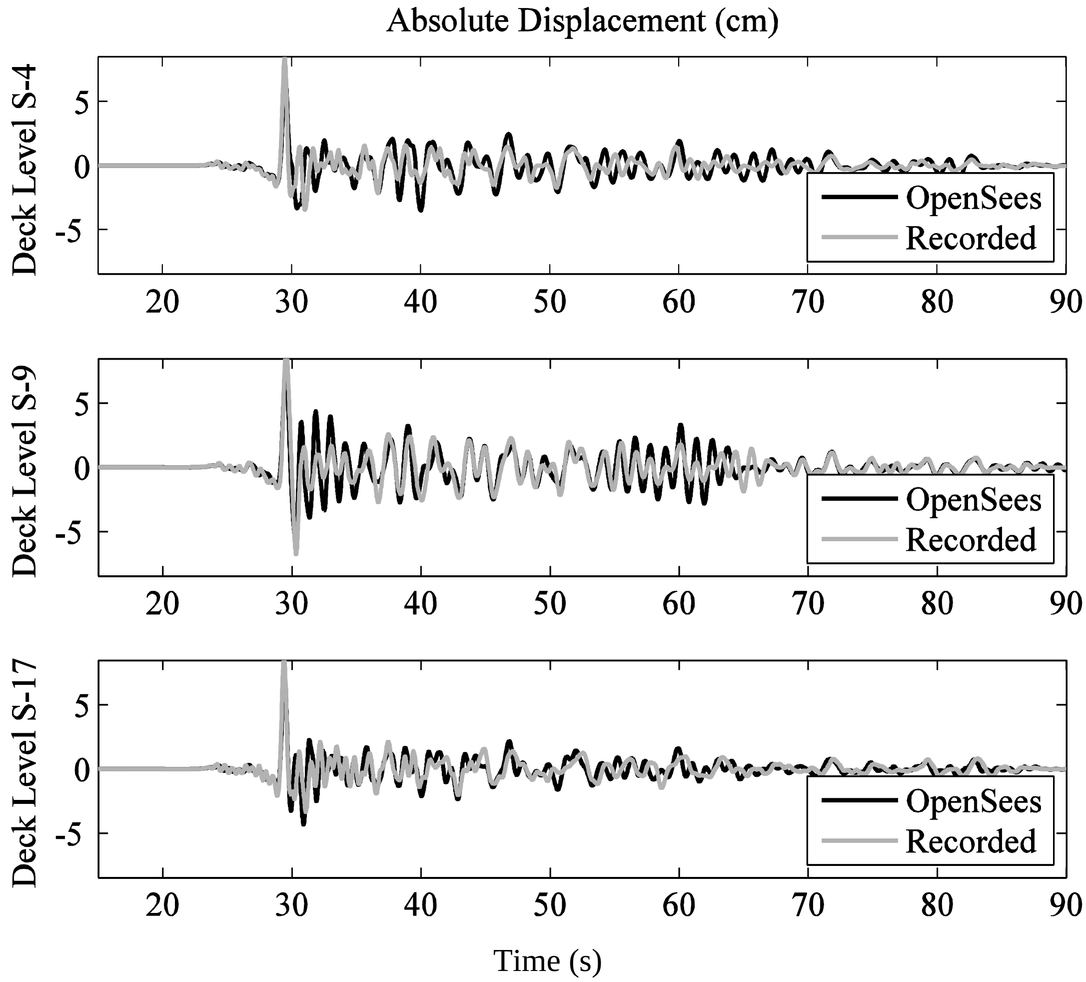

Figure 7.18: Comparisons of computed and measured displacement time histories at Pier S-4, S-9 and S-17 (deck level) during the moderate event

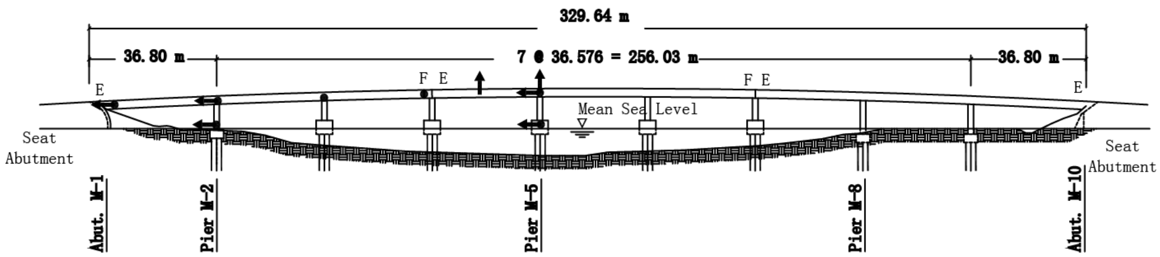

(a)

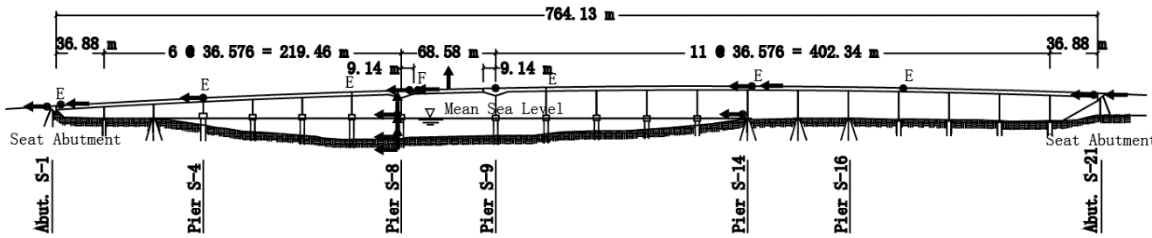

(b)

Figure 7.19: Side view of (a) the Middle Channel Bridge and (b) the Samoa Channel Bridge (http://www.strongmotioncenter.org)

Chapter 8

Recorded Seismic Response and Numerical Analysis of the Eureka Channel Bridge

Encouraged by the conclusions drawn from the Samoa Channel Bridge study, the observations during the 2010 Ferndale Earthquake (2010) and several earlier small earthquakes are employed to evaluate the Eureka Channel Bridge responses (including ground, pile foundation, and super-structure). System identification techniques and optimization approaches are used in this chapter. The recorded earthquake motions from this instrumented Eureka Channel Bridge structure along with the adjacent geotechnical downhole arrays stand to provide valuable information on the characteristics of structural response during seismic events. The Finite Element (FE) model of this long-span curved bridge is calibrated based on the recorded motions and identified bridge/foundation properties. The bridge model with optimized base springs considering soil-structure interaction is found to reasonably represent the seismic response of this ground-foundation-bridge system.

8.1 Introduction

Recorded seismic motions of the instrumented bridge foundation together with the adjacent downhole-array records provide a unique opportunity for documenting and analyzing salient ground-foundation-structure response mechanisms as discussed in Chapter 6 and Chapter 7. As shown, case study of the Samoa Channel Bridge based on such full-scale seismic performance data sets advances our understanding of the underlying actual soil-structure interaction (SSI) characteristics and leads to an improved Finite Element model capturing the actual structure behavior more accurately.

In this chapter, data from the extensively instrumented Eureka Channel Bridge and the Eureka geotechnical downhole array (Figure 8.1) are employed to elucidate the seismic response of this ground-foundation-bridge system. Accelerometers were embedded inside one of the retrofitted pile group foundations at the elevation of -10.36 m (-34 ft) and -16.46 m (-54 ft) below mean sea level (MSL). The acquired full-scale seismic performance data sets are shedding more light on the involved seismic soil-structure-interaction mechanisms.

Time histories, frequency spectra and system identification analyses are presented for documenting the ground-foundation-bridge response mechanisms. Focus is placed on the seismic response of the instrumented pile-group during the 2010 Ferndale Earthquake and the 2007 Ferndale Earthquake. Additional sets of recorded small seismic motions are studied as well for comparison. Extending the effort in Chapter 7, motions at the bridge free fields (Samoa Channel Bridge, Middle Channel Bridge and Eureka Channel Bridge), deeply embedded pile below Pier E-7 and the nearby free-field geotechnical array (Eureka Geotechnical Array) are compared and discussed in detail.

On this basis, a linear FE model representing the instrumented Eureka Channel Bridge Pier E-7 and its pile group foundation is developed and calibrated. To maintain focus, attention is directed to the bridge transverse response. The representative stiffness for the pier column and the pile foundation beneath is estimated by matching the computed dominant natural frequency of the model with the identified values.

Furthermore, a simple FE model for the entire bridge with springs at the column base was developed. Optimization techniques are employed to identify the spring values at the base of the column which represent the effects of the soil-foundation system. This calibrated FE model is found to mimic the seismic response of the Eureka Channel Bridge and yield comparable results with the recorded earthquake strong motion data.

Together with the identified deep-foundation soil-structure characteristics from Samoa Channel Bridge, the results of this additional research are of significant consequence towards refining our understanding of the involved SSI mechanisms.

8.2 General Bridge Information

8.2.1 The Bridge Description

The Eureka Channel Bridge connecting Eureka and Woodley Island (Figure 8.1) is one of three bridges crossing Humboldt Bay in Eureka, California. This 15-span bridge is a 553.44 m long and 10.36 m wide structure, supported by 14 single hexagonal concrete column type piers and seat-type abutments (Figure 8.2). The bridge piers are labeled from Eureka to Samoa as Pier E-1 (abutment), Pier E-2, Pier E-3 and so on. This bridge includes a curved section (Figure 8.2) with a radius of 548.64 m for a total length of 309.15 m from Pier E-1 up to 11.677 m NW of Pier E-9.

The continuous cast-in-place (CIP) pre-stressed (PS) 3-cell box girder superstructure is resting on reinforced concrete (RC) "T" piers from E- 1 to E-3. Four PS RC I-girders along with CIP concrete slabs (0.165 m in thickness) are supported on the hammer head of column type piers from E- 4 to E-15 and the RC seat-type abutments E-16. Between Pier E-7 and Pier E-8, there is a 42.67 m long prestressed precast concrete drop-in span. Seven separation joints allowing movement during seismic events are located at the top of Piers E-3, E-4, E-6, E-9, E-13 and the two abutments supports (Figure 8.2).

The height of the single hexagonal concrete pier columns ranges from 2.39 m at Pier E-15 to 12.25 m at Pier E-6. The abutments and pier columns are founded on pile-groups consisting of driven pre-cast prestressed concrete piles. Referenced to the mean sea level (MSL), the mudline elevation varies from +2.8 m at Pier E-3 to a -5.0 m at Pier E-8. Nearly all pile caps are embedded in soil except for pile caps from E-7 to E-10 which are around 7.35 m – 8.35 m above the mudline (Figure 8.2).

When designed in 1968, pile groups under the main span (below Pier E-7 and Pier E-8) consisted of 8 (2x4) cylindrical (diameter D=1.37 m) concrete piles (filled with concrete for it entire length) with center to center spacing of 2D. The foundation of Piers E-9 and E-10 consist of five RC piles with a RC skirt. At the reinforced concrete seat type abutments E-1 and E-16, there are 12 square-shaped concrete pile (d=35.6 cm). The front row consists of 8/7 piles battered at a 1:3 ratio and the back row consists of 4/5 vertical piles. Detailed design drawings along with soil borings are reported in (Caltrans 2002b).

8.2.2 Geology and Site Description

The Eureka Channel Bridge is located in an area of complex interaction among three tectonic plates (North American, Pacific and Gorda) with high seismic activity. The ‘Little Salmon’ fault is the nearest seismic source from the site (Caltrans 2000a).

The geology map of Eureka area (Figure 7.1b) shows that alluvial deposits (Qal) are identified (Clay, silt, sand, gravel, and boulders, deposited in stream beds, alluvial fans, terraces, flood plains and ponds) on Woodley Island. Non-marine terrace deposits (Qt) were found at Eureka area (McLaughlin et al. 2000).

Thirteen borings were drilled to a maximum depth of about 37.19 m below the mean sea level (MSL) along HWY 255 in 1968 (Figure 8.3). It is revealed that the bridge site is mantled by very soft silty clay underlain by dense gray medium to compact gray sand. Stiff grey was encountered at the elevation of -12.2 m and continues to the maximum explored depth. Soil layers vary in thickness and are not continuous horizontally (Caltrans 2002b).

8.2.3 Seismic Retrofit Effort

The Eureka Channel Bridge was designed by the California Department of Transportation (Caltrans) in 1968 and the construction was completed in 1971. Minor damage was reported after earthquakes in 1992 and 1994. Some repairs and subsequently an initial seismic retrofit (Caltrans 2002b) were completed by Caltrans prior to 1997 (e.g., the bent caps were reinforced and transversely stressed; pipe extenders and cable assemblies were added to selected bents, etc.).

In order to further strengthen this bridge, a seismic retrofit program was carried out by Caltrans in 2002, which included (Caltrans 2002b): (1) strengthening of the foundations by installing additional cast-in-steel shell (CISS) piles (e.g. 2 additional 0.914 m diameter and 13 mm thickness piles at both noses of the pier footing at Pier E-7 through E-10, as shown in Figure 8.4); (2) adding or enlarging pile caps to cover the new piles. The original skirt was retained at each pier. The retrofit skirt extended through the overall length of the pier but retained the original width; and (3) encasing the bridge columns in reinforced concrete column jackets to improve ductility. Accelerometers were installed inside one of the retrofitted CISS piles at Pier E-7 at two different elevations (-10.36 m and -16.46 m) during the structural retrofit. Detailed design drawings, retrofit information along with soil borings are reported by Caltrans (Caltrans 1968; 2002b).

8.3 Strong-Motion Instrumentations at the Eureka Channel Bridge

8.3.1 Instrumentations of the Eureka Channel Bridge

To obtain insights for both the characteristics of seismicity and earthquake response of the structure, the Eureka Channel Bridge was heavily instrumented (CGS station 89736) with a total of 27 accelerometers (mostly deployed in 1996). Side view and deck level plan view of the sensor network layout are shown in Figure 8.2. Locations of sensors are marked with numbered arrows indicating the direction of measured motion.

There are 18 sensors placed on the Eureka Channel Bridge to measure the translational motion of the structure, including 10 on the deck, 3 at the abutments and 5 at the pile caps of Pier E-3 and Pier E-7 (Figure 8.2). Sensors on the structure are oriented in the longitudinal and transverse direction of the bridge (positive direction of transverse motion defined as radially inward for this curved bridge). At a nearby ground surface station (EGS, 33.53 m south of the Abutment E-1 and 7.62 m west of E-1), three sensors were installed at elevation of +1.9 m approximately, oriented in the north-south (NS), east-west (EW) and vertical directions (Figure 8.2). In addition, 6 accelerometers were embedded inside one of the retrofitted CISS piles at Pier E-7 (Figure 8.4). Foundation seismic response at two different elevations (-10.36 m and -16.46 m) was included after the structural retrofit.

Of particular interest in this instrumentation is the dynamic response of the foundation relative to bridge structure in the transverse direction at the mid-span (Pier E-7). For this purpose, records from sensors 5, 3, 24 and 27 are studied in detail in this chapter to obtain salient resonant frequencies for both the superstructure and the entire ground-foundation-bridge system.

8.3.2 Recorded Earthquake Motions

Records from a total of nine earthquakes in the period of June 2002 through March 2014 are currently available with Magnitudes from 4.5 M_L to 7.2 M_W (M_L: local magnitude, and Mw: regional moment magnitude). Corrected acceleration, velocity, displacement and acceleration response spectra are available. Varying in peak acceleration (from 0.006 g to 0.256 g), epicentral distances (from 20.8 km to 155.1 km), shaking duration, and frequency content bandwidth, these earthquakes provide valuable information on the soil-foundation-structure seismic behavior over a broad range of excitations. Table 8.1 depicts time, magnitude, epicentral distance, peak horizontal acceleration at ground surface and structure of the recorded earthquakes (where one of events exceeds 0.2 g in peak ground acceleration).

Notable in Table 8.1 is the 2010 Ferndale Earthquake (M_w of 6.5) which is the first significant earthquake data set obtained since the retrofit in 2002 and is the largest motion recorded on the bridge. The bridge at a distance of 54.5 km from the epicenter of this earthquake reached peak acceleration of the order of 0.26 g at the ground surface and 0.51 g on the bridge deck. The largest movement on the bridge structure was 6.8 cm longitudinally and 6.1 cm transversely referenced to the motions of the pile at -16.46 m depth (Figure 8.4) during this earthquake event.

8.4 Evaluation of Earthquake Records

8.4.1 Ground Motions at the Bridge and Adjacent Downhole Sites

Comparison of the ground surface motions at three Caltrans bridge sites: the Samoa Channel Bridge (SCB), the Middle Channel Bridge (MCB), and the Eureka Channel Bridge (ECB) crossing the Humboldt Bay and at the Eureka Geotechnical Downhole Array (GDA) is shown in Figure 8.5 and Figure 8.6. Synchronization between the bridges and GDA records was done based on the actual digital time stamp for each site. In addition, arrival time of the ground surface seismic waves at the GDA and bridge sites differed by less than 0.2 second as judged by cross-correlation analysis. Overall, the ground surface displacement responses are of the same pattern (Figure 8.5). Generally, Fourier transformations of the acceleration time histories indicate the same dominant frequencies (Figure 8.6 and Figure 8.7).

Figure 8.8 and Figure 8.9 present ground displacement of: 1) the Eureka Channel Bridge ground surface station (EBGS), 2) the Eureka Channel Bridge pile foundation (EBPF) at the elevation of -16.46 m (re-oriented based on cross-correlation calculation as described in section 8.4.3), and 3) the adjacent geotechnical downhole array (GDA) in EW and NS directions.

As may be noted, motions at the EBGS and the EBPF (estimated at about 12.46 m below the mudline at this location) are of the same pattern as that of the GDA stations (being somewhere between the ground surface and elevation of -16 m). The pseudo-acceleration response spectra, with 5% damping, for the recorded free field motions of the bridge as well as those of the adjacent downhole array are shown in Figure 8.10 for the moderate event. There is a noticeable amplification effect for the motion at the downhole ground surface compared to those at depth. In particular, spectral acceleration of the EBPF falls between those of downhole at the ground surface and 33 m depth in the short period range. It is noteworthy that the pseudo-acceleration of the bridge at the ground surface station is significantly high at low period. This observed high energy response at low period might be partly due to the soil profile characteristics at the site and partly due to the impact of the bridge.

Generally, the location of -16.46 m along the pile depth will be assumed to be practically moving along with the ground (Figure 8.8 and Figure 8.9), indicating a level of firm embedment (fixity). Similar conclusions can be obtained based on comparisons of records from other available small earthquakes.

8.4.2 Seismic Response along the Bridge Deck

As shown in Figure 8.11b - Figure 8.14b, relative displacement time histories (referenced to the motions at EBPF station) generally display in-phase behavior in both directions (Transverse defined as radially inward for this curved bridge) for two representative earthquake events. Overall, the bridge is noticeably flexible in the mid-span (Channels 4 and 5 at Pier E-7). For the moderate event, maximum relative displacement at pier E-7 is 60% larger in amplitude compared to that at the abutment (E-16) in the transverse direction. In addition, relative displacement time histories highlight the period of vibration in both translational directions for this curved bridge during the small shaking events.

Sharp spikes were observed from the deck acceleration time histories in the translational directions (Long and Tran directions) for the moderate event (Figure 8.12a). Among these, the highest spike is 0.95 g at Chan4 in the longitudinal direction and 0.51 g at Chan19 in the transversal direction, whereas the peak ground acceleration at the bridge site is only about 0.26 g (Table 8.1). Such spikes were likely caused by a head-on impact between adjacent bridge deck segments (Huang and Shakal 1995; Malhotra et al. 1995). No spikes were observed during the small shaking event.

8.4.3 Seismic Response of Pier E-7

Given the discontinuity of the bridge structure due to the existence of separation joints near Pier E-7, transverse motion of the central intermediate bent may be analyzed individually (in an approximate manner, independent of the rest of the bridge). In addition, the high translational motion observed at Pier E-7 near the mid-length of the bridge, indicates that this might be a vulnerable location of the bridge. Of particular interest in this study was the dynamic response of the bridge structure relative to the pile foundation in the transverse direction at the mid-span Pier E-7.

Due to the uncertainty of sensor orientations within the retrofitted pile, cross-correlation analyses were performed to check for potential azimuthal error. It was found that sensors at the elevation of -16.46 m need to be rotated 8.5 degrees (clockwise) based on cross-correlation between the EBGS motion and the EBPF responses. For the sensors at elevation of -10.36 m, 22.1 degrees rotation is needed for the highest correlation with the recorded pile cap response.

As such, based on comparisons of the displacement time histories in Figure 8.15-Figure 8.18, it can be concluded that the pile cap and bridge deck displacements are noticeably different. Relative displacement time histories during the low amplitude shanking event (the 2007 Ferndale Earthquake) show a clear dominant fundamental response period. The bridge displacements are due to deformation of the pile and the pier as well (Figure 8.19 and Figure 8.20).

8.4.4 Abutment and Bridge Response along Mud-line

Figure 8.21 and Figure 8.22 compare the acceleration and displacement time histories of bridge base along the ground surface (including motions at the EBGS, the EBPF, on the pile cap near ground surface and at the bridge abutments). It was observed that displacement time histories are of the similar pattern. In the longitudinal direction, spikes were observed at the abutment and on the pile cap of Pier E-3 during the moderate event. All these observations indicate that the motions recorded on the E-3 pier footing, on the pile at elevation of -10.36 m and on the abutment of Pier E-16 are affected by the bridge response. For this curved bridge, motions recorded at the ground surface and at the EBPF (-16.46 m below MSL) can potentially be used as input excitation for general numerical modeling procedures.

8.5 System Identification for the Ground-Foundation-Bridge System

8.5.1 Site Response and Nonlinearity

During the moderate event, nonlinearity of the site seismic response was evident through analysis of the nearby Eureka geotechnical downhole (GDA) array data. The recorded data at this downhole site allows for a better understanding of the ground seismic response in which the Eureka Channel Bridge foundations are embedded. Details of the strong motion data analysis for the GDA can be found in Chapter 5.

8.5.2 Bridge Sub-system Resonances

Transfer Function (TF) defined as the ratio of the cross power spectral density ($P_{yx}(f)$ with seismic input signal x and output response y) and the power spectral density

(P_{xx} (f)) is employed to assess the system and sub-system resonant frequencies. In the transverse direction, the fundamental frequency for Deck-Pier sub-system (deck response referenced to pile cap response) at Pier E-7 is in range of 2.42-2.54 Hz for the low amplitude earthquakes. The same logic is then employed to relate the deck response to that of the pile at -16.46 m (taken here to be the fixed base), and also related to the nearby free-field ground surface motion. A Hanning window and 50% overlap is adopted to reduce the effects of spectral leakage. The first natural frequency for this bent of the bridge system was found to be around 1.5 Hz during these low amplitude earthquakes. Short time Fourier transfer function contours in Figure 8.23 - Figure 8.25 indicate that the dominant frequencies stay the same with time. A summary of the TF results for 4 small earthquakes (Table 8.2 and Table 8.3) is presented in Figure 8.26 and Figure 8.27.

8.6 Finite Element Analysis

8.6.1 Finite Element Modeling

Based on time history data analysis, Pier E-7 could be considered, in an approximate manner, to move independently of the influence of the rest of the bridge (in the transverse direction). In the following sections, a linear elastic OpenSees FE model of Pier E-7 (including the deck, the Pier, and the pile group below) is developed based on the "as-built" geometry of the bridge and updated with column/pile foundation stiffness based on the identified characteristics. This model consisting of point masses at the bridge deck level and the pile cap level is connected by linear elastic beam-column elements. With the aid of the SNOPT optimization tool implemented in the OpenSees platform, an attempt is made to demonstrate variations of flexibilities for the ground-foundation system. In particular, valuable insights can be gained about: (i) nonlinear stiffness reduction levels for the column, (ii) nonlinear stiffness reduction levels for the foundation, (iii) equivalent base spring to represent the ground-foundation system below Pier E-7, and (iv) variation of spring values at the bridge pile group foundations.

8.6.2 Structural Modeling of the Column at Pier E-7

The bridge column at Pier E-7 (Figure 8.28) was modeled with elastic beam-column elements. Center-to-center mass of the bridge deck above E-7 (including mass of deck, longitudinal I-girder and transversal beams), mass of the hammerhead column top and half mass of the column is defined as the point mass at the center of gravity for the Deck-Girder system. Calculations of masses were based on the density and volume of structural components. Since seismic motion at the pile cap level is known from the records (Channel 3), boundary condition at the base of the column is considered to be fixed in all DOFs with this prescribed motion time history (Figure 8.28).

The following material parameters were used for this idealized FE model (Caltrans 2002b): reinforced concrete mass density ρ= 2560 kg/m3, Young's modulus E=2.51×10^7 kPa (compressive strength $f_c' = 28\text{MPa}$) for existing reinforced concrete and Young's modulus E=2.39×10^7 kPa (compressive strength $f_c' = 25\text{MPa}$) for retrofit reinforced concrete, Poisson's ratio ν=0.2 for concrete and Young's modulus $E_s = 2.0 \times 10^8$ kPa for steel.

For the FE analysis, gross moment of inertia for the concrete column based on the uncracked section is employed. Flexural stiffness (EI) of the connecting bending beams is then calibrated through eigenvalue analysis to match the identified bridge-bent resonant frequencies in Table 8.2. The pier column stiffness (Table 8.4) appears to be noticeably smaller than calculations might imply (about 54% times of the gross EI is engaged). It agrees well with the common Caltrans practice where effective moment of inertia is the range between gross and cracked moment of inertia (Caltrans 2012; 2013). As such, the calibrated pier stiffness includes contributions from interaction (resistance) due to the overall bridge connectivity. It is noted here that no recorded deck motion was available for the moderate event, which did not permit for conducting a similar analysis.

8.6.3 Structural Modeling of the Pile Foundation below Pier E-7

As shown in Figure 8.29, center-to-center mass of the bridge deck above E-7 (including mass of deck, longitudinal I-girder and transversal beams), mass of the hammerhead column top and half mass of the column is defined as the 1st point mass at the center of gravity for the Deck-Girder system. Half mass of the column, mass of the pile cap, and half mass of the pile groups is lumped at the elevation of the pile cap level (2nd point mass). As presented earlier, seismic motion at the pile -16.46 m below the mean sea level is known from the records (Chan 27). Base boundary condition for the pile foundation is considered to be fixed in all DOFs with prescribed motion time history at this location. The pile cap mass location was assumed to be fixed against rotation (due to the spatial extent of the underlying pile group).

The pier column and pile foundation (taken as a single equivalent super-pile with the union of the cross section of all the piles) is modeled with linear beam-column elements (Figure 8.29). A large EI is set for the element representing the pile cap in order to achieve rigidity.

Based on eigenvalue analysis, one might calibrate the pile group foundation lateral stiffness to match with the identified bridge resonant frequency (Figure 8.30). It turns out that the employed quantities amounted to a factor of about 2.90 for the stiffness of pile group foundation (Table 8.5 low amplitude earthquakes). This stiffness for the pile might be reasonable considering the support provided by the surrounding soil. Unlike the Samoa Channel Bridge, most of pile foundation below Pier E-7 is embedded in the ground. It is noted here that no recorded deck motion was available for the moderate event, which did not permit for conducting a similar analysis.

Computational simulation results show a reasonable match from the pile cap to the deck (column part, Figure 8.31) and from the base to the deck (Figure 8.32 and Figure 8.33). As such, the calibrated stiffness includes contributions from interaction (resistance) due to the overall bridge connectivity, and the pile foundation lateral stiffness implicitly accounts for SSI. Stiffness adjusting factors obtained from this study provide a reference for seismic and SSI considerations and are to be further refined based on additional more representative investigations.

8.7 Numerical Simulation for the Eureka Channel Bridge

A Finite Element model of the Eureka Channel Bridge representing the super-structure down to the pile cap locations was developed using linear beam-column elements. The recently developed software MSBridge (Elgamal et al. 2014) is employed to generate the mesh for this curved bridge (Figure 8.34).

8.7.1.1 Modeling of Super-Structure

The section properties of the cast-in-place deck slab on prestressed I-girder sections are calculated as a box girder shape using the software CTBridge. A reduction factor of 0.54 for the uncracked EI of the columns was employed as suggested from the above analysis of bent E-7 response. Properties of the bridge deck section and pier column section are listed in Table 8.6 and Table 8.7 on the basis of the blue prints (Caltrans 2002b).

8.7.1.2 Modeling of Joints between E-7 and E-8

Generally, longitudinal stiffness is a function of the interaction between pier stiffness, bearing types and joint locations. For the simplified FE model presented in this chapter, separation joints between bent 7 and bent 8 are defined simply by a hinge system composed of zero-length elements in OpenSees to represent cables, bearing pads and compression connectors (with equalDOF constraints for vertical translations and rotations).

8.7.1.3 Modeling of Abutments

An elastic abutment model consisting of a series of rigid elements and zero-length elements at each end of the bridge is employed. A rigid element with abutment width orientated in the transverse direction is connected through a rigid joint to the bridge center line. Two zero-length elements are distributed along the rigid element at each bridge end. In the longitudinal direction, the abutment stiffness (K_{abut}) is specified as 760.8 kN/mm, obtained from equation 7.43 and 7.44 of SDC 2010 (Caltrans 2013). In the transverse direction, a zero-length element is defined at each end of the rigid link with an assigned elastic spring of K=225.42 kN/mm, by multiplying the longitudinal stiffness with wing wall effectiveness of 2/3, participation coefficients of 4/3 and 1/3 length of the back wall (Caltrans 2013; Elgamal et al. 2014). An elastic spring with very high stiffness is defined at each end of the rigid link in the vertical direction.

8.7.1.4 Modeling of Base Springs

Linear lateral springs were attached to the base of superstructure (at the pile cap location) to account for stiffness of the underlying pile foundations and the soil-foundation-structure interaction (Figure 8.35). Recorded motion at -16.46 m of the retrofitted pile is employed as the uniform base dynamic excitation at the ends of springs along the bridge length. Base springs representing the stiffness of the pile foundation at pier E-7 in the local transverse direction is identified using the SNOPT optimization tool (Table 8.8). To this end, the FE model for the isolated Pier E-7 with optimized spring value provided a good match with the recorded pier response (Figure 8.36 and Figure 8.37).

A Finite Element Model for the Pier E-7 ground-pile foundation system is developed (details in section 8.8). Pushover analysis is performed bi-directionally and the longitudinal stiffness for this pile foundation is identified as 87% of that in the transverse direction. As such, an initial trial value for all base springs (except the one below Pier E-7) was defined as 90,000 kN/m in the transverse direction and with a reduction factor (0.87) in the longitudinal direction.

A challenging task is to calibrate the spring values to satisfactorily match the data set simultaneously. Determination of linear foundation stiffness at individual locations was achieved by using the extended OpenSees-SNOPT framework (Gu 2008). Optimized spring values along the bridge are shown in Figure 8.38. Corresponding displacement/ acceleration time histories during the moderate event are shown in Figure 8.39-Figure 8.41. Overall, it is found that computed response of the bridge model is in good agreement with the recorded motions at various locations of the bridge.

8.8 3D FE Modeling of Pile Groups at Pier E-7

Using OpenSeesPL, a computational study based on 3D OpenSees finite element modeling is performed to evaluate the large pile-ground system stiffness under static lateral load. A model that is representative of salient characteristics of the Eureka Bridge (California) Pier E-7 (Figure 8.42) pile-group foundation geometry was studied. The pile group consists of 8 original concrete piles and 4 cast-in-steel-shell (CISS) retrofit piles (Figure 8.43). The existing piles are configured in a 4 x 2 arrangement with spacing of 2 pile diameters (2D) in the longitudinal and transversal directions on center.

The original pile is 1.37 m in diameter with a wall thickness h = 0.127 m. Each concrete pile is encased by a prestressed concrete shell and filled with class B concrete for their entire length of 25.3 m (Caltrans 2002b). The group is rigidly connected by a pile cap 4.915 m above the mudline.

The gross bending stiffness for the original pile was modeled as EI = 2.9 x 10^6 kN-m^2 and 1.51 x 10^6 kN-m^2 for retrofit pile based on the as-built geometry (Caltrans 2002b). Pile response was assumed to remain linear. As modeled in this study (Table 8.9), the top soft clay layer is 6.0 m in thickness, overlying a medium clay layer. The bottom stiff clay layer had a thickness of 32 m. A Poisson's ratio of 0.33 was specified for all layers. Due to the presence of water submerged density is employed for the simulation.

In the employed ½ mesh of (due to symmetry), a lateral pile cap longitudinal load was applied to a maximum of 2500 kN (Figure 8.44). The length of the mesh in the longitudinal direction is 317.81 m, with 153.425 m transversally (in this half-mesh configuration, resulting in a 317.81 m x 306.85 m soil domain in plan view). Total layer thickness was 44.2 m (the base of the soil domain is 23.816 m below the pile tip). The soil domain was modeled by eight-node brick elements and the piles were modeled by beam-column elements. Rigid beam-column elements were used around each pile to model the actual circumferential pile size (diameter).

Five case scenarios were conducted and compared to each other (Table 8.10): When the piles are considered embedded in soil instead of rock, with a reduction factor of 0.3 for pile uncracked cross-section (k_{trans} = 1.90 x 10^5 kN/m, k_{long} = 1.52 x 10^5 kN/m), the k_{trans} value is in the range of what was obtained from the bridge model optimization for Pier E-7 during the small earthquakes. With a pinned head boundary condition, relatively low value of k =118,000 kN/m with gross pile properties revealing the effect of pile cap connection.

8.9 Conclusions

In this chapter, a comparison of the measured displacement time-history records indicated that: (1) unlike seismic response of the Samoa Channel Bridge, the relative displacement between the top and bottom of Pier E-7 is noticeable indicating a relatively stiffer pile group behavior, (2) displacement time histories at ground surface and at the -16.5 m depth location of the pile followed similar wave patterns.

An OpenSees FE model of the bridge was developed and calibrated based on the observed seismic response. Computed bridge response was generally comparable to the actual measurement in the time domain indicating that the adopted strong motion data analysis techniques have captured salient seismic characteristics and are helpful for calibration of the FE model.

8.10 Acknowledgements

Chapter 8 of this dissertation is based on material from a manuscript under preparation for publication, tentatively titled “Recorded Seismic Response of Eureka Channel Bridge-Foundation System and Adjacent Downhole Array”, with co-author Ahmed Elgamal. The dissertation author is the first author and primary investigator of this paper.

Table 8.1: Recorded peak acceleration for recent earthquakes at the Bridge Site (arranged by order of peak acceleration)

Earthquake	Magnitude	Epicentral Distance (km)	Horiz. Peak Acc. (g)	
			Ground	Structure
Ferndale Jan 09, 2010	6.5 (M_w)	54.5	0.256	0.510
Ferndale Mar 09, 2014	6.8 (M_w)	82.6	0.027	0.072
Trinidad August 16, 2008	4.6 (M_w)	41.7	0.022	0.061
Humboldt Hill August 02, 2013	4.5 (M_L)	20.8	0.022	0.022
Trinidad June 24, 2007	5.1 (M_L)	65.6	0.020	0.081
Ferndale February 04, 2010	5.9 (M_w)	77.8	0.018	0.046
Willow Creek April 29, 2008	5.4 (M_w)	55.4	0.012	0.026
Ferndale February 26, 2007	5.4 (M_L)	63.2	0.011	0.021
Crescent City June 14, 2005	7.2 (M_L)	155.1	0.006	0.021

Table 8.2: Identified resonant frequency of bridge pier in the transverse direction

EQ	Fundamental Frequency (Hz) in transverse direction	
	Transfer Function $\frac{\text{deck}}{\text{Pile Cap}}$	MATLAB toolbox Parametric identification
Trinidad June 24, 2007	2.49	2.22
Willow Creek April 29, 2008	2.42	2.12
Trinidad August 16, 2008	2.54	2.16
Ferndale February 26, 2007	2.50	2.22

Table 8.3: Identified resonant frequency of bridge system in the transverse direction

EQ	Fundamental Frequency (Hz) in transverse direction		
	Transfer Function $\frac{\text{Deck}}{-16.5\text{ m}}$	Transfer Function $\frac{\text{Deck}}{\text{free field}}$	MATLAB toolbox Parametric identification
Trinidad June 24, 2007	1.52	1.52	1.59
Willow Creek April 29, 2008	1.57	1.43	1.56
Trinidad August 16, 2008	1.46	1.43	1.63
Ferndale February 26, 2007	1.59	1.63	1.59

Table 8.4: Optimized frequency and stiffness factor for pier at Pier E-7 based on uncracked section

Earthquake Event	Frequency (Hz)	Column Stiffness Factor
Trinidad June 24, 2007	2.34	0.54
Willow Creek April 29, 2008	2.46	0.60
Trinidad August 16, 2008	6.05	3.61
Ferndale February 26, 2007	2.33	0.53

Table 8.5: Optimized spring value representing pile foundation below Pier E-7

Earthquake	Optimized frequency (Hz)	Optimized stiffness factor for pile group
Trinidad June 24, 2007	1.51	2.93
Willow Creek April 29, 2008	1.52	2.98
Trinidad August 16, 2008	1.46	2.68
Ferndale February 26, 2007	1.54	3.07

Table 8.6: Employed Bridge Deck Properties for the FE Model

Cross Section	Span 1	Span 2	Span 3	E-7 & E-8	between E-7 and E-8	all other locations
Area of Cross Section (m^2)	3.57-3.72	3.72-4.17	4.17-4.68	4.75	4.05	3.77
Moment of Inertia @ Longitudinal Axis (m^4)	0.33-0.53	0.53-1.41	1.41-3.03	5.16	2.44	1.68
Moment of Inertia @ Vertical Axis (m^4)	27.90-29.17	29.17-32.93	32.93-37.22	41.10	35.25	32.91
Torsion Constant (m^4)	0.99-1.53	1.53-3.69	3.69-7.09	0.82	0.46	0.35

Table 8.7: Bridge Pier Column Properties

	E-7 and E-8	Piers except E-7 and E-8
Area of Cross Section	7.01 m^2	5.66 m^2
Transverse Moment of Inertia	7.06 m^4	5.11 m^4
longitudinal Moment of Inertia	1.88 m^4	1.15 m^4
Torsion Constant	5.77 m^4	3.53 m^4

Table 8.8: Optimized spring value representing pile foundation below Pier E-7

Earthquake	Optimized spring value K (kN/m)	Computed Frequency (Hz)
Trinidad Jun 24, 2007	1.77×10^5	1.51
Ferndale Feb 26, 2007	1.87×10^5	1.54
Trinidad Aug 16, 2008	1.61×10^5	1.46
Willow Creek Apr 29, 2008	1.79×10^5	1.52

Table 8.9: Soil Material Properties

Material Property	Thickness (m)	Total ρ (Mg/m^3)	V_s (m/s)
Soft clay	6.0	1.6	147.2
Medium clay	6.2	1.8	273.9
Stiff clay	32	2.0	387.3

Table 8.10: Effects of nonlinearity of pile and soil

Soil	Pile	K=F/D (kN/m)
Rock	Linear	24.76×10^6
	0.3 I_g*	8.26×10^5
Linear Soil	Linear	3.37×10^5
	0.3 I_g	1.90×10^5
	Pinned head	1.18×10^5

* I_g=moment of inertia of uncracked section

(a)

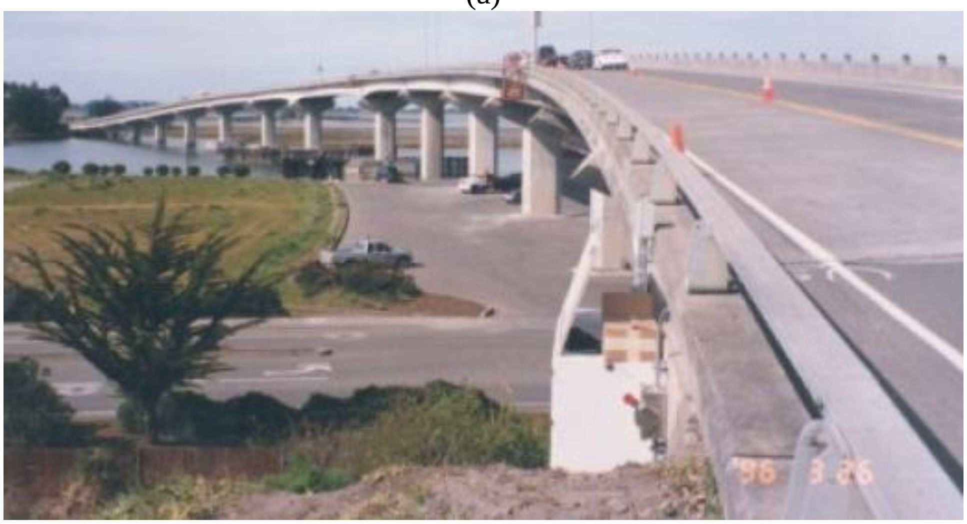

(b)

Figure 8.1: Bridge Configuration: (a) Samoa Channel Bridge, Eureka Geotechnical Array, Middle Channel Bridge and Eureka Channel Bridge (Map Data @ 2015 Google) and (b) photo of the Eureka Channel Bridge (http://www.strongmotioncenter.org)

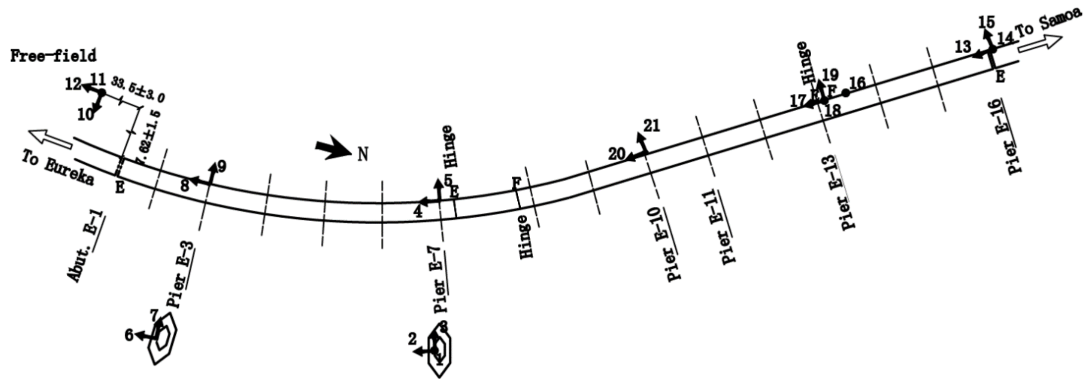

(a)

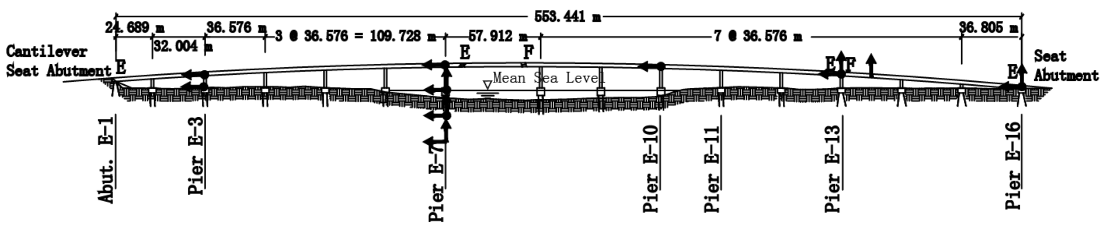

(b)

Figure 8.2: Layout of instrumentation at the Eureka Channel Bridge: (a) deck level plan and (b) elevation (http://www.strongmotioncenter.org)

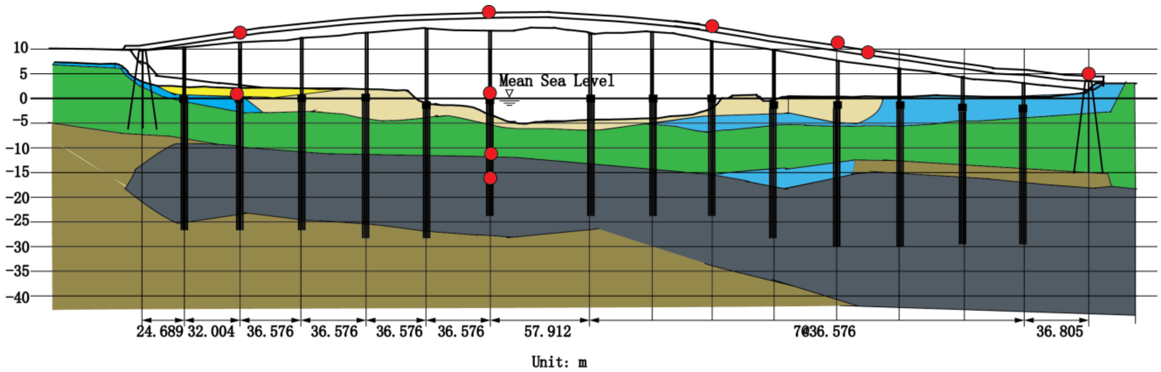

Figure 8.3: Soil Profile along the bridge (Caltrans 2002b)

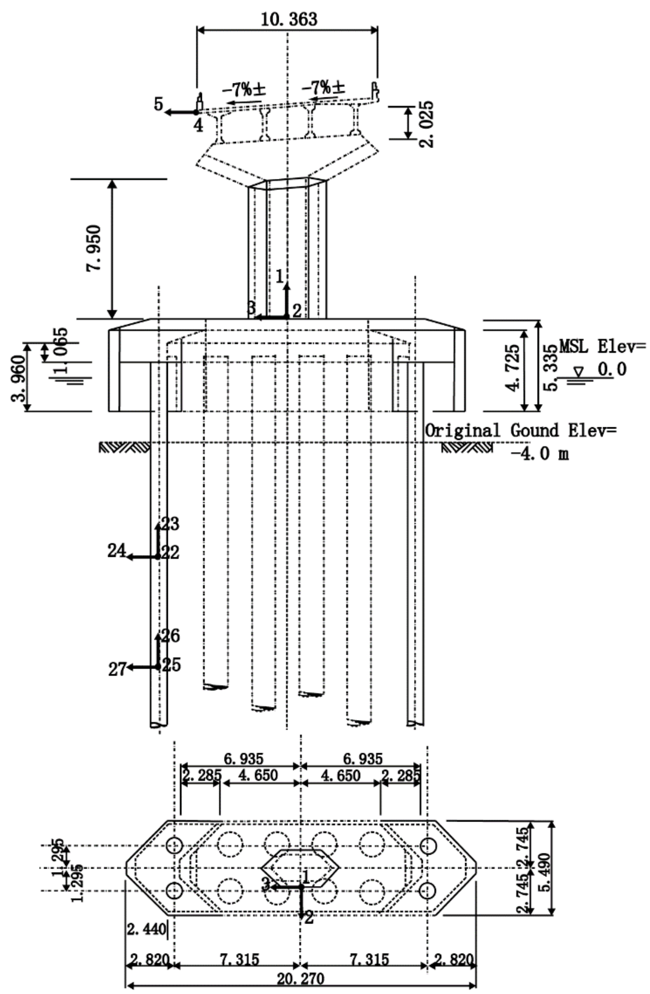

Figure 8.4: Layout of instrumentation and retrofit efforts at the Eureka Channel Bridge Pier E-7 (Caltrans 2002b)

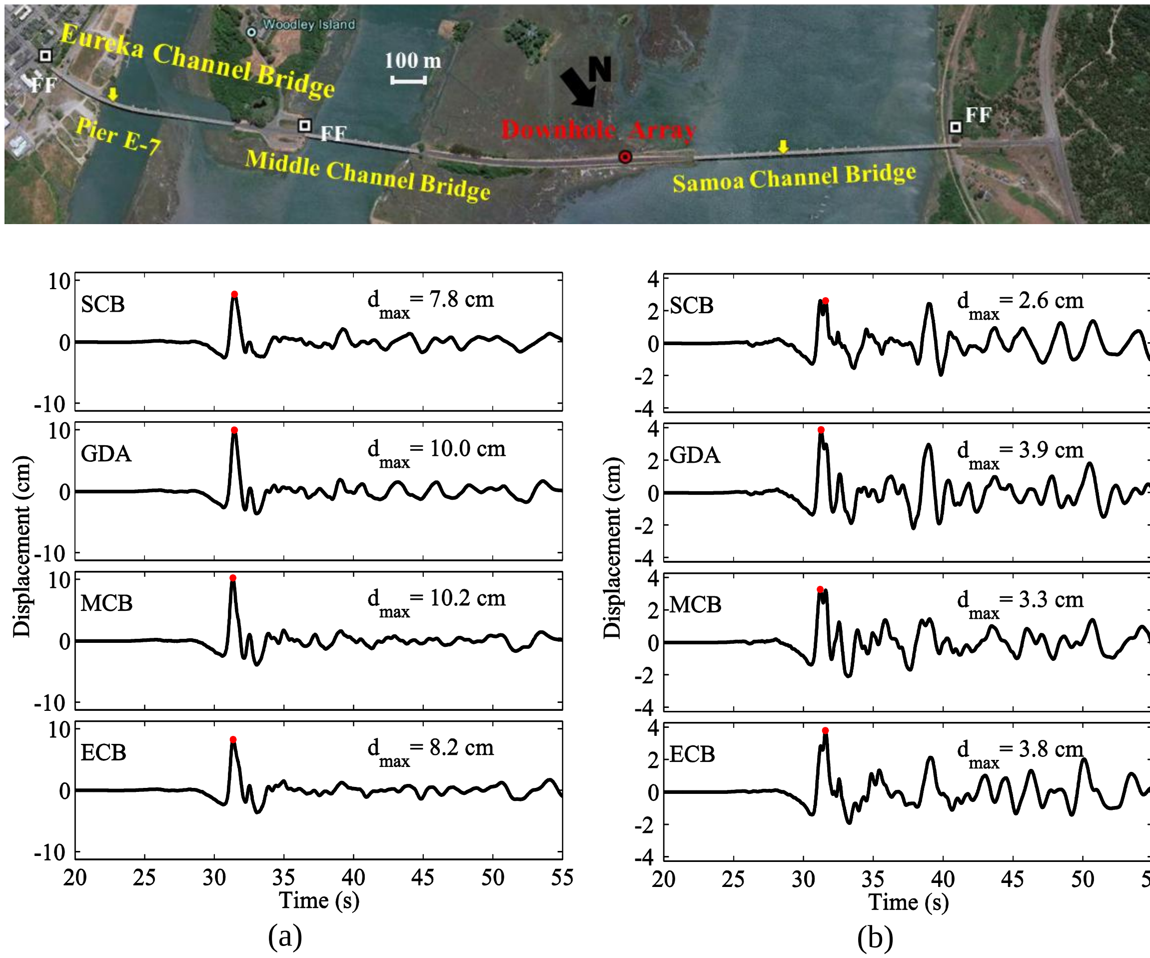

Figure 8.5: Displacements at the ground surface of the Samoa Channel Bridge (SCB), the Geotechnical downhole array (GDA), the Middle Channel Bridge (MCB) and the Eureka Channel Bridge (ECB) in the (a) NS and (b) EW directions during the moderate event

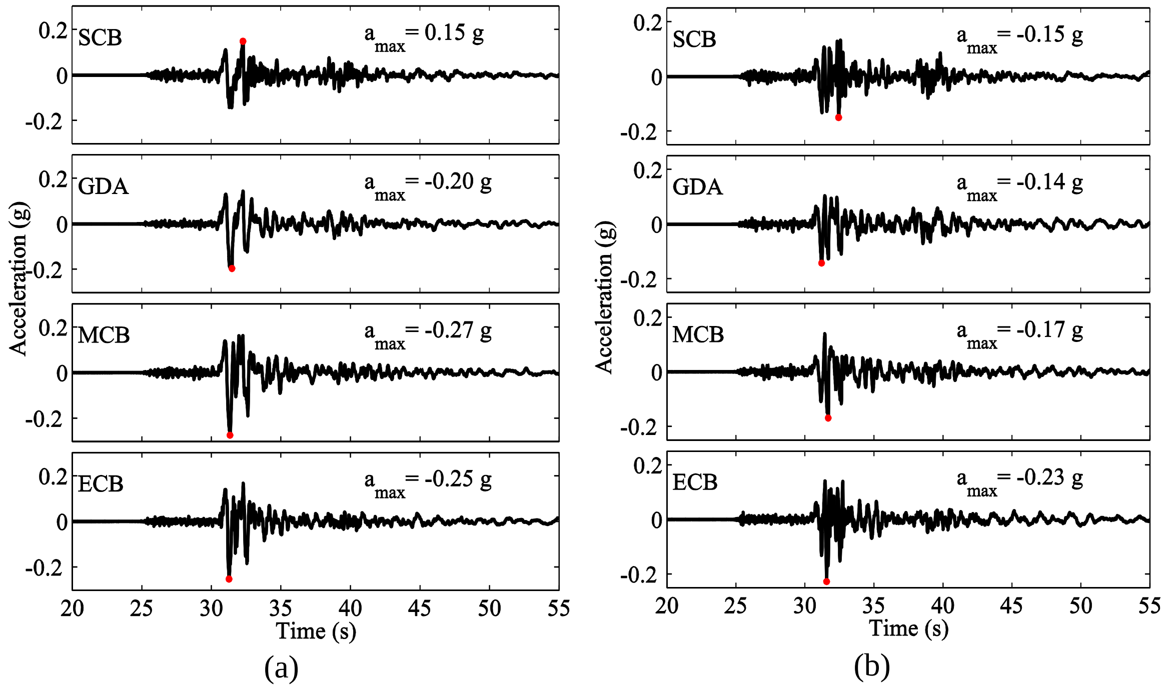

Figure 8.6: Accelerations at the ground surface of SCB, GDA, MCB and ECB in the (a) NS and (b) EW directions during the moderate event

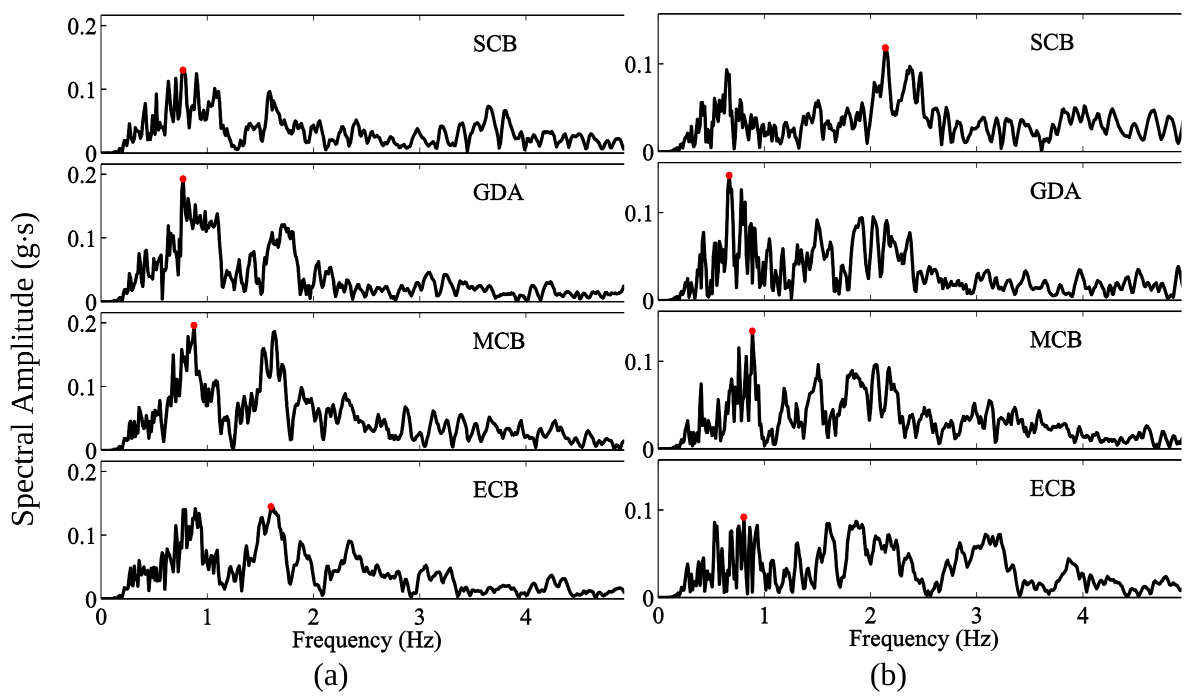

Figure 8.7: Fourier transformation of ground surface acceleration of SCB, GDA, MCB and ECB in the (a) NS and (b) EW directions during the moderate event

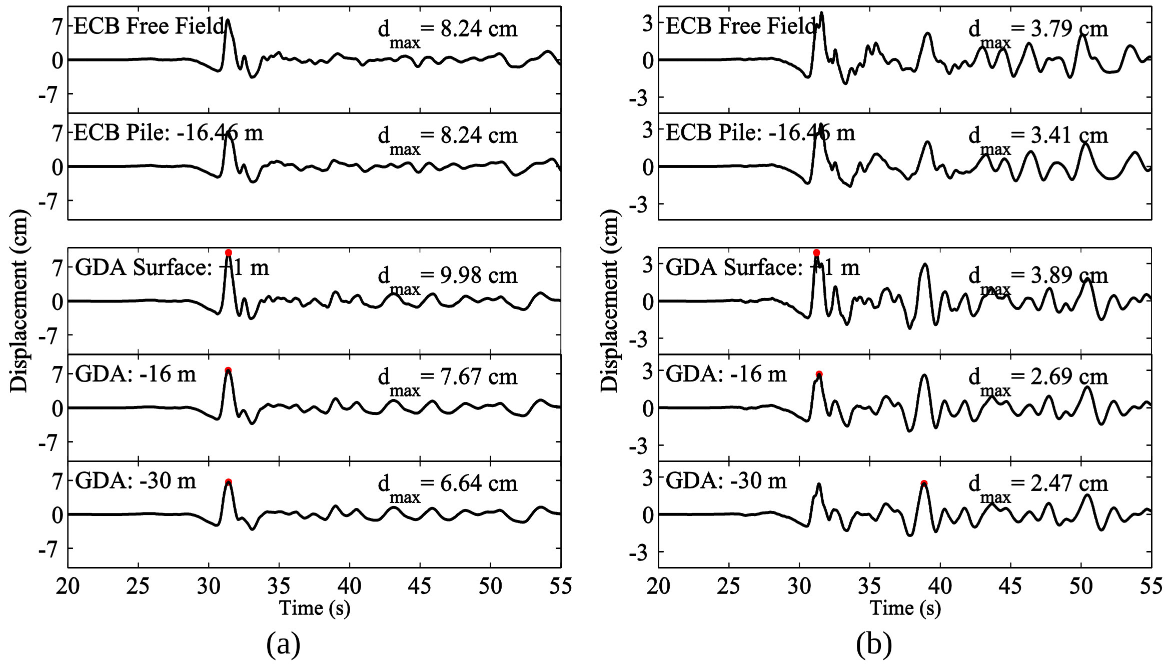

Figure 8.8: Displacement time histories in the (a) east-west (EW) and (b) north- south (NS) directions during the moderate event

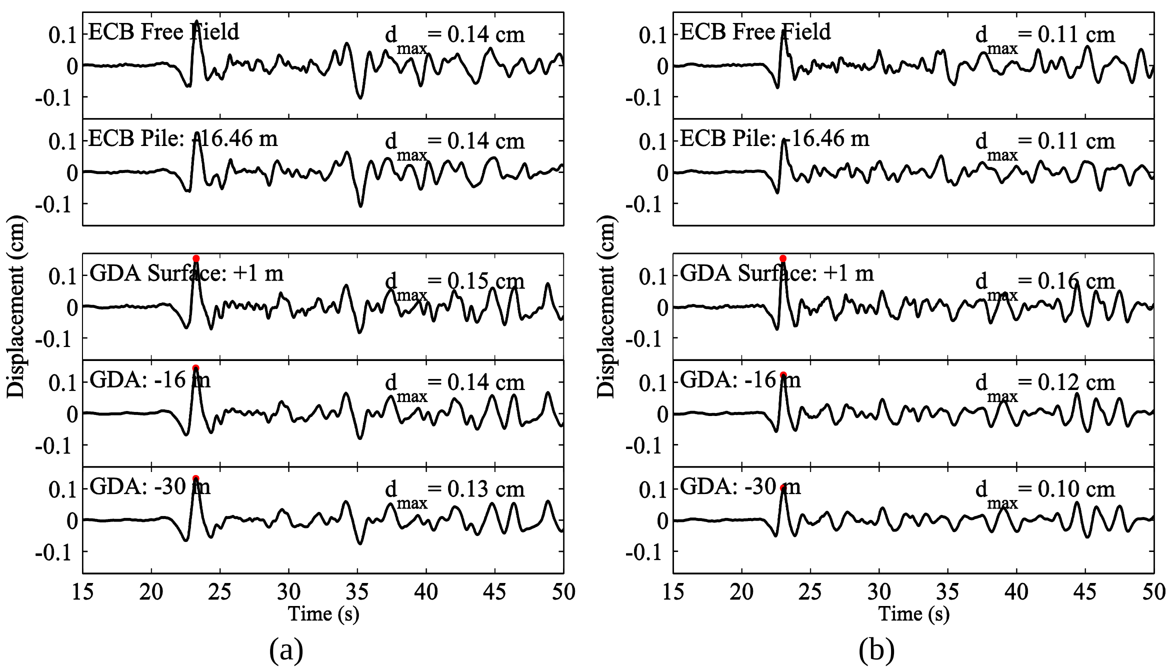

Figure 8.9: Displacement time histories in the (a) east-west (EW) direction and (b) north-south (NS) directions during the 2007 Ferndale Earthquake

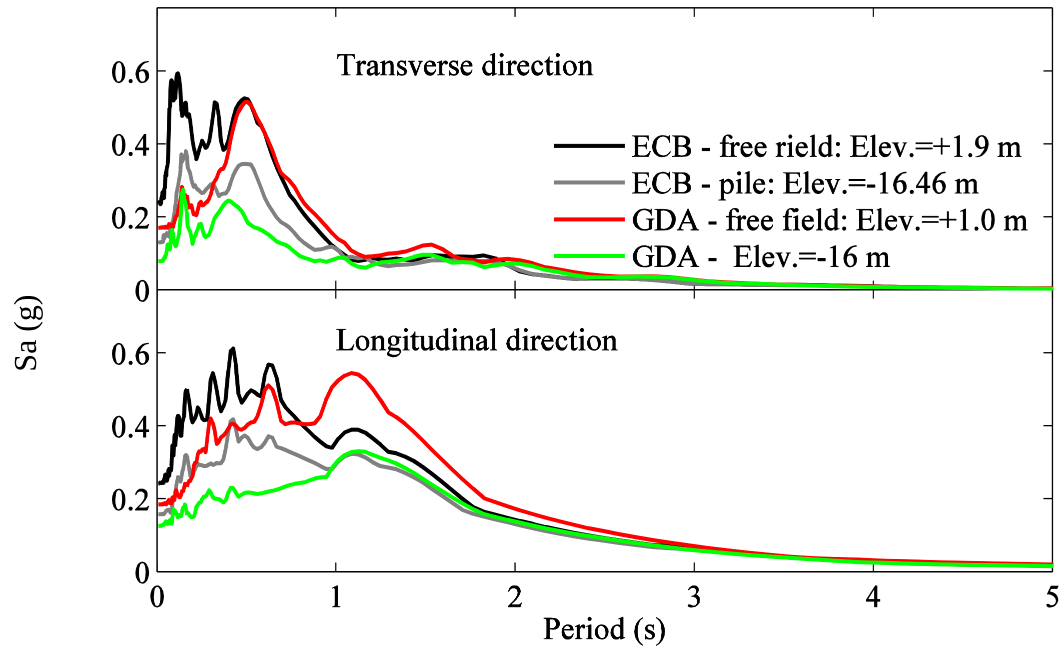

Figure 8.10: Eureka Channel bridge response spectra of free-field in the transverse and the longitudinal directions of Pier E-7 during the moderate event

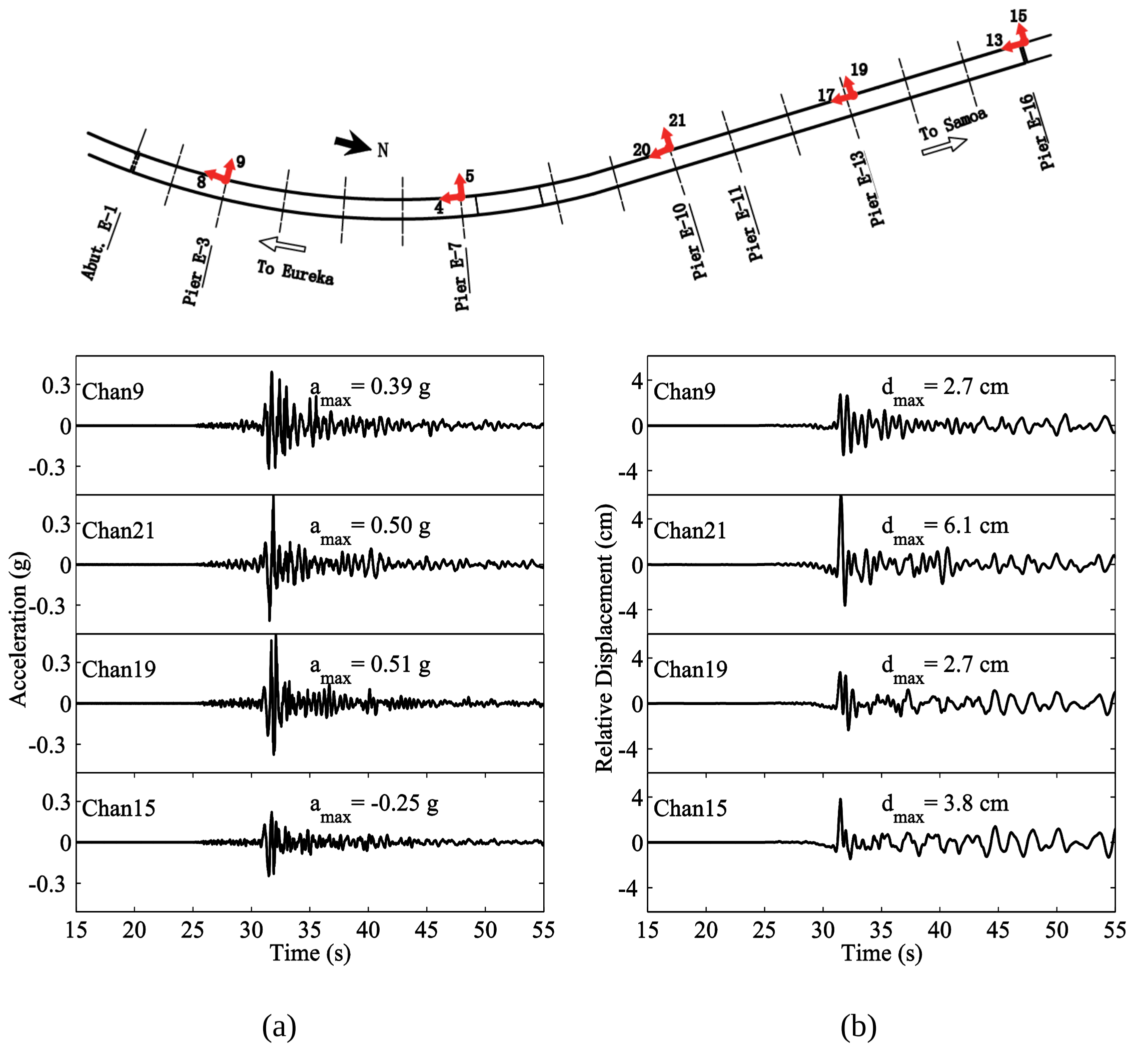

Figure 8.11: Variation of time histories at bridge deck level during the moderate event for (a) acceleration and (b) relative displacement time histories (Transverse shown)

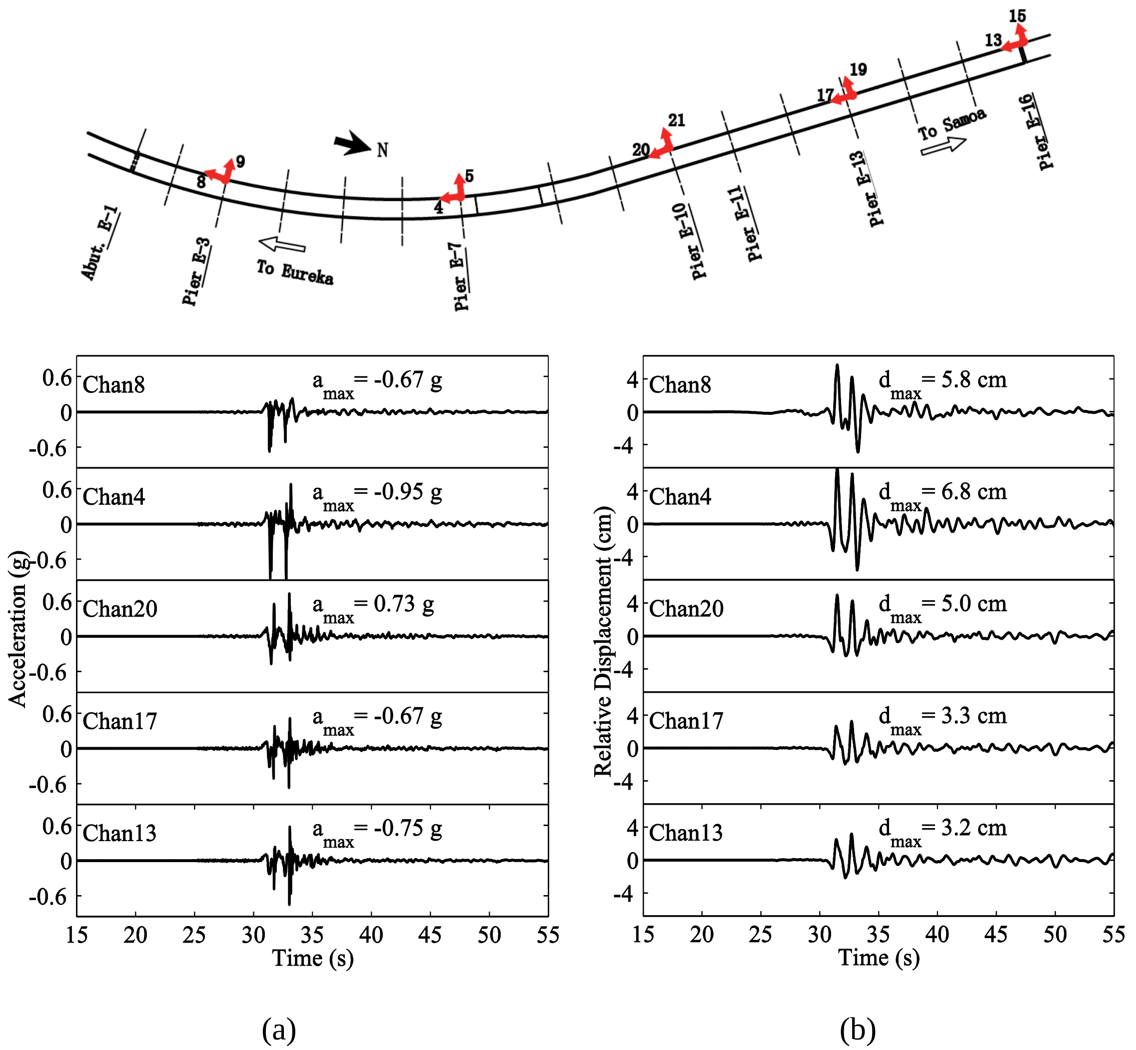

Figure 8.12: Variation of time histories at bridge deck level during the moderate event for (a) acceleration and (b) relative displacement time histories (Longitudinal shown)

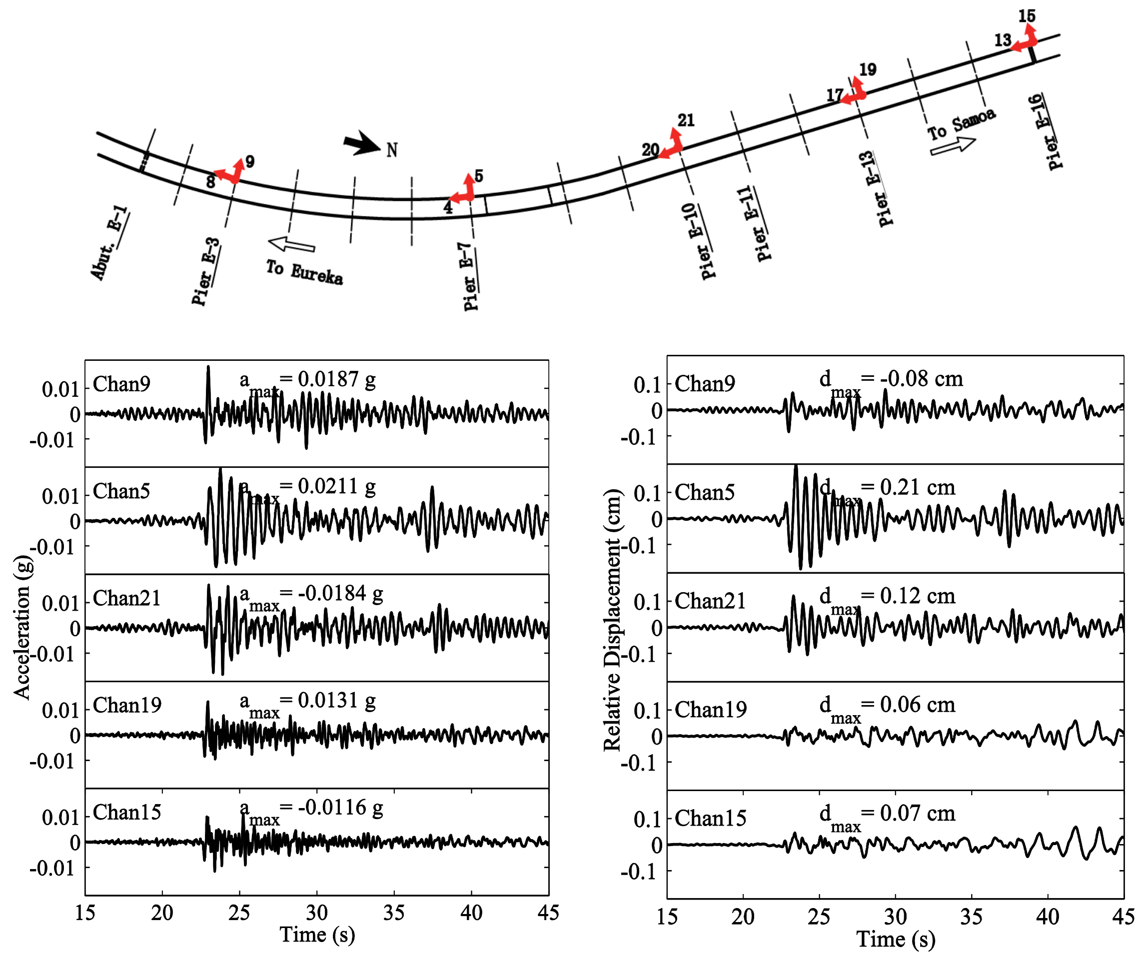

(a) (b)

Figure 8.13: Variation of time histories at bridge deck level during the 2007 Ferndale Earthquake for (a) acceleration and (b) relative displacement time histories (Transverse shown)

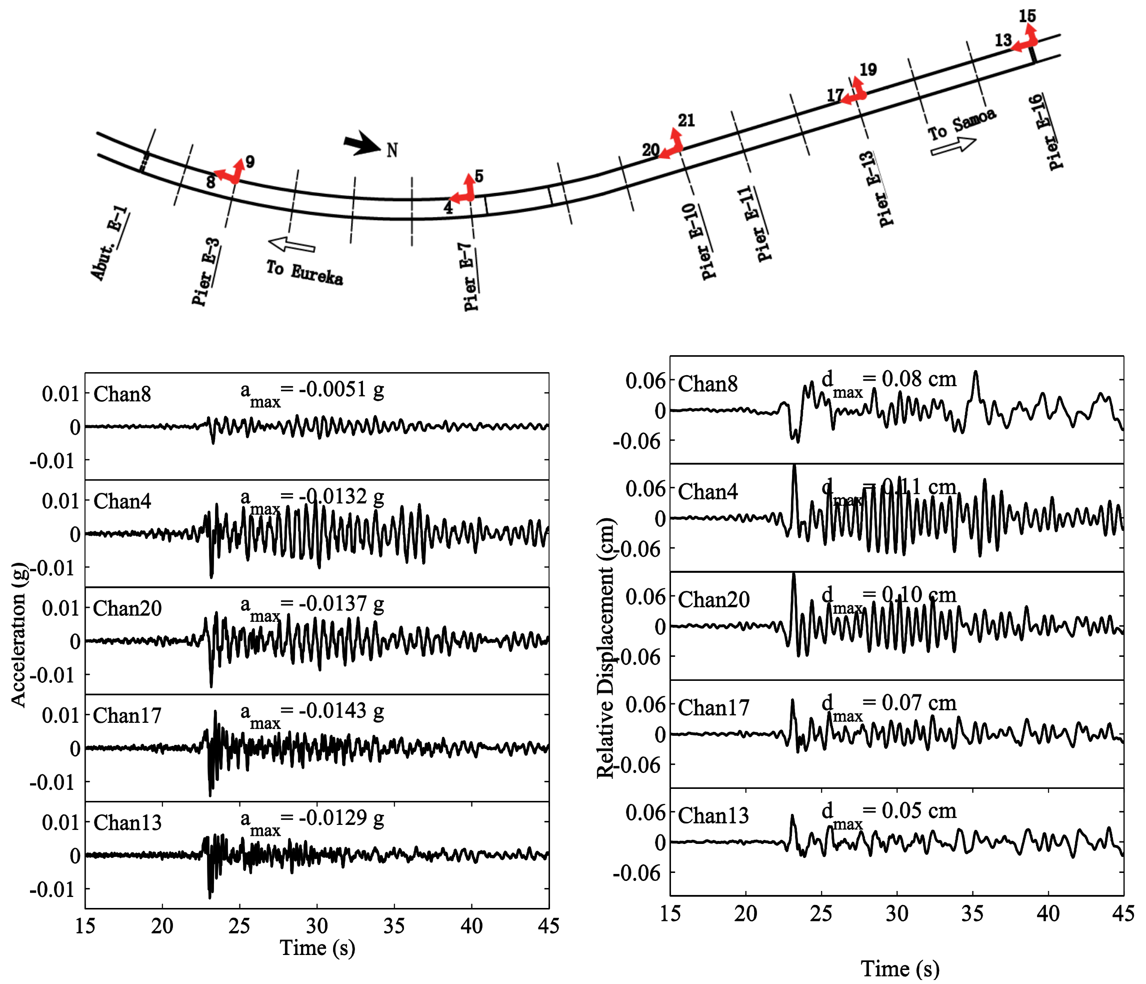

(a) (b)

Figure 8.14: Variation of time histories at bridge deck level during the 2007 Ferndale Earthquake for (a) acceleration and (b) relative displacement time histories (Longitudinal shown)

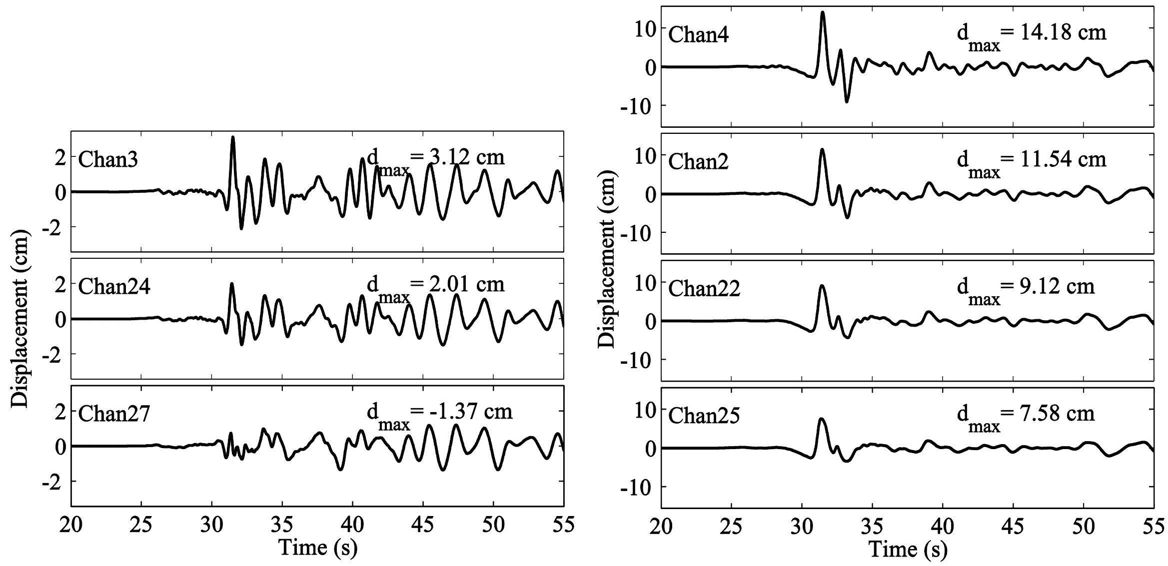

(a) (b)

Figure 8.15: Displacement time histories along Pier E-7: (a) in the transverse direction, (b) in the longitudinal direction during the moderate event

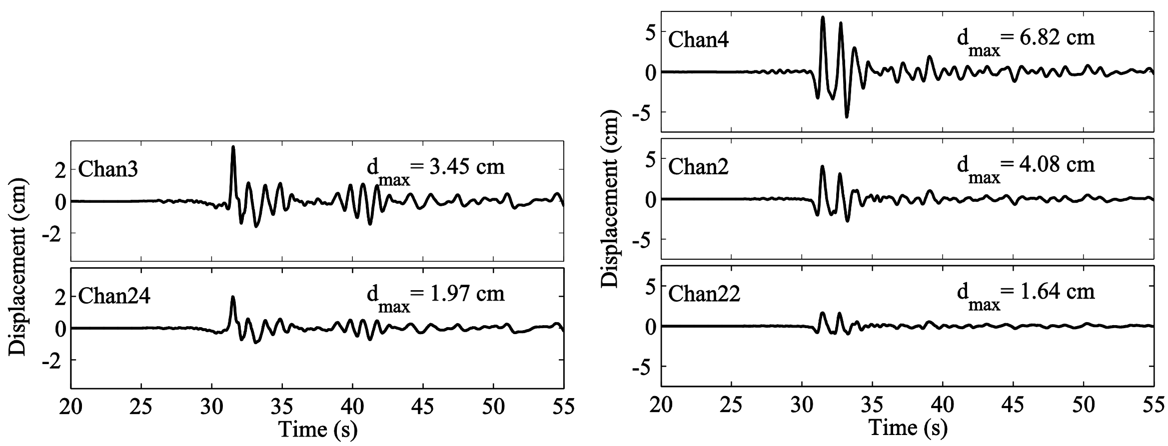

(a) (b)

Figure 8.16: Relative displacement time histories (referenced to the motions at EBPF station) along Pier E-7: (a) in the transverse direction, (b) in the longitudinal direction during the moderate event

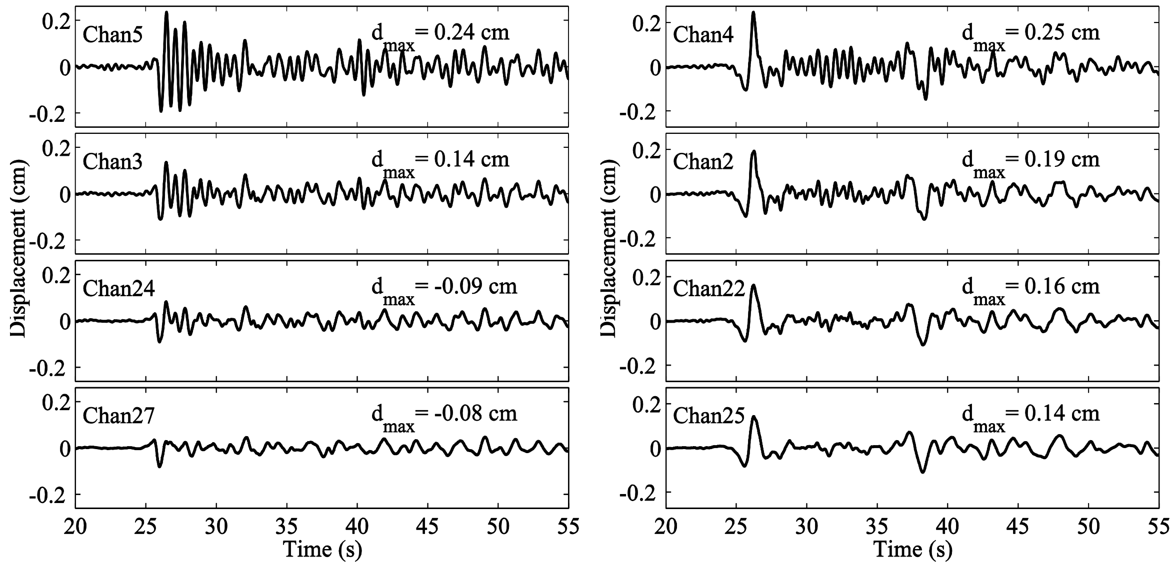

(a) (b)

Figure 8.17: Displacement time histories along Pier E-7: (a) in the transverse direction, (b) in the longitudinal direction during the 2007 Ferndale Earthquake

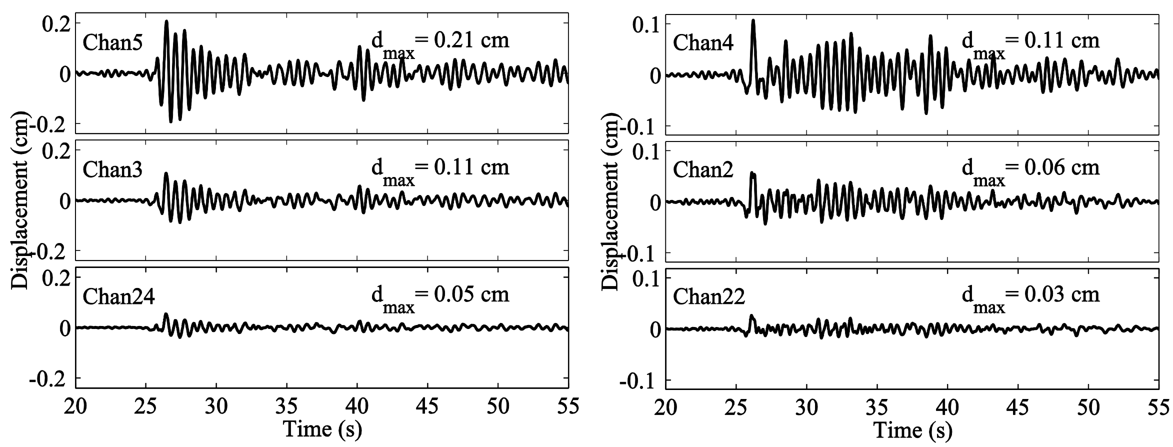

(a) (b)

Figure 8.18: Relative displacement time histories (referenced to the motions at EBPF station) along Pier E-7 during the 2007 Ferndale Earthquake: (a) Transverse and (b) Longitudinal

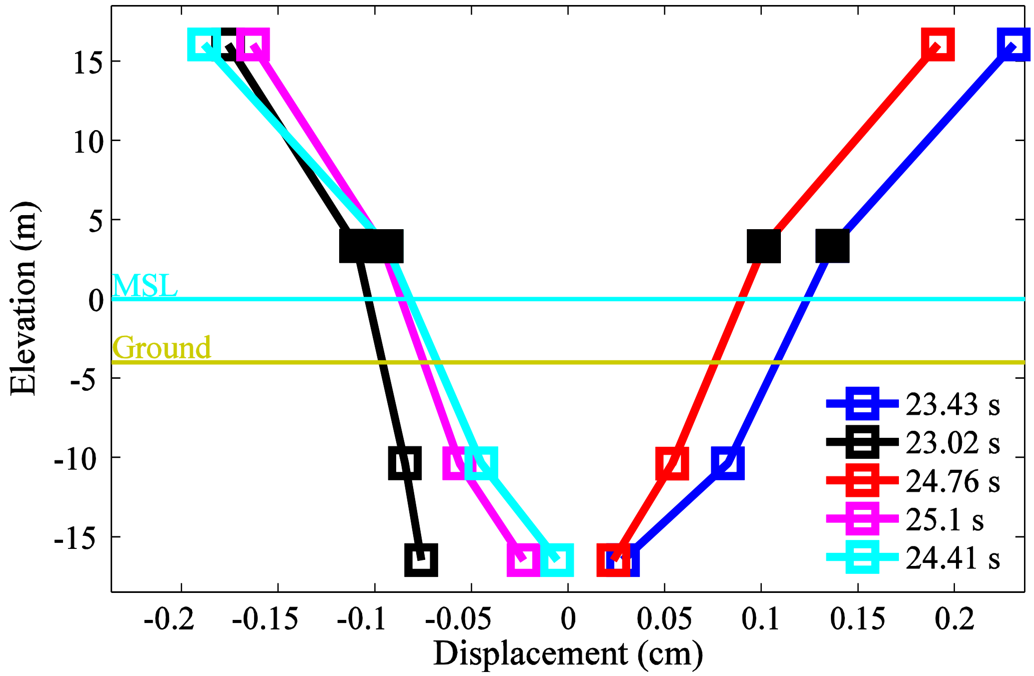

(a)

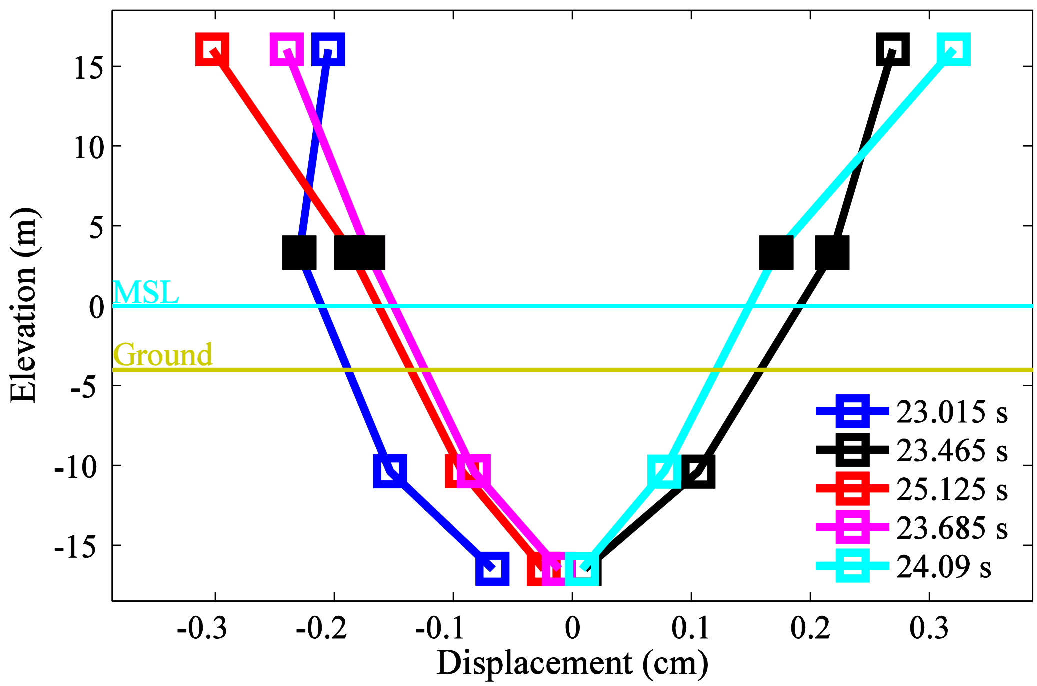

(b)

Figure 8.19: Displaced configuration of Pier E-7 for selected time instants during (a) the 2007 Ferndale Earthquake and (b) the 2007 Trinidad Earthquake (Transverse)

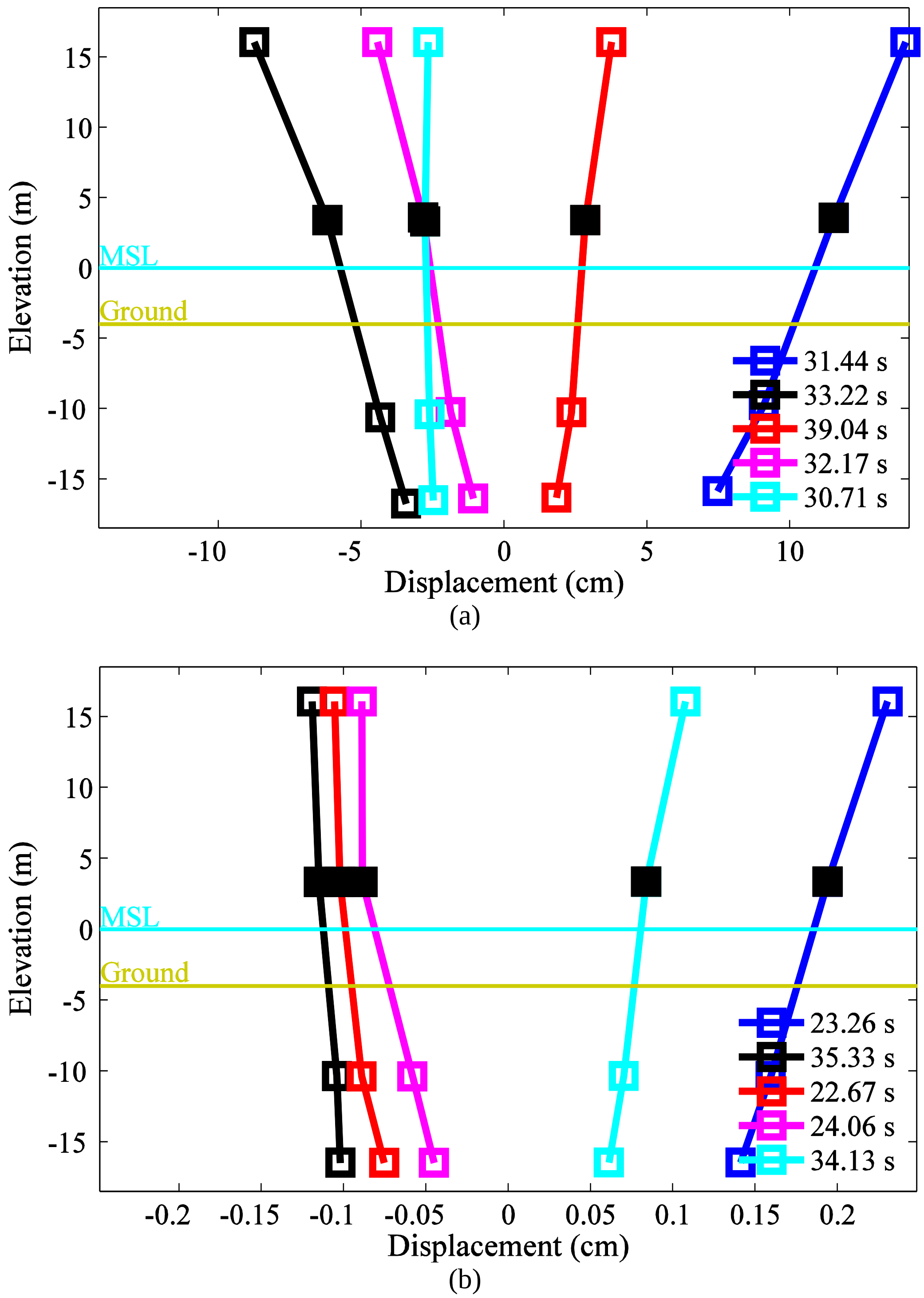

Figure 8.20: Displaced configuration of Pier E-7 for selected time instants during (a) the moderate event and (b) the 2007 Ferndale Earthquake (Longitudinal)

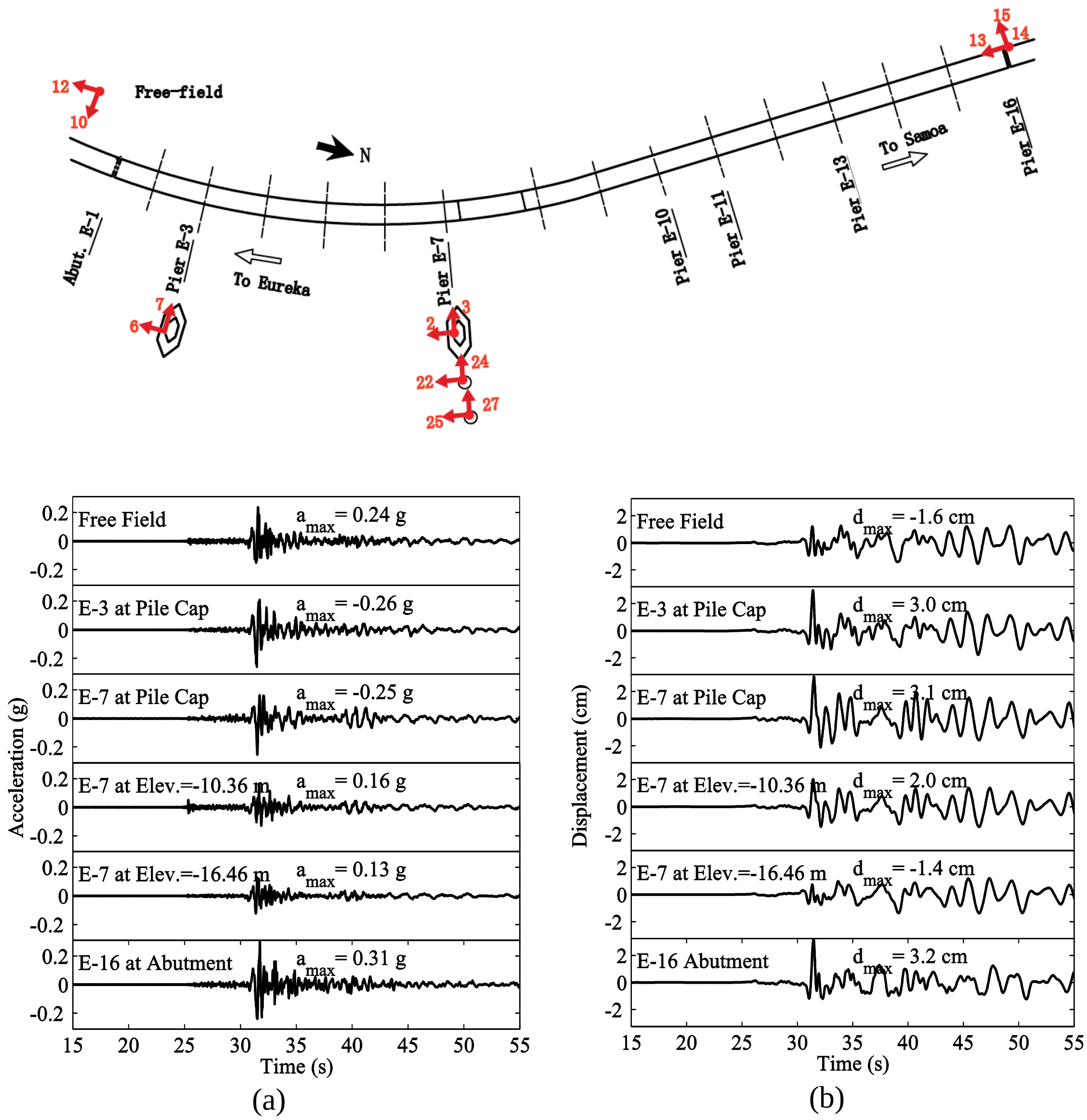

Figure 8.21: Variation of (a) acceleration and (b) displacement time histories along ground surface for the moderate event (in Tran direction of Pier E-7 shown)

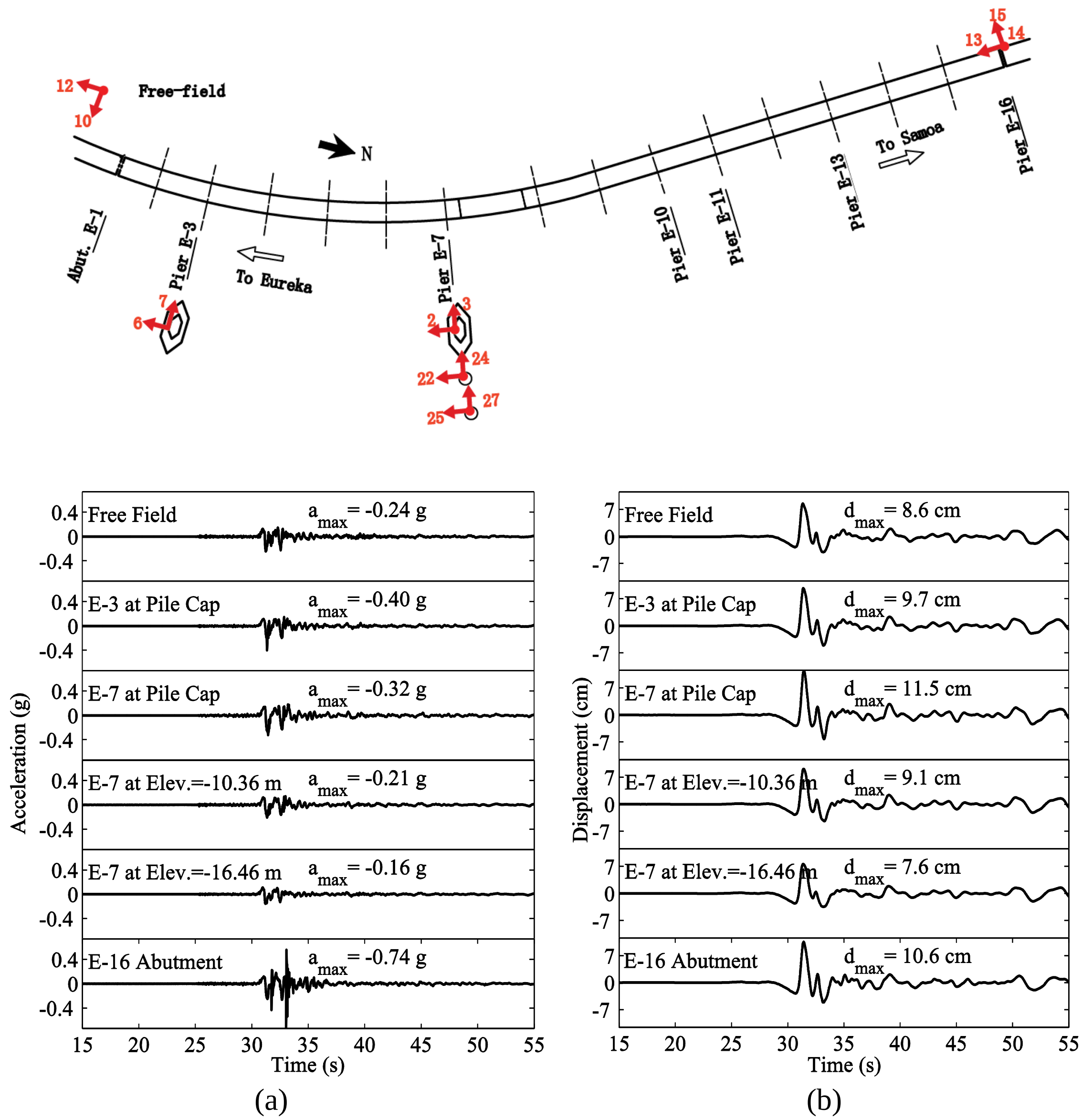

Figure 8.22: Variation of (a) acceleration and (b) displacement time histories along ground surface for the moderate event (in Long direction of Pier E-7 shown)

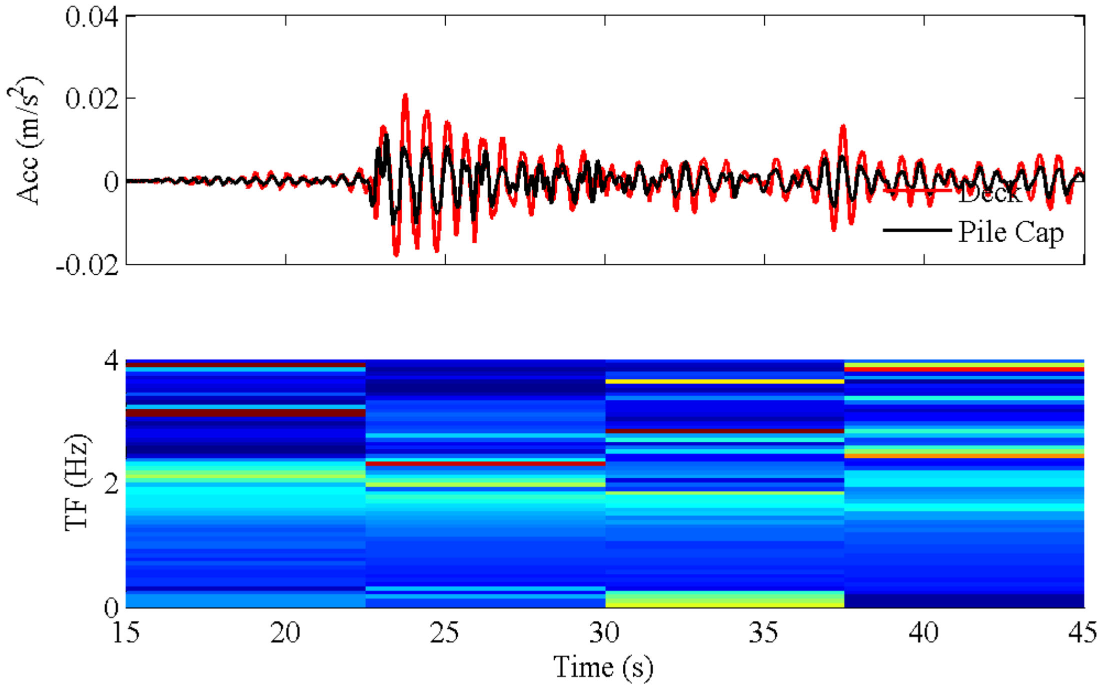

(a)

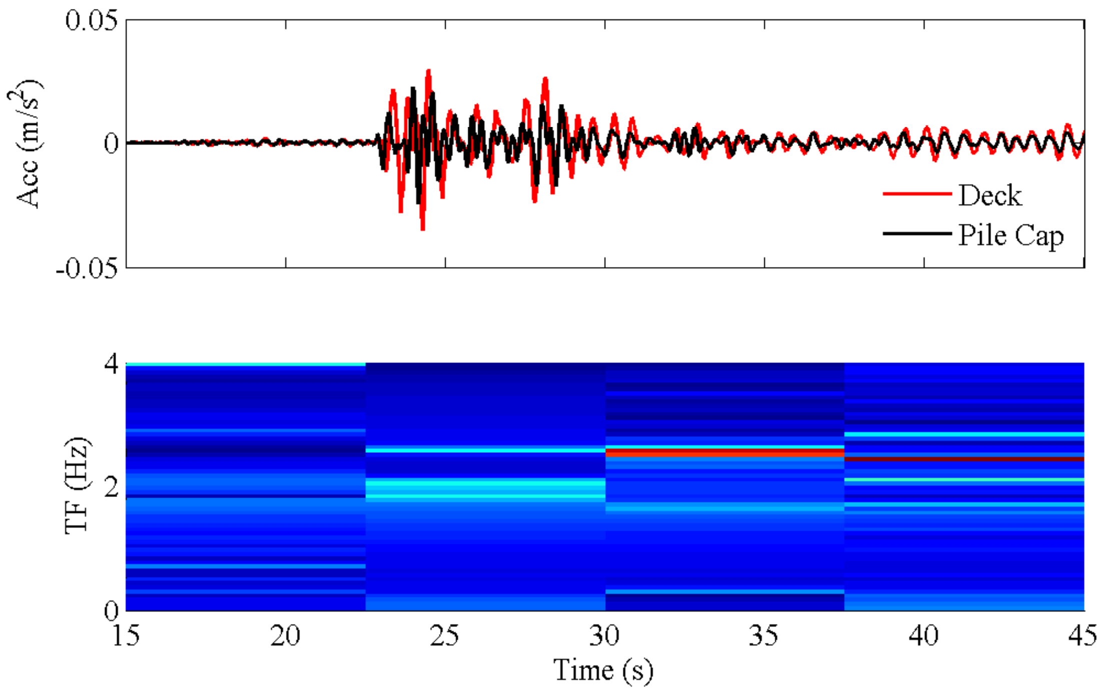

(b)

Figure 8.23: Short time transfer function plots in the transverse direction for deck response over pile cap response during (a) the 2007 Ferndale Earthquake and (b) the 2007 Trinidad Earthquake

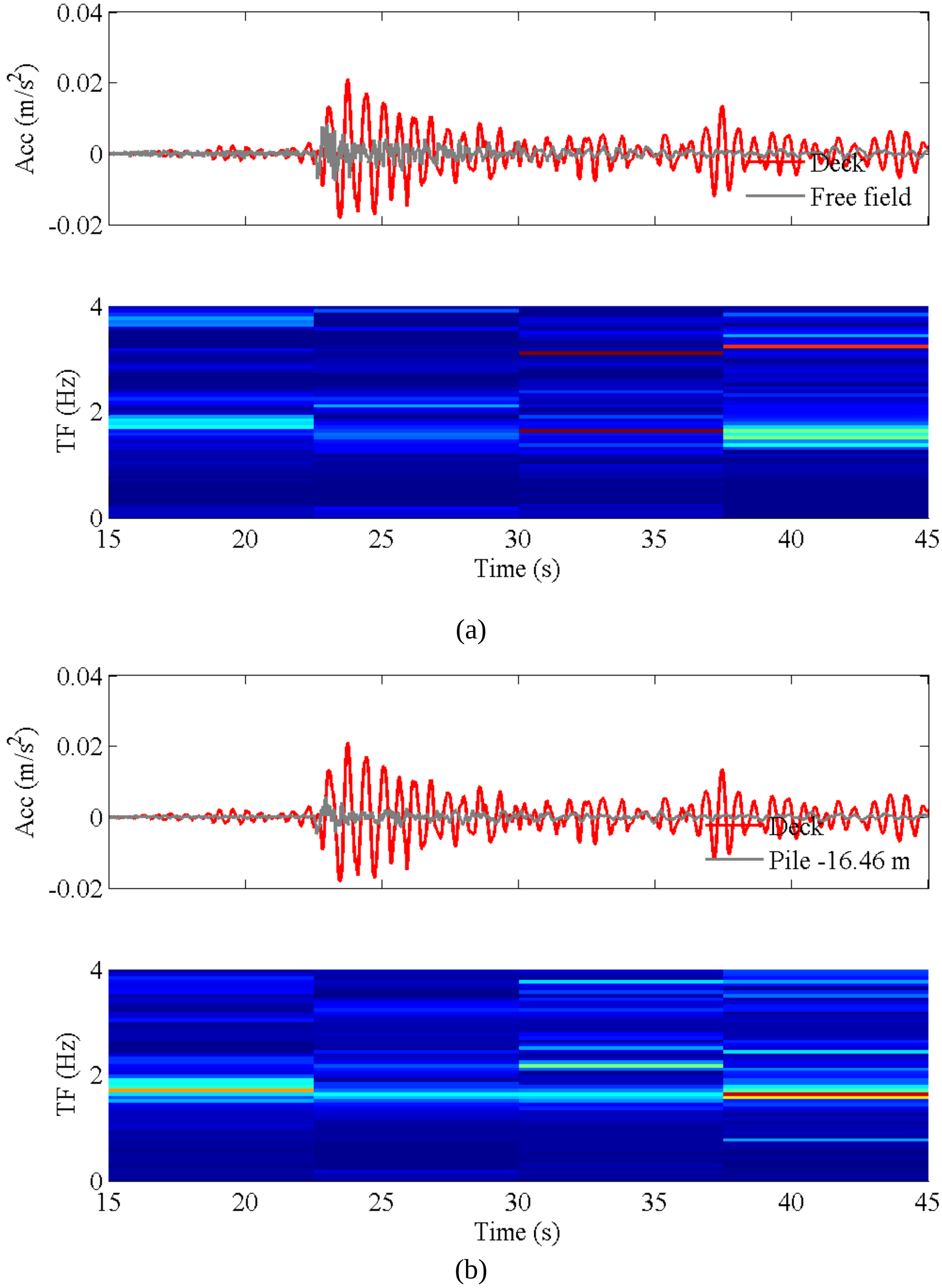

Figure 8.24: Short time transfer function plots in the transverse direction for (a) deck response over free field response and (b) deck response over pile response at -16.46 m during the 2007 Ferndale Earthquake

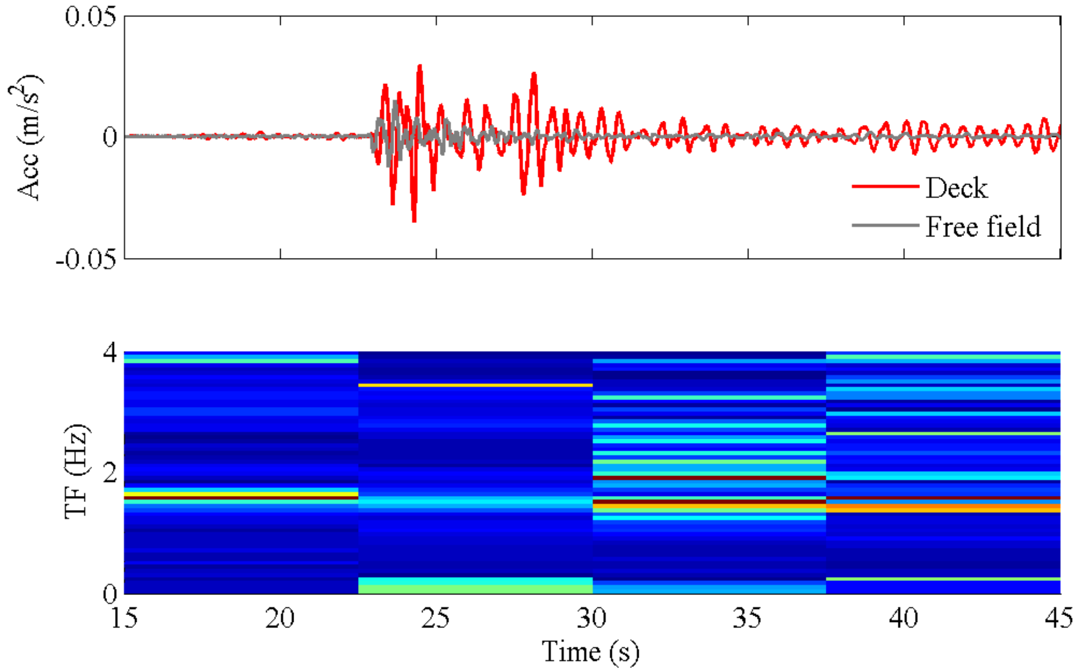

(a)

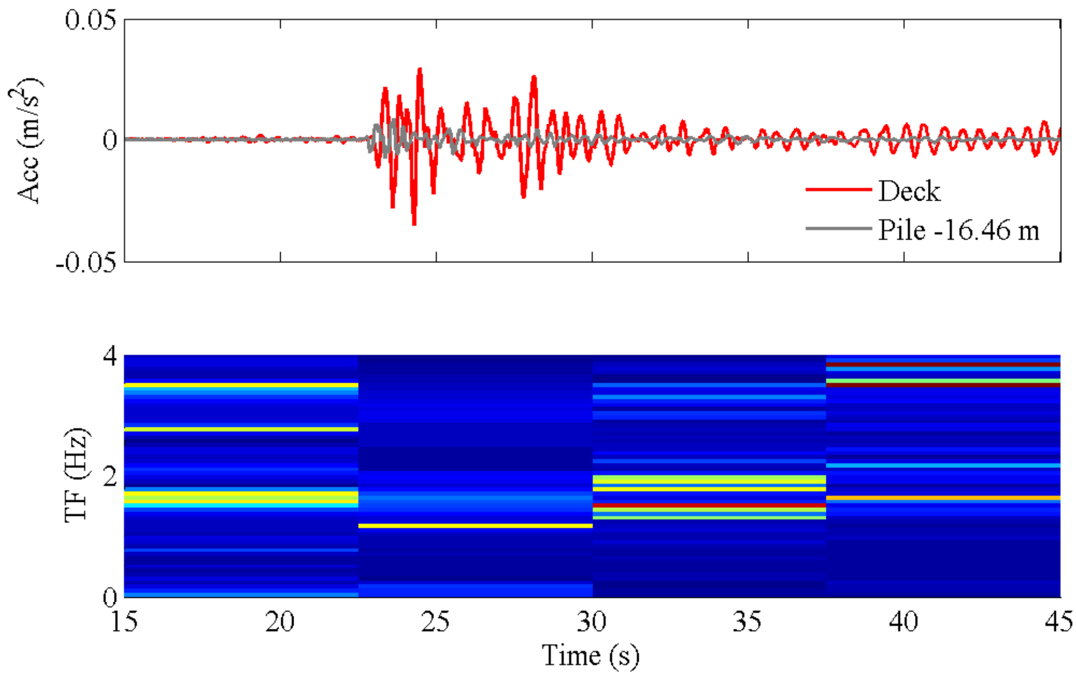

(b)

Figure 8.25: Short time transfer function plots in the transverse direction for (a) deck response over free field response and (b) deck response over pile response at -16.46 m during the 2007 Trinidad Earthquake

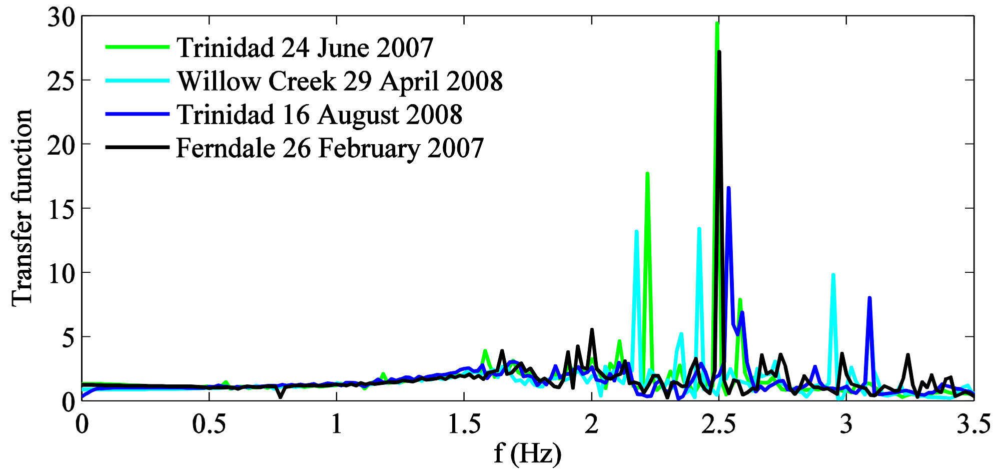

Figure 8.26: Transfer function in the transverse direction for deck response over pile cap response

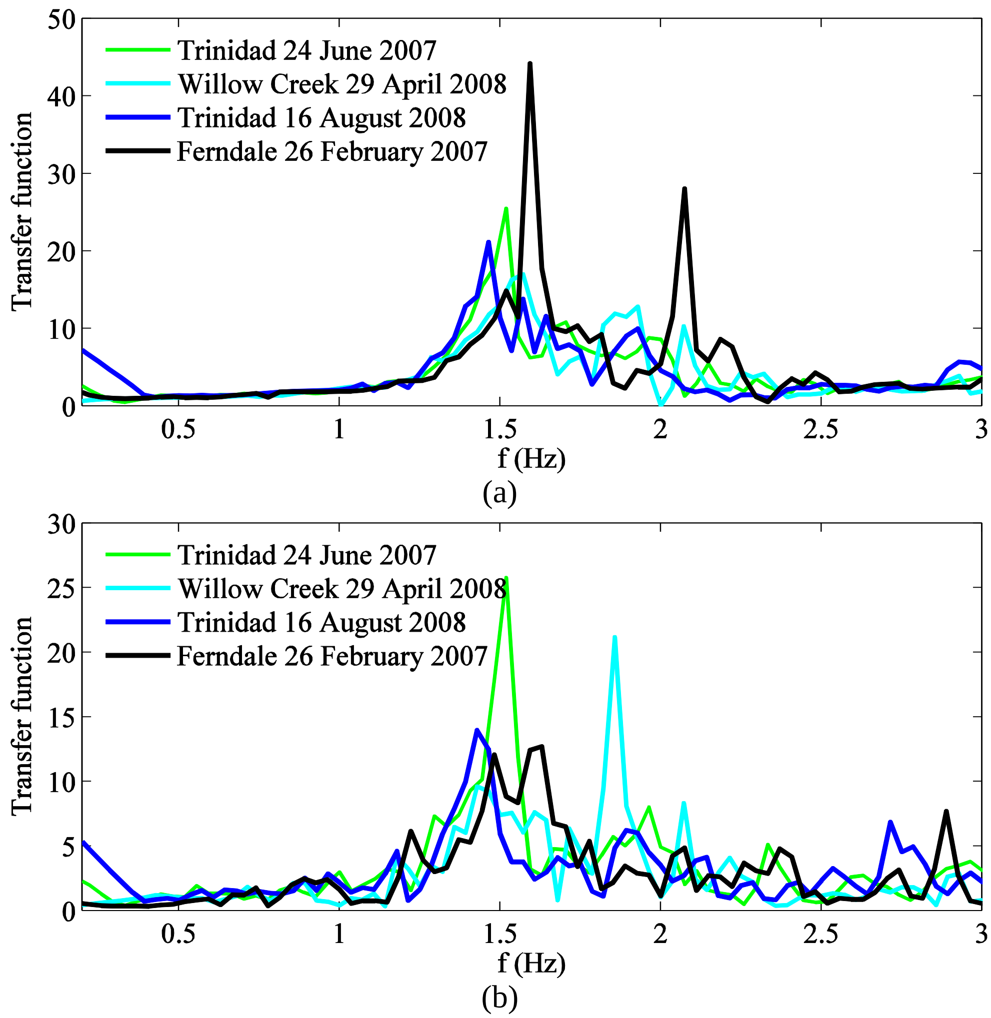

Figure 8.27: Transfer function in the transverse direction for (a) deck response over pile response at -16.46 m and (b) deck response over free field response

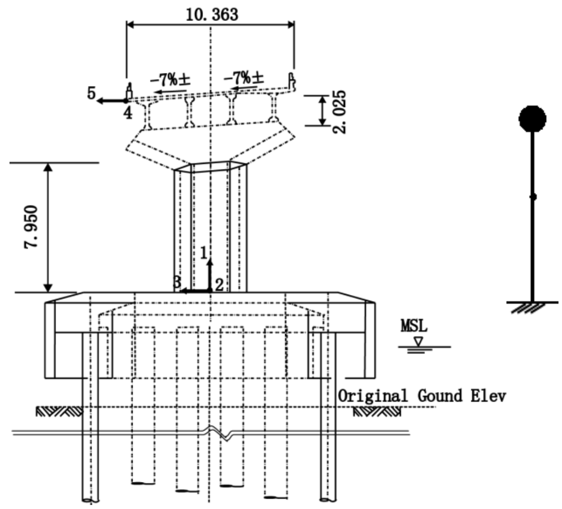

Figure 8.28: Pier E-7 single column type pier model

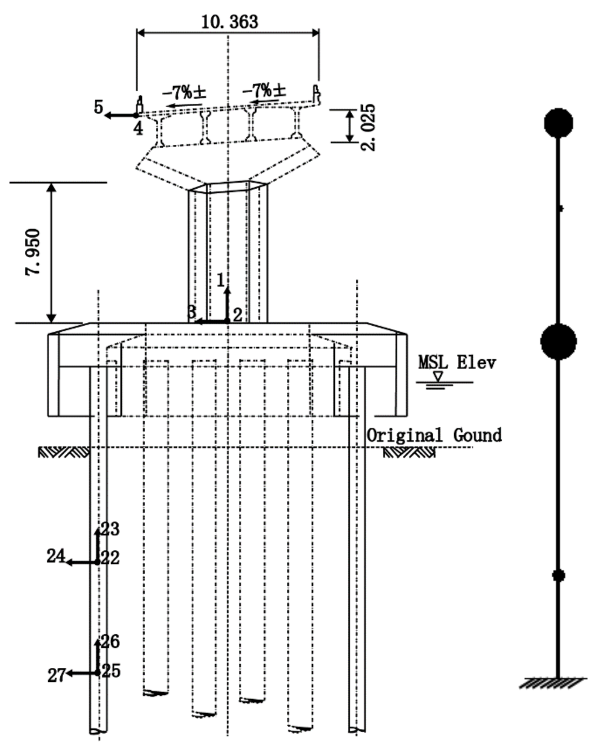

Figure 8.29: Pier E-7 foundation-pier model

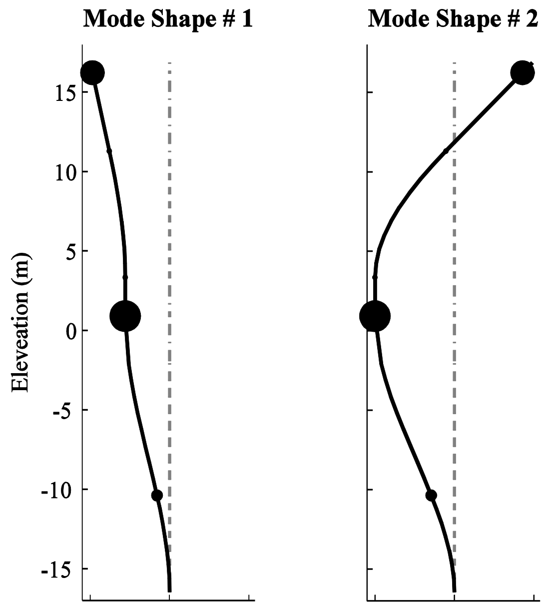

(a) (b)

Figure 8.30: Transverse mode shapes of pile-column system (at Pier E-7) with fixed base at the elevation of -16.46 m with (a) f_1=1.51 Hz and (b) f_2=3.50 Hz

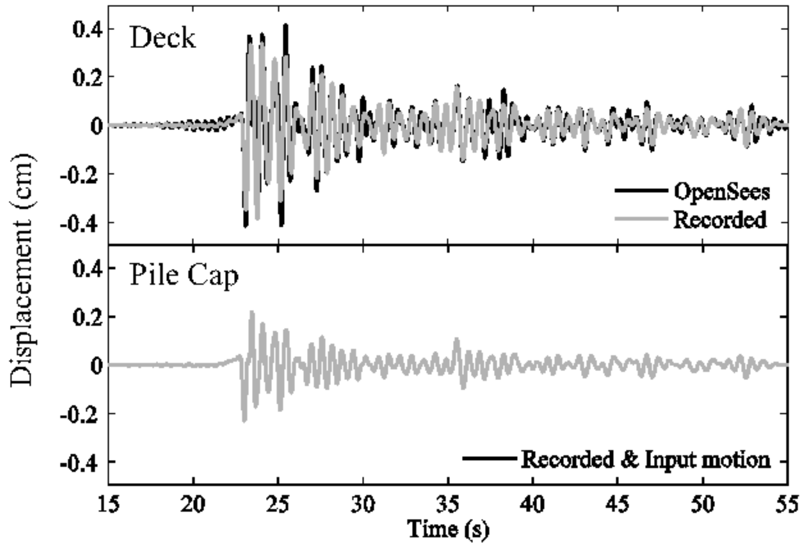

(a)

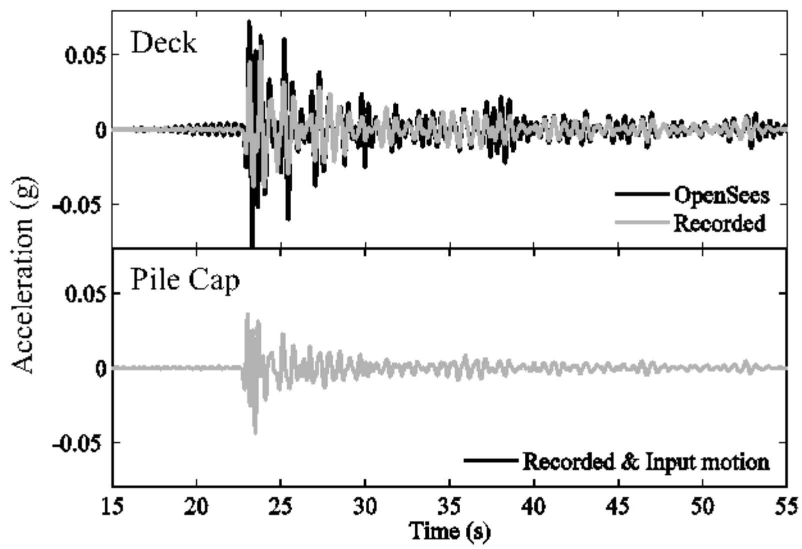

(b)

Figure 8.31: Comparison of computed and measured response at Pier E-7 during the 2007 Trinidad Earthquake

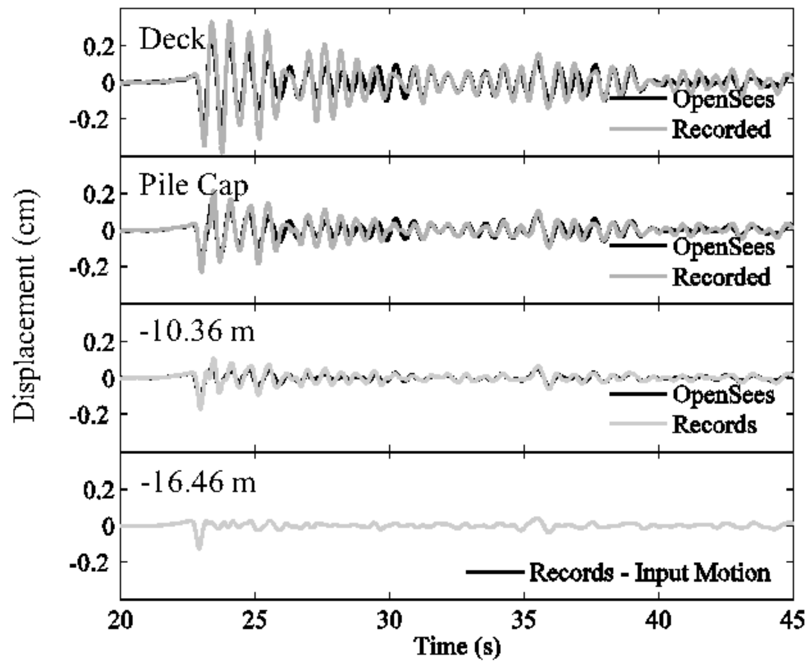

(a)

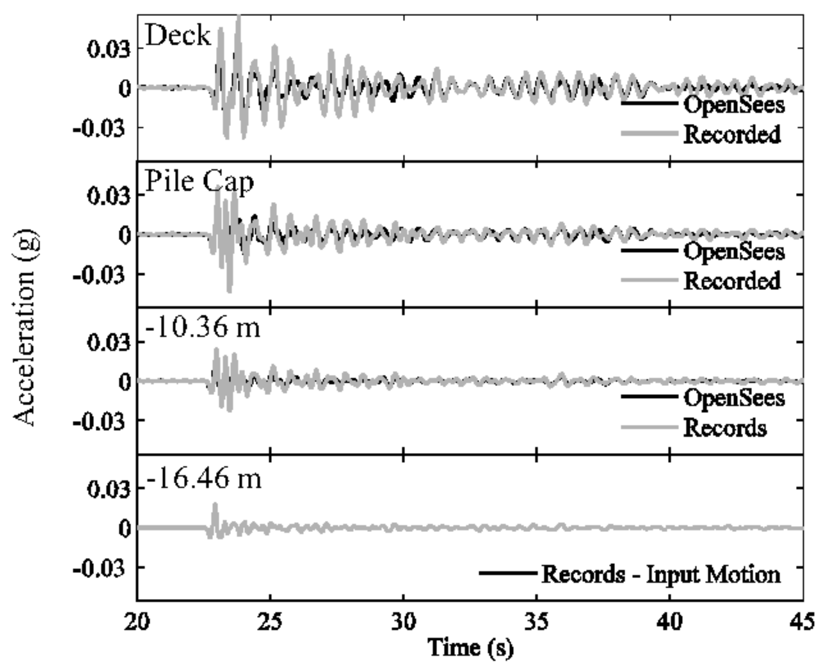

(b)

Figure 8.32: Time histories comparisons along Pier E-7 from deck level to elevation of -16.46 m during the 2007 Trinidad Earthquake

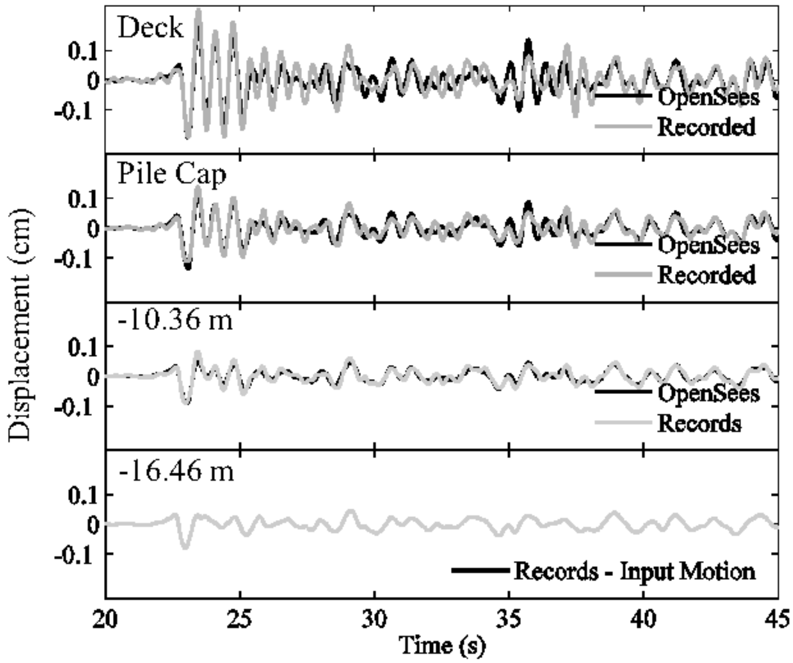

(a)

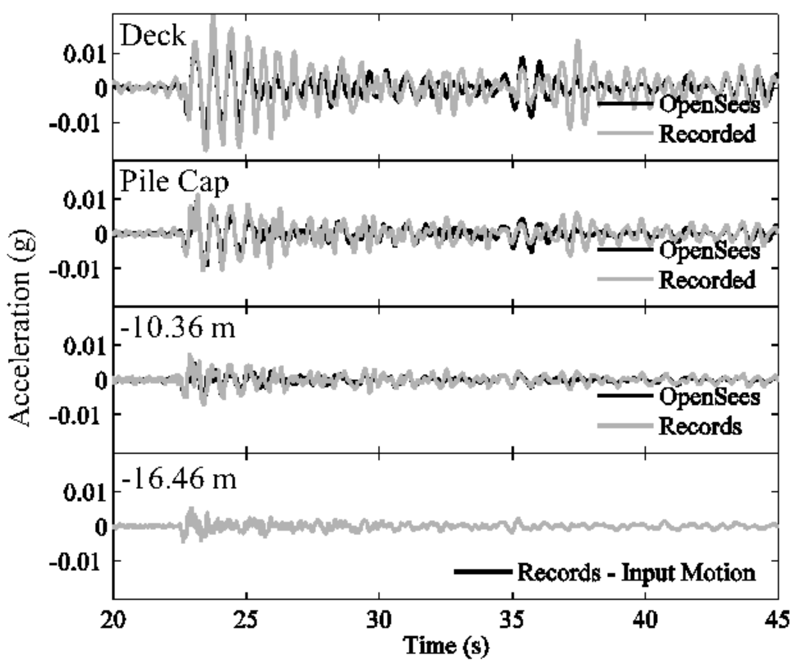

(b)

Figure 8.33: Time histories comparisons along Pier E-7 from deck level to elevation of -16.46 m during the 2007 Ferndale Earthquake

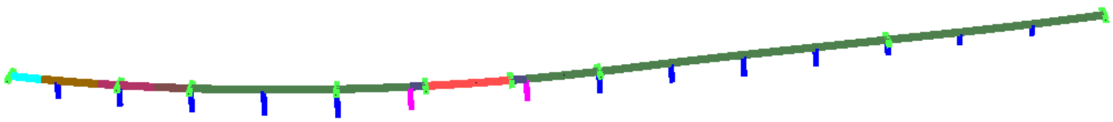

Figure 8.34: Beam-Column Model of the Eureka Channel Bridge

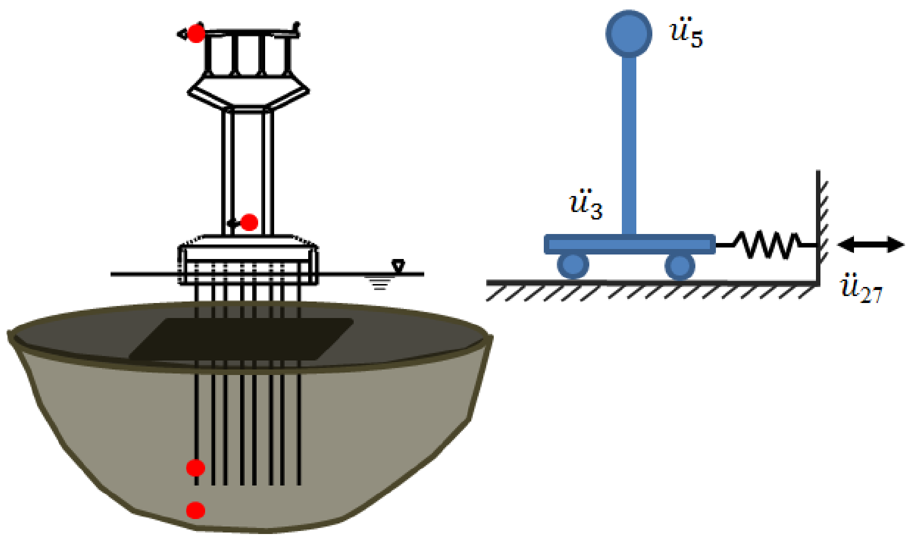

Figure 8.35: Estimation of the spring value at the base of Pier E-7 using SNOPT

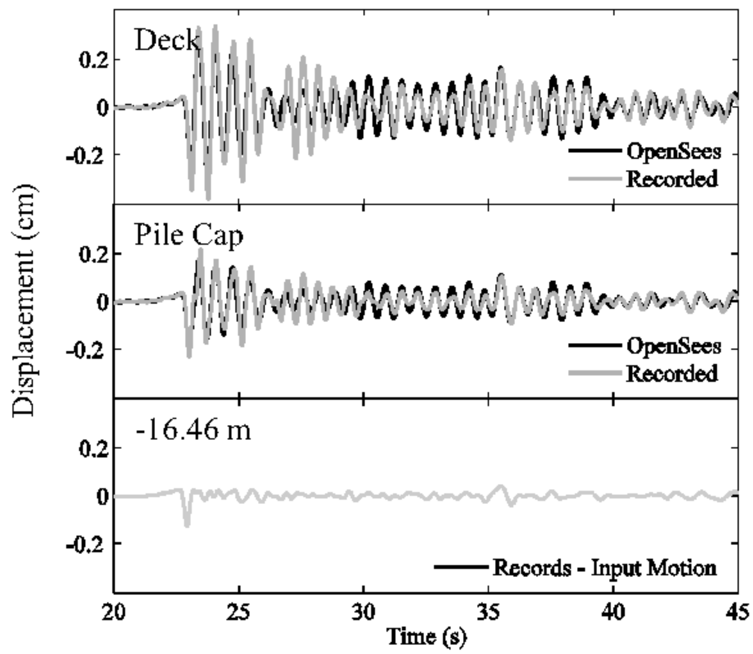

(a)

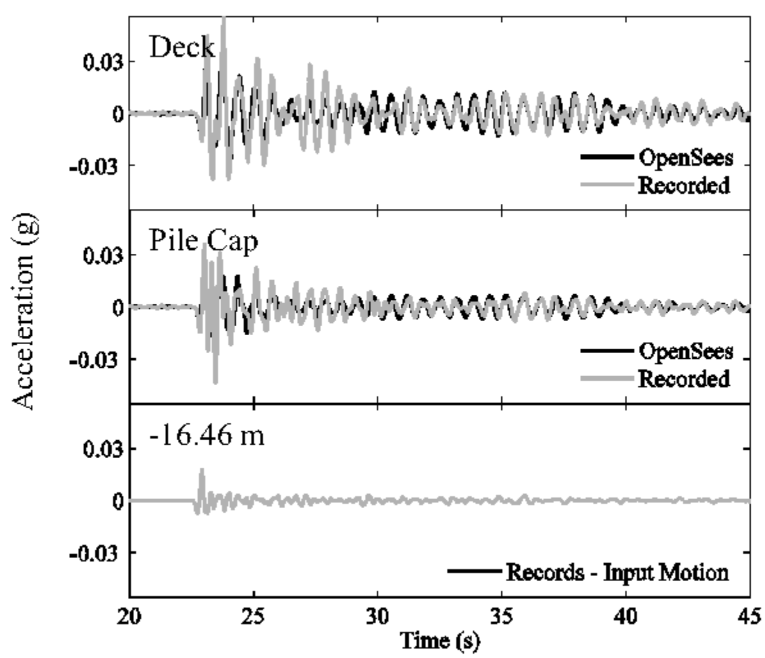

(b)

Figure 8.36: The recorded and optimized time histories at Pier E-7 during the 2007 Trinidad Earthquake

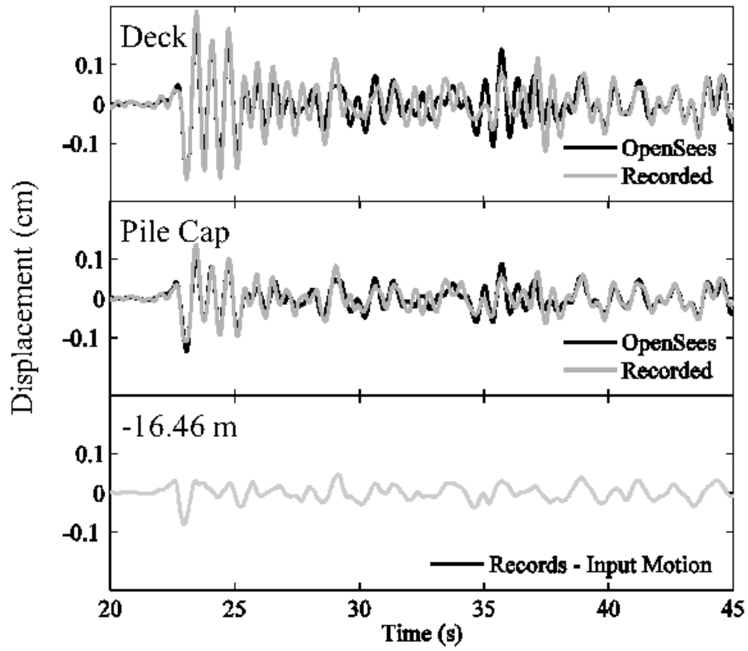

(a)

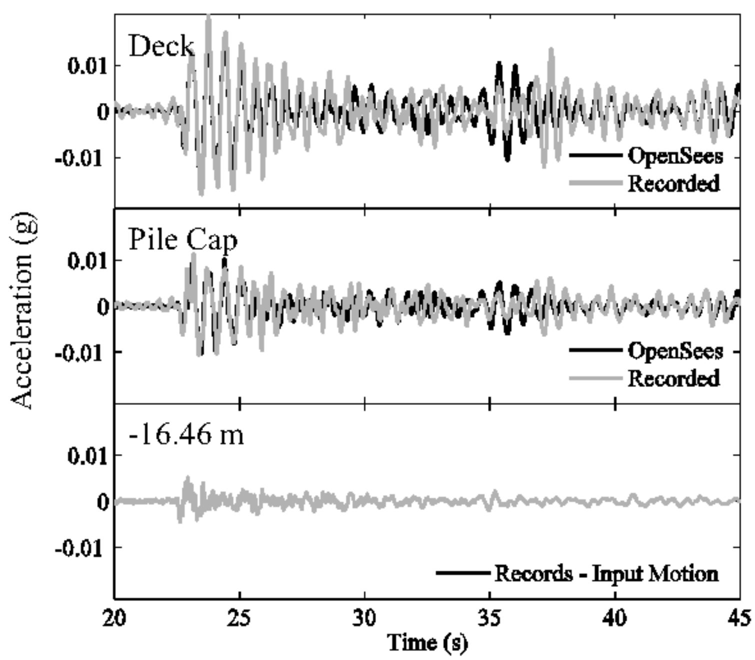

(b)

Figure 8.37: The recorded and optimized time histories at Pier E-7 during the 2007 Ferndale Earthquake

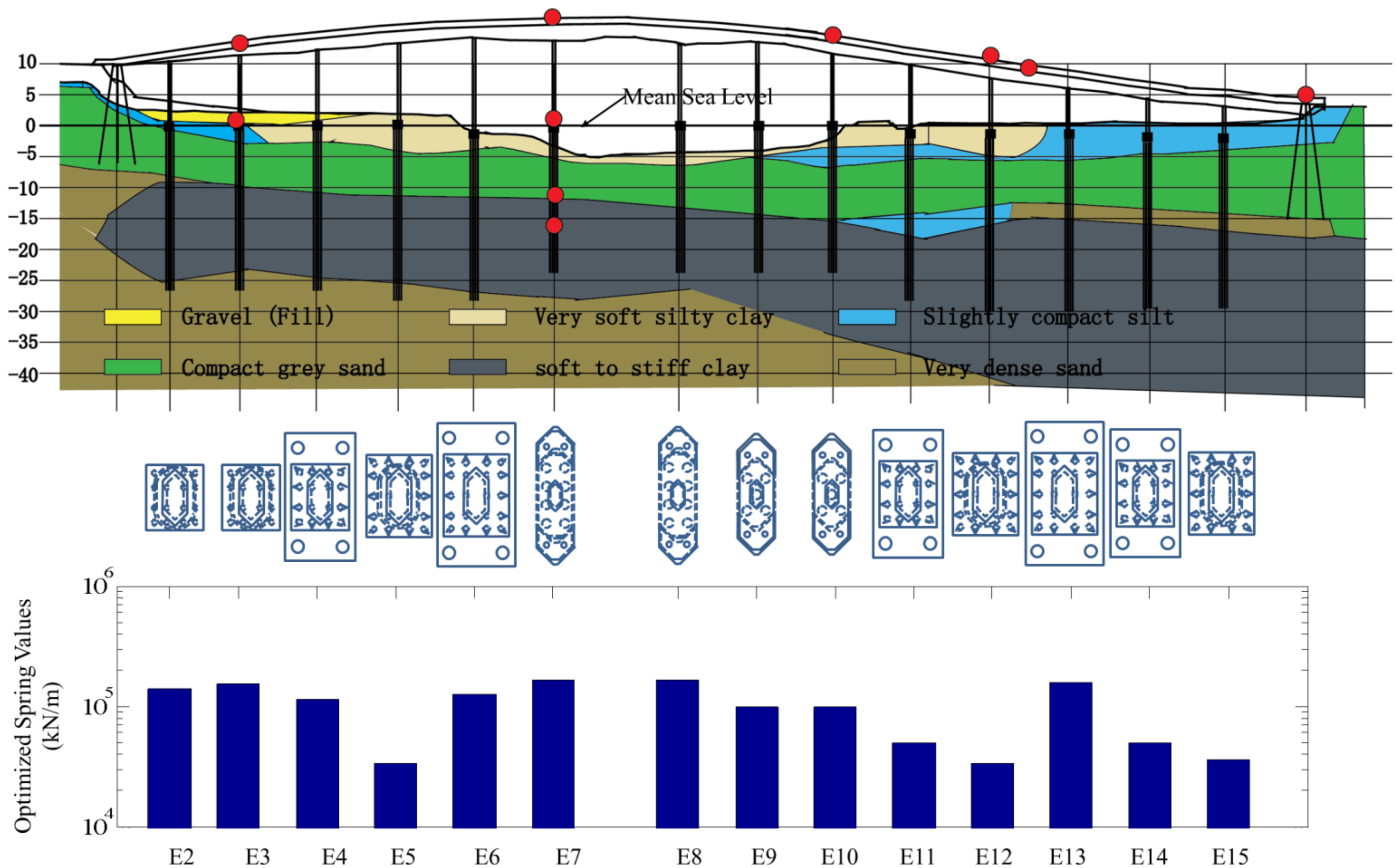

Figure 8.38: Identified lateral base spring values along the bridge

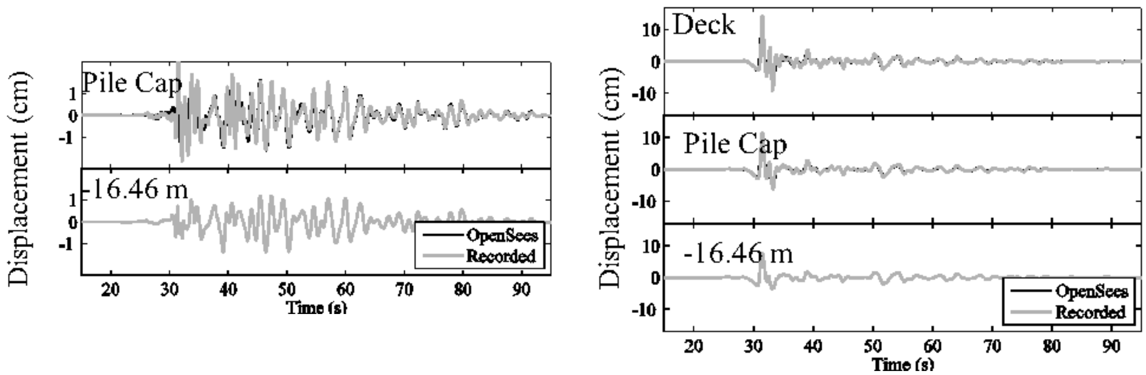

(a) (b)

Figure 8.39: Comparison of computed and measured displacement time histories at Pier E-7 in (a) Transverse and (b) Longitudinal during the moderate event

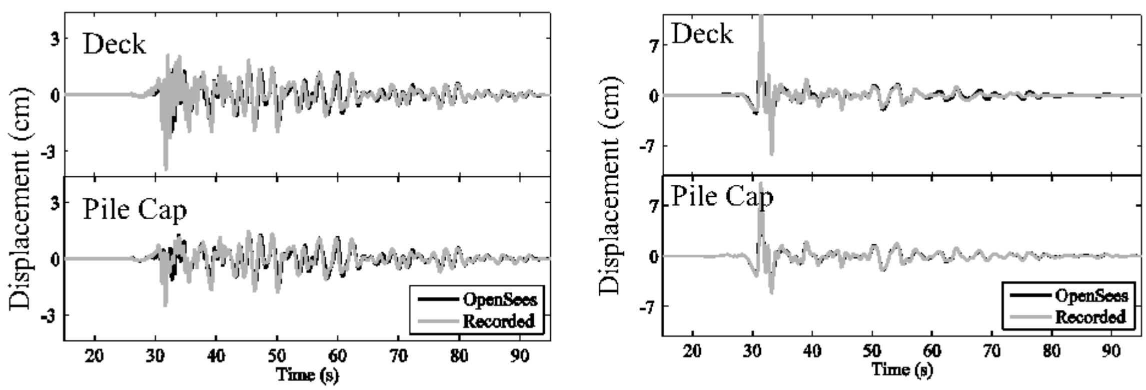

(a) (b)

Figure 8.40: Comparison of computed and measured displacement time histories at Pier E-7 in (a) Transverse and (b) Longitudinal during the moderate event

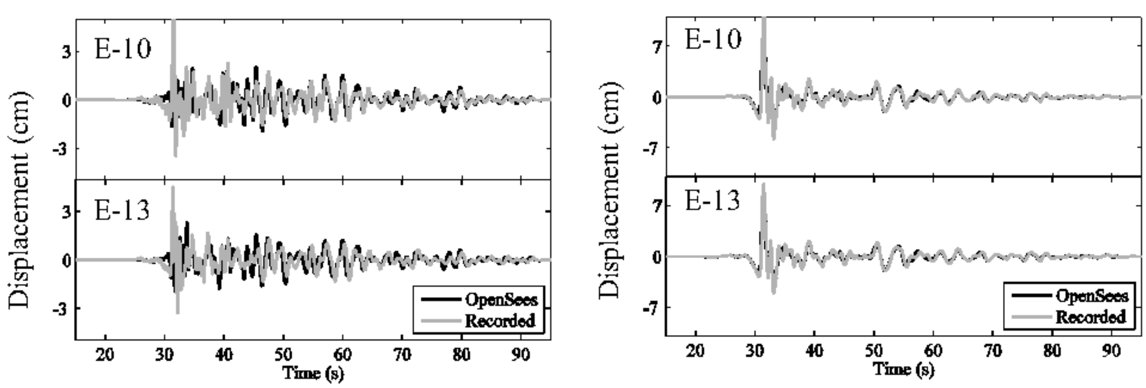

(a) (b)

Figure 8.41: Comparison of computed and measured displacement time histories at E-10 and E-13 in (a) Transverse and (b) Longitudinal during the moderate event

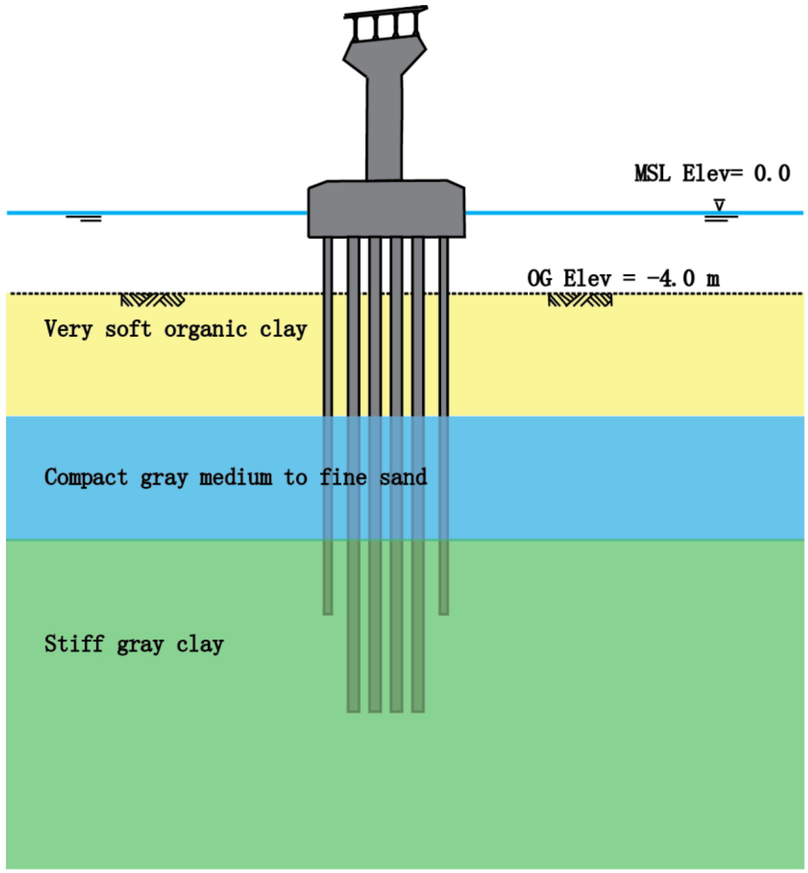

Figure 8.42: Soil Profile at Pier E-7 of Eureka Channel Bridge

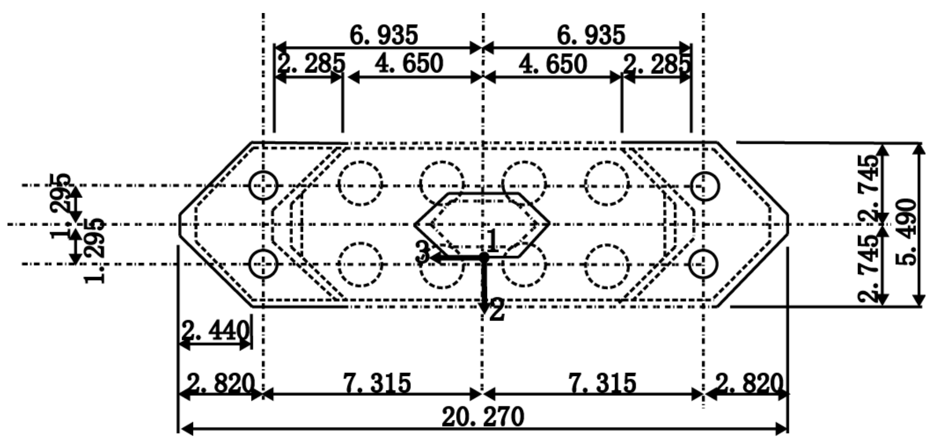

Figure 8.43: Plan view of pile group layout after retrofit

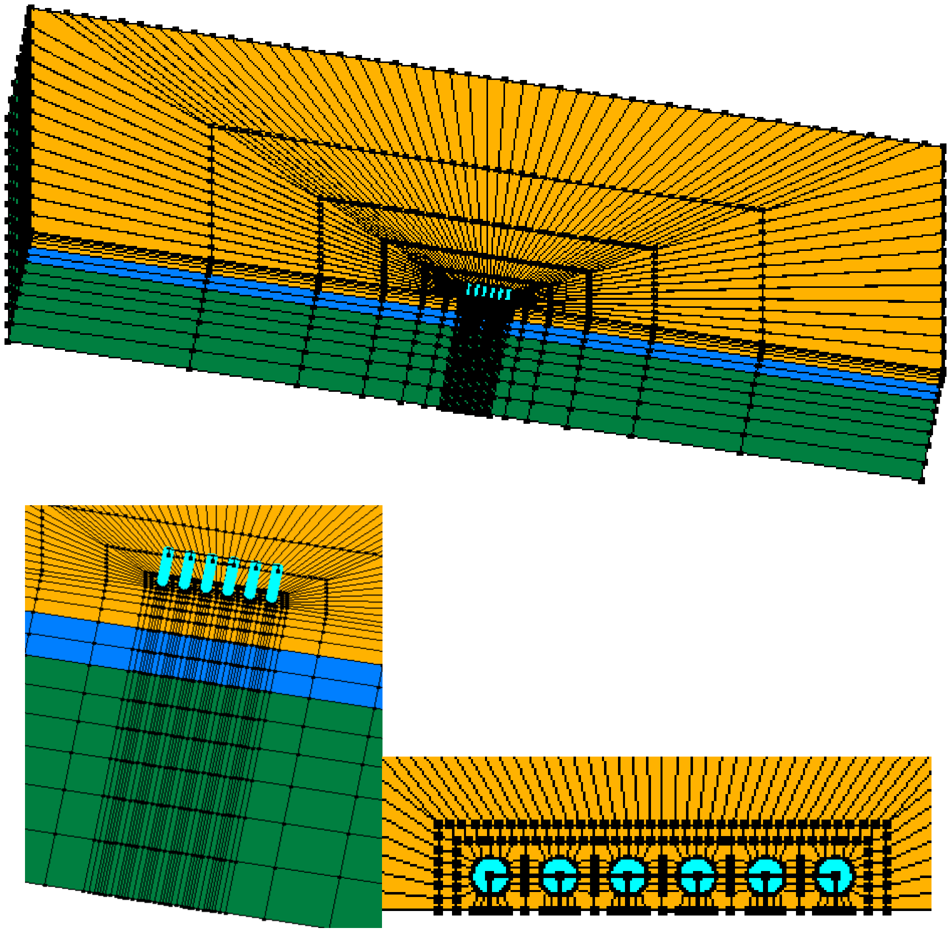

Figure 8.44: Finite element mesh and close-up view of pile group

Chapter 9

Conclusions and Future Work

9.1 Conclusions

Finite element modeling along with other numerical techniques has been providing valuable insights into the lateral/seismic response of ground-foundation-structure systems.

The contributions to the investigation of soil-structure interaction presented in this dissertation can be split into three broad categories: i) Large-scale 3D geotechnical Finite Element analysis for laterally loaded pile foundations; ii) strong motion data documentation and analysis for geotechnical downhole array and adjacent long-span bridges, and iii) Finite Element Model calibration on the basis of recorded strong motion data using system identification and optimization techniques. As a whole, this dissertation provides insights into a number of key mechanisms in the field of SSI.

9.1.1 3D Finite Element Modeling of Pile Groups

9.1.1.1 Laterally Loaded Pile Groups

Three-dimensional FE analyses for pile and pile groups were presented. Conclusions include:

(1) Displacement efficiency of the studied pile group dropped to as little as about 27% for close pile-spacing scenarios. Such decrease in efficiency would be expected as the immediate soil regions providing resistance around each pile heavily overlap.

(2) As spacing increased, group displacement efficiency becomes higher and more rapidly so in the nonlinear soil cases. This observation implies that the loaded zone of influence around each pile decreases with the level of nonlinearity in soil response.

(3) The center pile shoulders a lower share of the overall lateral load. Soil within this zone translates laterally due to the action of all surrounding piles, a mechanism that reduces available resistance to the center pile translation.

(4) The mechanism of soil tension cut-off (as a simple soil-pile interface mechanism) might play a significant role in dictating the analysis outcome. Along with a potentially reduced overall lateral stiffness, the front piles shoulder a higher portion of the overall load, and experience higher bending moments and shear forces. Conversely, a reduction in shear force and moment was noted in the back piles.

(5) Due to application of lateral load, back piles may experience a significant reduction in compressive axial load, resulting eventually in possible tensile axial forces. This may in turn adversely affect the reinforced concrete pile bending stiffness and strength.

9.1.1.2 Parametric Study for Effects of Soil Permeability and Loading Rate

(1) On the basis of a constitutive soil model with a soil-fluid fully coupled formulation, soil-pile system behavior with drainage conditions ranging from undrained to fully drained was investigated (piles in dense relatively cohesionless soils). Parametric studies that examine the effect of soil permeability coefficients loading rate were conducted. Under instantaneous or fast cyclic lateral load, the low permeability of dense cohesionless soils might lead to higher lateral stiffness with lower pile head displacement.

(2) Cyclic mobility and cavitation associated with the interaction between soil and fluid were examined. It is shown that fluid cavitation can prevent the effective confinement from further superfluous increases. The observations in this study can serve as a reference when selecting p-y curves or evaluating the pile foundation lateral response in saturated soil (for instantaneous loading scenarios).

(3) Additional FE numerical simulations were conducted to explore the effect of the existence of pile wings and their location/dimensions on the lateral behavior of piles. The results reveal that lateral resistance can be greatly improved when pile wings are introduced.

9.1.2 Strong Motion Data Analysis

At present, uncertainties remain regarding input ground motion and role of the foundation in bridge system analyses. Recorded seismic response at the Eureka geotechnical downhole array, and two nearby heavily instrumented bridges – the Samoa Channel Bridge and Eureka Channel Bridge has the potential to provide valuable insights. Overview and highlights of the conducted studies include:

(1) Sensors placed in the pile during the retrofit phase along with the adjacent subsurface geotechnical array allowed for comparisons of the site and foundation seismic responses.

(2) During the moderate shaking event (the 2010 Ferndale earthquake), soil nonlinearity was documented. In addition, the ground-foundation-bridge system for both the Samoa Channel Bridge and the Eureka Channel Bridge experienced a clear reduction in stiffness.

(3) For the Samoa Channel Bridge, the pile cap of Pier S-8 (at the center bent) is 16.7 m above the mudline. As such, much of the observed bridge deflections (both in the transverse and longitudinal directions) was emanating from movement of the pile.

(4) Significant effects of SSI on the bridge structure may be assessed with the help of recorded strong motion data and optimization techniques. The conducted studies attempt to provide a preliminary framework for such efforts.

Overall, insights obtained from this study concerning observed behavior of a full-scale bridge and pile foundation during actual earthquake events are extremely valuable and contribute considerably to our current understanding of this important SSI mechanism.

9.1.3 Numerical Modeling for Ground-Foundation-Structure system

A goal of this dissertation is to characterize and identify the effects of foundation flexibility on the ground-foundation-bridge system by developing a simple reliable method to assess recorded earthquake motions. Optimization techniques were employed to predict lateral stiffness of the pile groups at mid-span of two instrumented bridges as well as the base spring values for the whole bridge structure. Overview and highlights of this effort include:

(1) The earthquake response of the two bridges was examined with stick model and springs attached to the pier base to account for the presence of the pile foundation. These simplified FE models yielded comparable seismic response characteristics to the recorded observations.

(2) A major effort undertaken in this thesis addressed the use of optimization techniques for FE model calibration purposes (and knowledge extraction). Procedures for optimization of structure parameters (column stiffness, foundation stiffness and base spring values) using an optimization method are described and optimization results are analyzed. Overall, global optimization of model parameters in terms of minimizing the difference between the recorded and computed time histories provide valuable insights into the structure behavior.

9.2 Future work

To extend the work presented in this dissertation, further research to investigate the effects of SSI for bridges is needed. The following is a partial list of topics that are likely to advance the field:

(1) Herein, 8-node brick elements are employed for the soil domain and elastic beam-column elements are used to represent the bridge deck and pier column. More representative FE models with 20-node solid elements for soil (for instance), shell elements for the bridge deck and nonlinear beam-column elements for bridge piers may provide for more accurate simulations.

(2) Currently, there is limited information regarding the property of separation joints, abutments, and shear keys for the investigated bridges. Follow-up investigations about these issues may be of great value.

(3) Instrumentation of highway bridges in seismically active regions is a promising undertaking. Compared to the cost of shaking table testing facilities, monitoring of a long-span bridge might be among the efficient methods to evaluate real field conditions of an operation bridge. With additional sensors attached to pile foundations in the future, it is believed that valuable additional insights will gleaned.

BIBLIOGRAPHY

Abedzadeh, F., and Pak, R. Y. S. (2004), "Continuum Mechanics of Lateral Soil-Pile Interaction," *Journal of Engineering Mechanics*, 130(11), 1309-1318.

Allotey, N., and El Naggar, M. H. (2008), "A numerical study into lateral cyclic nonlinear soil-pile response," *Canadian Geotechnical Journal*, 45(9), 1268-1281.

Allotey, N., and Foschi, R. (2005), "Coupled P-Y T-Z analysis of single piles in cohesionless soil under vertical and/or horizontal ground motion," *Journal of Earthquake Engineering*, 9(6), 755-775.

Amiri, S. K. (2008), "The earthquake response of bridge pile foundations to liquefaction induced lateral spread displacement demands," Ph.D. Dissertation, University of Southern California, Los Angeles, CA.

Arici, Y., and Mosalam, K. (2000), "System identification and modeling of bridge systems for assessing current design procedures," *Proceedings of Proceedings of SMIP2000 Seminar*, 77-95.

Arici, Y., and Mosalam, K. M. (2003), "System identification of instrumented bridge systems," *Earthquake Engineering & Structural Dynamics*, 32(7), 999-1020.

ASCE (2010), "Minimum Design Loads for Buildings and Other Structures," *ASCE7-10*, Reston, VA.

Assimaki, D., Li, W., Steidl, J. M., and Schmedes, J. (2008), "Quantifying nonlinearity susceptibility via site response modeling uncertainty at three sites in the Los Angeles basin," *Bulletin of the Seismological Society of America*, 98(5), 2364-2390.

Banerjee, P. K., and Davies, T. G. (1978), "Behavior of axially and laterally loaded single piles embedded in nonhomogeneous soils," *Geotechnique*, 28(3), 309-326.

Bao, Y., Ye, G., Ye, B., and Zhang, F. (2012), "Seismic evaluation of soil–foundation–superstructure system considering geometry and material nonlinearities of both soils and structures," *Soils and Foundations*, 52(2), 257-278.

Basu, D., and Salgado, R. (2007), "Elastic analysis of laterally loaded pile in multi-layered soil," *Geomechanics and Geoengineering*, 2(3), 183-196.

Bendat, J. S., and Piersol, A. G. (1980), "Engineering applications of correlation and spectral analysis," *New York, Wiley-Interscience, 1980. 315 p.*, 1.

Bezgin, O., Najm, H., and Nassif, H. (2004), "Modeling of Laterally Loaded Shaft Foundations Using Continuous Soil Medium," *Proceedings of Proc., Structures Congress 2004*, ASCE, Nashville, Tennessee, USA, 137.

Bouafia, A. (2007), "Single piles under horizontal loads in sand: determination of P – Y curves from the prebored pressuremeter test," *Geotechnical and Geological Engineering*, 25(3), 283-301.

Briaud, J.-L., Smith, T., and Meyer, B. (1984), "Laterally loaded piles and the pressuremeter: Comparison of existing methods," *Proceedings of Laterally Loaded Deep Foundations: Analysis and Performance*, ASTM, ASTM STP 835, Kansas City, MO, USA, 97-111.

Broms, B. B. (1964), "Lateral resistance of piles in cohesionless soils," *Proceedings of the American Society of Civil Engineers, Journal of the Soil Mechanics and Foundations Division*, 90(SM3, Part 1), 123-156.

Brown, D. A., Reese, L. C., and Oneill, M. W. (1987), "Cyclic Lateral Loading of a Large-Scale Pile Group," *Journal of Geotechnical Engineering*, 113(11), 1326-1343.

Brown, D. A., and Shie, C.-F. (1990), "Numerical experiments into group effects on the response of piles to lateral loading," *Computers and Geotechnics*, 10(3), 211-230.

Budek, A. M., Priestley, M. J. N., and Benzoni, G. (2000), "Inelastic seismic response of bridge drilled-shaft RC pile/columns," *Journal of Structural Engineering*, 126(4), 510-517.

Budhu, M., and Davies, T. G. (1988), "Analysis of Laterally Loaded Piles in Soft Clays," *Journal of Geotechnical Engineering*, 114(1), 21-39.

Caltrans (1968), "As-Built Plans, Samoa Channel Bridge," California Department of Transportation, Sacramento, CA, personal communication.

Caltrans (2000a), "Caltrans studies re Humboldt Bay foundationa and soil," *peertestbeds*, Geotechnical studies - PEER.

Caltrans (2000b), "Memorandum: Foundation stiffness for Middle Channel Bridge," file 01-Hum-255-0.7, Engineering Service Center, Division of Structural Foundation - MS5, California Department of Transportation.

Caltrans (2001), "Guidelines on Foundation Loading and Deformation Due to Liquefaction Induced Lateral Spreading," California Department of Transportation, Sacramento, CA.

Caltrans (2002a), "As-Built Plans, Earthquake Retrofit Project for Samoa Channel Bridge," California Department of Transportation, Sacramento, CA, personal communication.

Caltrans (2002b), "As-Built Plans, Earthquake Retrofit Project for Eureka Channel Bridge," California Department of Transportation, Sacramento, CA, personal communication.

Caltrans (2008), "Strong Motion Instrumentation of Bridges and Downhole sites," *Research notes*, California Department of Transportation, Sacramento, CA.

Caltrans (2012), "Bridge Design Practice Manual," California Department of Transportation, Sacramento, CA.

Caltrans (2012a), "Guidelines on Foundation Loading and Deformation Due to Liquefaction Induced Lateral Spreading," California Department of Transportation, Sacramento, CA.

Caltrans (2012b), "San Francisco Bay Area Toll Bridge Seismic Retrofit and Regional Measure 1 Programs," Toll Bridge Program Oversight Committee, California Department of Transportation, Sacramento, CA.

Caltrans (2012c), "Post Earthquake Investigation Team (PEQIT) Manual," California Department of Transportation, Sacramento, CA.

Caltrans (2013), "Seismic Design Criteria Version 1.7," California Department of Transportation, Sacramento, CA.

Çelebi, M., Lysmer, J., and Luco, J. E. (1992), "Recommendations for a Soil-Structure Interaction Experiment " *Open-file report 92-295*, U.S. Geological Survey, San Francisco.

Chae, K. S., Ugai, K., and Wakai, A. (2004), "Lateral Resistance of Short Single Piles and Pile Groups Located Near Slopes," *International Journal of Geomechanics*, 4(2), 93-103.

Chai, Y. H., and Hutchinson, T. C. (2002), "Flexural Strength and Ductility of Extended Pile-Shafts. II: Experimental Study," *Journal of Structural Engineering*, 128(5), 595-602.

Chan, A. H.-C. (1988), "A unified finite element solution to static and dynamic problems of geomechanics," Ph.D. Dissertation, University College of Swansea, UK.

Chang, C.-Y., Mok, C. M., and Tang, H.-T. (1996), "Inference of Dynamic Shear Modulus from Lotung Downhole Data," *Journal of Geotechnical Engineering*, 122(8), 657-665.

Chang, C. Y., Mok, C. M., Power, M. S., Tang, Y. K., Tang, H. T., and Stepp, J. C. (1990), "Equivalent linear versus nonlinear ground response analyses at lotung seismic experiment site," *Proceedings of the US National Conference on Earthquake Engineering*, 327-327.

Chang, C. Y., Power, M. S., Tang, Y. K., and Mok, C. M. (1989), "Evidence of nonlinear soil response during a moderate earthquake," Publ by A.A. Balkema, Rio de Janeiro, Br, 1927-1930.

Chaudhary, M. T. A., Abé, M., and Fujino, Y. (2001), "Identification of soil–structure interaction effect in base-isolated bridges from earthquake records," *Soil Dynamics and Earthquake Engineering*, 21(8), 713-725.

Crouse, C. B., and Hushmand, B. (1989), "Soil-Structure interaction at CDMG and USGS accelerograph stations," *Bulletin of the Seismological Society of America*, 79(1), 1-14.

Datta, T. K. (2010), *Seismic analysis of structures*, John Wiley & Sons.

Dodds, A. (2005), "A numerical study of pile behavior in large pile groups under lateral loading," Ph.D. Dissertation, University of Southern California, Los Angeles, CA.

Dührkop, J., and Grabe, J. (2008), "Laterally loaded piles with bulge," *Journal of Offshore Mechanics and Arctic Engineering*, 130(4), 041602.

Dungca, J. R., Kuwano, J., Takahashi, A., Saruwatari, T., Izawa, J., Suzuki, H., and Tokimatsu, K. (2006), "Shaking table tests on the lateral response of a pile buried in liquefied sand," *Soil Dynamics and Earthquake Engineering*, 26(2-4), 287-295.

El Naggar, M. H., and Wei, J. Q. (1999), "Response of tapered piles subjected to lateral loading," *Canadian Geotechnical Journal*, 36(1), 52-71.

Elfass, S., Norris, G., and Ashour, M. (2004), "Analysis of Laterally Loaded Long or Intermediate Drilled Shafts of Small or Large Diameter in Layered Soil," *No. CCEER 01-02/CA04-0252*, California Department of Transportation, Sacramento, CA.

Elgamal, A., Lai, T., Yang, Z., and He, L. (2001), "Dynamic soil properties, seismic downhole arrays and applications in practice," *Proceedings of 4th Intl. Conf. on Recent Advances in Geote. E.Q. Engrg. Soil Dyn.*, San Diego, CA.

Elgamal, A., and Lu, J. (2009), "A Framework for 3D Finite Element Analysis of Lateral Pile System Response," ASCE GSP 186, Orlando, FL, 616–623.

Elgamal, A., Lu, J., and Forcellini, D. (2009), "Mitigation of Liquefaction-Induced Lateral Deformation in a Sloping Stratum: 3D Numerical Simulation," *Journal of Geotechnical and Geoenvironmental Engineering*, 135(11), 1672-1682.

Elgamal, A., Lu, J., and Mackie, K. (2014), "MSBrindge: OpenSees Pushover and Earthquake Analysis of Multi-span Bridges - User Manual," Department of Structural Engineering, University of California, San Diego.

Elgamal, A., Yan, L., Yang, Z., and Conte, J. P. (2008), "Three-Dimensional Seismic Response of Humboldt Bay Bridge-Foundation-Ground System," *J. Struct. Eng.*, 134(7), 1165.

Elgamal, A., Yang, Z., Lai, T., Kutter, B., and Wilson, D. (2005), "Dynamic Response of Saturated Dense Sand in Laminated Centrifuge Container," *Journal of Geotechnical and Geoenvironmental Engineering*, 131(5), 598-609.

Elgamal, A., Yang, Z. H., Parra, E., and Ragheb, A. (2003), "Modeling of cyclic mobility in saturated cohesionless soils," *Int. J. Plast.*, 19(6), 883-905.

Elgamal, A., Zeghal, M., and Parra, E. (1995), "Identification and Modeling of Earthquake Ground Response," *Proceedings of First International Conference on Earthquake Geotechnical Engineering*, Tokyo, Japan.

Elgamal, A., Zeghal, M., Tang, H., and Stepp, J. (1995), "Lotung Downhole Array. I: Evaluation of Site Dynamic Properties," *Journal of Geotechnical Engineering*, 121(4), 350-362.

Elgamal, A. W., Zeghal, M., Parra, E., Gunturi, R., Tang, H. T., and Stepp, J. C. (1996), "Identification and modeling of earthquake ground response - I. Site amplification," *Soil Dynamics and Earthquake Engineering*, 15(8), 499-522.

EPRI (1993), "Guidelines for determining design basis ground motions," *Final Rep. No. TR-102293*, Electric Power Research Institute, Palo Alto, California.

FEMA (2005), "Improvement of Nonlinear Static Seismic Analysis Procedures (FEMA 440)," Federal Emergency Management Agency (FEMA), Washington, D.C.

FEMA (2009), "NEHRP Recommended Seismic Provisions for New Buildings and Other Structures. 2009 Edition," Federal Emergency Management Agency (FEMA), Washington, D.C.

Fenves, G. L., and DesRoches, R. (1994), "Response of the Northwest Connector in the Landers and Big Bear earthquakes," Earthquake Engineering Research Center, University of California, Berkeley.

Fenves, G. L., and DesRoches, R. (1995), "Evaluation of the Response of I-10/215 Interchange Bridge near San Bernardino in the 1992 Landers and Big Bear Earthquakes," California Department of Conservation, Division of Mines and Geology, Office of Strong Motion Studies.

FHWA (2011), "LRFD Seismic Analysis and Design of Transportation Geotechnical Features and Structural Foundations," *Publication No. FHWA-NHI-11-032*, US Department of Transportation, Federal Highway Administration, Washington DC.

Gazetas, G. (1983), "Analysis of machine foundation vibrations: State of the art," *International Journal of Soil Dynamics and Earthquake Engineering*, 2(1), 2-42.

Gazetas, G., Fan, K., and Kaynia, A. (1993), "Dynamic response of pile groups with different configurations," *Soil Dynamics and Earthquake Engineering*, 12, 239-257.

Georgiadis, M., Anagnostopoulos, C., and Saflekou, S. (1992), "Centrifugal Testing of Laterally Loaded Piles in Sand," *Canadian Geotechnical Journal*, 29(2), 208-216.

Gerolymos, N., Escoffier, S., Gazetas, G., and Garnier, J. (2009), "Numerical modeling of centrifuge cyclic lateral pile load experiments," *Earthquake Engineering and Engineering Vibration*, 8(1), 61-76.

Gill, P. E., Murray, W., and Saunders, M. A. (2002), "SNOPT: An SQP algorithm for large-scale constrained optimization," *SIAM journal on optimization*, 12(4), 979-1006.

Glaser, S. D., and Baise, L. G. (2000), "System identification estimation of soil properties at the Lotung site," *Soil Dynamics and Earthquake Engineering*, 19(7), 521-531.

Goel, R. K., and Chopra, A. K. (1997), "Evaluation of bridge abutment capacity and stiffness during earthquakes," *Earthquake Spectra*, 13(1), 1-23.

Gomez, H. C., Ulusoy, H. S., and Feng, M. Q. (2013), "Variation of modal parameters of a highway bridge extracted from six earthquake records," *Earthquake Engineering & Structural Dynamics*, 42(4), 565-579.

Graizer, V., Shakal, A., and Hipley, P. (2000), "Recent data recorded from downhole geotechnical arrays," *Proceedings of SMIP2000 Seminar Proceedings*.

Gu, Q. (2008), "Finite element response sensitivity and reliability analysis of soil-foundation-structure-interaction (SFSI) systems," Ph.D. dissertation, University of California, San Diego, CA.

Hansen, J. B. (1961), "Ultimate resistance of rigid piles against transversal forces," *Geoteknisk Institut -- Bulletin (Danish Geotechnical Institute -- Bulletin)*, (12), 5-9.

Hansen, N. E. O., and Gislason, K. (2007), "Soil Reactions in Saturated Sand Caused by Impulsive Loads," *Journal of Waterway, Port, Coastal, and Ocean Engineering*, 133(1), 39-49.

Harichane, Z., Afra, H., and Elachachi, S. M. (2005), "An identification procedure of soil profile characteristics from two free field acclerometer records," *Soil Dynamics and Earthquake Engineering*, 25(6), 431-438.

Hipley, P., and Huang, M. (1997), "Caltrans/CSMIP bridge strong motion instrumentation," *Proceedings of Second National Seismic Conference on Bridge and Highways*, Sacramento, California, 227-236.

Hipley, P., Huang, M., and Shakal, A. (1998), "Bridge Instrumentation and Post-Earthquake Evaluation of Bridges," *Proceedings of SMIP98 Seminar on Utilization of Strong-Motion Data*, CA, U.S.A., 53-62.

Hoit, M., Hays, C., and McVay, M. (1997), "The Florida Pier analysis program methods and models for pier analysis and design," *Transportation Research Record: Journal of the Transportation Research Board*, 1569(1), 1-7.

Holtz, R. D., and Kovacs, W. D. (1981), *An Introduction to Geotechnical Engineering* Prentice Hall, Englewood Cliffs, NJ.

Huang, M., and Shakal, A. F. (1995), "CSMIP strong-motion instrumentation and records from the I10/215 interchange bridge near San Bernardino," *Earthquake Spectra*, 11(2), 193-215.

Irvine, J. H., Allan, P. G., Clarke, B. G., and Peng, J. R. (2003), "Improving the lateral stability of monopile foundations," *Proceedings of BGA International Conference on Foundations, Innovations, Observations, Design and Practice, September 2, 2003 - September 5, 2003*, Thomas Telford Services Ltd, Dundee, United kingdom, 371-380.

Ismael, N. (2010), "Behavior of Step Tapered Bored Piles in Sand under Static Lateral Loading," *Journal of Geotechnical and Geoenvironmental Engineering*, 136(5), 669-676.

Itani, R. (2003), "Effects of retrofitting applications on reinforced concrete bridges."

Ke, T.-C., Law, H., Lam, P., Maroney, B., Mohan, S., and Weinstein, J. (2010), "Ground motion study on Dumbarton toll bridge," *Proceedings of Fifth International Conference on Recent Advances in Geotechnical Earthquake Engineering and Soil Dynamics and Symposium in Honor of Professor I.M. Idriss*, San Diego, CA.

Kim, S., and Stewart, J. P. (2003), "Kinematic soil-structure interaction from strong motion recordings," *Journal of Geotechnical and Geoenvironmental Engineering*, 129(4), 323-335.

Kumar, S., Lalvani, L., and Omar, M. (2006), "Nonlinear Response of Single Piles in Sand Subjected to Lateral Loads using k hmax Approach," *Geotech Geol Eng*, 24(1), 163-181.

Kwon, O., and Elnashai, A. (2008), "Seismic Analysis of Meloland Road Overcrossing Using Multiplatform Simulation Software Including SSI," *Journal of Structural Engineering*, 134(4), 651-660.

Lam, I. P., Kapuskar, M., and Chaudhuri, D. (1998), "Modeling of pile footings and drilled shafts for seismic design," *No. MCEER-98-0018*, US Multidisciplinar Center for Earthquake Engineering Research.

Lam, I. P., and Law, H. (2000), "Soil Structure Interaction of Bridges for Seismic Analysis," MCEER, Fountain Valley, California.

Lam, I. P., Law, H. K., and Martin, G. R. (2007), "Bridge Foundations: Modeling Large Pile Groups and Caissons for Seismic Design," *No. MCEER-07-0018*, University at Buffalo, NY.

Lam, I. P., and Martin, G. R. (1986), "Seismic Design of Highway Bridge Foundations, FHWA Report," Federal Highway Administration, Washington D.C.

Lam, I. P., Martin, G. R., and Imbsen, R. (1991), "Modeling Bridge Foundations for Seismic Design and Retrofitting," *Transportation Research Recoed 1290*, 113-126.

Lam, I. P., and Martion, G. R. (1986), "Sesimic Design of Highway Bridge Foundations," Federal Highway Administration, Washington D.C.

Law, H. K., and Lam, I. P. (2001), "Application of Periodic Boundary for Large Pile Group," *Journal of Geotechnical and Geoenvironmental Engineering*, 127(10), 889-892.

Li, W., and Assimaki, D. (2010), "Site- and Motion-Dependent Parametric Uncertainty of Site-Response Analyses in Earthquake Simulations," *Bulletin of the Seismological Society of America*, 100(3), 954-968.

Li, X. S., Shen, C. K., and Wang, Z. L. (1998), "Fully Coupled Inelastic Site Response Analysis for 1986 Lotung Earthquake," *Journal of Geotechnical and Geoenvironmental Engineering*, 124(7), 560-573.

Liu, X., Scarpas, A., and Blaauwendraad, J. (2005), "Numerical modelling of nonlinear response of soil. Part 2: Strain localization investigation on sand," *International Journal of Solids and Structures*, 42(7), 1883-1907.

Ljung, L. (1999), *System Identification: Theory for the User*, Upper Saddle River, New Jersey: Prentice Hall PTR.

Lu, J., Elgamal, A., Sikorsky, C., and Shantz, T. (2010), "Computational Modeling of a Large Pile Group under Lateral Load," *Fifth International Conference on Recent*

Advances in Geotechnical Earthquake Engineering and Soil Dynamics San Diego, California.

Lu, J., Elgamal, A., Yan, L., Law, K., and Conte, J. (2011), "Large-Scale Numerical Modeling in Geotechnical Earthquake Engineering," *International Journal of Geomechanics*, 11(6), 490-503.

Lu, J., Yang, Z., and Ahmed, E. (2006), "OpenseesPL: three-dimensional lateral pile-ground interaction," *User's Manual, Version 0.8*.

Lu, J., Yang, Z., and Elgamal, A. (2010), "OpenseesPL: three-dimensional lateral pile-ground interaction," *User's Manual, Version 0.6*.

Luco, J., and Wong, H. (1992), "Identification of Soil Properties from Foundation Impedance Functions," *Journal of Geotechnical Engineering*, 118(5), 780-795.

Luco, J. E. (1975), "Impedance functions for a rigid foundation on a layered medium," *Nuclear Engineering and Design*, 31(2), 204-217.

Luco, J. E., and Contesse, L. (1973), "Dynamic structure-soil-structure interaction," *Bulletin of the Seismological Society of America*, 63(4), 1289-1303.

Luco, J. E., Trifunac, M. D., and Wong, H. L. (1987), "On the apparent change in dynamic behavior of a nine-story reinforced concrete building," *Bulletin of the Seismological Society of America*, 77(6), 1961-1983.

Maheshwari, B. K., Truman, K. Z., El Naggar, M. H., and Gould, P. L. (2004), "Three-dimensional finite element nonlinear dynamic analysis of pile groups for lateral transient and seismic excitations," *Canadian Geotechnical Journal*, 41(1), 118-133.

Maheshwari, B. K., Truman, K. Z., El Naggar, M. H., and Gould, P. L. (2004), "Three-dimensional nonlinear analysis for seismic soil-pile-structure interaction," *Soil Dynamics and Earthquake Engineering*, 24(4), 343-356.

Maki, T., Maekawa, K., and Mutsuyoshi, H. (2006), "RC pile-soil interaction analysis using a 3D-finite element method with fibre theory-based beam elements," *Earthquake Engineering & Structural Dynamics*, 35(13), 1587-1607.

Malhotra, P. K., Huang, M. J., and Shakal, A. F. (1995), "Seismic interaction at separation joints of an instrumented concrete bridge," *Earthquake Engineering & Structural Dynamics*, 24(8), 1055-1067.

Matlock, H. (1970), "Correlations for design of laterally loaded piles in soft clay," *Proceedings of Proc., Offshore Technology Conference*, OTC 1204, Houston, TX, USA, 577-594.

Mazzoni, S., McKenna, F., Scott, M. H., and Fenves, G. L. (2006), "Open System for Earthquake Engineers Simulation User Manual," *Pacific Earthquake Engineering Research Center*, University of California, Berkeley, CA.

McLaughlin, R. J., Ellen, S. D., Blake, M. C., Jayko, A. S., Irwin, W. P., Aalto, K. R., Carver, G. A., and Clarke, S. H. (2000), "Geology of the Cape Mendocino, Eureka, Garberville, and Southwestern part of the Hayfork," *U.S. Department of the Interior, U.S. Geological Survey*.

McVay, M., Casper, R., and Shang, T. I. (1995), "Lateral Response of Three-Row Groups in Loose to Dense Sands at 3D and 5D Pile Spacing," *Journal of Geotechnical Engineering*, 121(5), 436-441.

McVay, M., Zhang, L. M., Molnit, T., and Lai, P. (1998), "Centrifuge testing of large laterally loaded pile groups in sands," *Journal of Geotechnical and Geoenvironmental Engineering*, 124(10), 1016-1026.

Menéndez, C., Nieto, P. J. G., Ortega, F. A., and Bello, A. (2010), "Non-linear analysis of the consolidation of an elastic saturated soil with incompressible fluid and variable permeability by FEM," *Applied Mathematics and Computation*, 216(2), 458-476.

Mokwa, R. L. (1999), "Investigation of the resistance of pile caps to lateral loading," Ph.D. Dissertation, Virginia Polytechnic Institute and State University, Blacksburg, Virginia.

Mosquera, V., Smyth, A. W., and Betti, R. (2012), "Rapid evaluation and damage assessment of instrumented highway bridges," *Earthquake Engineering & Structural Dynamics*, 41(4), 755-774.

Muqtadir, A., and Desai, C. S. (1986), "Three-dimensional analysis of a pile-group foundation," *International Journal for Numerical and Analytical Methods in Geomechanics*, 10(1), 41-58.

Mylonakis, G., and Gazetas, G. (2000), "Seismic soil structure interaction: Beneficial or Detrimental?," *Journal of Earthquake Engineering*, 04(03), 277-301.

Mylonakis, G., Nikolaou, A., and Gazetas, G. (1997), "SOIL–PILE–BRIDGE SEISMIC INTERACTION: KINEMATIC AND INERTIAL EFFECTS. PART I: SOFT SOIL," *Earthquake Engineering & Structural Dynamics*, 26(3), 337-359.

Nazarian, S., and Desai, M. R. (1993), "Automated Surface Wave Method: Field Testing," *Journal of Geotechnical Engineering*, 119(7), 1094-1111.

Norris, G., Siddharthan, R., Zafir, Z., Abdel-Ghaffar, S., and Gowda, P. (1991), "Soil-Foundation-Structure Behavior at the Oakland Outer Harbor Wharf," *CCEER-91-2*, Center for Civil Engineering Earthquake Research, University of Nevada, Reno.

Norris, G., Siddharthan, R., Zafir, Z., and Gowda, P. (1993), "Soil and foundation conditions and ground motion at Cypress Street viaduct," *Transportation research record*(1411).

Novak, M. (1991), "Piles under Dynamic Loads," *Proceedings of Second International Conference on Recent Advances In Geotechnical Earthquake Engineering and Soil Dynamics*, St. Louis, Missouri, 2433-2456.

NRC (1985), "Liquefaction of soils during earthquakes," G. W. Housner, ed., National Research Council, Committee on Earthquake Engineering, Washington, D.C.

Olson, L. D. (2005), "Dynamic Bridge Substructure Evaluation and Monitoring," No. FHWA-RD-03-089. 2005.

Pandey, B. H., Ventura, C. E., and Finn, W. L. (2012), "Vibration Characteristics of Foundation and Free-Field Motions of Instrumented Buildings During Earthquakes," *Topics on the Dynamics of Civil Structures, Volume 1*, Springer, 433-441.

Parra, E. (1996), "Numerical Modeling of Liquefaction and Lateral Ground Deformation Including Cyclic Mobility and Dilation Response in Soil Systems,"Ph.D. Dissertation, Rensselaer Polytechnic Institute, Troy, NY.

Peng, J.-R. (2006), "Behaviour of finned piles in sand under lateral loading," Ph.D. Dissertation, Newcastle University, UK.

Peng, J., Clarke, B., and Rouainia, M. (2011), "Increasing the Resistance of Piles Subject to Cyclic Lateral Loading," *Journal of Geotechnical and Geoenvironmental Engineering*, 137(10), 977-982.

Peng, J., Lu, J., Law, K. H., and Elgamal, A. (2004), "ParCYCLIC: Finite element modelling of earthquake liquefaction response on parallel computers," *International Journal for Numerical and Analytical Methods in Geomechanics*, 28(12), 1207-1232.

Peng, J. R., Rouainia, M., and Clarke, B. G. (2010), "Finite element analysis of laterally loaded fin piles," *Computers & Structures*, 88(21–22), 1239-1247.

Petrasovits, G., and Awad, A. (1972), "Ultimate lateral resistance of a rigid pile in cohesionless soil," *Proceedings of proc., 5th European Conf. on SMFE*, Madrid, Spain, 407-412.

PG&E (2006), "Humboldt Bay Repowering Project Application for Certification," *Geologic and Foundation Design Criteria*, California Energy Commission.

Pise, P. J. (1984), "Lateral response of free-head pile," *Journal of Geotechnical Engineering*, 110(12), 1805-1809.

Pitarka, A., Thio, H. K., and Somerville, P. (2012), "3D Wave Propagation and Site Effects in the Humboldt Bay Area using Strong Grond Motion Records from the M6.5 Ferndale Earthquake," *Proceedings of SMIP12 Seminar Proceedings*, Sacramento, CA.

Poulos, H. G. (1971), "Behavior of laterally loaded piles: I-single piles," *Journal of the Soil Mechanics and Foundations Division*, 97(5), 717-731.

Poulos, H. G. (1971), "Behavior of Laterally Loaded Piles: II-Pile Groups," *Journal of the Soil Mechanics and Foundations Division*, 97(5), 733-751.

Power, M. S., Chang, C. Y., and Idriss, I. M. (1986), "Engineering characterization of ground motion. Task II. Summary report," *No. NUREG/CR-3805*, Office of Nuclear Regulatory Reasearch, Woodward-Clyde Consultants, Walnut Creek, CA; Structural Mechanics Associates, Newport Beach, CA, 369-380.

Pressley, J. S., and Poulos, H. G. (1986), "Finite element analysis of mechnisms of pile group behaviour," *International Journal of Numerial Analysis Mehthods in Geomechnics*, 10, 213-221.

Prevost, J. H. (1985), "A Simple Plasticity Theory for Frictional Cohesionless Soils," *Soil Dynamics and Earthquake Engineering*, 4(1), 9-17.

Priestley, M., Verma, R., and Xiao, Y. (1994), "Seismic shear strength of reinforced concrete columns," *Journal of Structural Engineering*, 120(8), 2310-2329.

Pyke, R. M. (1980), "Nonlinear soil models for irregular cyclic loadings," *Journal of Geotechnical and Geoenvironmental Engineering*, 106(ASCE 15829).

Randolph, M. F. (1981), "Response of flexible piles to lateral loading," *Geotechnique*, 31(2), 247-259.

Rayamajhi, D., Nguyen, T., Ashford, S., Boulanger, R., Lu, J., Elgamal, A., and Shao, L. (2012), "Effect of discrete columns on shear stress distribution in liquefiable soil," *Proceedings of Proc., Geo-Congress 2012*, 1908-1917.

Reese, L. C. (1997), "Analysis of laterally loaded piles in weak rock," *Journal of Geotechnical and Geoenvironmental Engineering*, 123(11), 1010-1017.

Reese, L. C., Cooley, L. A., and Radhakrishnan, N. (1984), "Laterally loaded liles and computer program COM624G," *Tech. Rep. K-84-2*, U.S. Army Engineer Waterways Experiment Station, Vicksburg, Miss.

Reese, L. C., and Matlock, H. (1956), "Non-dimensional solutions for laterally loaded piles with soil modulus assumed proportional to depth," *Proceedings of Proceedings of the eighth Texas conference on soil mechanics and foundation engineering*, Austin, Texas, 1-23.

Reese, L. C., and Wang, S.-T. (2006), "Verification of computer program LPile as a valid tool for design of a single pile under lateral loading," Ensoft, Inc, Austin , TX.

Reese, L. C., and Wang, S. T. (1986), "Method of Analysis of Piles under Lateral Loading," ASTM, Shanghai, China, 199-211.

Reese, L. C., and Welch, R. C. (1975), "Lateral loading of deep foundations in stiff clay," *Journal of the Geotechnical Engineering Division*, 101(7), 633-649.

Rollins, K., and Brown, D. (2011), "Design Guidelines for Increasing the Lateral Resistance of Highway-Bridge Pile Foundations by Improving Weak Soils," *Report 697*, National Cooperative Highway Research Program.

Rollins, K. M., Olsen, R. J., Egbert, J. J., Jensen, D. H., Olsen, K. G., and Garrett, B. H. (2006), "Pile Spacing Effects on Lateral Pile Group Behavior: Load Tests," *Journal of Geotechnical and Geoenvironmental Engineering*, 132(10), 1262-1271.

Rollins, K. M., Peterson, K. T., and Weaver, T. J. (1998), "Lateral load behavior of full-scale pile group in clay," *Journal of Geotechnical and Geoenvironmental Engineering*, 124(6), 468-478.

Şafak, E. (1991), "Identification of Linear Structures Using Discrete-Time Filters," *Journal of Structural Engineering*, 117(10), 3064-3085.

Sakr, M., Naggar, M. H. E., and Nehdi, M. (2005), "Lateral behaviour of composite tapered piles in dense sand," *Proceedings of the ICE - Geotechnical Engineering*, 145-157.

Scott, R. F. (1981), "Pile testing in a centrifuge," *Proceedings of Proceedings of the International Conference on Soil Mechanics and Foundation Engineering*, A. A. Balkema, Rotterdam, Neth, Stockholm, Swed, 839-842.

Seed, H. B., and Idriss, I. M. (1970), "Soil moduli and damping factors for dynamic response analyses," Earthquake Engineering Research Center, Report No. EERC 70-10, University of California, Berkeley, California.

Seed, H. B., Romo, M. P., Sun, J. I., Jaime, A., and Lysmer, J. (1988), "The Mexico Earthquake of September 19, 1985-Relationships Between Soil Conditions and Earthquake Ground Motions," *Earthquake Spectra*, 4(4), 687-729.

Shakal, A., and Huang, M. (2013), "Recent Developments and Status of the California Strong Motion Instrumentation Program," *Proceedings of SMIP2013 Seminar on Utilization of Strong-Motion Data Proceedings*, Los Angeles, California, 101-118.

Shamsabadi, A., Abazarsa, F., Ghahari, S., Nigbor, R., and Taciroglu, E. (2014), "Bridge Instrumentation: Needs, options, and consequences," *Proceedings of Istanbul Bridge Conference*, Istanbul, Turkey.

Shamsabadi, A., and Taciroglu, E. (2013), "A Frequency-Time Domain Handshake Method For Seismic Soil-Foundation-Structure Interaction Analysis of Long-Span Bridges," *Seventh National Seismic Conference on Bridges and Highways*Oakland, California.

Shantz, T. (2013), "Guidelines on foundation loading and deformation due to liquefaction induced lateral spreading," *California Department of Transportation, Sacramento, CA.*

Spyrakos, C. C. (1990), "Assessment of SSI on the longitudinal seismic response short span bridges," *Construction and Building Materials*, 4(4), 170-175.

Stewart, J. P., and Fenves, G. L. (1998), "System identification for evaluating soil–structure interaction effects in buildings from strong motion recordings," *Earthquake Engineering & Structural Dynamics*, 27(8), 869-885.

Stewart, J. P., Kwok, A. O.-L., Hashash, Y. M. A., Matasovic, N., Pyke, R., Wang, Z., and Yang, Z. (2008), *Benchmarking of Nonlinear Geotechnical Ground Response Analysis Procedures*, Pacific Earthquake Engineering Research Center.

Stewart, J. P., Seed, R. B., and Fenves, G. L. (1998), "Empirical evaluation of inertial soil-structure interaction effects," *Rep. No. PEER-98/07*, Pacific Earthquake Engineering Research Center, University of California, Berkeley, CA.

Storesund, R., Dengler, L., Mahin, S., Collins, B. D., Hanshaw, M., Turner, F., and Welsh, K. (2010), "M6.5 Earthquake Offshore Northern California January 9, 2010," GEER Field Reconnaissance Summary.

Takahashi, A., Kuwano, Y., Aria, Y., and Yano, A. (2002), "Lateral resistance of buried cylinder in liquefied sand," *Proceedings of Proceedings of the International Conference on physical modelling in geotechnics, ICPMG-02, St. John's, Newfoundland, Canada*.

Tileylioglu, S. (2008), "Evaluation of soil-structure interaction effects from field performance data," Ph.D. dissertation, University of California, Los Angeles, CA.

Ting, J. M. (1987), "Full-Scale Cyclic Dynamic Lateral Pile Responses," *Journal of Geotechnical Engineering*, 113(1), 30-45.

Travis, M. G., and Kyle, M. R. (2008), "Cyclic P-Y curves for a pile in cohesive soil," *Proceedings of Geotechnical Earthquake Engineering and Soil Dynamics IV*, ASCE, GSP 181, Sacramento, California, 1-10.

Tsai, C.-C., and Hashash, Y. M. A. (2009), "Learning of Dynamic Soil Behavior from Downhole Arrays," *Journal of Geotechnical and Geoenvironmental Engineering*, 135(6), 745-757.

Turek, M., Ventura, C. E., Dowling, J., Molnar, S., and Kaya, Y. (2014), "Ambient Vibration Testing of the Eureka-Samoa Channel Bridge," *Dynamics of Civil Structures, Volume 4*, Springer, 403-409.

Uzuoka, R., Sento, N., Kazama, M., Zhang, F., Yashima, A., and Oka, F. (2007), "Three-dimensional numerical simulation of earthquake damage to group-piles in a liquefied ground," *Soil Dynamics and Earthquake Engineering*, 27(5), 395-413.

Van Den Einde, L., Restrepo, J., Conte, J., Luco, E., Seible, F., Filiatrault, A., Clark, A., Johnson, A., Gram, M., and Kusner, D. (2004), "Development of the George E. Brown Jr. network for earthquake engineering simulation (NEES) large high performance outdoor shake table at the University of California, San Diego," *Proceedings of Proceedings of the 13th World Conference on Earthquake Engineering*, 1-6.

Wakai, A., Gose, S., and Ugai, K. (1999), "3-D elasto-plastic finite element analyses of pile foundations subjected to lateral loading " *Soils and Foundations*, 39(1), 97-111.

Wang, N., and Elgamal, A. (2013), "Bridge and adjacent downhole array responses during earthquakes at Eureka, California," *Proceedings of 110th International Conference on Urban Earthquake Engineering*, Tokyo, Japan.

Werner, S., Crouse, C., Katafygiotis, L., and Beck, J. (1994), "Use of strong motion records for model evaluation and seismic analysis of a bridge structure," *Proceedings of Proceedings Fifth US National Conference on Earthquake Engineering*, Earthquake Engineering Research Institute, Chicago, 511-520.

Werner, S. D., Beck, J. L., and Levine, M. B. (1987), "Seismic response evaluation of Meloland Road Overpass using 1979 Imperial Valley earthquake records," *Earthquake Engineering & Structural Dynamics*, 15(2), 249-274.

Wilson, J. C. (1986), "Analysis of the observed seismic response of a highway bridge," *Earthquake Engineering & Structural Dynamics*, 14(3), 339-354.

Wilson, J. C., and Tan, B. S. (1990), "Bridge Abutments: Assessing Their Influence on Earthquake Response of Meloland Road Overpass," *Journal of Engineering Mechanics*, 116(8), 1838-1856.

Wolf, J. P. (1985), *Dynamic soil-structure interaction*, Prentice-Hall, Englewood Cliffs, N.J.

Wong, H. L., and Luco, J. E. (1985), "Tables of impedance functions for square foundations on layered media," *International Journal of Soil Dynamics and Earthquake Engineering*, 4(2), 64-81.

Wong, H. L., and Luco, J. E. (1986), "Dynamic interaction between rigid foundations in a layered half-space," *Soil Dynamics and Earthquake Engineering*, 5(3), 149-158.

WSDOT (2014), "WSDOT Bridge Design Manual - Chapter 7 Substructure Design," Washington State Department of Transportation, Olympia, Washington.

Yang, Z. (2000), "Numerical Modeling of Earthquake Site Response Including Dilation and Liquefaction,"Ph.D. Thesis, Columbia University, New York, NY.

Yang, Z. (2002), "Development of geotechnical capabilities into OpenSees platform and their applications in soil-foundation-structure interaction analyses,"Ph.D., University of California, Davis, CA.

Yang, Z., and Elgamal, A. (2002), "Influence of Permeability on Liquefaction-Induced Shear Deformation," *Journal of Engineering Mechanics*, 128(7), 720-729.

Yang, Z., and Elgamal, A. (2003), "Application of unconstrained optimization and sensitivity analysis to calibration of a soil constitutive model," *International Journal for Numerical and Analytical Methods in Geomechanics*, 27(15), 1277-1297.

Yang, Z., Elgamal, A., and Parra, E. (2003), "Computational Model for Cyclic Mobility and Associated Shear Deformation," *Journal of Geotechnical and Geoenvironmental Engineering*, 129(12), 1119-1127.

Yang, Z., and Jeremic, B. (2003), "Numerical study of group effects for pile groups in sands," *International Journal for Numerical and Analytical Methods in Geomechanics*, 27(15), 1255-1276.

Yang, Z., and Jeremic, B. (2005), "Study of Soil Layering Effects on Lateral Loading Behavior of Piles," *Journal of Geotechnical and Geoenvironmental Engineering*, 131(6), 762-770.

Zafir, Z. (2002), "Seismic Foundation Stiffness for Bridges," *Proceedings of Deep Foundations 2002: An International Perspective on Theory, Design, Construction, and Performance*, ASCE, GSP 116, Orlando, Florida, 1421-1437.

Zeghal, M., and Elgamal, A. (1994), "Analysis of Site Liquefaction Using Earthquake Records," *Journal of Geotechnical Engineering*, 120(6), 996-1017.

Zeghal, M., Elgamal, A., Tang, H. T., and Stepp, J. C. (1995), "Lotung Downhole Array. II: Evaluation of Soil Nonlinear Properties," *Journal of Geotechnical Engineering*, 121(4), 363-378.

Zhang, J., and Makris, N. (2002), "Seismic response analysis of highway overcrossings including soil–structure interaction," *Earthquake Engineering & Structural Dynamics*, 31(11), 1967-1991.

Zhang, L. (2009), "Nonlinear analysis of laterally loaded rigid piles in cohesionless soil," *Computers and Geotechnics*, 36(5), 718-724.

Zhang, Y. (2006), "Probabilistic structural seismic performance assessment methodology and application to an actual bridge-foundation-ground system," Ph.D. Dissertation, University of California, San Diego, CA.

Zhang, Y., Conte, J. P., Yang, Z., Elgamal, A., Bielak, J., and Acero, G. (2008), "Two-Dimensional Nonlinear Earthquake Response Analysis of a Bridge-Foundation-Ground System," *Earthquake Spectra*, 24(2), 343-386.

Appendix A.

Additional Parametric Study for Effects of Loading Rate

Effects of loading rate are evaluated with an undrained-clay model interfacing layer (thickness of 0.17 m) employed between the pile and adjacent soil domain. Stiff clay with low permeability is used for the interfacing layer, whereas soil inside the pile zone is defined as soft clay (Lu et al. 2010). A tension cutoff logic is activated in this stiff clay model to eliminate the dilation of soil behind the pile due to the pile moving away from the soil. In this appendix, results are shown for bending stiffness of the pile EI = 2×10^6 kN-m^2 (same as the EI employed in the Dumbarton Pier 23 pile group). Load-displacement curves and variation of EPP with pile head displacement are shown below.

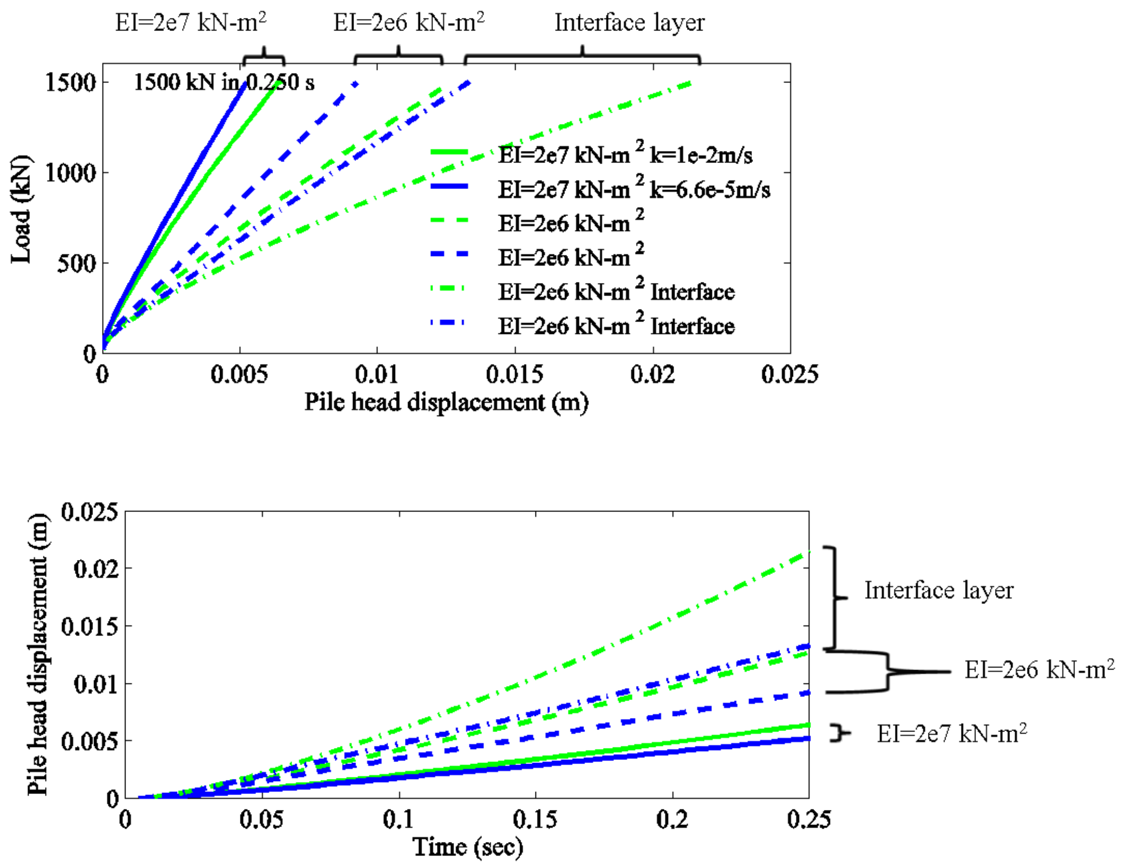

Figure A.1: Load-displacement for 1500 kN in 0.25 s with EI=2×10^{7} kN-m^{2}, EI=2×10^{6} kN-m^{2} (more realistic) and EI=2×10^{6} kN-m^{2} (with interfacing layer)

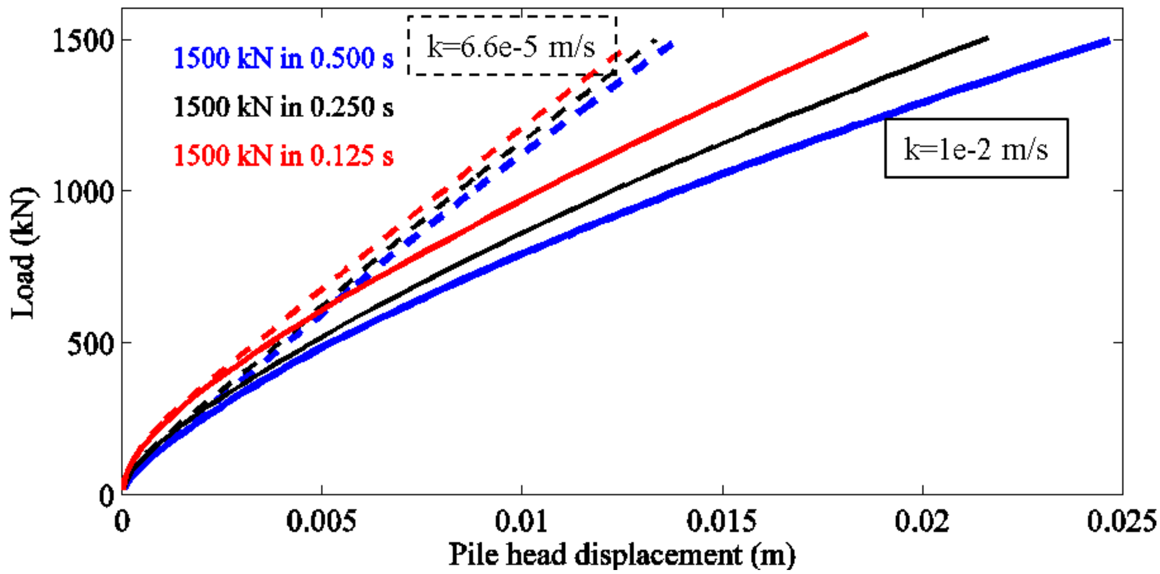

Figure A.2: Load-displacement curve for k=6.6e-5 m/s and k=1e-2 m/s (with interfacing layer)

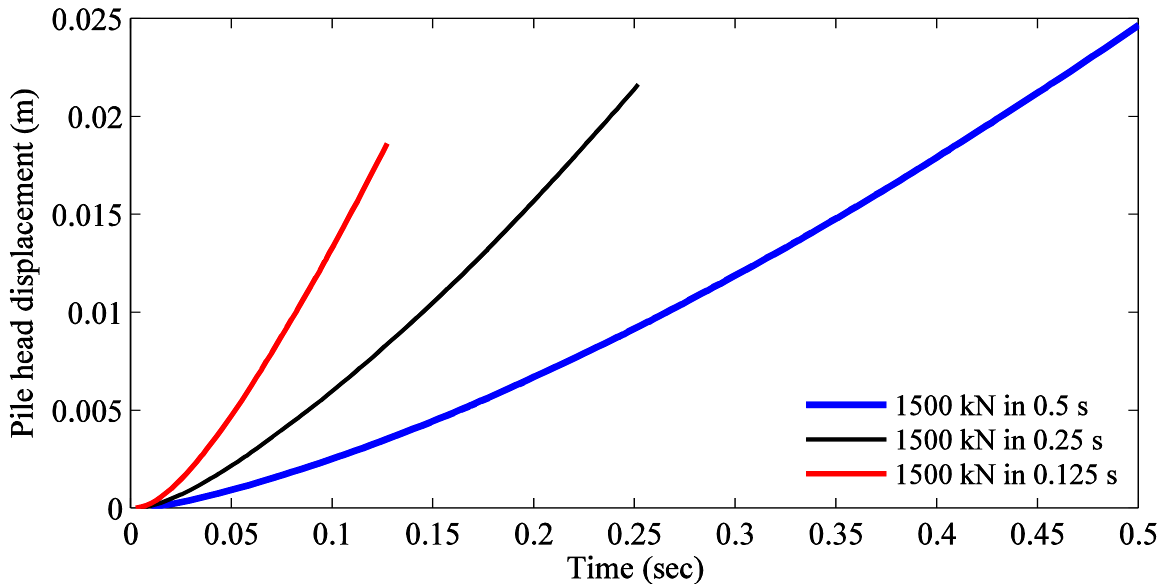

Figure A.3: Pile head displacement-time relationship for k=1e-2 m/s (with interfacing layer)

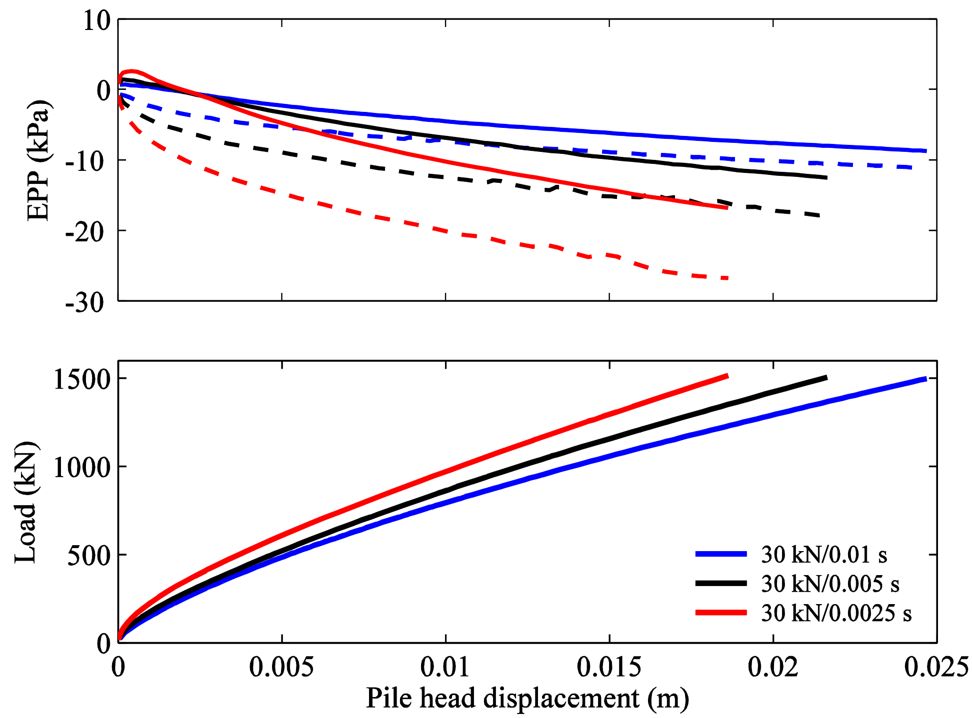

(a)

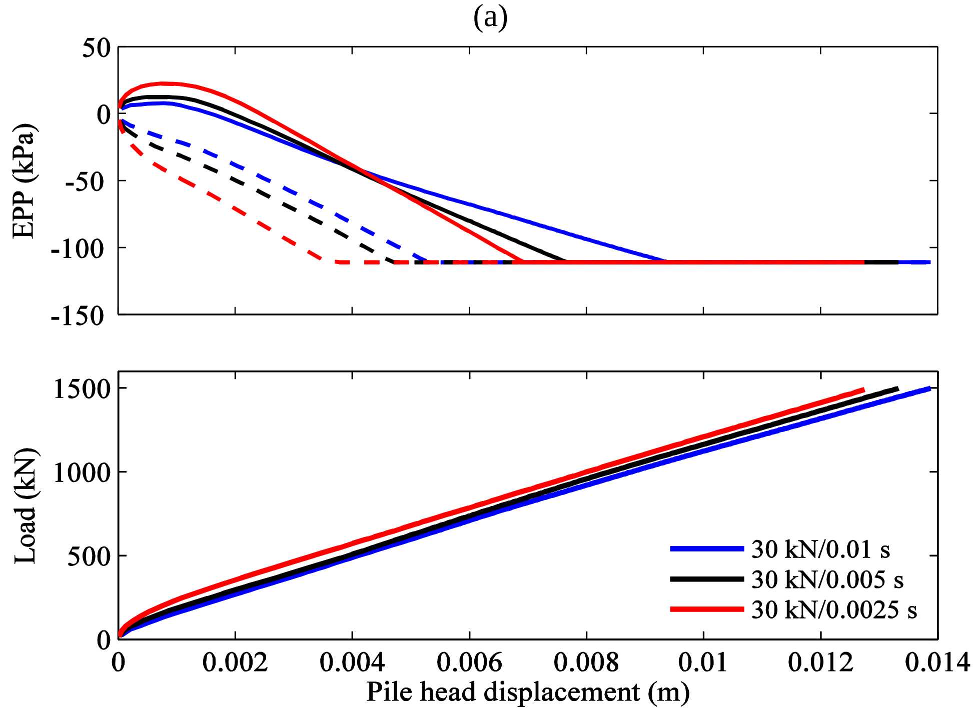

(b)

Figure A.4: EPP versus lateral load behind (dash line) and in front of (solid line) the pile for three loading rate cases for (a) k=1e-2 m/s and (b) k=6.6e-5 m/s (with interfacing layer)

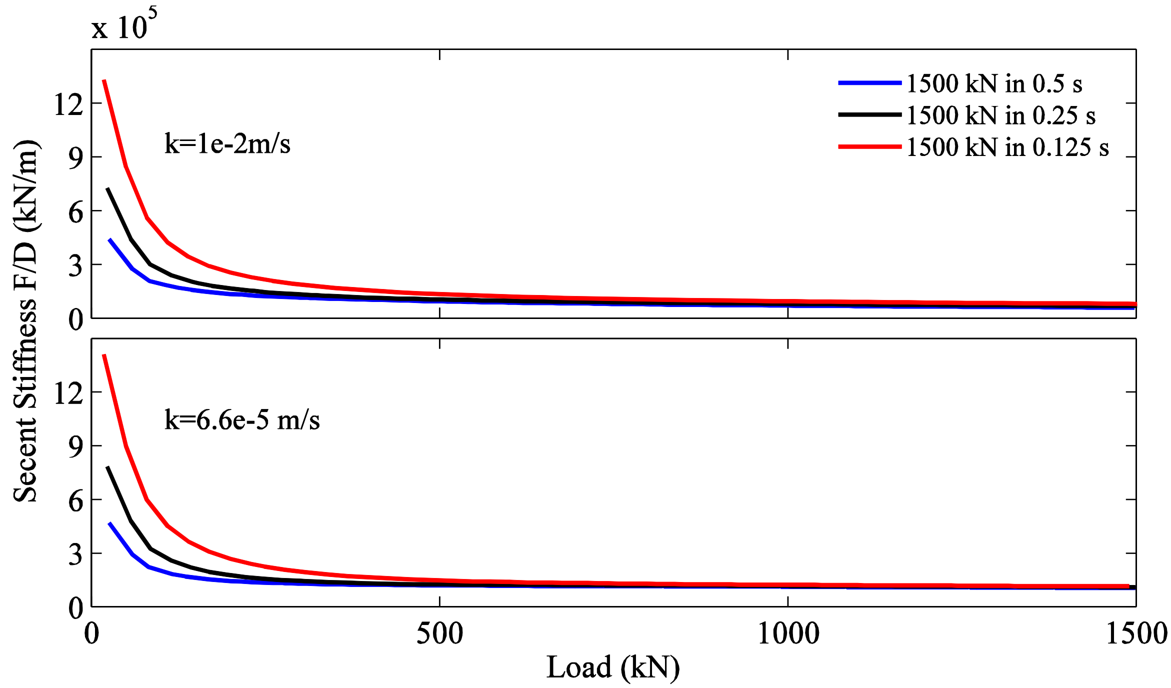

Figure A.5: Secant Stiffness versus load for 3 different constant loading rate scenarios (with interfacing layer)

F (kN)	PWP (kPa)		
	Case 1 1500 kN in 0.5 s	Case 2 1500 kN in 0.25 s	Case 3 1500 kN in 0.125 s
700	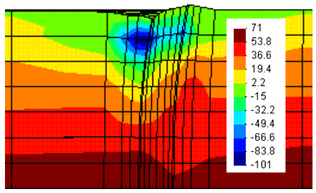	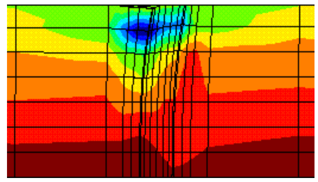	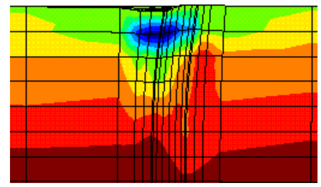
1500	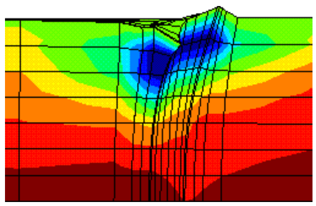	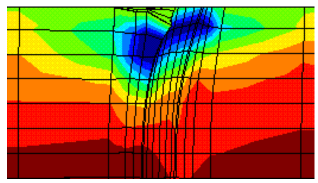	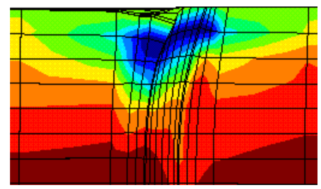

Figure A.6: Pore Water Pressure contour for permeability coefficient of 6.6e-5 m/s (with interfacing layer)

F (kN)	EPP (kPa)		
	Case 1 1500 kN in 0.5 s	Case 2 1500 kN in 0.25 s	Case 3 1500 kN in 0.125 s
700	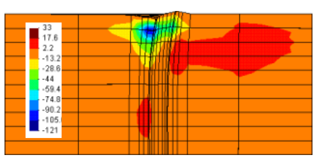	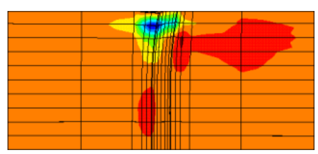	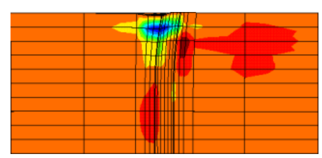
1500	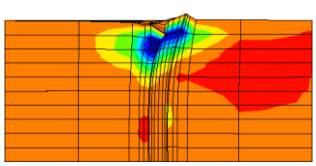	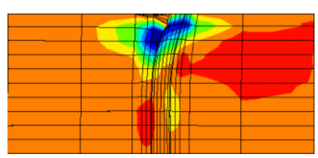	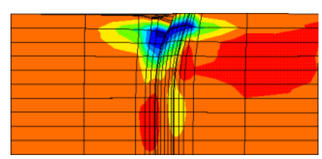

Figure A.7: EPP contour for permeability coefficient of 6.6e-5 m/s (with interfacing layer)

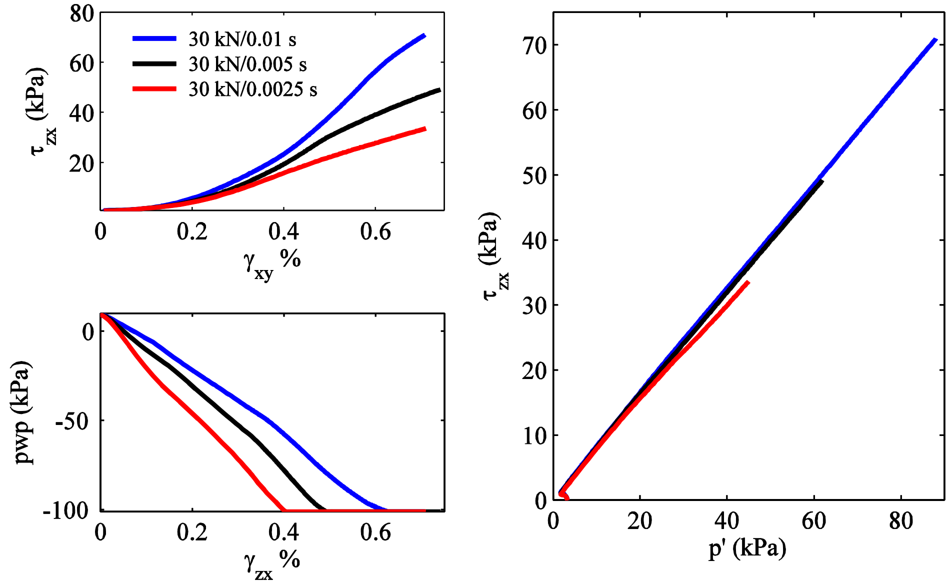

Figure A.8: Soil response at 0.685 m from pile center in transverse direction at 0.7887 m depth (with interfacing layer)

Appendix B.

Estimation of Soil Shear Modulus and Raleigh Damping

The downhole acceleration records in NS direction from the Eureka geotechnical array are employed as the base excitation. The site response during the 2010 Ferndale Earthquake and the 2000 Eureka Offshore Earthquake are studied with aid of the recently developed user interface OpenSees2DPS (http://www.soilquake.net/opensees2dps, Figure B.1). The optimization tool – SNOPT is employed to identify the soil shear wave velocity and Rayleigh Damping (Table B.1). The following boundary conditions are implemented:

(i) Lateral excitation was defined along the base with the recorded NS seismic motion at the depth of 136 m (Chan15)

(ii) At any given depth, displacement degrees of freedom of the left and right boundaries were tied together (both horizontally and vertically)

Table B.1: Soil Layer Properties (Linear Soil Case, Optimized value) for the moderate event

Soil layer	Mass density (kg/m^3)	V_s (m/s)	Poisson's ratio	Damping ratio*
Layer 1 (17m)	1600	108.5-200.9	0.49	20%
Layer 2 (14m)	1740	185.7-242.5	0.48	15%
Layer 3 (23m)	2000	311.1-413.2	0.47	15%
Layer 4 (80m)	2100	416.0-465.4	0.43	8%

*Rayleigh damping is employed with optimized damping ratio at frequencies of 2.13 Hz (f_1) and 6.3 Hz ($f2$).

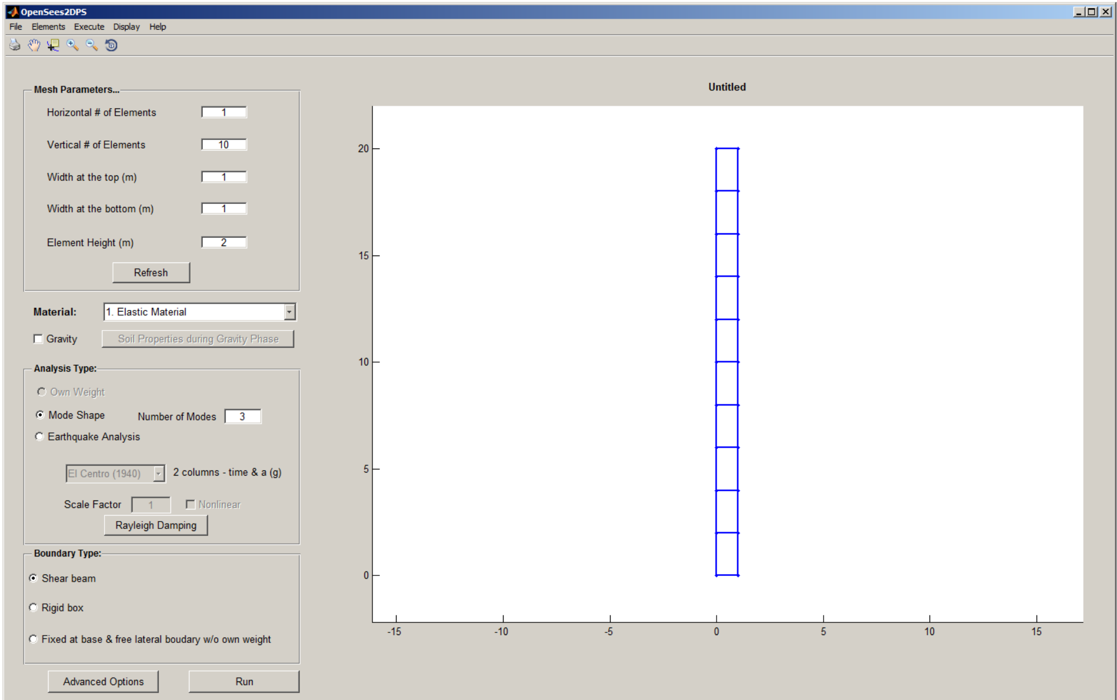

Figure B.1: OpenSees2DPS main window

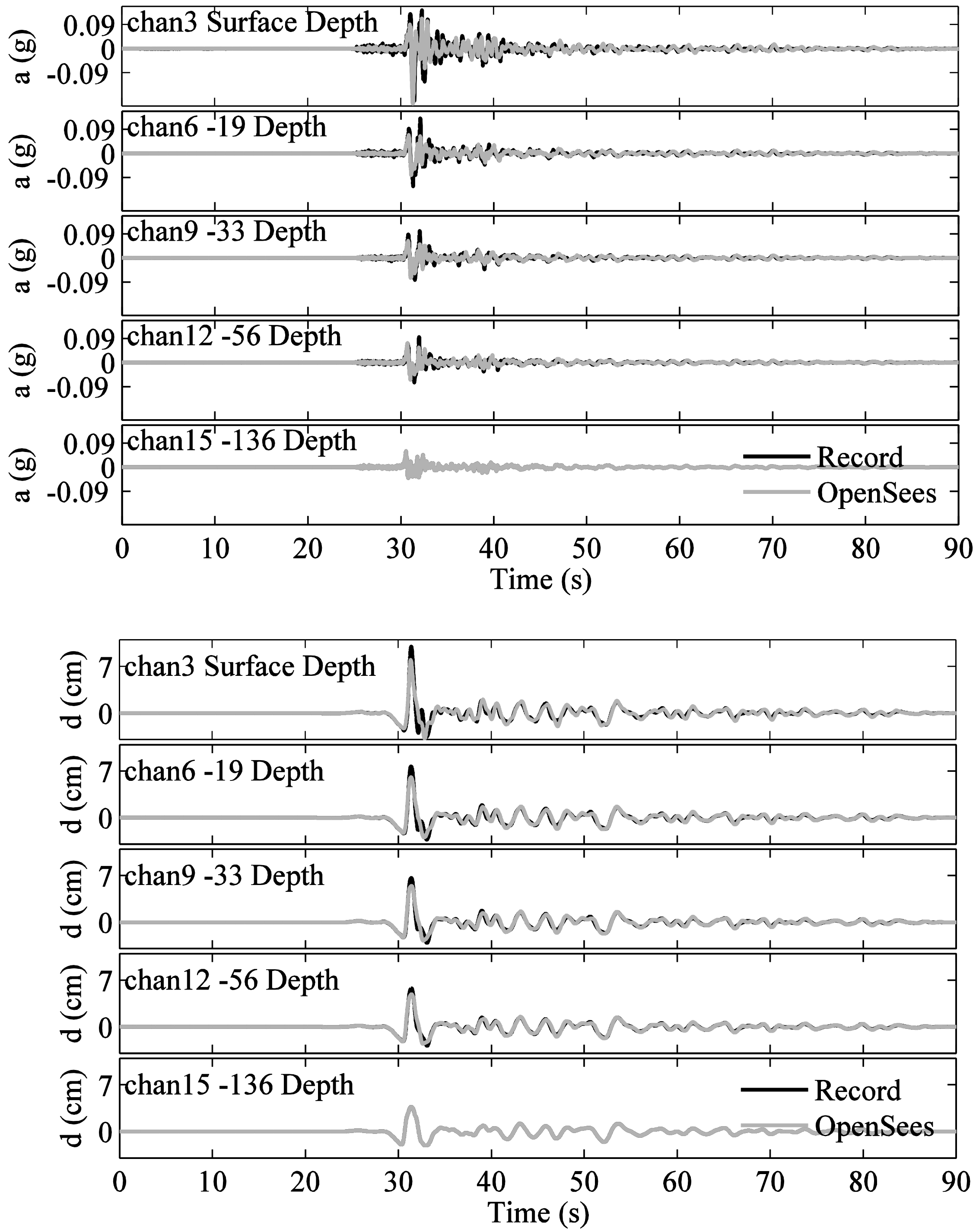

Figure B.2: The moderate event - Linear analysis (Damping ratio of 20% at $f_1 = 2.13$ Hz, $f_2 = 6.3$ Hz)

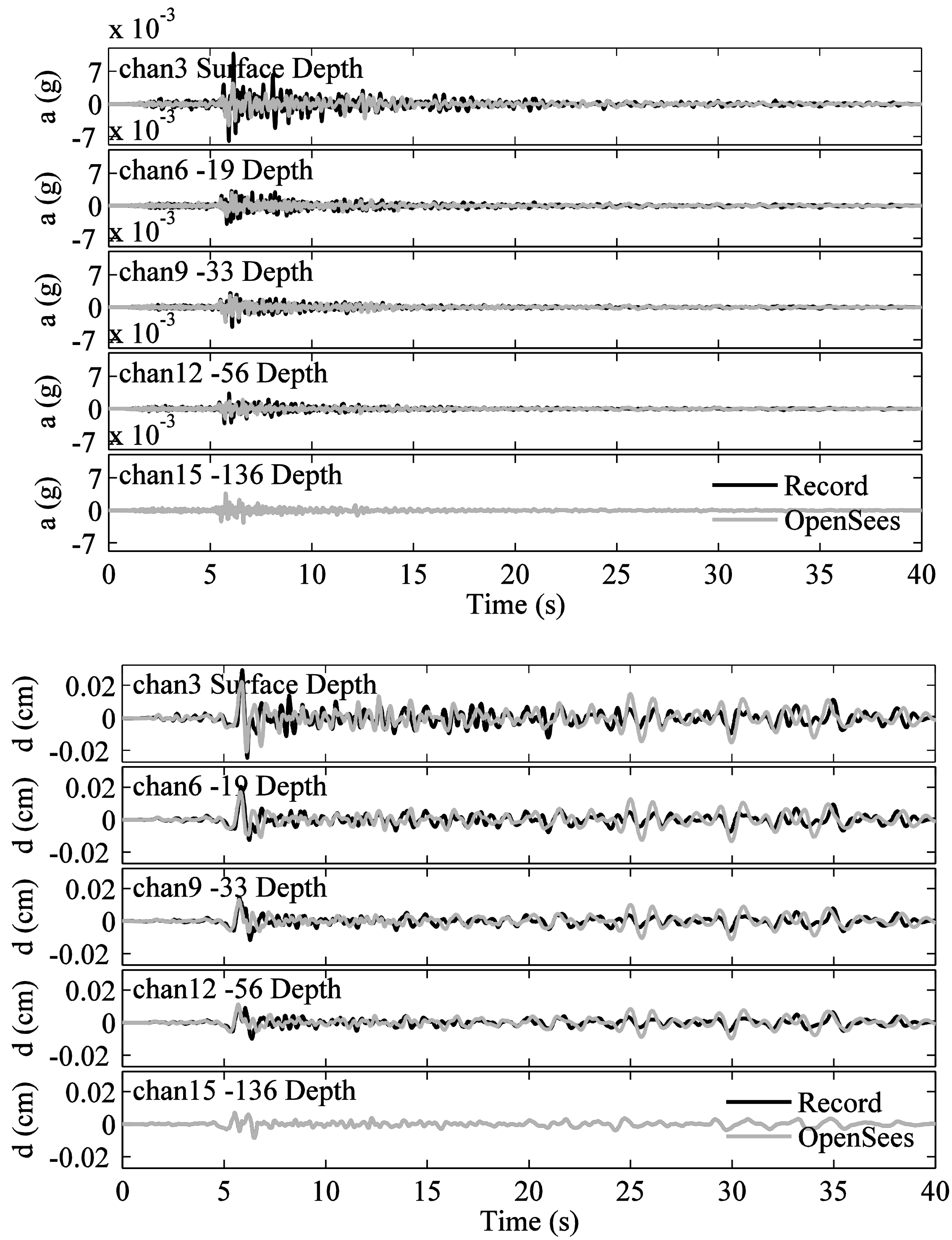

Figure B.3: The 2000 Eureka Offshore Earthquake - Linear analysis (Damping ratio of 5% at f1 = 2.63 Hz, f2 = 6.75 Hz)

Appendix C.

Moment Curvature (M−φ) Analysis for Pier Column S-8

Moment curvature (M−φ) analysis was performed for the single hexagonal concrete column of Samoa Channel Bridge. Caltrans idealized the elastic portion of the M−φ curve to be passing through the point marking the first reinforcing bar yield. And the idealized plastic moment capacity is obtained by balancing the areas between the actual and the idealized M−φ curves beyond the 1st reinforcing bar yield point (Caltrans).

$$I_{crack} = \frac{M_y}{\varphi_y E}$$

For the Samoa Channel Bridge, Mander's stress-strain model for confined and unconfined concrete was used in the moment curvature analysis. The initial ascending curve may be represented by the same equation for both the confined and unconfined model since the confining steel has no effect in this range of strain. As the curve approaches the compressive strength of the unconfined concrete, the unconfined stress begins to fall to an unconfined strain level before rapidly degrading to zero. The confined concrete model should continue to ascend until the confined compressive strength f'_{cc} is reached. This segment should be followed by a descending curve dependent on the parameters of the confining steel.

Concrete Modulus of Elasticity was derived based on following equations and CTBridge:

$E_c = 33 \times w^{1.5}\sqrt{f'_c}$ (psi) $\qquad$ $E_c = 0.043 \times w^{1.5}\sqrt{f'_c}$ (MPa)

where w is unit weight of concrete in lb/ft3 and kg/m3

Unconfined concrete compressive strain at the maximum compressive stress:

$$\epsilon_{c0} = 0.002$$

Ultimate unconfined compression strain:

$$\epsilon_{sp} = 0.005$$

The transverse steel percentage (reinforcement ratio) for a spirally confined circular column is (MSBridge User Manual, Elgamal et al. 2014):

$$\rho_t = \frac{\pi d_{bt}^2}{s' d_{cc}}$$

where d_{bt} is the diameter of the transverse reinforcement

s' is the spacing between transverse bars

d_{cc} is the gross diameter minus twice the cover and minus the diameter of the transverse bars $d_{cc} = D_L - 2c - d_{bt}$

The confined concrete strength f_{cc} is derived as following (MSBridge User Manual):

$$A_{cc} = \frac{\pi(d_{cc})^2}{4}$$

$$\rho_{cc} = \frac{A_s}{A_{cc}}$$

$$K_e = \frac{(1 - \frac{s'}{2d_{cc}})^2}{1 - \rho_{cc}}$$

$$f'_e = \frac{1}{2} K_e \rho_t f_y$$

$$f_{cc} = f'_c(-1.254 + 2.254\sqrt{1 + 7.94\frac{f'_e}{f'_c}} - 2\frac{f'_e}{f'_c})$$

Concrete strain at maximum strength $\epsilon_c = \frac{2f_{cc}}{E_c}$

Concrete strain at crushing strength $\epsilon_{cu} = 0.004 + \epsilon_s \frac{f_y}{f'_c} \rho_t$ (with $\epsilon_s = 0.12$)

Crushing Strength f_{cu}:

$$\epsilon_{c0} = \epsilon_c(1 + 5(\frac{f_{cc}}{f'_c} - 1))$$

$$\epsilon_{cr} = \frac{E_c}{E_c - \frac{f_{cc}}{\epsilon_{c0}}}$$

$$f_{cu} = \frac{f_{cc}\epsilon_{cu}}{\epsilon_{c0}} \frac{\epsilon_{cr}}{\epsilon_{cr} - 1 + (\frac{\epsilon_{cu}}{\epsilon_{c0}})^{\varepsilon_{cr}}}$$

The Samoa Channel Bridge was designed in 1968, built in 1971, and has been the object of two seismic retrofit efforts by California Department of Transportation (CalTrans): the first one was designed in 1985 and completed in 1987, and the second was designed in 2001 and completed in 2002 (Figure C.4).

Properties of concrete and steel of columns used for Moment Curvature analysis are listed in Table C.1. Cross-sections of pier column before and after retrofit are shown in Figure C.3 and Figure C.4. Moment-curvature curves in Figure C.5 and Figure C.6 demonstrate that factored flexural stiffness of Pier column S-8 agrees well with the moment curvature curve after retrofit.

Table C.1: Constitutive model parameters for concrete materials and steel material before Retrofit

Concrete01	Confined concrete		Unconfined concrete
	S-2 to S-20	S-8 &9	S-2 – S-20
Compressive strength at 28 days $f_c^{'}$ (MPa)	-34.795	-34.6969	-34
Strain at max. compressive strength ε_c	-0.0025	-0.0025	-0.0020
Crushing strength f_{cu} (MPa)	-30.7291	-30.701	0
Strain at crushing strength ε_{cu}	-0.005	-0.0048	-0.005
Young's modulus E_c (GPa)	27.90		

Steel01	Reinforcing steel
Yield strength f_y (MPa)	414
Initial elastic tangent E_s (kPa)	2×10^8
Strain-hardening ratio (b)	0.008

Table C.2: Constitutive model parameters for concrete materials and steel material after Retrofit

Concrete01	confined concrete		unconfined concrete
	S-2 – S-20	S-8 &9	S-2 – S-20
Compressive strength at 28 days $f_c^{'}$(MPa)	-35.8736	-35.6506	-28
Strain at max. compressive strength ε_c	-0.0028	-0.0028	-0.002
Crushing strength f_{cu} (MPa)	-33.3192	-33.1136	0
Strain at crushing strength ε_{cu}	-0.0157	-0.152	-0.005
Young's modulus E_c (GPa)	25.32		

steel01	Reinforcing steel
Yield strength f_y (MPa)	303
Initial elastic tangent E_s (kPa)	2×10^8
Strain-hardening ratio (b)	0.008

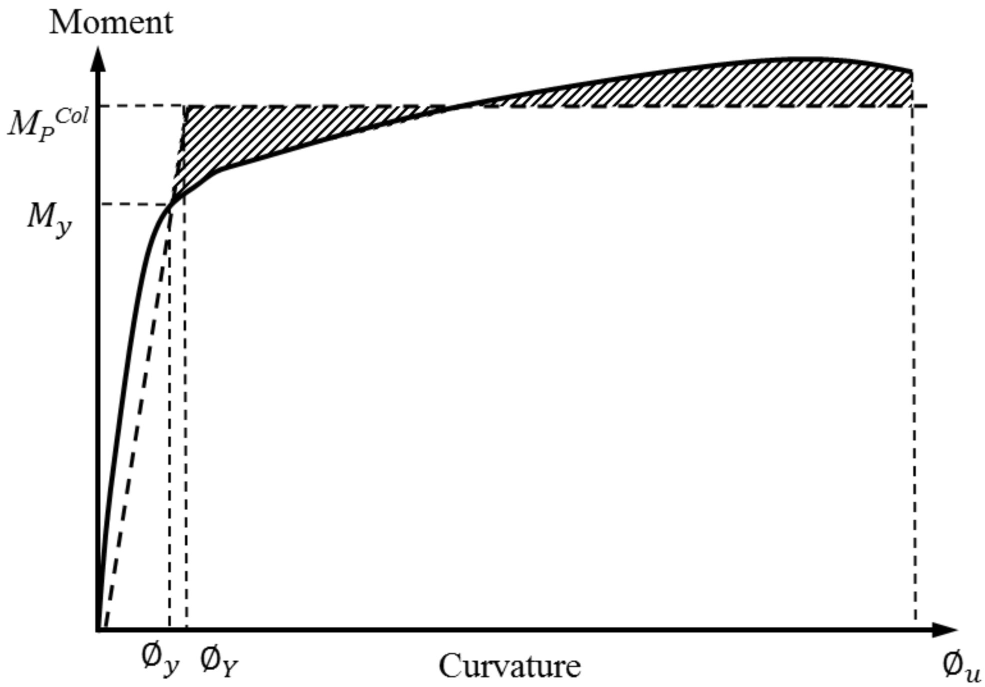

Figure C.1: Moment Curvature Curve (Caltrans)

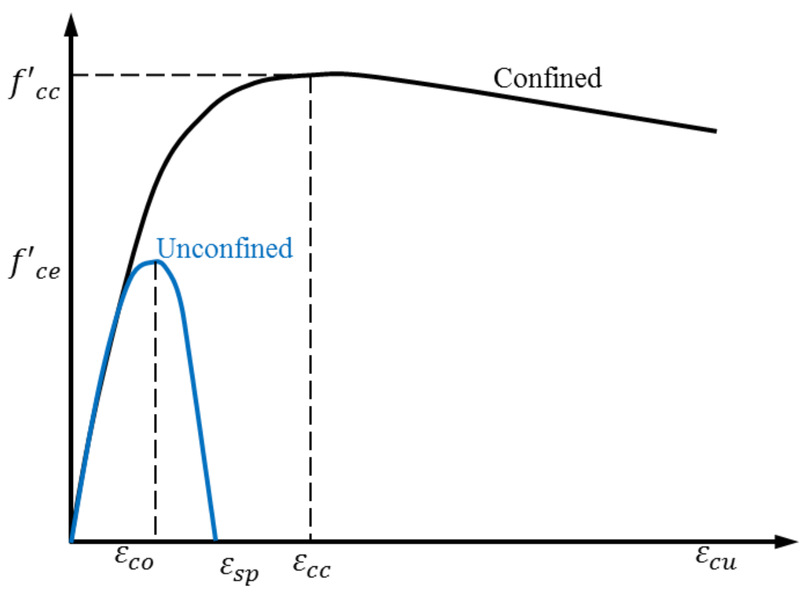

Figure C.2: Concrete Stress-Strain Model (Caltrans)

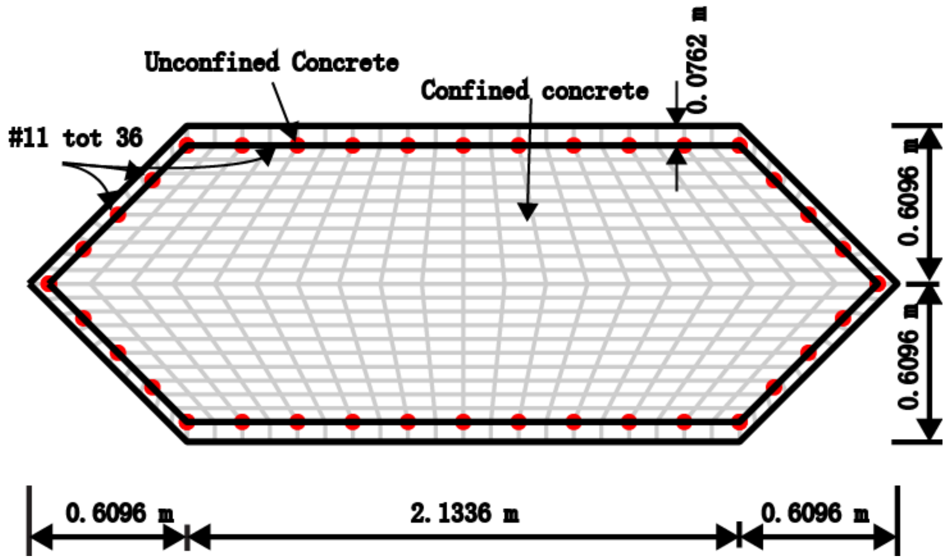

(a) Pier S-14

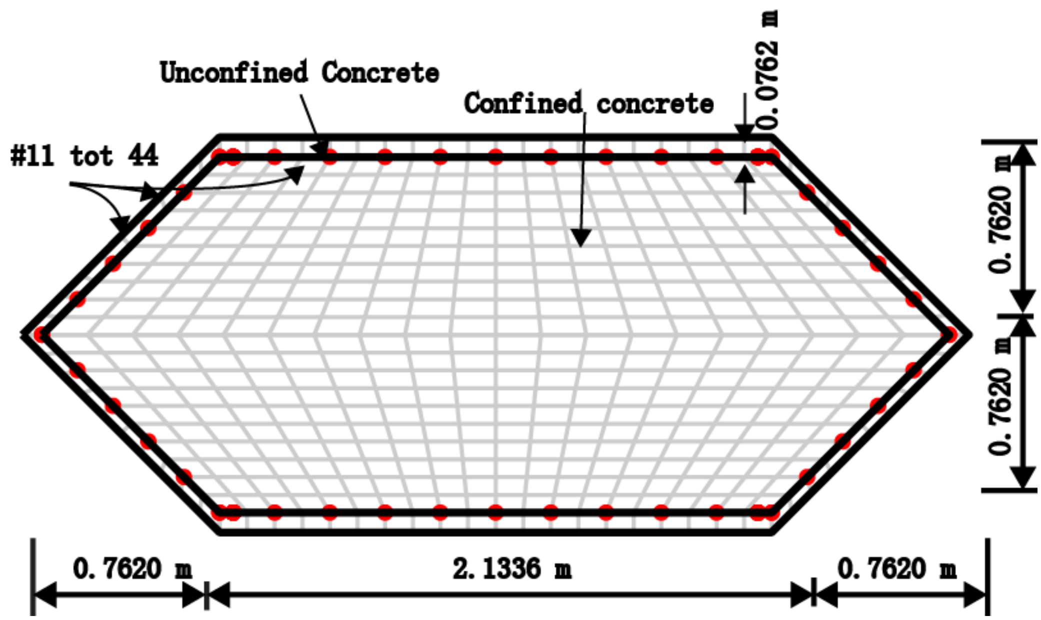

(b) Pier S-8

Figure C.3: Pier Columns before retrofit

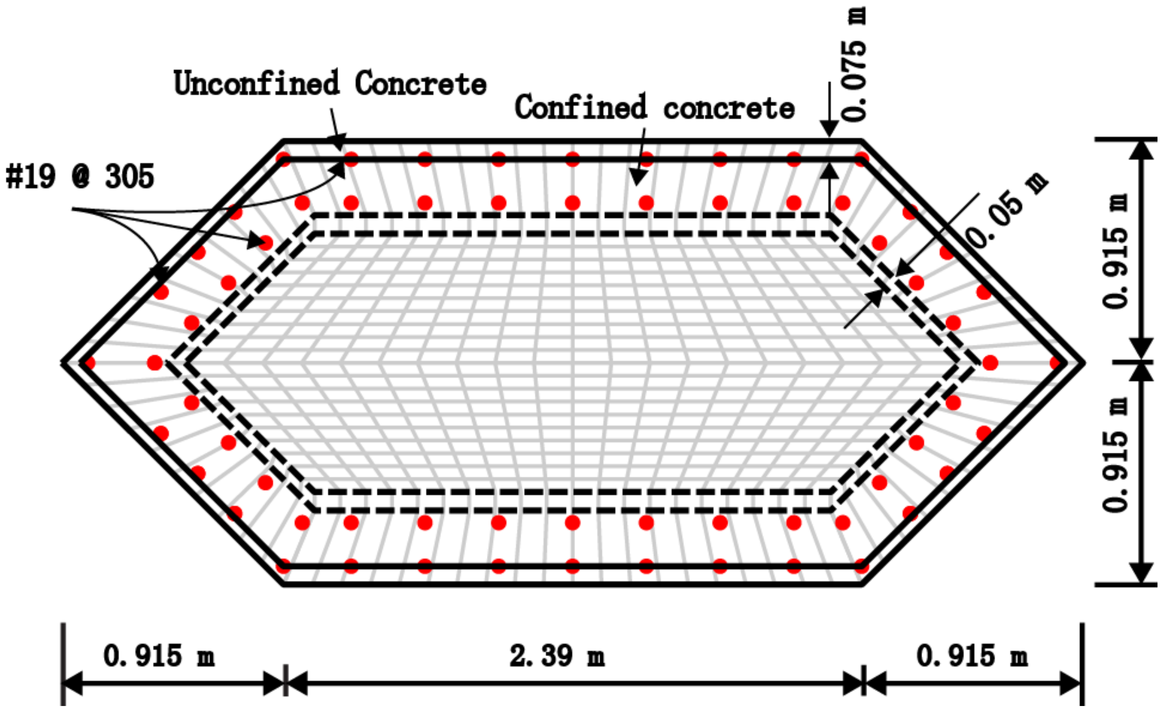

(a) Pier S-14

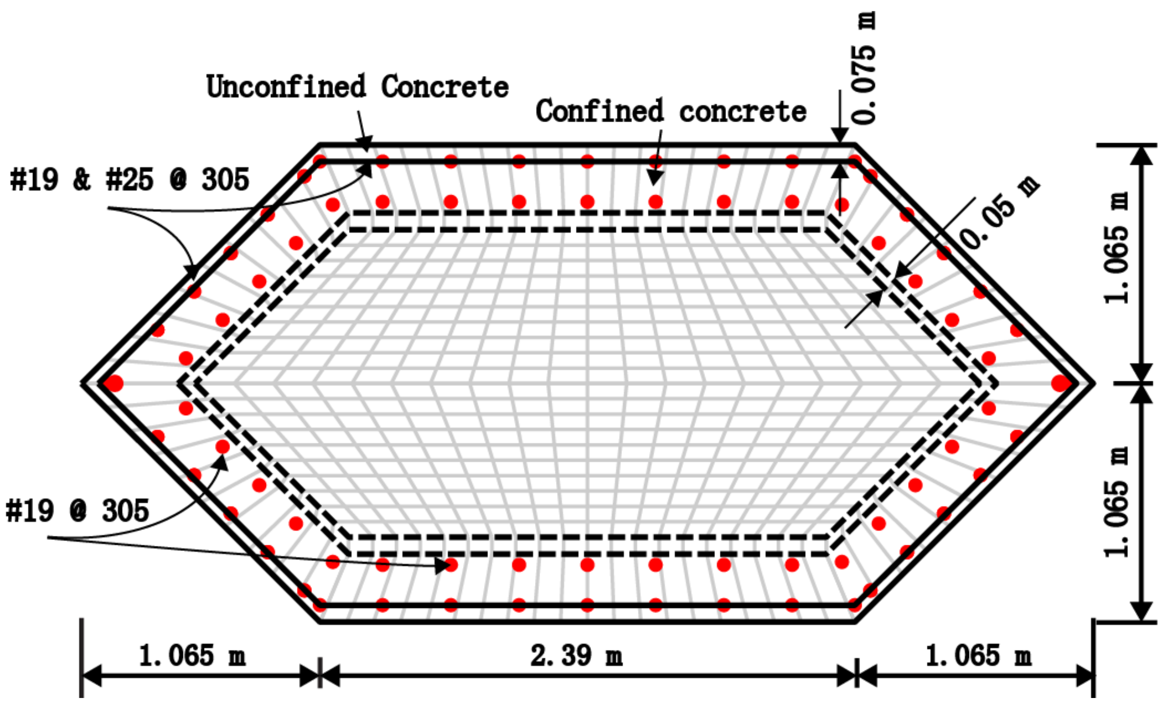

(b) Pier S-8

Figure C.4: Pier Columns after retrofit

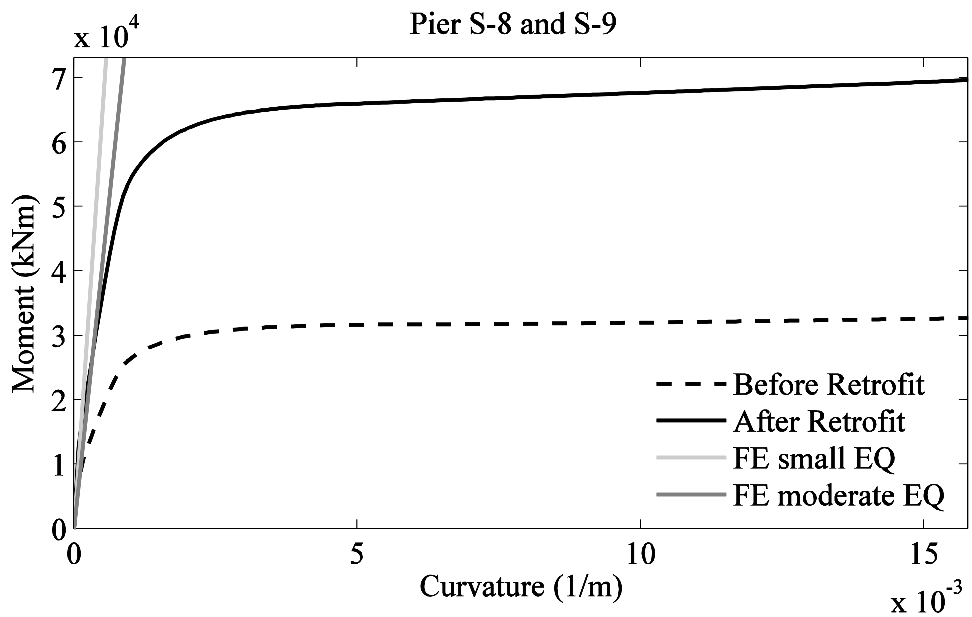

Figure C.5: Comparison of EI of pier S-8 and S-9 from FE and Moment curvature analysis

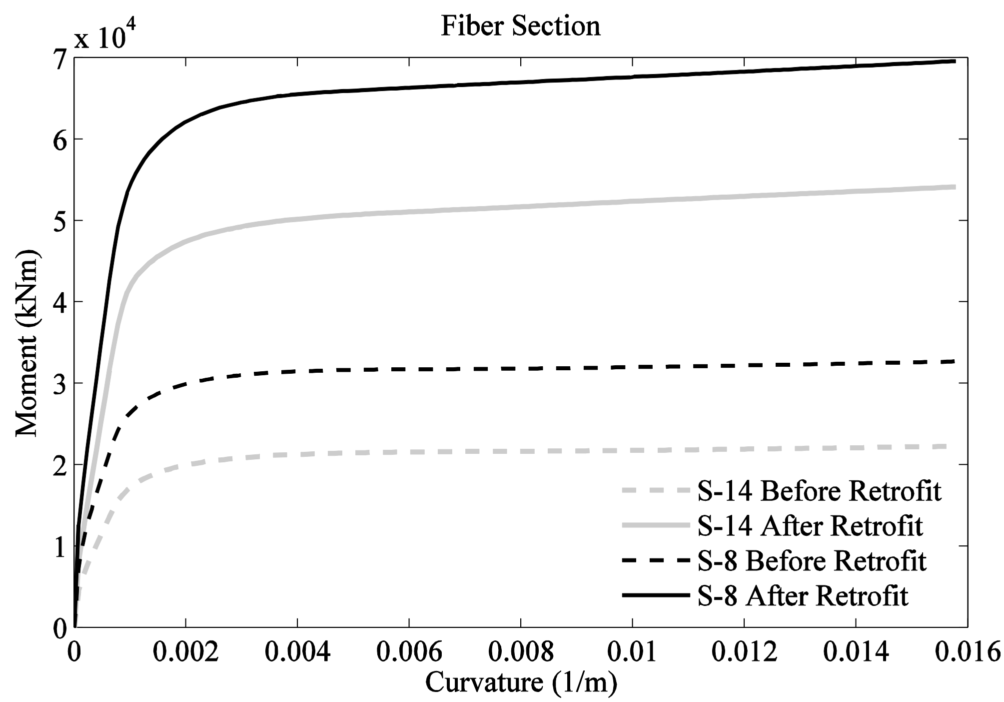

Figure C.6: Moment curvature analysis for pier columns cross section

Appendix D.

3D Modeling of Pile Groups below Pier S-8

A computational study based on 3 dimensional OpenSees finite element modeling was performed to evaluate the large pile-ground system stiffness under static lateral load. A robust and versatile framework (OpenSeesPL, http://cyclic.ucsd.edu/openseespl/) for computational analysis of pile-ground systems is employed to facilitate the pre- and post-processing phases.

A model that is representative of salient characteristics of the Samoa Bridge (California) Pier 8 (Figure D.1) pile-group foundation geometry was studied (Figure D.2). The pile group consists of 8 existing concrete piles and 6 cast-in-steel-shell (CISS) retrofit piles. The existing piles is configured in a 4 x 2 arrangement with spacing of 2 pile diameters (2D) in longitudinal and transversal directions on center.

Existing pile is 1.37 m in diameter with a wall thickness h = 0.127 m. Each concrete pile is encased by a prestressed concrete shell and filled with class B concrete for their entire length (25.6 m). The group is rigidly connected by a pile cap 16.715 m above the mudline.

The gross bending stiffness for existing pile was modeled as EI = 2.9 x 10^6 kN-m2 and 1.12 x 10^7 kN-m2 for retrofit pile. Pile response was assumed to remain linear.

As modeled in this study (Table D.1), the top soft clay layer is 1.5 m in thickness with underlying of a medium sand layer. The bottom layer of dense sand had a thickness of 35.115 m. A Poisson's ratio of 0.33 was specified for all layers. Due to the presence of water submerged density is employed for the simulation. For pressure-dependent material shear modulus is derived from:

$$p' = \frac{\sigma_1+\sigma_2+\sigma_3}{3}$$
$$G = G_r(\frac{p'}{80})^{0.5}$$

where p is mean effective confining pressure

G_r is the reference low-shear modulus specified at a reference mean effective confining pressure of 80 kPa.

In the employed ½ mesh of (due to symmetry), a lateral pile cap longitudinal load was applied to a maximum of 2500 kN. The length of the mesh in the longitudinal direction is 323.29 m, with 153.425 m transversally (in this half-mesh configuration, resulting in a 323 m x 306.85 m soil domain in plan view). Total layer thickness was 44 m (the base of the soil domain is 35.115 m below the pile tip). The soil domain was modeled by eight-node brick elements (8866 in total) and the piles were modeled by beam-column elements. Rigid beam-column elements were used around each pile to model the actual circumferential pile size (diameter).

Six case scenarios were conducted and compared with each other (Table D.2):

For the linear runs with pile groups embedded in rock / soil shows that there is about 62% reduction when considering cracked (factor of 0.3) pile cross-section. When we embed the pile in soil instead of rock, there is reduction of around 50%. With a reduction factor of 0.3 for pile cross-section (k= 3.77e4 kN/m) or for both pile and soil (k=3.02e4 kN/m), the K values are in the range of what we obtained for bridge model optimization – 3.00e4 kN/m and 3.94e4 kN/m for Pier S-8 optimization along during the strong earthquake.

The K value (9.69e4 kN/m) for linear soil run is 1.3-1.69 times of earlier estimated K during small earthquakes (~5.8e4 kN/m from bridge optimization and 7.5e4 kN/m from Pier S-8 optimization). With a pinned head BC, we got very low value of k=2.67e4 kN/m.

Table D.1: Soil Material Properties

Material Property	Thickness (m)	Total ρ (Mg/m^3)	Eff. p (kN/m^2)	Ref G_r (kPa)	V_s (m/s)
Soft clay	1.5	1.6	0-5.89	4000	81.6
Medium sand	7.385	2.0	5.89-54.18	7.50E4	142.4- 248.0
Dense sand	35.115	2.1	54.18-306.78	1.30E5	311.3-480.2

Table D.2: Effects of nonlinearity of pile and soil

Soil	Pile	K=F/D (kN/m)	Normalization
Rock	Linear Pile	20.59e4	1
	0.3 Crack Factor	6.53e4	32%
Linear Soil	Linear Pile	9.69e4	47%
	0.3 I_g*	3.69e4	18%
	Pinned head	2.67e4	5%
Linear Soil	Reduced shear modulus (30%) & 0.3 I_g	3.03e4	14%

* I_g=moment of inertia of uncracked section

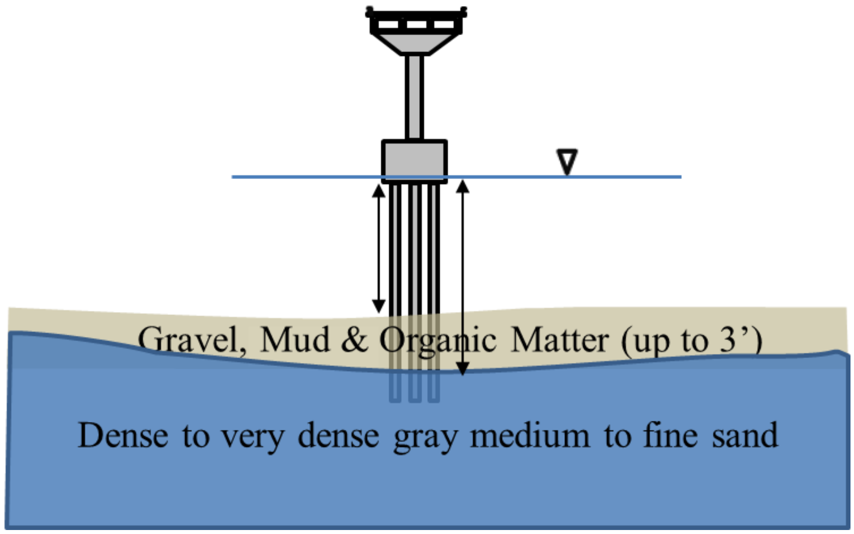

Figure D.1: Soil Profile at Pier S-8 of Samoa Channel Bridge

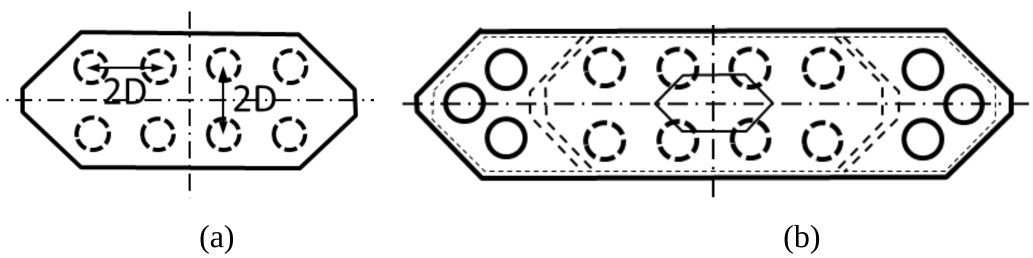

Figure D.2: Plan view of pile group layout (a) before and (b) after retrofit

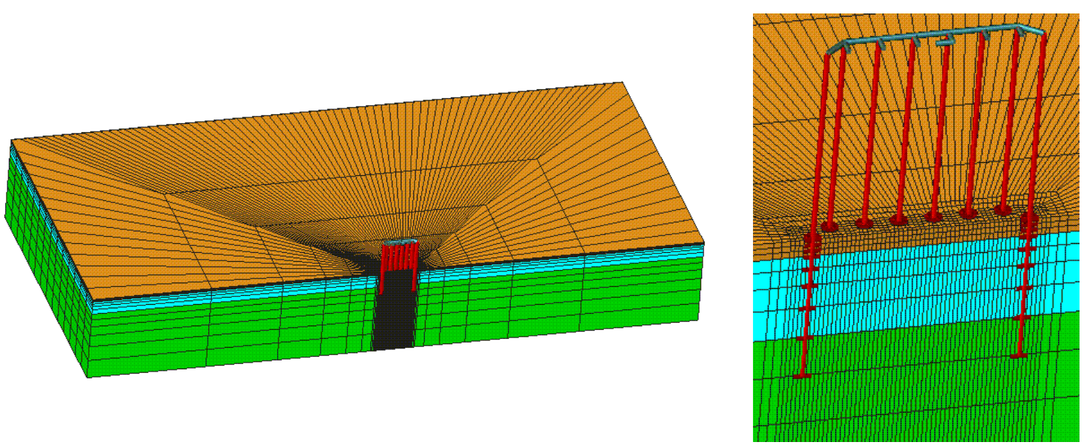

Figure D.3: Finite element mesh and close-up view of pile group